

ІНСТИТУТ МАГНЕТИЗМУ
НАЦІОНАЛЬНОЇ АКАДЕМІЇ НАУК УКРАЇНИ
ТА МІНІСТЕРСТВА ОСВІТИ І НАУКИ УКРАЇНИ

Кваліфікаційна наукова праця
на правах наукової доповіді

ВЕРБА Роман Володимирович

Прим. № _____

УДК 537.6/.8, 537.86, 537.39

ДИСЕРТАЦІЯ

**СПІНОВІ ХВИЛІ У НАДТОНКИХ МАГНІТНИХ ПЛІВКАХ ТА
НАНОСТРУКТУРАХ ПІД ДІЄЮ ЕЛЕКТРИЧНОГО ПОЛЯ ТА СТРУМУ**

01.04.11 — магнетизм

фізико-математичні науки

Подається на здобуття наукового ступеня доктора фізико-математичних наук

Дисертація містить результати власних досліджень. Використання ідей,
результатів і текстів інших авторів мають посилання на відповідне джерело

_____ Верба Р. В.

Науковий консультант

Горобець Юрій Іванович,

доктор фіз.-мат. наук, професор,

чл.-кор. НАПН України

КИЇВ — 2021

[зворотній бік титульної сторінки]

АНОТАЦІЯ

Верба Р. В. Спінові хвилі у надтонких магнітних плівках та наноструктурах під дією електричного поля та струму. — Кваліфікаційна наукова праця на правах наукової доповіді.

Дисертація на здобуття наукового ступеня доктора фізико-математичних наук за спеціальністю 01.04.11 - «Магнетизм». — Інститут магнетизму Національної академії наук України та Міністерства освіти і науки України, Київ, 2021.

Дисертаційна робота присвячена вирішенню наукової проблеми розробки нових та удосконалення існуючих методів збудження та контролю спінових хвиль у надтонких феромагнітних плівках та хвилеводах, які були б придатними для створення енергоефективних нанорозмірних пристроїв магнетронної логіки та інших систем спін-хвильової електроніки.

Спінові хвилі, які розповсюджуються у магнітовпорядкованих матеріалах, розглядаються як перспективні носії інформації для створення новітніх елементів та інтегрованих систем обробки інформації та НВЧ сигналів. Справді, малі довжини хвиль, до десятків й одиниць нанометрів, високі власні частоти — від одиниць до 100 ГГц у феромагнетиках і навіть більше у фери- та антиферомагнетиках, широкі можливості маніпулювання дисперсією та іншими характеристиками розповсюдження як за допомогою вибору геометрії, так і завдяки прикладанню зовнішнього впливу, велика різноманітність нелінійних ефектів, та ін. відкривають широкі можливості створення окремих різноманітних функціональних елементів та інтегрованих систем обробки інформації та НВЧ сигналів. Галузь магнетроніки, яка і досліджує можливості застосування спінових хвиль для інформаційних технологій, активно розвивається протягом останніх двох десятиріч, і на сьогодні успішно продемонстровані прототипи багатьох окремих елементів магнетронної логіки та магнетронних аналогових систем обробки сигналів.

Однією з найсуттєвіших проблем розвитку магнетроніки є необхідність розробки енергоефективних та придатних для застосування у нанорозмірних

системах методів збудження, контролю та зчитування спін-хвильових сигналів. Саме такі перетворення зовнішніх електричних сигналів у спін-хвильові і зворотно є головним джерелом втрат у класичних магнетонних системах із використанням магнітних полів, створюваних електричним струмом, які, до того ж, практично неможливо застосувати на субмікронних та наномасштабах. У дисертаційній роботі розглянуті альтернативні методи збудження та впливу на спінові хвилі — за допомогою електричних полів (через магнітоелектричний ефект) та електричних струмів із використанням ефекту спін-трансферу.

Метою дисертації було визначено вирішення проблеми розробки нових та удосконалення існуючих енергоефективних та сумісних з нанотехнологіями методів збудження та контролю спінових хвиль у надтонких феромагнітних плівках та хвилеводах, а також дослідження особливостей лінійної та нелінійної спін-хвильової динаміки у таких структурах і вивчення можливості застосування відповідних процесів для створення функціональних елементів магнетонної логіки та інших систем спін-хвильової електроніки. Для досягнення мети у роботі проведено цикл досліджень спін-хвильової динаміки у надтонких феромагнітних плівках та наноструктурах, у першу чергу — під впливом квазістатичного чи НВЧ електричного поля або спінового струму, та побудовані теоретичні моделі відповідних лінійних та нелінійних процесів.

Перші три розділи дисертації присвячено дослідженню спін-хвильової динаміки під впливом електричного поля завдяки ефекту електрично керованої магнітної анізотропії (ЕКМА). Цей нещодавно відкритий манітоелектричний ефект проявляється на границі провідний феромагнетик — діелектрик і, на думку автора, є одним з найперспективніших для електричного контролю спінових хвиль на субмікронних та наномасштабах.

Спершу, розглянуто можливість збудження спінових хвиль НВЧ електричним полем за допомогою ефекту ЕКМА. Встановлено, що за відсутності зовнішнього магнітного поля збудження можливе лише за механізмом параметричного збудження, тобто, на подвійній частоті. При цьому, у випадку перпендикулярної статичної намагніченості (плівки та хвилеводи тонші за

критичну товщину, яка, зазвичай, складає порядку 1 нм) взаємодія НВЧ модульованої анізотропії зі спіновими хвилями аналогічна до параметричної взаємодії з паралельною накачкою і визначається еліптичністю прецесії намагніченості. Натомість, у випадку площинної намагніченості (товщина плівок більша за критичну) параметричний зв'язок відбувається через перпендикулярну компоненту динамічної намагніченості. Такий механізм є більш ефективним і, найголовніше, не має обмежень щодо довжини спінової хвилі; зокрема, він ефективно працює і в обмінній області спектру спінових хвиль, де еліптичність, а, отже, і взаємодія з паралельною накачкою, прямує до нуля. Характерні напруги, необхідні для збудження спінових хвиль, складають до 0.1-1 В при оптимальних товщинах діелектрику і є досяжними в експерименті. У співпраці з колегами вперше успішно експериментально реалізовано параметричне збудження основної моди магнітної наноточки за допомогою НВЧ електричного поля, і результати експериментів повністю підтверджують теоретичні передбачення автора.

Розроблено нелінійну теорію параметричного збудження спінових хвиль у нанорозмірних хвилеводах локалізованою накачкою, яка дозволяє розрахувати амплітуди параметрично збуджених хвиль. Вперше встановлено, що окрім фазового механізму обмеження росту параметричної нестійкості (S-теорія В.С. Львова), який є єдиним суттєвим механізмом в об'ємних зразках, у нанорозмірних хвилеводах стає важливим додатковий механізм, а саме нелінійна зміна групової швидкості внаслідок нелінійного зсуву спектру. Поява цього механізму призводить не лише до зменшення амплітуд збуджених спінових хвиль, а й до якісно інших залежностей потужності збуджених хвиль від потужності накачки при невеликих перевищеннях порогу збудження — замість кореневої залежності має місце лінійна залежність.

Розглянуто механізм керованої зміни амплітуди чи/та фази спінової хвилі за допомогою прикладання квазістатичного електричного поля. Встановлено, що окрім локального зсуву дисперсії з'являється ще один суттєвий механізм, який впливає на проходження спінової хвилі через таку внутрішню електрично керовану границю розділу — зміна поляризації хвилі. Розроблено теорію

проходження спінових хвиль через границю розділу з урахуванням поляризації. Продемонстровано, що зміна поляризації призводить до трьох ефектів. По-перше, поблизу границі розділу з'являються експоненційно локалізовані спінові хвилі, з довжиною локалізації рівною або меншою за довжину біжучої хвилі відповідної частоти та ортогональною до неї поляризацією. По-друге, з'являється додатковий зсув фаз відбитої та переданої хвиль, який, залежно від різниці поляризацій, може приймати будь-яке значення в діапазоні $[-\pi, \pi]$, у той час як за відсутності різниці поляризацій фаза переданої хвилі завжди рівна фазі падаючої хвилі, а відбита хвиля може бути у фазі або в протифазі з нею. По-третє, різниця поляризації призводить до зменшення коефіцієнту проходження та збільшення коефіцієнту відбиття хвилі. При цьому зміна фази лінійна щодо різниці поляризації, а зміна коефіцієнтів проходження та відбивання — квадратична, тому при помірних прикладених електричних полях помітно проявляється тільки перший ефект. Незважаючи на різницю поляризації, спінова хвиля може проходити скінченну область з відмінною анізотропією резонансно, однак резонансні умови відрізняються від класичних внаслідок вищеописаного додаткового зсуву фаз. Встановлені залежності є характерними для спінових хвиль з домінантною обмінною взаємодією. У дипольній області спектру вплив поляризації може зникати повністю. Вищевказані властивості, однак, не стосуються розповсюдження спінових хвиль в геометрії поверхневих хвиль (геометрія Деймона-Ешбаха), які навіть в обмінній частині спектру демонструють стійкість до розсіяння на поверхневих дефектах і зменшене відбивання внаслідок відмінної симетрії динамічних дипольних полів хвилі.

Досліджено динаміку біжучих спінових хвиль при проходженні області локалізованої параметричної накачки, яка створюється НВЧ електричним полем, або в інший спосіб. Вперше продемонстровано ефект зменшення ефективності параметричного підсилення при збільшенні амплітуди вхідної хвилі, що пояснюється нелінійною чотиримагнотною взаємодією сигнальної та холостої хвиль. Характерна амплітуда вхідної хвилі, за якої проявляється ефект, обернено залежить від довжини області накачки, тому для підсилення спінових хвиль

великої амплітуди необхідно використовувати накачку з довжиною локалізації, суттєво меншою за довжину вільного пробігу хвилі. За певного значення амплітуди вхідної хвилі, яке визначається довжиною та величиною накачки, можлива реалізація стабілізації амплітуди — амплітуда вхідної та вихідної хвиль стають однаковими, а розкид амплітуд (шуми) зменшуються після проходження області накачки. Ефект стабілізації амплітуди краще проявляється за великих довжин накачки. Крім того, продемонстровано ефект стабілізації фази спінової хвилі під час проходження області неадіабатичної накачки. Показано, що даний ефект дозволяє реалізувати корекцію фазових помилок спін-хвильових сигналів у системах магнетронної логіки величиною приблизно до $|\Delta\varphi| < \pi/4$. Встановлено, що ефект фазової стабілізації є стійким по відношенню амплітуди вхідної хвилі.

У четвертому розділі розглянуто окремі випадки спін-хвильової динаміки під дією спін-поляризованого електричного чи чистого спінового струму. Хоча такий спосіб збудження спін-хвильової динаміки є суттєво енергозатратнішим за використання магнітоелектричних ефектів, він дозволяє отримати певні типи динаміки, недосяжні будь-якими іншими способами, зокрема, збудження автоколивань намагніченості. Пояснено ряд експериментів по збудженню спінових хвиль у спін-торк та спін-Холл осциляторах (СТО та СХО). Встановлено вирішальну роль дипольної взаємодії у стабілізації магнітних солітонів — спін-хвильових булетів — у квазіодновимірних СТО (СХО), що дозволяє реалізувати стійку монохроматичну генерацію в осциляторах з активною областю довжиною в одиниці мікрометрів μm , таким чином, підвищити потужність осцилятора. Продемонстровано, що неоднорідний профіль густини спінового струму (наприклад, у випадку активної зони осцилятора у вигляді наносмужки змінного перерізу) призводить до появи додаткової зворотної сили, що діє на булет, а також до просторового рознесення булетів у режимі двомодової генерації. У підсумку, така неоднорідність густини струму накачки призводить до збільшення когерентності та стабільності режиму одномодової генерації СТО. Також продемонстровано, що наявність потенціальної ями може змінювати тип збудженої моди у СТО з нелінійного булета на лінійно локалізовану моду за умови

достатньої глибини потенціальної ями та її розмірів, сумірних із розмірами активної зони. На експерименті така зміна типу моди проявляється зміною типу збудження автогенератора — з жорсткого на м'який режим збудження, а у випадку несиметричного розташування ями та активної зони також можлива суттєва якісна зміна профілів спін-хвильової моди, яку можна детектувати на експерименті.

Також у дисертації досліджено вплив інтерфейсної взаємодії Дзялошинського-Морія (ІВДМ) на параметричні та нелінійні процеси, а також на динаміку СХО. ІВДМ завжди присутня у СХО через наявність границі феромагнетик - важкий метал, і її роль збільшується зі зменшенням товщини феромагнітного шару. Також не повинно складати проблем у створенні структур, у яких поєднується ІВДМ та ЕКМА, у яких, як показано, наявність ІВДМ призводить до практично корисних ефектів. Продемонстровано збільшення ефективності та завадостійкості параметричного підсилювача при використанні спінових хвиль із невзаємним зсувом спектру, викликаного ІВДМ, що пов'язано з можливістю вибору робочої точки так, що холоста хвиля стає локалізованою. Узагальнено метод розрахунку коефіцієнтів нелінійної спін-хвильової взаємодії на випадок наявності несиметричних магнітних взаємодій, зокрема, ІВДМ, та отримані готові для використання рівняння для розрахунку нелінійних коефіцієнтів у намагнічених до насичення феромагнітних плівках та наносмужках. За допомогою розробленої теорії продемонстровано нелінійність невзаємного зсуву спектру спінових хвиль, викликаного ІВДМ — при збільшенні амплітуди спінової хвилі невзаємне розщеплення спектру зменшується, що може бути використаним для створення невзаємних пристроїв, керованих потужністю. Також розроблено теорію збудження невзаємних спінових хвиль в одно- та двовимірних СТО за наявності ІВДМ. За допомогою теорії, зокрема, пояснено появу червоного зсуву частоти генерації зі збільшенням ІВДМ, яке було спостережене у мікромагнітному моделюванні.

Насамкінець, у п'ятому розділі дисертації розглянуті питання розповсюдження, структури та взаємодії спінових хвиль у нанорозмірних феромагнітних хвилеводах та структурах. Розроблено методики розрахунку

дисперсійних характеристик, сталих затування за наявності різноманітних неоднорідних та/або нелокальних механізмів дисипації, а також коефіцієнтів зв'язку між спіновими хвилями дипольно взаємодіючих хвилеводів. Виявлено явище “розкріплення” профілю моди при зменшенні ширини хвилеводу менше за певне критичне значення, яке пов'язане не тільки зі зростанням впливу обмінної взаємодії, а й зі зменшенням неоднорідності динамічних дипольних полів на краях хвилеводу; отримано емпіричне наближення залежності критичної ширини від товщини хвилеводу та матеріальних параметрів. Виявлено основний механізм нелінійності у системі дипольно зв'язаних хвилеводів, який може бути використаний для створення компактних елементів магنونної логіки.

Одержані в роботі теоретичні результати відкривають шлях до створення енергоефективних електрично керованих елементів магنونної логіки та інших магنونних систем обробки НВЧ сигналів, а також до створення магнетичних наногенераторів на основі ефекту спін-трансферу з покращеними характеристиками. Варто відзначити, що частина з описаних явищ є загальною і не обмежуються спін-хвильовою динамікою під дією ефекту ЕКМА. Зокрема, виявлені явища стабілізації амплітуди та фази спінових хвиль і спосіб підвищення завадостійкості параметричного підсилювача можуть бути реалізовані і з будь-яким іншим типом НВЧ параметричної накачки. Загальні ж методики розрахунку дисперсії, сталих затування та коефіцієнтів нелінійної взаємодії спінових хвиль знайдуть своє застосування при розрахунку і проектуванні будь-яких магنونних систем на основі нанорозмірних феромагнетичних хвилеводів.

Ключові слова: спінова хвиля, магنونіка, динаміка намагнетиченості, електрично керована магнетична анізотропія, ефект спін-трансферу, надтонкі феромагнетичні плівки, магнетичні наноструктури, параметричні процеси, магнетичні солітони, спін-торк осцилятор, багатомангонні процеси.

ABSTRACT

Verba R. V. Spin waves in ultrathin magnetic films and nanostructures under electric fields and currents. — Qualifying scientific work – scientific report.

Thesis for a scientific degree of Doctor of Science in Physics and Mathematics, specialty 01.04.11 – Magnetism. – Institute of Magnetism of National Academy of Sciences of Ukraine and Ministry of Education and Science of Ukraine, Kyiv, 2021.

The thesis is devoted to the solution of scientific problem of the development of novel and improvement of existing methods of spin wave excitation and control in ultrathin ferromagnetic films and waveguides, which would be suitable for the creation of energy-efficient nanoscale elements of magnonic logic and other spin-wave electronics systems.

Spin waves, propagating in magnetically ordered materials, are considered as promising information carriers for the creation of novel elements and integrated circuits for information and microwave signals processing. Indeed, such features as small wavelengths, up to tens of nanometers and less, high eigenfrequencies – 1-100 GHz for ferromagnets and even more for ferri- and antiferromagnets, reach possibilities of the manipulation of dispersion and other propagation characteristics both by geometry choice and by an external influence, a wide variety of nonlinear effects, etc., open reach opportunities for the creation of various functional elements and integrated systems for information and microwave signals processing. The field of magnonics, which is exploring the possibilities of using spin waves for information technologies, has been actively developing over the last two decades, and, to the date, many prototypes of magnonic logic units and magnonic analog signal processing systems have been successfully demonstrated.

One of the most significant current problems in the magnonics is the development of energy-efficient and nanoscale-compatible methods of excitation, control and read-out of spin-wave signals. Such conversions of external electrical signals into spin waves and back are the main losses source in classical magnonics systems, which use Oersted magnetic fields of an electric current; additionally, this method is almost inapplicable at submicron- and nanoscale. In this thesis, alternative methods of spin wave excitation

and control are considered, namely, by electric fields (via magnetoelectric effect) and electric currents via the spin-transfer-torque effect.

The **aim of the thesis** is the solution of the problem of the creation of novel and improvement of existing energy efficient and nanoscale-compatible methods of spin-wave excitation and control in ultrathin ferromagnetic films and waveguides, as well as the investigation of peculiarities of linear and nonlinear spin-wave dynamics in such nanostructures with studying the possibility to use these processes for the development of functional elements of magnonic logic and other spin-wave electronics systems. To achieve this goal, a series of studies of spin-wave dynamics in ultrathin ferromagnetic films and nanostructures, mostly, under electric field or spin current drive, is performed, and theoretical models of the corresponding processes are developed.

The first three chapters of the thesis are devoted to the study of spin-wave dynamics under an electric field via the effect of voltage-controlled magnetic anisotropy (VCMA). This recently discovered magnetoelectric effect manifests itself at the conductive ferromagnet-dielectric interface and, in author's opinion, is one of the most promising for voltage control of spin waves at submicron- and nanoscales.

First, the possibility of spin wave excitation by a microwave electric field via VCMA is considered. It is found that in zero external magnetic field, the excitation is possible only via the parametric excitation mechanism, i.e., at the half excitation frequency. In the case of perpendicular static magnetization (thickness of films and waveguides below the critical thickness, which is of the order of 1 nm), the interaction of microwave modulated anisotropy with spin waves is similar to the parametric interaction with parallel pumping and is determined by the ellipticity of magnetization precession. Instead, in the case of in-plane magnetization (thickness above the critical one), the parametric interaction is mediated by out-of-plane dynamic magnetization component. This mechanism is more efficient and, importantly, has no restrictions on the spin wave wavelength; in particular, it still be efficient for exchange-dominated spin waves, for which the ellipticity, and, hence, the interaction with parallel pumping, are vanishing. The characteristic voltages required for spin wave excitation are about 0.1-1 V for optimal dielectric thicknesses, which is achievable in an experiment. In collaboration, we observe for the first time the parametric excitation of the fundamental

mode of a magnetic nanodot by a microwave voltage, and the experimental results coincide well with author's theoretical predictions.

A nonlinear theory of parametric spin wave excitation in nanosized waveguides by a localized pumping, which allows to calculate the amplitudes of excited waves, is developed. While in bulk samples the only significant mechanism, which limits the growth of parametric instability, is the phase mechanism (S-theory of V.S. L'vov), an additional novel mechanism was found at nanoscale – nonlinear change of the group velocity due to nonlinear spectrum shift. This mechanism leads not only to a decrease of the amplitudes of excited spin waves, but, also, to qualitatively different dependence of the excited wave power on the pump power at small overthreshold powers – the linear dependence appears instead of the standard square root dependence.

Spin wave amplitude and phase control by the application of a local quasistatic electric field is considered. In addition to a local dispersion shift, another significant mechanism, which affects spin wave transmission through such a voltage-controlled internal boundary, is found, namely, a variation of the wave polarization. A theory of spin waves transmission passing through an internal boundary accounting for the polarization variation is developed. A change of polarization is shown to lead to three effects. First, exponentially localized spin waves appear near the interface; their localization length is equal to or less than the wavelength of propagating spin wave of the same frequency and polarization is orthogonal to one of the propagating wave. Second, an additional phase shift of the reflected and transmitted waves appears. This shift, depending on the polarization difference, can take any value in the range $[-\pi, \pi]$, while in the absence of polarization difference, the phase of the transmitted wave is always equal to phase of the incident one, and the reflected wave can be in-phase or in antiphase with the incident. Third, the polarization difference leads to a decrease of the wave transmission rate and an increase of the reflection rate. The phase change is linear in polarization difference, while the change in the transmission and reflection rates demonstrates square dependence; thus, only the first effect is pronounced at a moderate applied voltage. Despite the polarization mismatch, a spin wave can pass through a finite region with a different anisotropy resonantly, but the resonance conditions differs from the classical ones due to the additional phase shift described above. The described

features are pronounced for exchange-dominated spin waves, while for dipole-dominated spin waves the effect of polarization mismatch can disappear completely. The above features, however, do not apply to the propagation of spin waves in the geometry of surface waves (Damon-Eshbach geometry), which, even in the exchange-dominated range, demonstrate back-scattering immunity on surface defects and reduced reflection due to different symmetry of dynamic dipolar fields.

The dynamics of spin waves propagating through a localized parametric pumping area, created by a microwave voltage or in another way, has been studied. The efficiency of parametric amplification is found to decrease with an increase of the input spin wave amplitude, which is explained by a nonlinear four-magnon interaction between signal and idler waves. The characteristic input wave amplitude, at which the effect becomes pronounced, inversely depends on the pumping length; thus, to amplify relatively large-amplitude spin waves one needs to use a pumping with a localization length, which is significantly smaller than the mean free path of the wave. At a certain input spin wave amplitude, which depends on the pumping length and strength, the amplitude of the input and output waves become the same, and the amplitude spread (noise) decreases after passing the pumping area, which constitutes the amplitude stabilization effect. The amplitude stabilization is more pronounced at large pumping lengths. Also, the effect of spin wave phase stabilization by a nonadiabatic parametric pumping is demonstrated. This effect is shown to allow for the correction of phase errors of spin-wave signals in magnonic logic circuits up to $|\Delta\varphi| < \pi/4$. The effect of spin wave phase stabilization is confirmed to be robust respective to the input spin wave amplitude and is possible both for linear and large-amplitude nonlinear waves.

The fourth chapter concerns several cases of spin-wave dynamics under spin-polarized electric or pure spin current. Although this method of spin-wave dynamics excitation is much less energy efficient than ones involving magnetoelectric effects, it allows to realize certain types of dynamics, which are inaccessible by any other means, in particular, self-sustained magnetization oscillations. Several experimental results on the spin wave excitation in spin-torque and spin-Hall oscillators (STO and SHO) are explained. It is shown that in quasi-one-dimensional STO (SHO) the dipolar interaction could play a crucial role in the stabilization of magnetic solitons – spin-wave bullets. It

allows to achieve a stable monochromatic generation in an oscillator with micron-sized active area and, thus, to increase SHO power. An inhomogeneous profile of spin current density (for example, due to a tapered shape of a nanowire forming a SHO) is shown to lead to the appearance of additional restoring force acting on the bullet, as well as to the spatial separation of bullets in two-bullet generation mode. As a result, such inhomogeneity of the driving current density leads to an increase of the coherence and stability of the single-bullet generation regime. It is also demonstrated that the presence of a potential well can change the type of excited mode in a STO from a nonlinear bullet to a linearly localized mode, provided significant well depth and its sizes, which should be similar to the active area size. In an experiment, such a change of the generation mode type manifests itself in the change from hard to soft mode of the auto-oscillator excitation; also, in the case of an asymmetric position of the well and active area, a significant qualitative change of the excited spin-wave mode profiles is also possible, which can be detected in an experiment.

The influence of the interfacial Dzyaloshinski-Moriya interaction (IDMI) on parametric and nonlinear processes, as well as on the dynamics of a SHO, is also considered in the thesis. IDMI is always present in SHOs due to the presence of the ferromagnetic-heavy metal interface, and its role increases with decreasing of the ferromagnetic layer thickness. There should be also no problems to create structures which combine IDMI and VCMA, in which, as is shown, the presence of IDMI leads to useful for practice effects. It is shown, that nonreciprocal spin wave spectrum shift in the presence of IDMI could lead to an increased efficiency and robustness of a parametric amplifier, which is a consequence of the possibility of choosing the working point so that the idler wave becomes evanescent. The Hamiltonian formalism for the nonlinear spin-wave interaction is generalized to the case of the presence of antisymmetric magnetic interactions, like IDMI, and ready-to-use equations for calculations of nonlinear coefficients in saturated ferromagnetic films and nanostructures are derived. Using the developed formalism, the nonlinearity of spin wave nonreciprocity, induced by IDMI, is demonstrated – as the spin wave amplitude becomes larger, the nonreciprocal splitting of the spectrum decreases, which can be used for the development of nonreciprocal power-dependent devices. The theory of excitation

of nonreciprocal spin waves in one- and two-dimensional STOs in the presence of IDMI is also developed. The theory, in particular, explains the appearance of a red shift of the generation frequency with an increase in IDMI, which was observed in micromagnetic simulations.

Finally, in the fifth chapter, the propagation, structure and interaction of spin waves in nanoscale ferromagnetic waveguides and structures are considered. Methods for calculation of the dispersion, damping rates in the presence of various inhomogeneous and/or nonlocal dissipation mechanisms, as well as of the spin wave coupling strength in nearby located dipolarly coupled waveguides, are developed. The phenomenon of spin wave “unpinning” in a waveguide narrower than a certain critical width, is found, and is shown to be related not only to increased role of the exchange interaction, but, also, to a decrease of the nonuniformity of dynamic dipolar fields at the waveguide edges. An empirical equation for the dependence of the critical width on the waveguide thickness and material parameters is derived. The main nonlinear mechanism in the system of dipolarly coupled waveguides is determined, and is shown to be useful for the development of magnonic logic gates.

Theoretical results obtained in this work open a way for the creation of energy-efficient voltage-controlled elements of magnonic logic and other magnonic microwave signal processing systems, as well as of magnetic nanogenerators with enhanced characteristics. It should be noted that several described phenomena are general and are not limited to the spin wave dynamics under VCMA action. In particular, the spin wave amplitude and phase stabilization effects and the method of increasing the robustness of a parametric amplifier can be implemented with any other type of microwave parametric pumping. General methods for the calculation of spin wave dispersion, damping rates and nonlinear interaction coefficients could find application in the investigation and development of any magnonic systems based on nanoscale ferromagnetic waveguides.

Keywords: spin wave, magnonics, magnetization dynamics, voltage-controlled magnetic anisotropy, spin-transfer-torque effect, ultrathin ferromagnetic films, magnetic nanostructures, parametric processes, magnetic solitons, spin-torque oscillator, multimagnon interaction.

**СПИСОК ОПУБЛІКОВАНИХ ПРАЦЬ ЗА ТЕМОЮ ДИСЕРТАЦІЇ
(PUBLICATION LIST)**

**Наукові праці, в яких опубліковані основні наукові результати дисертації
(Publications representing main thesis results):**

1. **R. Verba**, M. Carpentieri, G. Finocchio, V. Tiberkevich, and A. Slavin, Chapter 13 - Parametric excitation and amplification of spin waves in ultrathin ferromagnetic nanowires by microwave electric field. In: *Spin wave confinement: Propagating waves (2nd edition)*, ed. by S. O. Demokritov (Pan Stanford Publishing, Singapore, 2017), - P. 385-426.
2. **R. Verba**, V. Tiberkevich, I. Krivorotov, and A. Slavin, Parametric excitation of spin waves by voltage-controlled magnetic anisotropy, *Phys. Rev. Appl.* **1**, 044006 (2014).
3. **R. Verba**, V. Tiberkevich, and A. Slavin, Influence of interfacial Dzyaloshinskii-Moriya interaction on the parametric amplification of spin waves, *Appl. Phys. Lett.* **107**, 112402 (2015).
4. L. Yang, **R. Verba**, V. Tiberkevich, T. Schneider, A. Smith, Z. Duan, B. Youngblood, K. Lenz, J. Lindner, A. N. Slavin, and I. N. Krivorotov. Reduction of phase noise in nanowire spin orbit torque oscillators, *Sci. Rep.* **5**, 16942 (2015).
5. **R. Verba**, M. Carpentieri, G. Finocchio, V. Tiberkevich, and A. Slavin, Excitation of propagating spin waves in ferromagnetic nanowires by microwave voltage-controlled magnetic anisotropy, *Sci. Rep.* **6**, 25018 (2016).
6. A. Giordano, **R. Verba**, R. Zivieri, A. Laudani, V. Puliafito, G. Gubbiotti, R. Tomasello, G. Siracusano, B. Azzerboni, M. Carpentieri, A. Slavin, and G. Finocchio, Spin-Hall nano-oscillator with oblique magnetization and Dzyaloshinskii-Moriya interaction as generator of skyrmions and nonreciprocal spin-waves, *Sci. Rep.* **6**, 36020 (2016).
7. Y.-J. Chen, H. K. Lee, **R. Verba**, J. A. Katine, I. Barsukov, V. Tiberkevich, J. Q. Xiao, A. N. Slavin, and I. N. Krivorotov, Parametric resonance of magnetization excited by electric field, *Nano Lett.* **17**, 572 (2017).

8. **R. Verba**, M. Carpentieri, G. Finocchio, V. Tiberkevich, and A. Slavin, Excitation of spin waves in an in-plane-magnetized ferromagnetic nanowire using voltage-controlled magnetic anisotropy, *Phys. Rev. Appl.* **7**, 064023 (2017).
9. Q. Wang, P. Pirro, **R. Verba**, A. Slavin, B. Hillebrands, and A. V. Chumak, Reconfigurable nanoscale spin-wave directional coupler, *Sci. Adv.* **4**, e1701517 (2018).
10. **R. Verba**, M. Carpentieri, G. Finocchio, V. Tiberkevich, and A. Slavin, Amplification and stabilization of large-amplitude propagating spin waves by parametric pumping, *Appl. Phys. Lett.* **112**, 042402 (2018).
11. R. Zivieri, A. Giordano, **R. Verba**, B. Azzerboni, M. Carpentieri, A. N. Slavin, G. Finocchio, Theory of nonreciprocal spin-wave excitations in spin Hall oscillators with Dzyaloshinskii-Moriya interaction, *Phys. Rev. B* **97**, 134416 (2018).
12. **R. Verba**, V. Tiberkevich, A. Slavin, Damping of linear spin-wave modes in magnetic nanostructures: Local, nonlocal, and coordinate-dependent damping, *Phys. Rev. B* **98**, 104408 (2018).
13. M. Mohseni, **R. Verba**, T. Brächer, Q. Wang, D. A. Bozhko, B. Hillebrands, and P. Pirro, Backscattering Immunity of Dipole-Exchange Magnetostatic Surface Spin Waves, *Phys. Rev. Lett.* **122** (19), 197201 (2019).
14. **R. Verba**, M. Carpentieri, Y.-J. Chen, I. N. Krivorotov, G. Finocchio, V. Tiberkevich, and A. Slavin, Correction of Phase Errors in a Spin-Wave Transmission Line by Nonadiabatic Parametric Pumping, *Phys. Rev. Appl.* **11**, 054040 (2019).
15. **R. Verba**, V. Tiberkevich, and A. Slavin, Hamiltonian formalism for nonlinear spin wave dynamics under antisymmetric interactions: Application to Dzyaloshinskii-Moriya interaction, *Phys. Rev. B* **99**, 174431 (2019).
16. Q. Wang, B. Heinz, **R. Verba**, M. Kewenig, P. Pirro, M. Schneider, T. Meyer, B. Lägél, C. Dubs, T. Brächer, and A. V. Chumak, Spin Pinning and Spin-Wave Dispersion in Nanoscopic Ferromagnetic Waveguides, *Phys. Rev. Lett.* **122** (24), 247202 (2019).

17. **R. V. Verba**, Interplay of linear and nonlinear localization mechanisms in spin-torque oscillators with a field well, *Ukr. J. Phys.* **64** (10), 947 (2019).
18. **R. Verba**, V. Tiberkevich, and A. Slavin, Spin-wave transmission through an internal boundary: Beyond the scalar approximation, *Phys. Rev. B* **101**, 144430 (2020).
19. **R. V. Verba**, V. S. Tiberkevich and A. N. Slavin, Dipole-dominated dissipative magnetic solitons in quasi-one-dimensional spin-torque oscillators, *Фізика низьких температур* **46**, 920 (2020) [*Low Temp. Phys.* **46**, 773 (2020)].
20. Q. Wang, M. Kewenig, M. Schneider, **R. Verba**, F. Kohl, B. Heinz, M. Geilen, M. Mohseni, B. Lägel, F. Ciubotaru, C. Adelman, C. Dubs, S. D. Cotofana, O. V. Dobrovolskiy, T. Brächer, P. Pirro and A. V. Chumak, A magnonic directional coupler for integrated magnonic half-adders, *Nature Electronics* **3**, 765 (2020).

Публікації, які засвідчують апробацію матеріалів дисертації

(Conference abstracts and proceedings):

1. **R. V. Verba**, V. S. Tiberkevich, I. N. Krivorotov, and A. N. Slavin, Parametric excitation of spin waves in thin films by electric field. In: *58th Annual Conference on Magnetism and Magnetic Materials. Abstracts. (Denver, CO, USA, November 4 - 8, 2013)*, GB-04, p. 621.
2. **R. V. Verba**, V. S. Tiberkevich, and A. N. Slavin, Voltage control of spin waves in ultra-thin ferromagnetic waveguide. In: *INTERMAG 2014. Digest book (Dresden, Germany, 4 - 8 May 2014)*, AH-11, p. 237.
3. **R. V. Verba**, V. S. Tiberkevich, and A. N. Slavin, Damping of spin wave modes in the presence of spin pumping and spin diffusion. In: *INTERMAG 2014. Digest book (Dresden, Germany, 4 - 8 May 2014)*, HH-2, p. 3210.
4. **R. Verba**, V. Tiberkevich, O. Gorobets, and A. Slavin, Resonant and nonresonant transmission of spin waves through a barrier induced by voltage-controlled magnetic anisotropy. In: *59th Annual Conference on Magnetism and Magnetic Materials. Abstracts (Honolulu, HI, USA, November 3 - 7, 2014)*, CE-05, p. 250.

5. **R. V. Verba**, V. S. Tyberkevych, and A. N. Slavin, Excitation of propagating spin waves in an in-plane magnetized ferromagnetic strip by voltage-controlled magnetic anisotropy. In: *2015 IEEE International Magnetics Conference (INTERMAG) (Beijing, China, 11 - 15 May 2015)*, DB-02.
6. **R. V. Verba**, V. S. Tyberkevych, and A. N. Slavin, Influence of interfacial Dzyaloshinskii-Moriya interaction on parametric amplification of spin waves in ultrathin magnetic films. In: *2015 IEEE International Magnetics Conference (INTERMAG) (Beijing, China, 11 - 15 May 2015)*, GT-12.
7. **Verba R. V.**, Dipolar stabilization of a large size bullet mode in one-dimensional spin-torque oscillators. In: *Proceedings of the XI international conference "Electronics and applied physics" (Kyiv, October 21-24, 2015)*, p. 28.
8. **R. V. Verba**, L. Yang, V. Tyberkevych, T. Schneider, A. Smith, Z. Duan, J. Lindner, A. N. Slavin, and I. Krivorotov, Enhancement of single bullet mode stability in nanowire spin-Hall oscillator with spatially nonuniform current bias. In: *MMM | INTERMAG 2016 Joint Conference. Abstracts (San Diego, CA, USA, 11 – 15 January 2016)*, GU-07, p. 899.
9. Y. Chen, H. Lee, **R. V. Verba**, J. Katine, I. Barsukov, V. Tyberkevych, A. N. Slavin, and I. Krivorotov, Parametric excitation of magnetization by electric field. In: *MMM | INTERMAG 2016 Joint Conference. Abstracts (San Diego, CA, USA, 11 – 15 January 2016)*, GW-13, p. 915.
10. **R. V. Verba**, M. Carpentieri, G. Finocchio, V. Tyberkevych, and A. N. Slavin, Excitation of propagating spin waves in ferromagnetic nanowires by microwave voltage-controlled magnetic anisotropy. In: *MMM | INTERMAG 2016 Joint Conference. Abstracts (San Diego, CA, USA, 11 – 15 January 2016)*, HF-04, p. 956.
11. **R. Verba**, L. Yang, V. Tiberkevich, T. Schneider, A. Smith, Z. Duan, B. Youngblood, K. Lenz, J. Lindner, A. Slavin, and I. Krivorotov, Effect of dipolar interaction and bias nonuniformity on nanowire spin-Hall oscillator dynamics. In: *Baltic Spin 2016. Abstract book (Jurmala, Latvia, 9-13 August 2016)*, p. 22.

12. A. Giordano, **R. V. Verba**, R. Zivieri, A. Laudani, V. Puliafito, G. Gubbiotti, R. Tomasello, G. Siracusano, B. Azzerboni, M. Carpentieri, A. N. Slavin, and G. Finocchio, Spin-Hall nano-oscillator with oblique magnetization and Dzyaloshinskii-Moriya interaction as generator of skyrmions and nonreciprocal spin-waves. In: *61th Annual Conference on Magnetism and Magnetic Materials. Abstracts (New Orleans, LA, USA, 31 October – 4 November 2016)*, BB-08, p. 122.
13. A. Chumak, Q. Wang, P. Pirro, B. Hillebrands, **R. V. Verba**, and A. N. Slavin, Reconfigurable nano-scale spin-wave directional coupler. In: *61th Annual Conference on Magnetism and Magnetic Materials. Abstracts (New Orleans, LA, USA, 31 October – 4 November 2016)*, DB-02, p. 344.
14. **R. V. Verba**, V. Tyberkevych, and A. N. Slavin, Stabilization of spin wave amplitude by parametric pumping in ferromagnetic nanowires. In: *61th Annual Conference on Magnetism and Magnetic Materials. Abstracts (New Orleans, LA, USA, 31 October – 4 November 2016)*, DB-06, p. 346.
15. Y. Chen, **R. V. Verba**, V. Tyberkevych, A. N. Slavin, and I. Krivorotov, Parametric amplifier of spin waves using electric field. In: *61th Annual Conference on Magnetism and Magnetic Materials. Abstracts (New Orleans, LA, USA, 31 October – 4 November 2016)*, FE-09, p. 603.
16. **R. V. Verba**, V. S. Tiberkevich, and A.N. Slavin, Linear and nonlinear spin-wave mode localization in a spin-torque oscillator with a field well. In: *2017 IEEE International Magnetism Conference (INTERMAG) (Dublin, Ireland, 24-28 April 2017)*, BC-08.
17. **R. V. Verba**, M. Carpentieri, Y. Chen, V. Tyberkevych, G. Finocchio, I. Krivorotov, and A. N. Slavin. Correction of phase errors in spin wave signals by nonadiabatic parametric pumping. In: *62nd Annual Conference on Magnetism and Magnetic Materials. Abstracts (Pittsburgh, PA, USA, 6-10 November 2017)*, AE-04, p. 24.
18. A. Chumak, Q. Wang, B. Heinz, M. Kewenig, M. Schneider, T. Fischer, T. Meyer, B. Laegel, T. Löber, P. Pirro, C. Dubs, **R. V. Verba**, and T. Brächer. Spin-wave

- dynamics in yttrium iron garnet nano-structures. In: *62nd Annual Conference on Magnetism and Magnetic Materials. Abstracts (Pittsburgh, PA, USA, 6-10 November 2017)*, AE-10, p. 27.
19. **R. V. Verba**, V. Tyberkevych, and A. N. Slavin. Nonlinear spin-wave interaction in ultrathin ferromagnetic films with interfacial Dzyaloshinskii-Moriya interaction. In: *62nd Annual Conference on Magnetism and Magnetic Materials. Abstracts (Pittsburgh, PA, USA, 6-10 November 2017)*, FD-10, p. 556.
20. **R. Verba**, Voltage-controlled magnonics. In: *3rd International Advanced School on Magnonics 2018 (17–21 September, 2018, Kyiv, Ukraine)*, p. 36.
21. **R. V. Verba**, R. Zivieri, A. Giordano, B. Azzerboni, M. Carpentieri, A. N. Slavin, and G. Finocchio, Nonreciprocal spin waves in spin-Hall oscillators with Dzyaloshinskii-Moriya interaction. In: *2019 Joint MMM-INTERMAG conference. Book of Abstracts (January 14-18, 2019, Washington, DC, USA)*, AJ-10, p. 66.
22. A. Chumak, Q. Wang, B. Heinz, **R. V. Verba**, M. Kewenig, P. Pirro, M. Schneider, B. Lägél, C. Dubs, and T. Brächer, Spin-Wave Modes in sub-100 nm YIG Waveguides. In: *2019 Joint MMM-INTERMAG conference. Book of Abstracts (January 14-18, 2019, Washington, DC, USA)*, HE-07, p. 791.
23. **R. Verba**, Q. Wang, A. Chumak, Nonlinear Operation of Nanoscale Spin-Wave Directional Coupler. In: *Proceedings of the 2019 IEEE 9th International Conference on Nanomaterials: Applications & Properties (NAP-2019) (September 15-20, 2019, Odesa, Ukraine)*, p. 02M03-1.
24. Q. Wang, M. Kewenig, M. Schneider, **R. V. Verba**, B. Heinz, M. Geilen, M. Mohseni, B. Lägél, F. Ciubotaru, C. Adelman, S. Cotofana, C. Dubs, T. Brächer, P. Pirro, and A. Chumak, Realization of a Nanoscale Magnonic Directional Coupler for All-Magnon Circuits. In: *64th Annual conference on Magnetism and Magnetic Materials. Abstracts (November 4-8, 2019, Las Vegas, NV, USA)*, CE-08, p. 258.

Наукові праці, які додатково відображають наукові результати дисертації**(Publications which additionally shed light on the thesis results):**

1. M. Mohseni, M. Kewenig, **R. Verba**, Q. Wang, M. Schneider, B. Heinz, F. Kohl, C. Dubs, B. Lägel, A. A. Serga, B. Hillebrands, A. V. Chumak, and P. Pirro, Parametric Generation of Propagating Spin Waves in Ultrathin Yttrium Iron Garnet Waveguides, *Phys. Status Solidi RRL* **14**, 2000011 (2020).
2. O. V. Prokopenko, D. A. Bozhko, V. S. Tyberkevych, A. V. Chumak, V. I. Vasyuchka, A. A. Serga, O. Dzyapko, **R. V. Verba**, A. V. Talalaevskij, D. V Slobodianiuk, Yu. V. Kobljanskyj, V. A. Moiseienko, S. V. Sholom, and V. Yu. Malyshev, Recent trends in microwave magnetism and superconductivity, *Ukr. J. Phys.* **64** (10), 888 (2019).
3. B. Heinz, Q. Wang, **R. Verba**, V. Vasyuchka, M. Kewenig, P. Pirro, M. Schneider, T. Meyer, B. Lägel, C. Dubs, T. Brächer, O. Dobrovolskiy, and A. Chumak, Temperature Dependence of Spin Pinning and Spin-Wave Dispersion in Nanoscopic Ferromagnetic Waveguides, *Ukr. J. Phys.* **65** (12), 1094 (2020).

ЗМІСТ

Перелік умовних позначень	25
Вступ	27
Розділ 1. Збудження спінових хвиль надвисокочастотним електричним полем	47
1.1. Пороги збудження у випадку перпендикулярної статичної намагніченості хвилеводу	49
1.2. Запорогова динаміка спінових хвиль, збуджених локалізованою накачкою	55
1.3. Збудження спінових хвиль у планарно намагніченому хвилеводі	63
1.4. Параметричне збудження коливань намагніченості у наноточках	70
Розділ 2. Амплітудно-фазовий контроль спінових хвиль квазістатичним електричним полем	85
2.1. Теорія проходження спінових хвиль через внутрішню границю розділу з урахуванням зміни їх поляризації	86
2.2. Стійкість до розсіяння спінових хвиль у геометрії Деймона-Ешбаха у нанорозмірних хвилеводах	97
Розділ 3. Взаємодія біжучих спінових хвиль з локалізованою параметричною накачкою	103
3.1. Параметричне підсилення спінових хвиль великої амплітуди, стабілізація амплітуди спінових хвиль	105
3.2. Стабілізація фази спінових хвиль неадіабатичною параметричною накачкою	114
3.3. Вплив взаємодії Дзялошинського-Морія на параметричне підсилення спінових хвиль	121
Розділ 4. Вплив дипольної взаємодії, неоднорідності внутрішнього поля та струму, та взаємодії Дзялошинського-Морія на спін-хвильову динаміку у спін-торк осциляторах	125
4.1. Дипольні солітони у квазіодновимірних спін-Холл осциляторах	127

4.2. Зменшення фазового шуму у спін-Холл осциляторах на базі магнітних наносмужок змінного перерізу	134
4.3. Конкуренція лінійного та нелінійного механізмів локалізації у спін-торк осциляторах за наявності потенціальної ями	144
4.4. Збудження невзаємних та спіральних спінових хвиль у спін-Холл осциляторах за наявності взаємодії Дзялошинського-Морія	153
4.5. Теорія збудження невзаємних спінових хвиль у двовимірних спін-Холл осциляторах зі взаємодією Дзялошинського-Морія ...	162
Розділ 5. Розрахунок дисперсійних залежностей, сталих затухання та коефіцієнтів нелінійної взаємодії спінових хвиль у нанорозмірних магнітних хвилеводах	171
5.1. Затухання спінових хвиль за наявності неоднорідних та нелокальних механізмів дисипації	174
5.2. Дипольний пінінг та дисперсія спінових хвиль у нанорозмірних феромагнітних хвилеводах	184
5.3. Передача енергії спінових хвиль у дипольно взаємодіючих хвилеводах, спрямований відгалужувач	190
5.4. Нелінійність спрямованого спін-хвильового відгалужувача	202
5.5. Узагальнення гамільтонового формалізму нелінійної взаємодії спінових хвиль на випадок несиметричних магнітних взаємодій	225
Висновки	237
Додаток А. Список опублікованих праць за тематикою дисертації	242

ПЕРЕЛІК УМОВНИХ ПОЗНАЧЕНЬ

ЕКМА	електрично керована магнітна анізотропія
ІВДМ	інтерфейсна взаємодія Дзялошинського-Морія
ЗІГ	залізо-іттрієвий гранат
МЕ	магнітоелектричний
НВЧ	надвисокочастотний
СТ	спін-трансфер
СТО	спін-торк осцилятор
СХО	спін-Холл осцилятор
СХ	спінова хвиля, спін-хвильовий
BLS	Brillouin light scattering
BVMSW	backward volume magnetostatic wave
CMSSW	chiral magnetostatic surface wave
DMI	Dzyaloshinski-Moriya interaction
FM	ferromagnetic
FMR	ferromagnetic resonance
IDMI	interfacial Dzyaloshinski-Moriya interaction
IP	in-plane
MTJ	magnetic tunnel junction
LLG	Landau-Lifshitz-Gilbert
LLGS	Landau-Lifshitz-Gilbert-Slonczewski
OOP	out-of-plane
PMA	perpendicular magnetic anisotropy
PSD	power spectral density

SAF	synthetic antiferromagnet
SHE	spin-Hall effect
SHO	spin-Hall oscillator
ST	spin torque
STO	spin-torque oscillator
ST-FMR	spin-torque ferromagnetic resonance
STT	spin transfer torque
SW	spin wave
VCMA	voltage-controlled magnetic anisotropy
VM	volume mode
YIG	Yttrium-iron-garnet

ВСТУП

Невпинно зростаючі обсяги передачі та обробки даних та інформатизації суспільства підвищують потребу подальшого розвитку елементної бази інформаційних та комунікаційних технологій, роблячи акцент на їх швидкодії, енергоефективності та доступності для масового виробництва. Це спонукає не тільки розвивати існуючу технологію кремнієвих інтегральних схем, а й проводити дослідження і розробки альтернативних підходів, від розробки нової елементної бази класичних обчислювальних систем на основі двійкової логіки до принципово нових підходів в обробці інформації та сигналів: апаратних нейронних мереж та інших нейроморфних підходів, хвильових методів обчислень, квантових обчислень, тощо.

Одним з таких перспективних напрямків є магنونіка [1-4] — дослідницька галузь, основною ідеєю якої є використання спінових хвиль (СХ) у магнітовпорядкованих матеріалах як носіїв інформації для створення новітніх елементів та інтегрованих систем обробки інформації та надвисокочастотних (НВЧ) сигналів. Важливими властивостями магнітовпорядкованих матеріалів є порівняно малі втрати у магнітній підсистемі (для достатньо широкого кола матеріалів), зокрема, втрати на розповсюдження СХ, що робить магнітні системи запису та обробки інформації перспективно найбільш енергоефективними серед інших альтернатив [5], а також велике різноманіття нелінійних ефектів, які проявляються за невеликих та помірних потужностей [6-9] — а нелінійні ефекти є принципово важливими для створення систем обробки інформації, як класичних систем двійкової логіки, так і різноманітних нейроморфних систем. Окрім того, малі довжини СХ, до десятків й одиниць нанометрів [10], високі власні частоти — від одиниць до 100 ГГц у ферромагнетиках [11-13] і навіть більше у фери- та антиферромагнетиках [14-15], широкі можливості маніпулювання дисперсією та іншими характеристиками розповсюдження як за допомогою вибору геометрії [1, 16-17], так і завдяки прикладанню зовнішнього впливу [2, 18-20], та ін. відкривають широкі можливості створення окремих різноманітних нанорозмірних

швидкодіючих функціональних елементів та інтегрованих систем обробки інформації та НВЧ сигналів на основі СХ.

Галузь магنونіки активно розвивається протягом останніх двох десятиріч, і на сьогодні отримано ряд суттєвих результатів. Зокрема, успішно розроблені та досліджені прототипи багатьох окремих елементів магنونної логіки, таких як мажоритарний елемент [21-22], магنونний транзистор [23], XOR, NAND та інші логічні елементи [24-28], магنونних пристроїв аналогової обробки сигналів: мультиплексорів, демультиплексорів, кореляторів, аналізаторів спектру, та багатьох інших [18, 29-33], а також елементів та систем для реалізації нейроморфних підходів до обчислень [34-35]. Однак, необхідно зазначити, що більшість експериментів проводилась на прототипах, які, в першу чергу, зручні для досліджень та перевірки закладених принципів роботи. Зокрема, у дослідженнях зазвичай використовувались феромагнітні хвилеводи та структури мікронного і навіть субміліметрового розміру [18, 21-24, 26-30, 32-33], що дозволяє, зокрема, досліджувати СХ динаміку з гарною просторовою роздільною здатністю за допомогою розсіяння світла Брілюена. Однак, для створення конкурентноспроможних пристроїв необхідно переходити до наномасштабів, адже це дозволяє суттєво зменшити час затримки сигналів (тобто, підвищити швидкодію), а також зменшити енергетичні втрати, які, грубо, є пропорційними до об'єму магнітного матеріалу. Крім того, у більшості робіт використовується збудження СХ та вплив на них за допомогою магнітних полів, створюваних електричними струмами у провідних лініях, розташованих поблизу чи у контакті з феромагнітним хвилеводом чи іншою магнітною структурою [18, 22-24, 29-30, 32-33]. Великі омичні втрати електричного струму повністю нівелюють усі переваги застосування СХ з точки зору енергоефективності. Зокрема, наші оцінки показують, що ці втрати можуть на кілька порядків перевищувати втрати у магнітній підсистемі у СХ пристроях мікронних розмірів (див. таблицю I у п. 5.4). Також, такий підхід практично незастосовний на наномасштабах, адже мінімальні розміри провідної лінії (НВЧ антени) обмежуються як зростанням її індуктивності, так і проблемами перегрівання. Практично у всіх роботах розміри

провідних антен (їх ширина) складають не менше 0.5-1 мкм, а за необхідності створити магнітне поле з меншим масштабом неоднорідності застосовують додаткові структури між антеною та феромагнітним зразком [36-37].

Таким чином, існує потреба розробки інших підходів до збудження та впливу на СХ, які б були суттєво енергоефективнішими та придатними до застосування на наномасштабах. З точки зору енергоефективності найбільшу увагу приділяють впливу на магнітну підсистему електричним полем завдяки магнітоелектричним (МЕ) ефектам. При використанні МЕ ефектів зникає необхідність прикладати великі густини струмів (залишаються лише невеликі тунельні чи паразитні струми) і омичні втрати зменшуються практично до нуля. Наприклад, оцінки, зроблені у [5] показують, що 32-бітний суматор на основі МЕ комірок може споживати на два порядки менше енергії за будь-які інші відомі чи досліджувані технології.

Серед великого різноманіття МЕ ефектів (див., наприклад, огляди [38-40]) найбільшу увагу з точки зору НВЧ застосувань приділяли МЕ ефекту у композитних структурах п'єзоелектрик - феромагнетик [41-44]. Цей МЕ ефект є, фактично, комбінацією п'єзоелектричного ефекту та ефекту магнітострикції, зв'язок між якими забезпечується поширенням деформацій. Із використанням цього МЕ ефекту було, зокрема, реалізовано збудження та прийом СХ сигналів [45-46], модуляцію СХ [47], ведуться розробки електрично керованих елементів магнітної логіки та інтегрованих кіл [48-49]. Не применшуючи перспективи використання даного МЕ ефекту, необхідно відзначити певні проблеми на шляху його використання у пристроях магнітоніки, такі як наявність паразитних (механічних) резонансів, сильна нелінійність та наявність гістерезису, складність локалізації деформації на наномасштабі, та ризик механічного руйнування структури при прикладанні відносно великих сигналів (наприклад, для реалізації нелінійних СХ процесів). Також відзначимо ще два МЕ ефекти — спіновий флексоелектричний ефект [50-51] та ефект електрично керованої міжшарової обмінної взаємодії [52], які можуть бути цікавими для магнітних застосувань, однак, на сьогодні не достатньо вивчені, щоб досліджувати прикладні проблеми.

У цій роботі досліджується динаміка СХ під впливом іншого, нещодавно відкритого МЕ ефекту — ефекту електрично керованої магнітної анізотропії (ЕКМА) [53-55]. Цей ефект проявляється у приповерхневому шарі провідних феромагнетиків як зміна перпендикулярної магнітної анізотропії під впливом прикладеного електричного поля (напруги). Головною, хоч і не єдиною, причиною появи ЕКМА є спін-залежне екранування електронів провідності [56-57]. Оскільки ЕКМА є поверхневим ефектом, він найкраще проявляється у структурах провідний феромагнетик - діелектрик з надтонким шаром феромагнетика (тут і далі під надтонким шаром розуміється шар, у якому поверхневі ефекти, зокрема, ЕКМА, поверхнева анізотропія, тощо, визначають стан всього шару як цілого; характерні товщини для різних матеріалів складають до 1-2 нм). ЕКМА виявляє наступні властивості: лінійність (у деяких гетероструктурах можливе переважаювання квадратичного ефекту), відсутність гістерезису, високу швидкодію (зокрема, інерційних ефектів у гігагерцовому діапазоні частот помічено не було) [54]. За допомогою ЕКМА можна досягти значних змін магнітної анізотропії феромагнетика, зокрема, достатньої для його перемагнічування [54, 58-59]. Також, очевидно, немає ніяких проблем із застосуванням ЕКМА у нанорозмірних системах — достатньо створити провідний контакт на структурі діелектрик - феромагнетик відповідного розміру, а використання діелектричного шару нанометрової товщини забезпечить гарну локалізацію електричного поля в області під контактом. Усі ці особливості роблять ЕКМА одним з найбільш перспективних МЕ ефектів для створення енергоефективних субмікронних та нанорозмірних пристроїв та елементів магنونіки.

Здебільшого, увага до ефекту ЕКМА приверталась з точки зору застосування у новітніх елементах магнітної пам'яті, а, отже, досліджувались процеси перемагнічування магнітних нанoeлементів під дією імпульсних чи НВЧ електричних полів [58-59], а також рух доменних стінок і солітонів під впливом ЕКМА [60-62]. На момент початку роботи над дисертаційними дослідженнями (2013 рік) було зроблено лише 2 експериментальні роботи по дослідженню збудження феромагнітного резонансу у магнітних тунельних контактах спільним

впливом ЕКМА та спін-поляризованого струму [63-64] та дослідження зсуву частоти феромагнітного резонансу під дією статичного електричного поля [65]. Тому, вивчення можливості та перспектив створення електрично керованих пристроїв магنونіки із використанням ЕКМА необхідно було починати з базових питань — збудження СХ електричним полем, контроль проходження та фази СХ, та пов'язаних із ними ефектів та особливостей, і тільки потім переходити до дослідження інших ефектів, які можуть лягти в основу створення безпосередньо елементів магنونної логіки чи допоміжних елементів магنونних інтегрованих кіл.

Іншим важливим і цікавим для застосувань методом впливу на магнітну динаміку є використання ефекту спін-трансферу (СТ), який проявляється у виникненні моменту сил, що діє на намагніченість феромагнетика, при інжекції в нього спін-поляризованого електричного струму чи чистого спінового струму завдяки спін-Холл ефекту [66-67]. Хоча при використанні ефекту СТ необхідно прикладати великі густини електричного струму і енергоефективність такого методу не може конкурувати з МЕ ефектами (проте, є кращою за використання мікрохвильових антен), СТ має важливу особливість — завдяки йому можна досягти таких типів магнітної динаміки, які недосяжні при використанні електричного чи магнітного полів [68-69]. Зокрема, завдяки СТ можна досягти компенсації втрат та збудження автоколивань намагніченості, що лежить в основі роботи нанорозмірних магнітних автогенераторів — спін-торк та спін-Холл осциляторів (СТО та СХО) [70-73]. Також, ефект СТ без жодним проблем застосовний на наномасштабі (навіть навпаки, у багатьох випадках можливість його використання у структурах з латеральними розмірами, більшими за 1-10 мкм, знаходиться під великим питанням).

На відміну від динаміки намагніченості під дією ЕКМА, динаміка під впливом спін-поляризованого та чистого спінового струму вивчена достатньо детально і багато фундаментальних аспектів є відомими [74-79]. Однак, характеристики пристроїв на основі ефекту СТ, зокрема, потужність та когерентність генерації СТО та СХО, потребують подальшого удосконалення. У сучасних експериментах отримано ряд результатів [80-81], які є цікавими для

потенційних прикладних застосувань, у тому числі, і для вирішення вищезазначених проблем, але які не мають пояснення в рамках розвинених моделей, що створює необхідність подальшого розвитку теоретичних та модельних уявлень про СХ динаміку під впливом СТ.

Актуальність теми, таким чином, пов'язана зі значними перспективами застосування СХ у новітніх системах обробки інформації та НВЧ сигналів і необхідністю розробки принципів збудження та впливу на СХ, які були б енергоефективними та придатними для застосування у субмікронних та нанорозмірних системах. Важливо зазначити, що успішна розробка таких принципів не просто підвищить енергоефективність магنونних пристроїв, але й може, за оцінками, вивести магنونіку у лідери за енергоефективністю серед інших наявних та перспективних технологій обробки інформації та сигналів. Окрім цього, важливими залишаються дослідження особливостей СХ динаміки у нанорозмірних хвилеводах та розробка методів розрахунку характеристик СХ, які є необхідними для проектування елементів та інтегрованих систем магنونіки, а також продовження вивчення динаміки СТО та СХО з метою покращення характеристик цих нанорозмірних магнетичних автогенераторів.

Зв'язок роботи з науковими програмами, планами, темами. Робота над дисертацією була виконана в Інституті магнетизму НАН України та МОН України в рамках наступних науково-дослідних робіт (НДР):

- держбюджетна НДР МОН України “Вплив електричного та магнетичного полів на високочастотні та морфологічні властивості магнетичних наноструктур” (№ державної реєстрації 0115U002716);
- грант Президента України для молодих вчених на 2018 р. № Ф75/151-2018 “Нелінійні спіно-хвильові процеси у феромагнетичних наноструктурах з інтерфейсною взаємодією Дзялошинського-Морія” (№ державної реєстрації 0118U006294);
- конкурсна НДР молодих вчених НАН України на 2019-2020 рр. № 23-04/01 “Ефекти квантування та дипольного закріплення спінових хвиль у

мікрохвильовій динаміці магнітних наноструктур” (№ державної реєстрації 0119U102487);

— держбюджетна НДР МОН України “Спінова динаміка в магнітовпорядкованих матеріалах з метаповерхнями” (№ державної реєстрації 0118U004007).

У перших трьох НДР автор дисертації був керівником роботи. Дослідження також підтримувались Дослідницькою програмою “Center of Nanoferroic Devices” Національного інституту стандартів та технологій (National Institute of Standards and Technology, США) та Semiconductor Research Corporation (США), Національним науковим фондом США (U.S. National Science Foundation), гранти № ECCS-1708982 “Novel Terahertz Generators Based on Magnetic Materials” та № EFMA-1641989 “Non-Reciprocal Magneto-Acoustic Waves in Chiral Magnetic Systems”, програмою ЄС “Горизонт 2020”, Marie Sklodowska-Curie Research and Innovation Staff Exchange (RISE) project No. 644348 “MagIC – Magnonics, Interactions and Complexity: a multifunctional aspects of spin wave dynamics”, та Європейською дослідницькою радою (European Research Council), Starting Grant № 678309 “Magnon Circuits”.

Метою дисертації є вирішення проблеми розробки нових та удосконалення існуючих енергоефективних та сумісних з нанотехнологіями методів збудження та контролю спінових хвиль у надтонких феромагнітних плівках та хвилеводах, а також дослідження особливостей лінійної та нелінійної спін-хвильової динаміки у таких структурах і вивчення можливості застосування відповідних процесів для створення функціональних елементів магنونної логіки та інших систем спін-хвильової електроніки. *Об’єктом дослідження* є спінові хвилі у надтонких феромагнітних плівках та наноструктурах. За безпосередній предмет дослідження було обрано лінійну, параметричну та нелінійну НВЧ спін-хвильову динаміку у надтонких феромагнітних плівках та наноструктурах під впливом квазістатичних та НВЧ електричних полів за рахунок ефекту ЕКМА, а також спін-поляризованого електричного чи чистого спінового струму.

Для досягнення мети були сформульовані та розв'язувались наступні задачі:

1. Теоретичний розгляд можливості збудження СХ за допомогою НВЧ електричного поля у надтонких феромагнітних плівках та наноструктурах, визначення механізмів, за якими можливе збудження.
2. Побудова теорії запорогової динаміки параметрично збуджених СХ локалізованою накачкою; встановлення механізмів, які визначають стаціонарні амплітуди параметрично збуджених СХ.
3. Розгляд особливостей проходження СХ через ЕКМА керовану внутрішню границю розділу у феромагнетику, побудова теорії проходження СХ через внутрішню границю розділу з урахуванням впливу зміни поляризації СХ.
4. Розгляд нелінійної динаміки СХ під час проходження області локалізованої накачки, дослідження механізмів, які обмежують ефективність параметричного підсилення за великих амплітуд СХ, та розгляд можливості реалізації ефекту стабілізації амплітуди СХ.
5. Вивчення фазових характеристик параметричного підсилювача біжучих СХ, дослідження можливості корекції фазових помилок СХ сигналів.
6. Теоретичне пояснення експериментально спостережених особливостей збудження СХ мод у СТО та СХО, зокрема, визначення впливу розмірності активної області осцилятора, неоднорідностей густини спінового струму накачки та внутрішнього магнітного поля.
7. Вивчення впливу ІВДМ на СХ динаміку у СХО та параметричних підсилювачах. Розвиток теорії збудження СХ в одно- та двовимірних СХО за наявності ІВДМ.
8. Розробка методів розрахунку сталих затухання СХ під впливом нелокальних та неоднорідних дисипативних механізмів та коефіцієнтів нелінійної СХ взаємодії за наявності ІВДМ.
9. Розгляд особливостей дисперсії та структури СХ у нанорозмірних феромагнітних хвилеводах, а також лінійної та нелінійної взаємодії СХ у дипольно взаємодіючих нанорозмірних хвилеводах.

Методи дослідження:

1. Методи числового розв'язання диференціальних та інтегро-диференціальних рівнянь — у дослідженні СХ динаміки під дією локалізованої параметричної накачки та динаміки СТО й СХО.
2. Теорія збурень — при дослідженні параметричного підсилення СХ великої амплітуди та згасання СХ мод.
3. Мікромагнітне моделювання — при дослідженні проходження СХ через внутрішню границю розділу.
4. Об'єднаний метод колокації та найменших квадратів — при отриманні частоти та порогів збудження СХ у двовимірному СХО за наявності ІВДМ.
5. Гамільтонів формалізм СХ динаміки та класичні перетворення Голстейна-Прімакова — при дослідженні коефіцієнтів нелінійної СХ взаємодії.
6. Аналітичні методи теорії диференціальних рівнянь, математичної фізики, математичного аналізу.

Наукова новизна одержаних результатів полягає в наступному:

1. Запропоновано та обґрунтовано спосіб збудження СХ у надтонких феромагнітних плівках та наноструктурах НВЧ електричним полем за допомогою ефекту ЕКМА у нульовому зовнішньому магнітному полі. Продемонстровано можливість ефективного параметричного зв'язку з короткими обмінними СХ у хвилеводах з планарною намагніченістю.
2. Виявлено новий механізм обмеження амплітуд параметрично збуджених СХ локалізованою накачкою — нелінійну зміну групової швидкості СХ, який починає відігравати суттєву роль при субмікронних та нанорозмірних довжинах області накачки .
3. Узагальнено теорію проходження СХ через внутрішню границю розділу з урахуванням можливої зміни векторної структури (поляризації) хвилі.
4. Виявлено та пояснено зменшення ефективності параметричного підсилення СХ при збільшенні їх амплітуди. Запропоновано спосіб

мінімізації цього явища для збереження ефективності підсилення нелінійних СХ. Вперше виявлено ефект стабілізації амплітуди СХ параметричною накачкою.

5. Запропоновано та обґрунтовано спосіб підвищення ефективності та завадостійкості параметричного підсилювача СХ за рахунок невзаємного зсуву спектру СХ, викликаного, наприклад, ІВДМ, що дає змогу локалізувати холосту хвилю.
6. Вперше виявлено та досліджено утворення стійких дисипативних дипольних магнітних солітонів — дипольних СХ булетів — у квазіодновимірних СТО та СХО.
7. Пояснено механізм зменшення фазового шуму та збільшення області одномодової генерації у СХО з неоднорідним розподілом струму накачки.
8. Систематично вивчено вплив неоднорідного ландшафту внутрішнього статичного поля на динаміку СТО та СХО, продемонстровано можливість зміни типу збудженої моди з лінійно локалізованої на самолокалізовану нелінійну (СХ булет); пояснено експериментальні дані по спостереженню мод нетипового профілю у СТО впливом асиметричної потенціальної ями.
9. Вперше розроблено теорію збудження біжучих СХ в одно- та двовимірних СТО та СХО за наявності ІВДМ, пояснено спостережені у моделюванні червоний зсув частоти генерації та зменшення порогового струму зі збільшенням величини ІВДМ, а також природу спіральних СХ.
10. Розроблено метод розрахунку характеристик спрямованого відгалужувача на основі дипольно взаємодіючих нанорозмірних хвилеводів у лінійному та помірно нелінійному режимах роботи.
11. Узагальнено метод аналізу нелінійної СХ взаємодії на основі гамільтонового формалізму на випадок наявності антисиметричних взаємодій. Вперше виявлено нелінійність невзаємності спектру СХ, викликаного ІВДМ.

Практичне значення одержаних результатів. Запропоновані та обґрунтовані методи збудження та впливу на СХ електричним полем за допомогою ефекту ЕКМА відкривають шлях до створення енергоефективних нанорозмірних пристроїв магنونіки, які, за оцінками, можуть стати найбільш енергоефективними пристроями обробки інформації та НВЧ сигналів серед наявних та досліджуваних альтернатив. Запропоновані методи реалізації стабілізації (нормалізації) амплітуди СХ та корекції фазових відхилень СХ за допомогою взаємодії з параметричною накачкою, які є необхідними операціями для створення інтегрованих магنونних кіл. Пояснені механізми стабілізації “великих” дипольних солітонів у СХО і СТО та впливу неоднорідності струму накачки на динаміку цих солітонів відкривають шлях до збільшення потужності генерації та підвищення когерентності СХО та СТО. Виявлений ефект нелінійності невзаємного розщеплення спектру СХ за наявності ІВДМ може лягти в основу невзаємних пристроїв, керованих потужністю. Насамкінець, розроблені методи розрахунку дисперсійних характеристик, сталих затухання, коефіцієнтів нелінійної взаємодії СХ, а також величини дипольного зв'язку між СХ у сусідніх хвилеводах будуть корисними для планування та аналізу експериментів і розробки пристроїв в області магنونіки.

Особистий внесок здобувача. Усі аналітичні розрахунки, представлені в роботі, окрім отримання наближеного загального розв'язку для профілів СХ у СХО з ІВДМ та аналізу кутової залежності хвильового числа (п. ШВ, ШС підрозділу 4.5), проведені автором особисто. Автором також проведені числові моделювання динаміки намагніченості на основі вкорочених рівнянь під дією параметричної накачки (підрозділи 1.2, 3.1, 3.2) та СТ (підрозділи 4.1, 4.2, 4.3), аналіз симетрії дипольних полів поверхневих СХ мод (підрозділ 2.2), запропоновані пояснення появи спіральних мод у СХО з ІВДМ (підрозділ 4.4) та ефекту розкріплення профілів СХ мод у нанорозмірних хвилеводах (підрозділ 5.2), та зроблені оцінки енергоспоживання параметричного підсилювача на основі ЕКМА (підрозділ 5.4). Мікромагнітне моделювання проходження СХ через ЕКМА-керовану область (підрозділ 2.1) проведене автором особисто, інші

мікромагнітні моделювання проведені співавторами публікацій: М. Карпентієрі, Дж. Фіноккіо, Чі Ванг, Т. Шнайдер, Ю.-Дж. Чен, М. Мосхені. При цьому автор брав безпосередню участь у розробці методики та обробці даних мікромагнітного моделювання динаміки СХ під впливом ЕКМА (підрозділи 1.2-1.4, 3.1-3.2). Експерименти проведені співавторами (групи І. Криворотова та А. Чумака); автор брав безпосередню участь в обробці експериментальних даних по збудженню параметричного резонансу у наноточці НВЧ електричним полем та надавав рекомендації щодо коригування методики та подальших вимірів (підрозділ 1.4). У статтях [2-3, 5, 8, 10, 12, 14-15, 18-19] (нумерація згідно Додатку А) автор, спільно з проф. А. Славінім та В. Тиберкевичем брав участь у постановці задачі; в усіх опублікованих статтях автор брав участь в обговоренні результатів та написанні тексту. Особистий внесок у кожну з публікацій описаний детально у Додатку А. Співавторами публікацій захищено наступні дисертації: Liu Yang, “Magnetization dynamics in Pt/Ni₈₀Fe₂₀ nanowires induced by spin Hall effect”, Ph.D. thesis, University of California Irvine, 2015 [<https://escholarship.org/content/qt7b36f6mr/qt7b36f6mr.pdf>] (експериментальні дослідження динаміки СХО); Qi Wang, “Linear and nonlinear spin waves in nanoscale magnonic structures for data processing”, Ph.D. thesis, Technical University of Kaiserslautern, 2019 [<https://scholar.google.com/scholar?oi=bibs&cluster=17368862475438069002&btnI=1&hl=en>] (мікромагнітні дослідження СХ у нанорозмірних хвилеводах, мікромагнітні та експериментальні дослідження спрямованого СХ відгалужувача).

Апробація результатів дисертації. Основні результати, викладені в дисертації, доповідались та обговорювались на науковому семінарі Інституту магнетизму НАН України та МОН України, на семінарі лабораторії квантової радіофізики Київського національного університету імені Тараса Шевченка, та були представлені на 14 конференціях:

- 58th Annual Conference on Magnetism and Magnetic Materials (Denver, CO, USA, November 4-8, 2013);
- 2014 IEEE International Magnetism Conference (INTERMAG) (Dresden, Germany, 4-8 May 2014);

- 59th Annual Conference on Magnetism and Magnetic Materials (Honolulu, HI, USA, November 3-7, 2014);
- 2015 IEEE International Magnetism Conference (INTERMAG) (Beijing, China, 11-15 May 2015);
- XI international conference “Electronics and applied physics” (Kyiv, October 21-24, 2015);
- 2016 Joint MMM-INTERMAG Conference (San Diego, CA, USA, 11-15 January 2016);
- Baltic Spin 2016 (Jurmala, Latvia, 9-13 August 2016);
- 61th Annual Conference on Magnetism and Magnetic Materials (New Orleans, LA, USA, 31 October - 4 November 2016);
- 2017 IEEE International Magnetism Conference (INTERMAG) (Dublin, Ireland, 24-28 April 2017);
- 62nd Annual Conference on Magnetism and Magnetic Materials (Pittsburgh, PA, USA, 6-10 November 2017);
- 3rd International Advanced School on Magnonics 2018 (Kyiv, 17-21 September, 2018);
- 2019 Joint MMM-INTERMAG conference (Washington, DC, USA, January 14-18, 2019);
- 9th IEEE International Conference on Nanomaterials: Applications & Properties (NAP-2019) (Odesa, September 15-20, 2019);
- 64th Annual conference on Magnetism and Magnetic Materials (Las Vegas, NV, USA, November 4-8, 2019).

Усього представлено 24 доповіді та постерні презентації, з них 13 — особисто автором, включаючи 3 запрошені доповіді ([22, 31, 40] у Додатку А).

Публікації. Усього за результатами дисертації опубліковано 47 друкованих праць. Основні результати відображені в одному розділі колективної монографії, 19 статтях у наукових фахових журналах, з яких 17 опубліковані у журналах, які входять до квартилю Q1 відповідно до Scimago Scientific Journal Rankings (SJR) (статті [2-16, 18, 20] у додатку А), та 24 тезах та працях конференцій. Додатково

результати відображені у 3 статтях ([45-47] у додатку А). Статті [5] та [6], а також [17] та [46] опубліковані в одному випуску (номері) журналу.

Структура та обсяг дисертації. Дисертація підготована у вигляді наукової доповіді. До основної частини дисертації включено 19 статей у фахових наукових журналах, які згруповані у 5 розділів. Загальний обсяг дисертації — 249 сторінок, з яких основна частина складає 194 сторінки.

Список використаних джерел

1. V. V. Kruglyak, S. O. Demokritov, and D. Grundler, Magnonics, *J. Phys. D* **43**, 264001 (2010).
2. M. Krawczyk, and D. Grundler, Review and prospects of magnonic crystals and devices with reprogrammable band structure, *J. Phys. Cond. Matter* **26**, 123202 (2014).
3. A. V. Chumak, V. I. Vasyuchka, A. A. Serga, and B. Hillebrands, Magnon spintronics, *Nat. Phys.* **11**, 453 (2015).
4. *Magnonics. From Fundamentals to Applications*, ed. by S. O. Demokritov and A. N. Slavin (Springer, Berlin, 2013)
5. D. E. Nikonov, and I. A. Young, Overview of Beyond-CMOS Devices and a Uniform Methodology for Their Benchmarking, *Proc. IEEE* **101**, 2498 (2013).
6. V. S. L'vov, *Wave Turbulence under Parametric Excitation* (Springer-Verlag, New York, 1994).
7. G. Bertotti, I. Mayergoyz, and C. Serpico, *Nonlinear Magnetization Dynamics in Nanosystems* (Elsevier, Oxford, 2009).
8. А. Г. Гуревич. Г. А. Мелков, *Магнитные колебания и волны* (Москва, Наука, 1994).
9. O. R. Sulymenko, O. V. Prokopenko, V. S. Tyberkevych, A. N. Slavin, and A. A. Serga, Bullets and droplets: Two-dimensional spin-wave solitons in modern magnonics (Review Article), *Физ. низких температур* **44**, 775 (2018).
10. T. Balashov, P Buczec, L Sandratskii, A Ernst, and W Wulfhekel, Magnon dispersion in thin magnetic films, *J. Phys.: Condens. Matter.* **26**, 394007 (2014).

11. M. A. Popov, I. V. Zavislyak, and G. Srinivasan, Sub-THz dielectric resonance in single crystal yttrium iron garnet and magnetic field tuning of the modes, *J. Appl. Phys.* **110**, 24112 (2011).
12. M. A. Popov, I. V. Zavislyak, and G. Srinivasan, Magnetic field tunable 75-110 GHz dielectric phase shifter, *Electronics Lett.* **46**, 569 (2010).
13. I. Harward, Y. Nie, D. Chen, J. Baptist, et al., Physical properties of Al doped Ba hexagonal ferrite thin films, *J. Appl. Phys.* **113**, 043903 (2013).
14. Е. Г. Галкина, Б. А. Иванов, Динамические солитоны в антиферромагнетиках, *Физ. низких температур* **44**, 794 (2018).
15. V. Baltz, A. Manchon, M. Tsoi, T. Moriyama, et al., Antiferromagnetic spintronics, *Rev. Mod. Phys.* **90**, 015005 (2018).
16. C. Behncke, M. Hänze, C. F. Adolff, M. Weigand, and G. Meier, Band structure engineering of two-dimensional magnonic vortex crystals, *Phys. Rev. B* **91**, 224417 (2015).
17. J. W. Kłos, D. Kumar, M. Krawczyk, and A. Barman, Magnonic Band Engineering by Intrinsic and Extrinsic Mirror Symmetry Breaking in Antidot Spin-Wave Waveguides, *Sci. Rep.* **3**, 2444 (2013).
18. A. V. Chumak, V. S. Tiberkevich, A. D. Karenowska, A. A. Serga, et al., All-linear time reversal by a dynamic artificial crystal, *Nat. Commun.* **1**, 141 (2010).
19. R. Verba, G. Melkov, V. Tiberkevich, and A. Slavin, Fast switching of a ground state of a reconfigurable array of magnetic nano-dots, *Appl. Phys. Lett.* **100**, 192412 (2012).
20. M. Vogel, A. V. Chumak, E. H. Waller, T. Langer, et al., Optically reconfigurable magnetic materials, *Nat. Phys.* **11**, 487 (2015).
21. S. Klingler, P. Pirro, T. Brächer, B. Leven, B. Hillebrands, and A. V. Chumak, Design of a spin-wave majority gate employing mode selection, *Appl. Phys. Lett.* **105**, 152410 (2014).
22. T. Fischer, M. Kewenig, D. A. Bozhko, A. A. Serga, et al., Experimental prototype of a spin-wave majority gate, *Appl. Phys. Lett.* **110**, 152401 (2017).

23. A. V. Chumak, A. A. Serga, and B. Hillebrands, Magnon transistor for all-magnon data processing, *Nat. Commun.* **5**, 4700 (2014).
24. T. Schneider, A. A. Serga, B. Leven, B. Hillebrands, R. L. Stamps, M. P. Kostylev, Realization of spin-wave logic gates, *Appl. Phys. Lett.* **92**, 022505 (2008).
25. A. Khitun, M. Bao, and K. L. Wang, Magnonic logic circuits, *J. Phys. D Appl. Phys.* **43**, 264005 (2010).
26. N. Sato, K. Sekiguchi, Y. Nozaki, Electrical demonstration of spin-wave logic operation, *Appl. Phys. Express* **6**, 063001 (2013).
27. K. Ganzhorn, S. Klingler, T. Wimmer, S. Geprägs, et al., Magnon-based logic in a multi-terminal YIG/Pt nanostructure, *Appl. Phys. Lett.* **109**, 022405 (2016).
28. M. Balynsky, A. Kozhevnikov, Y. Khivintsev, T. Bhowmick, et al., Magnonic interferometric switch for multi-valued logic circuits, *J. Appl. Phys.* **121**, 024504 (2017).
29. K. Vogt, F. Y. Fradin, J. E. Pearson, T. Sebastian, et al., Realization of a spin-wave multiplexer, *Nat. Commun.* **5**, 3727 (2014).
30. F. Heussner, G. Talmelli, M. Geilen, B. Heinz, et al., Experimental realization of a passive gigahertz frequency division demultiplexer for magnonic logic networks, *Phys. Status Solidi* **14**, 1900695 (2020).
31. Á. Papp, W. Porod, Á. I. Csurgay, and G. Csaba, Nanoscale spectrum analyzer based on spin-wave interference. *Sci. Rep.* **7**, 9245 (2017).
32. A. V. Sadovnikov, E. N. Beginin, S. E. Sheshukova, D. V. Romanenko, Yu. P. Sharaevskii, and S. A. Nikitov, Directional multimode coupler for planar magnonics: side-coupled magnetic stripes, *Appl. Phys. Lett.* **107**, 202405 (2015).
33. A. V. Sadovnikov, S. A. Odintsov, E. N. Beginin, S. E. Sheshukova, Yu. P. Sharaevskii, and S. A. Nikitov, Toward nonlinear magnonics: Intensity-dependent spin-wave switching in insulating side-coupled magnetic stripes, *Phys. Rev. B* **96**, 144428 (2017).
34. J. Torrejon, M. Riou, F. Abreu Araujo, S. Tsunegi, et al., Neuromorphic computing with nanoscale spintronic oscillators, *Nature* **547**, 428 (2017).

35. T. Brächer and P. Pirro, An analog magnon adder for all-magnonic neurons, *J. Appl. Phys.* **124**, 152119 (2018).
36. C. Liu, J. Chen, T. Liu, F. Heimbach, et al., Long-distance propagation of short-wavelength spin waves, *Nat. Commun.* **9**, 738 (2018).
37. J. Chen, T. Yu, C. Liu, T. Liu. et al., Excitation of unidirectional exchange spin waves by a nanoscale magnetic grating, *Phys. Rev. B* **100**, 104427 (2019).
38. M. Fiebig, Revival of the magnetoelectric effect, *J. Phys. D* **38**, R123 (2005).
39. W.-Y. Tong, Y.-W. Fang, J. Cai, S.-J. Gong, and C.-G. Duan, Theoretical studies of all-electric spintronics utilizing multiferroic and magnetoelectric materials, *Comput. Mater. Sci.* **112**, Part B, 467 (2015).
40. F. Matsukura, Y. Tokura, and H. Ohno, Control of magnetism by electric fields, *Nat. Nanotechnol.* **10**, 209 (2015).
41. C.-W. Nan, M. I. Bichurin, S. Dong, D. Viehland, and G. Srinivasan, Multiferroic magnetoelectric composites: Historical perspective, status, and future directions, *J. Appl. Phys.* **103**, 031101 (2008).
42. N. X Sun and G. Srinivasan, Voltage control of magnetism in multiferroic heterostructures and devices, *SPIN* **2**, 1240004 (2012).
43. V. Garcia, M. Bibes, A. Barthélémy, Artificial multiferroic heterostructures for an electric control of magnetic properties, *Comptes Rendus Physique* **16**, 168 (2015).
44. I. V. Zavislyak, M. A. Popov, G. Srinivasulu, and G. Srinivasan, Electric field tuning of domain magnetic resonances in yttrium iron garnet films, *Appl. Phys. Lett.* **102**, 222407 (2013).
45. S. Cherepov, P. Khalili Amiri, J. G. Alzate, K. Wong, et al., Electric-field-induced spin wave generation using multiferroic magnetoelectric cells, *Appl. Phys. Lett.* **104**, 082403 (2014).
46. M. Balinskiy, A. C. Chavez, A. Barra, H. Chiang, et al., Magnetoelectric Spin Wave Modulator Based On Synthetic Multiferroic Structure, *Sci. Rep.* **8**, 10867 (2018).
47. F. Vanderveken, H. Ahmad, M. Heyns, B. Sorée, et al., Excitation and propagation of spin waves in non-uniformly magnetized waveguides, *J. Phys. D: Appl. Phys.* **53**, 495006 (2020).

48. D. Tierno, F. Ciubotaru, R. Duflou, M. Heyns, et al., Strain coupling optimization in magnetoelectric transducers, *Microelectronic Engineering* **187**, 144 (2015).
49. A. Mahmoud, F. Vanderveken, C. Adelman, F. Ciubotaru, et al., 2-output spin wave programmable logic gate, In: *2020 IEEE Computer Society Annual Symposium on VLSI (ISVLSI)*, p. 60.
50. X. Zhang, T. Liu, M.E. Flatté, and H.X. Tang, Electric-field coupling to spin waves in a centrosymmetric ferrite, *Phys. Rev. Lett.* **113**, 037202 (2014).
51. A. S. Savchenko and V. N. Krivoruchko, Electric-field control of nonreciprocity of spin wave excitation in ferromagnetic nanostripes, *J. Magn. Magn. Mater.* **474**, 9 (2019).
52. Q. Yang, Z. Zhou, N.X. Sun, and M. Liu, Perspectives of voltage control for magnetic exchange bias in multiferroic heterostructures, *Phys. Lett. A* **381**, 1213 (2017).
53. M. Weisheit, S. Fähler, A. Marty, Y. Souche, et al., Electric field-induced modification of magnetism in thin-film ferromagnets, *Science* **315**, 349 (2007).
54. S. Miwa, M. Suzuki, M. Tsujikawa, and T. Nozaki, Perpendicular magnetic anisotropy and its electric-field-induced change at metal-dielectric interfaces, *J. Phys. D: Appl. Phys.* **52**, 063001 (2019).
55. M. Endo, S. Kanai, S. Ikeda, F. Matsukura, and H. Ohno, Electric-field effects on thickness dependent magnetic anisotropy of sputtered MgO|Co₄₀Fe₄₀B₂₀|Ta structures, *Appl. Phys. Lett.* **96**, 212503 (2010).
56. C.-G. Duan, J. P. Velev, R. F. Sabirianov, Z. Zhu, et al., Surface Magnetoelectric Effect in Ferromagnetic Metal Films, *Phys. Rev. Lett.* **101**, 137201 (2008).
57. J. Zhang, P. V. Lukashev, S. S. Jaswal, and Evgeny Y. Tsymbal, Model of orbital populations for voltage-controlled magnetic anisotropy in transition-metal thin films, *Phys. Rev. B* **96**, 014435 (2017).
58. Y. Shiota, T. Nozaki, F. Bonell, S. Murakami, et al., Induction of coherent magnetization switching in a few atomic layers of FeCo using voltage pulses, *Nat. Mater.* **11**, 39 (2012).

59. W.-G. Wang, M. Li, S. Hageman, and C. L. Chien, Electric-field-assisted switching in magnetic tunnel junctions, *Nat. Mater.* **11**, 64 (2012).
60. A. Schellekens, A. van den Brink, J. Franken, H. Swagten, and B. Koopmans, Electric-field control of domain wall motion in perpendicularly magnetized materials, *Nat. Commun.* **3**, 847 (2012).
61. U. Bauer, S. Emori, and G. S. D. Beach, Voltage-gated modulation of domain wall creep dynamics in an ultrathin metallic ferromagnet, *Appl. Phys. Lett.* **101**, 172403 (2012).
62. X. Zhang, Y. Zhou, M. Ezawa, G. P. Zhao, and W. Zhao, Magnetic skyrmion transistor: skyrmion motion in a voltage-gated nanotrack, *Sci. Rep.* **5**, 11369 (2015).
63. T. Nozaki, Y. Shiota, S. Miwa, S. Murakami, et al., Electric-field-induced ferromagnetic resonance excitation in an ultrathin ferromagnetic metal layer, *Nat. Phys.* **8**, 491 (2012).
64. J. Zhu, J. A. Katine, G. E. Rowlands, Y.-J. Chen, et al., Voltage-Induced Ferromagnetic Resonance in Magnetic Tunnel Junctions, *Phys. Rev. Lett.* **108**, 197203 (2012).
65. S.-S. Ha, N.-H. Kim, S. Lee, C.-Y. You, et al., Voltage induced magnetic anisotropy change in ultrathin Fe₈₀Co₂₀|MgO junctions with Brillouin light scattering, *Appl. Phys. Lett.* **96**, 142512 (2010).
66. J.C. Slonczewski, Current-driven excitation of magnetic multilayers, *J. Magn. Magn. Mater.* **159**, L1 (1996).
67. L. Berger, Emission of spin waves by a magnetic multilayer traversed by a current, *Phys. Rev. B* **54**, 9353 (1996).
68. K. Ando, S. Takahashi, K. Harii, K. Sasage, et al., Electric manipulation of spin relaxation using the spin Hall effect, *Phys. Rev. Lett.* **101**, 036601 (2008).
69. A. Hamadeh, O. d'Allivy Kelly, C. Hahn, H. Meley, et al., Full control of the spin-wave damping in a magnetic insulator using spin-orbit torque, *Phys. Rev. Lett.* **113**, 197203 (2014).

70. S. I. Kiselev, J. C. Sankey, I. N. Krivorotov, N. C. Emley, et al., Microwave oscillations of a nanomagnet driven by a spin-polarized current. *Nature* **425**, 380 (2003).
71. W. H. Rippard, M. R. Pufall, S. Kaka, S. E. Russek, and T. J. Silva, Direct-current induced dynamics in $\text{Co}_{90}\text{Fe}_{10}/\text{Ni}_{80}\text{Fe}_{20}$ point contacts, *Phys. Rev. Lett.* **92**, 027201 (2004).
72. V. E. Demidov, S. Urazhdin, H. Ulrichs, V. Tiberkevich, et al., Magnetic nano-oscillator driven by pure spin current, *Nat. Mater.* **11**, 1028 (2012).
73. S. Tsunegi, H. Kubota, K. Yakushiji, M. Konoto, et al., High emission power and Q factor in spin torque vortex oscillator consisting of FeB free layer. *Appl. Phys. Express* **7**, 063009 (2014).
74. J. Slonczewski, Excitation of spin waves by an electric current, *J. Magn. Magn. Mater.* **195**, L261 (1999).
75. M. A. Hoefer, M. J. Ablowitz, B. Ilan, M. R. Pufall, and T. J. Silva, Theory of magnetodynamics induced by spin torque in perpendicularly magnetized thin films, *Phys. Rev. Lett.* **95**, 267206 (2005).
76. A. Slavin and V. Tiberkevich, Spin wave mode excited by spin-polarized current in a magnetic nanocontact is a standing self-localized wave bullet, *Phys. Rev. Lett.* **95**, 237201 (2005).
77. A. Slavin and V. Tiberkevich, Nonlinear auto-oscillator theory of microwave generation by spin-polarized current, *IEEE Trans. Magn.* **45**, 1875 (2009).
78. S. Bonetti, V. Tiberkevich, G. Consolo, G. Finocchio, et al., Experimental evidence of self-localized and propagating spin wave modes in obliquely magnetized current-driven nanocontacts. *Phys. Rev. Lett.* **105**, 217204 (2010).
79. S. M. Mohseni, S. R. Sani, J. Persson, T. N. Anh Nguyen, et al., Spin Torque–Generated Magnetic Droplet Solitons, *Science* **339**, 1295 (2013).
80. Z. Duan, A. Smith, L. Yang, B. Youngblood, et al., Nanowire spin torque oscillator driven by spin-orbit torques, *Nat. Commun.* **5**, 5616 (2014).
81. S. Bonetti, R. Kukreja, Z. Chen, F. Macià, et al., Direct observation and imaging of a spin-wave soliton with p-like symmetry, *Nat. Commun.* **6**, 8889 (2015).

РОЗДІЛ 1

**ЗБУДЖЕННЯ СПІНОВИХ ХВИЛЬ НАДВИСОКОЧАСТОТНИМ
ЕЛЕКТРИЧНИМ ПОЛЕМ**

У цьому розділі розглядається питання можливості збудження СХ електричним полем у надтонких феромагнітних плівках та наноструктурах за допомогою ефекту ЕКМА. Необхідно відзначити, що дія змінної в часі магнітної анізотропії, спричинена прикладанням НВЧ електричного поля, далеко не завжди еквівалентна дії НВЧ магнітного поля, тому механізми збудження СХ за допомогою ефекту ЕКМА можуть бути (і саме так і виявляється) суттєво відмінними від тих, які використовуються у класичній магнітоніці з керуванням магнітним полем.

З точки зору практичних застосувань дуже бажано працювати без прикладання постійного статичного магнітного поля, що обмежує вибір можливих конфігурацій статичної намагніченості хвилеводи чи нанoelementу. Як і в майже всіх роботах, присвячених магнітоніці, будемо розглядати випадок однорідної (чи квазіоднорідної) статичної намагніченості, так як такий стан є найбільш детермінованим і відтворюваним, на відміну від різноманітних доменних структур. Надтонкі феромагнітні плівки та хвилеводи, залежно від їх товщини, за відсутності магнітного поля можуть знаходитись у двох насичених станах: з намагніченістю у площині плівки або перпендикулярно цій площині, що пов'язано із впливом поверхневої перпендикулярної магнітної анізотропії^{1,2}. При цьому однорідний перпендикулярний стан є метастабільним у нульовому полі, однак стійким за достатньої величини ефективної анізотропії, а стан з планарною намагніченістю може бути основним станом системи, особливо у випадку достатньо вузьких наносмужок^{1,3}. Також варто відзначити, що перехід до суперпарамагнітного стану за кімнатних температур відбувається при товщинах плівки, менших за 2-3 моношари (0.3-0.4 нм для Fe) внаслідок розбиття плівки на

1 B. Heinrich and J. F. Cochran, Ultrathin metallic magnetic films: Magnetic anisotropies and exchange interactions, *Adv. Phys.* **42**, 523 (1993).

2 H. X. Yang, et al., First-principles investigation of the very large perpendicular magnetic anisotropy at Fe|MgO and Co|MgO interfaces, *Phys. Rev. B* **84**, 054401 (2011).

3 R. Skomski, et al., Micromagnetics of ultrathin films with perpendicular magnetic anisotropy, *Phys. Rev B* **58**, 3223 (1998).

острівці⁴; у роботі розглядаються плівки та наносмужки більших товщин, для яких подібні проблеми відсутні.

Нижче будуть розглянуті обидва можливі статичні стани. Як буде показано, у випадку перпендикулярної намагніченості задача зводиться до відомої задачі параметричного збудження паралельною накачкою, і головне питання у тому, які характерні поля необхідні для збудження і чи можливо їх досягнути. У випадку ж планарної намагніченості ситуація відмінна — хоча збудження теж, виявляється, можливе лише за параметричним механізмом, параметрична взаємодія має особливості, які не спостерігаються при параметричній взаємодії НВЧ магнітного поля зі СХ.

У підрозділі 1.2 розглянуто запорогову динаміку параметрично збуджених СХ у нанорозмірних хвилеводах, яка, як показано, виявляє якісні відмінності від динаміки в об'ємних зразках. Насамкінець, у підрозділі 1.4 представлені результати експериментальних досліджень параметричного резонансу у магнітній наноточці під дією електричного поля, які є першою експериментальною демонстрацією цього ефекту. Хоча збудження стоячих СХ мод у наноточці є дещо простішим за збудження біжучих СХ (менші пороги збудження), є всі підстави вважати реальною можливість збудження саме біжучих СХ за рахунок ЕКМА, особливо із використанням нещодавно відкритих більш ефективних ЕКМА матеріалів. Варто, насамкінець, зазначити, що згодом після публікації цих результатів збудження біжучих СХ за допомогою ЕКМА було реалізовано у випадку підмагніченого хвилеводу, коли можливе лінійне збудження⁵.

Особисто автором дисертації виконані аналітичні та числові розрахунки порогів збудження СХ, розвинута наближена теорія запорогової динаміки СХ, збуджених локалізованою параметричною накачкою, отримані аналітичні залежності амплітуди коливань намагніченості у наноточці під дією параметричної накачки як до порогу збудження, так і за ним. Також автор брав безпосередню участь у розробці методики та обробці даних мікромагнітного моделювання динаміки СХ під впливом ЕКМА, та в обробці й аналізі експериментальних даних по збудженню параметричного резонансу у наноточці НВЧ електричним полем.

4 C. Martínez Boubeta, et al., Coverage effects on the magnetism of FeMgO(001) ultrathin films *Phys. Rev. B* **71**, 014407 (2005).

5 B. Rana, et al., Excitation of coherent propagating spin waves in ultrathin CoFeB film by voltage-controlled magnetic anisotropy, *Appl. Phys. Lett.* **111**, 052404 (2017).

1.1. Пороги збудження у випадку перпендикулярної статичної намагніченості

ХВИЛЕВОДУ

PHYSICAL REVIEW APPLIED 1, 044006 (2014)

Parametric Excitation of Spin Waves by Voltage-Controlled Magnetic Anisotropy

Roman Verba,^{1*} Vasil Tiberkevich,² Ilya Krivorotov,³ and Andrei Slavin²

¹*Institute of Magnetism, Kyiv 03142, Ukraine*

²*Department of Physics, Oakland University, Rochester, Minnesota 48309, USA*

³*Department of Physics and Astronomy, University of California, Irvine, California 92697, USA*
(Received 20 January 2014; revised manuscript received 23 April 2014; published 28 May 2014)

A theory of parametric excitation of spin waves (SWs) in ultrathin ferromagnetic strips by a microwave electric field is developed. The excitation uses the effect of voltage-controlled magnetic anisotropy in ferromagnet-dielectric heterostructures. The characteristic values of the electric field necessary for parametric excitation of propagating SWs of 5–10 GHz frequency in Fe/MgO structure are found to be 0.1–1.5 V/nm. The minimum excitation threshold is achieved in narrow strip (strip width $w_x \sim 10$ –20 nm) for relatively long dipole-dominated SWs. In wider strips ($w_x \gtrsim 100$ nm) electric parametric pumping excites mostly short exchange-dominated SWs having higher excitation thresholds, but substantially wider range of possible SW frequencies.

DOI: [10.1103/PhysRevApplied.1.044006](https://doi.org/10.1103/PhysRevApplied.1.044006)

Information processing in ferromagnetic materials at microwave frequencies is a promising direction in modern functional electronic systems [1,2]. In such systems the amplitude and/or phase of spin waves (SWs) (which are the excitations of magnetic order of a ferromagnetic material) is used as the information signal. SWs as carriers of microwave signals have several important advantages, such as relatively small wavelengths, the possibility to vary their dispersion by both the patterning of the ferromagnetic film [3] and by dynamic manipulation of the external magnetic field [4], and low power thresholds of parametric and nonlinear interactions [5], allowing one to use nonlinear methods of signal processing. One of the main drawbacks of the existing SW technology is that the SW control using magnetic fields involves currents into adjacent conducting lines that create substantial Ohmic losses, limit (through inductances) minimum time constants of the devices, and complicate the compatibility of the SW devices with the conventional voltage-controlled silicon microelectronics.

Thus, it is tempting to find ways to use in the spin-wave electronics magnetoelectric (ME) effects [6], which, in general, allow one to manipulate the magnetization of a ferromagnet or the effective field in it directly by the application of an electric field or voltage. In our opinion, the most promising ME effect that can be used for the control of microwave SWs is the recently discovered effect of voltage-controlled magnetic anisotropy (VCMA) [7–9], which has been already proposed for use in magnetic random-access memory [10,11] and for the control of domain wall motion [12,13]. The VCMA effect takes place in conducting ferromagnetic films. In these films, due to the spin-dependent screening of the applied electric field,

magnetic anisotropy at the surface of a ferromagnetic metal varies with the applied field. The variation of the energy K_s of the surface magnetic anisotropy is linearly proportional to the component of the applied electric field E that is normal to the film surface: $\Delta K_s = \beta_s E$, where β_s is the ME coefficient dependent on the composition and thickness of the ferromagnetic film and the adjacent dielectric layer. We would like to note that such a simple linear relation between the applied signal and the system reaction on it is a very desirable feature for microwave applications.

In this paper we demonstrate theoretically that the VCMA effect driven by external microwave electric fields can be successfully used for the parametric excitation of propagating SWs, and, depending on the device geometry, both relatively long dipole-dominated waves and relatively short exchange-dominated SWs could be excited by this method in thin ferromagnetic strips.

The layout of a device for the excitation of SWs by electric field via the VCMA effect is presented in Fig. 1(a). A ferromagnetic metal (Fe) strip of the width w_x and thickness h grown, typically, on the GaAs(100) substrate is covered by a thin dielectric layer (MgO). The microwave-frequency voltage applied between the top gate electrode and the Fe strip causes the variation of the magnetic anisotropy at the Fe/MgO interface. The VCMA is a pure interface effect [8,14], therefore, it is more pronounced in ultrathin ferromagnetic metal films ($h \sim 1$ nm), which, typically, have perpendicular static magnetization owing to the perpendicular surface magnetic anisotropy [15,16]. Another advantage of the perpendicular static magnetization of a strip for the purpose of microwave signal processing is the possibility to locally control the effective internal bias magnetic field in the ferromagnetic strip by application of a *static* voltage to an additional gate electrode situated in the propagation path of excited

*Corresponding author.
verrv@ukr.net

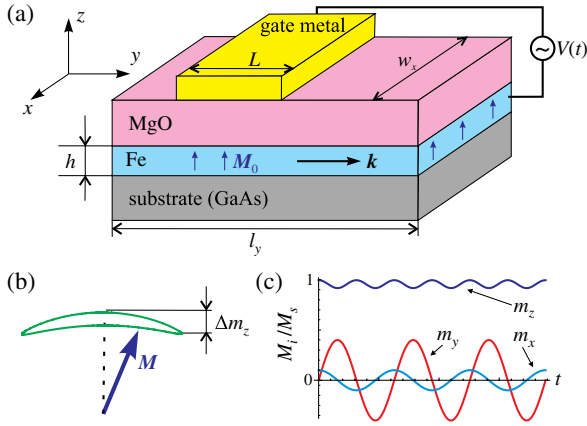


FIG. 1. (a) A layout of a device for the VCMA-induced parametric excitation of propagating SWs. Ferromagnetic metal (Fe) strip having perpendicular static magnetization \mathbf{M}_0 is covered by a dielectric (MgO) layer. The microwave voltage $V(t)$ applied to the gate electrode causes variation of the perpendicular magnetic anisotropy at the Fe/MgO interface. If the gate voltage is above a certain threshold, a SW having the wave vector \mathbf{k} is excited. (b),(c) An illustration showing the magnetization precession over an elliptic trajectory and corresponding time profiles of the in-plane and out-of-plane magnetization components.

SWs. This local variation of the internal magnetic field can lead to a phase shift of the propagating wave or/and to its partial or total reflection.

Since via VCMA one can modulate only the perpendicular component of the anisotropy field (H_z^a , below index z will be omitted), which is parallel to the static magnetization (see Fig. 1), the VCMA effect in unbiased ultrathin magnetic strips cannot be used for the linear excitation of SWs when the frequency of the excited wave is equal to the frequency of the applied voltage. Linear excitation requires a nonzero value of the in-plane (perpendicular to the static magnetization) component of the time-varying effective magnetic field, and in the considered geometry such a situation becomes possible when the static magnetization of the magnetic film is tilted from the perpendicular direction by the application of an external bias magnetic field [17,18].

At the same time, the geometry of an unbiased magnetic strip Fig. 1(a) is ideally suitable for the *parametric* excitation of SWs, when the frequency of the excited wave is twice smaller than the frequency of the applied microwave electric field (the geometry of the “parallel pumping” [5,19]). The mechanism of the parametric excitation can be described as follows: Owing to the thermal fluctuation, the magnetization vector of the film performs stochastic precession around the direction of static equilibrium of the magnetization vector $\mathbf{M}_0 = M_s \mathbf{e}_z$ (M_s is the saturation magnetization of the ferromagnetic film).

If the precession of magnetization with the frequency ω_k (Fourier component of the stochastic precession) goes over an elliptic trajectory (e.g., owing to a film sample shape or its crystallographic anisotropy), it creates a time variation of the longitudinal (m_z) magnetization component with double frequency $2\omega_k$ [see Figs. 1(b) and 1(c)]. The externally driven time-varying effective anisotropy field $\Delta H^a(t) = \Delta H^a e^{-i\omega_p t}$ couples to these out-of plane oscillations of the film magnetization and pumps energy into the magnetic system of the film. This pumping process is efficient (resonant) if the pumping frequency is close to $\omega_p \approx 2\omega_k$. When the pumping amplitude exceeds a certain threshold ΔH_{th}^a determined by the magnetic damping in the film material and the radiation losses (dependent on the size L of the region of pumping localization and on the SW group velocity), it excites a propagating SW of the frequency $\omega_k \approx \omega_p/2$ from the level of thermal fluctuations.

The parametric excitation of SWs by both spatially uniform and localized parallel pumping are extensively discussed in the literature [5,19,20]. In general, magnetization dynamics in ferromagnetic film is described by the well-known Landau-Lifshitz equation [5]. Representing the film magnetization as a sum of static magnetization and a series of propagating SWs having wave vector $\mathbf{k} = k\mathbf{e}_y$, frequency ω_k , damping rate Γ_k , and vector structure $\mathbf{m}_k = m_{k,x}\mathbf{e}_x + m_{k,y}\mathbf{e}_y$,

$$\mathbf{M}(\mathbf{r}, t) = M_s \left[\mathbf{e}_z + \sum_k (c_k \mathbf{m}_k e^{i(ky - \omega_k t)} + \text{c.c.}) \right], \quad (1)$$

one can obtain the following equation for the SW amplitude c_k under the action of parallel parametric pumping [20]:

$$\frac{dc_k}{dt} + i\omega_k c_k + \Gamma_k c_k = \sum_{k'=-\infty}^{\infty} \frac{L}{l_y} V_{kk'} \tilde{h}_{k+k'} e^{-i\omega_p t} c_{k'}^*. \quad (2)$$

Here, \tilde{h}_k is the Fourier image of a spatial profile of a pumping magnetic field [in our case, a profile of the voltage-induced anisotropy field variation along the magnetic strip, $\Delta H^a(y) = 2\beta_s E(y)/(M_s h)$], L and l_y are lengths of the gate electrode and the magnetic strip in the y direction, respectively [see Fig. 1(a)], and the superscript $*$ denotes complex conjugation. Note that in general the SW spectrum of a strip contains a set of SW modes, which differ by the profile along the strip width [i.e., $\mathbf{m}_k = \mathbf{m}_{k,n}(x)$]. However, since the pumping is uniform along the strip width, it does not lead to a coupling between the different SW modes, and dynamics of the SW modes having the same width profile is described by Eq. (2). Below, we restrict our attention to a case of a *lowest* SW mode, that is uniform along the strip width ($\mathbf{m}_k = \text{const}$).

The parameter $V_{kk'}$ is the efficiency of the parametric interaction of pumping and SWs and in the case when the condition $\omega_k = \omega_p/2$ of the exact parametric resonance is

satisfied for a certain SW wave vector $k = k_y$, this parameter is equal to

$$V_{kk} = -i\gamma\mu_0 \frac{\mathbf{m}_k^* \cdot \mathbf{m}_k^*}{2A_k}, \quad (3)$$

where γ is the gyromagnetic ratio of the strip ferromagnetic material, μ_0 is the vacuum magnetic permeability, and $A_k = i(\mathbf{m}_k^* \cdot \mathbf{e}_z \times \mathbf{m}_k)$ is the norm of the SW mode [21,22]. Analogously to Refs. [21,22] the eigenfrequencies ω_k and vectorial amplitudes \mathbf{m}_k of the SW modes existed in a ferromagnetic strip could be found from the solution of the eigenvalue problem $-i\omega_k \mathbf{m}_k = \mathbf{e}_z \times \hat{\Omega}_k \cdot \mathbf{m}_k$. The Hamiltonian tensor for linear SW excitations over the ground state $\mathbf{M} = M_s \mathbf{e}_z$ in our case of a thin magnetic strip of a finite width w_x has the form

$$\hat{\Omega}_k = \gamma(B + \mu_0 M_s \lambda_{\text{ex}}^2 k^2) \hat{\mathbf{I}} + \omega_M \hat{\mathbf{F}}_k. \quad (4)$$

Here $\omega_M = \gamma\mu_0 M_s$, λ_{ex} is the exchange length in the strip material and $B = 2K_s/(hM_s) - \mu_0 M_s N_0^{zz}$ is the static internal magnetic field in the strip, which consists of the effective anisotropy field (K_s is the surface anisotropy energy at zero applied gate voltage) and the demagnetization field (\hat{N}_0 is the demagnetization tensor of the strip).

The dynamic demagnetization tensor $\hat{\mathbf{F}}_k$, which depends on the strip width and height, has the form

$$\hat{\mathbf{F}}_k = \int_{-\infty}^{\infty} \frac{\sin^2[kw_x/2]}{k^2 w_x} \hat{\mathbf{N}}_k \frac{dk_x}{2\pi}. \quad (5)$$

The tensor $\hat{\mathbf{N}}_k$ in the above equation is defined by the expressions $N_k^{(\alpha\beta)} = k_\alpha k_\beta f(kh)/k^2$ for $\alpha, \beta = x, y$, $N_k^{(zz)} = 1 - f(kh)$, where $f(kh) = 1 - (1 - \exp[-kh])/kh$, all the other components of $\hat{\mathbf{N}}_k$ are equal to zero.

We note that the *finite width* w_x of the ferromagnetic strip in this problem is critically important. Indeed, in an infinite perpendicularly magnetized magnetic film the SW spectrum is isotropic, and waves with the same absolute value of the wave vector have the same frequency, damping rate and efficiency of parametric interaction. The difference between the directions of wave propagation could be introduced only by the shape of the gate electrode. If the gate electrode is a metal strip [as in Fig. 1(a)], the SWs propagating *along* the gate electrode will have the lowest threshold of parametric excitation owing to the vanishing radiation losses (waves never leave the region of pumping localization). Consequently, the waves propagating in other directions cannot be excited before the amplitude of the pumping signal exceeds a significantly higher threshold [5]. Naturally, such a case is not suitable for signal processing using propagating SWs, as for that purpose SWs excited by one gate should be processed in the film strip by another gate, and, then, received by the output gate. Thus, instead of infinite films we need to use strips of a

finite width, that should be smaller than the SW mean free path in the strip material, so that *only* the SW modes with the direction of propagation along the strip (k_y) are formed.

As mentioned above, the threshold E_{th} of parametric excitation depends both on the SW damping rate and on the length L of the pumping localization. Let us, first of all, ignore the finite length L of the gate electrode and consider the lowest possible excitation threshold of SWs, determined only by the SW damping $\Gamma_k = \alpha_G \omega_k + \Delta\omega_{\text{nu}}$, which consists of the homogeneous damping (α_G is the Gilbert damping constant) and the nonhomogeneous line broadening characterized by the parameter $\Delta\omega_{\text{nu}}$. In the case of a parametric resonance ($\omega_p/2 = \omega_k$) the threshold is given by the expression [5]: $\Delta H_{\text{th}}^a = \Gamma_k/|V_{kk}|$. The corresponding threshold magnitude of the applied microwave electric field is expressed as $E_{\text{th}} = \mu_0 \Delta H_{\text{th}}^a M_s h / (2\beta_s)$. These minimum threshold electric fields $E_{\text{th}}(k_y)$ as functions of the SW wave number k_y are shown in Fig. 2 for different values of the waveguide width w_x .

A typical dependence $E_{\text{th}}(k_y)$ has two local minima—one at $k_y = 0$ and the other at a higher value of the wave vector (see, e.g., a dashed line in Fig. 2). Such a dependence finds a natural explanation if one recalls that the parametric interaction efficiency is proportional to the precession ellipticity of the SW mode. At a small value of k_y , the precession ellipticity is determined by the in-plane shape anisotropy of the waveguide, and the long axis of the precession ellipse is directed along the waveguide. With the increase of k_y , the dynamic demagnetization along the y axis (component $F_k^{(yy)}$) also increases, and at some k_y becomes equal to the $F_k^{(xx)}$. At this point the precession is almost circular, and the excitation threshold is infinite ($V_{kk} = 0$). At higher k_y , the precession ellipticity becomes larger again owing to the influence of $F_k^{(yy)}$, that leads to the decrease of the threshold. Finally, with further increase of k_y the properties of the excited SW mode are mainly

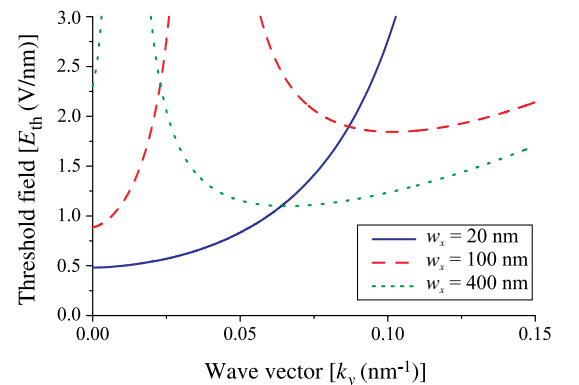


FIG. 2. Threshold electric field for the parametric excitation of SWs with the wave vector k_y for different waveguide widths w_x . Calculation parameters: Fe film of the thickness $h = 0.75$ nm ($M_s = 2.1$ T, $\lambda_{\text{ex}} = 3.4$ nm, $K_s = 1.36$ mJ/m², $\alpha_G = 0.004$, $\Delta\omega_{\text{nu}} = 2\pi \times 230$ MHz, $\beta_s = 100$ fJ/V m) [15,16,23].

determined by the exchange interaction which is isotropic, leading to the vanishing of the SW ellipticity and increase of E_{th} . Naturally, the characteristic value of the wave vector k_y at which the SW polarization becomes circular depends on the strip width w_x —at larger widths $w_x \gg h$ the point of circular polarization approaches $k_y = 0$ and the value of the parametric threshold at $k_y = 0$ increases significantly (see dotted line corresponding to $w_x = 400$ nm in Fig. 2).

The values of the parametric excitation threshold in certain limiting cases can be estimated analytically. When considering the local minimum of the parametric threshold taking place at zero wave number $k_y = 0$ we use the long-wave approximation for the dynamic demagnetization tensor \hat{F}_k . In this limit the only nonvanishing component of this tensor has the form

$$F_0^{(xx)} = 1 - F_0^{(zz)} \approx \frac{h}{2\pi w_x} \left(3 - 2 \ln \frac{h}{w_x} \right). \quad (6)$$

The SW frequency in this case is given by the expression $\omega_0^2 = \gamma B(\gamma B + \omega_M F_0^{(xx)})$, and the efficiency of the parametric interaction is $|V_{00}| = \gamma \mu_0 \omega_M F_0^{(xx)} / 4\omega_0$. Consequently, the threshold of parametric excitation is expressed as

$$E_{\text{th}} = 2 \frac{\mu_0 M_s^2 h}{\beta_s} \left(\alpha_G + \frac{\Delta \omega_{\text{nu}}}{\omega_0} \right) \frac{\omega_0}{\omega_M F_0^{(xx)}}. \quad (7)$$

For the case of a wide magnetic strip we can neglect the finiteness of the waveguide width in the expression Eq. (5) (at least for the lowest SW mode, that is uniform along the strip width) and use the approximation $\hat{F}_k \approx \hat{N}_k$ with $\mathbf{k} = k_y \mathbf{e}_y$. We can also use the exchange approximation for the SW spectrum, $\omega_k = \gamma B + \omega_M \lambda_{\text{ex}}^2 k^2$ since the second local minimum of the parametric threshold is located, typically, in the region $k_y h \ll 1$ (see Fig. 2), where the dynamic demagnetization is small and important only for the calculations of the SW ellipticity. The efficiency of the parametric interaction in this case can be estimated as $|V_{kk}| = \gamma \mu_0 \omega_M f(kh) / 4\omega_k$. Within these approximations one can show that the dependence $E_{\text{th}}(k_y)$ has a minimum at the point $k_y = \sqrt{\gamma B / 3\omega_M} / \lambda_{\text{ex}}$, and the corresponding minimum value of the parametric threshold is

$$E_{\text{th}} = 8 \frac{\mu_0 M_s^2 h}{\beta_s} \left(\alpha_G + \frac{\Delta \omega_{\text{nu}}}{\omega_k} \right) \frac{\lambda_{\text{ex}}}{h} \left(\frac{\omega_k}{\omega_M} \right)^{3/2}. \quad (8)$$

As one can see from Eqs. (7) and (8), the threshold of the parametric excitation has a power-law dependence on the SW frequency ω_k in the both above considered limiting cases. Since ω_k depends on the magnitude of the static internal magnetic field in the waveguide, which, in turn, depends on the waveguide width (via the size-dependent static demagnetization tensor \hat{N}_0), the dependence of the

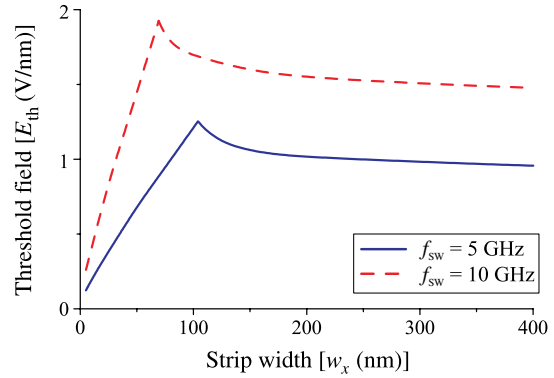


FIG. 3. Minimum threshold electric field for the parametric excitation of SWs as a function of the width w_x of the Fe waveguide for different frequencies f_{SW} of the excited SWs. Parameters of calculation, apart from the Fe film thickness (see text) are the same as in Fig. 2.

minimum parametric threshold on the waveguide width at a constant film thickness will be rather complex and noninformative. Instead, it would be more useful to plot the dependence $E_{\text{th}}(w_x)$ at a given value of the SW frequency. To get this dependence at each waveguide width w_x we chose the film thickness to minimize the parametric excitation threshold at a given frequency of the excited SW. These curves are shown in Fig. 3.

For each excitation frequency the dependence $E_{\text{th}}(w_x)$ has two qualitatively different regions. In the first region of the smaller waveguide widths the lowest parametric excitation threshold takes place for long SWs ($k \rightarrow 0$). In this first region the threshold almost linearly increases with the waveguide width, which is explained by the decrease of waveguide shape anisotropy and, consequently, the decrease of the precession ellipticity in the excited SW mode. The second region, after the inflection point in the dependence $E_{\text{th}}(w_x)$ (see Fig. 3), corresponds to the second local minimum of the parametric threshold shown in Fig. 2. In this region the threshold of parametric excitation decreases slightly with the increase of the waveguide width w_x and approaches the asymptotic value given by Eq. (8). The exact position of the inflection point separating these two regions depends on the frequency of the excited SW mode, and for larger SW frequencies it corresponds to narrower waveguides.

The lowest threshold at a given SW frequency is achieved for narrow waveguides having width $w_x \sim 10$ – 20 nm, which currently are rather difficult to fabricate. However, for such waveguides typical values of the threshold lie in the range 0.1 – 0.5 V/nm that could be easily realized in experiment. In this case relatively long dipole-dominated SWs will be excited parametrically, and, due to a weak dependence $\omega(k_y)$ the threshold electric field E_{th} strongly depends on the SW frequency (see solid line in Fig. 4). This property may create a significant difficulty when working with modulated electric signals having relatively wide modulation spectra—for such signals the

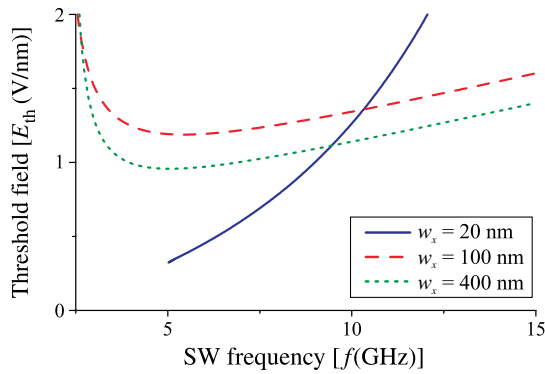


FIG. 4. Threshold electric field for the parametric excitation of SWs as a function of the SW frequency for different waveguide widths. The strip thickness for each w_x is chosen so that E_{th} is minimum for SW of 5 GHz frequency.

parametrically excited SW signal will be a nonlinear function of the gate voltage.

In contrast, when working with wider waveguides and shorter exchange-dominated SWs (second region in Fig. 3) this problem is absent since the threshold electric field is only weakly dependent on the frequency of the excited SW mode, as it is illustrated by Fig. 4. In particular, for the waveguide of the width $w_x = 400$ nm (see dotted line in Fig. 4) the parametric threshold varies by less than 10% in the SW frequency interval from 3.5 to 8.5 GHz. However, the price for this large working frequency band is a much larger parametric excitation threshold than in the case of narrower waveguides.

Now we discuss the influence of the finite gate length L [see Fig. 1(a)] on the parametric threshold. The spatial localization of the parametric pumping leads to the threshold increase due to the additional radiation losses of the excited SWs. These radiation losses are directly proportional to the SW group velocity v_{gr} and inversely proportional to the length of the pumping localization: $\Gamma_{rad} = Cv_{gr}/L$, where coefficient $C \in [1, \pi]$ depends on the ratio k_y/L [19,20]. The threshold of parametric excitation is determined by the total effective damping, $\Gamma_{tot} = \sqrt{\Gamma_k^2 + \Gamma_{rad}^2}$ [see Eq. (6.5.16) in Ref. [19]]. In the long-wavelength limit the SW group velocity can be roughly estimated as $v_{gr} \approx \omega_M h/4$ (group velocity of SW in a perpendicularly magnetized film [5]), that is of the order of $v_{gr} \sim 70$ m/s. Consequently, the radiation losses become smaller than the natural magnetic losses when the gate length $L \gtrsim 50$ –100 nm. On the other hand, when using a wide magnetic waveguide the acceptable value of the gate length L is significantly larger, $L \gtrsim 500$ nm, which is related to the larger group velocity of short exchange-dominated SWs. In both cases the value of L acceptable for signal processing applications is comparable to the width of a magnetic waveguide.

Finally, we should recall that we considered above the excitation of the lowest SW mode, that is uniform along the strip width. For narrow magnetic waveguides the higher width modes could be disregarded simply due to their significantly larger eigenfrequencies. On the other hand, for a wide waveguide the frequency distance between the different width modes is small, and the resonance condition $\omega_p = 2\omega_{k,n}$ could be satisfied for several width SW modes simultaneously. The detailed analysis of such a case could be a subject of a separate article and lies beyond the scope of this work.

In conclusion, we consider the parametric excitation of SWs in ultrathin ferromagnetic strips by a microwave electric field via the VCMA effect. It is found that the lowest threshold of the parametric excitation could be achieved for relatively long dipole-dominated SWs propagating in narrow magnetic waveguides having a width of the order of tens of nanometers. The corresponding value of the threshold electric field applied to the Fe/MgO interface is about 0.1–0.5 V/nm for the excitation of SWs having a frequency of the order of 5–10 GHz. In a wide magnetic strip ($w_x \gtrsim 100$ nm) it becomes more suitable to excite short exchange-dominated SWs having the wavelengths of the order of several tens of nanometers. Although the magnitude of the parametric excitation threshold in this case increases up to 1–2 V/nm for the same material, the threshold in this regime has a weak dependence on the SW frequency which allows one to work with modulated pumping signal having a relatively wide modulation spectrum. Finally, we note that, although the presented results are obtained for one particular heterostructure (Fe/MgO), these results qualitatively apply to other magnetic materials. In particular, for widely used CoFeB/MgO structures [24] one should expect a simple increase of the parametric threshold value by 2–3 times due to the smaller magnetoelectric coefficient [9].

We acknowledge the Center for NanoFerroic Devices (CNFD) and the Nanoelectronics Research Initiative (NRI) for partial funding of this work. The work was also supported by the U.S. National Science Foundation (Grants No. ECCS-1305586, No. DMR-1015175, No. DMR-1210850, No. ECCS-1309416), by the MTO/MESO Grant No. N66001-11-1-4114 from DARPA, and by contracts from the U.S. Army TARDEC, RDECOM.

- [1] D. D. Stancil and A. Prabhakar, *Spin Waves. Theory and Applications* (Springer, New York, 2009).
- [2] *Advanced Magnetic Nanostructures*, edited by D. J. Sellmyer and R. Skomski (Springer, New York, 2006).
- [3] S. Neusser and D. Grundler, Magnonics: Spin waves on the nanoscale, *Adv. Mater.* **21**, 2927 (2009).
- [4] A. V. Chumak, V. S. Tiberkevich, A. D. Karenowska, A. A. Serga, J. F. Gregg, A. N. Slavin, and B. Hillebrands,

- All-linear time reversal by a dynamic artificial crystal, *Nat. Commun.* **1**, 141 (2010).
- [5] A. G. Gurevich and G. A. Melkov, *Magnetization Oscillations and Waves* (CRC Press, New York, 1996).
- [6] M. Fiebig, Revival of the magnetoelectric effect, *J. Phys. D* **38**, R123 (2005).
- [7] M. Weisheit, S. Fähler, A. Marty, Y. Souche, C. Poinson, and D. Givord, Electric field-induced modification of magnetism in thin-film ferromagnets, *Science* **315**, 349 (2007).
- [8] C.-G. Duan, J. P. Velev, R. F. Sabirianov, Z. Zhu, J. Chu, S. S. Jaswal, and E. Y. Tsymlal, Surface magnetoelectric effect in ferromagnetic metal films, *Phys. Rev. Lett.* **101**, 137201 (2008).
- [9] M. Endo, S. Kanai, S. Ikeda, F. Matsukura, and H. Ohno, Electric-field effects on thickness dependent magnetic anisotropy of sputtered MgO/Co₄₀Fe₄₀B₂₀/Ta structures, *Appl. Phys. Lett.* **96**, 212503 (2010).
- [10] Y. Shiota, T. Nozaki, F. Bonell, S. Murakami, T. Shinjo, and Y. Suzuki, Induction of coherent magnetization switching in a few atomic layers of FeCo using voltage pulses, *Nat. Mater.* **11**, 39 (2012).
- [11] W.-G. Wang, M. Li, S. Hageman, and C. L. Chien, Electric-field-assisted switching in magnetic tunnel junctions, *Nat. Mater.* **11**, 64 (2012).
- [12] U. Bauer, S. Emori, and G. S. D. Beach, Voltage-gated modulation of domain wall creep dynamics in an ultrathin metallic ferromagnet, *Appl. Phys. Lett.* **101**, 172403 (2012).
- [13] A. Bernard-Mantel, L. Herrera-Diez, L. Ranno, S. Pizzini, J. Vogel, D. Givord, S. Auffret, O. Boulle, I. M. Miron, and G. Gaudin, Electric-field control of domain wall nucleation and pinning in a metallic ferromagnet, *Appl. Phys. Lett.* **102**, 122406 (2013).
- [14] M. Tsujikawa and T. Oda, Finite electric field effects in the large perpendicular magnetic anisotropy surface Pt/Fe/Pt(001): A first-principles study, *Phys. Rev. Lett.* **102**, 247203 (2009).
- [15] R. Urban, G. Woltersdorf, and B. Heinrich, Gilbert damping in single and multilayer ultrathin films: Role of interfaces in nonlocal spin dynamics, *Phys. Rev. Lett.* **87**, 217204 (2001).
- [16] H. X. Yang, M. Chshiev, B. Dieny, J. H. Lee, A. Manchon, and K. H. Shin, First-principles investigation of the very large perpendicular magnetic anisotropy at Fe|MgO and Co|MgO interfaces, *Phys. Rev. B* **84**, 054401 (2011).
- [17] T. Nozaki, Y. Shiota, S. Miwa, S. Murakami, F. Bonell, S. Ishibashi, H. Kubota, K. Yakushiji, T. Saruya, A. Fukushima, S. Yuasa, T. Shinjo, and Y. Suzuki, Electric-field-induced ferromagnetic resonance excitation in an ultrathin ferromagnetic metal layer, *Nat. Phys.* **8**, 491 (2012).
- [18] J. Zhu, J. A. Katine, G. E. Rowlands, Y.-J. Chen, Z. Duan, J. G. Alzate, P. Upadhyaya, J. Langer, P. K. Amiri, K. L. Wang, and I. N. Krivorotov, Voltage-induced ferromagnetic resonance in magnetic tunnel junctions, *Phys. Rev. Lett.* **108**, 197203 (2012).
- [19] V. S. L'vov, *Wave Turbulence Under Parametric Excitation* (Springer-Verlag, New York, 1994).
- [20] G. A. Melkov, A. A. Serga, V. S. Tiberkevich, Yu. V. Kobljanskij, and A. N. Slavin, Nonadiabatic interaction of a propagating wave packet with localized parametric pumping, *Phys. Rev. E* **63**, 066607 (2001).
- [21] V. V. Naletov, G. de Loubens, G. Albuquerque, S. Borlenghi, V. Cros, G. Faini, J. Grollier, H. Hurdequint, N. Locatelli, B. Pigeau, A. N. Slavin, V. S. Tiberkevich, C. Ulysse, T. Valet, and O. Klein, Identification and selection rules of the spin-wave eigenmodes in a normally magnetized nanopillar, *Phys. Rev. B* **84**, 224423 (2011).
- [22] R. V. Verba, Spin waves in arrays of magnetic nanodots with magnetodipolar coupling, *Ukr. J. Phys.* **58**, 758 (2013) [<http://ujp.bitp.kiev.ua/files/journals/58/8/580808p.pdf>].
- [23] M. K. Niranjana, C.-G. Duan, S. S. Jaswal, and E. Y. Tsymlal, Electric field effect on magnetization at the Fe/MgO(001) interface, *Appl. Phys. Lett.* **96**, 222504 (2010).
- [24] T. Devolder, P.-H. Ducrot, J.-P. Adam, I. Barisic, N. Vernier, Joo-Von Kim, B. Ockert, and D. Ravelosona, Damping of Co_xFe_{80-x}B₂₀ ultrathin films with perpendicular magnetic anisotropy, *Appl. Phys. Lett.* **102**, 022407 (2013).

SCIENTIFIC REPORTS

OPEN

Excitation of propagating spin waves in ferromagnetic nanowires by microwave voltage-controlled magnetic anisotropy

Received: 11 October 2015

Accepted: 05 April 2016

Published: 26 April 2016

Roman Verba¹, Mario Carpentieri², Giovanni Finocchio³, Vasil Tiberkevich⁴ & Andrei Slavin⁴

The voltage-controlled magnetic anisotropy (VCMA) effect, which manifests itself as variation of anisotropy of a thin layer of a conductive ferromagnet on a dielectric substrate under the influence of an external electric voltage, can be used for the development of novel information storage and signal processing devices with low power consumption. Here it is demonstrated by micromagnetic simulations that the application of a microwave voltage to a nanosized VCMA gate in an ultrathin ferromagnetic nanowire results in the parametric excitation of a propagating spin wave, which could serve as a carrier of information. The frequency of the excited spin wave is twice smaller than the frequency of the applied voltage while its amplitude is limited by 2 mechanisms: (i) the so-called “phase mechanism” described by the Zakharov-L’vov-Starobinets “S-theory” and (ii) the saturation mechanism associated with the nonlinear frequency shift of the excited spin wave. The developed extension of the “S-theory”, which takes into account the second limitation mechanism, allowed us to estimate theoretically the efficiency of the parametric excitation of spin waves by the VCMA effect.

Electric field control of magnetization in ferromagnets attracts a lot of attention of researchers in magnetism as it makes possible the development of novel magnetic recording and signal processing devices having low power consumption and compatible with standard CMOS technology. The electric field control could be realized using different magnetoelectric effects (see, e.g. review refs 1 and 2), among which of a particular interest is the recently discovered effect of the voltage-controlled magnetic anisotropy (VCMA)^{3–5}. The VCMA effect manifests itself as a variation of the *perpendicular* magnetic anisotropy at the interface between a ferromagnetic metal and an insulator under the application of an interface voltage. This effect has many attractive features, including linearity (variation of the anisotropy energy is directly proportional to the applied voltage)^{4,6}, absence of a hysteresis^{7,8}, possibility of relatively large variations of the anisotropy field^{9,10} and practical absence of inertia (at least, in the gigahertz frequency range)^{11,12}. These features make VCMA promising for various practical applications. In particular, the VCMA effect has been already proposed for use in magnetic recording^{13–15}, control of motion of domain walls^{16–18} and skyrmions¹⁹, and for excitation of a ferromagnetic resonance^{11,12,20}.

Recently, we have demonstrated analytically²¹ that by applying to a ferromagnetic metal - insulator interface a microwave voltage of a frequency $\omega_p = 2\pi f_p$ and a sufficient magnitude, it is possible to overcome the threshold of parametric excitation of half-frequency ($\omega_{SW} = \omega_p/2$) short spin waves (SWs) in ferromagnetic nanowires (at the same time, the linear excitation of SWs by VCMA, when $\omega_{SW} = \omega_p$, in a *zero bias magnetic field* is not possible^{12,21,22}). This means that the VCMA effect could be promising for excitation of propagating SWs in unbiased nanosized magnetic waveguides, where these SWs can be used for microwave signal processing.

It should be noted, however, that overcoming the parametric excitation threshold does not guarantee a stable excitation of propagating SWs. In the externally driven parametric process the excitation of monochromatic half-frequency propagating SWs could be hindered by many connected parasitic nonlinear phenomena, such as modulational instability, auto-oscillations and even developed turbulence of parametrically excited SWs²³. The

¹Institute of Magnetism, National Academy of Sciences of Ukraine, Kyiv 03142, Ukraine. ²Department of Electrical and Information Engineering, Politecnico of Bari, I-70125 Bari, Italy. ³Department of Electronic Engineering, Industrial Chemistry and Engineering, University of Messina, I-98166 Messina, Italy. ⁴Department of Physics, Oakland University, Rochester, MI 48309, USA. Correspondence and requests for materials should be addressed to R.V. (email: verrv@ukr.net)

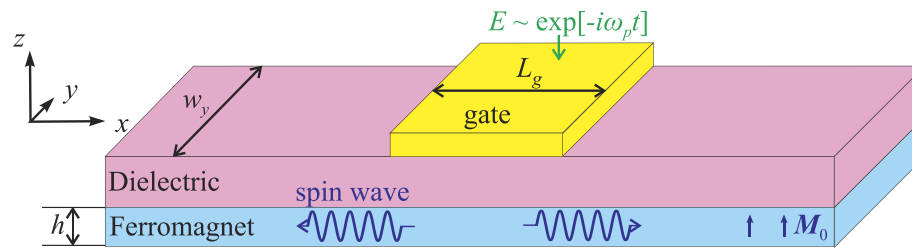


Figure 1. Considered system. A layout of a ferromagnetic nanowire spin wave waveguide grown on a dielectric layer and having a spatially localized conductive excitation (input) gate.

exact manifestation of these nonlinear phenomena depends on the strength of the microwave driving signal, SW spectrum of a magnetic sample and peculiarities of the parametric interaction between the driving signal and parametric SWs in a given sample geometry.

The conditions necessary for a stable parametric excitation of SWs were studied in details for two- and three-dimensional geometry in the case of spatially uniform parametric pumping in the framework of the so-called L'vov-Zakharov-Starobinets "S-theory"^{23–25}. The "S-theory" shows that the amplitudes of the excited SWs are limited by the "phase mechanism"²³, which is the disappearance of the phase correlation between the pumping signal and the excited SWs due to the nonlinear interaction between the SWs. The "S-theory" allows one to calculate the SW amplitudes, thus providing a theoretical estimate for the parametric excitation efficiency. Unfortunately, the conclusions of the conventional "S-theory"²³ cannot be directly translated to our case of VCMA-induced parametric excitation of SWs, where the ferromagnetic sample has to be quasi-one-dimensional (nanowire) in order to guarantee a definite direction of the SW propagation²¹, and the microwave parametric pumping is localized in the region of the VCMA gate electrode.

In our current work we study the peculiarities of the parametric excitation of SWs at a VCMA interface using the micromagnetic simulations. As it is shown below, in a real nanowire geometry the achievable magnitudes of the electric field of the microwave parametric pumping could reach the magnitudes that not only are above the threshold of parametric excitation, but are sufficient to sustain a stable generation of SWs propagating far away from the region of pumping localization and having narrow frequency linewidth. The comparison of our simulation results with the analytical results obtained using the modified "S-theory" demonstrates that in one-dimensional nanoscale ferromagnets the amplitudes of the parametrically excited SWs are limited not only by the classical "phase mechanism" (characteristic for the "S-theory" in bulk ferromagnets²³), but, also, by an additional limiting mechanism caused by the dependence of the SW group velocity on the SW amplitude, which appears due to a non-zero nonlinear SW frequency shift.

Results

Micromagnetic simulations. A sketch of a particular SW waveguide geometry used in our micromagnetic simulations is shown in Fig. 1. We consider a nanowire waveguide of the thickness h and width w_y , made from a conductive ferromagnetic material and grown on a thin MgO dielectric layer. Note, that since VCMA is a purely interface effect^{4,5,8}, the nanowire should be ultrathin ($h \sim 1\text{nm}$), and, owing to the perpendicular growth anisotropy, ultrathin magnetic nanowires and films in a zero bias magnetic field, typically, exist in the static magnetic state in which the film magnetization is directed out-of-plane^{26,27}. This magnetic configuration will be considered below.

On top of the nanowire there is a conductive excitation (or input) gate, which creates a microwave electric field E at the VCMA dielectric-ferromagnetic interface. This electric field drives microwave oscillation of the perpendicular interface anisotropy $K_{s,\perp} = \beta E$ (where β is the magnetoelectric coefficient). The input gate covers only a part of the length L_g of the nanowire waveguide. In such a geometry the SWs excited at the input gate could propagate outside the input gate region, where they could be influenced by other gates performing signal processing functions and, eventually, received by an output gate.

First, we performed the simulations for a CoFeB nanowire of the thickness $h = 0.8\text{ nm}$, width $w_y = 20\text{ nm}$ with a gate length of $L_g = 40\text{ nm}$ (see Methods). It is known²¹, that in a narrow nanowire waveguide the excitation threshold is lower than in a wider waveguides, and, therefore, the SW parametric excitation efficiency should be higher. The magnitude of the microwave anisotropy field was fixed at $\Delta B_a = 50\text{ mT}$, which corresponds to the experimentally reachable magnitude of the electric field $E = 0.78\text{ V/nm}$ ($\beta = 37\text{ fJ/V} \cdot \text{m}$)¹², while the frequency f_p of this field was varied.

In our simulations the in-plane components of the variable nanowire magnetization (normalized by the static magnetization M_s) were calculated under the center of the excitation gate as functions of the pumping frequency f_p . These curves are shown in Fig. 2(a). It is clear that in the range $f_p \in [4.73, 4.86]\text{ GHz}$ the amplitude of the excited magnetization precession significantly exceeds the thermal fluctuation level. The difference between the x and y components of the variable magnetization, i.e. nonzero precession ellipticity, naturally appears due to the in-plane shape anisotropy of the nanowire, and this ellipticity remains almost constant within frequency range of parametric excitation. Frequency spectrum of the excited magnetization precession contains one dominant peak (Fig. 2(b)), the maximum of which is located *exactly* at the half of the pumping frequency f_p (Fig. 2(d)). This means that the microwave voltage applied to the excitation gate leads to the *parametric* excitation of SWs. Note, that the frequency distribution of excited SWs is very narrow—its width (half width at half maximum, HWHM) is

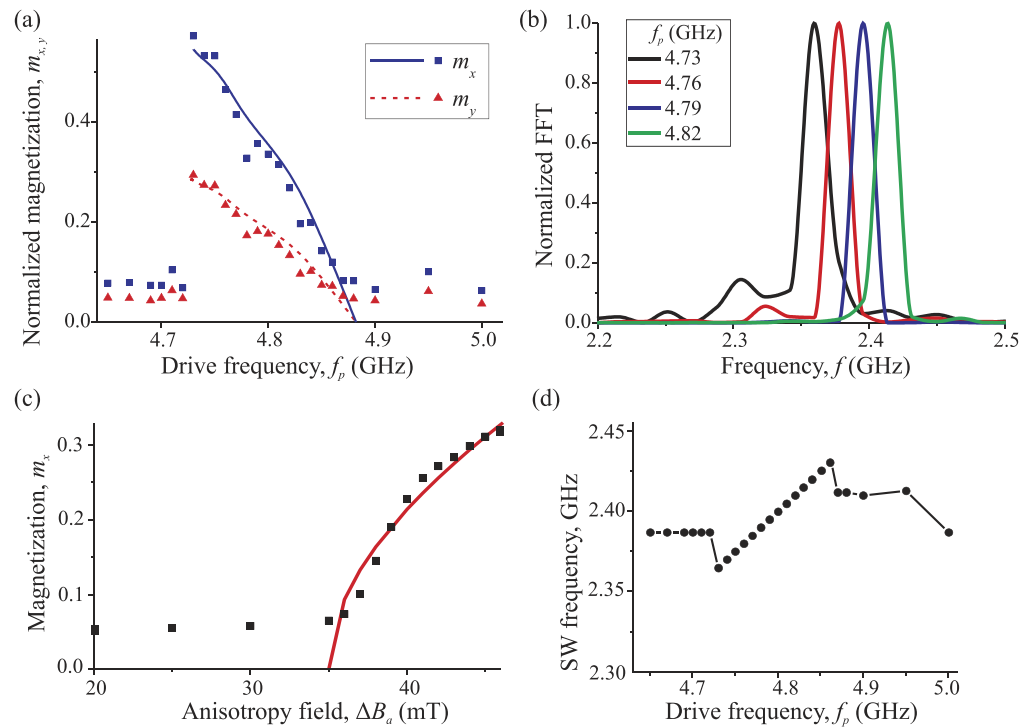


Figure 2. Amplitude and frequency of the excited spin waves. Normalized in-plane components $m_{x,y} = M_{x,y}/M_s$ of the variable nanowire magnetization under the center of the excitation gate as functions of the pumping frequency for $\Delta B_a = 50$ mT, wire width $w_y = 20$ nm and gate length $L_g = 40$ nm (a) and m_x as a function of the pumping amplitude ΔB_a at $f_p = 4.8$ GHz (c): symbols - micromagnetic simulations, lines - analytical theory. The frequency spectra of the micromagnetically calculated magnetization precession under the gate region and the position of their maximums as a function of the pumping frequency f_p are presented in the frames (b,d), respectively.

equal to 9–13 MHz. This is several times smaller than in the case of SWs of the same frequency excited linearly (i.e. by the in-plane microwave field), when $\text{HWHM} = \sqrt{3} \alpha_G f_{\text{SW}} = 41$ MHz. When the amplitude of the magnetization oscillations becomes larger, smaller additional peaks appear in the frequency spectrum (see curve for $f_p = 4.73$ GHz in Fig. 2(b)). However, even in that case of higher amplitude of the excited SWs the parametric excitation process remains stable, which is confirmed by the existence of only one dominant peak in the frequency spectrum of the excited SWs.

For a fixed pumping frequency the SW are excited, as expected, only above a certain threshold pumping magnitude ΔB_{th} , and above this threshold the SW amplitude increases monotonically (Fig. 2(c)). The threshold depends on the excitation frequency, mainly due to the frequency dependence of the SW group velocity (see Eq. (2)). In particular, the parametric excitation is absent for $f_p > 4.86$ GHz because at higher frequencies the threshold becomes larger than the applied pumping amplitude $\Delta B_a = 50$ mT. At the pumping frequencies below 4.73 GHz the parametric excitation is also absent, but for a different reason. For $f_p < 4.73$ GHz half of the pumping frequency lies below the bottom of the SW spectrum in the nanowire and, therefore no propagating SW can be excited parametrically in this frequency range at all.

However, when the pumping frequency is larger than $f_p > 4.73$ GHz, the pumping excites *propagating* SWs moving along the nanowire in both directions from the excitation gate. This is clearly illustrated by Fig. 3 where three instantaneous magnetization distributions in the nanowire, corresponding to three moments separated by a quarter of a period of the magnetization precession, are presented. It is clear that the maximum of the precession amplitude moves away from the gate region and propagates for a distance that is significantly larger than the gate length. The wave number of the excited SWs depends on the excitation frequency—in the considered geometry of a nanowire with perpendicular static magnetization a higher pumping frequency f_p corresponds to a higher SW wave number k . The shortest SW excited in the considered case at $f_p = 4.86$ GHz has the wave number $k \approx 8 \mu\text{m}^{-1}$. The determination of the SW wave number for $f_p = 4.73$ GHz is complicated, since the SW propagation length is comparable to the SW wavelength, so that the propagation maxima and minima of the dynamical magnetization are not clearly distinguishable. However, it should be noted, that, rather unexpectedly, even for this lowest excitation frequency, that should correspond to the excitation of a ferromagnetic resonance²¹, the propagation of SWs having a non-zero wave vector is seen (Fig. 3(a)). This unexpected feature will be explained below.

Note also, that, as always for the parametric excitation in a continuous media, SW wave number depends only on the pumping frequency and, due to the nonlinear frequency shift, on the pumping amplitude (see below), but not on the length of the excitation gate L_g . The propagation length $l_p = v/\Gamma$ of the excited SWs depends on their

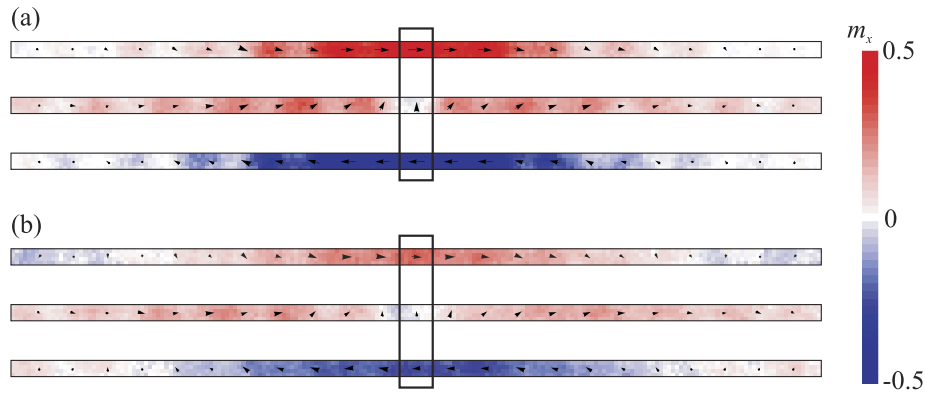


Figure 3. Spin wave profiles. Micromagnetic snapshots of the distributions of variable magnetization in a nanowire near the pumping gate at the moments separated by a time intervals equal to the quarter of the magnetization precession period. A part of the nanowire waveguide of the length equal to $1 \mu\text{m}$ is shown around the pumping gate, which is indicated by a black rectangle. The pumping frequency is $f_p = 4.73 \text{ GHz}$ (a) and $f_p = 4.8 \text{ GHz}$ (b), while the pumping amplitude is $\Delta B_a = 50 \text{ mT}$.

wave number—it increases with k , since the SW group velocity v increases with k faster than the SW damping rate Γ (until $k < \sqrt{\omega_0/(\gamma\mu_0 M_s)}/\lambda_{ex}$, where ω_0 is the ferromagnetic resonance frequency. Otherwise the opposite relation takes place).

From Fig. 3 one can also see that the excited SWs are uniform across the nanowire width. This is absolutely natural, since for such a narrow nanowire all the SW modes that are nonuniform across the nanowire width have much higher frequencies f_{SW} , which simply don't satisfy the parametric resonance condition $f_{SW} = f_p/2$. For much wider nanowires (hundreds of nanometers in width) the resonant condition could be satisfied for several SW modes having different profiles across the nanowire width. In this case the parametric pumping could excite a nonuniform mode—this depends on the interplay between the SW radiation losses and the coupling with pumping (e.g. see an example in ref. 28).

Theory. In order to find an explanation to the features of the SW excitation process seen in the numerical modeling and to derive an approximate analytical expression for the SW excitation efficiency we developed a theoretical model presented below. We start from the system of modified Bloembergen equations describing the process of parametric excitation of SWs^{29,30}:

$$\left(\frac{\partial}{\partial t} + v\frac{\partial}{\partial x} + \Gamma\right)a_1 = -iV\tilde{b}_0 a_2^* - iV\tilde{b}_{2k} a_1^* - i(T|a_1|^2 + 2S|a_2|^2)a_1, \quad (1)$$

which describes the temporal and spatial evolution of the envelope amplitudes a_1 and a_2 of the excited SWs having the carrier wave vectors k and $(-k)$ and frequency $\omega_k = \omega_p/2$, respectively (the second equation of the system could be obtained by the replacement $a_{1,2} \rightarrow a_{2,1}$ and $v \rightarrow (-v)$). Here v and Γ are the SW group velocity and damping rate (which includes both natural damping and nonuniform resonance line broadening due to technological imperfections), \tilde{b}_k is the Fourier image of the microwave anisotropy field, $V = V_{kk} = \gamma\omega_M(F_k^x - F_k^y)/(4\omega_k)$ is the efficiency of the parametric interaction, where \hat{F}_k is the Fourier transform of the coordinate-dependent demagnetization tensor²¹. Characteristics of SWs having the carrier wave vectors k and $(-k)$ are the same, since SW spectrum in the considered perpendicularly magnetized nanowire is reciprocal. Equation (1) contains the so-called nonadiabatic pumping term \tilde{b}_{2k} ³¹ which should be taken into account since the SW wavelength is greater than the pumping localization length.

We also take into account the nonlinear frequency shift T caused by the SW “self-interaction” and the nonlinear 4-wave (4-magnon) interaction between the parametrically excited “pairs” of SWs having wave vectors k and $(-k)$, which is described by the Hamiltonian $\mathcal{H} = \sum_k S_k c_k^* c_{-k}^* c_k c_{-k}$, where c_k is the SW amplitude (see “S-theory” in ref. 23). Note, that in bulk samples this 4-magnon interaction between the SW “pairs” is the only important mechanism limiting (or determining) the amplitudes of the parametrically excited SWs. All the other nonlinear interaction processes between the SWs could be disregarded, as in the traditional “S-theory” for bulk magnetic samples (see ref. 23). The validity of this approximation will be confirmed from the comparison between the analytical results of the above presented model and the results of the micromagnetic simulations. The magnitudes of the nonlinear coefficients in the model could be evaluated using the formalism of ref. 32 (see Methods). In the range of relatively long SWs ($k \ll 1/h, 1/\lambda_{ex}$) both nonlinear coefficients could be approximately evaluated as $T = S = -\gamma B_{int} - \omega_M(F_0^x + F_0^y)/2$, where B_{int} is the modulus of the static internal field in the nanowire.

The threshold of the parametric excitation of SWs could be calculated from Eq. (1) in the linear approximation, setting $T = S = 0$. Following the method from ref. 30 one can obtain an implicit equation determining the parametric excitation threshold:

$$\frac{\sqrt{|V\tilde{b}_0|^2 - (\Gamma - |V\tilde{b}_{2k}|)^2}}{\Gamma - |V\tilde{b}_{2k}|} = - \tan \left[\sqrt{|V\tilde{b}_0|^2 - (\Gamma - |V\tilde{b}_{2k}|)^2} \frac{L_g}{v} \right]. \quad (2)$$

In the limiting case of a small gate length $\Gamma \ll v/L_g$ one could obtain from Eq. (2) a well-known³¹ explicit expression $V\tilde{b}_{0,th} = \arccos \alpha / \sqrt{1 - \alpha^2} (v/L_g)$, where $\alpha = |\tilde{b}_{2k}/\tilde{b}_0|$ is the measure of the pumping “nonadiabaticity”; in our case of rectangular pumping profile $\alpha = \text{sinc}[kL_g]$. From this expression it is clear that the threshold becomes higher with the increase of the radiation losses $\Gamma_{rad} = v/L_g$. Since the SW group velocity v is higher for shorter SWs having higher eigenfrequencies, it is clear that the frequency range of the parametric excitation is larger for a larger gate size L_g at a fixed pumping amplitude and, naturally, this range increases with the increase of the pumping amplitude b_p . In principle, at a very high b_p the nonlinear processes other than those considered here could take place and could change this tendency. However, this issue lies beyond the scope of our current work.

To calculate the amplitudes of the parametrically excited SWs one needs to find stationary solutions of the system Eq. (1). Note, that at this stage the nonlinear frequency shift T could be disregarded, since the SW spectrum is *continuous*, and with the increase of the SW amplitude the SW wave vector changes in such a way, that the resonance condition $\omega_p = 2\omega_k(|a|)$ is satisfied. This process, which is not described by the system Eq. (1), will be explicitly discussed below.

The analytical solution of the system Eq. (1) could be found only in the simplest case, when the parametric pumping is spatially uniform and covers all the magnetic film^{23,30}, while in the general case this system allows only a numerical solution. The analysis of the numerical solutions of Eq. (1) has shown that the amplitude of the parametrically excited SW could be estimated with reasonable accuracy using the following approximate expression:

$$|a_1|_{max} = |a_2|_{max} = C \frac{(|\tilde{b}_0 V|^2 - |\tilde{b}_{0,th} V|^2)^{1/4}}{\sqrt{2|S|}}. \quad (3)$$

This approximate expression differs from the exact analytical one, obtained for the case of a spatially uniform pumping, only by the presence of the coefficient C . Here $|a_i|_{max}$ is the maximum value of the SW envelope amplitude in the nanowire, which commonly occurs at the boundary of the pumping area (left and right boundaries for a_1 and a_2 , respectively). Thus, it is the maximum amplitude of a SW propagating from the area of pumping localization. The coefficient C increases from 1 up to $C \sim 2$ when the radiation losses $\Gamma_{rad} = v/L_g$ (existing due to the finite pumping localization and finite SW group velocity) increase in comparison with the intrinsic SW damping Γ . Our simulations showed also that the dependence of the coefficient C on the degree of nonadiabaticity α is sufficiently weak to be neglected.

The appearance of the coefficient C in Eq. (3) is related to the spatial localization of the parametric pumping under the gate of the length L_g . In the case of a spatially localized pumping the spatial profiles of the parametrically excited spin waves become nonuniform. Namely, for weakly localized pumping, when $\Gamma L_g/v \gg 1$, SW profiles $a_i(x)$ are almost uniform within the pumping region except small regions near the pumping area boundaries. When the pumping becomes more localized (the ratio $\Gamma L_g/v$ decreases), these boundary regions occupy larger relative area and finally, for a sufficiently localized pumping, there are no regions with constant SW profiles at all. Nonuniform SW profiles affect both the values of the excitation (V) terms and nonlinear (S) terms in the right-hand-side part of Eq. (1), an interplay of which determines the excited SW amplitude. For a more localized pumping, when the region where $a_i(x) < a_{i,max}$ becomes larger, both pumping and nonlinear terms decrease, but the nonlinear S -term decreases faster since it contains three spin wave mode amplitudes contrary to one SW amplitude in the V -term. Consequently, the resulting maximal spin wave mode amplitude a_{max} increases when the pumping becomes more spatially localized (for a fixed value of the numerator in Eq. (3)). This effect is taken into account by the coefficient C which increases from 1 to roughly 2 with the decrease of the ratio $\Gamma L_g/v$, as was found from numerical simulations of Eq. (1). Note, that this does not mean that a decrease of the gate length L_g leads to an increase of excited SW amplitudes at *given pumping*, because the threshold $\tilde{b}_{0,th}$, which also determines excited SW amplitudes (Eq. (3)), becomes larger for a more localized pumping, as described by Eq. (2), and the increase of the threshold is significantly greater than the variation of the coefficient C .

Let us now discuss the effect of the nonlinear frequency shift (described by the coefficient T) on the process of parametric excitation of SWs. As it was pointed earlier, this frequency shift leads to the change of the SW wave vector with the increase of the SW amplitude. If all the parameters in Eq. (1) are only *weakly* dependent on the SW wave vector, one can simply neglect the nonlinear shift in Eq. (1) and use the approximate Eq. (3) for evaluation of amplitudes of the excited SWs. In our case, however, this assumption is not correct. Although the parameters V , Γ , and S are weak functions of the SW wave vector, the SW group velocity v changes significantly with the wave vector k variation. Note also, that the nonlinear frequency shift coefficient in our case is negative, $T < 0$, that is related to the perpendicular anisotropy of magnetic nanowire. Thus, with the increase of the SW amplitude the SW spectrum shifts down, and the half of the pumping frequency will now correspond to a higher SW wave vector and, therefore, to a higher value of the SW group velocity. Thus, with the increase of the SW amplitude the radiation losses increase, which leads to the additional limitation of the amplitude of the excited SWs.

To account for this effect rigorously, one needs to insert the dependence $v = f(k(|a|))$ into Eqs (2, 3) and to obtain a complex implicit equation for the excited SW amplitudes. On the other hand, to obtain an approximate analytical solution one can use an approximate dispersion relation for SWs in an *ultrathin* nanowire in the form: $\omega_k \approx \omega_0 + \omega_2 \lambda_{ex}^2 k^2$, and obtain a simple approximate expression for the SW group velocity in the form: $v \approx 2\omega_2 \lambda_{ex}^2 k$. Here ω_0 is the frequency of ferromagnetic resonance and $\omega_2 \approx \omega_M A_0 / \omega_0$ for $k \ll 1/\lambda_{ex}$ (see expres-

sion for A_k , Eq. (9), in the Methods section). The parametric excitation threshold Eq. (2) can be expressed as²³ $V^2 b_{0,th}^2 = \Gamma^2 + C_v(v/L_g)^2$, where $C_v \in [1, \pi] = f(\Gamma L_g/v, \alpha)$. In our case of a highly nonadiabatic pumping and relatively high radiation losses the coefficient C_v is equal to $C_v \approx 1$. Combining these expressions and taking into account the amplitude dependence of the SW frequency $\omega_k(a) = \omega_k(0) - |T||a_i|^2$ we find that the increase of the SW amplitude leads to the following increase of the total SW losses in the system: $\Delta\Gamma^2 = 4\omega_2\lambda_{ex}^2 C_v |T||a_i|^2 / L_g^2$. Solving now Eq. (3) taking into account the explicit power dependence of the SW losses, we finally get

$$|a_i|_{max} = \frac{C}{\sqrt{2|S|}} \left[\sqrt{|bV|^2 - |b_{th}V|^2 + \tilde{T}^2} - \tilde{T} \right]^{1/2}, \quad (4)$$

where $\tilde{T} = (\omega_2\lambda_{ex}^2 C_v C^2 |T|) / (L_g^2 |S|)$. It should be noted, that for a relatively large nonlinear frequency shift $\tilde{T} \gg \Gamma$, that is realized in our geometry, the resulting SW amplitude, given by Eq. (4), very weakly depends on the value of the coefficient C , which cannot be found analytically. Thus, in our case we can simply use $C = 2$, as for the case of a high radiation losses.

Using Eq. (4) we can describe the frequency dependence of the excited SW amplitudes, obtained from the micromagnetic simulations. The quantity calculated from the micromagnetic simulations is the sum of the partial SWs amplitudes at the center of the excitation gate, $a_\Sigma = |a_1 + a_2|$. This quantity can be expressed as $a_\Sigma = C_\Sigma \max a_i$, where the coefficient $C_\Sigma \in [1, 2]$. The value $C_\Sigma = 2$ corresponds to low radiation losses, when the amplitudes of the forward- and backward-propagating parametrically excited SWs are almost constant within the pumping region. With the increase of the SW group velocity (and, therefore, with the increase of the radiation losses) the value of the coefficient C_Σ decreases. The relation between envelope amplitude A_Σ and the real magnetization amplitude $M_{x,y}$ are given by^{23,32}

$$\max M_{y,x} = M_s \sqrt{2 - a_\Sigma^2} (u_k \pm v_k) a_\Sigma, \quad (5)$$

where

$$u_k = \sqrt{\frac{A_k + \omega_k}{2\omega_k}}, \quad v_k = -\text{sign} B_k \sqrt{\frac{A_k - \omega_k}{2\omega_k}}, \quad (6)$$

and A_k, B_k are the coefficients of the Holstein-Primakoff transformation (see Eqs (9 and 10) in the Methods section).

The resulting analytical expression for the frequency dependence of the amplitude (m_x) of the parametrically excited SWs gives a good quantitative description of the results of our micromagnetic simulations for $C_\Sigma = 1.7$ (see Fig. 2(a,c)). Note, that C_Σ is the only fitting parameter used, as all the other quantities were calculated from the nanowire geometry and the material parameters. Note also, that if we neglect the effect of the nonlinear frequency shift and use Eq. (3) instead of Eq. (4) the analytically calculated SW amplitudes will be significantly overestimated. Thus, the change of the SW group velocity due to the nonlinear adjustment of the SW wave vector is critically important in the process of parametric excitation of SWs in magnetic nanowires. Also, it is due to this adjustment that we see the propagating SW profiles at the lowest excitation frequency (Fig. 3). The standing ferromagnetic resonance at this frequency could be excited only when the pumping amplitude (and, therefore, the amplitude of the excited variable magnetization) is sufficiently low to produce any evident nonlinear shift of the SW wave vector.

In order to verify the developed analytical theory we performed micromagnetic simulations for a different width of the nanowire (50 nm) and a different gate length (100 nm), setting also the anisotropy constant to $K_1 = 1.6 \times 10^6 \text{ J/m}^3$. This change did not lead to any qualitative difference in the micromagnetic results, and we observed SW excitation in the frequency range $f_p \in [3.3, 3.57] \text{ GHz}$, which corresponds to the following wave number range of the excited SWs: $k \leq 11 \mu\text{m}^{-1}$. The developed analytical theory gave a good quantitative description of the micromagnetic results for $C_\Sigma = 1.9$ (see Fig. 4). The higher value of the coefficient C_Σ for this case then for the first studied geometry ($C_\Sigma = 1.7$) is natural, since in this case the radiation losses $\Gamma_{rad} = v/L_g$ are smaller due to larger length L_g of the pumping area.

Finally, let us discuss the issue of stability of the SW parametric excitation. As it follows from the results presented above, the only important nonlinear interactions between the excited SWs are the 4-wave processes responsible for “self-action” (described by the nonlinear coefficient T) and the processes of the interaction between the SW “pairs” (described by the nonlinear coefficient S). All the other 4-wave scattering processes, which could lead to the SW instability, are weak due to quasi-one-dimensional character of our system (nanowire) and the monotonic character of the of the SW spectrum of the nanowire. The 3-wave processes in our geometry have zero efficiency at all as long as the static magnetization is aligned with one of the symmetry axis of nanowire³². The 2-magnon scattering processes, which could take place due to the defects present in a nanowire, in the studied case of ultrathin magnetic nanowires should be weak, since the characteristic size of the possible defects in the nanowire material (nm) is substantially smaller than the characteristic SW wavelength (100 nm and more). Finally, the non-adiabatic character of the applied parametric pumping fixes not only the sum of phases of the excited SWs, but also the *difference* of these phases³¹, which makes the SW excitation process stable with respect to the appearance of magnetization auto-oscillations²³.

Discussion

In this work it has been demonstrated that a local microwave variation of the magnetic anisotropy caused by the application of a microwave electric field could excite propagating SWs in an ultrathin ferromagnetic nanowire via

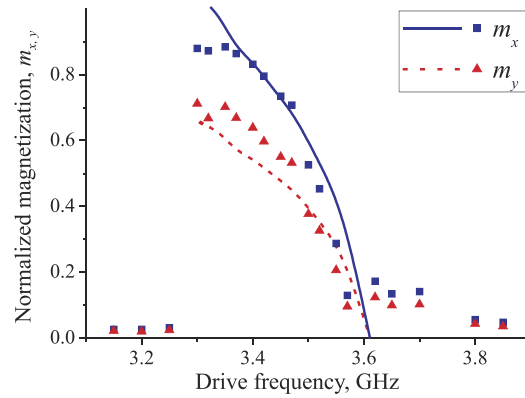


Figure 4. Amplitude of excited spin waves. Normalized in-plane components $m_{x,y} = M_{x,y}/M_s$ of the variable nanowire magnetization under the center of the excitation gate as functions of the pumping frequency for $\Delta B_a = 50$ mT, wire width $w_y = 50$ nm and gate length $L_g = 100$ nm. Symbols - micromagnetic simulations, lines - analytical theory.

the parametric excitation mechanism. The excited SWs could propagate for distances that are large compared to the size of the excitation gate, could have relatively large amplitudes and narrower spectral linewidth comparing to linearly excited SWs. These properties are very desirable for applications of the excited SWs in the nanoscale microwave signal processing devices. It is confirmed that, similar the case of a spatially uniform parametric pumping, the amplitudes of the excited SWs are limited by the “phase mechanism” resulting from 4-wave interaction between the excited SW “pairs”. However, in the case of a spatially localized parametric pumping in a magnetic nanowire due to a significant dependence of the SW group velocity on the wave vector a nonlinear shift of the SW frequency should be taken into account to obtain a correct estimation of the amplitude of the excited SW.

Methods

Micromagnetic simulations. Our micromagnetic simulations were performed using the parallel micromagnetic solver GPMagnet^{33,34}. The length of the nanowire $L = 2 \mu\text{m}$ was chosen to be sufficiently large to avoid the possible reflections from the far edges of the waveguide. The gate region of the length L_g was placed at the nanowire center. The material parameters of the ferromagnetic waveguide used in our simulations were: saturation magnetization $M_s = 1.6 \times 10^6$ A/m, exchange constant $A_{ex} = 2.0 \times 10^{-11}$ J/m, out-of-plane anisotropy constant $K_{\perp} = 1.55 \times 10^6$ J/m³, and Gilbert damping constant $\alpha_G = 0.01$, that corresponds to the typical parameters of CoFeB. Within the excitation gate region the anisotropy field was considered to be time varying: $B_a = B_{a,0} + \Delta B_a \sin[2\pi f_p t]$, where $B_{a,0} = 2K_{\perp}/M_s$ is the static part, whereas f_p and ΔB_a are the frequency and the amplitude of the microwave-frequency anisotropy field, respectively. Thermal fluctuations corresponding to the temperature $T = 1$ K were taken into account.

Calculation of nonlinear coefficients. A general way to calculate the coefficients of nonlinear SW interaction in ferromagnetic films is presented in ref. 32. In the notation of ref. 32 the coefficients T and S are the 4-magnon scattering coefficients $T \equiv W_{kk,kk}$ and $S \equiv W_{k(-k),k(-k)}$. Since the tensor \hat{F}_k is diagonal (in coordinate system shown in Fig. 1) all 3-magnon processes have zero efficiency until static magnetization is aligned with one of the symmetry axis of nanowire, so one doesn't need take into account the renormalization of 4-magnon coefficients due to nonresonant 3-magnon processes. Noting this one can obtain following expressions for the nonlinear coefficients in the case of zero external magnetic field

$$T = -A_k + \frac{B_k^2 \omega_M}{2\omega_k^2} (4\lambda_{ex}^2 k^2 - F_0^z + F_{2k}^z), \quad (7)$$

$$S = -A_k + \frac{A_k^2 \omega_M}{2\omega_k^2} (4\lambda_{ex}^2 k^2 - F_0^z + F_{2k}^z), \quad (8)$$

where

$$A_k = \gamma B_{int} + \frac{\omega_M}{2} (2\lambda_{ex}^2 k^2 + F_k^x + F_k^y), \quad (9)$$

$$B_k = \frac{\omega_M}{2} (F_k^y - F_k^x), \quad (10)$$

$\omega_k^2 = A_k^2 - B_k^2$ is the SW eigenfrequency, λ_{ex} is the material exchange length and $B_{int} = B_{an} - \mu_0 M_s F_0^z$ is the static internal field in nanowire. In the range of relatively long SWs ($k \ll 1/h, 1/\lambda_{ex}$) the above expressions reduce to $T = S = -\gamma B_{int} - \omega_M(F_0^x + F_0^y)/2$.

References

1. Fiebig, M. Revival of the magnetoelectric effect. *J. Phys. D: Appl. Phys.* **38**, R123 (2005).
2. Tong, W.-Y., Fang, Y.-W., Cai, J., Gong, Y.-W. & Duan, C.-G. Theoretical studies of all-electric spintronics utilizing multiferroic and magnetoelectric materials. *Comput. Mater. Sci.* **112**, part B, 467 (2015).
3. Weisheit, M. *et al.* Electric field-induced modification of magnetism in thin-film ferromagnets. *Science* **315**, 349 (2007).
4. Duan, C.-G. *et al.* Surface magnetoelectric effect in ferromagnetic metal films. *Phys. Rev. Lett.* **101**, 137201 (2008).
5. Endo, M., Kanai, S., Ikeda, S., Matsukura, F. & Ohno, H. Electric-field effects on thickness dependent magnetic anisotropy of sputtered MgO/Co₄₀Fe₄₀B₂₀/Ta structures. *Appl. Phys. Lett.* **96**, 212503 (2010).
6. Tsujikawa, M. & Oda, T. Finite electric field effects in the large perpendicular magnetic anisotropy surface Pt/Fe/Pt(001): A first-principles study. *Phys. Rev. Lett.* **102**, 247203 (2009).
7. Ha, S.-S. *et al.* Voltage induced magnetic anisotropy change in ultrathin Fe₈₀Co₂₀/MgO junctions with Brillouin light scattering. *Appl. Phys. Lett.* **96**, 142512 (2010).
8. Shiota, Y. *et al.* Quantitative evaluation of voltage-induced magnetic anisotropy change by magnetoresistance measurement. *Appl. Phys. Express* **4**, 043005 (2011).
9. Maruyama, T. *et al.* Large voltage-induced magnetic anisotropy change in a few atomic layers of iron. *Nat. Nanotech.* **4**, 158 (2009).
10. Nakamura, K. *et al.* Giant modification of the magnetocrystalline anisotropy in transition-metal monolayers by an external electric field. *Phys. Rev. Lett.* **102**, 187201 (2009).
11. Nozaki, T. *et al.* Electric-field-induced ferromagnetic resonance excitation in an ultrathin ferromagnetic metal layer. *Nat. Phys.* **8**, 491 (2012).
12. Zhu, J. *et al.* Voltage-induced ferromagnetic resonance in magnetic tunnel junctions. *Phys. Rev. Lett.* **108**, 197203 (2012).
13. Shiota, Y. *et al.* Induction of coherent magnetization switching in a few atomic layers of FeCo using voltage pulses. *Nat. Mater.* **11**, 39 (2012).
14. Wang, W.-G., Li, M., Hageman, S. & Chien, C. L. Electric-field-assisted switching in magnetic tunnel junctions. *Nat. Mater.* **11**, 64 (2012).
15. Nozaki, T. *et al.* Magnetization switching assisted by high-frequency-voltage-induced ferromagnetic resonance. *Appl. Phys. Express* **7**, 073002 (2014).
16. Schellekens, A., Van den Brink, A., Franken, J. & Swagten, H. J. M. & Koopmans, B. Electric-field control of domain wall motion in perpendicularly magnetized materials. *Nat. Commun.* **3**, 847 (2012).
17. Bauer, U., Emori, S. & Beach, G. S. D. Voltage-gated modulation of domain wall creep dynamics in an ultrathin metallic ferromagnet. *Appl. Phys. Lett.* **101**, 172403 (2012).
18. Bernand-Mantel, A. *et al.* Electric-field control of domain wall nucleation and pinning in a metallic ferromagnet. *Appl. Phys. Lett.* **102**, 122406 (2013).
19. Zhang, X., Zhou, Y., Ezawa, M., Zhao, G. P. & Zhao, W. Magnetic skyrmion transistor: skyrmion motion in a voltage-gated nanotrack. *Sci. Rep.* **5**, 11369 (2015).
20. Shiota, Y. *et al.* High-output microwave detector using voltage-induced ferromagnetic resonance. *Appl. Phys. Lett.* **105**, 192408 (2014).
21. Verba, R., Tiberkevich, V., Krivorotov, I. & Slavin, A. Parametric excitation of spin waves by voltage-controlled magnetic anisotropy. *Phys. Rev. Applied* **1**, 044006 (2014).
22. Verba, R., Tyberkevych, V. & Slavin, A. Excitation of propagating spin waves in an in-plane magnetized ferromagnetic strip by voltage-controlled magnetic anisotropy. in *Magnetics Conference (INTERMAG) 2015*, IEEE, doi:10.1109/INTMAG.2015.7157010.
23. L'vov, V. S. *Wave Turbulence Under Parametric Excitation* (Springer-Verlag, New York, 1994).
24. Zautkin, V. V., Zakharov, V. E., L'vov, V. S., Musher, S. L. & Starobinets, S. S. Parallel spin-wave pumping in yttrium garnet single crystals. *Sov. Phys. JETP* **62**, 1782 (1972).
25. Zakharov, V., L'vov, V. & Starobinets, S. Spin-wave turbulence beyond the parametric excitation threshold. *Sov. Phys. Usp.* **18**, 896 (1975).
26. Heinrich, B. & Cochran, J. F. Ultrathin metallic magnetic films: magnetic anisotropies and exchange interactions. *Adv. in Phys.* **42**, 523 (1993).
27. Yang, H. X. *et al.* First-principles investigation of the very large perpendicular magnetic anisotropy at Fe|MgO and Co|MgO interfaces. *Phys. Rev. B* **84**, 054401 (2011).
28. Brächer, T. *et al.* Mode selective parametric excitation of spin waves in a Ni₈₁Fe₁₉ microstripe. *Appl. Phys. Lett.* **99**, 162501 (2011).
29. Bloembergen, N. *Nonlinear optics* (Addison-Wesley Pub. Co., 1965).
30. Kalinikos, B. A. & Kostylev, M. P. Parametric amplification of spin wave envelope solitons in ferromagnetic films by parallel pumping. *IEEE Trans. Mag.* **33**, 3445 (1997).
31. Melkov, G. A., Serga, A. A., Tiberkevich, V. S., Kobljanskij, Y. V. & Slavin, A. N. Nonadiabatic interaction of a propagating wave packet with localized parametric pumping. *Phys. Rev. E* **63**, 066607 (2001).
32. Krivosik, P. & Patton, C. E. Hamiltonian formulation of nonlinear spin-wave dynamics: Theory and applications. *Phys. Rev. B* **82**, 184428 (2010).
33. Lopez-Diaz, L. *et al.* Micromagnetic simulations using graphics processing units. *J. Phys. D: Appl. Phys.* **45**, 323001 (2012).
34. Giordano, A., Finocchio, G., Torres, L., Carpentieri, M. & Azzèrboni, B. Semi-implicit integration scheme for Landau-Lifshitz-Gilbert-Slonczewski equation. *J. Appl. Phys.* **111**, 07D112 (2012).

Acknowledgements

We acknowledge the Center for NanoFerroic Devices (CNFD) and the Nanoelectronics Research Initiative(NRI) for the partial support of this work. The work was also supported in part by the National Science Foundation of the USA (grants Nos. ECCS-1305586, DMR-1015175), by the MTO/MESO grant N66001-11-1-4114 from DARPA, and by contracts from the U.S. Army TARDEC, RDECOM. The work of M.C. and G.F. was supported by the project PRIN2010ECA8P3 from Italian MIUR.

Author Contributions

M.C. and G.F. planned and performed micromagnetic simulations. R.V., V.T. and A.S. developed theoretical model. All authors analyzed the data and co-wrote the paper.

Additional Information

Competing financial interests: The authors declare no competing financial interests.

1.3. Збудження спінових хвиль у планарно намагніченому хвилеводі

PHYSICAL REVIEW APPLIED 7, 064023 (2017)

Excitation of Spin Waves in an In-Plane-Magnetized Ferromagnetic Nanowire Using Voltage-Controlled Magnetic Anisotropy

Roman Verba,^{1,*} Mario Carpentieri,² Giovanni Finocchio,³ Vasil Tiberkevich,⁴ and Andrei Slavin⁴

¹*Institute of Magnetism, Kyiv 03680, Ukraine*

²*Department of Electrical and Information Engineering, Politecnico di Bari, I-70125 Bari, Italy*

³*Department of Electronic Engineering, Industrial Chemistry and Engineering, University of Messina, I-98166 Messina, Italy*

⁴*Department of Physics, Oakland University, Rochester, Michigan 48309, USA*

(Received 21 February 2017; revised manuscript received 14 May 2017; published 16 June 2017)

It is demonstrated by analytical calculations and micromagnetic simulations that a microwave pumping by means of a voltage-controlled magnetic anisotropy (VCMA) could excite propagating spin waves in a ferromagnetic nanowire with in-plane static magnetization, and only the parametric excitation is possible. The efficiency of the parametric excitation is proportional to the out-of-plane component of the dynamic magnetization, and it is nonvanishing in the entire range of spin-wave wave vectors. This property ensures the excitation of spin waves in a wide frequency range (up to tens of gigahertz) using practically achievable amplitudes of the VCMA pumping. For a Fe/MgO nanowire, the threshold of parametric excitation of spin waves lies in the range 0.5–1 V/nm and only weakly depends on the nanowire width.

DOI: 10.1103/PhysRevApplied.7.064023

I. INTRODUCTION

The effect of voltage-controlled magnetic anisotropy (VCMA) manifests itself as a variation of the perpendicular magnetic anisotropy at the interface between a ferromagnetic metal and dielectric under the action of an electric field applied to the interface [1–3]. Similar to other magnetoelectric effects, e.g., in piezoelectric-piezomagnetic heterostructures, the effect of VCMA could provide an effective control of the magnetization in a ferromagnetic material with very low power consumption [4–6], much lower than using well-developed methods of magnetization control by magnetic field or electric current. The useful and convenient features of the VCMA effect, such as the technological simplicity of its application at nanoscale, high performance, and linearity as a function of the applied electric field [7–10] make VCMA one of the most attractive magnetoelectric effect for the application in spintronics and spin-wave (SW)-based signal processing, which currently attract significant research interest [11,12]. For example, the VCMA effect has been already proposed and tested for the application in magnetic recording [13,14], motion control of a domain wall [15,16], Skyrmions [17–19] and spin waves [20], and for the excitation of the ferromagnetic resonance [9,10,21].

In our previous works [22,23], we showed by both analytical calculations and micromagnetic simulations that microwave pumping by means of the VCMA could excite propagating SWs in an ultrathin ferromagnetic nanowire with an out-of-plane (OOP) static magnetization. In that

case, VCMA pumping leads to the variation of the OOP component of the effective magnetic field, which is parallel to the static magnetization (so-called parallel pumping geometry [24]). Thus, in the case of OOP magnetization, the SWs cannot be excited in a common linear regime, when the frequencies of the driving signal and the SWs are the same. Instead, the parametric excitation—a well-known method of SW excitation where the frequency of pumping is 2 times larger than the frequency of the excited SW [24–26]—is possible.

For practical applications, it is very desirable to use devices without permanent magnetic field bias. It is known that the static state of unbiased ultrathin ferromagnetic films and nanowires depends often on their thickness—below a certain critical thickness, the static magnetization is OOP; above this thickness, in plane (IP) [27,28]. The critical value depends on the perpendicular surface magnetic anisotropy and the saturation magnetization and, typically, is on the order of 1 nm. Here, we show that, in the case of IP magnetization—as in the case of OOP magnetization—only the parametric excitation of SWs is possible. It is also shown that the parametric excitation in thicker IP-magnetized magnetic nanowires could be more efficient than in thinner OOP-magnetized nanowires, despite the fact that VCMA is a purely interface effect, and its efficiency therefore decreases with an increase of the nanowire thickness.

The relatively high efficiency of SW parametric excitation is not the only advantage of IP-magnetized thicker nanowires. Thicker nanowires are usually easier to fabricate, and they have better uniformity. Therefore, thicker IP-magnetized nanowires have a lower inhomogeneous

*Corresponding author.
verrv@ukr.net

broadening of the SW linewidth [29]. Because of the vanishing static demagnetization fields, in the case of IP magnetization, it is possible to achieve higher SW frequency at zero bias field. Also, the IP-magnetization geometry allows one to combine the VCMA-based SW excitation with the advantages of the interfacial Dzyaloshinskii-Moriya interaction (IDMI), which takes place in ferromagnetic films grown on a heavy-metal substrate [30,31]. The IDMI is known to result in a nonreciprocal SW propagation [30,32,33], and the largest nonreciprocity is achieved for the case of IP magnetization, while, for OOP static magnetization, nonreciprocity is absent [33,34]. Obviously, the nonreciprocity of the SW propagation could provide additional functionality of the SW signal-processing devices [35].

II. THEORY

The considered layered structure is shown in Fig. 1. It consists of a thin layer of a ferromagnetic metal (e.g., Fe) covered by a dielectric layer (e.g., MgO) formed as a nanowire of the width w_y . The metal excitation gate of the length L_g is placed on top of the nanowire. The static magnetization of the ferromagnetic layer lies in plane along the nanowire length (the x axis). Below, we use the material parameters of an Fe-MgO structure, which is often used in the VCMA experiments: saturation magnetization of $\mu_0 M_s = 2.1$ T, exchange length $\lambda_{\text{ex}} = 3.4$ nm, perpendicular surface anisotropy energy $K_s = 1.36$ mJ/m², Gilbert damping $\alpha_G = 0.004$, nonuniform line broadening $\Delta\omega_{\text{nu}} = 2\pi \times 230$ MHz, magnetoelectric coefficient $\beta_s = 100$ fJ/(V m) [28,29,36]. The thickness of the Fe layer is chosen to be $h = 1$ nm. The parameters used are the same as in Ref. [22], except for the thickness [the critical thickness, corresponding to the OOP-to-IP state transition for Fe/MgO film, is $h_{\text{cr}} = 2K_s/(\mu_0 M_s^2) = 0.78$ nm, and it slightly increases for nanowires], which allows us to compare the excitation efficiencies in the OOP and IP geometries.

Magnetization dynamics in a nanowire is described by the Landau-Lifshitz equation for the magnetization vector $\mathbf{M}(\mathbf{r}, t)$:

$$\frac{\partial \mathbf{M}}{\partial t} = -\gamma \mathbf{M} \times \mathbf{B}_{\text{eff}} - \frac{\gamma \alpha_G}{M_s} \mathbf{M} \times (\mathbf{M} \times \mathbf{B}_{\text{eff}}), \quad (1)$$

where γ is the gyromagnetic ratio, α_G is the Gilbert damping constant (strictly speaking, effective; see below),

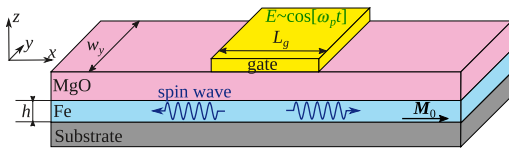


FIG. 1. A layout of the Fe-MgO nanowire with a VCMA excitation gate.

M_s is the saturation magnetization and \mathbf{B}_{eff} is the effective field consisting of external field (absent in our case), exchange, anisotropy, and magnetodipolar contributions. The variable microwave electric field $E(t) \sim \cos[\omega_p t]$ at the frequency ω_p , applied to the excitation gate, creates the variation of the perpendicular surface anisotropy $\Delta K_s = \beta E$. Corresponding variation of the effective field $\Delta \mathbf{B}_{\text{eff}}$ can be found as a variational derivative of the anisotropy energy density $W_{\text{an}} = -\Delta K_s M_z^2 / (h M_s^2)$:

$$\Delta \mathbf{B}_{\text{eff}}(t, \mathbf{r}) = -\frac{\delta}{\delta \mathbf{M}} \left(-\frac{\beta E M_z^2}{h M_s^2} \right) = \frac{2\beta E(t, \mathbf{r}) M_z(t, \mathbf{r})}{h M_s^2} \mathbf{e}_z. \quad (2)$$

As one can see, the electrically driven component of the effective field is not orthogonal to the dynamic magnetization since both of them have nonzero z components, and, consequently, the effective field can linearly affect dynamic magnetization and SWs. This relation is in contrast to the case of OOP static magnetization, for which $\Delta \mathbf{B}_{\text{eff}}$ [described by the same Eq. (2)] is parallel to the static magnetization. However, note, that $M_z(t)$ is the *dynamic* magnetization component having zero static value and varying at the frequency ω_k of the excited SW, if the excitation of SWs takes place. Thus, there are no terms in the expression for \mathbf{B}_{eff} proportional solely to the external force $E(t)$ and varying at the frequency of the external electric field. Consequently, the linear excitation of SWs in this geometry is impossible; nevertheless, the microwave VCMA-induced effective field is perpendicular to the static magnetization. It can be shown that the linear excitation of SWs becomes possible if the nanowire is magnetized at a finite angle to the surface $\theta_M \neq 0, \pi/2$ [10]. At the same time, if the variable electric field has the frequency component $\omega_p \approx 2\omega_k$, the effective magnetic field contains the *resonant* term at the SW frequency ω_k , and the *parametric* excitation of SWs may become possible.

To investigate SW dynamics, we use a standard expansion of magnetization as the sum of a static one and a series of SW modes: $\mathbf{M}(\mathbf{r}, t) = M_s [\mathbf{e}_x + \sum_{n,k} (c_{n,k} \mathbf{m}_{n,k} e^{i(kx - \omega_{n,k} t)} + \text{c.c.})]$. SW modes are characterized by the wave vector $\mathbf{k} = k \mathbf{e}_x$ and quantization number $n = 0, 1, 2, \dots$, which defines the SW mode profile $\mathbf{m}_{n,k} = \mathbf{m}_{n,k}(y)$ in the y direction (across the nanowire width). Substituting this representation into Eq. (1), one can obtain the following equation describing the dynamics of SW mode amplitude c_k [37]:

$$\frac{dc_k}{dt} + i\omega_k c_k + \Gamma_k c_k = \sum_{k'=-\infty}^{\infty} \frac{L_g}{L_x} V_{kk'} \tilde{b}_{k+k'} e^{-i\omega_p t} c_{k'}^*. \quad (3)$$

Since pumping is uniform across the nanowire width, it does not lead to a coupling between modes with different width profiles (different n 's), and the dynamics of SWs with a certain definite n is described by the same Eq. (3). For this

reason, we omit the index n in Eq. (3) and below. Value $\tilde{b}_k = L_g^{-1} \int b(x) e^{-ikx} dx$ in Eq. (3) is the Fourier image of a spatial profile of effective microwave pumping field $b(x) = 2\beta E(x)/(hM_s)$, l_x is the full length of the nanowire, and Γ_k is the SW damping rate which includes the Gilbert damping and the nonuniform SW line broadening. Equation (3) is absolutely the same as in the case of a parallel pumping [22,37], but the efficiency of the parametric interaction for the resonant case ($k' = -k$) is now equal to

$$|V_{k(-k)}| = |V_{kk}| = \gamma \frac{\langle |m_{k,z}|^2 \rangle}{2A_k}. \quad (4)$$

Here, $A_k = i\langle \mathbf{m}_k^* \cdot \mathbf{e}_x \times \mathbf{m}_k \rangle$ is the norm of the SW mode [38], with the symbols $\langle \dots \rangle$ mean averaging over the nanowire width. As one can see, the efficiency of the parametric excitation of SWs V_{kk} is proportional to the *out-of-plane magnetization component* $m_{k,z}$, and not to the difference of dynamic magnetization components $\langle |m_{k,y}|^2 - |m_{k,z}|^2 \rangle$, as is the case for the usual parallel pumping (see, e.g., Ref. [37]). The appearance of such a dependence follows from Eq. (2). Indeed, $\Delta \mathbf{B}_{\text{eff}}$ is proportional to the z component of the dynamic magnetization and has only a z component, acting, thus, on the dynamical magnetization component m_z . In total, these factors result in the dependence $V_{kk} \sim |m_{k,z}|^2$. Equation (4) is one of the key results of this work, and it remains valid for any in-plane direction of static magnetization of the nanowire. We would like to note that parametric coupling with an efficiency like Eq. (4) cannot be realized by a microwave magnetic field and is intrinsic for anisotropy pumping.

For the lowest SW mode, which is uniform along the nanowire width, Eq. (4) is simplified to

$$|V_{kk}| = \frac{\gamma |m_{k,z}|}{4 |m_{k,y}|} = \frac{\gamma}{4} \sqrt{\frac{\gamma B + \omega_M (\lambda_{\text{ex}}^2 k^2 + F_k^{(yy)})}{\gamma (B - B_{\text{an}}) + \omega_M (\lambda_{\text{ex}}^2 k^2 + F_k^{(zz)})}}, \quad (5)$$

where B is the static internal field in the nanowire, \hat{F}_k is the dynamic demagnetization tensor [22] and $B_{\text{an}} = 2K_s/(M_s h)$ is the anisotropy field. The wave-number dependence of the parametric interaction efficiency V_{kk} for the lowest SW mode is shown in Fig. 2. The efficiency V_{kk} increases as the excited SW becomes shorter, and it saturates at the value $\gamma/4$ in the high- k range due to the circular polarization of the SWs [$|m_{k,y}| = |m_{k,z}|$, the limit $\lambda_{\text{ex}} k \gg 1$ in Eq. (5)] in this range of wave numbers. Thus, in the case of in-plane magnetization, there are no principal restrictions on the wave number of the excited SW. This property is in sharp contrast to the case of OOP magnetization, where the excitation efficiency V_{kk} could have a zero value at a certain wave number and vanishes completely at high wave numbers k [22]. For small values of the

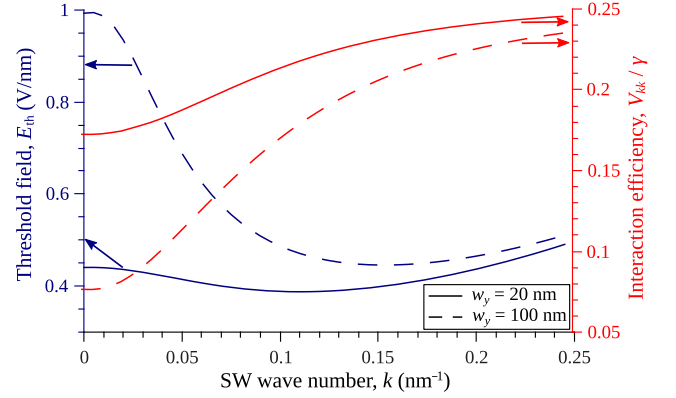


FIG. 2. Minimum parametric excitation threshold (the left axis) and efficiency of the VCMA-induced parametric interaction of spin waves (the right axis) as functions of the SW wave number for different widths of the ferromagnetic nanowire waveguide. Calculations are made for the lowest, uniform across the nanowire width, SW mode. Arrows show which curves belong to which axes.

SW wave number k , the interaction efficiency is higher in narrower nanowires, as they have stronger in-plane demagnetization fields resulting in higher OOP dynamic magnetization (a larger $F_k^{(yy)}$ component).

It is well known that the parametric excitation of SWs is a threshold excitation—the SWs are excited only if the pumping strength overcomes a certain threshold [24]. The minimum possible excitation threshold is equal to $b_{\text{th}} = \Gamma_k/V_{kk}$ and is realized in the case of relatively large gate size, $L_g \gg \Gamma_k/v$ (where v is the SW group velocity), and when the pumping frequency is 2 times as large as the frequency of the excited SW, $\omega_p = 2\omega_k$ (this condition, along with the SW dispersion law, determines the wave number of the excited SW). The corresponding threshold amplitude of the microwave electric field $E_{\text{th}} = b_{\text{th}} M_s h / 2\beta = \Gamma_k M_s h / (2\beta V_{kk})$ is shown in Fig. 2. It is clear that, in a relatively wide nanowire, it is easier to excite relatively short SWs, while the excitation of SWs with $k \rightarrow 0$ requires a higher amplitude of the electric-field pumping. In a relatively narrow nanowire, this difference becomes less and less pronounced. Consequently, it is desirable to use the narrow nanowire waveguides, having the width on the order of 10–20 nm, only when working with a small k , i.e., close to the ferromagnetic resonance (FMR) frequency. Away from the FMR (at a several-gigahertz distance) the difference in the nanowire width is practically insignificant, as, at $w_y > 30$ nm, the dependence of the parametric excitation threshold on the nanowire width saturates. This property also presents a contrast to the case of OOP magnetization, where the SW excitation threshold increases linearly up to $w_y \sim 70$ –100 nm, so that the use of relatively narrow nanowires creates a significant advantage [22]. It should also be noted that the minimum values of characteristic threshold in the case of IP

magnetization are similar to that in the OOP case (about 0.5 V/nm). However, the range of the excited SW frequencies is much larger. For example, for a 20-nm-wide waveguide, the wave number range shown in Fig. 2, in which the threshold varies insignificantly, corresponds to the SW frequency range $6 \text{ GHz} < \omega_k/2\pi < 50 \text{ GHz}$. In a nanowire with the same geometry (except for the thickness) and OOP magnetization, the excitation threshold is smaller than 1 V/nm only in the range 5–9 GHz [22]. Thus, excitation of relatively high-frequency SWs is more efficient in the IP-magnetized case, which is a consequence of a different coupling of the pumping to SWs.

Of course, for practical applications, the excitation gate should have a finite length L_g , and the excited SWs should propagate from the gate to be processed and received by other gates. A finite gate length leads to an increase of the threshold, which is determined from the following implicit equation [23]:

$$\frac{\sqrt{(Vb)^2 - (\Gamma - \alpha Vb)^2}}{\Gamma - \alpha Vb} = -\tan \frac{\sqrt{(Vb)^2 - (\Gamma - \alpha Vb)^2} L_g}{v}. \quad (6)$$

Here, $V = |V_{kk}|$ and $\alpha = |\tilde{b}_{2k}/\tilde{b}_0|$ is the so-called measure of the pumping nonadiabaticity, which describes interaction of copropagating SWs with parametric pumping and is significant only when the pumping length L_g becomes comparable to or less than the SW wavelength [37]. For example, for the case of a rectangular pumping profile, $\alpha = |\text{sinc}[kL_g]|$. The threshold increases from the minimum magnitude shown in Fig. 2, as the radiation losses $\Gamma_{\text{rad}} = v/L_g$ increase in comparison to the natural damping rate Γ_k , which is equivalent to an increase of the SW propagation length $l_p = v/\Gamma_k$ compared to the gate length L_g . In the limiting case of a small gate length where $L_g \ll l_p$, the threshold is equal to $b_{\text{th}} V_{kk} = \arccos(\alpha)(1 + \alpha^2)^{-1/2} v/L_g$ [37]. For our parameters, the maximum propagation path is achieved for SWs of the wavelength $2\pi/k \sim 20\text{--}30 \text{ nm}$, and it is about $l_p \approx 1 \mu\text{m}$.

III. MICROMAGNETIC SIMULATIONS

In order to verify the above-presented theoretical predictions, we perform micromagnetic simulations using the GPMagnet solver [39,40]. The nanowire-waveguide width is chosen to be $w_y = 20 \text{ nm}$, the gate length is $L_g = 100 \text{ nm}$, and the effective Gilbert constant is chosen to be $\alpha_G = 0.033$, which approximately takes into account both the real Gilbert damping and the nonuniform SW line broadening in the studied range of SW frequencies. The thermal fluctuations corresponding to the temperature of $T = 1 \text{ K}$ are also taken into account.

For these parameters, the FMR frequency, which is the lowest frequency in the SW spectrum, is $\omega_0/2\pi = 6 \text{ GHz}$.

When the pumping frequency exceeds the double of the FMR frequency $\omega_p > 2\omega_0$, the propagating SWs can be excited at a certain threshold pumping amplitude, and the amplitude of excited SW increases monotonically above this threshold (Fig. 3). The wave number k of the parametrically excited SW is determined by the pumping frequency ($\omega_k = \omega_p/2$) and increases with an increase of the pumping frequency ω_p . Since the SW group velocity v also increases with an increase of the SW wave number k , the threshold of the SW excitation by a gate of a *finite length* increases with an increase of ω_p .

Our simulations also show that the parametric excitation of SWs is possible even when the pumping frequency ω_p is slightly lower than the double FMR frequency (the curve for 11.6 GHz in Fig. 3). However, in this case, the SW excitation is of a “subcritical” type—the amplitude of the excited SW has a large finite value at the threshold. The excitation in this frequency range becomes possible due to a nonlinear shift of the SW frequency, which is negative in our case—common for thin films and nanowires with IP static magnetization [24,41]. In this geometry, an increase of the SW amplitude leads to a decrease of the SW frequency $\omega_k(|c_k|^2)$, meaning that the parametric resonance condition $\omega_k(|c_k|^2) = \omega_p/2$ can be satisfied for $\omega_p < 2\omega_0$. The SW mode excited in such a case has an evanescent nonpropagating character and is localized in the region close to the excitation gate since it lies below the spectrum of linear propagating SWs.

The excitation thresholds observed in the simulations are $b_{\text{th}} = 58, 78, \text{ and } 90 \text{ mT}$ for $\omega_p/2\pi = 12.2, 12.6, \text{ and } 12.8 \text{ GHz}$, while Eq. (6) gives the threshold values of 55, 98, and 114 mT, respectively. The overestimation of the threshold for $\omega_p/2\pi = 12.6, 12.8 \text{ GHz}$ in the analytical theory is related to the small theoretical values of the pumping nonadiabaticity $\alpha = |\text{sinc}[kL_g]|$. In these cases,

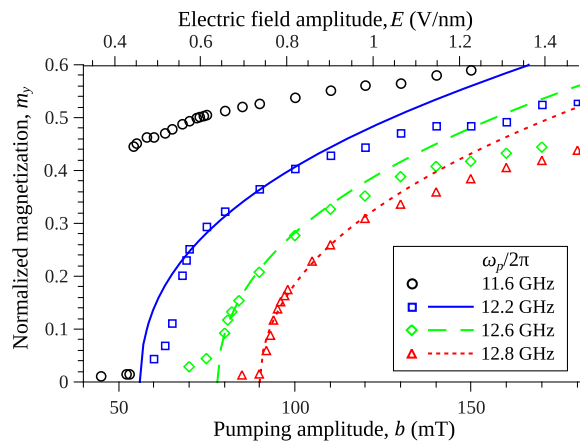


FIG. 3. Amplitudes of the excited SWs (normalized magnetization $m_y = M_y/M_s$ under the excitation-gate center) as functions of the pumping strength. Symbols, results of the micromagnetic simulations; lines, analytic theory.

$kL_g \approx \pi/2$ and the theoretical value of the coefficient α is vanishingly small. In reality, the excited SW modes are not ideal plane waves, and they have a finite spread of wave numbers k . Thus, the effective nonadiabaticity parameter α cannot be zero, which results in a lower excitation threshold, as was shown in Ref. [37]. For the case $\omega_p/2\pi = 12.2$ GHz, the theoretical value of α is not small and pumping nonadiabaticity is not underestimated, resulting in a better theoretical prediction of the threshold.

Similar to the case of OOP magnetization, the amplitudes of parametrically excited SWs are determined by two mechanisms: (i) the “phase mechanism” related to the four-wave interaction between the excited SWs, and (ii) the amplitude dependence of the radiation losses existing due to the negative nonlinear frequency shift [23]. The simulated amplitudes of the excited SWs could be adequately described by the theory presented in Ref. [23] with the single fitting coefficients $C_\Sigma = 1.5, 1.2,$ and 1.1 for $\omega_p/2\pi = 12.2, 12.6,$ and 12.8 GHz, respectively (this fitting parameter depends on the degree of pumping localization and varies in the interval $1 < C_\Sigma < 2$ [23]). At high SW amplitudes, theoretical descriptions become less accurate since additional nonlinear SW interaction processes become important. It should be noted that, for the pumping frequency $\omega_p < 2\omega_0$, the analytical theory developed in Ref. [23] is not applicable and should be generalized.

IV. NOTES ON MULTIMODE NANOWIRES AND VCMA MATERIALS

All the above-presented calculations are made for the *lowest* SW mode, having a uniform profile along the nanowire width ($n = 0$). However, with an increase of the nanowire width, the higher SW width modes become closer in frequency to the uniform mode, and the parametric resonance condition $\omega_p = 2\omega_{n,k}$ could be satisfied for several SW width modes simultaneously [see, an example, Fig. 4(a)]. In such a case, it is not clear which SW mode

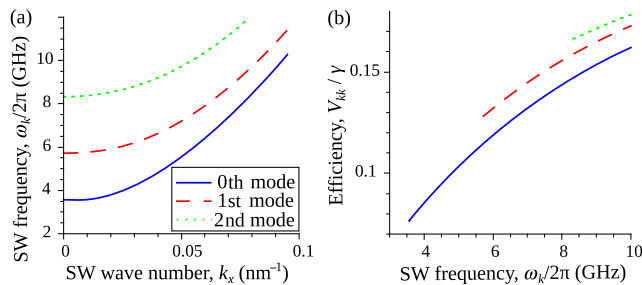


FIG. 4. (a) Spectrum of the three lowest SW width modes in a 100-nm-wide nanowire waveguide, and (b) efficiency of the parametric excitation of these modes as a function of their frequency. SW spectrum and mode structure in a finite-width waveguide are calculated using Ref. [42] and assuming “free” boundary conditions at the width edges of a nanowire.

would be excited in the waveguide. To answer this question, we plot the parametric interaction efficiency V_{kk} for different SW width modes in Fig. 4(b). As one can see, at a given frequency, V_{kk} has the largest value for the highest SW width mode since the spatially nonuniform width profile of a higher mode creates a larger dynamic demagnetization field along the y axis. This field results in a larger relative value of the z component of the dynamic magnetization, and, as shown above, the interaction efficiency V_{kk} is proportional to this z component of the dynamic magnetization. Also, at a given frequency, a higher SW mode has a lower k , and thus a lower SW group velocity $v \sim 2\omega_M \lambda_{\text{ex}}^2 k$. Thus, the highest mode has the lowest excitation threshold and will be excited by the parametric pumping. The other SW width modes may be excited only when the highest width mode reaches a sufficiently large amplitude [24]. It should be noted that the excitation of higher-order modes, having lower group velocity, limits the maximum propagation distance of the excited SWs, which is equal to the propagation length of the highest mode satisfying the conditions of parametric resonance. This property stimulates the use of narrow ferromagnetic nanowires in which a single-mode propagation regime exists in a wide range of frequencies.

Finally, we note that, in all of the above-presented calculations, we use the parameters of a typical VCMA material—a Fe-MgO multilayer. These calculations yield reasonable and experimentally reachable magnitude of the driving microwave electric fields needed for the parametric excitation of propagating SWs using the VCMA effect. Recent experimental and theoretical studies have found (or predicted) materials with substantially better VCMA characteristics, such as SrTiO₃/Fe bilayers, which have a 2 times larger magnetoelectric coefficient β than the Fe/MgO system [43], or a Cr/Fe/MgO multilayer having an almost 3 times larger β [44]. The use of these alternative materials should result in better characteristics of the SW processing devices based on parametric excitation of propagating spin waves through the VCMA effect.

V. SUMMARY

In this paper, we demonstrate that a microwave VCMA pumping can parametrically excite propagating SWs in an ultrathin ferromagnetic nanowire with in-plane static magnetization. The efficiency of the parametric interaction of propagating SWs by the VCMA pumping is proportional to the out-of-plane component of the dynamic magnetization of a nanowire. Such a type of parametric coupling is inherent to the case where the pumping is created by the time-dependent anisotropy of the magnetic film, and it cannot be realized by an application of a microwave magnetic field. The parametric interaction efficiency is nonvanishing in a wide range of SW wave numbers, including the region of short exchange-dominated SWs, where it tends to be $V_{kk} \rightarrow \gamma/4$. This useful property of the

VCMA-based parametric excitation of SWs in in-plane magnetized magnetic waveguides provides the practical method of excitation of short SWs, having sufficiently large group velocities for the development of energy-efficient signal-processing devices based on exchange-dominated short propagating SWs. The minimum excitation threshold is found to be about 0.5 V/nm in the Fe-MgO nanowire, and this threshold weakly depends on the nanowire width. At a large width of the nanowire, where the nanowire essentially becomes a multimode waveguide, the parametric VCMA pumping excites the highest SW width mode satisfying the parametric resonance condition.

ACKNOWLEDGMENTS

This work was supported in part by a grant from the Center for NanoFerriic Devices (CNFD) and the Nanoelectronics Research Initiative (NRI), by Grant No. EFMA-1641989 from the U.S. National Science Foundation, by a grant from DARPA, and by a contract from the U.S. Army TARDEC, RDECOM. R. V. acknowledges support from the Ministry of Education and Science of Ukraine, Project No. 0115U002716. The work of M. C. and G. F. was supported by the “Progetto Premiale—SIES Strategic Initiatives for the Environment and Security” and the executive program of scientific and technological cooperation between Italy and China (Code No. CN16GR09) funded by Ministero degli Affari Esteri e della Cooperazione Internazionale.

-
- [1] M. Weisheit, S. Fähler, A. Marty, Y. Souche, C. Poinsignon, and D. Givord, Electric field-induced modification of magnetism in thin-film ferromagnets, *Science* **315**, 349 (2007).
- [2] C.-G. Duan, J. P. Velez, R. F. Sabirianov, Z. Zhu, J. Chu, S. S. Jaswal, and E. Y. Tsymlal, Surface Magnetoelectric Effect in Ferromagnetic Metal Films, *Phys. Rev. Lett.* **101**, 137201 (2008).
- [3] M. Endo, S. Kanai, S. Ikeda, F. Matsukura, and H. Ohno, Electric-field effects on thickness dependent magnetic anisotropy of sputtered MgO/Co₄₀Fe₄₀B₂₀/Ta structures, *Appl. Phys. Lett.* **96**, 212503 (2010).
- [4] M. Fiebig, Revival of the magnetoelectric effect, *J. Phys. D* **38**, R123 (2005).
- [5] W.-Y. Tong, Y.-W. Fang, J. Cai, S.-J. Gong, and C.-G. Duan, Theoretical studies of all-electric spintronics utilizing multiferroic and magnetoelectric materials, *Comput. Mater. Sci.* **112**, Part B, 467 (2015).
- [6] F. Matsukura, Y. Tokura, and H. Ohno, Control of magnetism by electric fields, *Nat. Nanotechnol.* **10**, 209 (2015).
- [7] S.-S. Ha, N.-H. Kim, S. Lee, C.-Y. You, Y. Shiota, T. Maruyama, T. Nozaki, and Y. Suzuki, Voltage induced magnetic anisotropy change in ultrathin Fe₈₀Co₂₀/MgO junctions with Brillouin light scattering, *Appl. Phys. Lett.* **96**, 142512 (2010).
- [8] Y. Shiota, S. Murakami, F. Bonell, T. Nozaki, T. Shinjo, and Y. Suzuki, Quantitative evaluation of voltage-induced magnetic anisotropy change by magneto-resistance measurement, *Appl. Phys. Express* **4**, 043005 (2011).
- [9] T. Nozaki, Y. Shiota, S. Miwa, S. Murakami, F. Bonell, S. Ishibashi, H. Kubota, K. Yakushiji, T. Saruya, A. Fukushima, S. Yuasa, T. Shinjo, and Y. Suzuki, Electric-field-induced ferromagnetic resonance excitation in an ultrathin ferromagnetic metal layer, *Nat. Phys.* **8**, 491 (2012).
- [10] J. Zhu, J. A. Katine, G. E. Rowlands, Y.-J. Chen, Z. Duan, J. G. Alzate, P. Upadhyaya, J. Langer, P. K. Amiri, K. L. Wang, and I. N. Krivorotov, Voltage-Induced Ferromagnetic Resonance in Magnetic Tunnel Junctions, *Phys. Rev. Lett.* **108**, 197203 (2012).
- [11] A. Khitun, M. Bao, and K. L. Wang, Magnonic logic circuits, *J. Phys. D* **43**, 264005 (2010).
- [12] A. V. Chumak, V. I. Vasyuchka, A. A. Serga, and B. Hillebrands, Magnon spintronics, *Nat. Phys.* **11**, 453 (2015).
- [13] Y. Shiota, T. Nozaki, F. Bonell, S. Murakami, T. Shinjo, and Y. Suzuki, Induction of coherent magnetization switching in a few atomic layers of FeCo using voltage pulses, *Nat. Mater.* **11**, 39 (2012).
- [14] W.-G. Wang, M. Li, S. Hageman, and C. L. Chien, Electric-field-assisted switching in magnetic tunnel junctions, *Nat. Mater.* **11**, 64 (2012).
- [15] A. Schellekens, A. van den Brink, J. Franken, H. Swagten, and B. Koopmans, Electric-field control of domain wall motion in perpendicularly magnetized materials, *Nat. Commun.* **3**, 847 (2012).
- [16] U. Bauer, S. Emori, and G. S. D. Beach, Voltage-gated modulation of domain wall creep dynamics in an ultrathin metallic ferromagnet, *Appl. Phys. Lett.* **101**, 172403 (2012).
- [17] X. Zhang, Y. Zhou, M. Ezawa, G. P. Zhao, and W. Zhao, Magnetic skyrmion transistor: skyrmion motion in a voltage-gated nanotrack, *Sci. Rep.* **5**, 11369 (2015).
- [18] G. Finocchio, M. Ricci, R. Tomasello, A. Giordano, M. Lanuzza, V. Puliafito, P. Burrascano, B. Azzarboni, and M. Carpentieri, Skyrmion based microwave detectors and harvesting, *Appl. Phys. Lett.* **107**, 262401 (2015).
- [19] F. H. Tung, G. W. Liang, and L. W. Siang, Gateable Skyrmion transport via field-induced potential barrier modulation, *Sci. Rep.* **6**, 21099 (2016).
- [20] K. Nawaoka, Y. Shiota, S. Miwa, H. Tomita, E. Tamura, N. Mizuochi, T. Shinjo, and Y. Suzuki, Voltage modulation of propagating spin waves in Fe, *J. Appl. Phys.* **117**, 17A905 (2015).
- [21] Y.-J. Chen, H. K. Lee, R. Verba, J. A. Katine, I. Barsukov, V. Tiberkevich, J. Q. Xiao, A. N. Slavin, and I. N. Krivorotov, Parametric resonance of magnetization excited by electric field, *Nano Lett.* **17**, 572 (2017).
- [22] R. Verba, V. Tiberkevich, I. Krivorotov, and A. Slavin, Parametric Excitation of Spin Waves by Voltage-Controlled Magnetic Anisotropy, *Phys. Rev. Applied* **1**, 044006 (2014).
- [23] R. Verba, M. Carpentieri, G. Finocchio, V. Tiberkevich, and A. Slavin, Excitation of propagating spin waves in ferromagnetic nanowires by microwave voltage-controlled magnetic anisotropy, *Sci. Rep.* **6**, 25018 (2016).
- [24] V. S. L'vov, *Wave Turbulence Under Parametric Excitation* (Springer-Verlag, New York, 1994).

- [25] T. Brächer, P. Pirro, F. Heussner, A. A. Serga, and B. Hillebrands, Localized parallel parametric generation of spin waves in a $\text{Ni}_{81}\text{Fe}_{19}$ waveguide by spatial variation of the pumping field, *Appl. Phys. Lett.* **104**, 092418 (2014).
- [26] A. Capua, C. Rettner, and S. P. Parkin, Parametric Harmonic Generation as a Probe of Unconstrained Spin Magnetization Precession in the Shallow Barrier Limit, *Phys. Rev. Lett.* **116**, 047204 (2016).
- [27] B. Heinrich and J. F. Cochran, Ultrathin metallic magnetic films: Magnetic anisotropies and exchange interactions, *Adv. Phys.* **42**, 523 (1993).
- [28] H. X. Yang, M. Chshiev, B. Dieny, J. H. Lee, A. Manchon, and K. H. Shin, First-principles investigation of the very large perpendicular magnetic anisotropy at Fe|MgO and Co|MgO interfaces, *Phys. Rev. B* **84**, 054401 (2011).
- [29] R. Urban, G. Woltersdorf, and B. Heinrich, Gilbert Damping in Single and Multilayer Ultrathin Films: Role of Interfaces in Nonlocal Spin Dynamics, *Phys. Rev. Lett.* **87**, 217204 (2001).
- [30] L. Udvardi and L. Szunyogh, Chiral Asymmetry of the Spin-Wave Spectra in Ultrathin Magnetic Films, *Phys. Rev. Lett.* **102**, 207204 (2009).
- [31] K.-S. Ryu, L. Thomas, S.-H. Yang, and S. Parkin, Chiral spin torque at magnetic domain walls, *Nat. Nanotechnol.* **8**, 527 (2013).
- [32] R. L. Melcher, Linear Contribution to Spatial Dispersion in the Spin-Wave Spectrum of Ferromagnets, *Phys. Rev. Lett.* **30**, 125 (1973).
- [33] V. L. Zhang, K. Di, H. S. Lim, S. C. Ng, M. H. Kuok, J. Yu, J. Yoon, X. Qiu, and H. Yang, In-plane angular dependence of the spin-wave nonreciprocity of an ultrathin film with Dzyaloshinskii-Moriya interaction, *Appl. Phys. Lett.* **107**, 022402 (2015).
- [34] J.-H. Moon, S.-M. Seo, K.-J. Lee, K.-W. Kim, J. Ryu, H.-W. Lee, R. D. McMichael, and M. D. Stiles, Spin-wave propagation in the presence of interfacial Dzyaloshinskii-Moriya interaction, *Phys. Rev. B* **88**, 184404 (2013).
- [35] R. Verba, V. Tiberkevich, and A. Slavin, Influence of interfacial Dzyaloshinskii-Moriya interaction on the parametric amplification of spin waves, *Appl. Phys. Lett.* **107**, 112402 (2015).
- [36] M. K. Niranjana, C.-G. Duan, S. S. Jaswal, and E. Y. Tsybal, Electric field effect on magnetization at the Fe/MgO(001) interface, *Appl. Phys. Lett.* **96**, 222504 (2010).
- [37] G. A. Melkov, A. A. Serga, V. S. Tiberkevich, Y. V. Kobljanskij, and A. N. Slavin, Nonadiabatic interaction of a propagating wave packet with localized parametric pumping, *Phys. Rev. E* **63**, 066607 (2001).
- [38] R. V. Verba, Spin waves in arrays of magnetic nanodots with magnetodipolar coupling, *Ukr. J. Phys.* **58**, 758 (2013).
- [39] L. Lopez-Diaz, D. Aurelio, L. Torres, E. Martinez, M. A. Hernandez-Lopez, J. Gomez, O. Alejos, M. Carpentieri, G. Finocchio, and G. Consolo, Micromagnetic simulations using graphics processing units, *J. Phys. D* **45**, 323001 (2012).
- [40] A. Giordano, G. Finocchio, L. Torres, M. Carpentieri, and B. Azzèrboni, Semi-implicit integration scheme for Landau-Lifshitz-Gilbert-Slonczewski equation, *J. Appl. Phys.* **111**, 07D112 (2012).
- [41] P. Krivosik and C. E. Patton, Hamiltonian formulation of nonlinear spin-wave dynamics: Theory and applications, *Phys. Rev. B* **82**, 184428 (2010).
- [42] K. Y. Guslienko and A. N. Slavin, Magnetostatic Green's functions for the description of spin waves in finite rectangular magnetic dots and stripes, *J. Magn. Magn. Mater.* **323**, 2418 (2011).
- [43] I. Kota and H. Imamura, Electric field effect on magnetic anisotropy in Fe-monolayer on SrTiO_3 and MgO insulating layer: A first-principles study, in *Proceedings of the 59th Annual Magnetism and Magnetic Materials (MMM) Conference, Honolulu, 2014*, p. CE-11, http://magnetism.org/doc/past_conferences/mmm_conference_59.pdf.
- [44] T. Nozaki, A. Koziol-Rachwał, W. Skowroński, V. Zayets, Y. Shiota, S. Tamaru, H. Kubota, A. Fukushima, S. Yuasa, and Y. Suzuki, Large Voltage-Induced Changes in the Perpendicular Magnetic Anisotropy of an MgO-Based Tunnel Junction with an Ultrathin Fe Layer, *Phys. Rev. Applied* **5**, 044006 (2016).

Parametric Resonance of Magnetization Excited by Electric Field

Yu-Jin Chen,^{*,†} Han Kyu Lee,[†] Roman Verba,[‡] Jordan A. Katine,[¶] Igor Barsukov,[†] Vasil Tiberkevich,[§] John Q. Xiao,^{||} Andrei N. Slavin,[§] and Ilya N. Krivorotov[†]

[†]Department of Physics and Astronomy, University of California, Irvine, California 92697, United States

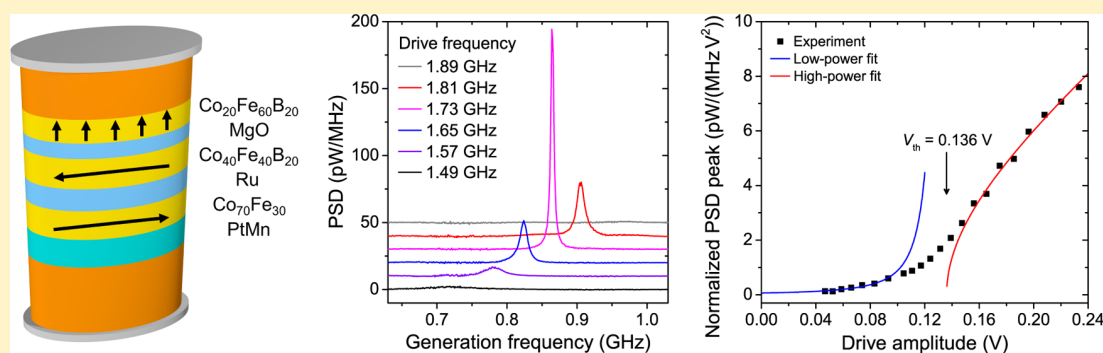
[‡]Institute of Magnetism, Kyiv 03142, Ukraine

[¶]HGST, San Jose, California 95135, United States

[§]Department of Physics, Oakland University, Rochester, Michigan 48309, United States

^{||}Department of Physics and Astronomy, University of Delaware, Newark, Delaware 19716, United States

S Supporting Information



ABSTRACT: Manipulation of magnetization by electric field is a central goal of spintronics because it enables energy-efficient operation of spin-based devices. Spin wave devices are promising candidates for low-power information processing, but a method for energy-efficient excitation of short-wavelength spin waves has been lacking. Here we show that spin waves in nanoscale magnetic tunnel junctions can be generated via parametric resonance induced by electric field. Parametric excitation of magnetization is a versatile method of short-wavelength spin wave generation, and thus, our results pave the way toward energy-efficient nanomagnonic devices.

KEYWORDS: Parametric resonance, voltage-controlled magnetic anisotropy, spin waves, magnetic tunnel junction

Magneto-electric coupling in magnetic materials and heterostructures enables control of magnetization by electric field, which is the key requirement for realization of energy-efficient spintronic devices.¹ Recent progress in this field includes demonstration of electric field induced magnetization reversal^{2–8} and ferromagnetic resonance.^{9,10} However, ferromagnetic resonance driven by electric field cannot be used for generation of spin waves with wavelengths smaller than the excitation region, which limits its applicability in nanomagnonic devices based on short-wavelength spin waves.¹¹ Here we report parametric excitation of spin waves in a ferromagnet by alternating electric field. Unlike ferromagnetic resonance, parametric resonance can be employed for generation and amplification of short-wavelength spin waves, and thus, our work is an important step toward the development of energy-efficient nanomagnonics.

A prominent manifestation of the magneto-electric coupling in magnetic films and heterostructures is modification of magnetic anisotropy by electric field.^{12–14} This recently discovered effect takes place at the interface between a ferromagnetic metal (e.g., Fe) and a nonmagnetic insulator

(e.g., MgO)¹⁴ and originates from different rates of filling of d -like electron bands in response to electric field applied perpendicular to the interface.¹⁵ Since electrons in different bands contribute unequally to the uniaxial perpendicular magnetic anisotropy (PMA) at the interface, electric field can be used to modulate PMA. This voltage-controlled magnetic anisotropy (VCMA) is promising for energy-efficient manipulation of magnetization^{4,16,17} because, unlike spin torque (ST), VCMA does not rely on high electric current density resulting in large Ohmic losses. In this work, we employ VCMA modulation at microwave frequencies in order to excite parametric resonance of magnetization in a nanomagnet.^{18–20}

Parametric excitation of magnetization by external magnetic field has been thoroughly studied in bulk and thin-film ferromagnets.²¹ In these experiments, a parameter of the magnetic system (external field) is modulated with a frequency at twice a spin wave frequency f_{SW} of the system. Parametric

Received: November 11, 2016

Revised: December 20, 2016

Published: December 21, 2016

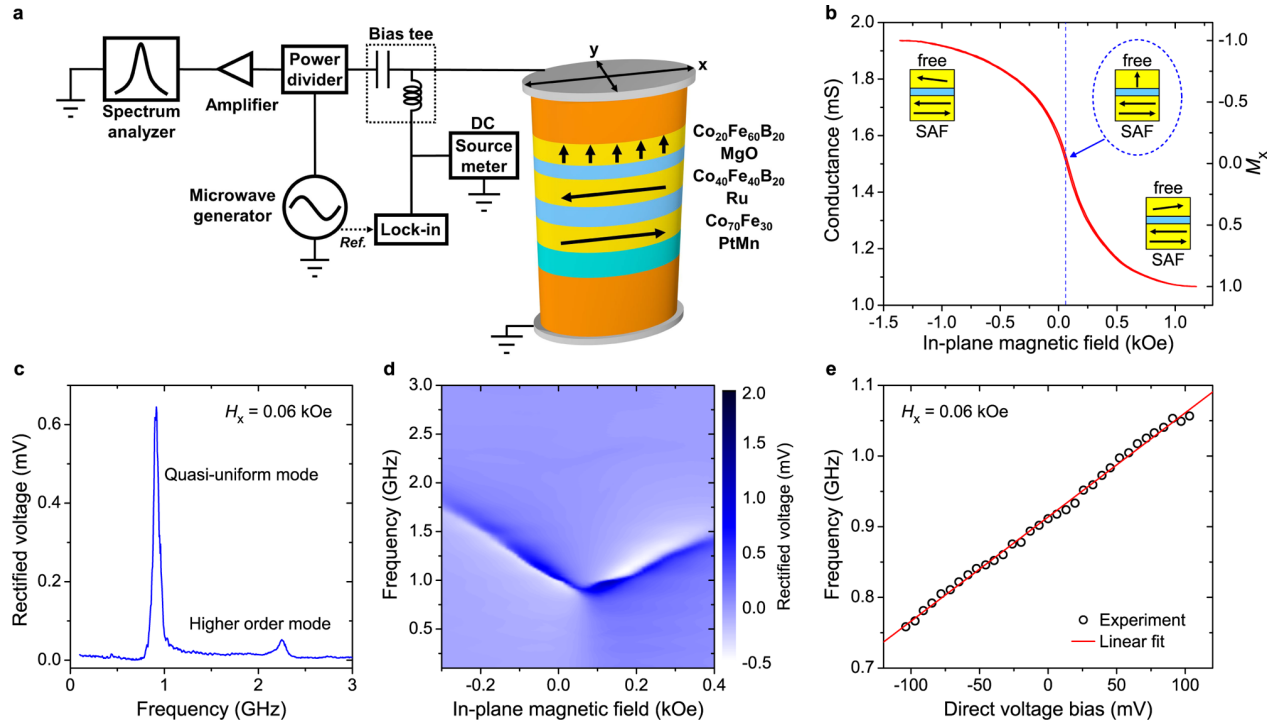


Figure 1. Measurement setup and MTJ characterization. (a) Schematic of experimental setup for DC and microwave characterization of MTJ. (b) MTJ conductance as a function of in-plane magnetic field H_x applied parallel to the MTJ long axis. (c) ST-FMR spectrum of the MTJ at $H_x = 0.06$ kOe. (d) Dependence of ST-FMR spectra on H_x . (e) Quasi-uniform mode frequency versus direct voltage bias V_{dc} measured at $H_x = 0.06$ kOe.

excitation is a nonlinear process, in which the parametric drive acts as negative effective magnetic damping that competes with positive intrinsic damping.²¹ At a threshold amplitude of the parametric drive, the negative damping exceeds the intrinsic damping and magnetization oscillations at half the drive frequency are excited.

Parametric excitation of magnetization has several important advantages over direct excitation by external magnetic field with a frequency at f_{SW} . First, parametric excitation efficiently couples not only to the uniform precession of magnetization but also to spin wave eigenmodes.²¹ This allows excitation of short-wavelength spin waves by simply choosing the parametric drive frequency to be twice the desired spin wave frequency. Second, parametric pumping can be used for frequency-selective amplification of spin waves²² and phase error corrections.²³ All these properties of parametric pumping form a highly desirable set of tools for the nascent field of nanomagnetics.^{24,25} However, parametric excitation of spin waves by microwave magnetic field in metallic ferromagnets is not energy-efficient because of the relatively high threshold fields (tens of Oe).²⁶ Here we show that replacing magnetic field pumping by electric field (VCMA) pumping solves this problem and allows parametric excitation of magnetic oscillations in metallic ferromagnets by a low-power microwave drive.

We demonstrate parametric excitation of magnetization in 70 nm × 150 nm elliptical nanoscale magnetic tunnel junctions (MTJs) schematically shown in Figure 1a. The junctions are patterned from (bottom lead)/Ta(5)/PtMn(15)/SAF/MgO(0.83)/Co₂₀Fe₆₀B₂₀(1.58)/Ta(5)/(cap) multilayers (thicknesses in nm) deposited by magnetron sputtering. Here SAF = Co₇₀Fe₃₀(2.3)/Ru(0.85)/Co₄₀Fe₄₀B₂₀(2.4) is the pinned synthetic antiferromagnet, which has magnetic moments lying

in the plane of the sample. The equilibrium direction of the Co₂₀Fe₆₀B₂₀ free layer magnetization is normal to the sample plane due to interfacial PMA.¹⁰ Prior to patterning, the multilayers are annealed for 2 h at 300 °C in a 10 kOe in-plane magnetic field that sets the pinned layer exchange bias direction parallel to the MTJ long axis.

All measurements reported in this Letter are made in the setup schematically shown in Figure 1a that allows application of DC and microwave voltages to the MTJ and measurement of DC and microwave signals generated by the MTJ. Figure 1b shows conductance G of the MTJ measured as a function of in-plane magnetic field H_x applied parallel to the MTJ long axis. The shape of the $G(H_x)$ curve is congruent to the shape of the $M_x(H_x)$ hysteresis loop,¹⁰ where M_x is normalized projection of the free layer magnetization onto the applied field direction. The hysteresis loop and micromagnetic simulations confirm the out-of-plane easy axis of the free layer (see Supporting Information Section 1). The center of the loop is shifted from zero field due to a residual 0.06 kOe stray field from the SAF.

We employ spin torque ferromagnetic resonance (ST-FMR) to characterize the spectral properties of spin wave eigenmodes of the MTJ. In this technique, a small amplitude microwave drive current $GV_{ac} \sin(2\pi f_d t)$ applied to the MTJ excites oscillations of magnetization at the drive frequency f_d . The resulting resistance oscillations $R_{ac} \sin(2\pi f_d t + \phi)$ of the MTJ at the drive frequency lead to partial rectification of the microwave drive voltage V_{ac} and generate a direct voltage V_r . Peaks in ST-FMR spectra $V_r(f_d)$ arise from resonant excitation of spin wave eigenmodes of the MTJ.^{27,28}

Figure 1c shows a ST-FMR spectrum of the MTJ measured at $H_x = 0.06$ kOe. Two spin wave eigenmodes are present in this spectrum with the lowest-frequency ($f_{SW} = 0.91$ GHz)

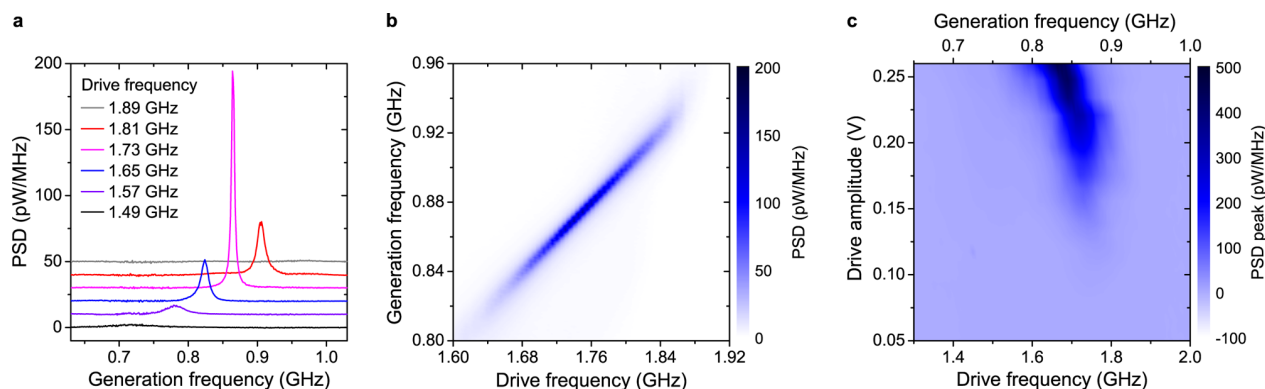


Figure 2. Parametric resonance. (a) Power spectral density (PSD) of the microwave signal emitted by the MTJ under VCMA parametric drive of $V_{ac} = 0.185$ V. Curves are vertically offset for clarity and are listed in order of drive frequency. (b) Dependence of the parametrically generated emission spectra on the drive frequency for $V_{ac} = 0.185$ V. (c) PSD peak plotted versus drive frequency and drive amplitude reveals typical Arnold tongue shape characteristic of parametric excitation.

mode being the quasi-uniform mode of the free layer.²⁹ From the spectral line width of the quasi-uniform mode we can estimate the Gilbert damping parameter $\alpha \approx 0.033$ (see Supporting Information Section 2), which is typical for a CoFeB layer of this thickness.¹⁰ Dependence of ST-FMR spectra on H_x is summarized in Figure 1d. The frequency of the quasi-uniform mode increases with increasing absolute value of the net in-plane field due to the second-order uniaxial PMA.¹⁰

Figure 1e shows dependence of the quasi-uniform mode frequency on direct voltage bias V_{dc} applied to the MTJ. From the slope of the line in Figure 1e we can estimate VCMA efficiency $\frac{dH_u}{dV_{dc}} = 526$ Oe/V (see Supporting Information Section 3), where H_u is the PMA field and the value of VCMA efficiency is typical for this material system.¹⁰

We use the parallel pumping geometry to parametrically excite the free layer quasi-uniform mode¹⁸ in which magnetization of the free layer is parallel to the oscillating PMA field H_u . We apply a constant 0.06 kOe in-plane magnetic field along the long axis of the ellipse to compensate the in-plane SAF stray field acting on the free layer so that its magnetization is aligned perpendicular to the sample plane. We then apply a parametric drive voltage V_{ac} to the MTJ and vary the drive frequency f_d about $2f_{SW}$ (twice the quasi-uniform mode resonance frequency). The resulting modulation of PMA at the drive frequency due to VCMA can parametrically excite magnetization oscillations at half the drive frequency,¹⁸ which gives rise to the MTJ resistance oscillations $R_{ac} \cos\left(2\pi\frac{f_d}{2}t + \phi\right)$. These resistance oscillations can be detected via their mixing with the microwave current $GV_{ac} \cos(2\pi f_d t)$ through the junction, which generates mixing voltage signals $V_{mix}(t)$ at frequencies $f_d/2$ and $3f_d/2$:

$$\begin{aligned} V_{mix}(t) &= GV_{ac} \cos(2\pi f_d t) R_{ac} \cos\left(2\pi\frac{f_d}{2}t + \phi\right) \\ &= \frac{1}{2} GV_{ac} R_{ac} \left[\cos\left(2\pi\frac{f_d}{2}t - \phi\right) + \cos\left(2\pi\frac{3f_d}{2}t + \phi\right) \right] \end{aligned} \quad (1)$$

As illustrated in Figure 1a, we amplify $V_{mix}(t)$ and measure its spectrum with a microwave spectrum analyzer. In this Letter, we present power spectra of $V_{mix}(t)$ measured near $f_d/2$; similar spectra are observed near $3f_d/2$. Figure 2a displays power

spectral density (PSD) $P(f)$ of $V_{mix}(t)$ measured at several fixed values of the drive frequency f_d near $2f_{SW}$ and drive amplitude $V_{ac} = 0.185$ V. The maximum of each power spectrum is observed exactly at $f_d/2$, clearly illustrating that magnetization dynamics of the free layer is excited parametrically at half the drive frequency. The line widths of the measured spectral peaks are in the range of several MHz. This line width mostly arises from thermal fluctuations of the free layer magnetization (fluctuations of the phase ϕ in eq 1). Figure 2b illustrates that parametric excitation of the quasi-uniform mode has well-pronounced resonant character: significant amplitude of the parametric oscillations is observed only in a narrow range of the drive frequencies near $2f_{SW}$.

Figure 2c displays dependence of $P(f_d/2)$ on the drive amplitude V_{ac} and drive frequency f_d . This figure illustrates the parametric excitation efficiency and clearly demonstrates that the observed microwave emission from the sample has a threshold character in V_{ac} . This threshold behavior is expected for parametric resonance that is excited when effective negative damping from the parametric drive exceeds the positive natural damping of the excited mode.²¹ Figure 2c also shows that the parametric resonance frequency f_{pr} (defined as f_d that gives maximum $P(f_d/2)$ at a given value of V_{ac}) shifts to lower values with increasing drive amplitude due to nonlinear frequency shift, as expected for a uniaxial ferromagnet.²¹ The shape of the parametric instability region in Figure 2c is a typical Arnold tongue of a nonlinear parametric oscillator.³⁰

In order to quantitatively determine the threshold drive voltage V_{th} needed to excite parametric resonance of the quasi-uniform mode, we analyze reduced power of this mode p as a function of the drive amplitude V_{ac} . By definition, $p = |c|^2$ where c is dimensionless amplitude of the quasi-uniform mode (see Supporting Information Section 4), which is proportional to the amplitude of the MTJ resistance oscillations, so that $p \approx (GR_{ac})^2$. It is clear from eq 1 that PSD of the reduced power $p(f)$ is proportional to $P(f)/V_{ac}^2$ for any V_{ac} . In Figure 3, we plot its resonant value $P(f_{pr}/2)/V_{ac}^2$, which is proportional to $p(f_{pr}/2)$, as a function of V_{ac} .

Analytical expressions for $p(f_{pr}/2)$ can be derived in the limit of $V_{ac} \ll V_{th}$. In this limit, magnetization dynamics are small-amplitude thermal fluctuations amplified by the parametric drive, for which

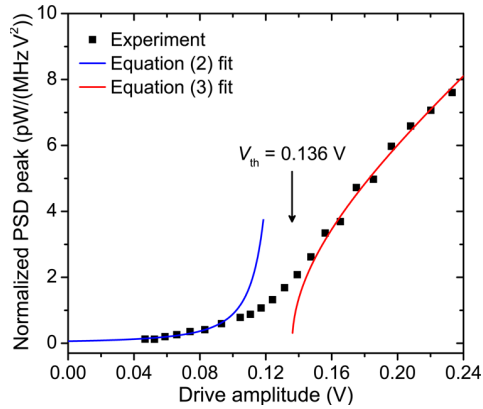


Figure 3. Parametric resonance threshold. Normalized peak amplitude of PSD, $P(f_{pr}/2)/V_{ac}^2$, measured at parametric resonance as a function of the parametric drive amplitude V_{ac} . Best fits of eqs 2 and 3 to the data (solid lines) give the parametric resonance threshold voltage $V_{th} = 0.136$ V.

$$p(f_{pr}/2) = \frac{A}{(V_{th} - V_{ac})^2} \quad (2)$$

where A is a constant (see Supporting Information Section 5).

In the opposite limit of $V_{ac} \gg V_{th}$, thermal fluctuations can be neglected and the following analytical expression for the reduced power p can be derived by

$$p = B\sqrt{V_{ac}^2 - V_{th}^2} \quad (3)$$

where B is a constant (see Supporting Information Section 5).

For our system, p in eq 3 can be replaced by $p(f_{pr}/2)$ because the measured spectral line width of $P(f)$ at $f_d = f_{pr}$ depends weakly on V_{ac} for $V_{ac} > 0.16$ V. Therefore, we can fit the data in Figure 3 using eq 2 in the small amplitude limit and eq 3 in the large amplitude limit. The best fit shown by the blue (small amplitude) and red (large amplitude) lines in Figure 3 gives $V_{th} = 0.136$ V. In this fitting procedure, A and B are free fitting parameters, while V_{th} is treated as a common fitting parameter for both the small and large amplitude limits (see Supporting Information Section 5).

It is instructive to compare the measured V_{th} to its theoretically expected value for our MTJ geometry and the measured VCMA efficiency (see Supporting Information Section 4). The calculated threshold voltage in the macrospin approximation is $V_{th} = 0.086$ V, while that given by micromagnetic simulations is $V_{th} = 0.156$ V. The measured value is similar to the micromagnetic prediction, which lends support to VCMA origin of the observed parametric resonance.

In our experiment, spin-polarized tunneling current flows through the MTJ, which results in ST and Oersted field acting on the free layer. However, these types of drive play a negligible role in exciting parametric resonance compared to the VCMA drive. The Oersted field has nearly circular symmetry, and therefore, it poorly couples to the quasi-uniform mode. The effective fields of both the field-like and damping-like ST lie in the sample plane, which corresponds to perpendicular pumping geometry. Parametric excitation of the quasi-uniform mode at $f_d = 2f_{SW}$ is inefficient in this geometry.²¹

Our experiment employs MTJ magnetic configuration with in-plane SAF and out-of-plane free layer that is convenient for unambiguous demonstration and quantitative analysis of parametric resonance excited by VCMA. However, we find

that VCMA-driven parametric resonance can be observed in other types of MTJ configurations. Figure 4 shows out-of-plane

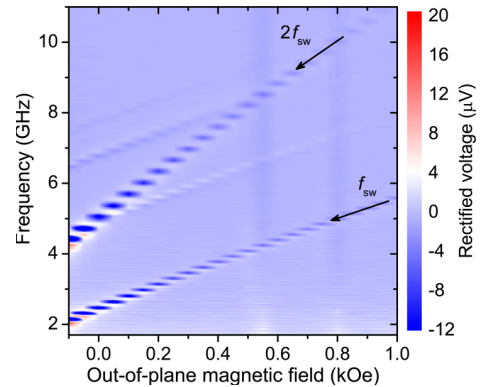


Figure 4. Parametric resonance in ST-FMR. ST-FMR spectra of an MTJ with out-of-plane SAF and free layers measured as a function of out-of-plane magnetic field. Resonance at twice the quasi-uniform mode frequency arises from parametric excitation of the quasi-uniform mode.

magnetic field dependence of ST-FMR spectra measured for a 30 nm × 95 nm MTJ with out-of-plane equilibrium configuration of both the free and SAF layers. Owing to the smaller amplitude of the rectified voltage in this collinear geometry, we employ ultrasensitive ST-FMR with magnetic field modulation²⁹ rather than conventional ST-FMR with amplitude modulation.

The ST-FMR spectra measured at a large value of the microwave drive voltage $V_{ac} = 0.4$ V reveal several spin wave eigenmodes of the free layer. Another prominent resonance is observed at twice the frequency of the lowest-frequency (quasi-uniform) spin wave eigenmode. In this collinear MTJ geometry, the microwave resistance oscillations of the device have a significant component at twice the excited spin wave mode frequency and mix with the parametric drive at twice the mode frequency to give rise to a rectified voltage peak at $2f_{SW}$ measured by ST-FMR. The amplitude of this additional resonance at $2f_{SW}$ relative to the amplitude of the resonance at f_{SW} increases with increasing V_{ac} , which is a signature of a thermally smeared threshold behavior similar to that in Figure 3. The out-of-plane collinear geometry is commonly employed in ST magnetic memory (STT-MRAM), and parametric resonance signals in ST-FMR of STT-MRAM can potentially be used for characterization of the free layer properties such as magnetic damping.

While magnetic damping in ultrathin films of metallic ferromagnets is significant, signal processing devices based on spin wave propagation in nanowires made from these films are feasible if short-wavelength spin waves are employed.¹⁸ The group velocities of such exchange-dominated spin waves can be sufficiently high to enable micrometer-scale spin wave propagation. For example, we calculate the decay length of a 0.1 μm wavelength spin wave in a 1 nm thick, 100 nm wide Fe/MgO nanowire to be 2 μm, assuming the damping constant $\alpha = 0.004$ ³¹ and the spin wave dispersion appropriate for the nanowire.¹⁸ This decay length is sufficiently long to enable signal propagation between neighboring spin wave logic gates separated by submicrometer distances.³² Furthermore, large VCMA at the Fe/MgO interface¹⁴ can be employed for

parametric amplification of spin waves propagating between the gates to counteract the spin wave amplitude decay.³³

In summary, our work shows that magneto-electric coupling can be used to excite parametric resonance of magnetization by electric field. We employ voltage-controlled magnetic anisotropy at the CoFeB/MgO interface to excite parametric oscillations of a CoFeB free layer magnetization in nanoscale magnetic tunnel junctions. The threshold voltage for parametric excitation in this system is found to be well below 1 V, which is attractive for applications in energy-efficient spintronic and magnonic nanodevices such as spin wave logic.³⁴ This work opens a new energy-efficient route for excitation of magnetization dynamics in thin films of metallic ferromagnets and nanodevices based on magnetic multilayers.

■ ASSOCIATED CONTENT

Supporting Information

The Supporting Information is available free of charge on the ACS Publications website at DOI: [10.1021/acs.nanolett.6b04725](https://doi.org/10.1021/acs.nanolett.6b04725).

Micromagnetic simulations of the ground state of the MTJ, estimate of the Gilbert damping, estimate of the VCMA efficiency, theoretical calculation of the parametric resonance threshold, and details of evaluating the parametric resonance threshold in experiment (PDF)

■ AUTHOR INFORMATION

Corresponding Author

*E-mail: yujin.chen@uci.edu.

ORCID

Yu-Jin Chen: [0000-0002-3006-7308](https://orcid.org/0000-0002-3006-7308)

Author Contributions

Y.-J.C., H.K.L., and R.V. contributed equally to this work. Y.-J.C. and H.K.L. performed electrical characterization of the MTJ samples. J.A.K. made the samples. R.V., V.T., and A.N.S. developed the theoretical model. I.N.K., A.N.S., I.B., and J.Q.X. formulated the experimental and theoretical approaches. I.N.K. and A.N.S. managed the project. All authors analyzed the data and cowrote the paper.

Notes

The authors declare no competing financial interest.

■ ACKNOWLEDGMENTS

We acknowledge the Center for NanoFerroic Devices (CNFD) and the Nanoelectronics Research Initiative (NRI) for funding of this work. This work was also supported by NSF Grants EFMA-1641989, ECCS-1309416, ECCS-1305586, and DMR-1610146, by DTRA Grant HDTRA1-16-1-0025, and by the FAME Center, one of six centers of STARnet, an SRC program sponsored by MARCO and DARPA.

■ REFERENCES

- Matsukura, F.; Tokura, Y.; Ohno, H. *Nat. Nanotechnol.* **2015**, *10*, 209–220.
- Chiba, D.; Yamanouchi, M.; Matsukura, F.; Ohno, H. *Science* **2003**, *301*, 943–945.
- Baek, S. H.; Jang, H. W.; Folkman, C. M.; Li, Y. L.; Winchester, B.; Zhang, J. X.; He, Q.; Chu, Y. H.; Nelson, C. T.; Rzechowski, M. S.; Pan, X. Q.; Ramesh, R.; Chen, L. Q.; Eom, C. B. *Nat. Mater.* **2010**, *9*, 309–314.
- Shiota, Y.; Nozaki, T.; Bonell, F.; Murakami, S.; Shinjo, T.; Suzuki, Y. *Nat. Mater.* **2012**, *11*, 39–43.
- Cuellar, F. A.; Liu, Y. H.; Salafranca, J.; Nemes, N.; Iborra, E.; Sanchez-Santolino, G.; Varela, M.; Garcia Hernandez, M.; Freeland, J. W.; Zhernenkov, M.; Fitzsimmons, M. R.; Okamoto, S.; Pennycook, S. J.; Bibes, M.; Barthélémy, A.; te Velthuis, S. G. E.; Sefrioui, Z.; Leon, C.; Santamaria, J. *Nat. Commun.* **2014**, *5*, 4215.
- Heron, J. T.; Trassin, M.; Ashraf, K.; Gajek, M.; He, Q.; Yang, S. Y.; Nikonov, D. E.; Chu, Y.-H.; Salahuddin, S.; Ramesh, R. *Phys. Rev. Lett.* **2011**, *107*, 217202.
- He, X.; Wang, Y.; Wu, N.; Caruso, A. N.; Vescovo, E.; Belashchenko, K. D.; Dowben, P. A.; Binek, C. *Nat. Mater.* **2010**, *9*, 579–585.
- Bauer, U.; Yao, L.; Tan, A. J.; Agrawal, P.; Emori, S.; Tuller, H. L.; van Dijken, S.; Beach, G. S. D. *Nat. Mater.* **2015**, *14*, 174–181.
- Nozaki, T.; Shiota, Y.; Miwa, S.; Murakami, S.; Bonell, F.; Ishibashi, S.; Kubota, H.; Yakushiji, K.; Saruya, T.; Fukushima, A.; Yuasa, S.; Shinjo, T.; Suzuki, Y. *Nat. Phys.* **2012**, *8*, 491–496.
- Zhu, J.; Katine, J. A.; Rowlands, G. E.; Chen, Y.-J.; Duan, Z.; Alzate, J. G.; Upadhyaya, P.; Langer, J.; Khalili Amiri, P.; Wang, K. L.; Krivorotov, I. N. *Phys. Rev. Lett.* **2012**, *108*, 197203.
- Yu, H.; d'Allivy Kelly, O.; Cros, V.; Bernard, R.; Bortolotti, P.; Anane, A.; Brandl, F.; Heimbach, F.; Grundler, D. *Nat. Commun.* **2016**, *7*, 11255.
- Weisheit, M.; Fähler, S.; Marty, A.; Souche, Y.; Poinson, C.; Givord, D. *Science* **2007**, *315*, 349–351.
- Chiba, D.; Sawicki, M.; Nishitani, Y.; Nakatani, Y.; Matsukura, F.; Ohno, H. *Nature* **2008**, *455*, 515–518.
- Maruyama, T.; Shiota, Y.; Nozaki, T.; Ohta, K.; Toda, N.; Mizuguchi, M.; Tulapurkar, A. A.; Shinjo, T.; Shiraishi, M.; Mizukami, S.; Ando, Y.; Suzuki, Y. *Nat. Nanotechnol.* **2009**, *4*, 158–161.
- Niranjan, M. K.; Duan, C.-G.; Jaswal, S. S.; Tsybal, E. Y. *Appl. Phys. Lett.* **2010**, *96*, 222504.
- Wang, W.-G.; Li, M.; Hageman, S.; Chien, C. L. *Nat. Mater.* **2012**, *11*, 64–68.
- Schellekens, A. J.; van den Brink, A.; Franken, J. H.; Swagten, H. J. M.; Koopmans, B. *Nat. Commun.* **2012**, *3*, 847.
- Verba, R.; Tiberkevich, V.; Krivorotov, I.; Slavin, A. *Phys. Rev. Appl.* **2014**, *1*, 044006.
- Kurebayashi, H.; Dzyapko, O.; Demidov, V. E.; Fang, D.; Ferguson, A. J.; Demokritov, S. O. *Appl. Phys. Lett.* **2011**, *99*, 162502.
- Manuilov, S. A.; Du, C. H.; Adur, R.; Wang, H. L.; Bhallamudi, V. P.; Yang, F. Y.; Hammel, P. C. *Appl. Phys. Lett.* **2015**, *107*, 042405.
- Gurevich, A. G.; Melkov, G. A. *Magnetization Oscillations and Waves*; CRC Press: Boca Raton, FL, 1996.
- Melkov, G. A.; Kobljanskyj, Y. V.; Serga, A. A.; Tiberkevich, V. S.; Slavin, A. N. *Phys. Rev. Lett.* **2001**, *86*, 4918.
- Chumak, A. V.; Vasyuchka, V. I.; Serga, A. A.; Kostylev, M. P.; Tiberkevich, V. S.; Hillebrands, B. *Phys. Rev. Lett.* **2012**, *108*, 257207.
- Kruglyak, V. V.; Demokritov, S. O.; Grundler, D. *J. Phys. D: Appl. Phys.* **2010**, *43*, 264001.
- Chumak, A. V.; Vasyuchka, V. I.; Serga, A. A.; Hillebrands, B. *Nat. Phys.* **2015**, *11*, 453–461.
- Urazhdin, S.; Tiberkevich, V.; Slavin, A. *Phys. Rev. Lett.* **2010**, *105*, 237204.
- Tulapurkar, A. A.; Suzuki, Y.; Fukushima, A.; Kubota, H.; Maehara, H.; Tsunekawa, K.; Djayaprawira, D. D.; Watanabe, N.; Yuasa, S. *Nature* **2005**, *438*, 339–342.
- Sankey, J. C.; Braganca, P. M.; Garcia, A. G. F.; Krivorotov, I. N.; Buhrman, R. A.; Ralph, D. C. *Phys. Rev. Lett.* **2006**, *96*, 227601.
- Gonçalves, A. M.; Barsukov, I.; Chen, Y.-J.; Yang, L.; Katine, J. A.; Krivorotov, I. N. *Appl. Phys. Lett.* **2013**, *103*, 172406.
- Bortolotti, P.; Grimaldi, E.; Dussaux, A.; Grollier, J.; Cros, V.; Serpico, C.; Yakushiji, K.; Fukushima, A.; Kubota, H.; Matsumoto, R.; Yuasa, S. *Phys. Rev. B: Condens. Matter Mater. Phys.* **2013**, *88*, 174417.
- Kardasz, B.; Montoya, E. A.; Eyrieh, C.; Girt, E.; Heinrich, B. J. *Appl. Phys.* **2011**, *109*, 07D337.
- Dutta, S.; Chang, S.-C.; Nickvash, K.; Nikonov, D. E.; Sasikanth, M.; Young, I. A.; Naeemi, A. *Sci. Rep.* **2015**, *5*, 9861.
- Verba, R.; Tiberkevich, V.; Slavin, A. *Appl. Phys. Lett.* **2015**, *107*, 112402.

(34) Khitun, A.; Bao, M.; Wang, K. L. *J. Phys. D: Appl. Phys.* **2010**, *43*, 264005.

Supporting Information: Parametric resonance of magnetization excited by electric field

Yu-Jin Chen,^{*,†} Han Kyu Lee,[†] Roman Verba,[‡] Jordan A. Katine,[¶]
 Igor Barsukov,[†] Vasil Tiberkevich,[§] John Q. Xiao,^{||} Andrei N. Slavin,[§] and
 Ilya N. Krivorotov[†]

[†]*Department of Physics and Astronomy, University of California, Irvine, California 92697,
 USA*

[‡]*Institute of Magnetism, Kyiv 03142, Ukraine*

[¶]*HGST, San Jose, California 95135, USA*

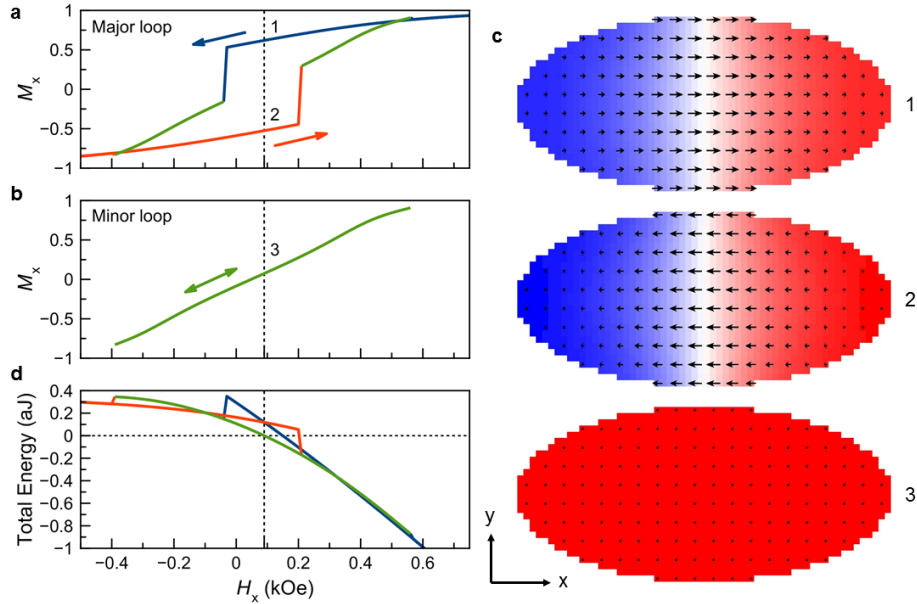
[§]*Department of Physics, Oakland University, Rochester, Michigan 48309, USA*

^{||}*Department of Physics and Astronomy, University of Delaware, Newark, Delaware 19716,
 USA*

E-mail: yujin.chen@uci.edu

S1 Micromagnetic simulations

To determine the magnetic ground state of the MTJ nanopillar studied in this work, we perform micromagnetic simulations of the entire nanopillar stack (including the free and the SAF layers) using OOMMF software.¹ The magnetic material parameters of the free and the SAF layers employed in the simulations were determined in previous studies of these MTJ devices.^{2,3} We simulate the hysteresis loops of the device at zero temperature as a function of in-plane magnetic field H_x . Supplemental Figure 1a shows the major loop of the normalized free layer magnetization M_x as a function of H_x (the SAF layer magnetization



Supplementary Figure 1: Micromagnetic simulations. **a,b**, Normalized magnetization of the free layer M_x as a function of in-plane magnetic field H_x applied parallel to the MTJ long axis, given by zero-temperature micromagnetic simulations (**a** - major loop of the free layer, **b** - minor loop of the free layer). Arrows indicate field sweep direction. **c**, Three stable micromagnetic states of the free layer in the middle of the hysteresis loop: two Néel domain wall states with opposite directions of magnetization in the middle of the domain wall (1 and 2) and the quasi-uniform state (3). Arrows show the in-plane magnetization component while the colors represent the out-of-plane magnetization component with red (blue) being positive (negative). **d**, Total micromagnetic energy of the MTJ as a function of H_x . Colors correspond to the free layer micromagnetic states shown in **a**, **b**, and **c**.

does not switch for the range of H_x employed). This loop is shifted from zero field by a value similar to that observed in the experiment (see Fig. 1b of the main text) due to stray magnetic field from the SAF layer acting on the free layer.

The simulations reveal the presence of three stable states of the free layer magnetization at low fields as illustrated in Supplemental Fig. 1c: two Néel domain wall states with opposite directions of magnetization in the middle of the domain wall (1 and 2) and the quasi-uniform state (3). A minor hysteresis loop shown in Supplemental Fig. 1b demonstrates that the quasi-uniform state of the free layer is stable in a wide range of magnetic fields near zero, suggesting that this state is the ground state near zero field. This is directly confirmed by plotting the total micromagnetic energy of the MTJ as a function of H_x for all three

micromagnetic states of the system (Supplemental Fig. 1d). This plot clearly shows that the quasi-uniform state of the free layer magnetization is the lowest energy state in a significant range of fields near zero. The asymmetry of the total energy in H_x is due to a non-zero net magnetic moment of the SAF layer.

Micromagnetic simulations of the hysteresis loop at room temperature ($T \approx 300$ K) and magnetic field sweep rate employed in our experiment are prohibitively time consuming. However, given the importance of thermal fluctuations for a free layer nanomagnet of the small size and low magnetic anisotropy employed in our measurements, we can expect the free layer is in its lowest energy state for magnetic field values near zero. This assumption is supported by the absence of hysteresis in the experimentally measured $M_x(H_x)$ curve shown in Fig. 1b of the main text. Furthermore, the data in Supplementary Fig. 1d show that the Boltzmann probability of the quasi-uniform state is much greater than that of the domain wall state in the middle of the hysteresis curve. For any two states, the Boltzmann ratio of probabilities of being in those states is:

$$\frac{p_i}{p_j} = \exp [-(E_i - E_j)/k_B T], \quad (\text{S1})$$

where p_i and p_j are the probabilities of being in state i and state j , E_i and E_j are the total micromagnetic energies of the states, k_B is the Boltzmann constant, and T is the temperature. The energy difference between the domain wall state and the quasi-uniform state in the middle of the hysteresis loop is 1.19×10^{-19} J, with the quasi-uniform state being lower in energy as shown in Supplementary Fig. 1d. Therefore, the Boltzmann probability of the domain wall state is 3.5×10^{-13} of that of the quasi-uniform state at $T = 300$ K.

S2 Gilbert damping

The Gilbert damping of the free layer was estimated from the spectral linewidth of the quasi-uniform mode measured by ST-FMR technique at $H_x = 0.06$ kOe. Assuming uniax-

ial anisotropy, the Gilbert damping parameter is given by the ratio of half width at half maximum Δf of the ST-FMR resonance curve $V_r(f_d)$ to the quasi-uniform mode resonance frequency f_{SW} :⁴

$$\alpha = \frac{\Delta f}{f_{\text{SW}}}. \quad (\text{S2})$$

In the experiment (see Fig. 1c of the main text), we find $\Delta f \approx 0.03$ GHz. By using this value of the linewidth and the measured resonance frequency $f_{\text{SW}} = 0.91$ GHz, we obtain an estimate of the free layer Gilbert damping constant $\alpha \approx 0.033$.

S3 VCMA efficiency

The observed linear shift of the quasi-uniform mode resonance frequency f_{SW} with applied direct voltage V_{dc} shown in Fig. 1e of the main text arises exclusively from VCMA. The effective fields due to field-like and damping-like spin torque are perpendicular to the free layer magnetization for the perpendicular orientation of the free and the SAF magnetic moments employed in our experiment. Such perpendicular fields can only induce a quadratic shift of the quasi-uniform mode frequency. The frequency shift due to Ohmic heating is independent of the current polarity and thus is also quadratic in V_{dc} to leading order. Given the linear relation between the resonance frequency f_{SW} and the anisotropy field H_{u} for a uniaxial ferromagnet, the slope of the line in Fig. 1e in the main text is

$$\frac{\gamma}{2\pi} \frac{dH_{\text{u}}}{dV_{\text{dc}}}, \quad (\text{S3})$$

where the gyromagnetic ratio γ is taken to be 176 GHz/T. The data in Fig. 1e in the main text gives VCMA efficiency $\frac{dH_{\text{u}}}{dV_{\text{dc}}} = 526$ Oe/V, which is typical for this material system.²

S4 Theory of parametric resonance threshold

For the theoretical description of parametric resonance of the MTJ free layer we employ a single-mode approximation. We expand the free layer magnetization into static and dynamic parts: $\mathbf{M}(\mathbf{r}, t) = M_s(\boldsymbol{\mu} + c(t)\mathbf{m}(\mathbf{r}) + c^*(t)\mathbf{m}^*(\mathbf{r}))$, where $\boldsymbol{\mu}$ is the unit vector in the direction of the static magnetization, $\mathbf{m}(\mathbf{r})$ is the coordinate-dependent vector structure of the spin wave mode, and c is the dimensionless amplitude of this mode. Starting from the Landau-Lifshitz-Gilbert equation, the following nonlinear equation describing the dynamics can be derived:^{4,5}

$$\frac{dc}{dt} + i(\omega_{\text{SW}} + \Psi|c|^2)c + \Gamma c = hV_{00}e^{i\omega_p t}c^* + \eta(t), \quad (\text{S4})$$

where $\omega_{\text{SW}} = 2\pi f_{\text{SW}}$ is the spin wave mode angular frequency, Ψ is the nonlinear frequency shift of the mode, Γ is the damping rate of the mode, h is the effective pumping field amplitude, ω_p is the pumping frequency, V_{00} is the efficiency of parametric interaction, and $\eta(t)$ describes thermal noise (see Ref.⁶ for details). In these notations, the parametric resonance threshold field is $h_{\text{th}} = \Gamma/|V_{00}|$, where $|V_{00}| = \frac{\gamma\mu_0}{2}\varepsilon$, γ is the gyromagnetic ratio taken to be 176 GHz/T, $\mu_0 = 4\pi \times 10^{-7} \text{ T}\cdot\text{m/A}$ is the permeability of vacuum, and the damping rate $\Gamma = 2\pi\Delta f = 2\pi \times 0.03 \text{ GHz}$.^{4,5} Averaged ellipticity of the spin wave mode ε is given by:⁵

$$\varepsilon = \left| \frac{\langle \mathbf{m}^* \cdot \mathbf{m}^* \rangle_{\mathbf{r}}}{\langle \mathbf{m}^* \cdot (\boldsymbol{\mu} \times \mathbf{m}) \rangle_{\mathbf{r}}} \right|, \quad (\text{S5})$$

where $\langle \dots \rangle_{\mathbf{r}}$ denotes a spatial average over the free layer volume.

We calculate the quasi-uniform mode ellipticity from the micromagnetic mode profile. This calculation gives $\varepsilon = 0.26$, which results in $h_{\text{th}} = 6.5 \text{ kA/m} = 82 \text{ Oe}$. This gives the threshold voltage for excitation of parametric resonance $V_{\text{th}} = h_{\text{th}} \frac{dV_{\text{dc}}}{dH_{\text{u}}} = 0.156 \text{ V}$. This micromagnetic value of V_{th} is significantly higher than that given by the macrospin approximation with $\varepsilon = \omega_{\text{M}}|N_x - N_y|/(2\omega_{\text{SW}})$, where $\omega_{\text{M}} = \gamma\mu_0 M_s$ (with $M_s = 950 \text{ kA/m}$), $N_x = 0.014$ and $N_y = 0.040$ are components of the free layer demagnetization tensor,⁷ and $\omega_{\text{SW}} = 2\pi \times 0.91 \text{ GHz}$ is the spin wave mode frequency. The higher value of ellipticity

($\varepsilon = 0.478$) in the macrospin approximation leads to a lower parametric threshold: $h_{\text{th}} = 45$ Oe and $V_{\text{th}} = 0.085$ V. As expected, the experimentally measured value of the threshold voltage $V_{\text{th}} = 0.136$ V is much higher than that given by the macrospin approximation but it is similar to that appropriate for micromagnetic profile of the quasi-uniform mode. The 15% discrepancy between the measured and the theoretically predicted threshold could arise from deviation of the free layer shape from the ideal elliptical shape assumed in the simulations and from over-estimation of the damping parameter of the free layer.

S5 Evaluation of the parametric resonance threshold from experiment

To determine the threshold voltage for parametric excitation V_{th} from the experimental data in Fig. 3 of the main text, we fit these data to theoretical expressions of the oscillation power as a function of the drive amplitude V_{ac} . These expressions are derived below for two limits: $V_{\text{ac}} \ll V_{\text{th}}$ and $V_{\text{ac}} \gg V_{\text{th}}$.

S5A Below the threshold

Well below the threshold ($V_{\text{ac}} \ll V_{\text{th}}$), the nonlinear frequency shift in Eq. (S4) can be neglected and the parametric resonance frequency f_{pr} is equal to twice the spin wave mode frequency ($f_{\text{pr}} = 2f_{\text{SW}}$). In this limit, the reduced integrated power p of the spin wave mode is given by the expression below when the free layer is driven exactly at the parametric resonance frequency f_{pr} :

$$p = \langle |c|^2 \rangle = \frac{C_1}{\Gamma - |hV_{00}|} + \frac{C_1}{\Gamma + |hV_{00}|} = \frac{D}{(V_{\text{th}} - V_{\text{ac}})} + \frac{D}{(V_{\text{th}} + V_{\text{ac}})}, \quad (\text{S6})$$

where $\langle \dots \rangle$ denotes a thermal average. In deriving this expression, we assumed white thermal noise: $\langle \eta(t)\eta(\tau) \rangle = C_2\delta(t - \tau)$ and $\langle \eta(t)\eta^*(\tau) \rangle = C_1\delta(t - \tau)$, where C_1 , C_2 and $D = C_1V_{\text{th}}/\Gamma$

are constants. Here we also employed the linear relation between the effective (VCMA) pumping field amplitude h and the microwave voltage amplitude V_{ac} , which is evident from Fig. 1e of the main text.

By expanding the noise term into Fourier series, we obtain the following expression for reduced power spectral density $p(f)$ of the spin wave mode oscillations:

$$p(f) = \langle |c(f)|^2 \rangle = \frac{C_2}{(\Gamma - |hV_{00}|)^2 + (2\pi(f - f_{SW}))^2} + \frac{C_2}{(\Gamma + |hV_{00}|)^2 + (2\pi(f - f_{SW}))^2} \quad (S7)$$

$$= \frac{A}{(V_{th} - V_{ac})^2 + (2\pi(f - f_{SW})V_{th}/\Gamma)^2} + \frac{A}{(V_{th} + V_{ac})^2 + (2\pi(f - f_{SW})V_{th}/\Gamma)^2}, \quad (S8)$$

where $A = C_2 V_{th}^2 / \Gamma^2$ is a constant. Setting $f = f_{SW}$ in Eq. (S8), we obtain an expression for the peak value of the reduced PSD that is observed at $f = f_{SW} = f_{pr}/2$:

$$p(f_{pr}/2) = \langle |c(f_{pr}/2)|^2 \rangle = \frac{A}{(V_{th} - V_{ac})^2} + \frac{A}{(V_{th} + V_{ac})^2}. \quad (S9)$$

The second term in Eq. (S9) is much smaller than the first one for V_{ac} approaching V_{th} and it can be neglected in fitting the experimental data of Fig. 3 of the main text:

$$p(f_{pr}/2) = \langle |c(f_{pr}/2)|^2 \rangle = \frac{A}{(V_{th} - V_{ac})^2}. \quad (S10)$$

S5B Above the threshold

Well above the threshold ($V_{ac} \gg V_{th}$), the integrated power of the parametrically excited quasi-uniform mode is nearly temperature independent and can be approximated by its zero-temperature value.⁸ Neglecting the thermal noise term in Eq. (S4), we derive:

$$p = |c|^2 = \frac{1}{|\Psi|} \left(\sqrt{(hV_{00})^2 - (h_{th}V_{00})^2} + 2\pi(f_{pr}/2 - f_{SW})\text{sign}(\Psi) \right). \quad (S11)$$

We assume that the deviation of f_{pr} from $2f_{SW}$ is small, so that the second term in the parentheses can be neglected compared to the first term. In this case, Eq. (S11) takes a

simple form:

$$p = B\sqrt{V_{ac}^2 - V_{th}^2}, \quad (\text{S12})$$

where $B = \Gamma/(|\Psi|V_{th})$ is a constant.

S5C Details of the fitting procedure

The fitting of the normalized peak power data shown in Fig. 3 of the main text to Eq. (S10) and Eq. (S12) was performed by the least squares method with A , B and V_{th} as fitting parameters. A range of data near the threshold voltage must be excluded in the fitting procedure because neither Eq. (S10) nor Eq. (S12) is valid at the threshold voltage. We chose the data range where $V_{ac} < 0.1 \text{ V}$ for the low-power fit and the data range where $V_{ac} > 0.16 \text{ V}$ for the high-power fit (the excluded data range is $0.1 \text{ V} - 0.16 \text{ V}$) because the best fit parameters do not change significantly upon further extension of the excluded data range. The threshold voltage given by this fitting procedure is $V_{th} = 0.136 \text{ V}$.

References

- (1) Donahue, M. J.; Porter, D. G. OOMMF Users Guide, Version 1.0, Interagency Report NISTIR 6376, National Institute of Standards and Technology, Gaithersburg, MD (1999).
- (2) Zhu, J.; Katine, J. A.; Rowlands, G. E.; Chen, Y.-J.; Duan, Z.; Alzate, J. G.; Upadhyaya, P.; Langer, J.; Khalili Amiri, P.; Wang, K. L.; Krivorotov, I. N. *Phys. Rev. Lett.* **2012**, *108*, 197203.
- (3) Gonçalves, A. M.; Barsukov, I.; Chen, Y.-J.; Yang, L.; Katine, J. A.; Krivorotov, I.N. *Appl. Phys. Lett.* **2013**, *103*, 172406.
- (4) Gurevich, A. G.; Melkov, G. A. *Magnetization Oscillations and Waves*; CRC Press: Boca Raton, FL, 1996.

- (5) Verba, R.; Tiberkevich, V.; Krivorotov, I.; Slavin, A. *Phys. Rev. Appl.* **2014**, *1*, 044006.
- (6) Verba, R.; Tiberkevich V.; Guslienko, K.; Melkov, G.; Slavin, A. *Phys. Rev. B* **2013**, *87*, 134419.
- (7) Beleggia, M.; De Graef, M.; Millev, Y. T.; Goode, D. A.; Rowlands, G. *J. Phys. D: Appl. Phys.* **2005**, *38*, 3333-3342.
- (8) Slavin, A.; Tiberkevich, V. *IEEE Trans. Magn.* **2009**, *45*, 1875-1918.

РОЗДІЛ 2

**АМПЛІТУДНО-ФАЗОВИЙ КОНТРОЛЬ СПІНОВИХ ХВИЛЬ
КВАЗІСТАТИЧНИМ ЕЛЕКТРИЧНИМ ПОЛЕМ**

Зазвичай, для контрольованої динамічної зміни фази СХ, повного або часткового її відбиття використовують локально прикладене магнітне поле, яке локально змінює дисперсію СХ. Аналогом цього методу у підході електрично керованої магнетоники є локальне прикладання квазістатичного електричного поля, яке призводить до локальної зміни анізотропії. Як показано нижче, у випадку зміни анізотропії суттєву роль починає відігравати зміна поляризації СХ, яка є несуттєвою при прикладанні магнітного поля. Детальному дослідженню впливу поляризації на проходження СХ через внутрішні границі розділу присвячено підрозділ 2.1. У ньому здебільшого розглянуті СХ в обмінному наближенні (відносно короткі СХ) і якісно розглянуті особливості, які очікуються для дипольних СХ. Зокрема, показано, що СХ у геометрії Деймона-Ешбаха можуть поводити себе суттєво відмінно від інших СХ. Детально особливості розсіювання СХ у геометрії Деймона-Ешбаха розглянуті у підрозділі 2.2. Хоча у підрозділі 2.2 у якості магнітного матеріалу розглядається залізо-іттрієвий гранат (ЗІГ), який не виявляє ефекту ЕКМА (для ЗІГ було виконане моделювання співавторами), у тонких хвилеводах провідних феромагнетиків очікуються такі ж ефекти. Справді, обмінна довжина у типових провідних феромагнетиків (Fe, CoFeB) у 4-5 разів менша за обмінну довжину у ЗІГ, тому ефекти, продемонстровані для ЗІГ товщиною 30 нм будуть проявлятися у плівках провідних феромагнетиків товщиною 5 нм і менше, для яких вже можливе електричне керування завдяки ЕКМА.

Автором дисертації було побудовано теорію проходження СХ з урахуванням зміни їх поляризації, проведене мікромагнітне моделювання проходження СХ через ЕКМА керовану область, а також проаналізовано симетрію СХ у геометрії Деймона-Ешбаха, і дано якісне пояснення підвищеній стійкості цих хвиль до розсіювання.

2.1. Теорія проходження спінових хвиль через внутрішню границю розділу з урахуванням зміни їх поляризації

PHYSICAL REVIEW B **101**, 144430 (2020)

Spin-wave transmission through an internal boundary: Beyond the scalar approximation

Roman Verba¹, Vasil Tiberkevich² and Andrei Slavin²

¹*Institute of Magnetism, Kyiv 03142, Ukraine*

²*Department of Physics, Oakland University, Rochester, Michigan 48309, USA*



(Received 15 January 2020; revised manuscript received 25 March 2020; accepted 27 March 2020; published 20 April 2020)

The transmission and reflection of a spin wave at an internal boundary created by the local variation of anisotropy (or a bias magnetic field) are studied taking into account not only the changes in the wave amplitude, but also the changes in the wave polarization. It is shown that the account of the changes in the spin-wave polarization before and after the boundary leads to (i) increase of the spin-wave amplitude reflection coefficient, (ii) appearance of an additional phase shift $\Delta\phi \neq 0, \pi$ in both transmitted and reflected waves, and (iii) creation of additional evanescent waves in the vicinity of the boundary. It is also shown that even when significant changes in the transmitted wave polarization take place at the boundary, a spin wave could pass a finite-width boundary without reflection, if a certain resonance condition is satisfied. The effect of the polarization change at an internal boundary is especially pronounced for the exchange-dominated spin waves, while in the case of the dipole-dominated spin waves, this effect can vanish completely for certain configurations of the static magnetization.

DOI: [10.1103/PhysRevB.101.144430](https://doi.org/10.1103/PhysRevB.101.144430)

I. INTRODUCTION

Spin waves (SWs) in ferromagnetic materials are considered as promising candidates for signal carriers in the next generation of signal processing devices. This is closely related to the attractive intrinsic properties of spin waves, such as relatively low damping, high frequency, small wavelength, down to tens of nanometers, and a variety of possible nonlinear SW interactions [1–5]. In order to process information, one should be able to perform different linear and nonlinear operations with SWs. In particular, the operations of interest for signal processing are controllable reflection/transmission of SWs and variation of the SW phase, which can be performed by a local variation of the SW spectrum. Such local spectrum variations were realized many times in bulk and submillimeter ferromagnetic (FM) samples by the application of an additional localized static magnetic field. In particular, attenuation [6,7] and frequency-dependent reflection [8] of SWs by a field-induced inhomogeneity were realized, as well as the resonance tunneling of SWs through a potential barrier [9], and generation of SW pulse trains by magnetic field-induced mirrors [10].

At nanoscale, however, application of local (10–100 nm) magnetic field is technically complicated and inefficient. Instead, it is much more convenient and energy efficient to vary the local magnetic properties of the propagation medium using a variety of magnetoelectric effects [11–14], among which one of the most promising for application at a nanoscale is the effect of voltage-controlled magnetic anisotropy (VCMA) in ferromagnetic metal/dielectric heterostructures [15–17]. The use of the VCMA effect has been already proposed for magnetic recording [18,19], excitation of SWs [20–23] and magnetic solitons [24]. In the VCMA effect, as well as in several other magnetoelectric effects, the application of an

electric field results in the variation of the FM *magnetic anisotropy* which, of course, leads to the variation of the SW spectrum [25,26].

It is important to note that SWs are characterized not only by their dispersion relation, but also by the vector structure. Magnetization precession is circular only in an isotropic ferromagnetic sample. The presence of crystalline or shape anisotropy, as well as dynamic dipolar interaction, which is anisotropic, leads to an elliptic trajectory of the magnetization precession, i.e., to the appearance of a nonzero SW ellipticity $\varepsilon = 1 - m_{\min}/m_{\max}$, where $m_{\min, \max}$ are the dynamic magnetization components in the propagating SW. As the SW ellipticity is determined by the total effective anisotropy, the variation of the material anisotropy in the propagation medium, caused, e.g., by an external bias electric field through the VCMA effect, could *significantly* modify the ellipticity of a propagating SW. Strictly speaking, the application of a localized external static magnetic field also changes the SW ellipticity, except in some symmetric cases (like the case of SW propagation in the perpendicularly magnetized isotropic FM film), because it changes the relation between the components of total effective magnetic field acting on the magnetization. However, this effect is much weaker, than the effect of the local anisotropy variation.

This is illustrated by Fig. 1, where the SW spectra and ellipticity are shown for SWs propagating in an in-plane magnetized FM nanowire subjected to different in-plane bias magnetic fields [Figs. 1(a) and 1(c)] and different perpendicular electric fields [Figs. 1(b) and 1(d)], which modify the local magnetic anisotropy due to the VCMA effect. One can see, that in this example the parameters of the applied static magnetic and electric fields were chosen in such a way, that the SW spectral variations caused by the application of these fields were very similar. At the same time, the variation of

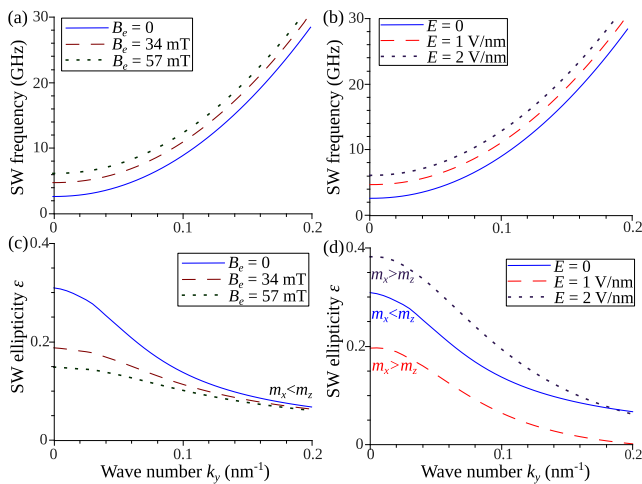


FIG. 1. Spectrum [(a) and (b)] and ellipticity [(c) and (d)] of SWs propagating in a ferromagnetic nanowire under different applied static magnetic fields [(a) and (c)] and electric fields, causing the local anisotropy modification via VCMA effect [(b) and (d)]. Parameters: Fe/MgO nanowire of the 20 nm width, Fe thickness 0.86 nm, static magnetization and the bias magnetic field are directed along the nanowire, saturation magnetization $M_s = 2.1$ T, exchange length $\lambda_{\text{ex}} = 3.4$ nm, constant of the perpendicular surface anisotropy $K_s = 1.36$ mJ/m², and magnetoelectric coefficient $\beta = 100$ fJ/(Vm) [27].

the SW ellipticity in the case of the anisotropy modification caused by the electric field are much more pronounced. With the anisotropy modification, the ellipticity variation takes place in a wider range of the SW wave numbers, and even the major and minor axes of the magnetization precession in the propagating SW could be interchanged by the action of the external electric field through the VCMA effect [see Fig. 1(d)].

Thus it is only natural to ask a question on how such a significant modification of the SW vectorial structure would affect the transmission and reflection of SWs from the internal boundary created by the local variation of the FM anisotropy, and under which circumstances this effect becomes practically important.

Theoretically the problem of SW transmission between different ferromagnetic materials or different regions of the same material was studied for many years. Starting from seminal work by Rado and Weertman [28] there were many research interest to the boundary conditions at the ferromagnet interface, including study of the effect of magnetoelastic interaction [29], finite width and diffusive character of interfaces [30–32], nonuniform dipolar fields [33,34], Dzyaloshinski-Moriya interaction [35], magnetic anisotropy of interface [36,37], etc. The problem of the SW reflection from a sharp boundary was studied in details for exchange-dominated SWs in isotropic, uniaxial and biaxial anisotropic ferromagnets [38–40]. The case of smooth interface was studied for both dipolar [6,7] and exchange-dominated SWs [30,31]. A closely related problem of the phase accumulation of SWs propagating in a nonuniform field was considered in Refs. [41,42]. Recently, the problem of transmission and reflection of exchange-dominated SWs from

an interface between two biaxial magnetic materials has been considered again [43] and formation of surface exchange SWs at the boundary has been predicted for the first time.

In almost all the previously published papers, the problem of the SW transmission through a boundary (or a region with modified magnetic parameters) was considered within a scalar approximation, in which SW was described by a single effective scalar variable. This scalar variable can be introduced in a multiple ways. Either a spin density formalism can be employed [38,39] or a single variable describing circularly polarized dynamic magnetization can be introduced [41] or one of the dynamic magnetization components is simply neglected [6,7].

In our current work, we go beyond the scalar approximation and study the SW transmission and reflection using the full *vector* equations of motion, accounting, thus, for the SW *polarization*. As it will be shown below, the variation of the SW polarization results in a qualitatively different behavior of a SW transmitted through a boundary, such as the appearance of localized modes near the boundary, and appearance of a nonzero phase shift in the transmitted wave. We develop an analytical theory of the SW transmission through a sharp internal boundary for dipole-exchange and exchange-dominated SWs, and derive a criterion allowing one to determine the range of validity of the commonly used scalar approximation. The developed theory is general, and is not limited to the case when the internal boundary is introduced by the VCMA. This case will be discussed below simply to illustrate the developed general formalism.

The paper is organized as follows. In Sec. II, the geometry of the problem, and the general equations of motion for the magnetization are introduced. The boundary conditions, and the vectorial structure of SWs modes, localized near the boundary, are described in Sec. III. Analytical expressions for the coefficients of SW transmission and reflection from an isolated boundary, and from a finite-width region with modified magnetic parameters (two consequent boundaries separated by a finite distance) are derived and discussed in Sec. IV within the exchange approximation. Effects of the dipolar interaction on the obtained results are discussed in Sec. V. Finally, conclusions are given in Sec. VI.

II. MODEL AND INITIAL EQUATIONS

The geometry of the considered problem is shown in Fig. 2. We consider a quasi-one-dimensional problem, when SWs propagate in a ferromagnetic waveguide (e.g., stripe or nanowire) along the axis of a waveguide (y axis in Fig. 2). The boundary between the regions with different magnetic properties is perpendicular to the SW propagation direction (x -axis). We also assume that the SW profile in the x - z plane (perpendicular to the propagation direction) remains unchanged in both regions. This assumption is absolutely natural for relatively thin ferromagnetic films and nanowires with the thickness of the order of several exchange lengths for a given FM material. In such a case, the SW profile along the film thickness is maintained uniform by the exchange interaction, and the width profiles of different SW modes are defined by

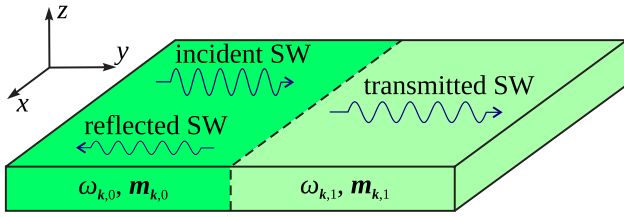


FIG. 2. Geometry of an SW waveguide with a single internal boundary: SW propagates along the FM waveguide through a sharp internal boundary between the two waveguide regions which have different magnetic properties, and, therefore, different SW dispersion relations and different vector structure (polarization) of the SW modes.

the effective dipolar boundary conditions, which are almost independent of the SW wave vector and values of the bias magnetic field or anisotropy [33,34,44]. The assumption of a constant SW transverse profile works also in much larger samples, like micrometer-sized ferromagnetic strips or films, if the propagation of the *bulk* SW modes is considered. For example, such a case is realized if a FM film or a strip is magnetized in the y or z directions. A well-known exemption, which cannot be considered within the above mentioned assumption, is the Damon-Eshbach surface SW mode, which propagates in an in-plane magnetized film perpendicularly to the direction of the static magnetization (i.e., the static magnetization is along the x direction in Fig. 2). The thickness profile of the Damon-Eshbach mode depends on its wave number [45] (in relatively thick films), and the solution of the boundary problem in such a case requires accounting of *all* the SW modes of the film.

We consider the SW propagation in an FM waveguide through an internal boundary—a boundary between two regions of the same FM waveguide. This boundary can be created by any external influence, e.g., by the application of an external bias magnetic field, electric field or strain. Thus the regions of the FM waveguide separated by the boundary can differ by the values of the static internal magnetic field or magnetic anisotropy, while the saturation magnetization M_s and the exchange length λ_{ex} are the same in both regions. The static magnetization is assumed to be uniform, and have the same direction in both separated regions of the waveguide. The boundary is considered to be sharp, which physically means that the area in which the external control parameter (magnetic field, electric field, strain, etc.) varies is much smaller than the SW wavelength. For ultrathin nanowires, where the magnetic anisotropy could be modified by the VCMA effect, this is an absolutely natural approximation for all the range of the experimentally achievable SW wavelengths. It should be noted, that below we do not use any specific features of VCMA-induced anisotropy variation. All the theory uses only the SW dispersion relation and vector structure, and, thus, could be applied to boundaries created by any physical effects within the limits described above. Also, the theory can be generalized to the case of the interface between the *different* ferromagnetic materials, and one should expect qualitatively similar effects.

Within the above formulated approach the propagation of SWs is described by the following equation (see Refs. [46–48]

for the details of this formalism):

$$\frac{\partial \mathbf{m}(y, t)}{\partial t} = \boldsymbol{\mu} \times \hat{\boldsymbol{\Omega}} * \mathbf{m}(y', t), \quad (1)$$

where the tensor operator

$$\hat{\boldsymbol{\Omega}} = \delta(y - y') \left(\gamma B - \omega_M \lambda_{\text{ex}}^2 \frac{\partial^2}{\partial y^2} + \omega_M \hat{N}_{\text{an}} \right) + \omega_M \int dy' \hat{\mathbf{G}}_{\text{dip}}(y - y'). \quad (2)$$

Here, $\boldsymbol{\mu}$ ($|\boldsymbol{\mu}| = 1$) and $\mathbf{m}(y, t)$ are the dimensionless static and dynamic magnetization components, so that the full magnetization vector is written as $\mathbf{M}(y, t) = M_s(\boldsymbol{\mu} + \mathbf{m}(y, t))$, B is the static internal magnetic field inside the FM waveguide, λ_{ex} is the exchange length of the FM material, tensor $\hat{N}_{\text{an}} = -B_{\text{an}}/(\mu_0 M_s)(\mathbf{e}_z' \otimes \mathbf{e}_z')$ describes the uniaxial anisotropy with effective anisotropy field B_{an} and anisotropy axis \mathbf{e}_z' [47], and $\hat{\mathbf{G}}_{\text{dip}}$ is the magnetostatic Green's function, which depends on the sample geometry [49]. For the considered problem, obviously, B and \hat{N}_{an} can be different in different regions of the FM waveguide. Since the magnetic damping is not of a qualitative importance for the particular scattering problem considered here, in the following it is neglected. Note, that if the profile of the propagating SW mode is not uniform in the x - z plane, Eq. (2) remains valid, but proper expression for the Green's function $\hat{\mathbf{G}}_{\text{dip}}$ should be used (i.e., when averaging standard two-dimensional Green's function over the nanowire width actual SW profile should be taken into account [49]).

Considering transmission of a monochromatic SW with the angular frequency ω , we represent the SW dynamic magnetization via its complex amplitudes: $\mathbf{m}(y, t) = (\mathbf{m}(y) \exp[-i\omega t] + \text{c.c.})$, which results in the replacement $\partial \mathbf{m}(y, t)/\partial t \rightarrow -i\omega \mathbf{m}(y)$ in Eq. (1). In a general case, the resulting integral-differential equation can not be solved analytically. However, for a sufficiently large SW wave number k (see criteria below), the exchange interaction becomes dominant, and the integral operator in Eq. (2) can be replaced with its Fourier-transform $\hat{\mathbf{F}}_k = \int \hat{\mathbf{G}}_{\text{dip}}(y) e^{-iky} dy$. Consequently, Eq. (1) becomes an ordinary differential equation, which for the considered case of a sharp boundary can be solved in each region separately, and a proper boundary conditions should be applied. In both regions separated by the boundary, the SW has the form of a harmonic wave with the wave vector $\mathbf{k} = k\mathbf{e}_y$: $\mathbf{m}(y, t) = (\mathbf{m}_k \exp[i(ky - \omega_k t)] + \text{c.c.})$. The SW dispersion relation $\omega_k(k)$ and the vector structure \mathbf{m}_k of the propagating SW mode are determined from the following eigenvalue problem [46,47]:

$$-i\omega_k \mathbf{m}_k = \boldsymbol{\mu} \times \hat{\boldsymbol{\Omega}}_k \cdot \mathbf{m}_k, \quad (3)$$

$$\hat{\boldsymbol{\Omega}}_k = (\gamma B + \omega_M \lambda_{\text{ex}}^2 k^2) \hat{\mathbf{I}} + \omega_M (\hat{\mathbf{F}}_k + \hat{N}_{\text{an}}). \quad (4)$$

The range of validity of the above described exchange approximation can be easily evaluated from Eqs. (3) and (4). Comparing the exchange contribution to the SW energy (frequency) and maximal possible dipolar contributions one finds that the last one is negligible if $\lambda_{\text{ex}}^2 k^2 \gg \max_{\alpha, \beta} |F_{k, \alpha\beta} - F_{0, \alpha\beta}|$. Note that $\hat{\mathbf{F}}_0$ is the simple static demagnetization tensor of the used FM waveguide.

III. BOUNDARY CONDITIONS AND EVANESCENT SPIN WAVES

In the case when M_0 and λ_{ex} are the same in both regions, the following conditions of continuity of the dynamic magnetization $\mathbf{m}(y)$ and its derivative should be satisfied at the boundary (located at $y = 0$):

$$\mathbf{m}(y = 0_-) = \mathbf{m}(y = 0_+), \quad \left. \frac{\partial \mathbf{m}}{\partial y} \right|_{y=0_-} = \left. \frac{\partial \mathbf{m}}{\partial y} \right|_{y=0_+}. \quad (5)$$

If the SW vector structure is the same in both regions, one can represent dynamic magnetization using a scalar variable $a(y)$: $\mathbf{m}(y) = \mathbf{m}_0 a(y)$. In such a scalar approximation, the conditions (5) are reduced to two scalar equations, and it is easy to calculate the SW reflection R and transmission T coefficients at the boundary by choosing the solution as a sum of incident and reflected waves before the boundary, $a(y < 0) = e^{ik_0 y} + R e^{-ik_0 y}$, and a single transmitted wave after the boundary, $a(y > 0) = T e^{ik_1 y}$. This solution is well-known

$$R = \frac{k_0 - k_1}{k_0 + k_1}, \quad T = \frac{2k_0}{k_0 + k_1}. \quad (6)$$

The wave number k_1 , of course, is determined from the dispersion relation, so that the frequencies of the incident and transmitted SWs are the same: $\omega_0(k_0) = \omega_1(k_1)$. From Eq. (6), it is clear that the SW reflection coefficient increases when the difference of SW wave numbers, determined by the difference of the external control parameters before and after the boundary becomes larger. One can also see, that the transmitted SW is always in phase with the incident one, while the reflected SWs could be in phase, or acquire a phase shift $\Delta\phi = \pi$ depending whether $k_0 > k_1$ or not.

In a general “vectorial” case, however, one should use the full boundary conditions (5). It is clear, that choosing solution as a sum of the incident and reflected SWs before the boundary and as a single transmitted SW after the boundary, it is not possible to satisfy the boundary conditions as there are only two scalar parameters to be determined (R and T) and four scalar equations to be satisfied (since \mathbf{m} is, effectively, a two-component vector perpendicular to the static magnetization). Consequently, there should be the *other* waves, which, together with the incident, reflected and transmitted SWs, will allow us to satisfy the boundary conditions.

To understand what are these “other” additional SWs, let us look closer at Eq. (3). For a fixed SW frequency ω , Eq. (3) can be considered as an eigenvalue problem for the SW wave vector k^2 and the vector \mathbf{m}_k characterizing the vectorial structure of the SW mode. In the range of existence of the propagating SW mode this eigenvalue problem has two solutions: one with the $k^2 > 0$, which describes the propagating SWs having the vectorial profile \mathbf{m}_k , and the second solution with $k^2 = -\kappa^2 < 0$, which corresponds to the *exponentially localized (evanescent)* SWs with the spatial distribution $\mathbf{m}(y) \sim \exp[\pm\kappa y]$. The “wave number” of these evanescent SWs for an arbitrary anisotropy and static magnetization can be represented as

$$\kappa^2 = \frac{2\omega_k |\mathbf{m}_k|^2}{\omega_M \lambda_{\text{ex}}^2 A_k} - k^2, \quad (7)$$

where $A_k = i(\mathbf{m}_k^* \cdot \boldsymbol{\mu} \times \mathbf{m}_k)$ is the norm of the propagating SW mode \mathbf{m}_k [46]. The vector structure of these localized waves (to the accuracy of an arbitrary multiplier) is determined as

$$\mathbf{m}_{\text{ev}} = \boldsymbol{\mu} \times \mathbf{m}_k^*. \quad (8)$$

For example, if a propagating SW has polarization $\mathbf{m}_k = m_x \mathbf{e}_x + i m_y \mathbf{e}_y$, then the structure of the evanescent SW is described by $\mathbf{m}_{\text{ev}} = m_y \mathbf{e}_x - i m_x \mathbf{e}_y$. In other words, the evanescent wave has the opposite direction of the magnetization vector rotation compared to the incident SW, and the precession ellipse in the case of an evanescent wave is rotated on 90° . Note that in a general case the polarizations of the propagating incident and the localized evanescent SWs are *orthogonal*, in the sense $\mathbf{m}_{\text{ev}}^* \cdot \mathbf{m}_k = 0$, that is expected. The existence of the similar evanescent SWs near the boundary was first predicted in Ref. [43].

The existence of these evanescent SWs is natural. The SWs with orthogonal polarization cannot propagate in a FM waveguide. Consequently, if such an SW is injected into the waveguide, it should decay at a certain decay length. Equation (7) determines the magnitude of the characteristic decay length $l = 1/\kappa$ of these evanescent SWs. It can be shown that $\kappa^2 > k^2$ for any parameters of the waveguide, i.e., the evanescent SW decays on the length which is of the order, or smaller, than the wavelength of the propagating SW of the same frequency.

IV. TRANSMISSION AND REFLECTION OF THE SPIN WAVES AT A BOUNDARY IN THE EXCHANGE APPROXIMATION

A. Single internal boundary

In this section, we calculate the transmission and reflection coefficients for a SW passing through a single internal boundary, as shown in Fig. 2. As it was pointed out in the previous section, for the proper description of scattering from the boundary one should represent the dynamical magnetization before the boundary as a sum of incident, reflected, and evanescent SWs:

$$\mathbf{m}(y < 0) = \mathbf{m}_{k,0}(e^{ik_0 y} + R e^{-ik_0 y}) + C_1 \mathbf{m}_{\text{ev},0} e^{\kappa_0 y}, \quad (9)$$

and the magnetization after the boundary as a sum of a transmitted and another evanescent SWs:

$$\mathbf{m}(y > 0) = T \mathbf{m}_{k,1} e^{ik_1 y} + C_2 \mathbf{m}_{\text{ev},1} e^{-\kappa_1 y}. \quad (10)$$

The amplitude of the incident propagating SW is assumed to be equal to 1. Substituting these equations for the wave amplitudes into the boundary conditions (5), one obtains four linear equations for the coefficients R , T , C_1 , and C_2 , which can be solved by well-known methods.

An example of the SW profiles (9) and (10) calculated using the full vectorial approach is presented in Fig. 3(b), and, for comparison, the similar profiles calculated within the traditional scalar approximation are presented in Fig. 3(a). For clarity, we have chosen the parameters of the scattering problem in such a way, that the incident and reflected SWs are circularly polarized (dynamic magnetization components $|m_x| = |m_z|$), while the transmitted SW has the elliptical polarization. In Fig. 3(b), one can clearly see the influence of

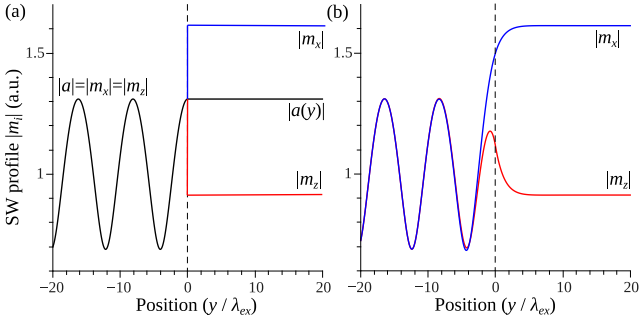


FIG. 3. Profiles of an SW mode near the boundary of two regions with different dispersion relation and different SW polarizations: (a) scalar approximation [Eq. (6)] and (b) full vectorial solution. Figures show the profiles of both components of the SW dynamical magnetization and, also, the profile of the effective scalar variable $a(y)$ [in (a) only]. The position of the boundary is shown by a vertical dashed line. Calculation parameters: $\lambda_{\text{ex}}k_0 = 0.39$, $\mathbf{m}_{k,0} = [1, 1]$, and $\lambda_{\text{ex}}k_1 = 0.2$, $\mathbf{m}_{k,1} = [1.77, 1]$ (which correspond to an FM waveguide magnetized in the y direction by the bias magnetic field $B_e = 0.1\mu_0M_s$, isotropic in the zeroth region, and having perpendicular hard-axis anisotropy in the first region $N_{zz,1}^{(an)} = 0.3$. The SW frequency is $\omega = 0.25\omega_M$).

the localized evanescent SWs, which allow the components of the dynamic magnetization to vary continuously across the boundary. In contrast, in the scalar approximation Fig. 3(a), only the effective scalar parameter $a(y)$ (e.g., spin density) is continuous, while dynamic magnetization components have an unphysical discontinuity at the boundary. The oscillations before the boundary are caused by the interference of the incident and reflected SWs. We would like to note that the localization length of the evanescent SWs does not depend on the polarization difference in the two regions, and that these waves always appear if any polarization difference exists.

The transmission and reflection coefficients in the vectorial formalism have the following form:

$$T = \frac{2k_0(\kappa_0 + \kappa_1)|\mathbf{m}_{k,0}|^2/(\mathbf{m}_{k,0}^* \cdot \mathbf{m}_{k,1})}{(k_0 + k_1)(\kappa_0 + \kappa_1) - i\mathcal{E}_{01}^2(k_0 + i\kappa_1)(k_1 + i\kappa_0)}, \quad (11a)$$

$$R = \frac{(k_0 - k_1)(\kappa_0 + \kappa_1) - i\mathcal{E}_{01}^2(k_0 - i\kappa_1)(k_1 + i\kappa_0)}{(k_0 + k_1)(\kappa_0 + \kappa_1) - i\mathcal{E}_{01}^2(k_0 + i\kappa_1)(k_1 + i\kappa_0)}. \quad (11b)$$

Here the quantity \mathcal{E}_{01} is defined as

$$\mathcal{E}_{01} = \left| \frac{\mathbf{m}_{k,0} \cdot \boldsymbol{\mu} \times \mathbf{m}_{k,1}}{\mathbf{m}_{k,0}^* \cdot \mathbf{m}_{k,1}} \right|. \quad (12)$$

This quantity serves as a natural *measure of difference in the SW polarization* $\mathbf{m}_{k,0}$ and $\mathbf{m}_{k,1}$. In particular, it is equal to zero, if $\mathbf{m}_{k,0} = \mathbf{m}_{k,1}$, and $\mathcal{E} \rightarrow \infty$ for almost orthogonal SW polarizations when $\mathbf{m}_{k,0}^* \cdot \mathbf{m}_{k,1} \rightarrow 0$.

It is clear that for identical SW polarizations, when $\mathcal{E}_{01} = 0$, the vectorial expressions for the SW transmission and reflection coefficients (11) are reduced to Eq. (6), obtained in the scalar approximation. Inequality of the SW polarizations before and after the boundary leads to an increase of the SW reflection from the boundary, and a consequent decrease of the SW transmission. Additionally, it leads to the appearance of the phase shifts in both the reflected and transmitted waves

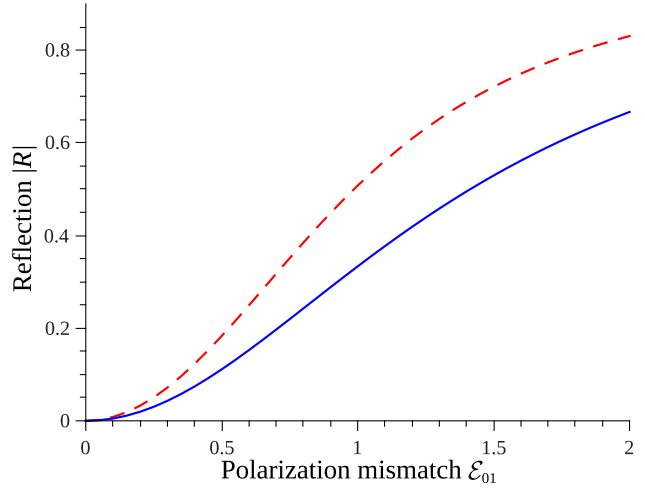


FIG. 4. Dependence of the SW reflection coefficient on the SW polarization mismatch for the case of identical SW wave numbers, but different vector structure of the SWs before and after the boundary: solid line $-\kappa = k$ and dashed line $-\kappa = 3k$.

relative to the incident one, which can take any value $\Delta\phi \in [-\pi, \pi]$ (recall that in the scalar approximation $\Delta\phi = 0, \pi$ for the reflected wave, and there is now phase shift for the transmitted wave). It is important to note that even if the SW wave vectors are identical, the SW would not be fully transmitted through the boundary if the polarization mismatch exists: $T \neq 1$, $R \neq 0$ for $k_0 = k_1$, and $\mathcal{E}_{01} \neq 0$. Finally, it is interesting to note that for a large SW polarization difference ($\mathcal{E}_{01} \gg 1$) the transmission coefficient is reduced to zero, $T \rightarrow 0$, while the reflection coefficient approaches the value:

$$R \rightarrow \frac{k_0 - i\kappa_1}{k_0 + i\kappa_1}, \quad (13)$$

which coincides with Eq. (6), obtained in the scalar approximation, assuming that the only SW existing after the boundary is the evanescent one, having the inverse localization length κ_1 . Naturally, $|R| \rightarrow 1$ in this case.

Let us now look quantitatively at the influence of the SW polarization mismatch on the SW reflection and transmission coefficients. For this purpose, we calculate the R and T coefficient for a model system, assuming that the SW wave numbers in both regions are the same, $k_0 = k_1$ and $\kappa_0 = \kappa_1$, while the polarization difference \mathcal{E}_{01} is nonzero. In this case, the SW reflection is caused only by the SW polarization difference. Such a situation is not just an abstract theoretical model, but it can be realized, for example, at the interface between the FM waveguides having the same anisotropy field, but the anisotropy axes that are perpendicular to each other.

The calculated dependencies of the SW reflection coefficient $|R|$ are shown in Fig. 4. As one can see, the effect of the polarization mismatch on the SW reflection and transmission depends, also, on the ratio of the SW wave number k to the inverse localization length of the corresponding evanescent wave κ ; for a larger ratio κ/k , the reflection is stronger.

This can be easily understood by recalling, that in the well-known scalar case the reflection is proportional to

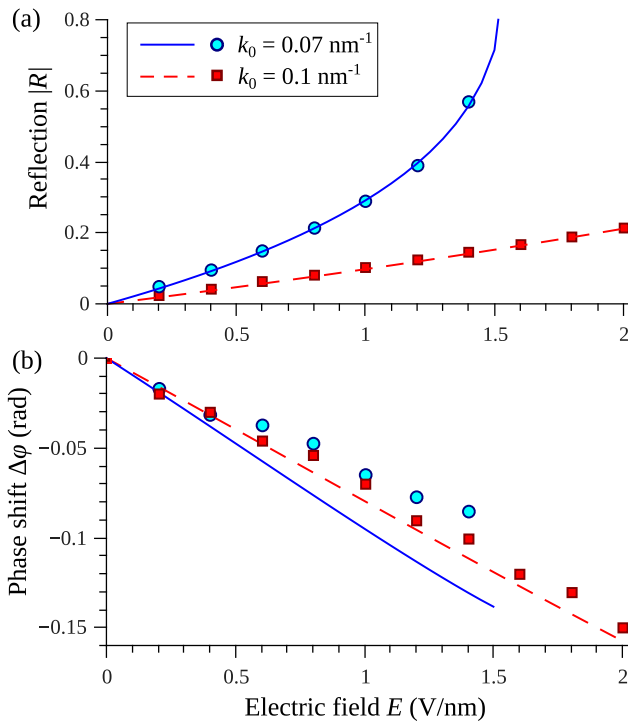


FIG. 5. Dependence of the SW reflection coefficient (a) and the phase shift of the reflected SW (b) on the control parameter (electric field applied in the region after the boundary) for different wave number of the incident SW; lines: theory and symbols: results of micromagnetic simulations. The material and geometrical parameters are as in Fig. 1.

the difference of the wave vectors of between the incident and the transmitted waves. Similarly, in our case when the difference in characteristic scales of the incident and the localized waves increases, a greater part of the incident SW is reflected from the boundary. As it was pointed out earlier, $\kappa^2 \geq k^2$ for any stable magnetic configuration, and the ratio κ/k increases with the increase of the band gap in the SW spectrum (i.e., with the increase of the value ω_0).

It should be noted that the influence of the polarization mismatch on the reflection is proportional to \mathcal{E}_{01}^2 , and, consequently, it is almost unnoticeable for the small polarization difference ($\mathcal{E}_{01} < 0.1$ – 0.2 in Fig. 4). Obviously, when the SW wave vectors are also different, which results in a nonzero reflection for $\mathcal{E}_{01} = 0$, the effect of the polarization mismatch on the amplitude of the reflected wave will be pronounced only for even higher values of \mathcal{E}_{01} .

As an example, in Fig. 5, we calculated the reflection coefficient $|R|$ and the phase shift $\Delta\phi$ of an SW reflected in an ultrathin nanowire where the sharp internal boundary was created by an external electric field via VCMA, so the perpendicular magnetic anisotropy was changed at the boundary. As it was shown in Fig. 1, the SW polarization can significantly change in such a case, resulting in the polarization mismatch up to $\mathcal{E}_{01} = 0.3$ in the studied range of applied electric field values. We found that the difference between the values of the reflection coefficient $|R|$ in the full vectorial solution Eq. (11) and in the scalar approximation Eq. (6) does not exceed 1%.

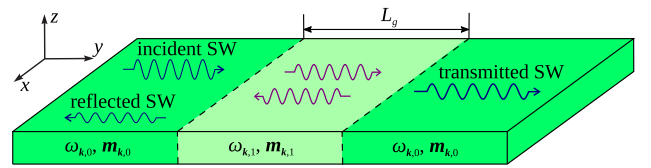


FIG. 6. Geometry of an SW waveguide with two internal boundaries: SW in the course of propagation in an FM waveguide encounters a region of a finite length L_g with different magnetic parameters

However, at the same time one can clearly see in Fig. 5 an additional phase shift in the reflected SW up to 0.15 rad, which could be easily detected and should be taken into account in the design of SW signal processing devices.

We have also verified our theoretical calculations by micromagnetic simulations using MuMax3 micromagnetic solver [50]. In these simulations, we set the nanowire length to $4 \mu\text{m}$, SWs are excited by a local, 50 nm in length, application of microwave magnetic field b_z of the magnitude $b_z = 0.1 \text{ mT}$ and the frequency of 5.52 GHz (corresponding to $k_0 = 0.07 \text{ nm}^{-1}$) and 8.85 GHz ($k_0 = 0.1 \text{ nm}^{-1}$), and the internal boundary is separated by $1 \mu\text{m}$ from the excitation source. To increase the precision of the determination of reflected wave amplitude and phase, the damping rate is set to $\alpha_G = 10^{-4}$, except for the regions near the nanowire beginning and end, where it increases quadratically, which ensures absence of SW reflections from these edges. The complex reflection coefficient R is extracted from the magnetization dynamics in the region between the excitation area and internal boundary (but not close to the boundary, so that evanescent waves become negligible), by its fitting by the sum of incident and reflected waves.

As one can see in Fig. 5, the modulus of the reflection rate $|R|$ is nicely reproduced by micromagnetic simulations. In the case of shorter incident SW having $k_0 = 0.1 \text{ nm}^{-1}$, our theory predicts well also the phase shift of the reflected wave. In the case of longer incident SW, $k_0 = 0.07 \text{ nm}^{-1}$, we also see clear additional phase shift of the reflected SWs, induced by the polarization mismatch, however, this shift is somewhat smaller than predicted one. The reason of this discrepancy is the increased role of the dipolar interaction in the propagation of longer SWs, which is discussed in more details in Sec. V.

Thus, we can conclude that the SW polarization mismatch before and after the boundary leads to three main effects. The first one, which is clearly visible for any polarization mismatch, is the appearance of the localized evanescent SWs at the boundary. The second effect is the additional phase shift for both reflected and transmitted SWs. Finally, the third one is a decrease of the transmission and increase of reflection coefficients which, however, is measurable only for sufficiently large values of the polarization mismatch \mathcal{E}_{01} .

B. Finite region with different SW dispersion and polarization

In this section, we consider the SW scattering from a region (“gate”) of a finite gate length L_g , inside which the magnetic parameters (magnetic field or anisotropy) of a waveguide are modified (see Fig. 6). Such structures can be used for the effective control of the phase and amplitude of a propagating SW in the SW-based signal processing. In experiment, such

a geometry can be realized by applying a control voltage in a spatially extended region of the SW waveguide (middle region in Fig. 6).

Within a standard scalar approximation the solution of this transmission problem is well-known, and the transmission coefficient T is given by

$$|T|^2 = \left[1 + \frac{1}{4} \left(\frac{k_0}{k_1} - \frac{k_1}{k_0} \right)^2 \sin^2(k_1 L_g) \right]^{-1}. \quad (14)$$

The reflection coefficient can be calculated from the equality $|T|^2 + |R|^2 = 1$. Of course, this solution is valid if the gate length L_g is significantly smaller, than the SW mean free path.

For the calculation of the transmission coefficient within the full vectorial approach one should take into account an incident ($e^{ik_0 y}$), reflected ($R e^{-ik_0 y}$), and one evanescent ($C_1 e^{\kappa_0 y}$) SW in the first region (left one in Fig. 6), two propagating ($C_2 e^{ik_1 y}$ and $C_3 e^{-ik_1 y}$) and two evanescent [$C_4 e^{-\kappa_1 y}$ and $C_5 e^{\kappa_1(y-L_g)}$] SWs inside the middle (gate) region, and one transmitted propagating SW ($T e^{ik_0(y-L_g)}$) and one evanescent SW ($C_6 e^{-\kappa_0(y-L_g)}$) in the last (right) region. In this geometry, the positions of the sharp internal boundaries are assumed to be at $y = 0$ and L_g , respectively. By the application of two pairs of conditions Eq. (5) at both boundaries, one can obtain the amplitudes of all the propagating and evanescent waves. The exact solution of the problem is too cumbersome to be presented here. Thus below we will show only the solutions obtained in several most important particular cases.

To illustrate the qualitative influence of the polarization mismatch on the SW propagation through a gate of a finite length, we present below the dependence of the transmission coefficient on the gate length L_g for a model problem illustrated in Fig. 7 and compare it with the similar results obtained in the scalar approximation Eq. (14). The following features of the SW scattering from the finite-size gate can be seen from Fig. 7. First, the function $|T|^2(L_g)$ is still a periodic function, except in the case of small gate lengths, when the amplitudes of the evanescent SWs localized at one of the boundaries are not vanishing the other another boundary, i.e., when $\exp[\kappa_1 L_g]$ is not a negligible value. The period of the function $|T|^2(L_g)$ is the same as in the scalar approximation, and is equal to $2\pi/k_1$. Second, the minimum value of the transmission coefficient becomes smaller due to the influence of polarization difference. Finally, the most interesting feature is the fact, that the maximum value of transmission coefficient can be $\max |T|(L_g) = 1$, i.e., an SW can pass the gate region resonantly. This resonance transmission could appear to be rather surprising, since the SW passes two boundaries where a part of the SW polarization is lost. In a certain sense, this is an analog of the well-known resonance tunneling of particles in quantum mechanics, and the role of the tunnel barriers is played by the internal boundaries. The resonant transmission takes place if the condition $k_1 L_g + \psi = \pi n$, $n \in \mathbb{Z}$ is satisfied (see the definition of ψ below). In a scalar approximation, the resonant transmission also takes place, under the condition $k_1 L_g = \pi n$ (see Eq. (14) or Ref. [40]). The appearance of the phase ψ in the resonance conditions is related to the additional phase shift, which is acquired by an SW reflected from a boundary due to a nonzero polarization mismatch.

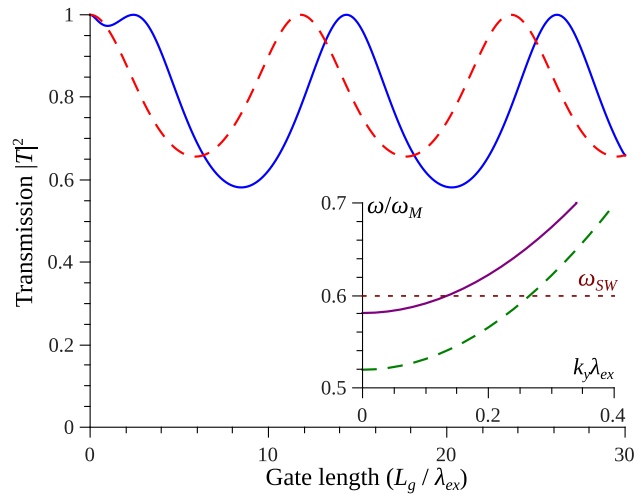


FIG. 7. Coefficient of SW transmission through a gate of a finite length L_g ; solid lines: full vectorial solution and dashed lines: scalar approximation. Parameters: internal field $B/\mu_0 M_s = 0.1$, effective anisotropy tensor (including static demagnetization tensor) $N_{xx}^{(an)} = 0.8$, $N_{yy}^{(an)} = 0.2$ within the gate region, and $N_{xx,0}^{(an)} = 0.35$, $N_{yy,0}^{(an)} = 0.65$ outside this region, SW frequency $\omega_{SW} = 0.6\omega_M$. The corresponding SW spectra are shown in the inset, dashed line; within the gate region, solid; outside this region; for these parameters, the SW polarization difference is $\mathcal{E}_{01} = 0.37$.

An reasonably simple analytical expression for the SW transmission coefficient can be derived assuming that amplitude of the evanescent SW localized at one of the boundaries is vanishingly small at the other boundary, i.e., if $\exp[-\kappa_1 L_g] \ll 1$. Within this approximation the SW transmission coefficient can be written as

$$|T|^2 = \left[1 + \frac{1}{4} \left[\left(\frac{k_0}{k_1} - \frac{k_1}{k_0} \right)^2 + \mathcal{E}_{01}^2 f \right] \sin^2(k_1 L_g + \psi) \right]^{-1}. \quad (15)$$

Here, f and ψ are the coefficients which depend on the SW wave numbers k_i , “wave numbers” κ_i of the localized evanescent waves, and the SW vector structure. In a general case, the explicit expressions for f and ψ are rather cumbersome, and we will not present them below. It is clear, that for a negligible difference of the SW polarization, $\mathcal{E}_{01} \ll 1$, the above presented equation is reduced to Eq. (14) ($\psi = 0$ for $\mathcal{E}_{01} = 0$, see below).

The expressions for f and ψ in a compact explicit form can be also derived in several limiting cases. For a small polarization mismatch, $\mathcal{E}_{01} \ll 1$ these expressions have the following form:

$$f = 2 \frac{(k_0^2 - k_1^2)(k_0^2 \kappa_0 - k_1^2 \kappa_1)}{k_0^2 k_1^2 (\kappa_0 + \kappa_1)}, \quad (16a)$$

$$\psi = \frac{1}{2} \arcsin \left[4 \mathcal{E}_{01}^2 \frac{k_1 (k_0^2 + \kappa_0 \kappa_1)}{(k_0^2 - k_1^2)(\kappa_0 + \kappa_1)} \right]. \quad (16b)$$

It is clear, that for $\mathcal{E}_{01} = 0$ the phase $\psi = 0$, as it was pointed out above. In particular, using Eq. (16), we can calculate the effect of the polarization mismatch on the SW transmission for a VCMA gate (all the parameters used are the

same as in Fig. 5). When the applied gate voltage $E = 2 \text{ V/nm}$ the value $\mathcal{E}_{01}^2 f$ is only 4% of the polarization-independent term $(k_0/k_1 - k_1/k_0)^2$. Consequently, the minimum transmission coefficient also decreases by around 4%. The phase ψ which affects the condition of the resonance transmission through the finite-length gate is equal to $\psi = 0.15 \text{ rad}$, which is not a negligible value, and should be taken into account.

Another limiting case, in which compact expressions for f and ψ can be derived, is the case of a large polarization mismatch, i.e., the case when $\mathcal{E}_{01} \gg 1$. In this limit, the coefficients in Eq. (15) can be calculated as

$$f = \mathcal{E}_{01}^2 \frac{(k_0^2 + \kappa_1^2)^2 (k_1^2 + \kappa_0^2)^2}{k_0^2 k_1^2 (\kappa_0 + \kappa_1)^4}, \quad (17a)$$

$$\psi = \frac{1}{2} \arcsin \left[\frac{4k_1 \kappa_0 (\kappa_0^2 - k_1^2)}{(\kappa_0^2 + k_1^2)^2} \right]. \quad (17b)$$

The case of a large polarization mismatch is, basically the case of a large ellipticity of the SW precession, for which typically $\kappa \gg k$. Consequently, one can see that in such a case $\psi \rightarrow 0$, similarly to the case of small values of \mathcal{E}_{01} .

V. EFFECT OF DIPOLAR INTERACTION

In the previous sections, we neglected the effect of the dynamic dipolar interaction on the SW propagation and transmission through an internal boundary. For a sufficiently short SWs and thin ferromagnetic films, this approximation is natural and correct. However, in the range of relatively small SW wave numbers the dynamic dipolar interaction becomes important, and, also, its influence is more pronounced in relatively thick ferromagnetic films.

The problem of transmission of dipole-exchange SWs through an internal boundary is a complex challenging task, which has not been solved analytically even within the scalar approximation. In order to understand main features of the SW transmission in the dipole-exchange case we, first, consider the case of purely dipolar SWs (magnetostatic waves), neglecting the exchange interaction. This approximation is valid if all the dimensions of a ferromagnetic waveguide and the SW wavelength are much larger than the exchange length in the waveguide FM material.

The propagation of the dipolar SWs is described by the Walker's equation [51] for magnetostatic potential ψ :

$$\text{div}(\hat{\boldsymbol{\mu}} \cdot \nabla \psi) = 0, \quad (18)$$

where $\hat{\boldsymbol{\mu}} = \hat{\boldsymbol{\mu}}(\omega) = \hat{\mathbf{I}} + \hat{\boldsymbol{\chi}}$ is the tensor of magnetic permeability, and $\hat{\boldsymbol{\chi}}$ is the tensor of magnetic susceptibility. In the coordinate system where the z' axis is aligned along the direction of static magnetization the susceptibility tensor $\hat{\boldsymbol{\chi}}$ has only four nonzero components:

$$\hat{\boldsymbol{\chi}} = \frac{\omega_M}{\omega_0^2 - \omega^2} \begin{pmatrix} \omega_H + \omega_{\text{an},y'} & i\omega & 0 \\ -i\omega & \omega_H + \omega_{\text{an},x'} & 0 \\ 0 & 0 & 0 \end{pmatrix}, \quad (19)$$

where $\omega_{\text{an},i} = \gamma B_{\text{an},i}$, $B_{\text{an},x'}$, and $B_{\text{an},y'}$ are the anisotropy fields in the x' and y' directions (anisotropy is assumed to be biaxial), and $\omega_0^2 = (\omega_H + \omega_{\text{an},x})(\omega_H + \omega_{\text{an},y})$ is the ferromagnetic resonance frequency in the waveguide.

In order to make the calculations simple and clear, we consider a metalized FM waveguide where the static magnetization direction is along the z axis (the case of a perpendicularly magnetized waveguide). The coordinate system is the same as the one shown in Fig. 2. In this case from the boundary conditions at the metalized surfaces, which require $(\hat{\boldsymbol{\mu}} \nabla \psi)_z = 0$, one gets a profile of the dipolar SW eigenmodes: $\psi_n = \cos[\kappa_n z] e^{ik_y y}$, where $\kappa_n = \pi/t_z$, where t_z is the film thickness. Also, from Eq. (18), one can get a dispersion relation for the magnetostatic waves in the form: $\kappa_n^2 = \mu_{yy}(\omega) k^2$. The thickness profile of a magnetostatic SW mode does not depend on its wave vector, so we can consider the transmission problem for only one magnetostatic mode.

The magnetostatic boundary conditions at an internal boundary require continuity of the tangential components of the magnetic field $\mathbf{H} = \nabla \psi$ (x and z components in our geometry) and of the normal component of the magnetic induction $\mathbf{B} = \hat{\boldsymbol{\mu}} \cdot \nabla \psi$ (y component). These conditions can be satisfied by the selection of a solution as a sum of incident, reflected and transmitted waves: $\psi(y < 0) = \cos[\kappa z] (e^{ik_0 y} + R e^{-ik_0 y})$ and $\psi(y > 0) = T \cos[\kappa_n z] e^{ik_1 y}$. Then, the transmission and reflection coefficients are equal to

$$R = \frac{\mu_{yy,0} k_0 - \mu_{yy,1} k_1}{\mu_{yy,0} k_0 + \mu_{yy,1} k_1}, \quad T = \frac{2\mu_{yy,0} k_0}{\mu_{yy,0} k_0 + \mu_{yy,1} k_1}. \quad (20)$$

This solution is similar to the one obtained in the scalar exchange approximation [Eq. (6)]. The only difference is the fact, that the magnetostatic wave is sensitive to the variation of the product of a wave number by the yy component of the magnetic permeability tensor, but not sensitive to the variation of the SW wave vector alone. Another two features of this solution should be pointed out: (i) the solution of the transmission problem in the range of dipolar SWs *does not contain any localized SW modes* independently of the presence or absence of the SW polarization mismatch and (ii) there is no explicit dependence of the SW transmission coefficient on the SW polarization.

A dependence of the SW transmission coefficient on SW polarization may, however, be present implicitly in the dependence $\hat{\boldsymbol{\mu}}(\omega)$. To check this point, let us look at the case when the SW wave vectors in the regions before and after the boundary are the same, $k_0 = k_1$. From the dispersion law, it follows that this case requires $\mu_{yy,0} = \mu_{yy,1}$. Consequently, the reflected wave is absent [see Eq. (20)], and the incident wave passes fully through internal boundary. The polarization of the magnetostatic wave is given by $\mathbf{m} = \hat{\boldsymbol{\chi}} \nabla \psi$, i.e., the relation between the dynamic magnetization components has the form: to $m_x/m_y = \chi_{xy}/\chi_{yy} = i\omega/(\omega_H + \omega_{\text{an},x})$. As it was mentioned above, the yy components of the susceptibility tensor χ_{yy} are the same in both regions, but the xy components *can be different*.

Indeed, one can easily find values of $\omega_{H,0(1)}$, $\omega_{\text{an},0(1)}$ such that $\chi_{yy,0} = \chi_{yy,1}$, but $\chi_{xy,0} \neq \chi_{xy,1}$ for a certain frequency ω , see Eq. (19). Note, that this is possible not only in a specific case of biaxial anisotropy, but also can happen in a case of an uniaxial anisotropy. Thus, we can conclude, that a dipolar SWs can be *absolutely* insensitive to the variation of the SW polarization, at least in certain geometries. This is in a sharp contrast with the properties of the exchange SWs, which are *always* sensitive to the SW polarization mismatch.

Absolutely the same calculations with the similar conclusions one can make for the case when the FM waveguide is magnetized in-plane along the direction of the wave propagation $\boldsymbol{\mu} = \mathbf{e}_y$. The only difference is in the values of the transmission and reflection coefficients [see Eq. (20)], where $\mu_{yy} = 1$ [since $\mu_{z'z'} = 1 + \chi_{z'z'} = 1$, see Eq. (19)]. For any other directions of the waveguide static magnetization such a simple analysis can not be performed, because the SW profile across the film thickness becomes dependent on the SW wave vector, and the conditions at an internal boundary can not be satisfied using a single thickness SW mode. Therefore, in a complex magnetization geometry, the scattering into multiple thickness magnetostatic modes takes place at a boundary. In such a complex case, obviously, it would be difficult to try to isolate the effect of SW polarization mismatch in the scattering problem.

Let us now return to the initial problem of the transmission of a dipole-exchange SWs through a boundary. If an FM waveguide is sufficiently thin (of the order of 10–100 nm, depending on the material exchange length), the thickness profile of a propagating SW is maintained uniform by the exchange interaction *independently* of the static magnetization direction. Based on the above described properties of the magnetostatic waves, one can expect, that, at least in certain geometries, the SW would become insensitive to the polarization mismatch when the role of the dipolar interaction increases. To verify this hypothesis, we performed numerical simulation of Eq. (1) accounting for the dipolar interaction via the integral operator with Green's function kernel [Eq. (2)]. Equation (1) was solved using finite-difference method in the stationary mode (i.e., $\partial \mathbf{m} / \partial t = -i\omega \mathbf{m}$). The length of simulation area was chosen 10–20 times larger than SW wavelength, and the boundary conditions were set as the sum of harmonic incident and reflected waves at one boundary, and transmitted wave at other boundary, with unknown reflection and transmission rates. This approach leads, finally, to a linear equation system for the coefficients R and T and a set discretized magnetization values.

These numerical calculations showed that the above described behavior takes place if the waveguide static magnetization does not have in-plane components that are perpendicular to the SW propagation direction, $\mu_x = 0$, i.e., it takes place for perpendicular magnetization ($\boldsymbol{\mu} = \mathbf{e}_z$), for “backward volume waves geometry” ($\boldsymbol{\mu} = \mathbf{e}_y$), and for any magnetization configuration between these two. For such magnetization geometries, the SW transmission through a boundary becomes less sensitive to the polarization mismatch with the increase of the role of the dipolar interaction (this increase was simulated by the increase of the film thickness), and in the limit of a negligible exchange interaction the effect of polarization disappears completely. The same feature was pointed above in our micromagnetic simulations (see Fig. 5).

However, if $\mu_x \neq 0$, in particular, in the case of a “Damon-Eshbach geometry” ($\boldsymbol{\mu} = \mathbf{e}_x$), the effect of the SW polarization does not disappear completely even for the dipole-dominated SWs. In particular, the SW reflection takes place if $k_0 = k_1$, but $\mathbf{m}_0 \neq \mathbf{m}_1$. Such a drastic dependence on the direction of the static magnetization can be understood recalling the above mentioned solution of the Walker's equation. In the above considered dipolar case of perpendicular

magnetization, the SW polarization is defined by the xy and yy components of the susceptibility tensor, however, the xy component of the same tensor *does not contribute* to the SW dispersion law, and, consequently, to the SW propagation and scattering. Thus the SW propagation would not be affected by the m_x component of the dynamic magnetization in the considered case. A similar situation takes place in the case of the dipole-exchange SW propagating in thin films when $\mu_x = 0$, because xx and xy components of the magneto-dipolar Green function in Eq. (1) are identically zero, $G_{xx} = G_{xy} = 0$. However, as soon as $\mu_x \neq 0$, both dynamic magnetization component have the y or/and z components, and, thus, both of them contribute to the SW propagation, since $G_{yy}, G_{zz} \neq 0$. Also, we should note, that different symmetry of dynamic magnetic fields of a SW in the Damon-Eshbach geometry leads to different SW transmission features in general, not only regarding the SW polarization [52].

Concluding this section we can state, that the effect of the SW polarization mismatch on the transmission through an internal boundary is more complex in the case of dipole-dominated SWs, compared to the case of the exchange-dominated SWs. In certain geometries ($\mu_x = 0$), this effect disappears, while in other geometries it is still present. Also, in the case of dipolar SWs the polarization difference does not lead to the formation of dipolar-dominated localized SWs. The evanescent SWs, discussed in Sec. III, are, of course, still present, because the exchange interaction requires the magnetization continuity. However, these localized SWs do not contribute to the transmission and reflection coefficients of the dipolar SWs. In the intermediate region, when both dipolar and exchange interaction are important, one should expect a smooth transition from the transmission rules for the exchange-dominated SWs to the transmission rules characteristic to the dipole-dominated SWs. In particular, one should expect a smooth disappearance of the effect of the SW polarization mismatch in the case of a static magnetization with $\mu_x = 0$. The characteristic values of the SW wave number, when this transition occurs can be obtained from the comparison of the term $\mathbf{m}_k^* \cdot (\hat{\mathbf{F}}_k - \hat{\mathbf{F}}_0) \cdot \mathbf{m}_k / A_k$ evaluating the dipolar contribution and the term $\lambda_{\text{ex}}^2 k^2$ evaluating the exchange contribution to the SW dispersion. If $\lambda_{\text{ex}}^2 k^2 \gg \mathbf{m}_k^* \cdot (\hat{\mathbf{F}}_k - \hat{\mathbf{F}}_0) \cdot \mathbf{m}_k / A_k$, one can safely neglect the dynamic dipolar interaction, and use the above developed analytical vectorial scattering theory for exchange-dominated SWs (see Sec. IV of the current paper). Otherwise a numerical solution of the full problem Eq. (1) should be used.

VI. SUMMARY

In this work, we have developed a theory of an SW transmission and reflection from a sharp internal boundary, taking into account the SW polarization. The difference in the SW polarizations before and after the boundary accompanies the difference in the SW wave numbers in almost all the cases, except some symmetric ones. However, the difference in polarizations is much more pronounced if the regions, separated by an internal boundary, differ by the value of anisotropy, as it happens in the case of a magnetoelectric (e.g., VCMA) control of the SW dispersion, or/and by the direction of anisotropy axes, as it takes place at an interface between two different

anisotropic ferromagnets. While the above presented theory was developed for an internal boundary within a single ferromagnet, assuming a constant static magnetization \mathbf{M}_0 , and exchange length λ_{ex} in all the sample, it can be generalized to the case of an interface of two different ferromagnets, and one should expect qualitatively similar SW behavior at the boundary.

The SW polarization difference leads to three main effects. First, the exponentially localized (evanescent) SWs appear in the vicinity of the boundary. The appearance of these localized evanescent SW modes is a direct consequence of the necessity to satisfy the continuity conditions for the magnetization and its derivative within the whole ferromagnetic sample, which cannot be satisfied by propagating SWs only. The localized SWs are orthogonal to the propagating SWs of the same frequency, and have the localization lengths equal or smaller than the wavelength of a corresponding propagating SW. The existence of the localized modes results in the second effect—appearance of an additional phase shift for both reflected and transmitted SWs. This phase shift can be of any value $\Delta\phi \in [-\pi, \pi]$, and only for the case of a zero SW polarization mismatch it is reduced to $\Delta\phi = 0, \pi$ for the reflected SW and to $\Delta\phi = 0$ for the transmitted SW. Finally, a nonzero SW polarization mismatch \mathcal{E}_{01} results in a decrease of the SW transmission coefficient and in an increase of the SW reflection coefficient. However, this effect is pronounced only for a sufficiently large polarization mismatch \mathcal{E}_{01} (characteristic value depends on the difference of the SW wave numbers for the incident and transmitted SWs).

In spite of a nonzero polarization mismatch before and after a finite-length region with different magnetic parameters, an SW can pass this region resonantly, i.e., without reflection and with a transmission coefficient $|T| = 1$, if the propagation losses within that region are negligible. The conditions of the resonant transmission through a finite-length “gate” are affected by the SW polarization mismatch, and has the form $k_1 L_g + \psi = \pi n$, $n \in \mathbb{Z}$, where the additional phase $\psi = \psi(\mathcal{E}_{01})$ is the function of the polarization difference. In particular, for relatively small polarization mismatch, the phase is proportional to $\psi \sim \mathcal{E}_{01}^2$.

All these features are intrinsic for the exchange-dominated SW, since exchange interaction requires continuity of the magnetization and its derivatives. In the case of dipole-dominated SWs, the influence of SW polarization difference is not as pronounced, and can disappear completely in certain magnetization geometries.

ACKNOWLEDGMENTS

This work was supported in part by the U.S. National Science Foundation (Grants No. EFMA-1641989 and No. ECCS-1708982), by the U.S. Air Force Office of Scientific Research under the MURI Grant No. FA9550-19-1-0307, and by the Oakland University Foundation. R.V. acknowledges support from the Ministry of Education and Sciences of Ukraine (Projects No. 0115U002716 and No. 0118U004007).

-
- [1] D. D. Stancil and A. Prabhakar, *Spin Waves. Theory and Applications* (Springer, New York, 2009).
- [2] A. A. Serga, A. V. Chumak, and B. Hillebrands, *J. Phys. D: Appl. Phys.* **43**, 264002 (2010).
- [3] V. V. Kruglyak, S. O. Demokritov, and D. Grundler, *J. Phys. D: Appl. Phys.* **43**, 264001 (2010).
- [4] *Magnonics. From Fundamentals to Applications*, edited by S. O. Demokritov and A. N. Slavin (Springer, Berlin, 2013).
- [5] *Magnetism of Surfaces, Interfaces, and Nanoscale Materials*, edited by R. E. Camley, Z. Celinski, and R. L. Stamps, Handbook of Surface Science Vol. 5 (Elsevier, Amsterdam, 2016).
- [6] S. O. Demokritov, A. A. Serga, A. André, V. E. Demidov, M. P. Kostylev, B. Hillebrands, and A. N. Slavin, *Phys. Rev. Lett.* **93**, 047201 (2004).
- [7] M. P. Kostylev, A. A. Serga, T. Schneider, T. Neumann, B. Leven, B. Hillebrands, and R. L. Stamps, *Phys. Rev. B* **76**, 184419 (2007).
- [8] T. Neumann, A. A. Serga, B. Hillebrands, and M. P. Kostylev, *Appl. Phys. Lett.* **94**, 042503 (2009).
- [9] U.-H. Hansen, M. Gatzel, V. E. Demidov, and S. O. Demokritov, *Phys. Rev. Lett.* **99**, 127204 (2007).
- [10] A. A. Serga, T. Neumann, A. V. Chumak, and B. Hillebrands, *Appl. Phys. Lett.* **94**, 112501 (2009).
- [11] M. Fiebig, *J. Phys. D: Appl. Phys.* **38**, R123 (2005).
- [12] C.-W. Nan, M. I. Bichurin, S. Dong, D. Viehland, and G. Srinivasan, *J. Appl. Phys.* **103**, 031101 (2008).
- [13] F. Matsukura, Y. Tokura, and H. Ohno, *Nat. Nano.* **10**, 209 (2015).
- [14] W.-Y. Tong, Y.-W. Fang, J. Cai, S.-J. Gong, and C.-G. Duan, *Comput. Mater. Sci.* **112**, Part B, 467 (2016).
- [15] M. Weisheit, S. Fähler, A. Marty, Y. Souche, C. Poinignon, and D. Givord, *Science* **315**, 349 (2007).
- [16] C.-G. Duan, J. P. Velev, R. F. Sabirianov, Z. Zhu, J. Chu, S. S. Jaswal, and E. Y. Tsybal, *Phys. Rev. Lett.* **101**, 137201 (2008).
- [17] S. Miwa, M. Suzuki, M. Tsujikawa, T. Nozaki, T. Nakamura, M. Shirai, S. Yuasa, and Y. Suzuki, *J. Phys. D: Appl. Phys.* **52**, 063001 (2018).
- [18] W.-G. Wang, M. Li, S. Hageman, and C. L. Chien, *Nat. Mater.* **11**, 64 (2012).
- [19] Y. Shiota, T. Nozaki, F. Bonell, S. Murakami, T. Shinjo, and Y. Suzuki, *Nat. Mater.* **11**, 39 (2012).
- [20] J. Zhu, J. A. Katine, G. E. Rowlands, Y.-J. Chen, Z. Duan, J. G. Alzate, P. Upadhyaya, J. Langer, P. K. Amiri, K. L. Wang, and I. N. Krivorotov, *Phys. Rev. Lett.* **108**, 197203 (2012).
- [21] R. Verba, M. Carpentieri, G. Finocchio, V. Tiberkevich, and A. Slavin, *Sci. Rep.* **6**, 25018 (2016).
- [22] Y.-J. Chen, H. K. Lee, R. Verba, J. A. Katine, I. Barsukov, V. Tiberkevich, J. Q. Xiao, A. N. Slavin, and I. N. Krivorotov, *Nano Lett.* **17**, 572 (2017).
- [23] B. Rana, Y. Fukuma, K. Miura, H. Takahashi, and Y. Otani, *Appl. Phys. Lett.* **111**, 052404 (2017).
- [24] A. O. Leon, M. G. Clerc, and D. Altbir, *Phys. Rev. E* **98**, 062213 (2018).

- [25] S.-S. Ha, N.-H. Kim, S. Lee, C.-Y. You, Y. Shiota, T. Maruyama, T. Nozaki, and Y. Suzuki, *Appl. Phys. Lett.* **96**, 142512 (2010).
- [26] K. Nawaoka, Y. Shiota, S. Miwa, H. Tomita, E. Tamura, N. Mizuochi, T. Shinjo, and Y. Suzuki, *J. Appl. Phys.* **117**, 17A905 (2015).
- [27] M. K. Niranjan, C.-G. Duan, S. S. Jaswal, and E. Y. Tsybal, *Appl. Phys. Lett.* **96**, 222504 (2010).
- [28] G. Rado and J. Weertman, *J. Phys. Chem. Sol.* **11**, 315 (1959).
- [29] V. A. Ignatchenko, *Fiz. Met. Metalloved.* **36**, 1219 (1973).
- [30] V. S. Tkachenko, V. V. Kruglyak, and A. N. Kuchko, *Metamaterials* **3**, 28 (2009).
- [31] V. S. Tkachenko, V. V. Kruglyak, and A. N. Kuchko, *Phys. Rev. B* **81**, 024425 (2010).
- [32] V. V. Kruglyak, O. Y. Gorobets, Y. I. Gorobets, and A. N. Kuchko, *J. Phys.: Cond. Matter.* **26**, 406001 (2014).
- [33] K. Y. Guslienko, S. O. Demokritov, B. Hillebrands, and A. N. Slavin, *Phys. Rev. B* **66**, 132402 (2002).
- [34] K. Y. Guslienko and A. N. Slavin, *Phys. Rev. B* **72**, 014463 (2005).
- [35] M. Kostylev, *J. Appl. Phys.* **115**, 233902 (2014).
- [36] P. Gruszecki, Y. S. Dadoenkova, N. N. Dadoenkova, I. L. Lyubchanskii, J. Romero-Vivas, K. Y. Guslienko, and M. Krawczyk, *Phys. Rev. B* **92**, 054427 (2015).
- [37] V. V. Kruglyak, C. S. Davies, V. S. Tkachenko, O. Y. Gorobets, Y. I. Gorobets, and A. N. Kuchko, *J. Phys. D: Appl. Phys.* **50**, 094003 (2017).
- [38] Y. I. Gorobets and S. A. Reshetnyak, *Tech. Phys.* **43**, 188 (1998).
- [39] S. A. Reshetnyak, *Phys. Solid State* **46**, 1061 (2004).
- [40] S. Mieszczak, O. Busel, P. Gruszecki, A. N. Kuchko, J. W. Kłos, and M. Krawczyk, An anomalous refraction of spin waves as a way to guide signals in curved magnonic multimode waveguides, [arXiv:2001.11356](https://arxiv.org/abs/2001.11356) [physics.app-ph].
- [41] S. V. Vasiliev, V. V. Kruglyak, M. L. Sokolovskii, and A. N. Kuchko, *J. Appl. Phys.* **101**, 113919 (2007).
- [42] C. S. Chang, M. Kostylev, E. Ivanov, J. Ding, and A. O. Adeyeye, *Appl. Phys. Lett.* **104**, 032408 (2014).
- [43] V. D. Poimanov and V. G. Shavrov, *J. Phys.: Conf. Ser.* **1389**, 012134 (2019).
- [44] Q. Wang, B. Heinz, R. Verba, M. Kewenig, P. Pirro, M. Schneider, T. Meyer, B. Lägél, C. Dubs, T. Brächer, and A. V. Chumak, *Phys. Rev. Lett.* **122**, 247202 (2019).
- [45] A. G. Gurevich and G. A. Melkov, *Magnetization Oscillations and Waves* (CRC Press, New York, 1996).
- [46] R. Verba, G. Melkov, V. Tiberkevich, and A. Slavin, *Phys. Rev. B* **85**, 014427 (2012).
- [47] R. Verba, G. Melkov, V. Tiberkevich, and A. Slavin, in *Magnetism of Surfaces, Interfaces, and Nanoscale Materials*, edited by R. E. Camley, Z. Celinski, and R. L. Stamps, Handbook of Surface Science Vol. 5, (Elsevier, Amsterdam, 2016), pp. 215–241.
- [48] O. Dzyapko, I. Lisenkov, P. Nowik-Boltyk, V. E. Demidov, S. O. Demokritov, B. Koene, A. Kirilyuk, T. Rasing, V. Tiberkevich, and A. Slavin, *Phys. Rev. B* **96**, 064438 (2017).
- [49] K. Y. Guslienko and A. N. Slavin, *J. Magn. Magn. Mater.* **323**, 2418 (2011).
- [50] A. Vansteenkiste, J. Leliaert, M. Dvornik, M. Helsen, F. Garcia-Sanchez, and B. Van Waeyenberge, *AIP Adv.* **4**, 107133 (2014).
- [51] D. D. Stancil, *Theory of Magnetostatic Waves* (Springer-Verlag, New York, 1993).
- [52] M. Mohseni, R. Verba, T. Brächer, Q. Wang, D. A. Bozhko, B. Hillebrands, and P. Pirro, *Phys. Rev. Lett.* **122**, 197201 (2019).

2.2. Стійкість до розсіяння спінових хвиль у геометрії Деймона-Ешбаха у нанорозмірних хвилеводах

PHYSICAL REVIEW LETTERS **122**, 197201 (2019)

Backscattering Immunity of Dipole-Exchange Magnetostatic Surface Spin Waves

M. Mohseni,¹ R. Verba,² T. Brächer,¹ Q. Wang,¹ D. A. Bozhko,¹ B. Hillebrands,¹ and P. Pirro^{1,*}

¹*Fachbereich Physik and Landesforschungszentrum OPTIMAS, Technische Universität Kaiserslautern, 67663 Kaiserslautern, Germany*

²*Institute of Magnetism, Kyiv 03680, Ukraine*



(Received 19 October 2018; published 14 May 2019)

The existence of backscattering-immune spin-wave modes is demonstrated in magnetic thin films of nanoscale thickness. Our results reveal that chiral magnetostatic surface waves (CMSSWs), which propagate perpendicular to the magnetization direction in an in-plane magnetized thin film, are robust against backscattering from surface defects. CMSSWs are protected against various types of surface inhomogeneities and defects as long as their frequency lies inside the gap of the volume modes. Our explanation is independent of the topology of the modes and predicts that this robustness is a consequence of symmetry breaking of the dynamic magnetic fields of CMSSWs due to the off-diagonal part of the dipolar interaction tensor, which is present both for long- (dipole-dominated) and short-wavelength (exchange-dominated) spin waves. Micromagnetic simulations confirm the robust character of the CMSSWs. Our results open a new direction in designing highly efficient magnonic logic elements and devices employing CMSSWs in nanoscale thin films.

DOI: [10.1103/PhysRevLett.122.197201](https://doi.org/10.1103/PhysRevLett.122.197201)

Protected transport of energy and information has gained a tremendous amount of interest during the last decade [1–4]. Magnons, the quanta of spin waves (SWs), which are the collective excitations of the spin ensemble of a magnetically ordered system, are considered as a promising counterpart to photons and phonons to serve as information carriers in future wave-based data processing devices [5–19]. For the design of magnon-based devices, decreasing propagation losses is considered one of the biggest challenges [18,20]. In addition to intrinsic magnetic losses manifesting themselves in a viscous damping, external losses mediated by surface defects such as fabrication-induced disorders, roughness, and magnetic inhomogeneities generally contribute to the total losses. Therefore, novel ways to avoid these scattering losses are highly desired.

In fact, this has motivated a large number of theoretical works, e.g., on the potential topological protection of SWs [21–26]. Nevertheless, the observation of protected magnon transport still remains a great challenge since most of the proposed systems obtain their topological protection from Dzyaloshinskii-Moriya interaction (DMI) [27–30] or strongly inhomogeneous magnetic ground states [21]. Such properties are hard to realize experimentally or can come along with a detrimental influence on the propagation properties [28,30]. Considering these facts, the prediction of protected magnon transport that does not rely on topological arguments would constitute a major breakthrough [20].

Here, we introduce a mechanism of wave backscattering immunity that is distinct to that topological protection. We

show that backscattering immune SW modes exist in simple thin film systems that have homogeneous magnetic parameters and do not exhibit DMI. In terms of applications, the studied system benefits largely from its simplicity in comparison to artificially created metamaterials and crystals for robust photonic [31,32], phononic [33], and magnonic transport. We show that the protection of these modes is caused by the chirality of the mode profiles of the counterpropagating SWs. In particular, we present a theory suggesting that chiral magnetostatic surface waves (CMSSWs) are robust against backscattering from surface defects. We further show that this protection is effective for both dipolar waves as well as for short-wavelength waves dominated by the exchange interaction. Using micromagnetic simulations, we confirm the predictions of our theory for an yttrium iron garnet (YIG) model system, which is the most suitable host for SW propagation due to its low intrinsic losses [6,8,9,12,13,18,34–38]. The obtained results can be generalized to other materials, like metallic alloys. The simulations also show that the protection against scattering is particularly strong if the CMSSW frequency is located in the frequency gap of the volume modes (VMs, also known as perpendicular standing spin waves), which opens due to the quantized exchange energy in thin films. Therefore, the backscattering protection is more pronounced in thinner films, in which the gap of VMs is larger.

To illustrate the mechanism that leads to the chiral protection of CMSSWs, Figs. 1(a) and 1(b) exemplarily shows its mode profiles and dispersion relations in a YIG film of thickness $d = 80$ nm for typical values of the

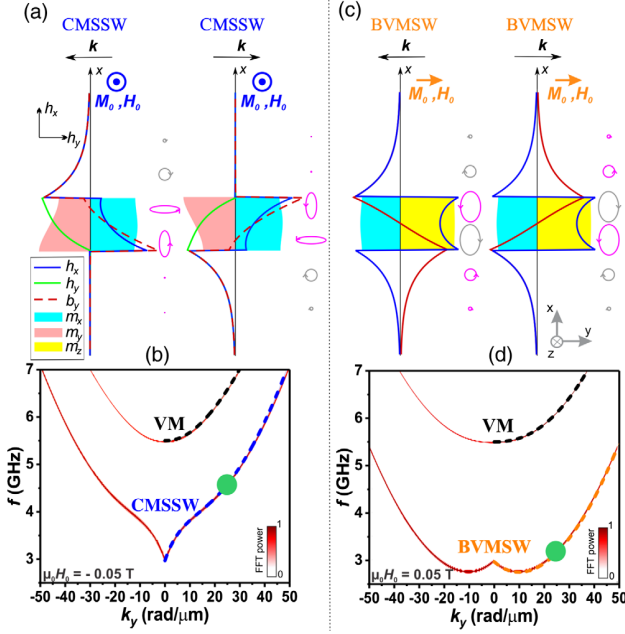


FIG. 1. (a),(c) Profiles of CMSSWs and BVMSWs, propagating in opposite directions (color coded), and corresponding distributions of the dynamic magnetic field \mathbf{h} and the induction \mathbf{b} . Ellipses show the vector structure of the dynamic magnetic field \mathbf{h} . The color code indicates the sign of rotation of the dynamic magnetic field. Film thickness 80 nm and $k_y = 25.9$ rad/ μm . (b),(d) Corresponding magnon band structures are calculated via numerical simulations (color plot) and analytical calculations according to [41] (dashed lines). The fundamental modes are distinguished via blue (CMSSW) and orange (BVMSW) lines, and the higher-order volume modes via black lines. Green dots indicate the modes exemplarily investigated in Fig. 2.

exchange constant $A_{\text{exch}} = 3.5$ pJ/m and saturation magnetization $M_s = 140$ kA/m. The case of CMSSWs is realized when the film is magnetized in plane, perpendicular to the wave propagation direction $\vec{M}_0 \perp \vec{k}$ [Fig. 1(a)]. This “Damon-Eshbach” geometry is well studied in the case of pure dipolar (magnetostatic) SWs in relatively thick films. SWs in this geometry are chiral due to the off-diagonal part of the dynamic dipole-dipole interaction, which breaks time-reversal symmetry (“ T symmetry”). This, among other things, leads to a nonreciprocal localization of CMSSWs at the surfaces of the film, which depends on the direction of the wave vector k_y [38–40]. Considering the nanoscale thickness of the system studied here, both dipolar and exchange interactions are important for the wave propagation.

Under these conditions, the dynamic magnetization components of CMSSWs are weakly localized at one of the surfaces [see Fig. 1(a) and 1(b)]. As also visible from the dispersion relations shown in Fig. 1(b), higher-order VMs are present in addition to CMSSWs. The exchange energy contribution, which is quantized over the thickness

with a quantum proportional to $1/d^2$, leads to a frequency shift of VMs above the CMSSW frequency. This implies a frequency gap where only the CMSSW is present.

For comparison, we also study the case of a nonchiral wave [Figs. 1(c) and 1(d)]: if the wave vector is parallel to the static magnetization ($\vec{k} \parallel \vec{M}_0$), so-called backward volume magnetostatic waves (BVMSWs) occur. For this orientation, the dipolar interaction does not lead to broken T symmetry.

As we already pointed out, the spatial localization of CMSSWs at a film surface is weak in the studied systems. To show how the chirality nevertheless leads to backscattering protection, the corresponding equations of motion are analyzed. For the appearance of any chiral and nonreciprocal effects, at least the T symmetry should be broken. In principle, magnetization dynamics always exhibits broken T symmetry, since magnetization precesses always counterclockwise around the static field direction. However, this is not a sufficient criterion. Indeed, the propagation of small-amplitude SWs is described by the following dynamical equations [41–42]:

$$\begin{aligned} \frac{dm_x}{dt} &= -(\omega_H - \omega_M \lambda^2 \nabla^2) m_y - \omega_M h_y, \\ \frac{dm_y}{dt} &= (\omega_H - \omega_M \lambda^2 \nabla^2) m_x + \omega_M h_x, \end{aligned} \quad (1)$$

where $\omega_H = \gamma B$, B is the static internal field, $\omega_M = \gamma \mu_0 M_s$, λ is the exchange length, $\mathbf{h}(\mathbf{r}) = \int \hat{\mathbf{G}}(\mathbf{r}, \mathbf{r}') \cdot \mathbf{m}(\mathbf{r}') d\mathbf{r}'$ is the dynamic dipolar field with $\hat{\mathbf{G}}$ being the magnetostatic Green function, and the static magnetization is assumed to be oriented along the z direction. If the off-diagonal part of the dynamic interaction is zero $G_{xy} = G_{yx} = 0$, the equation system (1) can be transformed to one equation for m_x (or m_y), which contains *only* second-order time derivatives of m_x , i.e., of the form $d^2 m_x(\mathbf{r}, t)/dt^2 = F[m_x(\mathbf{r}, t), \mathbf{r}]$ with F being the integrodifferential operator, which does not depend explicitly on the time t . In this scenario, SW propagation exhibits T symmetry and does not possess chirality by itself. This case is realized for BVMSWs, as for these waves, the dynamical components of magnetization (z and x in notation of Fig. 1) are not dipolarly coupled.

In contrast, in the CMSSW geometry, the dynamic magnetization components are coupled and $G_{xy} = G_{yx} \neq 0$. Consequently, Eq. (1) cannot be simplified to one equation that contains only even time derivatives of magnetization. Hence, T symmetry of CMSSW propagation is broken and these waves are chiral.

To understand how this chirality leads to protection against backscattering, one first has to note that the nonzero off-diagonal components of the dynamic dipolar interaction result in a completely different symmetry for the dipolar fields created by CMSSW and BVMSW (see Fig. 1). The dipolar fields have to satisfy the electromagnetic boundary conditions at any internal or external boundary, like the

boundary of a defect. Namely, this implies continuity of the tangential component of the magnetic field \mathbf{h} and of the normal component of the magnetic induction $\mathbf{b} = \mu_0(\mathbf{h} + \mathbf{m})$. In addition, the exchange interaction requires continuity of magnetization and its spatial derivative. The resulting different form of the created fields has direct implications on the reflection and transmission of the waves.

In the case of BVMSW, the dipolar fields for opposite propagation directions are related by mirroring with respect to the XOZ plane, and the spatial distribution of the magnitude of the fields is the same [see Figs. 1(c) and 1(d)]. In this sense, forward and reflected waves match each other, and direct reflection of BVMSWs into an oppositely propagating wave can easily occur, satisfying the boundary conditions. In contrast, dipolar fields of oppositely propagating CMSSWs are related by subsequent mirroring to the YOZ and XOZ planes, respectively. This is also sketched with the ellipses in Fig. 1, showing the precession of the dynamic magnetic field \mathbf{h} . Consequently, the field strength at a given vertical position differs significantly. This can, for instance, be seen in the regions above and below the film. This feature is due to the constructive and destructive interference of the dipolar fields produced by the x and y components of magnetization. In particular, this feature is still present even in the case when the dynamic magnetization distribution in the film is uniform. Thus, dipolar fields of forward and backscattered CMSSWs are “incompatible” and CMSSWs cannot simply scatter to oppositely propagating CMSSWs because of the impossibility of satisfying the boundary conditions.

In order to shed more light on this “mismatch” of the CMSSW profiles, we consider the following simple model. We assume that only propagating CMSSWs are involved in the dynamics. Furthermore, we represent the magnetic fields at the boundary as the sum of the fields created by incident CMSSWs, transmitted CMSSWs with amplitude T , and reflected CMSSWs with amplitude R . The regions before and after the boundary situated at $y = y_g$ are different only by their thickness. This corresponds, for instance, to an unperturbed film in contact with a defect, as is shown in Fig. 2. As was pointed out above, with propagating CMSSWs only, it is impossible to exactly satisfy the boundary conditions. In practice, other localized evanescent waves are involved in the scattering process. Nevertheless, we can find values of the transmission and reflection coefficients that minimize the mismatch of the fields at the boundary. The obtained values cannot be interpreted as real transmission and reflection coefficients, but they show the qualitative behavior of these coefficients in different conditions.

Using the analytically calculated profiles of CMSSWs, we construct the functional of integral mismatch of the field h_x at the boundary at the position $y = y_g$,

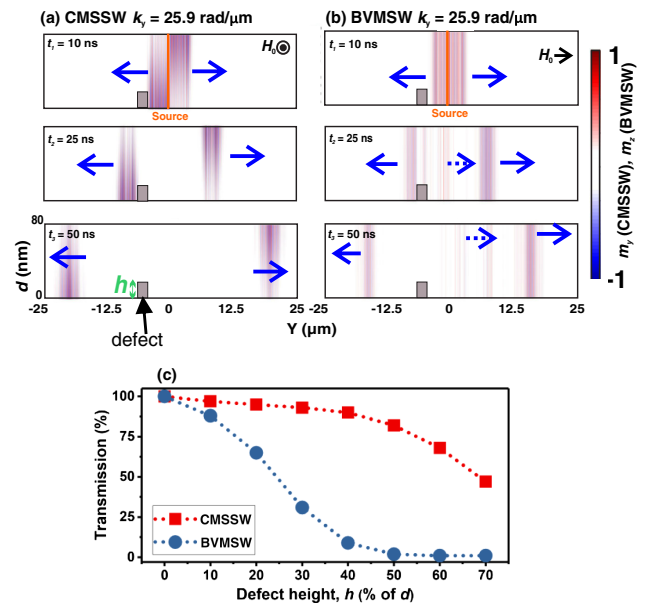


FIG. 2. Snapshots of the SW propagation in the presence of a defect (gray rectangular). (a) CMSSW ($f = 4.64$ GHz and $k_y = 25.9$ rad/ μm) (b) BVMSW ($f = 3.2$ GHz and $k_y = 25.9$ rad/ μm). Direction of the applied field H_0 is indicated in the right corner. Transmitted and reflected waves are marked with solid and dashed arrows, respectively. (c) SW transmission for different SW modes as a function of the topographic defect height. Lines are guides to the eye.

$$\Phi_h(R, T) = \int_{-\infty}^{+\infty} |h_{x,k_1} + Rh_{x,-k_1} + Th_{x,k_2}|^2 dx.$$

Here, k_1 and k_2 are the wave numbers of incident and transmitted spin waves, which are related by the dispersion relation $\omega_1(k_1) = \omega_2(k_2)$. The same functional was constructed for the mismatch of the component of the magnetic induction b_y . As one cannot directly compare magnetic field and induction, we minimize both functionals separately assuming complex-valued coefficients R and T , i.e., allowing for an arbitrary phase shift between waves.

From this, we infer that the minima of mismatches of b_y and h_x take place for approximately the same transmission rate T . However, at the same time, the reflection rate R has opposite signs with similar magnitude for the two components. In other words, the conditions of continuity of the normal component of the magnetic induction and the tangential component of the field imply that both act on the reflected wave oppositely, i.e., with a phase shift of π . This phase relation is a direct consequence of the specific symmetry of the field profiles of the CMSSW and it suppresses the formation of the reflected wave. This leads to almost 100% transmission from the defect. The calculations also show that this feature—opposite signs of R —remains valid for defect depths ranging from a vanishing depth up to depths of about 50% of the film thickness.

In the following, we will verify the analytical predictions using micromagnetic simulations. The simulations have been performed via the MuMax 3.0 open source software [43]. The simulated film parameters are equivalent to the ones of Fig. 1 and a Gilbert damping parameter of $\alpha = 0.0002$ has been assumed. The external magnetic field of 0.05 T is applied along the $-z$ direction or $+y$ direction (see Supplemental Material [44] for more information).

To check for backscattering immunity, in Fig. 2(a), the topographical defect ($2 \mu\text{m}$ long), with a height equal to $h = 20\%$ of the film thickness d , is placed at one of the surfaces of the film. Snapshots from micromagnetic simulations of propagating SW pulses with a length of 10 ns, excited with a SW source at the center ($y = 0 \mu\text{m}$), are shown in Fig. 2 for three different times (t_1-t_3) before and after reaching the defect.

In all presented cases, SWs with a wave vector of $k_y = 25.9 \text{ rad}/\mu\text{m}$, as indicated by the green dots in Fig. 1, have been studied. For the CMSSW [Fig. 2(a)], the system is excited with a carrier frequency of $f = 4.64 \text{ GHz}$. In very good agreement with our prediction, the CMSSW pulse (blue arrow to the left) passes the defect without any significant reflection and reaches an amplitude transmission close to 96% [see Supplemental Material Fig. 2(a) [44]]. However, in the case of the BVMSW, shown in Fig. 2(b), the SW pulse undergoes a strong backreflection when impinging on the defect and only 62% of the wave is transmitted [see Supplemental Material Fig. 2(b) [44]].

In Fig. 2(c), we present a systematic characterization of the scattering from topographical defects for the same parameters as used in Figs. 2(a) and 2(b). We vary the defect height (h) as displayed in Fig. 2(a) and evaluate the transmission of the propagating SWs. It can be seen that, for the CMSSW case, a defect can be as high as 40% of the thickness, and still a transmission in the range of 90% can be achieved. This is in good agreement with the estimation from the analytical part presented above. A further increase of the defect height creates a coupling channel, which allows the wave to scatter to the other surface and propagate backwards. In contrast, for the BVMSW case [Fig. 2(b)], already a defect as high as 40% of the thickness is enough to result in an almost complete reflection. Here, the scattering takes place between k_y and $-k_y$ of the same mode. In addition, we verified that this strong scattering can be observed over the whole wave vector range shown in Fig. 1(d).

In Fig. 3(a), the transmission of CMSSWs for the same system as discussed in Fig. 2(a) is shown as a function of the excited wave vector. From small wave vectors starting from $k_y = 2 \text{ rad}/\mu\text{m}$ (with dominant dipolar interaction) to midrange $k_y = 35 \text{ rad}/\mu\text{m}$ (dipole-exchange waves), the CMSSW transmission is around 95%. In this frequency range [which is marked by the blue colored area of Fig. 3(a)], the CMSSW lies inside the gap of the VM.

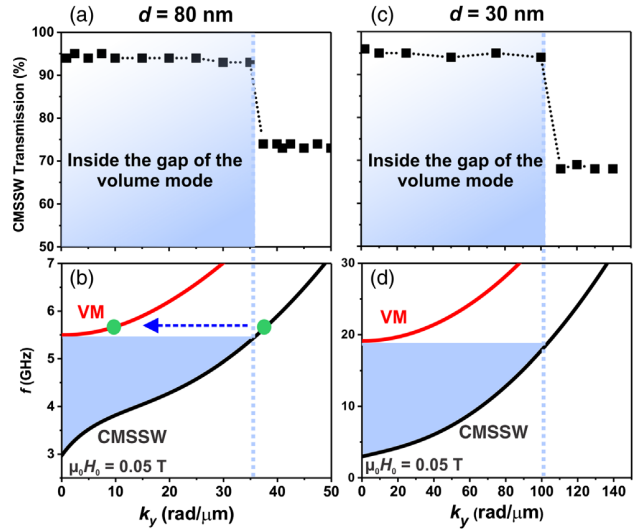


FIG. 3. CMSSW transmission as a function of wave vector in the presence of a $2 \mu\text{m} \times (20\% \text{ of } d)$ topographical defect for a film with (a) $d = 80 \text{ nm}$ and (c) $d = 30 \text{ nm}$. The blue area shows the range of wave vectors inside the gap of volume modes where the protection is strong. (b),(d) Indicates the relevant magnon band structure of the systems and the corresponding frequency gap, which is distinguished via the blue area. Please note the different scales.

Therefore, no resonant scattering to the VM is possible due to energy conservation.

A drop of the CMSSW transmission by roughly 20% is visible in Fig. 3(a). This drop appears for wave vectors $k_y > 36 \text{ rad}/\mu\text{m}$, when the CMSSW becomes frequency degenerated with the first VM. This degeneracy enables a resonant scattering from the CMSSW to the VM. This supplies a channel for backreflection of SW energy. The appearance of backscattered VMs is clearly visible in the simulations [see Supplemental Material Fig. 3 [44]].

It should be noted that the strong protection that is found even for low wave vectors provides evidence that the localization of the dynamic magnetization at a surface plays no direct role for the protection. Indeed, the localization on one surface is proportional to the in-plane wave vector k_y [40], and, e.g., for $k_y = 2 \text{ rad}/\mu\text{m}$, the amplitude decays by only 4.2% from one side to the other and the mode profile is nearly homogeneous.

As a next step, we will show that the strong protection of CMSSWs in the thin film is a general phenomenon that is present even for high wave vector SWs with a dominant exchange energy contribution. Theoretically, this can be predicted by evaluating the off-diagonal component of the Green function, which is responsible for the specific symmetry of dipolar fields of the CMSSW [41],

$$G_{xy}(k_y, x, x') = \frac{i}{2} \text{sgn}[x - x'] k_y e^{-|k_y(x-x')|}. \quad (2)$$

The strength of the asymmetry can be naturally measured by the difference of the off-diagonal contribution at the opposite surfaces of the film. These can be estimated as $(1 - \exp[-|k_y d|])$. This term increases with k_y , giving insight into why CMSSW protection is present even in the high- k exchange-dominated range.

In order to prove micromagnetically that the protection still exists for exchange-dominated SWs, the scattering study of Figs. 3(a) and 3(b) is repeated for a film with $d = 30$ nm, which is shown in Fig. 3(c). Because of the stronger quantization, this system shows a much larger gap of VMs and the protection of a shorter wavelength can be tested without the occurrence of the scattering channel to the VMs. Similar to the 80 nm film, the protection exists as long as no resonant scattering to the VM is possible. In this case, the maximal wave number at which CMSSWs are not degenerated with VMs is $k_y \sim 100$ rad/ μm . For these waves, the exchange contribution to the SW energy ($\sim \omega_M \lambda^2 k^2$) is almost 4 times larger than the dipolar one [$\sim \omega_M (1 - e^{-kd})$].

In conclusion, we showed that chiral magnetostatic surface waves, which propagate perpendicular to the static magnetization in an in-plane magnetized thin film, are robust against backscattering from surface defects. The protection of the CMSSW can be understood without a consideration of the topology of the system. It is strong if the frequency lies inside the gap of the volume modes, where no resonant scattering to or hybridization with other modes is possible. It should be emphasized that this protection takes place in ferromagnetic films with nanoscale thicknesses both for the dipole-dominated and the dipole-exchange range. It is also observed that the localization of the magnetization profile of CMSSWs is not the protecting mechanism for backscattering. At the same time, it is also observed for exchange-dominated waves, as long as they lie in the gap of the volume modes. Absolute protection of the CMSSWs is expected if the inversion symmetry of the system is broken, e.g., using a bilayer to design the magnon band structure and change the mode profiles of the counterpropagating SWs. This knowledge gives a new view on the role of the dipolar interaction on exchange-dominated SWs. The thin film system proposed here is the simplest medium for protected magnon transport and probably, in general, protected energy transport via waves.

Financial support by the Deutsche Forschungsgemeinschaft (SFB/TRR 173 “Spin + X,” Project B01), by the Nachwuchsring of the TU Kaiserslautern, and by the European Research Council Starting Grant No. 678309 MagnonCircuits is gratefully acknowledged. R. V. acknowledges support from Ministry of Education and Sciences of Ukraine (Project No. 0118U004007). The authors would like to thank K. Yamamoto for fruitful discussions about the topological properties of the MSSWs.

*ppirro@rhrk.uni-kl.de

- [1] L. Kou, S. C. Wu, C. Felser, T. Frauenheim, C. Chen, and B. Yan, *ACS Nano* **8**, 10448 (2014).
- [2] M. Malki and G. S. Uhrig, *Phys. Rev. B* **95**, 235118 (2017).
- [3] E. Thingstad, A. Kamra, A. Brataas, and A. Sudbø, *Phys. Rev. Lett.* **122**, 107201 (2019).
- [4] P. Roushan, J. Seo, C. V. Parker, Y. S. Hor, D. Hsieh, D. Qian, A. Richardella, M. Z. Hasan, R. J. Cava, and A. Yazdani, *Nature (London)* **460**, 1106 (2009).
- [5] F. Heussner, A. A. Serga, T. Brächer, B. Hillebrands, and P. Pirro, *Appl. Phys. Lett.* **111**, 122401 (2017).
- [6] A. V. Chumak, A. A. Serga, and B. Hillebrands, *Nat. Commun.* **5**, 4700 (2014).
- [7] S. M. Mohseni, H. F. Yazdi, M. Hamdi, T. Brächer, and S. M. Mohseni, *J. Magn. Magn. Mater.* **450**, 40 (2018).
- [8] S. Klingler, P. Pirro, T. Brächer, B. Leven, B. Hillebrands, and A. V. Chumak, *Appl. Phys. Lett.* **105**, 152410 (2014).
- [9] T. Fischer, M. Kewenig, D. A. Bozhko, A. A. Serga, I. I. Syvorotka, F. Ciubotaru, C. Adelman, B. Hillebrands, and A. V. Chumak, *Appl. Phys. Lett.* **110**, 152401 (2017).
- [10] T. Brächer, F. Heussner, P. Pirro, T. Meyer, T. Fischer, M. Geilen, B. Heinz, B. Lägell, A. A. Serga, and B. Hillebrands, *Sci. Rep.* **6**, 38235 (2016).
- [11] A. V. Chumak, A. A. Serga, B. Hillebrands, and M. P. Kostylev, *Appl. Phys. Lett.* **95**, 262508 (2009).
- [12] Q. Wang, P. Pirro, R. Verba, A. Slavin, B. Hillebrands, and A. V. Chumak, *Sci. Adv.* **4**, e1701517 (2018).
- [13] V. V. Kruglyak, S. O. Demokritov, and D. Grundler, *J. Phys. D* **43**, 260301 (2010).
- [14] M. Krawczyk and D. Grundler, *J. Phys. Condens. Matter* **26**, 123202 (2014).
- [15] M. Madami, S. Bonetti, G. Consolo, S. Tacchi, G. Carlotti, G. Gubbiotti, F. B. Mancoff, M. A. Yar, and J. Åkerman, *Nat. Nanotechnol.* **6**, 635 (2011).
- [16] S. M. Mohseni, S. R. Sani, J. Persson, T. N. A. Nguyen, S. Chung, Y. Pogoryelov, P. K. Muduli, E. Iacocca, A. Eklund, R. K. Dumas, S. Bonetti, A. Deac, M. A. Hoefer, and J. Åkerman, *Science* **339**, 1295 (2013).
- [17] F. Garcia-Sanchez, P. Borys, R. Soucaille, J. P. Adam, R. L. Stamps, and J. V. Kim, *Phys. Rev. Lett.* **114**, 247206 (2015).
- [18] A. V. Chumak, V. I. Vasyuchka, A. A. Serga, and B. Hillebrands, *Nat. Phys.* **11**, 453 (2015).
- [19] J. A. Otálora, M. Yan, H. Schultheiss, R. Hertel, and A. Kákay, *Phys. Rev. Lett.* **117**, 227203 (2016).
- [20] D. Sander, S. O. Valenzuela, D. Makarov, C. H. Marrows, E. E. Fullerton, P. Fischer, J. Mccord, P. Vavassori, S. Mangin, P. Pirro, B. Hillebrands, A. D. Kent, T. Jungwirth, O. Gutfleisch, C. G. Kim, and A. Berger, *J. Phys. D* **50**, 363001 (2017).
- [21] R. Shindou, R. Matsumoto, S. Murakami, and J. I. Ohe, *Phys. Rev. B* **87**, 174427 (2013).
- [22] L. Zhang, J. Ren, J. S. Wang, and B. Li, *Phys. Rev. B* **87**, 144101 (2013).
- [23] X. S. Wang, H. W. Zhang, and X. R. Wang, *Phys. Rev. Applied* **9**, 024029 (2018).
- [24] R. Chisnell, J. S. Helton, D. E. Freedman, D. K. Singh, R. I. Bewley, D. G. Nocera, and Y. S. Lee, *Phys. Rev. Lett.* **115**, 147201 (2015).
- [25] R. Shindou, J. I. Ohe, R. Matsumoto, S. Murakami, and E. Saitoh, *Phys. Rev. B* **87**, 174402 (2013).

- [26] E. Iacocca and O. Heinonen, *Phys. Rev. Applied* **8**, 034015 (2017).
- [27] H. T. Nembach, J. M. Shaw, M. Weiler, E. Jué, and T. J. Silva, *Nat. Phys.* **11**, 825 (2015).
- [28] Y. Tserkovnyak, A. Brataas, and G. E. W. Bauer, *Phys. Rev. Lett.* **88**, 117601 (2002).
- [29] Y. Tserkovnyak, A. Brataas, and G. E. W. Bauer, *Phys. Rev. B* **66**, 224403 (2002).
- [30] T. Brächer, O. Boule, G. Gaudin, and P. Pirro, *Phys. Rev. B* **95**, 064429 (2017).
- [31] A. B. Khanikaev, S. Hossein Mousavi, W. K. Tse, M. Kargarian, A. H. MacDonald, and G. Shvets, *Nat. Mater.* **12**, 233 (2013).
- [32] X. Cheng, C. Jouvaud, X. Ni, S. H. Mousavi, A. Z. Genack, and A. B. Khanikaev, *Nat. Mater.* **15**, 542 (2016).
- [33] C. He, X. Ni, H. Ge, X. C. Sun, Y. B. Chen, M. H. Lu, X. P. Liu, and Y. F. Chen, *Nat. Phys.* **12**, 1124 (2016).
- [34] A. A. Serga, A. V. Chumak, and B. Hillebrands, *J. Phys. D* **43**, 264002 (2010).
- [35] A. V. Chumak, P. Pirro, A. A. Serga, M. P. Kostylev, R. L. Stamps, H. Schultheiss, K. Vogt, S. J. Hermsdoerfer, B. Laegel, P. A. Beck, and B. Hillebrands, *Appl. Phys. Lett.* **93**, 022508 (2008).
- [36] S. Maendl, I. Stasinopoulos, and D. Grundler, *Appl. Phys. Lett.* **111**, 012403 (2017).
- [37] C. Hauser, T. Richter, N. Homonnay, C. Eisenschmidt, M. Qaid, H. Deniz, D. Hesse, M. Sawicki, S. G. Ebbinghaus, and G. Schmidt, *Sci. Rep.* **6**, 20827 (2016).
- [38] T. An, V. I. Vasyuchka, K. Uchida, A. V. Chumak, K. Yamaguchi, K. Harii, J. Ohe, M. B. Jungfleisch, Y. Kajiwara, H. Adachi, B. Hillebrands, S. Maekawa, and E. Saitoh, *Nat. Mater.* **12**, 549 (2013).
- [39] I. Lisenkov, V. Tyberkevych, A. Slavin, P. Bondarenko, B. A. Ivanov, E. Bankowski, T. Meitzler, and S. Nikitov, *Phys. Rev. B* **90**, 104417 (2014).
- [40] M. Kostylev, *J. Appl. Phys.* **113**, 053907 (2013).
- [41] B. A. Kalinikos and A. N. Slavin, *J. Phys. C* **19**, 7013 (1986).
- [42] B. A. Kalinikos, in *Linear and Nonlinear Spin Waves in Magnetic Films and Superlattices*, edited by M. G. Cottam (World Scientific, Singapore, 1994), pp. 89–156.
- [43] A. Vansteenkiste, J. Leliaert, M. Dvornik, F. Garcia-Sanchez, and B. Van Waeyenberge, *AIP Adv.* **4**, 107133 (2014).
- [44] See Supplemental Material at <http://link.aps.org/supplemental/10.1103/PhysRevLett.122.197201> for Methods of micromagnetic simulations and the animated versions of the simulated SW propagation in the presence of defects.

РОЗДІЛ 3

ВЗАЄМОДІЯ БІЖУЧИХ СПІНОВИХ ХВИЛЬ З ЛОКАЛІЗОВАНОЮ ПАРАМЕТРИЧНОЮ НАКАЧКОЮ

У цьому розділі розглядається взаємодія біжучих СХ з параметричною накачкою. Добре відомо, що така взаємодія може призводити до підсилення лінійних СХ (тобто, хвиль малої амплітуди), що використовується в параметричних підсилювачах СХ¹. Використання ефекту ЕКМА для створення параметричної накачки не призводить до появи ніяких відмінностей у такій взаємодії порівняно з добре вивченою взаємодією з параметричною накачкою, створюваною НВЧ магнітним полем. Єдина кількісна відмінність — це ефективність взаємодії СХ з накачкою, яка розглянута вище у Розділі 1. Варто, однак, зазначити, що параметричне підсилення електричним полем є значно ефективнішим. Оцінки, наведені у підрозділі 5.4, показують, що для типових субмікронних хвилеводів ЗІГ втрати (омічні) у класичному підсилювачі з використанням магнітного поля мікросмужкової антени перевищують типові втрати власне у магнітній підсистемі на 3-4 порядки (про що згадувалось вступі). У той же час для нанорозмірних провідних хвилеводів втрати в ЕКМА підсилювачі (діелектричні втрати та омічні втрати тунельних струмів) сумірні з магнітними втратами, і для оцінюваної там системи магнітної логіки складають у перерахунку всього 3 аДж/біт, що на порядок менше енергоспоживання перспективних напівпровідникових систем.

Однак, використання нанорозмірних феромагнітних хвилеводів дозволяє досягти режимів, недсяжних у мікронних та макросистемах. Сильна дискретизація спектру СХ призводить до суттєвого послаблення багатомангнетного розсіяння, що суттєво підвищує пороги нестійкості СХ щодо три- і чотирихвильового розпаду. Тому, у таких хвилеводах можуть поширюватись СХ великої амплітуди. Дослідженню взаємодії таких нелінійних СХ з параметричною накачкою присвячено підрозділ 3.1.

1 А. Г. Гуревич, Г. А. Мелков, *Магнитные колебания и волны* (Москва, Наука, 1994).

У підрозділі 3.2 запропонований спосіб корекції фази СХ за допомогою взаємодії з неадіабатичною параметричною накачкою. Хоча така взаємодія розглядалась раніше² і, зокрема, є відомою залежність коефіцієнту підсилення від фази СХ, фазові характеристики та можливість корекції фази раніше не розглядалися. Крім того, у роботі вперше розглянуто взаємодію нелінійних СХ з неадіабатичною накачкою.

Окрім ефекту ЕКМА у надтонких плівках та хвилеводах також може проявлятися ІВДМ, в тому числі одночасно з ЕКМА (оскільки за ЕКМА та ІВДМ відповідають різні інтерфейси — ферромагнетик - діелектрик та ферромагнетик - важкий метал, відповідно). Таке поєднання призводить до цікавих особливостей параметричної взаємодії, що досліджено у підрозділі 3.3.

Автором дисертації були проведені аналітичні та числові розрахунки характеристик неадіабатичного підсилювача та підсилювача за наявності ІВДМ, числове моделювання динамічних рівнянь при дослідженні параметричної взаємодії нелінійних СХ, та аналітичні оцінки меж різних режимів роботи підсилювача залежно від амплітуди СХ. Також автор брав безпосередню участь у розробці методики та обробці даних мікромагнітного моделювання.

² G. A. Melkov, A. A. Serga, V. S. Tiberkevich, Yu. V. Kobljanskij, and A. N. Slavin, Nonadiabatic interaction of a propagating wave packet with localized parametric pumping, *Phys. Rev. E* **63**, 066607 (2001).

3.1. Параметричне підсилення спінових хвиль великої амплітуди, стабілізація амплітуди спінових хвиль

APPLIED PHYSICS LETTERS 112, 042402 (2018)



Amplification and stabilization of large-amplitude propagating spin waves by parametric pumping

Roman Verba,^{1,a)} Mario Carpentieri,² Giovanni Finocchio,³ Vasil Tiberkevich,⁴ and Andrei Slavin⁴

¹*Institute of Magnetism, Kyiv 03680, Ukraine*

²*Department of Electrical and Information Engineering, Politecnico di Bari, I-70125 Bari, Italy*

³*Department of Electronic Engineering, Industrial Chemistry and Engineering, University of Messina, I-98166 Messina, Italy*

⁴*Department of Physics, Oakland University, Rochester, Michigan 48309, USA*

(Received 13 December 2017; accepted 10 January 2018; published online 22 January 2018)

The interaction of a localized parametric pumping with spin waves of different amplitudes, propagating in a ferromagnetic nanowire, is studied analytically and by micromagnetic simulations. It is shown that parametric amplification of spin waves by localized pumping becomes less efficient with an increase in the spin wave amplitude due to the influence of nonlinear 4-magnon processes. In a certain range of spin wave amplitudes, the parametric amplifier acts as a stabilizer of the spin wave amplitude, as its action significantly reduces the spread of the spin wave amplitude in the vicinity of a certain mean value. The stabilization effect becomes more pronounced for higher pumping strength and larger relative lengths of the pumping localization region, compared to the spin wave mean free path. In contrast, the use of relatively short pumping localization regions allows one to efficiently amplify large-amplitude nonlinear spin waves. *Published by AIP Publishing.*

<https://doi.org/10.1063/1.5019357>

Recent experimental and theoretical investigations^{1–6} have shown that spin waves (SWs) in magnetic micro- and nano-structures can be successfully used in microwave signal processing. These SWs have high frequencies (up to tens of gigahertz) and short wavelengths (down to several nanometers), and their dispersion characteristic can be effectively controlled by the structure sizes, as well as by the magnitude and direction of the applied bias magnetic field. The discovery of the interfacial Dzyaloshinskii-Moriya interaction, which can lead to SW nonreciprocity at the nanoscale,^{7–9} and studies of the effect of voltage-controlled magnetic anisotropy (VCMA),^{10,11} which enables low-loss excitation and manipulation of SWs using electric fields,^{12–15} create additional advantages for signal processing by means of microwave SWs.

To build a practical SW-based signal processing circuit, one should find a way to perform several basic operations with SWs, such as SW excitation and reception, controllable modification of the SW amplitude and phase, and logic operations. One of such necessary basic operations is the amplification of a propagating SW, which is required to compensate the SW propagation losses as well as the SW processing losses. Another basic operation that could be critically important in signal processing is the stabilization of the SW amplitude, i.e., the operation that could make the amplitude of an output SW almost the same in a certain range of input SW amplitudes. The operation of the amplitude stabilization is especially important in the SW-based signal processing circuits where phase modulation is used to code the transmitted information and the SW interference is used to perform signal-processing operations.^{2,5,16,17} Indeed, the result of interference of two or more SWs is sensitive to their phases

only if the SW amplitudes are almost the same. Otherwise, the result of the SW interference may substantially depend on the relative amplitudes of input SWs, while the SW phase information may be lost completely.

In this work, we will show that both amplification and amplitude stabilization of a SW-coded signal can be realized by localized parametric pumping—i.e., by the interaction of a propagating SW with a localized magnetic field (external or effective) of approximately double SW frequency. The parametric pumping is a well-known experimental method for the frequency-selective amplification of *linear* (small amplitude) propagating SWs.^{18–22} However, in ferromagnetic nanowires it is possible and, in order to increase the signal-to-noise ratio, often desirable to have relatively large-amplitude SWs.²³ Below, we will specifically study the influence of the amplitude of a propagating SW on the process of its parametric interaction with pumping and will clarify when the pumping could be used for effective SW amplification and when this pumping can work as a SW amplitude stabilizer.

A sketch of the studied system is shown in Fig. 1. It is a ferromagnetic nanowire of width w_y and thickness h , having

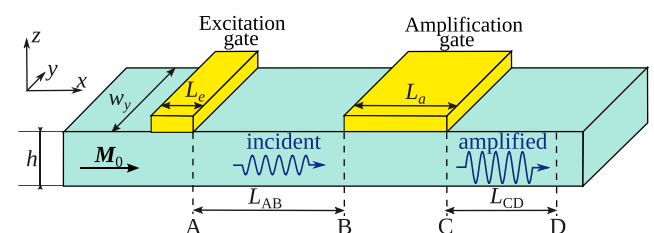


FIG. 1. A sketch of the parametric amplifier showing regions where excitation and amplification of the propagating spin waves take place. The reference points A–D used in the micromagnetic simulations are also shown.

^{a)}Author to whom correspondence should be addressed: verrv@ukr.net

the in-plane static magnetization due to the nanowire shape anisotropy. We considered the VCMA-based parametric pumping which is realized by variation of the perpendicular anisotropy at a ferromagnetic—dielectric interface at the microwave voltage applied across the interface. Our previous work²⁴ showed that in this geometry, microwave anisotropy couples parametrically to the propagating SWs, and it can be used for the efficient excitation or/and amplification of SWs. Note, also, that all the results presented below are rather general and could be used in a case when pumping is provided by other means (e.g., by a localized microwave magnetic field) and when other nanowire geometry and direction of the static magnetization are used.

The process of parametric pumping of small-amplitude SWs has been studied in detail in Refs. 18 and 25 and references therein. The parametric pumping, which in our case is created by microwave-frequency modulation of perpendicular magnetic anisotropy, couples with two propagating SWs having wave vectors k and k' and can pump energy into these waves. In particular, if a propagating SW having wave vector k and frequency ω_k passes through the region of pumping localization, the parametric interaction results in the partial compensation of the propagation losses or in the amplification of this SW and in the simultaneous creation of an idler SW having the wave vector k' and frequency $\omega_{k'}$. The parametric interaction is the most efficient if $k' \approx -k$ and the pumping frequency $\omega_p = \omega_k + \omega_{k'}$, i.e., if the conservation laws for the linear momentum and energy are fulfilled. In the simplest case of a *reciprocal* SW spectrum $\omega_k = \omega_{-k}$ leading to the parametric resonance condition $\omega_p = 2\omega_k$, the frequency of parametric pumping should be twice larger than the frequency of the propagating SW. In this case, the amplification rate (the ratio of the signal SW amplitude after and before the interaction with pumping) is equal to²⁰

$$K = \left[\cos \kappa L_a + \frac{\Gamma_k}{v\kappa} \sin \kappa L_a \right]^{-1}, \quad \kappa = \frac{\sqrt{|Vb_p|^2 - \Gamma_k^2}}{v}, \quad (1)$$

and is determined by the SW group velocity v , damping rate Γ_k , length of the pumping localization region L_a , and the efficiency of the parametric interaction $V = V_{kk}$, which in our case is equal to $V_{kk} = \gamma m_{k,z} / (4m_{k,y})$, where $m_{k,y}$ and $m_{k,z}$ are the dynamic magnetization components of SW.²⁴ The amplification rate increases with the pumping strength b_p (effective magnetic field of the pumping) and, at a certain value of $b_p = b_{th}$, becomes infinite, $K \rightarrow \infty$, meaning that two counter-propagating SWs are excited spontaneously by parametric pumping. Of course, for the purpose of the SW amplification, the pumping should be always below this critical value, $b_p < b_{th}$.

When the condition of the parametric resonance $\omega_p = 2\omega_k$ is not satisfied exactly, the amplification rate decreases rapidly at the frequency scale proportional to the SW damping rate Γ_k , resulting in the amplification that is strongly frequency-selective. Equation (1) uses the assumption of the *adiabatic* pumping, meaning that the pumping localization length L_a is larger than the SW wavelength (strictly speaking, if $|\text{sinc}[kL_a]| \ll 1$). Otherwise, the amplification rate becomes dependent on the SW phase^{26,27} that is undesirable in a general case (but could have its own specific applications²⁸).

Equation (1) is valid for moderate amplification rates K , when the amplitudes of both incident and amplified SWs, as well as the amplitude of the idler SW, are sufficiently small to neglect the nonlinear SW interaction.

To study effects of nonlinear interaction on the parametric amplification of SW, we, first of all, performed micromagnetic simulations using the GPMagnet solver.^{29,30} In the simulations, the SWs were excited linearly by microwave magnetic field $\mathbf{b} = b_y(t)\mathbf{e}_y$ applied at the excitation gate of the length $L_e = 30$ nm. The excitation frequency was 8.23 GHz, which corresponds to the SW wavelength of 100 nm. The microwave parametric pumping in the form of a perpendicular anisotropy $\Delta K_{\perp} = b_p M_s \cos[\omega_p t]$ modulated with the frequency $\omega_p / (2\pi) = 16.46$ GHz was applied at the amplification gate of the length $L_a = 500$ nm, separated from the excitation gate by the distance of $L_{AB} = 400$ nm. The transmission characteristic of the amplifier defined as the ratio of the SW amplitude at the amplification gate output (point C) to the SW amplitude at the amplification gate input (point B) was calculated for different magnitudes of the pumping strength (points B and C are shown in Fig. 1).

To avoid the incorrect determination of the SW amplitude due to the presence of the idler wave, the amplitude of the incident SW was obtained at a given excitation field and zero pumping, while the amplitude of the output SW at $x = x_C$ was retrieved from the amplitude at point D (separated from point C by the distance $L_{CD} = 400$ nm), where the idler wave is definitely absent, provided that the propagation losses are known. The following material parameters of the Fe/MgO structure (common for VCMA experiments) were used: saturation magnetization $\mu_0 M_s = 2.1$ T, exchange length $\lambda_{ex} = 3.4$ nm, surface perpendicular anisotropy energy $K_s = 1.36$ mJ/m², and effective Gilbert damping (including non-uniform broadening for a given SW frequency) $\alpha_G = 0.02$. The nanowire thickness was set to $h = 1$ nm and width $w = 20$ nm, and the bias magnetic field was absent. For such a width of a nanowire, all the SW modes, except the one that is uniform across the nanowire width, have the frequencies that are much higher than the studied one and, therefore, can be disregarded.

The simulated transmission characteristics calculated at the different values of the pumping strength are shown in Fig. 2. For the chosen parameters, the threshold of parametric excitation is equal to $b_p = 64$ mT, corresponding to the pumping electric field of 0.53 V/nm in the VCMA Fe/MgO structure. As one can see, in the interval of sufficiently small SW amplitudes, the transmission characteristics are linear, demonstrating that the amplification rate K is constant and is determined solely by the pumping amplitude. Then, the transmission characteristics demonstrate saturation, which corresponds to the decrease in the amplification rate. The saturation appears at different amplitudes of the incident SW for different magnitudes of the pumping strength: for a smaller pumping, the linear amplification regime is realized in a wider range of incident SW amplitudes. With a further increase in the incident SW amplitude, the parametric amplification becomes less and less efficient, and, finally, the output SW signal becomes almost insensitive to the presence of the parametric pumping (see below). If the pumping is switched off, SW decays at the pumping length with the rate $K = \exp[-L_a/l_{fp}]$, where $l_{fp} = v/\Gamma_k$ is the SW mean free

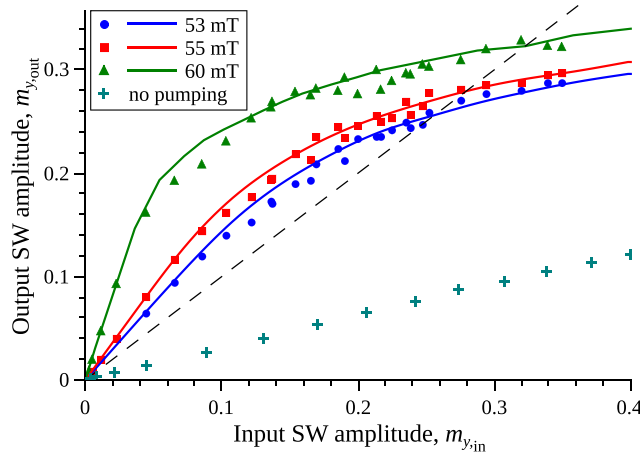


FIG. 2. Transmission characteristics of the parametric amplifier: symbols—micromagnetic simulations and lines—analytical model. The dashed line corresponds to the amplification rate $K=1$ ($m_{y,\text{out}}=m_{y,\text{in}}$). The SW amplitudes are shown as a dimensionless dynamic magnetization component $m_y = M_y/M_s$.

path; for the studied case, $l_{\text{fp}} \approx 440$ nm and is almost independent of the SW amplitude within the studied range (Fig. 2).

Figure 2 illustrates, also, another interesting feature of the nonlinear parametric amplification. It can be seen that at a certain incident SW amplitude m_0 , which depends on the pumping strength, the amplification rate is equal to $K=1$, which corresponds to the situation when the amplitudes of the incident and the output SWs are equal. Note that the derivative of the transmission characteristics $dm_{\text{out}}/dm_{\text{in}}$ at this point is less than 1. Then, if the incident SW near this point has an average amplitude m_0 with a certain amplitude spread Δm_{in} , $m_{\text{in}} = m_0 + \Delta m_{\text{in}}$, the output SW will also have the same mean amplitude m_0 , but a smaller amplitude spread: $m_{\text{out}} = m_0 + \Delta m_{\text{out}}$, where $\Delta m_{\text{out}} = \Delta m_{\text{in}}$ ($dm_{\text{out}}/dm_{\text{in}} < \Delta m_{\text{in}}$). Consequently, the parametric amplifier in this regime can be used for the stabilization of the output SW amplitude, which is a necessary operation for the processing of SW signals with phase modulation.

To give a further insight into the nonlinear parametric amplification process, we consider SW dynamics within a simplified analytical model. We use the so-called Bloembergen system of equations (see e.g., Ref. 26) which describes the evolution of envelope amplitudes of SW a_1 (signal wave) and a_2 (idler wave), which are related to the real magnetization by the equation $(M_y)_{1,2} = CM_s a_{1,2}(t, x) \exp[i(\pm kx - \omega_k t)]$, where the coefficient C is dependent on the SW vector structure.^{23,26} Then, the system of the Bloembergen equations can be written as

$$\left(\frac{\partial}{\partial t} + v \frac{\partial}{\partial x} + \Gamma\right) a_1 = -iVb_p(x)a_2^* - i(T|a_1|^2 + 2S|a_2|^2)a_1. \quad (2)$$

The second equation for the envelope amplitude a_2 can be obtained by the index replacement $1 \leftrightarrow 2$ and the change $v \rightarrow -v$. This system includes the effects of the SW propagation, damping, and interaction with pumping. The solution of Eq. (2) in the linear approximation ($T=S=0$) with natural

boundary conditions $a_1(x_B) = a_0$, $a_2(x_C) = 0$ gives the amplification rate Eq. (1).

In Eq. (2), we also include two nonlinear terms. The first one describes the nonlinear SW frequency shift $\omega = \omega_0 + T|c_k|^2$ (c_k is the SW amplitude), which is a result of 4-wave interaction of a SW with itself (corresponding Hamiltonian $\mathcal{H} = (1/2) \sum_k T_k |c_k|^4$). The second term describes the 4-wave interaction of the SW pairs with opposite wave vectors k and $-k$ (signal and idler SWs in our case), which is described by the Hamiltonian $\mathcal{H} = \sum_k S_k |c_k|^2 |c_{-k}|^2$. The S -term is known to be often the most important nonlinear term for the processes of parametric wave interaction, as it is responsible for the deviation of the phase relation between the SWs and the parametric pumping from the optimum, and, consequently, in a less efficient energy transfer from the pumping to the SWs.¹⁸ The coefficients $T = T_k$ and $S = S_k$ can be calculated using the formalism presented in Ref. 31 (also see Ref. 23).

The general analytical solution of Eq. (2) is not known, and before solving it numerically, it is useful to make one additional transformation of this equation. If one introduces new variables $a_1 = \tilde{a}_1 \exp[-i(T/v) \int_{-\infty}^x (|a_1|^2 + |a_2|^2) dx']$, $a_2^* = \tilde{a}_2^* \exp[-i(T/v) \int_{-\infty}^x (|a_1|^2 + |a_2|^2) dx']$, it is possible to get an equation for \tilde{a}_1, \tilde{a}_2 in the form similar to Eq. (2) but with $\tilde{T} = 0$ and $\tilde{S} = S - T/2$. This new equation is invariant with respect to the substitution $\tilde{a}' \sqrt{\tilde{S}'} = \tilde{a} \sqrt{\tilde{S}}$, i.e., the coefficient \tilde{S} only defines the amplitude scale, while the solution remains the same (except in the case $\tilde{S} \rightarrow 0$, when the currently ignored higher-order nonlinear interaction terms should be taken into account).

The transmission characteristics, calculated from the numerical solution of Eq. (2), are shown in Fig. 2. It is clear that they almost perfectly match the results of the previously performed micromagnetic simulations but with the coefficient \tilde{S} that is different from the analytically calculated one. The nonlinear coefficients calculated using Ref. 31 are $T/(2\pi) = -8.06$ GHz and $S/(2\pi) = -1.46$ GHz, resulting in $\tilde{S}/(2\pi) = 2.57$ GHz, while the good agreement with the micromagnetic results is achieved for $\tilde{S}/(2\pi) \approx 4.75$ GHz (85% higher value). We believe that this discrepancy is mainly related to the influence of the nonresonant 3-wave interaction processes between different SW branches, which leads to the renormalization of the 4-magnon coefficients T and S . Note that these 3-magnon processes do not result in any qualitative difference but only in a weak quantitative difference.

Using the analytical model Eq. (2), it is possible to investigate how the transmission characteristics change with the size variation of the amplification gate. The pumping strength for each gate size L_a was chosen in such a way that the amplification rate in the linear regime is the same. As one can see from Fig. 3(a), the nonlinear processes, resulting in a decrease in the amplification efficiency, become pronounced at a smaller amplitude of the incident SW for longer amplification gates. Such a behavior is expected, as the strength of the nonlinear SW interaction depends on the amplitudes of both the incident and idler SWs. In the case of a smaller gate, the idler wave reaches a smaller amplitude

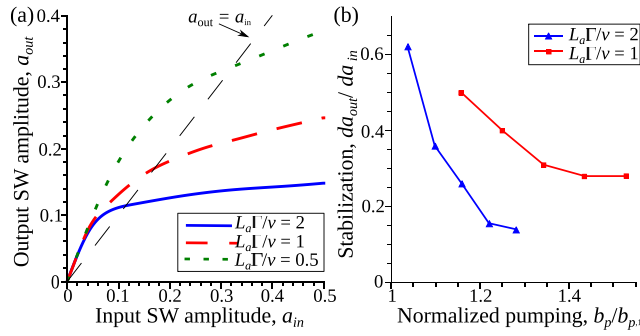


FIG. 3. (a) Transmission characteristics of the parametric amplifier calculated from the numerical solution of Eq. (2) for different lengths of the pumping localization region; (b) Stabilization ratio defined as a derivative da_{out}/da_{in} at the point $a_{out} = a_{in}$ for different pumping localization lengths. The pumping strength was normalized to the value $b_{p,1}$ at which $K = 1$ in the linear regime.

(remember that $a_2(x_C) = 0$), and the overall efficiency of the 4-wave interaction is also smaller. Thus, for the purpose of the SW amplification, it is desirable to use relatively small amplification gates with a length that is at least several times smaller than the SW mean free path $l_{fp} = v/\Gamma$.

In contrast, a better stabilization of the SW amplitude is achieved for larger gates having the size of the order or larger than the SW mean free path. The better stabilization properties correspond to a smaller derivative of the transmission characteristic at the point $a_{out} = a_{in}$. As one can see from Fig. 3(b), this amplitude stabilization effect is realized for a larger length of the pumping localization region and a higher pumping amplitude. Of course, the pumping amplitude should be smaller than the threshold of parametric excitation of SWs. For example, for $L_a\Gamma/v = 2$, the minimum value of the derivative da_{out}/da_{in} is $da_{out}/da_{in} \approx 0.13$, meaning that the amplitude spread in the output SW is 7.7 times smaller than the amplitude spread of the input SWs. Of course, in practical devices, the use of such large amplification gates is not convenient. A possible solution to this problem is a local variation of the SW dispersion, e.g., by the application of a static electric field (in the VCMA devices), or a variation of the nanowire shape. This dispersion variation allows one to change locally the SW wave vector and, therefore, the SW group velocity to satisfy the relation $v < L_a\Gamma$, while the SW mean free path outside of this region can be substantially larger.

The model Eq. (2) also allows one to estimate the characteristic amplitudes of the incident SW at which different amplification regimes can be realized. In particular, a linear amplification regime is realized in the range of $|a_{in}|^2 \ll 1/(\tilde{S}\sqrt{f^2(x)})$, where the function $f(x)$ is $f(x) = (K^2/v\kappa) \sin[\kappa(x_C - x)](\cos[\kappa(x_C - x)] + \Gamma/(v\kappa) \sin[\kappa(x_C - x)])$ and the symbol $\langle \dots \rangle$ denotes the averaging over the pumping region. In contrast, a SW is almost insensitive to the pumping and simply decays as $\exp[-\Gamma x/v]$ in the range of $|a_{in}|^4 \gg v/(2\Gamma L_a)|Vb_p/\tilde{S}|^2 \exp[2\Gamma L_a/v]$. The results calculated from these expressions are in good agreement with the results of our numerical simulations. The details of the derivation can be found in the [supplementary materials](#).

At the end, we would like to note that the nonlinear coefficients T_k and S_k could significantly depend on the

nanowire geometry and the static magnetization as well as on the SW wave vector k . Thus, by choosing a proper geometry and a proper working frequency, it is possible to both enhance and suppress the nonlinear interactions at a given SW amplitude, depending on what is desired.

In summary, we have studied a nonlinear stage of amplification of a propagating SW by a localized parametric pumping. It was shown that the nonlinear 4-wave interaction processes result in the decrease in a parametric amplification efficiency at sufficiently high SW amplitudes. The characteristic values of the SW amplitudes, at which the nonlinear interaction becomes important, are determined by 4-wave interaction efficiency (coefficient \tilde{S}) and are inversely proportional to the ratio of the pumping localization length L_a to the SW mean free path l_{fp} . As a result, for the purpose of the SW amplification, it is desirable to use relatively small amplification gates, which can efficiently amplify large-amplitude SWs. In contrast, larger gates ($L_a \geq l_{fp}$) with the pumping strength that is close to the parametric excitation threshold can be used for the stabilization of the SW amplitude.

See [supplementary materials](#) for the details of the estimation of SW amplitudes at which different regimes of the parametric amplification are realized.

This work was supported in part by the grant from the Center for NanoFerroic Devices (CNFD) and Nanoelectronics Research Initiative (NRI), by the Grants Nos. EFMA-1641989 and ECCS-1708982 from the NSF of the USA, and by the DARPA M3IC Grant under the Contract No. W911-17-C-0031. RV acknowledges support from the Ministry of Education and Science of Ukraine, project 0115U002716. G.F. and M.C. acknowledge the executive program of scientific and technological cooperation between Italy and China for the years 2016–2018 “Nanoscale broadband spin-transfer-torque microwave detector” (code CN16GR09) funded by Ministero degli Affari Esteri e della Cooperazione Internazionale.

¹A. Khitun, M. Bao, and K. L. Wang, *J. Phys. D: Appl. Phys.* **43**, 264005 (2010).

²A. V. Chumak, V. I. Vasyuchka, A. A. Serga, and B. Hillebrands, *Nat. Phys.* **11**, 453 (2015).

³A. V. Chumak, A. A. Serga, and B. Hillebrands, *Nat. Commun.* **5**, 4700 (2014).

⁴V. V. Kruglyak, S. O. Demokritov, and D. Grundler, *J. Phys. D: Appl. Phys.* **43**, 264001 (2010).

⁵T. Schneider, A. A. Serga, B. Leven, B. Hillebrands, R. L. Stamps, and M. P. Kostylev, *Appl. Phys. Lett.* **92**, 022505 (2008).

⁶N. Sato, K. Sekiguchi, and Y. Nozaki, *Appl. Phys. Express* **6**, 063001 (2013).

⁷R. L. Melcher, *Phys. Rev. Lett.* **30**, 125 (1973).

⁸L. Udvardi and L. Szunyogh, *Phys. Rev. Lett.* **102**, 207204 (2009).

⁹V. L. Zhang, K. Di, H. S. Lim, S. C. Ng, M. H. Kuok, J. Yu, J. Yoon, X. Qiu, and H. Yang, *Appl. Phys. Lett.* **107**, 022402 (2015).

¹⁰M. Weisheit, S. Fähler, A. Marty, Y. Souche, C. Poinsignon, and D. Givord, *Science* **315**, 349 (2007).

¹¹C.-G. Duan, J. P. Velez, R. F. Sabirianov, Z. Zhu, J. Chu, S. S. Jaswal, and E. Y. Tsymlal, *Phys. Rev. Lett.* **101**, 137201 (2008).

¹²J. Zhu, J. A. Katine, G. E. Rowlands, Y.-J. Chen, Z. Duan, J. G. Alzate, P. Upadhyaya, J. Langer, P. K. Amiri, K. L. Wang, and I. N. Krivorotov, *Phys. Rev. Lett.* **108**, 197203 (2012).

¹³K. Nawaoka, Y. Shiota, S. Miwa, H. Tomita, E. Tamura, N. Mizuochi, T. Shinjo, and Y. Suzuki, *J. Appl. Phys.* **117**, 17A905 (2015).

- ¹⁴Y.-J. Chen, H. K. Lee, R. Verba, J. A. Katine, I. Barsukov, V. Tiberkevich, J. Q. Xiao, A. N. Slavin, and I. N. Krivorotov, *Nano Lett.* **17**, 572 (2017).
- ¹⁵B. Rana, Y. Fukuma, K. Miura, H. Takahashi, and Y. Otani, *Appl. Phys. Lett.* **111**, 052404 (2017).
- ¹⁶K.-S. Lee and S.-K. Kim, *J. Appl. Phys.* **104**, 053909 (2008).
- ¹⁷S. Klingler, P. Pirro, T. Brächer, B. Leven, B. Hillebrands, and A. V. Chumak, *Appl. Phys. Lett.* **105**, 152410 (2014).
- ¹⁸V. S. L'vov, *Wave Turbulence under Parametric Excitation* (Springer-Verlag, New York, 1994).
- ¹⁹B. Kalinikos, N. Kovshikov, M. Kostylev, and H. Benner, *JETP Lett.* **64**, 171 (1996).
- ²⁰B. A. Kalinikos and M. P. Kostylev, *IEEE Trans. Mag.* **33**, 3445 (1997).
- ²¹P. A. Kolodin, P. Kabos, C. E. Patton, B. A. Kalinikos, N. G. Kovshikov, and M. P. Kostylev, *Phys. Rev. Lett.* **80**, 1976 (1998).
- ²²T. Brächer, P. Pirro, and B. Hillebrands, *Phys. Rep.* **699**, 1 (2017).
- ²³R. Verba, M. Carpentieri, G. Finocchio, V. Tiberkevich, and A. Slavin, *Sci. Rep.* **6**, 25018 (2016).
- ²⁴R. Verba, M. Carpentieri, G. Finocchio, V. Tiberkevich, and A. Slavin, *Phys. Rev. Appl.* **7**, 064023 (2017).
- ²⁵A. G. Gurevich and G. A. Melkov, *Magnetization Oscillations and Waves* (CRC Press, New York, 1996), p. 464.
- ²⁶G. A. Melkov, A. A. Serga, V. S. Tiberkevich, Y. V. Kobljanskij, and A. N. Slavin, *Phys. Rev. E* **63**, 066607 (2001).
- ²⁷A. A. Serga, S. O. Demokritov, B. Hillebrands, S.-G. Min, and A. N. Slavin, *J. Appl. Phys.* **93**, 8585 (2003).
- ²⁸T. Brächer, F. Heussner, P. Pirro, T. Meyer, T. Fischer, M. Geilen, B. Heinz, B. Lägél, A. A. Serga, and B. Hillebrands, *Sci. Rep.* **6**, 38235 (2016).
- ²⁹L. Lopez-Diaz, D. Aurelio, L. Torres, E. Martinez, M. A. Hernandez-Lopez, J. Gomez, O. Alejos, M. Carpentieri, G. Finocchio, and G. Consolo, *J. Phys. D: Appl. Phys.* **45**, 323001 (2012).
- ³⁰V. Puliafito, A. Giordano, A. Laudani, F. Garesci, M. Carpentieri, B. Azzerboni, and G. Finocchio, *Appl. Phys. Lett.* **109**, 202402 (2016).
- ³¹P. Krivosik and C. E. Patton, *Phys. Rev. B* **82**, 184428 (2010).

Supplementary materials: Amplification and stabilization of large-amplitude propagating spin waves by parametric pumping

Roman Verba,^{1, a)} Mario Carpentieri,² Giovanni Finocchio,³ Vasil Tiberkevich,⁴ and Andrei Slavin⁴

¹⁾*Institute of Magnetism, Kyiv 03680, Ukraine*

²⁾*Department of Electrical and Information Engineering, Politecnico of Bari, I-70125 Bari, Italy*

³⁾*Department of Electronic Engineering, Industrial Chemistry and Engineering, University of Messina, I-98166 Messina, Italy*

⁴⁾*Department of Physics, Oakland University, Rochester, MI 48309, USA*

(Dated: 23 December 2017)

^{a)}corresponding author, e-mail: verrv@ukr.net

In these Supplementary materials we provide details of the derivation of expressions that allow one to estimate the spin wave (SW) amplitude, at which different regimes of the parametric amplification are realized. The derivation is based on the following system of Bloembergen equations:

$$\begin{aligned} \left(\frac{\partial}{\partial t} + v \frac{\partial}{\partial x} + \Gamma \right) \tilde{a}_1 &= -iVb_p(x)\tilde{a}_2^* - 2i\tilde{S}|\tilde{a}_2|^2\tilde{a}_1 \\ \left(\frac{\partial}{\partial t} - v \frac{\partial}{\partial x} + \Gamma \right) \tilde{a}_2^* &= iV^*b_p^*(x)\tilde{a}_1 + 2i\tilde{S}|\tilde{a}_1|^2\tilde{a}_2^* . \end{aligned} \quad (\text{S1})$$

The conversion from the SW envelope amplitudes a_i to common dynamic magnetization is given by the expression:

$$M_{y,z}(x, t) = M_s \sqrt{2 - |a_i(x, t)|^2} (u_k \pm v_k) a_i(x, t), \quad (\text{S2})$$

where u_k and v_k are the coefficients of the third Holstein-Primakoff transformation (see, e.g. Ref. 1).

I. LINEAR REGIME OF AMPLIFICATION

In the linear approximation ($\tilde{S} \rightarrow 0$) the stationary solution of Eq. (S1) with the boundary conditions $\tilde{a}_1(0) = a_0$, $\tilde{a}_2(L_a) = 0$ is given by the expression:

$$\begin{aligned} \tilde{a}_1(x) &= a_0 \frac{v\kappa \cos[\kappa(L_a - x)] + \Gamma \sin[\kappa(L_a - x)]}{v\kappa \cos[\kappa L_a] + \Gamma \sin[\kappa L_a]} \\ \tilde{a}_2^*(x) &= \frac{ia_0 (\Gamma^2 + v^2\kappa^2) \sin[\kappa(L_a - x)]}{Vb_p v\kappa \cos[\kappa L_a] + \Gamma \sin[\kappa L_a]}, \end{aligned} \quad (\text{S3})$$

where $\kappa = \sqrt{|Vb_p|^2 - \Gamma^2}/v$ and the coordinate system is chosen in such a way, that the beginning of the amplification gate corresponds to $x = 0$ and the end, correspondingly, to $x = L_a$. Setting $x = L_a$ one can obtain the amplification rate K (see Eq. (1) in the main text).

In the linear approximation the phase relation between the signal and idler SWs is constant, $\phi_\Sigma = \phi_1 + \phi_2 = \phi_p - \pi/2$, where $\tilde{a}_i = A_i e^{i\phi_i}$, $\phi_p = \text{Arg}[b_p]$. In the first approximation of the perturbation theory the dynamics of the phase ϕ_Σ is described by the following equation:

$$\frac{\partial \phi_\Sigma}{\partial x} = 2\tilde{S} (A_1^2 + A_2^2) . \quad (\text{S4})$$

The solution of the above equation with the natural boundary condition $\phi_\Sigma(L_a) = \phi_{\Sigma,0} = \phi_p - \pi/2$, which means that the phase relation are not affected by 4-wave process at $x = L_a$ since $\tilde{a}_2(L_a) = 0$, yields $\phi_\Sigma = 2\tilde{S}A_0^2 f(x) + \phi_{\Sigma,0}$, where

$$f(x) = -\frac{\sin[\kappa(L_a - x)] (v\kappa \cos[\kappa(L_a - x)] + \Gamma \sin[\kappa(L_a - x)])}{(v\kappa \cos[\kappa L_a] + \Gamma \sin[\kappa L_a])^2}. \quad (\text{S5})$$

The linear amplification regime is realized when the averaged value of the phase deviation caused by 4-wave processes is negligible, i.e. when $\sqrt{\langle (\phi_\Sigma - \phi_{\Sigma,0})^2 \rangle} \ll \pi/2$, which results in the following condition (neglecting the value $\pi/4 \sim 1$):

$$A_0^2 \ll \frac{1}{\tilde{S} \sqrt{\langle f^2(x) \rangle}}. \quad (\text{S6})$$

II. REGIME OF AMPLITUDE STABILIZATION (WHEN THE SW AMPLITUDE IS INSENSITIVE TO PUMPING)

At a sufficiently high amplitude the incident SW becomes almost insensitive to the pumping, and simply decays with the natural damping rate as $\exp[-\Gamma x/v]$. Using this solution ($\tilde{a}_1(x) = a_0 \exp[-\Gamma x/v]$) as a zero-order approximation in Eq. (S1) one can obtain the amplitude of the idler SW in the first approximation of the perturbation theory (assuming, also, a moderate damping rate $\exp[-\Gamma L_a/v] \approx 1 - \Gamma L_a/v$):

$$\tilde{a}_2^* \approx \frac{V^* b_p^*}{2\tilde{S}A_0} e^{\frac{\Gamma x}{v}} \left(\exp \left[e^{\frac{2\Gamma L_a}{v}} \frac{2i\tilde{S}A_0^2(L_a - x)}{v} \right] - 1 \right). \quad (\text{S7})$$

Using this expression, one can calculate the full energy transferred from the pumping to the SWs per one oscillation period:

$$I_p = 2\omega_p |Vb_p| \int_0^{L_a} a_2^* a_1^* dx. \quad (\text{S8})$$

The maximum value of I_p is estimated as:

$$I_p \leq \frac{\omega_p |Vb_p|^2 v}{2\tilde{S}^2 A_0^2} e^{\frac{2\Gamma L_a}{v}}. \quad (\text{S9})$$

The losses of the signal wave are estimated as $2\Gamma\omega_k A_0^2 L_a$. If these losses significantly exceed the pumped energy, we can say that the signal SW is almost insensitive to the influence of pumping. This happens if:

$$A_0^4 \gg \frac{1}{2} \frac{v}{\Gamma L_a} \left| \frac{Vb_p}{\tilde{S}} \right|^2 e^{\frac{2\Gamma L_a}{v}}. \quad (\text{S10})$$

REFERENCES

¹P. Krivosik and C. E. Patton, Phys. Rev. B **82**, 184428 (2010).

Correction of Phase Errors in a Spin-Wave Transmission Line by Nonadiabatic Parametric Pumping

Roman Verba,^{1,*} Mario Carpentieri,² Yu-Jin Chen,³ Ilya N. Krivorotov,³ Giovanni Finocchio,⁴ Vasil Tiberkevich,⁵ and Andrei Slavin⁵

¹*Institute of Magnetism, Kyiv 03142, Ukraine*

²*Department of Electrical and Information Engineering, Politecnico di Bari, I-70125 Bari, Italy*

³*Department of Physics and Astronomy, University of California, Irvine, California 92697, USA*

⁴*Department of Electronic Engineering, Industrial Chemistry and Engineering, University of Messina, I-98166 Messina, Italy*

⁵*Department of Physics, Oakland University, Rochester, Michigan 48309, USA*

 (Received 12 January 2019; revised manuscript received 18 March 2019; published 15 May 2019)

It is shown that phase errors in a microwave spin-wave transmission line can be corrected by subjecting the signal-carrying propagating spin wave to the action of a localized nonadiabatic parametric pumping, having the localization length smaller than the spin-wave wavelength. In such a transmission line the phase-transmission characteristic has a “steplike” shape containing flat “stabilization plateaus” separated by intervals of size π . Within the “plateau” regions the phase of the output spin wave is practically constant in a rather wide range of phases of the input spin wave. This effect can be used in magnonic logic devices for the correction of phase errors of up to $\pm 0.25\pi$. It is also proved that this phase-stabilization effect is stable against the variations of the spin-wave amplitude and is present across the amplitude range of the stable spin-wave propagation.

DOI: [10.1103/PhysRevApplied.11.054040](https://doi.org/10.1103/PhysRevApplied.11.054040)

I. INTRODUCTION

Spin waves (SWs) propagating in nanoscale ferromagnetic waveguides are considered to be promising candidates for applications in a new generation of digital- and analog-signal-processing devices [1–5]. Recently, several novel concepts of magnonic logic elements and circuits have been proposed [6–12]. In magnonic logic, a digital signal can be coded via SW amplitude [6,13–15] or SW phase [2,16]. Obviously, in the case of phase-coded magnonic logic devices the spin-wave phase should be well defined, and should not fluctuate substantially in the course of the spin-wave propagation. This property of the SW phase stability is also crucial for amplitude-coded magnonic logic devices. Indeed, these devices often use SW interference for information processing and the phase relations between several processed SWs should be well defined for correct device operation [13,15,17,18].

For example, the result of the interference of two SWs having phases φ_1 and φ_2 and similar amplitudes is proportional to $\cos[(\varphi_1 - \varphi_2)/2]$. Deviation of the phase difference by 0.55π could be enough for incorrect interpretation of the interference result—instead of 1 in the ideal case $\varphi_1 - \varphi_2 = 0$ (or 0 if $\varphi_1 - \varphi_2 = \pi$), the resulting signal

becomes less than 2/3 (greater than 1/3), which is commonly interpreted as indeterminate in amplitude-coded logic [15]. Deviation of the phase difference by 0.8π leads to a wrong result—logic “0” instead of “1” and vice versa.

There are several reasons for the SW phase deviation in a magnonic circle. The first is the deviation of the SW waveguide length due to lithographic misprints. This deviation can occur, for example, due to a misposition of the waveguide bends and a spread of bend shapes in a circuit. Small length deviations, not exceeding 1 nm at each bend, can accumulate over a magnonic circle and, for exemplary SWs of 100-nm wavelength, could reach critical values (corresponding to 0.55π phase shift) after passing several tens of such bends. Similarly, a misprint of the waveguide width leads to a change of SW dispersion and, thus, SW wave number at a fixed frequency, which is another source of random phase accumulation. Finally, stability of the SW phase can be violated by thermal fluctuations and the phase deviations leading, eventually, to a signal-processing error can accumulate in the course of the SW propagation in a magnonic circuit. Therefore, the timely correction of these phase errors is very important for stable and error-free operation of magnonic logic circuits.

In this work, we demonstrate that the problem of phase-error correction can be solved by application of localized parametric pumping, i.e., by using the interaction of a

*verrv@ukr.net

propagating SW with a localized microwave magnetic field (external or internal) of approximately double the SW frequency. Parametric pumping is a well-known method for excitation and amplification of SWs [19–22]. It is also known that parametric interaction becomes phase sensitive in the case of so-called “nonadiabatic” localized pumping, having a localization length (or other characteristic length of the spatial variation) that is smaller than the SW wavelength [23–25]. In our current work we calculate the phase-transmission characteristics for a SW transmission line containing a region where nonadiabatic parametric pumping is acting and show that the phase-transmission characteristics of such a line demonstrate “stabilization plateaus,” within which the phase of the output SW signal is more or less constant in a rather wide range of phases of the input SW signal. Thus, the phase fluctuation of the SW signal acquired in the course of its propagation can be corrected. It is important that these phase-stabilization plateaus are separated by intervals of size almost exactly equal to π , which is thus perfectly suitable for phase-coded magnonic logic and/or signal processing.

II. THEORY

A sketch of the considered SW transmission line is shown in Fig. 1. It is a ferromagnetic nanowire of width w_y and thickness h . The SWs of the frequency ω_k , propagating in the $+x$ direction, are excited by the excitation gate or, in an integrated magnonic circuit, come from a preceding SW signal-processing device. The parametric pumping gate of length L_p is placed on the propagation path of the SWs. The parametric pumping can be created by a microwave magnetic field with polarization parallel to the direction of static magnetization of the nanowire [20,21], by the microwave electric field via various magnetoelectric effects [22], or by other means. The phase-stabilization effects discussed below do not depend on the nature of the pumping and are also independent of the direction of static magnetization of the nanowire.

To be specific with the coefficients used in our calculations, we consider the case of parametric pumping

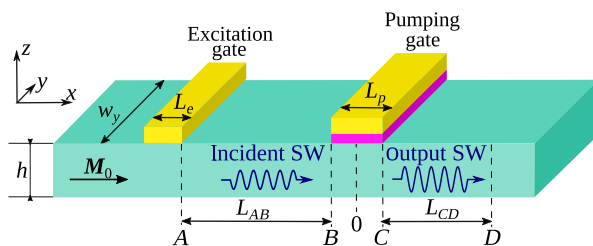


FIG. 1. A sketch of the considered magnonic transmission line showing regions of the SW excitation and the localization of the parametric pumping. The reference points A – D used in the micromagnetic simulations are also shown.

produced by a microwave voltage via the voltage-controlled magnetic anisotropy effect (VCMA) [26,27], which is the most efficient and convenient method for applications at the nanoscale. In this case the pumping gate consists of a strip of a normal metal separated by a dielectric layer from the conductive ferromagnetic material of the nanowire. The application of a microwave voltage of frequency ω_p to the gate results in oscillations of the perpendicular magnetic anisotropy at the ferromagnetic-dielectric interface with the same frequency [28,29]. It has been shown that these oscillations of anisotropy can couple parametrically to the SWs propagating in the nanowire, both in the case of the in-plane and out-of-plane static magnetization direction of the nanowire [22,29,30]. In the former case the coupling is stronger, and demonstrates no limits with respect to the SW wave number [30], so here we consider only this case of the in-plane static magnetization, as shown in Fig. 1.

In the parametric process of first order, the pumping is coupled to a pair of SWs having wave vectors k and k' . The efficiency of the parametric interaction is proportional to the $(k + k')$ th Fourier harmonic $b_{p,k+k'}$ of the spatial distribution of the effective pumping field $b_p(x)$. Therefore, in the case of weakly localized quasiuniform pumping, when $kL_p \gg 1$, only the SWs with opposite wave vectors, $k' = -k$, interact efficiently with the pumping, which is a consequence of the momentum conservation law (the case of “adiabatic pumping”).

In contrast, when the pumping localization length L becomes smaller than the SW wavelength (or if the pumping is spatially nonuniform with the characteristic length comparable to the SW wavelength), not only can the contrapropagating SWs ($k' = -k$) interact with the localized pumping field, but also other SWs ($k' \neq -k$), in particular copropagating SWs, can do so as well. This is the case of “nonadiabatic parametric pumping,” as described in Ref. [23].

It should be noted that the parametric interaction has maximum efficiency when the resonance condition $\omega_p = \omega_k + \omega_{k'}$ is satisfied. This condition severely limits the number of SWs that can efficiently interact with the pumping. In the simple, and most common case, when the pumping frequency is twice as large as the SW frequency, $\omega_p = 2\omega_k$, the only SWs efficiently interacting with the nonadiabatic pumping are the above-mentioned contrapropagating SWs having the same modulus of SW wave vectors k and $-k$; however, the nonadiabatic term results in additional coupling of these SWs with themselves (that is the limiting case of the coupling of copropagating SWs, when approaching exact parametric resonance).

The SW dynamics under a localized parametric pumping is convenient to study using Bloembergen’s system of equations. For the case of nonadiabatic pumping, it has been generalized in Ref. [23] and, neglecting the higher-order nonlinear SW interactions, it can be

written as

$$\begin{aligned} \left(\frac{\partial}{\partial t} + v\frac{\partial}{\partial x} + \Gamma\right) a_1 &= Vb_0 e^{-i\psi} a_2^* + Vb_{2k} e^{-i\psi} a_1^*, \\ \left(\frac{\partial}{\partial t} - v\frac{\partial}{\partial x} + \Gamma\right) a_2^* &= Vb_0 e^{i\psi} a_1 + Vb_{2k} e^{i\psi} a_2. \end{aligned} \quad (1)$$

This system describes the evolution of the envelope amplitudes $a_1(x, t)$ and $a_2(x, t)$ of the two SW wave packets, having carrier wave vectors k and $-k$, respectively. In our problem, a_1 describes the envelope amplitude of the incident SW, which propagates toward the pumping region, and a_2 is the envelope amplitude of the idler SW, which is counterpropagating to a_1 , and appears in the pumping region as a result of the parametric interaction. The relation of envelope amplitudes to the real magnetization amplitudes is given by the equation $\mathbf{m}_{1,2}(x, t) = [\mathbf{m}_k a_{1,2}(x, t) \exp(\pm ikx - i\omega_k t) + \text{c.c.}]$, where \mathbf{m}_k describes the vector structure (ellipticity) of a particular SW. In Eq. (1), v and Γ are the group velocity and the damping rate of the SWs, V is the efficiency of the parametric coupling, ψ is the phase of the pumping, and $b_k = (1/L_p) \int_{-L_p/2}^{L_p/2} b_p(x) e^{ikx} dx$ is the Fourier harmonic of the effective field of pumping with the spatial profile $b_p(x)$. The fact that pumping is nonadiabatic is reflected by the last term in the equations, which describes the parametric coupling of the copropagating SWs ($k' = k$). In the case of quasiuniform adiabatic pumping this term is naturally absent, since $b_{2k} \rightarrow 0$. The value $\alpha = |b_{2k}/b_0|$ describes the strength of the nonadiabatic term relative to the adiabatic one, and is called “the degree of nonadiabaticity of the pumping.”

In our particular case of the in-plane static magnetization and VCMA-induced pumping, the efficiency of the parametric coupling is given by $V = \gamma |m_{k,z}/4m_{k,y}|$, the pumping field is $b_p = 2\beta E/hM_s$ with β being the magnetoelectric coefficient, E is the amplitude of the microwave electric field applied to the pumping gate [30], and the pumping Fourier harmonics b_k are given by the expression $b_k = b_p \text{sinc}(kL_p/2) \equiv b_p \sin(kL_p/2)/(kL_p/2)$.

The pumping phase ψ is defined in such a way that the applied microwave electric field is $E(t) = E \sin(\omega_p t + \psi)$, with $\omega_p = 2\omega_k$ (exact parametric resonance). The real dynamic magnetization, corresponding to the steady propagating SW of the envelope amplitude $a_1 = |a_1| e^{-i\varphi}$, is $m_z(x, t) = 2m_{z,k} \sin(\omega_k t + \varphi - kx)$, where φ is the SW phase. Note that the point $x = 0$ is assumed to be at the center of the pumping gate, as shown in Fig. 1 and its position obviously affects the definitions of the phases φ and ψ . For other cases of the parametric pumping source and other directions of the static magnetization, the only differences in Eq. (1) come from the different values of the parametric coupling efficiency V [19,21,22], and the relations of the phases ψ and φ to the real time profiles

of the dynamic magnetization and applied pumping signal (microwave magnetic or electric field).

For further analysis it is convenient to introduce new real variables $A_{1\pm}$ and $A_{2\pm}$, as $a_1 = e^{-i\psi/2}(A_{1+} + iA_{1-})$ and $a_2 = e^{-i\psi/2}(A_{2+} - iA_{2-})$, which is possible if the pumping is harmonic, i.e., if the pumping phase is time independent, $\psi \neq \psi(t)$. This operation, in fact, is a decomposition of a harmonic wave with an arbitrary phase into two partial waves, sine and cosine. Then, Eq. (1) is transformed to [23]

$$\begin{aligned} \left(\frac{\partial}{\partial t} + v\frac{\partial}{\partial x} + \Gamma \mp Vb_{2k}\right) A_{1\pm} &= Vb_0 A_{2\pm}, \\ \left(\frac{\partial}{\partial t} - v\frac{\partial}{\partial x} + \Gamma \mp Vb_{2k}\right) A_{2\pm} &= Vb_0 A_{1\pm}. \end{aligned} \quad (2)$$

As one can see, the pairs of partial waves (A_{1+}, A_{2+}) and (A_{1-}, A_{2-}) evolve independently and are connected only by the boundary conditions. The action of the nonadiabatic term Vb_{2k} results in different effective damping for partial waves: effective damping for the “in-phase” partial waves (A_{1+}, A_{2+}) is decreased, while the “out-of-phase” SWs (A_{1-}, A_{2-}) acquire an additional damping term. Thus, the partial waves evolve differently under the action of pumping, since the pumping pumps energy more effectively into the “in-phase” partial waves.

To find a steady-state solution of the transmission problem, we consider a stationary regime, setting $\partial A_i/\partial t = 0$. Equation (2) should be accompanied by a boundary condition $a_1(-L_p/2) = A_0 e^{-i\varphi_0}$, which describes the incoming SW with amplitude A_0 and arbitrary phase φ_0 , and $a_2(L_p/2) = 0$, meaning that no idler wave is incident to the pumping region. Then, the envelope amplitude of the output SW $a_{out} = a_1(L_p/2)$ can be found to be

$$\begin{aligned} a_{out} &= A_0 e^{-i\psi/2} \left[\cos\left(\varphi_0 - \frac{\psi}{2}\right) K_+ \right. \\ &\quad \left. - i \sin\left(\varphi_0 - \frac{\psi}{2}\right) K_- \right], \end{aligned} \quad (3)$$

where

$$K_{\pm} = \left[\cos(\kappa_{\pm} L_p) + \frac{\tilde{\Gamma}_{\pm}}{v\kappa_{\pm}} \sin(\kappa_{\pm} L_p) \right]^{-1} \quad (4)$$

are the amplification rates for partial waves, $\tilde{\Gamma}_{\pm} = \Gamma \mp Vb_{2k}$, and $\kappa_{\pm}^2 = (Vb_0)^2 - \tilde{\Gamma}_{\pm}^2$.

As usual [21], the parametric pumping results in a partial amplification of the incident SW, until the pumping amplitude reaches a certain threshold, at which a spontaneous generation of SWs takes place (the threshold of generation is determined from the condition $K_+ \rightarrow \infty$). Due to the nonadiabatic term, the amplification rates of the partial waves are different, resulting in the dependence of the

output SW amplitude on its phase [23,24]. Simultaneously, this means that the ratio between the amplitudes of the partial waves A_{1+} and A_{1-} changes within the pumping region, and is different at the end of the pumping gate compared to that at the gate entrance. Thus, the phase of the incident SW a_1 changes during the propagation through the pumping gate. Since the “in-phase” partial wave A_{1+} grows faster (or decays slower) than the “out-of-phase” partial wave, the phase of the incident wave approaches the phase of the “in-phase” partial wave, which is fixed by the phase of pumping to an accuracy of an integer multiple of π : $\varphi(x) \rightarrow \psi/2 + \pi n$, $n \in \mathbb{Z}$.

The phase-transmission characteristics are obtained from Eq. (3) simply as $\varphi_{out} = -\text{Arg}(a_{out})$. In the case of adiabatic pumping, when $b_{2k} = 0$, the phase-transmission characteristic is a simple straight line, $\varphi_{out} = \varphi_0$ [Fig. 2(a)]. Recall that the SW phase φ was introduced as a phase of the SW envelope, so the propagation phase shift kL_p is not taken into account in Fig. 2. This leads to a simple vertical shift of all the curves.

In contrast, as soon as the pumping becomes nonadiabatic, the SW phase-transmission characteristics become

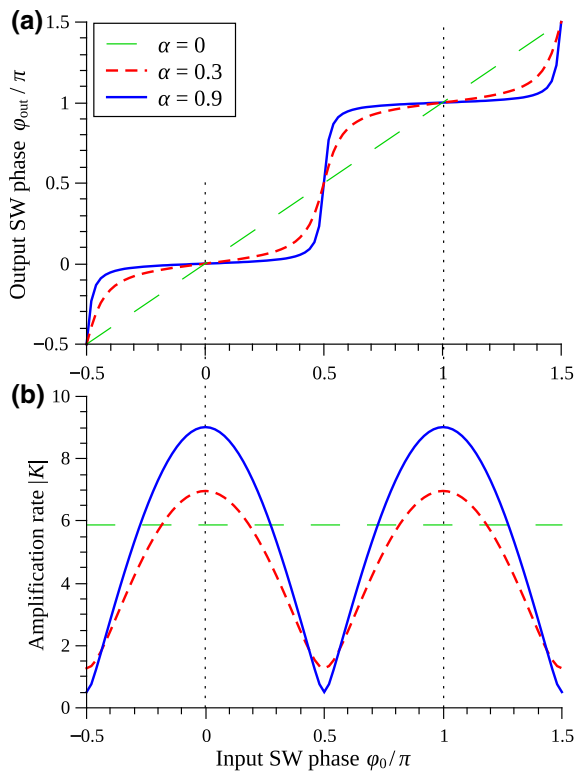


FIG. 2. (a) SW phase-transmission characteristics $\varphi_{out} = f(\varphi_0)$ and (b) amplification rates $|K| = f(\varphi_0)$ of a parametric pumping gate for different degrees of the pumping nonadiabaticity $\alpha = |b_{2k}/b_0|$. The pumping length $L_p = 0.1v/\Gamma$, the pumping strength is 90% of the SW generation threshold, and the pumping phase $\psi = 0$.

nonlinear. They demonstrate pronounced plateaus near the values $\varphi = 0, \pi$, which are the phases of the “in-phase” partial wave (since it is assumed that the pumping phase $\psi = 0$). Within these plateaus, the output SW phase is almost constant in a wide range of the input SW phases, i.e., nonadiabatic parametric pumping demonstrates the effect of SW phase stabilization. Importantly, the SW phase-stabilization plateaus are separated by phase intervals of size π , which perfectly matches the needs of the phase-coded magnonic logic, as under this approach the logic state “0” and the logic state “1” are coded by the SWs with a phase difference of π .

Stabilization plateaus become wider and more flat with an increase in the degree $\alpha = |b_{2k}/b_0|$ of the pumping “nonadiabaticity” [Fig. 2(a)]. A similar enhancement of the phase-stabilization properties is observed with an increase of the pumping strength, when this strength approaches the threshold of the parametric SW generation. In a limiting case, when $K_+ \gg K_-$ (which means that the pumping amplitude is close to the threshold or that the length of the pumping region is sufficiently large), the phase-transmission characteristic becomes almost a steplike function.

It should be noted that the pumping nonadiabaticity also results in the dependence of the output SW amplitude on the input SW phase, as shown in Fig. 2(b). When the phase stabilization becomes better, the variations of the SW amplitude also increase. Large variations of the SW amplitude, naturally, are not acceptable in SW processing devices, which limits the achievable ranges of the possible phase-error corrections in practice. Usually, about 10–15% of the SW amplitude variation can be considered acceptable, which defines the practical limits of the possible phase-error-correction interval as being about $\pm 0.25\pi$. Additional improvements can be achieved by placing a phase-insensitive amplitude-stabilization device after the phase stabilizer, which could use a nonlinear regime of the SW interaction with adiabatic pumping [31] or other nonlinear phenomena.

At the same time, a certain degree of SW amplitude variation can even be useful. When the SW phase is close to $\varphi_0 = \pi/2$, this means that the phase error is large and the interpretation of the SW phase as being the closest value to 0 or π may be incorrect. In the case of such large values of the phase errors it is often recommended to start the signal processing again. The above proposed phase-stabilization device indicates such large phase errors by a significant reduction of the amplitude of the output SW. In summary, by using the proposed phase-stabilization device small and moderate phase errors can be corrected, while the presence of large phase errors can clearly be determined and indicated.

Finally, we note that Fig. 2 illustrates the case when the phase stabilization is accompanied by amplification of the processed SWs. Often, this amplification is desirable

in magnonic circuits to compensate for propagation and processing losses, but sometimes a regime of no amplification [$K(0, \pi) \approx 1$] for in-phase waves needs to be realized. Fortunately, it is easy to vary the SW amplification rate by choice of the pumping amplitude and length. For example, the case of no amplification requires either a sufficiently long parametric pumping gate or enhanced magnetic damping within the parametric gate, so that the “out-of-phase” partial SWs decay significantly. The pumping nonadiabaticity in the case of a relatively long pumping gate can be realized by creating a spatially nonuniform pumping (e.g., a pumping gate consisting of several fingers having different polarities and/or strengths of the applied voltage). If the averaged pumping signal is nonzero (e.g., if fingers of opposite polarity are of unequal length), the SW dynamics is described by the same Eq. (1) in which the nonadiabatic term b_{2k} becomes large if $2k \approx 2\pi/P$, where P is the period of the fingers array. However, even in the case of zero averaged pumping one should expect the phase-stabilization effect to occur. In this case only the nonadiabatic term remains and one arrives at the limiting case of the parametric interaction of copropagating waves, when the idler wave is equivalent to the signal wave. In the case of copropagating waves, parametric pumping also can amplify waves (but cannot excite them) [32,33], and the nonadiabatic term is still phase sensitive; thus, one should expect qualitatively the same effect.

III. MICROMAGNETIC SIMULATIONS

To confirm our theoretical predictions about the SW phase stabilization we perform a series of micromagnetic simulations using the GPMagnet solver [34,35]. In our simulations the SWs are excited linearly by a microwave magnetic field applied at the excitation gate of length $L_e = 50$ nm. The excitation frequency is 6.49 GHz, which corresponds to a SW wavelength of 210 nm. Microwave parametric pumping in the form of modulation of the perpendicular anisotropy $\Delta K_{\perp} = b_p M_s \sin(\omega_p t)$ at a frequency $\omega_p/(2\pi) = 12.98$ GHz is applied at the pumping gate of length $L_p = 50$ nm, separated from the excitation gate by a distance $L_{AB} = 250$ nm. The corresponding degree of pumping nonadiabaticity in this case is $\alpha = 0.67$. To avoid the mistakes in the output SW phase determination due to the presence of the idler SW, the phase of the output SW is calculated at the point D . The SW phase at the end of the gate is retrieved by subtraction of the propagation phase accumulation kL_{CD} , where $L_{CD} = 250$ nm. The following material parameters of the Fe/MgO structure (common for VCMA experiments [36]) are used: saturation magnetization $\mu_0 M_s = 2.1$ T, exchange length $\lambda_{ex} = 3.4$ nm, surface perpendicular anisotropy energy $K_s = 1.36$ mJ/m², and effective Gilbert damping (including nonuniform broadening for a given SW frequency)

$\alpha_G = 0.02$. The nanowire thickness is set to $h = 1$ nm, the width is $w = 20$ nm, and the bias magnetic field is absent.

Simulations performed with no incident SW and a finite temperature of 1 K give a threshold of parametric excitation equal to $b_{p,th} = 130$ mT. It is somewhat smaller than the threshold of 169 mT calculated using the analytical equation Eq. (4) (from the condition $K_+ \rightarrow \infty$). We believe that the discrepancy is caused by the dispersion of SW group velocity.

In the simulations of the SW phase-transmission characteristics in the presence of an incident SW we set the pumping strength to $b_p = 100$ mT, which is 77% of the SW generation threshold. Thermal fluctuations are switched off to speed up the simulations—since we work sufficiently away from the threshold we do not expect a significant growth of thermal fluctuations under the parametric pumping gate. The simulated phase-transmission characteristic for small-amplitude (linear) SWs that are excited by a 1-mT excitation field are shown in Fig. 3 (blue dots). The figure shows definite phase-stabilization plateaus and matches well with the phase characteristics obtained in the analytical calculation (solid line) for a pumping strength equal to 77% of the theoretical SW generation threshold. We believe that the small upshift of the simulated phase characteristic is also related to the dispersion of the SW group velocity.

We also verify how phase-transmission characteristics change with the SW amplitude, when different nonlinear SW interactions become important. For this purpose we perform simulations for larger excitation fields, at 10 mT and 30 mT. For the excitation field of 30 mT the SW amplitude reaches a value of $M_y/M_s \approx 0.15$, which is definitely beyond the range where the excited SWs can be considered small amplitude (or linear) and in which our

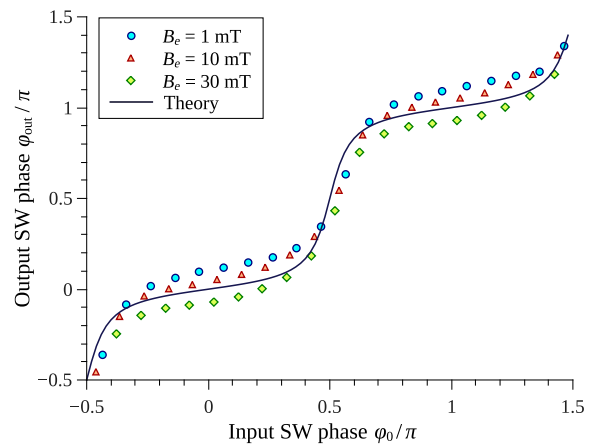


FIG. 3. Phase-transmission characteristics of a VCMA parametric pumping gate for different incident SW amplitudes created by different excitation fields B_e (symbols, micromagnetic simulations; solid line, theoretical curve for linear SWs).

analytical theory is valid. From Fig. 3 one can see that the phase-stabilization effect is still present in the case of the large-amplitude nonlinear SWs, and the sizes and slope of the phase-stabilization plateaus are almost the same, as in the linear case. The only difference is a downshift of these plateaus, which is a consequence of the nonlinear SW phase accumulation. Thus, nonadiabatic parametric pumping can be used for phase-error correction of both linear and nonlinear SWs.

IV. SUMMARY

In summary, we demonstrate that the interaction of a propagating SW with localized nonadiabatic parametric pumping leads to a shift of the SW phase, in addition to a simple propagation phase accumulation kL_p . As a result, the SW phase-transmission characteristics become nonlinear, demonstrating a “steplike” shape. They contain pronounced flat “stabilization plateaus,” within which the output SW phase is almost constant in a certain range of phases of the input SW. The phase-stabilization effect becomes more pronounced with the increased level of the pumping nonadiabaticity and when the pumping strength approaches the threshold of the parametric SW generation (but it should not exceed the threshold). Our findings open a way for the implementation of phase-error corrections in magnonic logic circuits. The range of possible phase-error corrections is limited mainly by the phase dependence of the output SW amplitude and is about $\pm 0.25\pi$ for both linear and nonlinear SWs.

ACKNOWLEDGMENTS

This work was supported in part by Grants No. EFMA-1641989, No. ECCS-1708982, and No. DMR-1610146 from the U.S. NSF, and by the DARPA M3IC grant under Contract No. W911-17-C-0031. R.V. acknowledges support from the Ministry of Education and Science of Ukraine (Project No. 0118U004007). I.N.K. acknowledges support by the Army Research Office through Grant No. W911NF-16-1-0472 and by the Defense Threat Reduction Agency through Grant No. HDTRA1-16-1-0025. G.F. and M.C. would like to acknowledge the contribution of the COST Action CA17123 “Ultrafast opto magneto electronics for non-dissipative information technology.”

-
- [1] V. V. Kruglyak, S. O. Demokritov, and D. Grundler, Magnonics, *J. Phys. D: Appl. Phys.* **43**, 264001 (2010).
 - [2] A. Khitun, M. Bao, and K. L. Wang, Magnonic logic circuits, *J. Phys. D: Appl. Phys.* **43**, 264005 (2010).
 - [3] S. O. Demokritov and A. N. Slavin, eds., *Magnonics. From Fundamentals to Applications* (Springer, Berlin, 2013).
 - [4] D. E. Nikonov and I. A. Young, Overview of beyond-CMOS devices and a uniform methodology for their benchmarking, *Proc. IEEE* **101**, 2498 (2013).

- [5] M. Krawczyk and D. Grundler, Review and prospects of magnonic crystals and devices with reprogrammable band structure, *J. Phys.: Cond. Matter.* **26**, 123202 (2014).
- [6] A. V. Chumak, A. A. Serga, and B. Hillebrands, Magnon transistor for all-magnon data processing, *Nat. Commun.* **5**, 4700 (2014).
- [7] A. V. Chumak, V. I. Vasyuchka, A. A. Serga, and B. Hillebrands, Magnon spintronics, *Nat. Phys.* **11**, 453 (2015).
- [8] S. Dutta, S.-C. Chang, N. Kani, D. E. Nikonov, S. Maniaturuni, I. A. Young, and A. Naeemi, Non-volatile clocked spin wave interconnect for beyond-CMOS nanomagnet pipelines, *Sci. Rep.* **5**, 9861 (2015).
- [9] A. Khitun, Parallel database search and prime factorization with magnonic holographic memory devices, *J. Appl. Phys.* **118**, 243905 (2015).
- [10] K. Ganzhorn, S. Klingler, T. Wimmer, S. Geprägs, R. Gross, H. Huebl, and S. T. B. Goennenwein, Magnon-based logic in a multi-terminal YIG/Pt nanostructure, *Appl. Phys. Lett.* **109**, 022405 (2016).
- [11] A. V. Sadovnikov, S. A. Odintsov, E. N. Beginin, S. E. Sheshukova, Yu. P. Sharaevskii, and S. A. Nikitov, Toward nonlinear magnonics: Intensity-dependent spin-wave switching in insulating side-coupled magnetic stripes, *Phys. Rev. B* **96**, 144428 (2017).
- [12] Q. Wang, P. Pirro, R. Verba, A. Slavin, B. Hillebrands, and A. V. Chumak, Reconfigurable nanoscale spin-wave directional coupler, *Sci. Adv.* **4**, e1701517 (2018).
- [13] T. Schneider, A. A. Serga, B. Leven, B. Hillebrands, R. L. Stamps, and M. P. Kostylev, Realization of spin-wave logic gates, *Appl. Phys. Lett.* **92**, 022505 (2008).
- [14] B. Lenk, H. Ulrichs, F. Garbs, and M. Münzenberg, The building blocks of magnonics, *Phys. Rep.* **507**, 107 (2011).
- [15] Q. Wang, R. Verba, T. Brächer, P. Pirro, and A. V. Chumak, “Integrated magnonic half-adder,” arXiv:1902.02855 [physics.app-ph].
- [16] S. Klingler, P. Pirro, T. Brächer, B. Leven, B. Hillebrands, and A. V. Chumak, Spin-wave logic devices based on isotropic forward volume magnetostatic waves, *Appl. Phys. Lett.* **106**, 212406 (2015).
- [17] M. Balynsky, A. Kozhevnikov, Y. Khivintsev, T. Bhowmick, D. Gutierrez, H. Chiang, G. Dudko, Y. Filimonov, G. Liu, C. Jiang, A. A. Balandin, R. Lake, and A. Khitun, Magnonic interferometric switch for multi-valued logic circuits, *J. Appl. Phys.* **121**, 024504 (2017).
- [18] B. Rana and Y. Otani, Voltage-Controlled Reconfigurable Spin-Wave Nanochannels and Logic Devices, *Phys. Rev. Appl.* **9**, 014033 (2018).
- [19] V. S. L’vov, *Wave Turbulence under Parametric Excitation* (Springer-Verlag, New York, 1994).
- [20] A. G. Gurevich, and G. A. Melkov, *Magnetization Oscillations and Waves* (CRC Press, New York, 1996), p. 464.
- [21] T. Brächer, P. Pirro, and B. Hillebrands, Parallel pumping for magnon spintronics: Amplification and manipulation of magnon spin currents on the micron-scale, *Phys. Rep.* **699**, 1 (2017).
- [22] R. Verba, M. Carpentieri, G. Finocchio, V. Tiberkevich, and A. Slavin, in *Spin Wave Confinement: Propagating Waves (2nd Edition)*, edited by S. O. Demokritov (Singapore, Pan Stanford Publishing Pte. Ltd., 2017), p. 385.

- [23] G. A. Melkov, A. A. Serga, V. S. Tiberkevich, Yu. V. Kobljanskij, and A. N. Slavin, Nonadiabatic interaction of a propagating wave packet with localized parametric pumping, *Phys. Rev. E* **63**, 066607 (2001).
- [24] A. A. Serga, S. O. Demokritov, B. Hillebrands, Seong-Gi Min, and A. N. Slavin, Phase control of nonadiabatic parametric amplification of spin wave packets, *J. Appl. Phys.* **93**, 8585 (2003).
- [25] T. Brächer, F. Heussner, P. Pirro, T. Meyer, T. Fischer, M. Geilen, B. Heinz, B. Lägel, A. A. Serga, and B. Hillebrands, Phase-to-intensity conversion of magnonic spin currents and application to the design of a majority gate, *Sci. Rep.* **6**, 38235 (2016).
- [26] M. Weisheit, S. Fähler, A. Marty, Y. Souche, C. Poinsignon, and D. Givord, Electric field-induced modification of magnetism in thin-film ferromagnets, *Science* **315**, 349 (2007).
- [27] C.-G. Duan, J. P. Velev, R. F. Sabirianov, Z. Zhu, J. Chu, S. S. Jaswal, and E. Y. Tsybal, Surface Magnetoelectric Effect in Ferromagnetic Metal Films, *Phys. Rev. Lett.* **101**, 137201 (2008).
- [28] J. Zhu, J. A. Katine, G. E. Rowlands, Y.-J. Chen, Z. Duan, J. G. Alzate, P. Upadhyaya, J. Langer, P. K. Amiri, K. L. Wang, and I. N. Krivorotov, Voltage-Induced Ferromagnetic Resonance in Magnetic Tunnel Junctions, *Phys. Rev. Lett.* **108**, 197203 (2012).
- [29] Y.-J. Chen, H. K. Lee, R. Verba, J. A. Katine, I. Barsukov, V. Tiberkevich, J. Q. Xiao, A. N. Slavin, and I. N. Krivorotov, Parametric resonance of magnetization excited by electric field, *Nano Lett.* **17**, 572 (2017).
- [30] R. Verba, M. Carpentieri, G. Finocchio, V. Tiberkevich, and A. Slavin, Excitation of Spin Waves in an In-Plane-Magnetized Ferromagnetic Nanowire Using Voltage-Controlled Magnetic Anisotropy, *Phys. Rev. Appl.* **7**, 064023 (2017).
- [31] R. Verba, M. Carpentieri, G. Finocchio, V. Tiberkevich, and A. Slavin, Amplification and stabilization of large-amplitude propagating spin waves by parametric pumping, *Appl. Phys. Lett.* **112**, 042402 (2018).
- [32] N. Bloembergen, *Nonlinear Optics* (W.A. Benjamin Inc., New York, 1965).
- [33] R. Verba, V. Tiberkevich, and A. Slavin, Influence of interfacial Dzyaloshinskii-Moriya interaction on the parametric amplification of spin waves, *Appl. Phys. Lett.* **107**, 112402 (2015).
- [34] L. Lopez-Diaz, D. Aurelio, L. Torres, E. Martinez, M. A. Hernandez-Lopez, J. Gomez, O. Alejos, M. Carpentieri, G. Finocchio, and G. Consolo, Micromagnetic simulations using graphics processing units, *J. Phys. D: Appl. Phys.* **45**, 323001 (2012).
- [35] V. Puliafito, A. Giordano, A. Laudani, F. Garesci, M. Carpentieri, B. Azzerboni, and G. Finocchio, Scalable synchronization of spin-hall oscillators in out-of-plane field, *Appl. Phys. Lett.* **109**, 202402 (2016).
- [36] T. Maruyama, Y. Shiota, T. Nozaki, K. Ohta, N. Toda, M. Mizuguchi, A. A. Tulapurkar, T. Shinjo, M. Shiraishi, S. Mizukami, Y. Ando, and Y. Suzuki, Large voltage-induced magnetic anisotropy change in a few atomic layers of iron, *Nature Nano.* **4**, 158 (2009).

3.3. Вплив взаємодії Дзялошинського-Морія на параметричне підсилення

СПІНОВИХ ХВИЛЬ

APPLIED PHYSICS LETTERS 107, 112402 (2015)



Influence of interfacial Dzyaloshinskii-Moriya interaction on the parametric amplification of spin waves

Roman Verba,^{1,a)} Vasil Tiberkevich,² and Andrei Slavin²

¹*Institute of Magnetism, National Academy of Sciences of Ukraine, Kyiv 03142, Ukraine*

²*Department of Physics, Oakland University, Rochester, Michigan 48309, USA*

(Received 17 August 2015; accepted 3 September 2015; published online 14 September 2015)

The influence of the interfacial Dzyaloshinskii-Moriya interaction (IDMI) on the parametric amplification of spin waves propagating in ultrathin ferromagnetic film is considered theoretically. It is shown that the IDMI changes the relation between the group velocities of the signal and idler spin waves in a parametric amplifier, which may result in the complete vanishing of the reversed idler wave. In the optimized case, the idler spin wave does not propagate from the pumping region at all, which increases the efficiency of the amplification of the signal wave and suppresses the spurious impact of the idler waves on neighboring spin-wave processing devices. © 2015 AIP Publishing LLC.

[<http://dx.doi.org/10.1063/1.4931089>]

Signal processing at microwave frequencies using spin waves (SWs) propagating in ferromagnetic films and layered structures attracts a significant interest of researchers during the several last decades.^{1,2} With the rapid current progress in spintronics of magnetic nanostructures, it became necessary to replace the well-developed macroscopic microwave devices based on yttrium iron garnet (YIG) films with the SW devices of submicron and/or nanoscale sizes based on metallic multilayers. When the size of a SW device is reduced to nanoscale, this device starts to experience a strong influence of surface effects,^{3,4} which were negligible for macroscopic systems. These effects can change the properties of the signal processing devices qualitatively and can open a route for the development of a qualitatively new SW processing techniques.

One of such phenomena of a significant current research interest is the interface antisymmetric exchange interaction, which is commonly called the interfacial Dzyaloshinskii-Moriya interaction (IDMI).^{5,6} The IDMI is the most pronounced at an interface between a ferromagnetic material and a heavy metal having a large spin-orbital coupling (e.g., Fe-W,⁷ Mn-W,⁸ and Co-Pt⁹ interfaces). It has been shown recently that the IDMI could stabilize a nontrivial chiral static magnetic structure in ultrathin ferromagnetic films,^{10,11} or could result in a substantial nonreciprocity of the spectrum of SWs propagating in a magnetic film.^{7,12–14}

In our current work, we consider the influence of the IDMI on the SW dynamics under microwave parametric pumping, in particular, in the context of its influence on the process of parametric amplification of a SW propagating in a thin ferromagnetic film. Commonly, the pumping in a microwave parametric amplifier^{15–18} is created by an external microwave signal having frequency that is approximately twice larger than the frequency of the amplified SW. In such a case, the parametric amplification process can be classified as a first-order parametric process (see, e.g., Ref. 1). As will be shown below, the use of a bilayer consisting of an

ultrathin ferromagnetic film and an adjacent layer of a heavy metal and having a sufficiently strong IDMI instead of a single ferromagnetic film could drastically improve the characteristics of a parametric amplifier of SWs.

The sketch of the considered parametric amplifier, where SWs propagate in the ferromagnetic-heavy metal bilayer, is shown in Fig. 1. The ferromagnetic film is magnetized in-plane by a bias magnetic field directed perpendicularly to the direction of the SW propagation (so called “Damon-Eshbach” geometry¹). In this case, the effect of the IDMI on the SW dispersion relation is maximum.^{13,14} The parametric pumping of the microwave frequency ω_p is localized within the region of the length L along the SW propagation path. The microwave magnetic field of the pumping is parallel to the static magnetization (so called “parallel pumping” configuration¹). The pumping could be created, e.g., by a microwave current in an adjacent transmission line. Alternatively, the pumping could be created by an oscillating magnetic anisotropy driven by an external microwave electric field via the effect of the voltage-controlled magnetic anisotropy^{19,20} or via the stress-mediated magnetoelectric effect.^{21,22} These magnetoelectric methods of pumping could be especially more efficient at the nanoscale.

The SW dispersion relation in the considered geometry and in presence of IDMI can be written as¹⁴

$$\omega_k = \sqrt{\omega_H + \omega_M(\lambda_{ex}^2 k^2 + f(kh))} \times \sqrt{\omega_H + \omega_M(\lambda_{ex}^2 k^2 + 1 - f(kh))} + D^* k, \quad (1)$$

where $k \equiv k_y$ is the SW wave number, $\omega_H = \gamma B_e$, $\omega_M = \gamma \mu_0 M_s$, $f(x) = 1 - (1 - e^{-|x|})/|x|$, B_e is the external bias magnetic field, M_s , λ_{ex} , and h are the saturation magnetization, exchange length, and thickness of the ferromagnetic film. The impact of the IDMI is accounted for by the last term, where $D^* = 2Db/(\mu_0 M_s^2 h)$, D is the modulus of the Dzyaloshinskii-Moriya vector,^{5,6} and b is the thickness of the interface atomic layer of the ferromagnetic film. In the above equation, we assume a uniform SW profile along the x -direction and a large width w_x of the ferromagnetic film

^{a)}Author to whom correspondence should be addressed. Electronic mail: verrv@ukr.net

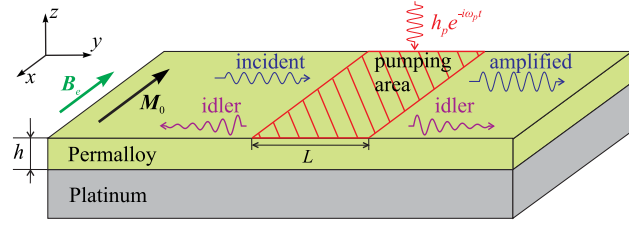


FIG. 1. A layout of the parametric amplifier. The parametric interaction of the incident SW, propagating in a ferromagnetic (permalloy) film, with the pumping of the frequency ω_p leads to its amplification and the appearance of two, in general, idler SWs propagating away from the pumping region.

compared to its thickness, $w_x \gg h$. We note that these restrictions are not critically important and will not change the results qualitatively.

From Eq. (1), it is clear that the SW spectrum of a magnetic film in the presence of IDMI is nonreciprocal, $\omega_k \neq \omega_{-k}$. If the IDMI is sufficiently strong, then the minimum of the SW spectrum is located at a nonzero wave number $k_{min} \neq 0$ and is monotonic for the positive k , while being non-monotonic for negative values of k (or vice-versa). The sufficient condition for the appearance of the spectrum minimum at $k_{min} \neq 0$ is

$$D^* > \frac{h}{4} \sqrt{\frac{\omega_H + \omega_M}{\omega_H}}, \quad (2)$$

which also becomes a necessary condition if the ferromagnetic film is ultrathin, having the thickness $h < 4\lambda_{ex} \sqrt{\omega_H/\omega_M}$.

An example of an SW spectrum having minimum at $k_{min} \neq 0$ calculated for a permalloy film of the thickness 0.7 nm deposited on a platinum substrate is shown in Fig. 2. The parameters for this calculation ($\mu_0 M_s = 1$ T, $B_e = 0.2$ T, $\lambda_{ex} = 4$ nm, $D = 3$ mJ/m², $b = 0.248$ nm, and damping constant $\alpha_G = 0.01$) were taken from Refs. 14 and 23. We use

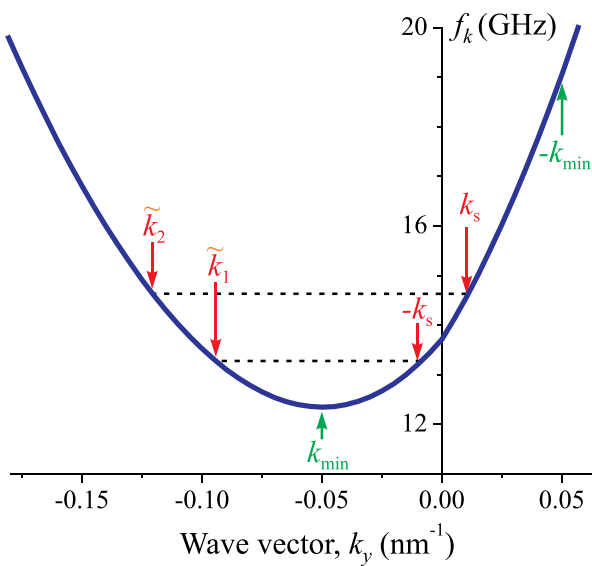


FIG. 2. SW spectrum of a permalloy film on a platinum substrate. Red arrows show the position of the main idler SW at $-k_s$ and 2 non-adiabatic idler SWs at \tilde{k}_1, \tilde{k}_2 for the signal SW situated at $k_s = 0.01$ nm⁻¹. Green arrows show the minimum of the SW spectrum $k_{min} = -0.05$ nm⁻¹ and the corresponding optimum position of the signal SW at $-k_{min} = 0.05$ nm⁻¹.

these parameters for all the numerical calculations described below, but all the qualitative features of the presented results are applicable to other materials while the condition Eq. (2) is satisfied.

We consider the evolution of a spectrally narrow SW packet having the central frequency ω_s , wave vector $k_s > 0$, and describe it by the amplitude $a_s(y)$. Naturally, in the absence of the parametric pumping the amplitude decreases in the propagation direction as $a_s(y) = a_s(0) \exp[-\Gamma_s y/v_s]$, where Γ_s and $v_s = \partial\omega_k/\partial k$ are the damping rate and the group velocity of the signal SW, respectively. The parametric pumping leads to the coupling of the signal SW with other SWs. If the pumping region is sufficiently large (see condition below) and the pumping field is almost uniform within this region, due to the momentum conservation law the signal SW is efficiently coupled with only one idler SW having the wave vector $-k_s$.^{1,24}

Due to the IDMI-induced SW non-reciprocity, the frequencies of the signal and idler SWs are different, $\omega_{k_s} \neq \omega_{-k_s}$, and the parametric interaction is the most efficient (resonant) if the pumping frequency $\omega_p = \omega_{k_s} + \omega_{-k_s}$. Also, as one can see from Fig. 2, in a large range of the wave vectors of the signal SW, $k_s \in [0, -k_{min}]$, the group velocities of both the signal and the idler SWs have the same sign, $v_s v_i > 0$. This means that the both SWs propagate in the same direction, and the reversed idler SW almost vanishes. Both these features are very desirable for practical applications, since the appearance of a reversed idler SW at the signal frequency ($\omega_i = \omega_s$) could lead to an instability of the whole SW signal processing device. Moreover, if the wave vector of the signal SW is opposite to the wave vector position of the spectrum minimum, $k_s = -k_{min}$, the group velocity of the idler SW vanishes, and this idler wave becomes *evanescent* outside the pumping region (see Fig. 4). It is clear, that this is the best situation for the effective use of the SW parametric amplifier.

For the quantitative description of the amplification rate and profiles of the interacting SWs, we use a well-known system of Bloembergen equations, which describes the temporal and spatial evolution of the signal (a_s) and idler (a_i) SWs under the parametric pumping $h_p(y)$ ¹⁶

$$\begin{aligned} \frac{\partial a_s}{\partial t} + v_s \frac{\partial a_s}{\partial y} + \Gamma_s a_s - i \frac{\sigma_s}{2} \frac{\partial^2 a_s}{\partial y^2} &= V_k h_p a_i^*, \\ \frac{\partial a_i^*}{\partial t} + v_i \frac{\partial a_i^*}{\partial y} + \Gamma_i a_i^* + i \frac{\sigma_i}{2} \frac{\partial^2 a_i^*}{\partial y^2} &= V_k^* h_p^* a_s. \end{aligned} \quad (3)$$

This system was derived for the case of parametric resonance ($\omega_p = \omega_{k_s} + \omega_{k_s}$). For the proper description in the case of a vanishing group velocity of the idler SW, $v_i \rightarrow 0$, we have to take into account the dispersion of the group velocity for the idler SW $\sigma_i \equiv \partial^2 \omega_k / \partial k^2|_{k_i}$ (note that for the signal SW this is not important, and, therefore, for the signal wave we set $\sigma_s = 0$ below). Also, for simplicity, we use identical damping rates for the signal and idler SWs, $\Gamma_s = \Gamma_i = \Gamma = \alpha_G \omega_s$. The coefficient V_k describes the efficiency of the parametric interaction of the SWs with the pumping. In the case when the pumping is created by an external magnetic field or by an effective variable anisotropy field parallel to the static

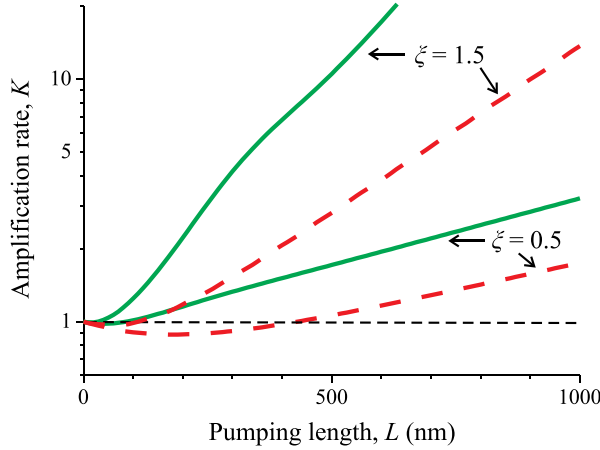


FIG. 3. Amplification rate of the signal SW as a function of the length L of a pumping region at different supercriticalities ξ (different pumping amplitudes). Red dashed lines correspond to the wave vector of the signal SW $k_s = 0.01 \text{ nm}^{-1}$, while green solid lines—to the optimum case $k_s = -k_{min} = 0.05 \text{ nm}^{-1}$ (see Fig. 2).

magnetization, $\mathbf{h}_p = h_p e^{-i\omega_p t} \mathbf{e}_x$, this coupling coefficient is equal to

$$V_k = \frac{\gamma\mu_0\omega_M}{4} \frac{1 - 2f(kh)}{\omega_k - kD^*}. \quad (4)$$

If the pumping is created by the microwave variation of the perpendicular anisotropy (e.g., if the voltage-controlled magnetic anisotropy effect is used²⁰), the efficiency is equal to

$$V_k = \frac{\gamma\mu_0}{4} \frac{\omega_H + \omega_M (\lambda_{ex}^2 k^2 + f(kh))}{\omega_k - kD^*}. \quad (5)$$

The calculated amplification rate $K = a_s(L)/a_s(0)$ in a stationary regime ($\partial a_{s,i}/\partial t = 0$ in Eq. (3)) is shown in Fig. 3. The pumping intensity is characterized by the supercriticality $\xi = [V_k h_p / \Gamma - 1]$.

The value $\xi = 0$ corresponds to the damping compensation for an infinitely extended pumping $L \rightarrow \infty$. For the parameters of our calculation, this is achieved for the pumping field $h_p \sim 100 - 150 \text{ Oe}$ depending on the value of the signal wave number k_s . For a finite L , the threshold value of ξ required to compensate the damping of the signal SW increases with the reduction of the length L of the pumping region. The amplification rate is, naturally, proportional to ξ and depends inversely on the group velocity v_i of the idler SW, since the smaller values of the v_i correspond to the lower radiation losses for the idler SW. The highest amplification rate at a given pumping amplitude could be achieved for the case when $v_i = 0$, i.e., when the idler SW is not propagating at all (see Fig. 3).

It should be noted that for a finite pumping length L and any finite pumping amplitude, the amplification rate K remains finite if the group velocities of the signal and idler SWs satisfy the condition $v_s v_i > 0$. In this case, the SW parametric instability could develop in space, but not in time.^{25,26} The analysis of Eq. (3) shows that in the case $v_i = 0$, the amplification rate is also always finite. Thus, the excitation of

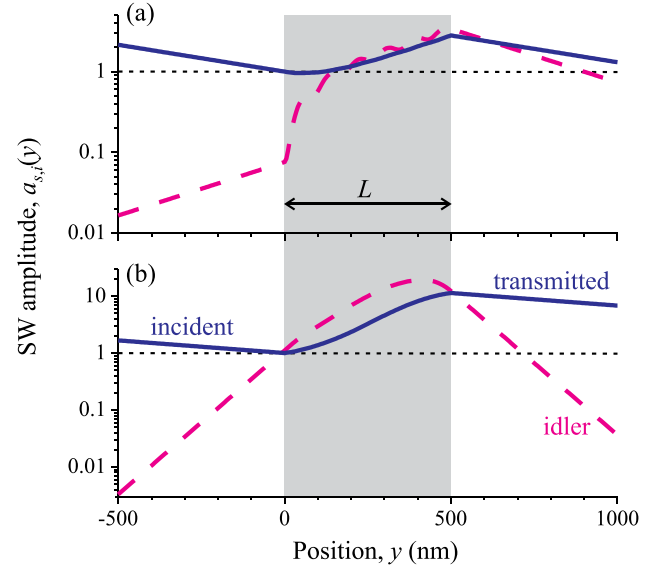


FIG. 4. Profiles of the signal (solid lines) and idler (dashed lines) SWs for the wave number of the signal SW $k_s = 0.01 \text{ nm}^{-1}$ (a), and for the optimum case $k_s = -k_{min} = 0.05 \text{ nm}^{-1}$ (b). Gray shaded area shows the pumping region, and the pumping supercriticality was $\xi = 1.5$.

SWs from the thermal level by the parametric pumping is impossible (it requires $K \rightarrow \infty$ at some ξ). This is an important feature, because one can apply practically any pumping needed for the signal wave amplification without creating a problem of a spurious generation of an idler wave at the same frequency. In particular, one can easily amplify a SW, which does not exactly satisfy the condition of the parametric resonance, i.e., when $\Delta\omega = \omega_p - (\omega_{k_s} + \omega_{-k_s}) \neq 0$. Naturally, the pumping amplitude required for the SW amplification in this case will be higher than in the resonance case.¹⁶

The corresponding profiles of the signal and idler SWs in the parametric amplifier are shown in Fig. 4. It is interesting to note that the localization length of the idler SW outside the pumping area, corresponding to the e times decrease of its amplitude a_i , is the same for both positive ($y > L$) and negative ($y < 0$) directions, and is given by $l_i = \sigma_i / \text{Im} \sqrt{v_i^2 - 2i\sigma_i\Gamma}$. When the group velocity of the idler SW is not small, $v_i \gg \sigma_i\Gamma$, the localization length of the idler wave is equal to $l_i = v_i/\Gamma$, but the amplitude of the reversed idler SW (for $y < 0$) is very small compared to both the amplitude the co-propagating idler SW (for $y > L$) and the magnitude of the incident signal SWs. Thus, the calculation shows that the amplitude of the reversed idler SW is practically vanishing, as it was pointed out earlier. In contrast, if $v_i \rightarrow 0$, the amplitude of the idler SW is similar at the both boundaries of the pumping region, and could be even larger than the signal amplitude a_s . However, the localization length of the idler wave becomes significantly smaller and is determined by the dispersion of the group velocity of the idler SW: $l_i \approx \sqrt{\sigma_i/\Gamma}$. For the parameters of our calculations, it is only about 80 nm, which is rather small compared to the mean free path of signal SW, which is of the order of 1 micron.

Now, we consider the limits of applicability of the presented results. Everywhere above, we used the adiabatic

approximation in the description of the parametric interaction, assuming that only the SWs with the wave vector k_s and $-k_s$ are coupled parametrically. In a general case, the resonant parametric pumping leads, also, to the coupling with the other 2 SWs having frequencies ω_{k_s} , ω_{-k_s} and wave vectors \tilde{k}_1 , \tilde{k}_2 (see Fig. 2). Note that these SWs have negative group velocities, i.e., they are counter-propagating compared to the signal SW. Thus, they may lead to the formation of a non-vanishing reversed idler SW, in particular, having the frequency that is equal to the frequency of the signal wave, which is undesirable. The wave vectors of these idler SWs could be estimated as $\tilde{k}_{1,2} \approx 2k_{min} \pm k_s$. The interaction efficiency with these idler SWs is given by $V_k \tilde{h}_{k_s + \tilde{k}_1}$ and $V_k \tilde{h}_{-k_s + \tilde{k}_2}$, respectively.²⁷ Here, \tilde{h}_k is the Fourier-image of the pumping profile, which, in our case, is equal to $\tilde{h}_k = h_p \text{sinc}[kL/2]$.

One can see that the interaction efficiency with idler SW at \tilde{k}_1 increases when the wave vector of the signal SW approaches its optimal value $k_s \rightarrow -k_{min}$. However, simultaneously, the group velocity of this idler SW decreases to zero, in particular, for $k_s = -k_{min}$, this SW simply coincides with the “main” idler SW at $-k_s$. Consequently, the idler SW having the wave vector \tilde{k}_1 could only weakly increase the total amplitude of the reversed SW.

The maximum possible interaction efficiency with the second idler SW at \tilde{k}_2 , which always has a non-vanishing group velocity, is equal to $\tilde{h}_{2k_{min}}$. For our case, it is ten times smaller than the interaction efficiency with the “main” idler SW as long as $L > 55$ nm. So, one could neglect this SW for almost all the practically achievable pumping length L .

In conclusion, we have shown that the IDMI-induced shift of the SW spectrum could qualitatively change the relation between the signal and idler SWs in a parametric amplifier, so that they become co-propagating. Consequently, the parametric amplification of the signal SW creates only a weak reversed idler SW, which cannot significantly affect the source of the signal SW or the other previous SW processing elements. Moreover, if the signal SW has a proper wave vector $k_s \approx -k_{min}$, the idler SW becomes completely non-propagating and is dissipated at the length of the order of 100–200 nm from the pumping region. Also, as long as the pumping is adiabatic ($L \gtrsim 100$ –200 nm), the parametric excitation of SWs from the thermal level is impossible, which prevents the noise generation in the parametric amplifier. All these features make ferromagnetic films with IDMI attractive for applications in the SW-based microwave signal processing devices at nanoscale.

We acknowledge the Center for NanoFerroic Devices (CNFD) and the Nanoelectronics Research Initiative (NRI) for the partial support of this work. The work was also supported by the National Science Foundation of the USA (Grant Nos. ECCS-1305586 and DMR-1015175), by the MTO/MESO Grant No. N66001-11-1-4114 from DARPA, and by contracts from the U.S. Army TARDEC, RDECOM.

- ¹A. G. Gurevich and G. A. Melkov, *Magnetization Oscillations and Waves* (CRC Press, New York, 1996), p. 464.
- ²*Magnonics: From Fundamentals to Applications*, edited by S. O. Demokritov and A. N. Slavin (Springer, Berlin, 2013).
- ³*Advanced Magnetic Nanostructures*, edited by D. J. Sellmyer and R. Skomski (Springer, New York, 2006).
- ⁴*Spin Wave Confinement*, edited by S. O. Demokritov (Pan Stanford Publishing, Singapore, 2009).
- ⁵I. E. Dzialoshinskii, *Sov. Phys. JETP* **5**, 1259 (1957), available at http://www.jetp.ac.ru/files/dzialoshiinsky1957_en.pdf.
- ⁶T. Moriya, *Phys. Rev.* **120**, 91 (1960).
- ⁷L. Udvardi and L. Szunyogh, *Phys. Rev. Lett.* **102**, 207204 (2009).
- ⁸M. Bode, M. Heide, K. von Bergmann, P. Ferriani, S. Heinze, G. Bihlmayer, A. Kubetzka, O. Pietzsch, S. Blügel, and R. Wiesendanger, *Nature* **447**, 190 (2007).
- ⁹K.-S. Ryu, L. Thomas, S.-H. Yang, and S. Parkin, *Nat. Nanotechnol.* **8**, 527 (2013).
- ¹⁰M. Heide, G. Bihlmayer, and S. Blügel, *Phys. Rev. B* **78**, 140403 (2008).
- ¹¹K.-W. Kim, H.-W. Lee, K.-J. Lee, and M. D. Stiles, *Phys. Rev. Lett.* **111**, 216601 (2013).
- ¹²K. Zakeri, Y. Zhang, J. Prokop, T.-H. Chuang, N. Sakr, W. X. Tang, and J. Kirschner, *Phys. Rev. Lett.* **104**, 137203 (2010).
- ¹³J.-H. Moon, S.-M. Seo, K.-J. Lee, K.-W. Kim, J. Ryu, H.-W. Lee, R. D. McMichael, and M. D. Stiles, *Phys. Rev. B* **88**, 184404 (2013).
- ¹⁴M. Kostylev, *J. Appl. Phys.* **115**, 233902 (2014).
- ¹⁵B. Kalinikos, N. Kovshikov, M. Kostylev, and H. Benner, *JETP Lett.* **64**, 171 (1996).
- ¹⁶B. A. Kalinikos and M. P. Kostylev, *IEEE Trans. Magn.* **33**, 3445 (1997).
- ¹⁷P. A. Kolodin, P. Kabos, C. E. Patton, B. A. Kalinikos, N. G. Kovshikov, and M. P. Kostylev, *Phys. Rev. Lett.* **80**, 1976 (1998).
- ¹⁸G. Melkov, A. Serga, V. Tiberkevich, A. Oliynyk, A. Bagada, and A. Slavin, *IEEE Trans. Magn.* **35**, 3157 (1999).
- ¹⁹J. Zhu, J. A. Katine, G. E. Rowlands, Y.-J. Chen, Z. Duan, J. G. Alzate, P. Upadhyaya, J. Langer, P. K. Amiri, K. L. Wang, and I. N. Krivorotov, *Phys. Rev. Lett.* **108**, 197203 (2012).
- ²⁰R. Verba, V. Tiberkevich, I. Krivorotov, and A. Slavin, *Phys. Rev. Appl.* **1**, 044006 (2014).
- ²¹C.-W. Nan, M. I. Bichurin, S. Dong, D. Viehland, and G. Srinivasan, *J. Appl. Phys.* **103**, 031101 (2008).
- ²²S. Cherepov, P. Khalili Amiri, J. G. Alzate, K. Wong, M. Lewis, P. Upadhyaya, J. Nath, M. Bao, A. Bur, T. Wu, G. P. Carman, A. Khitun, and K. L. Wang, *Appl. Phys. Lett.* **104**, 082403 (2014).
- ²³Z. Duan, A. Smith, L. Yang, B. Youngblood, J. Lindner, V. E. Demidov, S. O. Demokritov, and I. N. Krivorotov, *Nat. Commun.* **5**, 5616 (2014).
- ²⁴V. S. L’vov, *Wave Turbulence under Parametric Excitation* (Springer-Verlag, New York, 1994).
- ²⁵N. Bloembergen, *Nonlinear Optics* (Addison-Wesley Publishing Co., 1965).
- ²⁶N. M. Kroll, *J. Appl. Phys.* **36**, 34 (1965).
- ²⁷G. A. Melkov, A. A. Serga, V. S. Tiberkevich, Y. V. Kobljanskij, and A. N. Slavin, *Phys. Rev. E* **63**, 066607 (2001).

РОЗДІЛ 4

ВПЛИВ ДИПОЛЬНОЇ ВЗАЄМОДІЇ, НЕОДНОРІДНОСТІ ВНУТРІШНЬОГО ПОЛЯ ТА СТРУМУ, ТА ВЗАЄМОДІЇ ДЗЯЛОШИНСЬКОГО-МОРІЯ НА СПІН-ХВИЛЬОВУ ДИНАМІКУ У СПІН-ТОРК ОСЦИЛЯТОРАХ

Цей розділ присвячено дослідженню СХ динаміки під дією спінополяризованого чи чистого спінового струму у СТО та СХО, відповідно. Як вже вказувалось у вступі, динаміка СТО та СХО у багатьох випадках добре вивчена. Зокрема, відомо про визначальний вплив коефіцієнту нелінійного зсуву частоти СХ на динаміку — у випадку додатного нелінійного зсуву можливе збудження біжучих СХ, а у випадку від'ємного нелінійного зсуву збуджується нелінійна самокалізована мода (солітон), яку часто називають СХ булетом. Щоправда, збудження булету було відоме у двовимірних СТО та СХО з активною зоною розміром кількисот нанометрів, а при більших розмірах активної зони замість когерентного збудження відбувається підсилення сукупності теплових СХ мод¹.

У нещодавніх експериментах, однак, було виявлено динаміку осциляторів, яка не може бути пояснена в рамках раніше розроблених моделей. Зокрема, у СХО на основі магнітної наносмужки було виявлено стійку одномодову генерацію, незважаючи на від'ємний нелінійний зсув частоти та відносно велику (1.8 мкм) активну зону². Поясненню цього ефекту присвячено підрозділ 4.1, у якому показано визначальну роль розмірності осцилятора та дипольної взаємодії. Відзначимо, що згодом було детально експериментально досліджено перехід від квазіодновимірного СХО до двовимірного³, і ці експерименти повністю підтверджують теоретичні висновки, зроблені в даній роботі.

У підрозділі 4.2 досліджено вплив неоднорідності густини струму накачки на динаміку СХО. Експерименти, зроблені колегами в Університеті Каліфорнії в Ірвайні, показали цікаві і практично корисні особливості таких СХО на прикладі СХО на основі наносмужки змінного перерізу, і ці результати пояснюються у

1 V. E. Demidov, S. Urazhdin, E. R. J. Edwards, M. D. Stiles, R. D. McMichael, and S. O. Demokritov, Control of magnetic fluctuations by spin current, *Phys. Rev. Lett.* **107**, 107204 (2011).

2 Z. Duan, A. Smith, L. Yang, B. Youngblood, et al., Nanowire spin torque oscillator driven by spin-orbit torques, *Nature Commun.* **5**, 5616 (2014).

3 A. Smith, K. Sobotkiewicz, A. Khan, E. A. Montoya, et al. Dimensional crossover in spin Hall oscillators, *Phys. Rev. B* **102**, 054422 (2020).

підрозділі 4.2. Також відзначимо, що тут проводиться порівняння інтегральних характеристик СХО (частоти генерації, ширини лінії, тощо), які досліджувались експериментально, однак згодом були проведені безпосередні дослідження просторової динаміки намагніченості у схожій системі за допомогою розсіяння світла Бріллюена⁴, які додатково підтверджують зроблені висновки.

У підрозділі 4.3 представлено дослідження динаміки СТО за наявності неоднорідного профілю внутрішнього магнітного поля (потенціальної ями), мотивацією для яких стала робота С. Бонетті та співавторів⁵, у якій описано появу СХ моди нетипового профілю у СТО. Насамкінець, у підрозділах 4.4-4.5 досліджено СХ у СХО за наявності ІВДМ, яка, як згадано у вступі, присутня завжди у СХО через присутність інтерфейсу важкий метал -ферромагнетик і може бути суттєвою при зменшенні товщини ферромагнетику.

Автором дисертації були проведені числові моделювання динаміки намагніченості на основі вкорочених рівнянь (підрозділи 4.1-4.3), розрахунки порогів збудження СХ булету та лінійно локалізованої СХ моди (підрозділ 4.3), розроблено аналітичну модель одновимірного СХО за наявності ІВДМ та якісно пояснені особливості СХ динаміки, спостережені у мікромагнітному моделюванні, у тому числі червоний зсув частоти генерації та природу появи спіральних СХ (підрозділ 4.4). Також, із використанням наближеного загального розв'язку рівняння на власні значення для СХ у двовимірному СХО з ІВДМ, отриманого співавторами — А. Джіордано та Р. Зівієрі, автором запропонований метод наближеного розрахунку частоти та порогів збудження СХ та зроблені відповідні аналітичні розрахунки (підрозділ 4.5).

4 K. Wagner, A. Smith, T. Hache, J.-R. Chen, et al., Injection locking of multiple auto-oscillation modes in a tapered nanowire spin Hall oscillator, *Sci. Rep.* **8**, 16040 (2018).

5 S. Bonetti, R. Kukreja, Z. Chen, F. Macià, et al., Direct observation and imaging of a spin-wave soliton with p-like symmetry, *Nature Commun.* **6**, 8889 (2015).

4.1. Дипольні солітони у квазіодновимірних спін-Холл осциляторах

Low Temperature Physics/Fizika Nizkikh Temperatur, 2020, v. 46, No. 8, pp. 920–926

Dipole-dominated dissipative magnetic solitons in quasi-one-dimensional spin-torque oscillators

R.V. Verba

Institute of Magnetism NAS of Ukraine and MES of Ukraine, Kyiv 03142, Ukraine

E-mail: verrv@ukr.net

V.S. Tiberkevich and A.N. Slavin

Department of Physics, Oakland University, Rochester, Michigan 48309, USA

Received March 5, 2020, published online June 22, 2020

It is well-known that a spin-transfer torque caused by a dc electric current can excite in a two-dimensional ferromagnetic film exchange-dominated magnetic solitons, often called “spin-wave bullets”, under the condition of a negative nonlinear shift of spin wave frequency. In this work, we demonstrate that in a quasi-one-dimensional (1D) case, e.g., in a nanowire spin-Hall oscillator, it is possible to excite a stable dissipative magnetic soliton, which is dominated by the dipole-dipole interaction. This dissipative magnetic soliton can be described in the framework of a 1D Ginzburg–Landau auto-oscillator model, and has the shape similar to that of the exchange-dominated spin wave bullet, but with a different spatial localization law. The influence of the dipolar interaction makes possible the stabilization of a dissipative soliton in a relatively large (micron-sized) active area of the oscillator, which is in a sharp contrast with the two-dimensional case, where the excitation of a stable spin-wave bullet was observed only in relatively small active areas having typical sizes of the order of 100 nm. The characteristics and possible applications of these dipole-dominated spin wave bullets are discussed.

Keywords: spin-wave bullet, spin-torque oscillator, soliton, dipolar interaction.

1. Introduction

The inherent nonlinearity of magnetization dynamics, which is, mostly, of a topological origin [1], leads to the possibility of formation of a wide variety of static and dynamic magnetic solitons, which can exist in ferromagnetic samples [2,3]. The pioneering theoretical works describing the conditions of formation and classification of magnetic solitons were performed in 1970th [4–7], followed up by the experimental studies of the spin-wave (SW) envelope solitons in continuous ferrite films [8,9]. Recent progress in the nanopatterning, engineering of magnetic interfaces and multilayers allows for the experimental observation of many kinds of static magnetic solitons, for instance, vortices [10,11], skyrmions [12–15], magnetic bobbles [16], spin meron pairs [17].

An important turning point in the investigations of dynamic magnetic solitons was the discovery of the spin-transfer torque (STT) effect [18,19]. By means of the STT it becomes possible, under certain conditions, to completely compensate magnetic damping [20], and, thus, to realize experimentally highly nonlinear cases of the magnetization

dynamics described theoretically in [2,21]. First, it was theoretically predicted [22] and, then, experimentally confirmed [23] that in the case of an in-plane magnetized two-dimensional (2D) ferromagnetic film a local application of STT can lead to the excitation of a particular type of a dynamic magnetic soliton, called a “spin wave bullet”. Later, the excitation by means of STT of the other types of magnetic solitons, such as multibullets [24], droplets [25–27] and dynamic skyrmions [28] was also demonstrated.

The excitation of the SW bullets was extensively studied in the two-dimensional case, when a ferromagnet forming a free layer of a spin-torque oscillator (STO) or a spin-Hall oscillator (SHO) is an extended film, and the STT acts on it locally. In such cases the local STT action (or local injection of a spin current) is created by the use a point contact [23,29] or a current concentrator [30]. The SW bullets can be excited under the condition of a negative nonlinear shift of the SW frequency, which can be realized, e.g., in the case of an in-plane magnetized isotropic ferromagnetic film. In such a case, the frequency of the magnetization oscillations decreases with the increase of the oscillation amplitude, and, at a certain amplitude, goes below the spect-

rum of the linear SWs. This nonlinear transformation of a large-amplitude SW into an evanescent state constitutes a nonlinear self-localization mechanism leading to the formation of a spatially localized SW bullet. In a 2D case the formation of the SW bullets is dominated by the exchange interaction, and is well described within the purely exchange model [22]. The characteristic size of an SW bullet in such a case is determined by the exchange length of a ferromagnetic medium, and, typically, does not exceed 100–200 nm. If one applies an external STT to a much larger area, the coherent excitation of SW bullets (or any other mode) becomes impossible, and, instead, a sub-threshold “heating” of many different SW modes is observed [31].

In contrast, in a quasi-1D case taking place, e.g., in a nanowire SHO [32], the coherent single-mode generation was observed in the SHO devices having much larger sizes of the SHO active area (area where the STT is applied) exceeding $1\ \mu\text{m}$ [32,33]. Later, we found [34] that in this case the SW mode excited by the STT is also a nonlinear self-localized SW bullet, but its formation is dominantly affected by the dipole-dipole interaction. It should be noted, that the existence of dipole-dominated bullets is not trivial, as in this 1D geometry the Lighthill criterion [35], necessary for the formation of conservative dynamic solitons is not fulfilled. Thus, these dipole-dominated bullets can be classified as purely dissipative magnetic solitons (see, e.g., [2]), that can exist only in an active, externally pumped medium, like an active area of an SHO. In this work we present a detailed numerical study of such dipole-dominated magnetic solitons, and consider the conditions when the dipolar interaction dominates the formation of the SW bullets.

2. Model of 1D spin-torque oscillator

The most common realization of a quasi-1D case is a SHO based on a bilayer nanowire comprising a ferromagnet and a heavy metal, the sketch of which is presented in Fig. 1. If a nanowire is sufficiently narrow, the profile of the excited SW mode is determined by the lateral quantization and nonuniformity of the static magnetic field across the nanowire width, and this width profile remains almost unchanged with the increase of SW amplitude, both for bulk and edge modes of a nanowire [34]. In this case the development

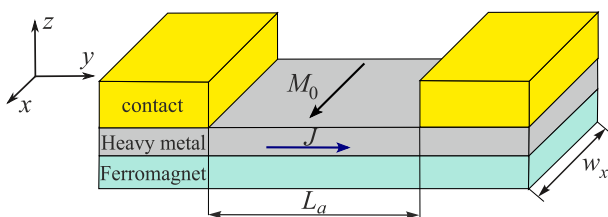


Fig. 1. Sketch of the considered quasi-1D SHO, comprising a ferromagnet–heavy metal nanowire and thick metal contacts, which define the active area between them.

of the magnetization dynamics takes place only along the nanowire length (y coordinate), and is determined by the distribution of bias current density $J(y)$, which exerts STT due to the spin-Hall effect. Below, we assume a rectangular profile of the bias current: $J(y) = J$ within the active region of the length L_a and $J(y) = 0$ outside it. We also assume the static magnetization to be directed along the x direction, that is the most efficient geometry for the SW excitation by the spin-Hall effect. Notes on the influence of the static magnetization direction on the magnetization dynamics will be given below.

The magnetization dynamics in this SHO is studied in the framework of a nonlinear Ginzburg–Landau equation which is derived from the corresponding Landau–Lifshitz equation accounting for linear and first nonlinear ($\sim |b|^3$) terms [22,34]:

$$\frac{\partial b}{\partial t} + (i + \alpha_G) \hat{\Omega} * b + iN |b|^2 b - \sigma J(y) (1 - |b|^2) b = 0. \quad (1)$$

Here $b = b(y, t)$ is the complex amplitude of the dynamic magnetization in the excited spin-wave mode, α_G is the effective damping constant, which could be different from the standard Gilbert constant due to the contribution of the spin pumping into a heavy metal layer and/or large precession ellipticity, the parameter N describes the nonlinear frequency shift [36], and the coefficient σ is the spin-transfer torque or spin-Hall efficiency for a STO or SHO, respectively, exact expressions for which is not important for our current work and can be found elsewhere [28,36].

The frequency operator $\hat{\Omega}$ is given by

$$\hat{\Omega} * b \equiv \omega_0 b - \omega_M \lambda_{\text{ex}}^2 \frac{\partial^2 b}{\partial y^2} + \frac{\omega_M^2}{2\omega_0} \int G_{yy}(y-y') b(y') dy', \quad (2)$$

where $\omega_M = \gamma \mu_0 M_s$, λ_{ex} is the exchange length of the ferromagnet, and ω_0 is the frequency of a spin wave resonance in the linear regime, which is assumed to be constant. A spatial dependence of the ω_0 can be induced, e.g., by the Oersted field of the bias current, and, in the case of a significant nonuniformity of this field, could affect the nature of the excited mode [37]. The last integral term, which was neglected in most of the previous studies, describes the dipole–dipole interaction with G_{yy} being the yy -component of the magnetostatic Green’s function for a nanowire geometry [38]. In several previous works the effect of the dipolar interaction on magnetic solitons was considered within a local approximation (as an effective anisotropy) [6]. Attempts to account long-range nature of dipolar interaction were done in [39,40]; however, the approximation made in these works is valid for small-amplitude solitons, which is not the case of solitons excited by STT. In the particular case presented below, rigorous accounting for the dipolar interaction is of a principal importance.

In the following, we present the results of a numerical solution of Eq. (1). As it is usually done in the SW bullet

simulations [41], we have chosen the initial condition in the form of a large-amplitude Gaussian-shape inhomogeneity. The numerical parameters, used in our simulations, are the following: $\omega_0 = 0.25\omega_M$, $N = -0.1\omega_M$, $\lambda_{\text{ex}} = 5.5$ nm, $\alpha_G = 0.02$, which are in the range of typical parameters of SHOs based on NiFe/Pt nanowires; the nanowire width was $w_x = 200$ nm, which is used in the expression for the Green's function.

3. Results

A typical dependence of the generation frequency on the bias current, which is obtained in the considered case, is shown in Fig. 2a. The generation starts at a certain threshold $J_{\text{th},1}$, which is determined by the size of the active area and the magnetic parameters of a nanowire. The threshold value is always larger than $J_{\text{th},0} = \Gamma_0 / \sigma$ (where $\Gamma_0 = \alpha_G \omega_0$), which corresponds to the damping compensation for linear SW in the case when the STT is applied to the whole sample (see Eq. (1)). At the threshold $J_{\text{th},1}$, the generation is a single-mode regime, with the frequency lying below the linear SW resonance frequency ω_0 . With the increase of the bias current the generation frequency decreases, as it is expected for a negative nonlinear frequency shift. At a certain second threshold value $J_{\text{th},2}$ the generation mode is switched to a different regime. It could be two-mode regime, shown in Fig. 2a, a more complex quasi-periodic regime, or even a generation failure. In this work we are discussing only the first, single-mode generation regime, which is the most important for applications.

The profiles of the excited SW mode are shown in Fig. 2b. At the threshold $J_{\text{th},1}$ the mode has large amplitude and is clearly localized in the vicinity of the active area. Further increase of the bias current leads to the spatial narrowing of the excited mode with simultaneous increase of its amplitude.

All these features of the excited SW mode (the frequency lying below the linear SW resonance, finite mode amplitude at the generation threshold, spatially localized profile)

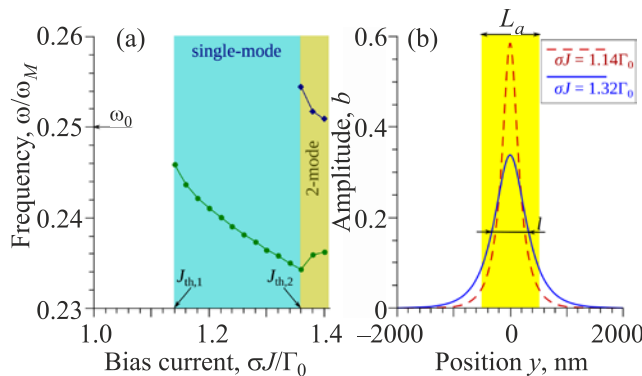


Fig. 2. (Color online) (a) Dependence of the generation frequency of a SHO on the bias current. (b) Profiles of the excited SW mode at the generation threshold $\sigma J_{\text{th},1} = 1.14\Gamma_0$, and at a higher bias current. Calculation parameters: active region length $L_a = 1$ μm , nanowire thickness $h = 5$ nm.

are characteristic for the excitation of self-localized SW soliton (SW bullet mode), and are similar to the corresponding characteristics obtained in the 2D case [22]. The only important difference is the size of the active area, in which we observe the bullet excitation, $L_a = 1$ μm , which is much larger than characteristic sizes of the active area, for which single-bullet mode excitation was reported in the 2D case.

We have systematically studied how the range of bias current, where the single mode generation is realized, evolves with the increase of the active area length L_a (see Fig. 3). First, let us look at the results within the purely exchange approximation, which is achieved by neglecting the integral term in Eq. (2). The excitation threshold of the first bullet mode (lower boundary of the single-mode region) becomes smaller for larger L_a , as one should expect because of a larger in size, and, consequently, smaller in amplitude, bullet can be excited at the threshold. The transition to non-single-mode generation regime also takes place at a smaller bias current in an oscillator with a larger active area, that is a consequence of a smaller exchange energy penalty for the excitation of a second bullet mode, or a more complex nonuniform dynamics. Also, in Fig. 3 we plot the threshold of a linear SW mode excitation, which would have been realized if the nonlinear frequency shift would be zero or positive. In a real experiment, the thermal fluctuations, which are neglected in our simulations, lead to a nonzero thermal level of the linear SWs, and the level of the thermal SWs increases substantially close to the formal threshold of a linear SW mode excitation. This means, that if the thresholds of excitation of

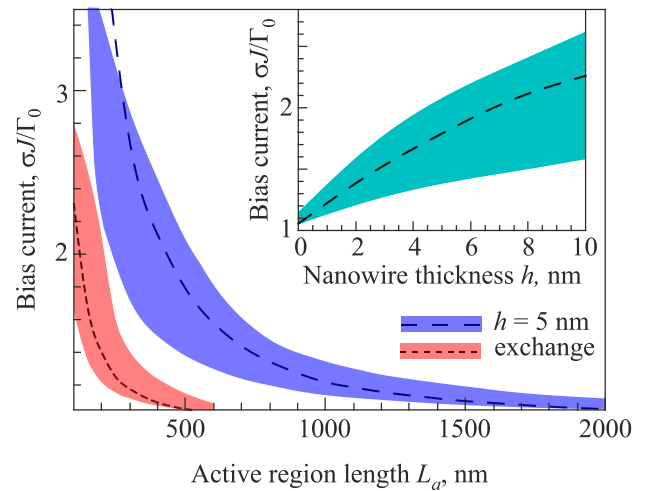


Fig. 3. (Color online) Region of the single-mode generation (shaded area) as a function of the active area length within the purely exchange approximation (red), and within the full dipole-exchange model for the nanowire thickness $h = 5$ nm (blue). Inset shows the region of the single mode generation as a function of the nanowire thickness for the active area length $L_a = 500$ nm. In both panels, dashed lines show the threshold of the linear mode excitation if the nonlinear frequency shift is neglected, $N = 0$.

the bullet and linear SW modes become too close to each other, the thermal noise could break the single-bullet mode generation regime, and a more complex dynamics (e.g., stochastic jumps between different modes, so called “mode hopping” [42]) can be observed. A similar situation takes place if the thresholds of a single-bullet and of a two-bullet mode excitation become close to each other. Single-bullet generation can be observed only if the threshold of its excitation is sufficiently lower than other thresholds. Within the purely exchange approximation this situation takes place if the active area is smaller than 300–400 nm, in full accordance with previous results obtained for the 2D case.

At the same time, if the dipolar interaction is taken into account, all the characteristic thresholds increase substantially (see Fig. 3), and, therefore, the single-bullet mode can be stabilized in a much larger active area, up to $L_a \lesssim 1.5 \mu\text{m}$. By varying the nanowire thickness h we found, that all the thresholds increase with the increase of h (see inset in Fig. 3). This increase of threshold is expected for the excitation of a linear mode, since a larger nanowire thickness corresponds to a larger SW group velocity at low wave numbers. This group velocity is approximately equal to $v_{\text{gr}} \approx h\omega_M^2 / (4\omega_0)$ for the considered geometry. The larger group velocity leads to the larger radiation losses which should be compensated by the STT. It is clear from Fig. 3, that the thickness dependence of the bullet excitation threshold follows the same trend as the threshold for the linear mode, meaning that it is also governed by the group velocity increase.

Summarizing this part, we can state, that: (i) dipolar interaction is crucial for the stabilization of the SW bullet mode in large, micron-sized active area of a SHO, and (ii) the amplitude range of existence of the single-bullet mode, as well as the maximum size of the active area in which generation of this mode can be achieved, are mainly determined by the SW group velocity, and increase with the increase of the group velocity. This fact can be explained by a more effective energy flow from the active area when v_{gr} is increased.

It should be noted, that the appearance of dipole-dominated solitons is not trivial, as they do not satisfy the Light-hill criterium $ND < 0$ [35], where $D = \partial^2\omega / \partial k^2$ is the dispersion of the SW group velocity. For the exchange-dominated spectrum $D = 2\omega_M\lambda_{\text{ex}}^2 > 0$, and the criterium is satisfied. However, for the dipole-exchange SW spectrum the dispersion is negative ($D < 0$) at low k . We also checked the pure dipolar case (setting $\lambda_{\text{ex}} = 0$), for which $D < 0$ in all the range of the SW wave numbers, and the results remain almost the same. Therefore, we can conclude that the dipole-dominated SW bullets are the solitons of a purely dissipative nature and they can exist only in an active medium with a local source of energy pumping, like it happens in the active area of our SHO. In contrast, 1D exchange-dominated SW bullets are not restricted by this limitation. Note, however, that in a conservative 2D case

the SW bullets are unstable in respect to splitting into multiple solitons.

Now we discuss the properties of the dipole-dominated SW bullets. Their spatial profiles are shown in Fig. 2b. We have found, that the profile of an SW bullet in this case is well-described by the same two-parameter function, i.e., $b(y) = B_0 f(y/l)$, where B_0 is the bullet amplitude, and l is its characteristic width. The normalized function $f(\eta)$ is almost the same for the different values of the bias currents and/or different lengths of the active region. Some differences are present at the bullet “tails”, away from the active region. However, a numerical simulation is not a particularly convenient tool to study the small details of the obtained bullet profiles due to the possible numerical errors and the finite size of the simulation area. Rather unexpectedly, the bullet profile is well-described by the function $f(\eta) = 1 / \cosh(2.62\eta)$, which is the exact solution for a 1D magnetic soliton in the purely exchange approximation. Some discrepancy with this analytically obtained profile takes place only at the tails, where the dynamic magnetization is small, $b(y) \ll B_0$. Thus, one can use the function $f(\eta) = 1 / \cosh(2.62\eta)$ for the analytical estimations of the bullet excitation threshold using the method described in Ref. 22, and expect a reasonably good accuracy. A more rigorous description of the spatial profile of a dipole-dominated bullet, especially at the tails, requires a more detailed analytical consideration.

In the exchange approximation, the SW bullet frequency is related to its amplitude by the expression (recall, that $N < 0$):

$$\omega_{\text{bul}} = \omega_0 + NB_0^2 / 2.2. \quad (3)$$

The frequency of dipole-dominated bullets follows the same dependence, as shown in Fig. 4a. This fact is not surprising, because this dependence is equivalent to $\omega_{\text{bul}} = \omega_0 + N \int |b|^3 dy / \int b dy$, which means that the bullet frequency is fully determined by the nonlinear frequency shift.

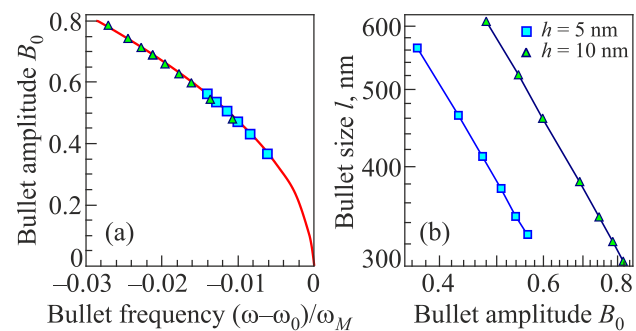


Fig. 4. (a) Dependence of the SW bullet amplitude on the bullet frequency. Points — simulations for $h = 5 \text{ nm}$ and $h = 10 \text{ nm}$, line — Eq. (3). (b) Bullet size l as a function of its amplitude. Lines are the guides for an eye.

A more interesting is the dependence of the bullet width on its amplitude. The bullet width here is defined as the width at half-maximum of its amplitude, as shown in Fig. 2b. In the exchange approximation one gets $l \sim 1/B_0$. From the numerical simulations we found, that the width of dipole-dominated SW bullets also follows the power-law dependence described by $l = C/B_0^\beta$, but the exponent $\beta \neq 1$ (see Fig. 4b and note the log–log scale). For various nanowire thicknesses h and SW resonance frequencies ω_0 we have found that the exponent is in the range $\beta \approx 1.25–1.35$. The coefficient C , naturally, increases with the SW group velocity (i.e. with the increase of the nanowire thickness), meaning that the SW bullets of the same amplitude are wider, if the dipolar interaction is stronger. A more rigorous determination of the localization rules for the dipolar SW bullets requires a detailed analytical model, and lies out of the scope of our current work. Also, note that approximate theory for low-amplitude dipolar solitons yields different exponent $\beta = 2$ [39,40], meaning that typical STT-driven bullets are definitely out of the applicability range of this approximation.

At the end, we would like to discuss the influence of the SHO geometry on the formation of the dipolar SW bullets. As it is shown above, the effect of the dipolar interaction on the SW bullet formation is mostly connected with the dipolar SW group velocity, which significantly depends on the orientation of the nanowire static magnetization in respect to the SW propagation direction. The maximum effect is expected in the case of “Damon–Eshbach” geometry, when the nanowire is magnetized along its width, while the SW propagates along the nanowire length. This case was considered in the above presented calculations.

In the case of a perpendicular magnetization of a nanowire, the formation of dipole-dominated SW bullets is also expected, but it can be realized only for a conventional STO, as the spin-Hall effect does not work in this geometry. The SW group velocity in this case is also positive, $v_{gr} \approx \omega_M h/4$, and for a relatively thick nanowire can be sufficiently large to support the formation of a dipolar SW bullet. In contrast, in the case of a nanowire magnetized along its axis (y direction in Fig. 1), the dipolar SW group velocity becomes negative. Thus, the dipolar interaction does not lead to the additional energy flow from the active area, and, therefore, cannot support large-size SW bullets.

The anisotropy of the SW dispersion in an in-plane magnetized magnetic film explains why in the 2D case only relatively small, exchange-dominated SW bullets were observed. Indeed, for a certain cone of the polar angles ϕ , $[\phi < \phi_0] \cup [(\phi + \pi) < \phi_0]$, where $\phi = 0$ corresponds to the direction parallel to the film static magnetization and ϕ_0 depends on the material parameters and the external bias magnetic field, the SW group velocity is negative. Therefore, in these directions the length of the active area cannot exceed several hundreds of nanometers, as, otherwise, the bullet instability develops in these directions. Since in practi-

cally all the experiments the active area of a STO or a SHO was approximately of a circular shape, only in active areas having the size of the order of hundreds of nanometers the stable single-mode SW generation was observed. Judging from our above presented simulations, we expect that if one designs a 2D SHO with an active area elongated along the direction, perpendicular to the static magnetization, an elliptic-shape 2D SW bullet with a micron-scale size in this direction and 100–200 nm size in the perpendicular direction can be formed and stabilized.

4. Conclusions

In conclusion, we studied theoretically the formation and properties of SW bullets in a quasi-1D STO. It is demonstrated that in the 1D case, the dipolar interaction can play a dominant role in the process of the SW bullet formation. In contrast with the exchange-dominated SW bullets [22], the dipole-dominated bullets are purely dissipative solitons can only exist in an active, externally pumped medium. The dipolar interaction can substantially enlarge the characteristic width of the SW bullet, and can make possible a stable single bullet mode excitation in a STO having a relatively large, micron-scale size of the active area. The stabilizing effect of the dipolar interaction scales with the group velocity of the linear SWs at $k \rightarrow 0$. The higher is the SW group velocity, the larger is the range of the bias currents corresponding to the single-mode generation for a given length of the active area, and the larger is the maximum length of the active area, in which a stable single-mode generation can be achieved. The spatial profiles of the large-size dipole-dominated dissipative SW bullets are very similar to the profiles of the small-size conservative exchange-dominated SW bullets, and they both demonstrate the same dependence of the bullet frequency on its amplitude. At the same time, the localization law for the dipolar SW bullets $l = C/B_0^\beta$ with $\beta \approx 1.25–1.35$ differs from the corresponding law in the exchange-dominated case, where $\beta = 1$. Our results show a way to increase the size of the SHO active area in which a single-mode SW generation can take place, which could be useful in the design of relatively high-power SHO-based generators of microwave signals.

Acknowledgements

This work was supported in part by the NSF of the USA (Grants # EFMA-1641989 and # ECCS-1708982), by the U.S. Air Force Office of Scientific Research under the MURI grant # FA9550-19-1-0307, by the Oakland University Foundation, and by the Ministry of Education and Sciences of Ukraine (project 0118U004007).

1. O. Prokopenko, D. Bozhko, V. Tyberkevych, A. Chumak, V. Vasyuchka, A. Serga, O. Dzyapko, R. Verba, A. Talalaevskij, D. Slobodianiuk, Yu. Kobljanskyj, V. Moiseienko, S. Sholom, and V. Malyshev, *Ukr. J. Phys.* **64**, 888 (2019).

2. A.M. Kosevich, B.A. Ivanov, and A.S. Kovalev, *Nonlinear Magnetization Waves. Dynamic and Topological Solitons*, Naukova dumka, Kyiv (1983).
3. O.R. Sulymenko, O.V. Prokopenko, V.S. Tyberkevych, A.N. Slavin, and A.A. Serga, *Fiz. Nizk. Temp.* **44**, 775 (2018) [*Low Temp. Phys.* **44**, 602 (2018)].
4. B.A. Ivanov and A.M. Kosevich, *Sov. Phys. JETP* **45**, 1050 (1977).
5. A.M. Kosevich, B.A. Ivanov, and A.S. Kovalev, *JETP Lett.* **25**, 486 (1977).
6. B.A. Ivanov, A.M. Kosevich, and I.M. Babich, *JETP Lett.* **29**, 714 (1979).
7. A.M. Kosevich, B.A. Ivanov, and A.S. Kovalev, *Phys. Rep.* **194**, 117 (1990).
8. B.A. Kalinikos, N.G. Kovshikov, and A.N. Slavin, *JETP Lett.* **38**, 413 (1983).
9. B.A. Kalinikos, N.G. Kovshikov, and A.N. Slavin, *Phys. Rev. B* **42**, 8658 (1990).
10. K.Yu. Guslienko, *J. Nanosci. Nanotechnol.* **8**, 2745 (2008).
11. R. Antos, Y. Otani, and J. Shibata, *J. Phys. Soc. Jpn.* **77**, 031004 (2008).
12. *Skyrmions. Topological Structures, Properties, and Applications*, J.P. Liu, Z. Zhang, and G. Zhao (eds.), CRC Press, (2016).
13. G. Finocchio, F. Büttner, R. Tomasello, M. Carpentieri, and M. Kläui, *J. Phys. D* **49**, 423001 (2016).
14. A. Fert, N. Reyren, and V. Cros, *Nat. Rev. Mater.* **2**, 17031 (2017).
15. D. Navas, R.V. Verba, A. Hierro-Rodriguez, S.A. Bunyaev, X. Zhou, A.O. Adeyeye, O.V. Dobrovolskiy, B.A. Ivanov, K.Y. Guslienko, and G.N. Kakazei, *APL Mater.* **7**, 081114 (2019).
16. F. Zheng, F.N. Rybakov, A.B. Borisov, D. Song, S. Wang, Z.-A. Li, H. Du, N.S. Kiselev, J. Caron, A. Kovács, M. Tian, Y. Zhang, S. Blügel, and R.E. Dunin-Borkowski, *Nat. Nanotechnol.* **13**, 451 (2018).
17. S. Wintz, C. Bunce, A. Neudert, M. Körner, T. Strache, M. Buhl, A. Erbe, S. Gemming, J. Raabe, C. Quitmann, and J. Fassbender, *Phys. Rev. Lett.* **110**, 177201 (2013).
18. J.C. Slonczewski, *J. Magn. Magn. Mater.* **159**, L1 (1996).
19. L. Berger, *Phys. Rev. B* **54**, 9353 (1996).
20. S.I. Kiselev, J.C. Sankey, I.N. Krivorotov, N.C. Emley, R.J. Schoelkopf, R.A. Buhrman, and D.C. Ralph, *Nature* **425**, 380 (2003).
21. G. Bertotti, I. Mayergoyz, and C. Serpico, *Nonlinear Magnetization Dynamics in Nanosystems*, Elsevier (2009).
22. A. Slavin and V. Tiberkevich, *Phys. Rev. Lett.* **95**, 237201 (2005).
23. S. Bonetti, V. Tiberkevich, G. Consolo, G. Finocchio, P. Muduli, F. Mancoff, A. Slavin, and J. Åkerman, *Phys. Rev. Lett.* **105**, 217204 (2010).
24. H. Ulrichs, V.E. Demidov, and S.O. Demokritov, *Appl. Phys. Lett.* **104**, 042407 (2014).
25. M.A. Hofer, T.J. Silva, and Mark W. Keller, *Phys. Rev. B* **82**, 054432 (2010).
26. S.M. Mohseni, S.R. Sani, J. Persson, T.N. Anh Nguyen, S. Chung, Ye. Pogoryelov, P.K. Muduli, E. Iacocca, A. Eklund, R.K. Dumas, S. Bonetti, A. Deac, M.A. Hofer, and J. Åkerman, *Science* **339**, 1295 (2013).
27. D.V. Slobodianiuk, O.V. Prokopenko, and G.A. Melkov, *J. Magn. Magn. Mater.* **439**, 144 (2017).
28. A. Giordano, R. Verba, R. Zivieri, A. Laudani, V. Puliafito, G. Gubbiotti, R. Tomasello, G. Siracusano, B. Azzerboni, M. Carpentieri, A. Slavin, and G. Finocchio, *Sci. Rep.* **6**, 36020 (2016).
29. V.E. Demidov, S. Urazhdin, A. Zholud, A.V. Sadovnikov, A.N. Slavin, and S.O. Demokritov, *Sci. Rep.* **5**, 8578 (2015).
30. V.E. Demidov, S. Urazhdin, H. Ulrichs, V. Tiberkevich, A. Slavin, D. Baither, G. Schmitz, and S.O. Demokritov, *Nat. Mater.* **11**, 1028 (2012).
31. V.E. Demidov, S. Urazhdin, E.R.J. Edwards, M.D. Stiles, R.D. McMichael, and S.O. Demokritov, *Phys. Rev. Lett.* **107**, 107204 (2011).
32. Z. Duan, A. Smith, L. Yang, B. Youngblood, J. Lindner, V.E. Demidov, S.O. Demokritov, and I.N. Krivorotov, *Nat. Commun.* **5**, 5616 (2014).
33. K. Wagner, A. Smith, T. Hache, J.-R. Chen, L. Yang, E. Montoya, K. Schultheiss, J. Lindner, J. Fassbender, I. Krivorotov, and H. Schultheiss, *Sci. Rep.* **8**, 16040 (2018).
34. L. Yang, R. Verba, V. Tiberkevich, T. Schneider, A. Smith, Z. Duan, B. Youngblood, K. Lenz, J. Lindner, A.N. Slavin, and I.N. Krivorotov, *Sci. Rep.* **5**, 16942 (2015).
35. M.J. Lighthill, *IMA J. Appl. Math.* **1**, 269 (1965).
36. A. Slavin and V. Tiberkevich, *IEEE Trans. Magn.* **45**, 1875 (2009).
37. R. Verba, *Ukr. J. Phys.* **64**, 947 (2019).
38. K.Y. Guslienko and A.N. Slavin, *J. Magn. Magn. Mater.* **323**, 2418 (2011).
39. A.S. Kovalev, A.M. Kosevich, I.V. Manzhos, and K.V. Maslov, *JETP Lett.* **44**, 222 (1986).
40. A.S. Kovalev, A.M. Kosevich, and I.V. Manzhos, *Sov. Phys. JETP* **67**, 2301 (1988).
41. G. Consolo, B. Azzerboni, G. Gerhart, G.A. Melkov, V. Tiberkevich, and A.N. Slavin, *Phys. Rev. B* **76**, 144410 (2007).
42. G. Consolo, G. Finocchio, G. Siracusano, S. Bonetti, A. Eklund, J. Åkerman, and B. Azzerboni, *J. Appl. Phys.* **114**, 153906 (2013).

Дипольні дисипативні магнітні солітони у квазіодновимірних спін-торк осциляторах

R.V. Verba, V.S. Tiberkevich, A.N. Slavin

Завдяки ефекту спін-трансферу постійний електричний струм, як відомо, може збуджувати у двовимірній феромагнітній плівці обмінні магнітні солітони, які ще називають «спін-хвильовими булетами», за умови від'ємного нелінійного зсуву частоти спінових хвиль. У роботі продемонстровано, що у квазіодновимірному випадку, наприклад, у спін-Холл осциляторі на основі магнітної наносмужки, можливе збу-

дження стійких дисипативних магнітних солітонів, динаміка яких визначається, в першу чергу, магнітодипольною взаємодією. Ці дисипативні магнітні солітони описуються у межах одновимірної моделі автогенератора Гінзбурга–Ландау та мають профіль близький до профілю обмінних солітонів, але виявляють відмінний закон просторової локалізації. Вплив дипольної взаємодії проявляється у можливості стабілізації дисипативного солітона в осциляторі з відносно великою (мікронних розмірів) активною зоною, що сильно відрі-

зняється від двовимірного випадку, у якому утворення спін-хвильових булетів спостерігалось лише у відносно малих активних зонах з типовими розмірами порядку 100 нм. Розглянуто характеристики та можливі застосування таких дипольних спін-хвильових булетів.

Ключові слова: спін-хвильовий булет, спін-торк осцилятор, солітон, магнітодипольна взаємодія.

SCIENTIFIC REPORTS

OPEN

Reduction of phase noise in nanowire spin orbit torque oscillators

Received: 24 August 2015

Accepted: 22 October 2015

Published: 23 November 2015

Liu Yang^{1,*}, Roman Verba^{2,*}, Vasil Tiberkevich³, Tobias Schneider⁴, Andrew Smith¹, Zheng Duan¹, Brian Youngblood¹, Kilian Lenz⁴, Jürgen Lindner⁴, Andrei N. Slavin³ & Ilya N. Krivorotov¹

Spin torque oscillators (STOs) are compact, tunable sources of microwave radiation that serve as a test bed for studies of nonlinear magnetization dynamics at the nanometer length scale. The spin torque in an STO can be created by spin-orbit interaction, but low spectral purity of the microwave signals generated by spin orbit torque oscillators hinders practical applications of these magnetic nanodevices. Here we demonstrate a method for decreasing the phase noise of spin orbit torque oscillators based on Pt/Ni₈₀Fe₂₀ nanowires. We experimentally demonstrate that tapering of the nanowire, which serves as the STO active region, significantly decreases the spectral linewidth of the generated signal. We explain the observed linewidth narrowing in the framework of the Ginzburg-Landau auto-oscillator model. The model reveals that spatial non-uniformity of the spin current density in the tapered nanowire geometry hinders the excitation of higher order spin-wave modes, thus stabilizing the single-mode generation regime. This non-uniformity also generates a restoring force acting on the excited self-oscillatory mode, which reduces thermal fluctuations of the mode spatial position along the wire. Both these effects improve the STO spectral purity.

The discovery of giant spin Hall effect in nonmagnetic heavy metals such as Pt¹⁻³, W⁴ and Ta^{3,5-7} creates new opportunities for the manipulation of magnetization by spin currents, including switching and excitation of self-oscillations of magnetization^{4-6,8-11}. Spin-orbit interaction in such heavy metals results in large spin-dependent deflection of electrons participating in electric charge current¹²⁻¹⁶, which can be viewed as a pure spin current flowing perpendicular to the charge current¹⁷⁻¹⁹. This pure spin current can be injected from the heavy metal into an adjacent ferromagnet and apply spin torque to its magnetization^{20,21}. Due to its non-conservative nature, this spin orbit torque can act as magnetic anti-damping^{22,23} leading to the decrease of the relaxation rates of spin waves (SWs), which was observed in both metallic^{2,24-26} and insulating^{3,27} ferromagnets.

A spin orbit torque uniformly applied to a spatially extended ferromagnetic film cannot reduce the spin wave damping to zero, and therefore, cannot excite self-oscillations of magnetization in the film even at high spin current densities²⁸. The origin of this anti-damping saturation is non-linear spin wave interactions, which distribute the injected energy and angular momentum among a continuum of SWs with different wave vectors, so that the net damping rate for any SW mode remains positive⁸. Patterning of the ferromagnetic film into nanoscale dots discretizes the spin wave spectrum and closes many of the nonlinear SW scattering channels. In such a case, the relaxation rate of the lowest-energy SW mode of the nanodot can reach zero, and self-oscillations of the mode can be excited by the spin current⁹. Another route to excitation of self-oscillations by spin orbit torques is the application of a

¹Department of Physics and Astronomy, University of California, Irvine, CA 92697, USA. ²Institute of Magnetism, National Academy of Sciences of Ukraine, Kyiv 03142, Ukraine. ³Department of Physics, Oakland University, Rochester, MI 48309, USA. ⁴Helmholtz-Zentrum Dresden - Rossendorf, Institute of Ion Beam Physics and Materials Research, Bautzner Landstraße 400, 01328 Dresden, Germany. *These authors contributed equally to this work. Correspondence and requests for materials should be addressed to L.Y. (email: YANGL2@UCI.EDU)

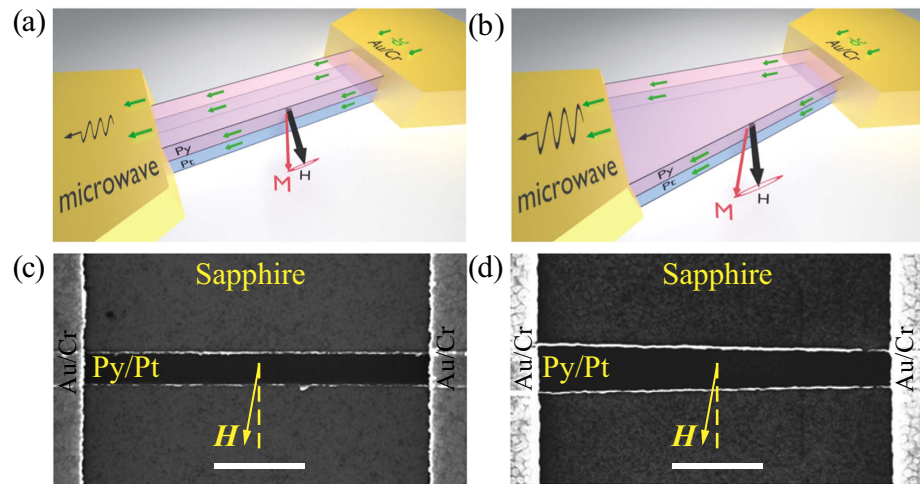


Figure 1. Samples. Schematic of the straight (a) and tapered (b) nanowire STO: applied magnetic field, electric bias current and precessing magnetization are shown by black, green and red arrows, respectively. Scanning electron micrographs (SEM) of the straight (c) and tapered (d) nanowire STO samples. 500 nm white scale bars are shown in each SEM image.

high spin current density to a nanoscale region of an extended ferromagnetic film by using the current concentrators^{8,10,29,30}. In this case a nonlinear self-localized spin wave “bullet” mode can be excited^{10,31,32}. Since the frequency of the bullet mode lies below the SW spectrum, the resonant scattering processes from this mode into a SW continuum are forbidden, which enables the self-sustained excitation of this large-amplitude mode^{8,10,29,30}. The characteristic dimensions of this bullet mode is determined by the exchange length of the ferromagnet, and are typically below 100 nm^{31,33}. Recently, we have shown that the spin orbit torques can excite self-oscillations of magnetization in micrometer-scale ferromagnets, namely in quasi-one-dimensional ferromagnetic nanowires¹¹. The geometric confinement of the spin waves in nanowires suppresses some nonlinear scattering channels such as four-magnon scattering^{34,35}, which turns out to be sufficient for the excitation of sustainable self-oscillations over micrometer-scale regions of the nanowire¹¹. In spite of the large excitation volume and the associated diminished impact of the random thermal torques on the magnetization dynamics, the spectral linewidth of the microwave signal generated by nanowire STOs was found to be comparable to that of nanoscale STOs^{22,36–50}. This result can be attributed to the simultaneous excitation of several SW modes in nanowire auto-oscillators, because it is known that the interactions between the simultaneously excited self-oscillatory modes can substantially increase the linewidths of the generated modes^{51,52}. Therefore, new methods for selective excitation of a single self-oscillatory mode in a nanowire STO are highly desirable for the development of STO devices with high spectral purity. In this paper, we report experiments demonstrating that the single-mode regime of operation and the associated phase noise reduction can be achieved via proper design of the nanowire STO shape. We show that STOs based on tapered nanowires, such as the one shown in Fig. 1(b,d) exhibit reduced phase noise, and a wider bias current range of single mode operation in comparison to the straight nanowire STOs of similar dimensions. We employ numerical simulations to show that the spatial non-uniformity of the spin current density in the tapered nanowire STO is the key factor contributing to the improved phase noise. These simulations also reveal that the spin orbit torques excite a self-localized micrometer-scale bullet mode if nanowire SW modes exhibit negative nonlinear frequency shift. In the tapered nanowire devices, the spatial nonuniformity of the spin current density stabilizes the single-mode generation regime at higher bias currents. It also generates a confining potential for the bullet, which reduces the thermal fluctuations of the spatial position of this mode along the nanowire length, resulting in the reduction of the STO phase noise.

Results

Experiment. The nanowire STO samples based on $\text{AlO}_x(2\text{nm})/\text{Py}(5\text{nm})/\text{Pt}(7\text{nm})$ multilayers were patterned on a sapphire substrate via e-beam lithography and liftoff as described in Methods (here Py = Permalloy = $\text{Ni}_{80}\text{Fe}_{20}$). The wires are $6\ \mu\text{m}$ long with two Au(35 nm)/Cr(7 nm) leads attached to each wire as shown in Fig. 1. The $1.9\ \mu\text{m}$ long nanowire section between the leads is the STO active region, in which direct bias current applied to the wire generates the anti-damping spin orbit torque. The width of the straight nanowires is 190 nm, while the width of the tapered nanowires increases from 190 nm to 250 nm within the active region.

In our measurements, the magnetization of nanowires is saturated by a 700 Oe in-plane external magnetic field applied at the angle of 80° with respect to the wire axis as shown in Fig. 1. Direct current

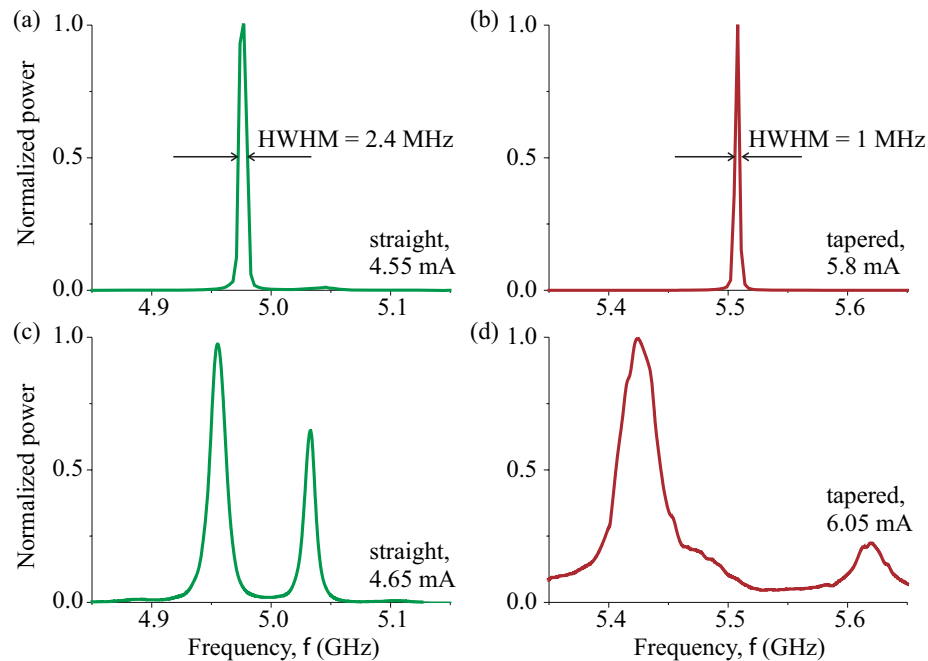


Figure 2. Microwave emission spectra. Normalized power spectra generated by the straight (a,c) and tapered (b,d) nanowire STOs at two bias current values.

I_{dc} applied to the nanowire excites self-oscillations of magnetization when the bias current exceeds a certain critical value ($I_{dc} > 4.45$ mA for the straight wire and $I_{dc} > 5.675$ mA for the tapered wire). The critical current is higher for the tapered nanowire because of its greater average width. Magnetization self-oscillations are converted into a microwave signal via anisotropic magneto-resistance of the Py layer¹¹. The output microwave signal is amplified by a low-noise amplifier and measured by a spectrum analyzer. All measurements reported in this paper were made at the bath temperature of 4.2 K, although the sample temperature near the critical current is approximately 150 K due to heating of the nanowire by the bias current¹¹. We studied 3 straight and 3 tapered nanowire samples and found similar results for all these devices. In this paper, we present the data for one representative straight and one representative tapered nanowire STO.

The spectra of microwave signals generated by the straight and tapered nanowire STOs at two bias current values above the critical current are presented in Fig. 2. Here we only show the low-frequency group of peaks observed in the spectra. At higher bias currents, we have also detected a group of low-amplitude peaks at 0.8 GHz above the low frequency group. Following the analysis of Ref. 11, we identify the low-frequency peaks as the spin wave modes localized at the wire edges (“edge modes”)^{53,54}, while the high-frequency peaks arise from the spin wave modes that have their maximum amplitudes within the central part of the wire (“bulk modes”). We also directly verified these conclusions using micromagnetic simulations of the spin wave spectra in the straight and tapered nanowires, as discussed in the next section. Since the critical current for the excitation of bulk modes is significantly higher than the range of the bias currents discussed in this work, we do not discuss the bulk modes in the rest of this paper.

For both the straight and tapered nanowire STOs, we observed a single spectral peak in a range of bias currents above the critical current I_c (Fig. 2(a,b)). The frequency of this first peak is higher in the tapered nanowire STO than in the straight nanowire STO. This happens because the average demagnetizing field decreases with the increase of the wire width and the average tapered wire width is greater than that of the straight wire. The emission power in the first peak increases with increasing bias current until the second peak appears in the spectrum at the second critical current ($I_2 = 4.55$ mA for the straight nanowire STO; $I_2 = 5.875$ mA for the tapered nanowire STO) as shown in Fig. 2(c,d). For $I > I_2$, the integrated power in the first mode decreases, and the spectral linewidth of this mode increases with increasing current, as illustrated in Fig. 2(c,d) and 3. At even higher bias current values, the third edge mode appears in the microwave emission spectra. Here we will not discuss this complicated regime, and will restrict our discussion to the single- and double-mode STO operation regimes, focusing on the differences between the straight and tapered nanowire devices.

While the general features of the emission spectra as a function of the bias current are qualitatively similar for the straight and tapered nanowire STOs, there are significant quantitative differences. First, the current range of the single-mode operation of the tapered nanowire STO (0.2 mA) is twice as wide as

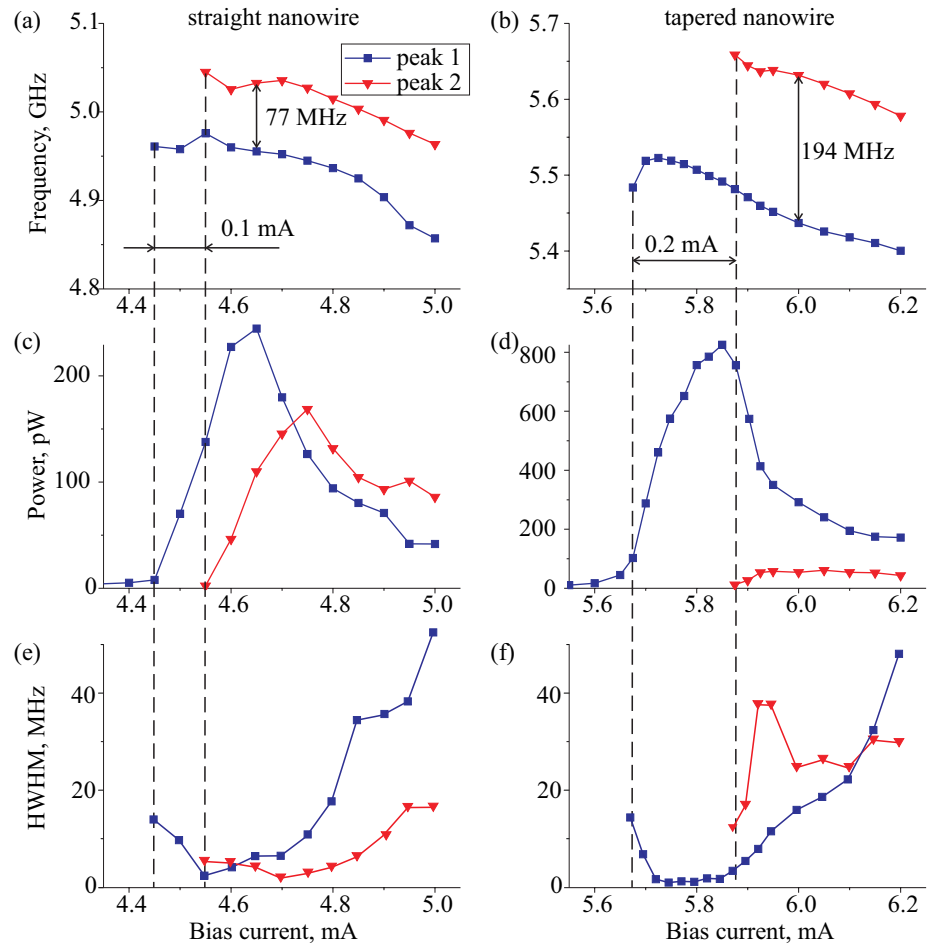


Figure 3. Auto-oscillatory mode frequency and power. Measured dependence of the auto-oscillation frequency (a,b), integrated microwave emission power (c,d) and HWHM (e,f) on the bias current for the first (blue squares) and second (red triangles) peaks in the auto-oscillation spectra.

that for the straight nanowire STO (0.1 mA) as illustrated in Fig. 3. Second, the frequency gap between the first and the second peaks in the generation spectrum is much wider for the tapered nanowire STO in comparison to the straight nanowire STO. Third, the minimum spectral linewidth (half width at half maximum or HWHM) in the single-mode auto-oscillation regime is significantly smaller for the tapered nanowire STO (1.0 MHz) than for the straight nanowire STO (2.4 MHz), as shown in Fig. 2. All these large quantitative differences between the two types of the STO cannot be attributed to a small difference of the average demagnetization fields, which results in a 10% difference in the edge mode frequency. In the next section we explain the origin of the observed significant impact of the nanowire shape on the spectral properties of nanowire STOs.

Theory. In order to visualize the spatial profiles of the observed self-oscillatory edge modes, we performed micromagnetic simulations of the magnetization dynamics in the nanowire STO. First, we employed the spectral mapping technique to calculate the edge spin wave mode profile in the linear regime (see Methods for details). Since the applied magnetic field makes different angles to the two edges of the tapered nanowire sample, the frequencies of the modes localized at the opposite edges are different. The spatial profile of the lowest-frequency edge mode calculated by the spectral mapping technique for the tapered nanowire STO is shown in Fig. 4(a). The mode extends over the entire nanowire length and is strongly localized near one of the edges. We have also performed micromagnetic simulations of the self-oscillatory magnetic dynamics in this nanowire sample driven by spin orbit torque. Such simulations are very time-consuming because of the significant spatial extent of the nanowire and long transient dynamics. For this reason, we performed these simulations for only a few values of the bias current above the critical current. The spatial profile of the self-oscillatory mode driven by direct current is shown in Fig. 4(b). It is clear from this figure that the self-oscillatory nonlinear mode directly originates from the linear edge mode but shows a higher degree of localization near the middle of the nanowire STO active

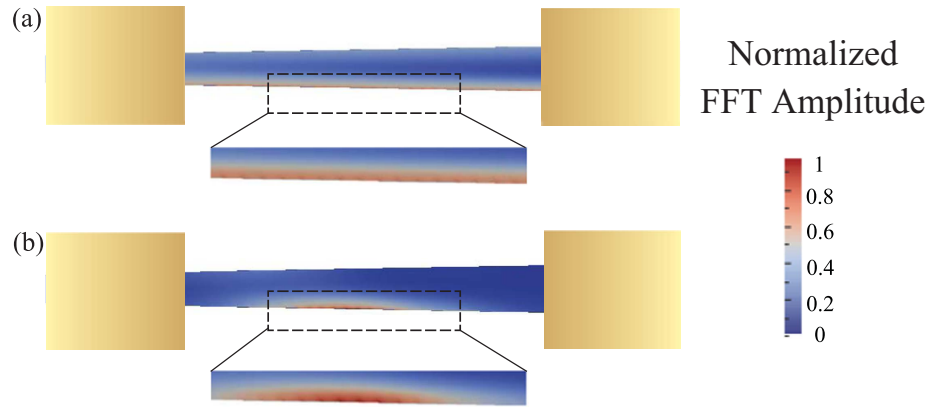


Figure 4. Micromagnetic simulations. (a) Spatial profile of the lowest-frequency linear SW mode of the tapered nanowire. (b) Spatial profile of the self-oscillatory bullet mode excited by direct current exceeding the critical value. Dashed rectangles show a zoomed in view of the edge mode. Yellow rectangles represent the Au/Cr leads.

region. We also applied this type of micromagnetic analysis to the straight nanowire STO and observed a similar behavior with the main difference being localization of the edge mode at both edges of the nanowire due to the higher symmetry of the system. We note that in real nanowire samples, equivalence of the two edges is broken due to the random edge roughness and non-uniform edge damage, and thus the localization of the lowest-frequency edge mode near one of the edges is expected as well.

Since detailed micromagnetic simulations of the self-oscillatory dynamics as a function of the direct bias current are prohibitively time-consuming, we developed a one-dimensional model describing current-driven magnetization dynamics in a nanowire STO. This model describes magnetization dynamics in the framework of nonlinear Ginzburg-Landau equation that is derived as a small-amplitude approximation of the Landau-Lifshitz equation:

$$\frac{\partial b}{\partial t} + (i + \alpha_G) \hat{\Omega} * b + iN|b|^2b - \sigma J(y)(1 - |b|^2)b = 0. \quad (1)$$

Here $b = b(y, t)$ is the complex amplitude of the dynamic magnetization in the excited SW mode, which depends only on the coordinate along the wire axis (y -axis), α_G is the Gilbert damping constant, N is the nonlinear frequency shift, $J(y)$ is the spatial distribution of the bias current density along the nanowire axis and σ is the spin orbit torque efficiency constant (see Methods). The one-dimensional model is valid if one can factorize the two-dimensional mode profile as $b(x, y) = b(y)f(x)$, where $f(x)$ does not depend on y . We explicitly verified that this assumption is valid via micromagnetic simulations of the mode profile shown in Fig. 4.

The frequency operator $\hat{\Omega}$ is given by:

$$\hat{\Omega} * b \equiv \omega_0 b - \omega_M \lambda_{ex}^2 \frac{\partial^2 b}{\partial y^2} + \frac{\omega_M}{2\omega_0} \int G_{yy}(y - y') b(y') dy', \quad (2)$$

where ω_0 is the spin wave resonance frequency in the linear regime, $\omega_M = \gamma\mu_0 M_s$ and λ_{ex} is the exchange length. In contrast to the previous studies³¹, we also take into account the magnetodipolar interaction in the Damon-Eshbach geometry via the magnetostatic Green's function G_{yy} . In all simulations presented in this paper, we neglect the current-induced Oersted field (< 50 Oe), which is much smaller than the applied field of 700 Oe. We verified the inclusion of the Oersted field into our Ginzburg-Landau simulations does not significantly change the simulation results.

The sign of the nonlinear frequency shift N is the key factor determining the type of self-oscillatory magnetization dynamics driven by spin orbit torque. It is known that for negative nonlinear shift, a nonlinear self-localized solitonic bullet mode is favored under the action of anti-damping spin torque; while for positive nonlinear shift, no self-localization is found^{10,31,32}. Figure 3 demonstrates that the nonlinear frequency shift of the edge SW mode in our system is *negative* ($N < 0$), and, therefore, we should expect self-localization of the excited self-oscillatory mode. We also note that in the previously studied nanowire STO samples prepared via Ar plasma etching¹¹, positive nonlinear shift of the edge mode was observed, and the nonlinear mode self-localization did not take place. This demonstrates a strong sensitivity of the

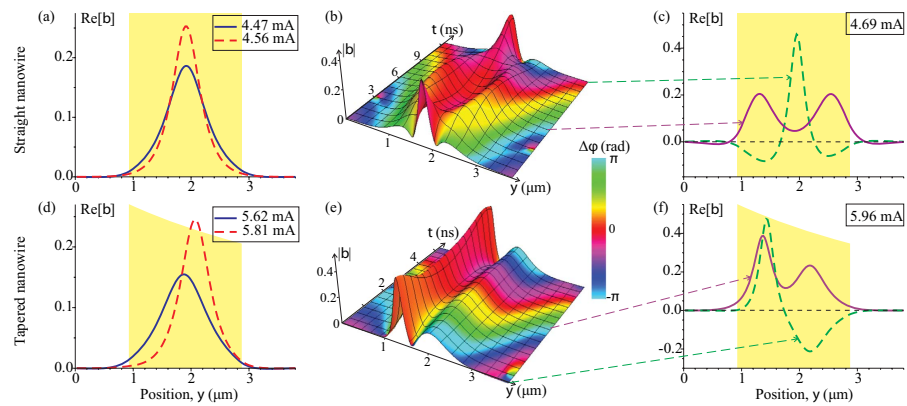


Figure 5. Self-oscillatory mode profiles. Profiles of the self-oscillatory bullet mode in the single-mode regime calculated from Eq. (1) for the straight (a) and tapered (d) nanowire STOs at different bias currents. The height of the yellow shaded area represents the spin current density within the STO active region. (b,e) Time evolution of the amplitude $|b|$ and relative phase $\Delta\phi$ (see Methods) of the magnetization oscillations in the double-bullet regime of self-oscillations. (c,f) Snapshots of the dynamic magnetization profile $\text{Re}[b]$ at two values of time.

nanowire STO properties to the degree of magnetic edge damage, which depends on the sample fabrication technique (see Methods for details).

Figure 4(b) illustrates that the excited self-oscillatory mode given by micromagnetic simulations is indeed a nonlinear self-localized bullet mode, as expected for $N < 0$. The self-localization is evident from the smaller spatial extent of the nonlinear mode in Fig. 4(b) along the wire length compared to the size of the linear mode in Fig. 4(a). The characteristic dimension of this bullet mode is approximately $1\ \mu\text{m}$, which is one order of magnitude larger than the size of the self-oscillatory bullet modes excited by spin torque in extended thin films in point contact STOs^{10,31–33,40,42}. Such increase of the bullet size is a result of the enhanced role of the magnetic dipole interaction in the nanowire geometry. A detailed study of the effect of dipolar interaction on the bullet size will be presented elsewhere.

The frequency of the self-oscillatory mode at the critical current given by micromagnetic simulation (5.8 GHz) is similar to the measured frequency of 5.5 GHz. The value of N derived from our micromagnetic simulations is approximately one third of the measured value. This is not surprising because we find N to be very sensitive to the wire fabrication process, and the value of N calculated for a nanowire with ideal edges can significantly differ from the measured value of N .

Figure 5 illustrates the bullet mode profiles obtained from the numerical solution of the Ginzburg-Landau equation (see Methods for details). In the straight nanowire STO, a single bullet mode with its maximum in the center of the wire is excited above the critical current as shown in Fig. 5(a). The amplitude of this bullet mode increases and its width decreases with increasing bias current, which is a clear evidence of the nonlinear self-localization. When the current density reaches a second critical current I_2 , another bullet mode is excited within the STO active region as illustrated in Fig. 5(c). A similar type of the two-bullet excitation was previously observed in a point contact STO⁵⁵. The double-bullet solution at $I > I_2$ is not stationary – the magnetization profile oscillates between the single-bullet and double-bullet configurations, as illustrated in Fig. 5(b,c). As a result of these mode profile oscillations, the spectrum of the voltage signal generated by the STO develops two prominent peaks in agreement with our experimental observations. At higher currents, additional bullet modes sequentially enter the active region, and the resulting magnetization dynamics becomes very complex.

For the tapered nanowire STO, we solve the same Ginzburg-Landau equation, but with a spatially dependent current density $J(y) \sim 1/w(y)$, where $w(y)$ is the nanowire width. Similar to the straight nanowire case, a nonlinear edge bullet mode is excited at the threshold current I_c . With increasing bias current, the size of this bullet mode decreases and the center of the mode shifts towards the wider end of the nanowire as shown in Fig. 5(d). At a higher critical current I_2 , a second bullet mode appears in the left part of the active region (where current density is higher). In contrast to the straight nanowire, where the mode profile oscillates between one- and two-bullet mode configurations, two different bullet modes coexist at all times in the tapered nanowire, as evident from Fig. 5(e). These two bullets oscillate with different frequencies – the left bullet experiencing higher current density has a lower oscillation frequency, as illustrated in Fig. 5(e) by the linear increase of the phase difference between the two bullet solutions $\Delta\phi$ with time (see Methods for details). This can be also seen in Fig. 5(f) where the two different bullet modes are in phase at one moment of time, and have opposite phases at a later moment. The Fourier transform of the voltage signal arising from this double-bullet dynamics exhibits two distinct spectral peaks corresponding to the two different bullet mode frequencies.

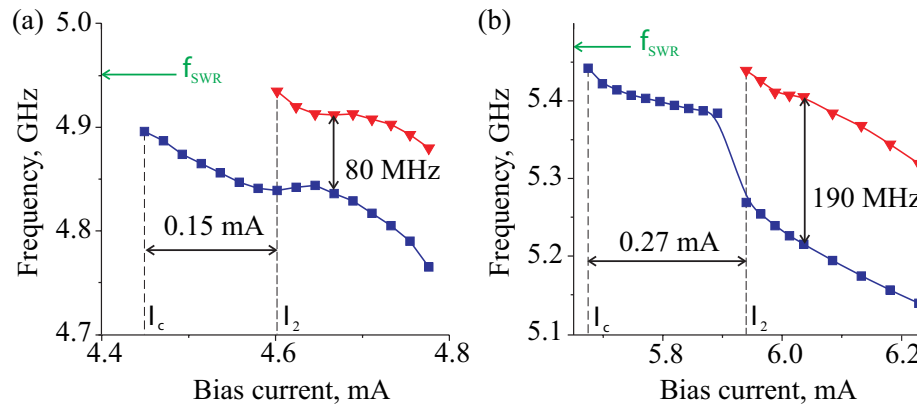


Figure 6. Frequency versus bias current: simulations. Self-oscillatory mode frequency as a function of the bias current calculated by numerically solving Eq. (1) for the straight (a) and tapered (b) nanowire STOs; blue squares - first bullet mode, red triangles - second bullet mode. Lines are guide for eyes and green arrows show the resonance frequency of the edge mode in the linear regime $f_{\text{SWR}} = \omega_0/2\pi$.

Figure 6 shows the calculated self-oscillatory mode frequencies given by Eq. (1) versus the magnitude of the direct bias current. These dependences are in good agreement with the experimental data in Fig. 3: the single-mode current range ($I_2 - I_c$) and the inter-mode frequency gap in the double-mode regime are significantly wider for the tapered nanowire STO. The wider single-mode current range is a direct consequence of the current-induced shift of the position of the first bullet mode away from the center of the active region towards the wider end of the nanowire (towards lower current density). This current-induced shift allows the first bullet mode to remain within a region of lower current density (and thus, within a single-mode regime) over a wider range of the applied bias currents. The wider inter-mode frequency gap in the tapered wire arises from the spatially non-uniform current density as well. Since the two bullet modes are spatially separated along the wire length, they are exposed to different spin current densities in the tapered nanowire device. This results in significantly different amplitudes of the two bullet modes, as illustrated in Fig. 5(e), and due to the nonlinear frequency shift, an enhancement of the inter-mode frequency gap.

The reduced phase noise of the tapered nanowire STO can be also explained by the spatially non-uniform spin current density. In the straight nanowire devices, the bullet mode position is weakly confined to the center of the nanowire by its interaction with the active region boundaries. Therefore, its position along the wire is highly susceptible to thermal fluctuations, resulting in fluctuations of measured voltage signal. In contrast, the bullet position in the tapered nanowire is mainly determined by the nonuniformity of the applied current density. Therefore, there is a current-induced restoring force that reduces the amplitude of thermal fluctuations of the bullet position along the wire length, thereby reducing the mode's phase noise. Another important effect which reduces the phase noise in the tapered nanowire STO is the enhanced bias current range of a single-mode generation. This results in higher generation power in the single-mode regime, which decreases the phase noise of the generated signal^{22,56}.

Discussion

In this work, we demonstrate that phase noise of nanowire-based spin orbit torque oscillators can be significantly reduced via the nanowire shape design. We experimentally show that the single-mode regime of the STO operation is extended over a wider current range in the tapered nanowire STOs compared to the straight nanowire STOs. The degree of spectral purity of the microwave signal generated by the tapered nanowire STO is also significantly improved in comparison to the straight nanowire STO devices.

To understand the observed effect of the nanowire shape on the STO operation, we developed a one-dimensional Ginzburg-Landau model of a nanowire STO. This model reveals that non-linear self-localized bullet modes are excited in the nanowire under the action of spin orbit torque if the excited spin wave modes possess negative non-linear frequency shift. These bullet modes have micrometer-scale spatial dimensions, which is an order of magnitude greater than the dimensions of the bullet modes excited in point contact STO devices, due to the enhanced role of magnetodipolar interaction in one-dimensional systems.

The model demonstrates that spatially non-uniform spin current density in tapered nanowire STOs is the key factor leading to the phase noise reduction in these devices. The non-uniform spin current density results in a current-induced displacement of the bullet mode from the nanowire center towards the region of lower current density, which extends the single-mode generation regime to a wider range of bias currents. In addition, the non-uniform current density provides a restoring force that reduces the amplitude of thermal fluctuations of the bullet mode position along the nanowire length, thereby

decreasing the STO phase noise. The model also predicts a transition to a double-mode regime of the STO operation experimentally observed at higher values of the bias current.

Methods

Sample fabrication. Fabrication of the STO devices starts with sputter deposition of a 5 nm thick Pt layer onto a c-plane sapphire substrate at 585 °C followed by annealing for 1 hour at the same temperature, which results in the growth of a continuous Pt film, as verified by high-resolution SEM and atomic force microscopy imaging. Then, straight and tapered nanowires are defined on top of the Pt film via e-beam lithography, brief Ar plasma cleaning immediately followed by *in situ* room temperature sputter deposition of AlO_x(2 nm)/Py(5 nm)/Pt(2 nm) trilayer and lift-off. The AlO_x(2 nm) capping layer is employed to prevent oxidation of the Py layer. The Au(35 nm)/Cr(7 nm) leads are defined via e-beam lithography and e-beam evaporation of the Au/Cr bilayer followed by lift-off. At the final fabrication step, Ar plasma etching is used to remove the 5 nm thick bottom Pt layer everywhere, but under the Py nanowire and the Au/Cr leads.

The liftoff technique employed for fabrication of the nanowire STOs minimizes the nanowire edge damage, thereby decreasing the critical current for excitation of the edge mode self-oscillations. The critical current for excitation of the edge modes is lower than that for the bulk modes for the samples studied in this work. This result is in contrast with our previous study of nanowire STOs¹¹, in which the critical currents of the bulk and edge groups of modes were nearly identical. The reason for this difference is the different methods of the device fabrication. Ar plasma etching of the nanowires employed in ref. 11 creates a significant edge damage, increases the damping parameter in the edge region, thereby increasing the critical current for excitation of the edge modes.

Micromagnetic simulations. Micromagnetic simulations are performed by using a modified version of the MuMax3 software package⁵⁷. The computational domain containing the entire 6 μm long nanowire is discretized into 4096 × 256 × 1 cells, which results in the cell size of approximately 1.5 × 1.5 × 5 nm³. The saturation magnetization $M_s = 530 \cdot 10^3$ A/m and the exchange stiffness $A = 0.5 \cdot 10^{-11}$ J/m were previously determined for this type of STO samples¹¹. Spin wave eigenmode frequencies of the nanowire are found as peak positions in the Fourier transform of the dynamics magnetization excited by a sinc-shaped out-of-plane magnetic field pulse of 0.5 Oe amplitude and 50 ps duration⁵⁸. The eigenmode spatial profiles are reconstructed by plotting the cell-specific Fourier amplitudes at the mode eigenfrequency. The auto-oscillatory mode of the system is found by solving the LLG equation with anti-damping spin torque applied to the 1.9 μm long active region of the nanowire. The simulation time is set to 2.5 μs to minimize the transient contributions to the self-oscillatory dynamics. The spatial profile of the auto-oscillatory mode is reconstructed by plotting the cell-specific Fourier amplitudes at the self-oscillatory mode frequency.

Numerical solution of the Ginzburg-Landau equation. The Ginzburg-Landau equation (Eq. (1)) is derived for a dimensionless complex magnetization amplitude b , which is related to the dynamic magnetization components as $b = (M_y + i\epsilon M_z) / \sqrt{1 + \epsilon^2} M_s$. Here ϵ describes the ellipticity of the magnetization precession, which is assumed to be constant. The values of ω_0 and σ used in the simulations are chosen to fit the experimentally measured frequency of self-oscillations at the threshold, and the threshold bias current I_c . The value of the nonlinear frequency shift $N = -0.1\omega_M$ is derived from the measured dependence of the first self-oscillatory mode frequency on the bias current²². The other material parameters: $\lambda_{ex} = \sqrt{2A/\mu_0 M_s^2}$, $\omega_M = \gamma\mu_0 M_s$, α_G are chosen to be identical to those used in our micromagnetic simulations. The integral kernel G_{yy} is approximated by the Green's function of a 25 nm wide wire⁵⁹, because the localization length of the edge mode given by our micromagnetic simulations is approximately 25 nm. The spatial domain is discretized into sufficiently small cells, and the resulting set of equations is solved in the time domain starting from a random distribution of b until a stationary state of magnetic self-oscillations is reached. To illustrate dynamics of the relative phase between the two bullets in the double-bullet solution of Eq. (1), we multiplied $b(t)$ by $\exp[i\omega_1 t]$, where ω_1 is the frequency of the first bullet mode. The relative phase between the two bullets shown in Fig. 5(b,e) is simply $\Delta\phi = \text{Arg}[b(t)e^{i\omega_1 t}]$.

References

- Kimura, T., Otani, Y., Sato, T., Takahashi, S. & Maekawa, S. Room-temperature reversible spin Hall effect. *Phys. Rev. Lett.* **98**, 156601 (2007).
- Ando, K. *et al.* Electric manipulation of spin relaxation using the spin Hall effect. *Phys. Rev. Lett.* **101**, 036601 (2008).
- Hahn, C., Loubens, G. de., Klein, O., Viret, M., Naletov, V. V. & Youssef, J. Ben. Comparative measurements of inverse spin Hall effects and magnetoresistance in YIG/Pt and YIG/Ta. *Phys. Rev. B.* **87**, 174417 (2013).
- Pai, C.-F., Liu, L., Tseng, H. W., Ralph, D. C. & Buhrman, R. A. Spin transfer torque devices utilizing the giant spin Hall effect of tungsten. *Appl. Phys. Lett.* **101**, 122404 (2012).
- Liu, L., Pai, C.-F., Li, Y., Tseng, H. W., Ralph, D. C. & Buhrman, R. A. Spin-torque switching with the giant spin Hall effect of tantalum. *Science* **336**, 555 (2012).
- Woo, S.-H., Mann, M., Tan, A. J., Caretta, L. & Beach, G. S. D. Enhanced spin-orbit torques in Pt/Co/Ta heterostructures. *Appl. Phys. Lett.* **105**, 212404 (2014).
- Kim, J. *et al.* Layer thickness dependence of the current-induced effective field vector in Ta[CoFeB]MgO. *Nature Mater.* **12**, 240 (2012).

8. Demidov, V. E. *et al.* Magnetic nano-oscillator driven by pure spin current. *Nat. Mater.* **11**, 1028 (2012).
9. Liu, L., Pai, C.-F., Ralph, D. C. & Buhrman, R. A. Magnetic oscillations driven by the spin Hall effect in 3-terminal magnetic tunnel junction devices. *Phys. Rev. Lett.* **109**, 186602 (2012).
10. Liu, R. H., Lim, W. L. & Urazhdin, S. Spectral characteristics of the microwave emission by the spin Hall nano-oscillator. *Phys. Rev. Lett.* **110**, 147601 (2013).
11. Duan, Z. *et al.* Nanowire spin torque oscillator driven by spin orbit torques. *Nature Comm.* **5**, 5616 (2014).
12. Zhang, S. Spin Hall effect in the presence of spin diffusion. *Phys. Rev. Lett.* **85**, 393 (2000).
13. Sinova, J., Culcer, D., Niu, Q., Sinitsyn, N. A., Jungwirth, T. & MacDonald, A. H. Universal intrinsic spin Hall effect. *Phys. Rev. Lett.* **92**, 126603 (2004).
14. Haney, P. M., Lee, H.-W., Lee, K.-J., Manchon, A. & Stiles, M. D. Current induced torques and interfacial spin-orbit coupling: Semiclassical modeling. *Phys. Rev. B* **87**, 174411 (2013).
15. Fan, X., Wu, J., Chen, Y., Jerry, M. J., Zhang, H. & Xiao, J. Q. Observation of the nonlocal spin-orbital effective field. *Nature Comm* **4**, 1799 (2013).
16. Bhowmik, D., You, L. & Salahuddin, S. Spin Hall effect clocking of nanomagnetic logic without a magnetic field. *Nature Nanotech.* **9**, 59 (2014).
17. Dyakonov, M. I. & Perel, V. I. Possibility of orienting electron spins with current. *Sov. Phys. JETP Lett.* **13**, 467 (1971).
18. Hirsch, J. E. Spin Hall effect. *Phys. Rev. Lett.* **83**, 1834 (1999).
19. Hoffmann, A. Spin Hall effects in metals. *IEEE Trans. Magn.* **49**, 5172 (2013).
20. Slonczewski, J. C. Current-driven excitation of magnetic multilayers. *J. Magn. Mater.* **159**, L1 (1996).
21. Berger, L. Emission of spin waves by a magnetic multilayer traversed by a current. *Phys. Rev. B* **54**, 9353 (1996).
22. Slavin, A. & Tiberkevich, V. Nonlinear auto-oscillator theory of microwave generation by spin-polarized current. *IEEE Trans. Magn.* **45**, 1875 (2009).
23. Bazaliy, Ya. B., Jones, B. A. & Zhang, S.-C. Modification of the Landau-Lifshitz equation in the presence of a spin-polarized current in colossal- and giant-magnetoresistive materials. *Phys. Rev. B* **57**, R3213 (1998).
24. Tserkovnyak, Y. & Bender, S. A. Spin Hall phenomenology of magnetic dynamics. *Phys. Rev. B* **90**, 014428 (2014).
25. Demidov, V. E., Urazhdin, S., Edwards, E. R. J. & Demokritov, S. O. Wide-range control of ferromagnetic resonance by spin Hall effect. *Appl. Phys. Lett.* **99**, 172501 (2011).
26. Rousseau, O. & Viret, M. Interaction between ferromagnetic resonance and spin currents in nanostructures. *Phys. Rev. B* **85**, 144413 (2012).
27. Hamadeh, A. *et al.* Full control of the spin-wave damping in a magnetic insulator using spin-orbit torque. *Phys. Rev. Lett.* **113**, 197203 (2014).
28. Demidov, V. E. *et al.* Control of magnetic fluctuations by spin current. *Phys. Rev. Lett.* **107**, 107204 (2011).
29. Demidov, V. E., Urazhdin, S., Zholud, A., Sadovnikov, A. V. & Demokritov, S. O. Nanoconstriction-based Spin-Hall nano-oscillator. *Appl. Phys. Lett.* **105**, 172410 (2014).
30. Demidov, V. E. *et al.* Spin-current nano-oscillator based on nonlocal spin injection. *Sci. Rep.* **5**, 8578 (2015).
31. Slavin, A. & Tiberkevich, V. Spin wave mode excited by spin-polarized current in a magnetic nanocontact is a standing self-localized wave bullet. *Phys. Rev. Lett.* **95**, 237201 (2005).
32. Bonetti, S. *et al.* Experimental evidence of self-localized and propagating spin wave modes in obliquely magnetized current-driven nanocontacts. *Phys. Rev. Lett.* **105**, 217204 (2010).
33. Consolo, G. *et al.* Excitation of self-localized spin-wave bullets by spin-polarized current in in-plane magnetized magnetic nanocontacts: A micromagnetic study. *Phys. Rev. B* **76**, 144410 (2007).
34. Pincus, P., Sparks, M. & LeCraw, R. C. Ferromagnetic relaxation II. The role of four-magnon processes in relaxing the magnetization in ferromagnetic insulators. *Phys. Rev.* **124**, 1015 (1961).
35. Dobin, A. Yu. & Vitoria, R. H. Intrinsic nonlinear ferromagnetic relaxation in thin metallic films. *Phys. Rev. Lett.* **90**, 167203 (2003).
36. Grollier, J., Cros, V. & Fert, A. Synchronization of spin-transfer oscillators driven by stimulated microwave currents. *Phys. Rev. B* **73**, 060409 (2006).
37. Georges, B. *et al.* Origin of the spectral linewidth in nonlinear spin-transfer oscillators based on MgO tunnel junctions. *Phys. Rev. B* **80**, 060404 (2009).
38. Houssameddine, D. *et al.* Spin-torque oscillator using a perpendicular polarizer and a planar free layer. *Nature Mater.* **6**, 447 (2007).
39. Ozyilmaz, B., Kent, A. D., Sun, J. Z., Rooks, M. J. & Koch, R. H. Current-induced excitations in single cobalt ferromagnetic layer nanopillars. *Phys. Rev. Lett.* **93**, 176604 (2004).
40. Tsoi, M. *et al.* Generation and detection of phase-coherent current-driven magnons in magnetic multilayers. *Nature* **406**, 46 (2000).
41. Kiselev, S. *et al.* Microwave oscillations of a nanomagnet driven by a spin polarized current. *Nature* **425**, 380 (2003).
42. Rippard, W. H., Pufall, M. R., Kaka, S., Russek, S. E. & Silva, T. J. Direct-current induced dynamics in point $\text{Co}_{90}\text{Fe}_{10}/\text{Ni}_{80}\text{Fe}_{20}$ contacts. *Phys. Rev. Lett.* **92**, 027201 (2004).
43. Deac, A. M. *et al.* Bias-driven high-power microwave emission from MgO-based tunnel magnetoresistance devices. *Nature Phys.* **4**, 803 (2008).
44. Arai, H., Matsumoto, R., Yuasa, S. & Imamura, H. Spin-torque-induced oscillation at zero bias field in a magnetoresistive nanopillar with a free layer with first- and second-order uniaxial anisotropy. *Appl. Phys. E* **8**, 8 (2015).
45. Mistral, Q. *et al.* Current-driven microwave oscillations in current perpendicular-to-plane spin-valve nanopillars. *Appl. Phys. Lett.* **88**, 192507 (2006).
46. Nazarov, A. V. *et al.* Spin transfer stimulated microwave emission in MgO magnetic tunnel junctions. *Appl. Phys. Lett.* **88**, 162504 (2006).
47. Tserkovnyak, Y. *et al.* Nonlocal magnetization dynamics in ferromagnetic heterostructures. *Rev. Mod. Phys.* **77**, 1375 (2005).
48. Zeng, Z. *et al.* Ultralow-current-density and bias-field-free spin-transfer nano-oscillator. *Sci. Rep.* **3**, 1426 (2013).
49. Krivorotov, I. N. *et al.* Time-domain measurements of nanomagnet dynamics driven by spin-transfer torques. *Science* **307**, 228 (2005).
50. Wang, Y. & Sham, L. J. Quantum dynamics of a nanomagnet driven by spin-polarized current. *Phys. Rev. B* **85**, 092403 (2012).
51. Iacocca, E., Heinonen, O., Muduli, P. K. & Åkerman, J. Generation linewidth of mode-hopping spin torque oscillators. *Phys. Rev. B* **89**, 054402 (2014).
52. Sharma, R., Dürrenfeld, P., Iacocca, E., Heinonen, O. G., Åkerman, J. & Muduli, P. K. Mode-hopping mechanism generating colored noise in a magnetic tunnel junction based spin torque oscillator. *Appl. Phys. Lett.* **105**, 132404 (2014).
53. Jorzick, J. *et al.* Spin wave wells in nonellipsoidal micrometer size magnetic elements. *Phys. Rev. Lett.* **88**, 047204 (2002).
54. Park, J. P., Eames, P., Engebretson, D. M., Berezovsky, J. & Crowell, P. A. Spatially resolved dynamics of localized spin-wave modes in ferromagnetic wires. *Phys. Rev. Lett.* **89**, 277201 (2002).

55. Ulrichs, H., Demidov, V. E. & Demokritov, S. O. Micromagnetic study of auto-oscillation modes in spin-Hall nano-oscillators. *Appl. Phys. Lett.* **104**, 042407 (2014).
56. Kim, J.-V., Tiberkevich, V. & Slavin, A. N. Generation linewidth of an auto-oscillator with a nonlinear frequency shift: spin-torque nano-oscillator. *Phys. Rev. Lett.* **100**, 017207 (2008).
57. Vansteenkiste, A. *et al.* The design and verification of MuMax3. *AIP Advances* **4**, 107133 (2014).
58. Venkat, G. *et al.* Proposal for a standard micromagnetic problem: Spin wave dispersion in a magnonic waveguide. *IEEE Trans. Magn.* **49**, 524 (2013).
59. Guslienko, K. Y. & Slavin, A. N. Magnetostatic Green's functions for the description of spin waves in finite rectangular magnetic dots and stripes. *J. Magn. Magn. Mater.* **323**, 2418 (2011).

Acknowledgements

We acknowledge the Center for NanoFerroic Devices (CNFD) and the Nanoelectronics Research Initiative (NRI) for funding of this work. This work was also supported by NSF Grants DMR-1210850, ECCS-1309416, ECCS-1305586 and by the FAME Center, one of six centers of STARnet, and SRC program sponsored by MARCO and DARPA. This work was also supported in part by the grant from DARPA MTO/MESO grant N66001-11-1-4114 and by contracts from the US Army TARDEC, RDECOM. Partial funding by the DFG/NSF in the framework of the Materials World Network program is also acknowledged. T.S. acknowledges support through PROMOS stipend.

Author Contributions

L.Y. made the samples and performed electrical characterization of the samples. R.V., V.T. and A.N.S. developed theoretical model. R.V. made numerical simulations. T.S. performed micromagnetic simulations. L.Y., A.S., B.Y. and Z.D. developed the sample fabrication process. L.Y., J.L., K.L. and I.N.K. formulated the experimental approach. I.N.K. and A.N.S. managed the project. All authors analyzed the data and co-wrote the paper.

Additional Information

Competing financial interests: The authors declare no competing financial interests.

How to cite this article: Yang, L. *et al.* Reduction of phase noise in nanowire spin orbit torque oscillators. *Sci. Rep.* **5**, 16942; doi: 10.1038/srep16942 (2015).



This work is licensed under a Creative Commons Attribution 4.0 International License. The images or other third party material in this article are included in the article's Creative Commons license, unless indicated otherwise in the credit line; if the material is not included under the Creative Commons license, users will need to obtain permission from the license holder to reproduce the material. To view a copy of this license, visit <http://creativecommons.org/licenses/by/4.0/>

4.3. Конкуренція лінійного та нелінійного механізмів локалізації у спін-торк осциляторах за наявності потенціальної ями

<https://doi.org/10.15407/ujpe64.10.947>

R.V. VERBA

Institute of Magnetism Nat. Acad. of Sci. of Ukraine
(36-b, Vernadskogo Blvd., Kyiv 03142, Ukraine; e-mail: verrv@ukr.net)

INTERPLAY OF LINEAR AND NONLINEAR LOCALIZATION MECHANISMS IN SPIN-TORQUE OSCILLATORS WITH A FIELD WELL

The magnetization dynamics in a spin-torque oscillator with nonuniform profile of a static magnetic field creating a field well is studied by analytic calculations and numerical simulations. It is demonstrated that, in the case of sufficiently deep and narrow field well, the linear localization in the field well dominates the nonlinear self-localization, despite a negative nonlinear frequency shift. A change of the localization mechanism results in a qualitatively different dependence of the generation power on the driving current. For the dominant linear localization, the soft generation mode is realized, while, for the nonlinear self-localization, we observe a hard mode of auto-oscillator excitation. Simultaneously, a difference in the profiles of the excited spin-wave mode can become evident and distinguishable in experiments only in the case of a nonsymmetric field well.

Keywords: spin-torque oscillator, spin-wave bullet, localized mode, magnetization dynamics.

1. Introduction

Spin current injected into a ferromagnet creates a torque on its magnetization. Due to the nonconservative nature, this spin-transfer torque can result in the magnetization reversal [1, 2], partial compensation of magnetic losses [3, 4], and excitation of self-sustained magnetization oscillations driven by a dc current [5, 6]. Nanoscale magnetic oscillators, which utilize this effect – spin-torque oscillators (STOs) – are promising for various applications such as compact microwave generators [7, 8], sources of spin waves in magnonics [9, 10], neuromorphic computing [11], etc. Earlier researches utilized the spin-transfer torque of a spin-polarized electric current [1, 5, 6]; the usage of pure spin currents coming from the spin-Hall effect in heavy metals [12] or nonlocal spin current injection [13] enlarges the functionality of STOs.

STOs can demonstrate various types of the nonlinear magnetization dynamics depending on their geometry. In an STO with a nanoscale confined free layer, the spin current excites mostly the lowest quasi-uniform spin-wave mode of the free layer [14] or, in the case of the free layer in a vortex state, the gyrotropic mode of a vortex [15], which is also the lowest among spin-wave modes of a vortex state. In

the case of spatially extended free layer (film or nanowire), the dynamics of an STO becomes more complex. It was shown that the injection of a spin current into a large micron-size area of a ferromagnetic film does not allow the excitation of coherent spin waves because of the nonlinear scattering, which redistributes the energy to many spin-wave modes [16]. If the size of the active area, into which the spin current is injected, is reduced down to hundreds of nanometers, the coherent generation becomes possible. Features of the excited spin-wave mode in this case are determined by a nonlinear frequency shift N , which depends on the geometry and static magnetization direction [14]. In the case of positive nonlinear frequency shift, $N > 0$, which is typically realized for the out-of-plane static magnetization direction, the linear spin waves propagating from the active area are excited [17–19]. In contrast, if $N < 0$ (in-plane static magnetization), the excited mode is a nonlinear self-localized spin-wave bullet having characteristic sizes of 100-200 nm [20–22]. Characteristic sizes of the bullet and, consequently, sizes of the STO active area, which supports the coherent generation can be enlarged by the dipolar interaction to the micron-scale in a one-dimensional geometry related to nanowire spin-Hall oscillators [23, 24].

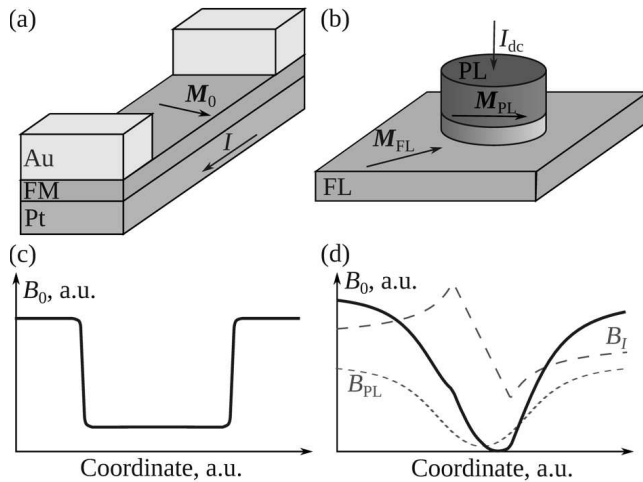


Fig. 1. Sketches of a common nanowire spin-Hall oscillator consisting of a ferromagnetic (FM) – heavy metal (Pt) bilayer with Au electrodes defining the active area between them (a), and nanocontact STO with a continuous ferromagnetic film as a free layer (FL) and a nanodot ferromagnetic pinned layer (PL) separated by a dielectric spacer (b); (c, d) show the corresponding schematic profiles of a static internal magnetic field B_0 (projection of the total magnetic field on the static magnetization direction) in the ferromagnetic layer of SHO (c) and in the free layer of nanocontact STO (d); in (d), dashed lines show separate contributions of the Oersted field B_I and stray fields B_{PL} of the pinned layer

This simple picture, however, takes place only in the case of spatially uniform free layers. In a real device, the presence of the Oersted field of a driving current or stray fields from a pinned layer creates a nonuniform energy landscape even in a geometrically uniform magnetic film or nanowire. As an illustration, we show the common geometry of a nanowire spin-Hall oscillator (SHO) [25] and the corresponding profile of a static internal magnetic field affected by the Oersted field of a dc current in Fig. 1, a, c. The presence of a field well or field hill in the nanowire depends on the sign of the spin-Hall angle of a heavy metal (as it determines the direction of a current necessary for the spin-wave excitation) and the mutual position of ferromagnetic and heavy metal layers (i.e. which one is on the top). In the case of nanocontact STO with a ferromagnetic film as a free layer (Fig. 1, b), the field landscape can be more complex, as it is exemplarily shown in Fig. 1, d. In this case, the superposition of the Oersted field of a dc current and the magnetostatic stray fields of the pinned layer can create a complex landscape with a nonsymmetric field well.

Naturally, the presence of a geometric or magnetic nonuniformity in a ferromagnetic free layer affects the STO dynamics and, in particular, may affect the nature of an excited spin-wave mode. Recently, it was shown that the excited spin-wave mode in a nanoconstriction SHO, in which a ferromagnetic layer is patterned, is often a linearly localized mode independent of the static magnetization direction. It is a consequence of the strong nonuniformity of the internal magnetic field and different nonlinear properties of the edge modes compared to the bulk ones [26–28]. In [29], the mode hopping between linearly localized and bullet modes in an SHO with extended active area was found. This means that the excitation thresholds of both these modes are close to each other. Similar hoppings were observed in a constriction-based SHO [27].

In this work, we study the features of localized excitations in an STO within a simple one-dimensional model with a field well. We consider the conditions, when a linear or nonlinear localization mechanism dominates, and how it affects the experimentally measured properties of STO.

2. Model

In this work, the interplay of the linear and nonlinear localization mechanisms is studied within a simple one-dimensional model (e.g., nanowire STO or SHO). We assume that the driving electric current density $J(y)$ and, consequently, spin current density, are constant within the active region of the length L_a and are zero outside it (Fig. 2). The nonuniform energy landscape in a ferromagnetic layer is modeled by the rectangular profile of a static internal magnetic field containing a finite-depth field well of the length L_w . It is described by the spatial dependence of the local ferromagnetic resonance (FMR) frequency $\omega_0(y)$, which is the “fictive” frequency, which a zero-wavenumber spin-wave excitation would have, if the parameters of a sample and the external conditions (e.g., static field) were equal to given local parameters. Obviously, the spatial distribution $\omega_0(y)$ has also rectangular profile with a well (Fig. 2). In a general case, the nonuniformity of a local FMR frequency can be created not only by a nonuniform total external field, but also by a spatial dependence of the magnetic anisotropy, nanowire width or thickness, etc. The lengths of the active area and the field well

can be different in the general case, $L_a \neq L_w$. In the most of this work, except for Subsec. 3.3, we consider a symmetric location of the field well and the active area, meaning that their centers coincide, as shown in Fig. 2.

The magnetization dynamics of STO is studied in the framework of the nonlinear Ginzburg–Landau equation, which is derived as an approximation of the Landau–Lifshitz equation accounting for the linear and first nonlinear ($\sim|b|^3$) terms [10, 20, 23]:

$$\begin{aligned} \frac{\partial b}{\partial t} + (i + \alpha_G) \left(\omega_0(y) - D \frac{\partial^2}{\partial y^2} \right) b + \\ + iN|b|^2b - \sigma J(y) (1 - |b|^2) b = 0. \end{aligned} \quad (1)$$

Here, $b = b(y, t)$ is the complex amplitude of the dynamic magnetization in the excited spin-wave mode; it is related to the real dynamic magnetization components M_ξ and M_η (orthogonal to each other and to the static magnetization direction) as $b = (M_\xi + i\varepsilon M_\eta)/\sqrt{1 + \varepsilon^2} M_s$ with M_s being the saturation magnetization and ε being the ratio of dynamic magnetization components, which describes the ellipticity of the magnetization precession. The magnetic damping is described by the effective damping constant α_G , which could be different from the standard Gilbert constant due to a contribution of the spin pumping into the heavy metal layer (in SHOs) and/or large precession ellipticity. The parameter N describes a nonlinear frequency shift [14]. The coefficient σ is the spin-transfer-torque or spin-Hall efficiency for STO or SHO, respectively, exact expressions for which are not important for our current work and can be found elsewhere [10, 14]. The parameter D describes the spin-wave dispersion and can be achieved from the Taylor expansion of the linear spin wave dispersion relation as $\omega_k \approx \omega_0 + Dk^2 + \dots$ [10, 20]. In the case of a soft ferromagnetic film or thin wide nanowire, it is equal to $D = \omega_M \lambda^2 (2\omega_H + \omega_M \sin^2 \theta_M) / (2\omega_0)$, where $\omega_M = \gamma \mu_0 M_s$, $\omega_H = \gamma B_0$, γ is the gyromagnetic ratio, λ is the exchange length of the ferromagnetic, B_0 is the modulus of the static effective magnetic field, and θ_M is the angle between the static magnetization direction and the film normal. The FMR frequency in this case is equal to $\omega_0 = [\omega_H (\omega_H + \omega_M \sin^2 \theta_M)]^{1/2}$. Formally, it appears that the parameter D is spatially dependent in the presence of a field well. This weak dependence, however, can be easily neglected, by setting

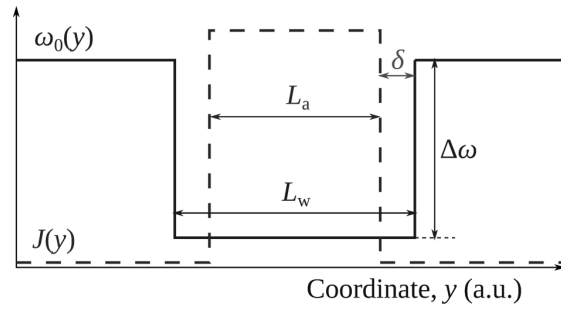


Fig. 2. Studied model of an STO with a field well, showing a spatial distribution of the driving current density $J(y)$ and the local FMR frequency $\omega_0(y)$

the constant D to the value calculated outside the well, since the solution in this region is more sensitive to D , as it determines the radiation losses. Finally, in Eq. (1), we neglect the nonlocal term describing the magnetodipolar interaction (expression including the dipolar term can be found in [23]). It is correct for a sufficiently thin ferromagnetic films and nanowires. Simultaneously, as shown in [23], the dipolar interaction just changes the characteristic length scale, while it does not lead to a qualitatively new behavior of an STO.

It should be noted that the model assumes the well width and depth and a nonlinear frequency shift independent of the amplitude of magnetization precession b . Therefore, it is not directly applicable to the case of wells created by the self-demagnetization fields or excitation of spin-wave modes with anomalous nonlinearity. This more complex case takes place, for example, in constriction-based SHOs [27, 28].

3. Interplay of Localization Mechanisms

3.1. Excitation thresholds of linearly localized and bullet modes

The excitation of a magnetization dynamics in an STO is a threshold process. The generation starts, if the driving current is higher than the threshold value, at which the antidamping spin-transfer torque overcomes total losses (Gilbert damping and radiation losses). Naturally, the mode having the lowest threshold is excited firstly. At large currents, the generation can switch to another regime, e.g., the excitation of higher-order propagating modes [30], second bullet mode [31], multibullet mode [23], mode hopping [32], *etc.* Here, we are not interested in this high-driving-current dynamics and consider only the lowest excited

mode. Therefore, to understand which mode – linear or bullet one – is excited in an STO with a field well, we firstly calculate the excitation threshold for both of them.

A way to calculate the excitation threshold for a linear spin-wave mode is well-known. For this purpose, one needs to find a stationary solution $b(y, t) = b(y)e^{-i\omega t}$ of Eq. (1), neglecting all the nonlinear terms in it [10, 17, 19]. In our case of piecewise constant functions $J(y)$ and $\omega_0(y)$, the solution in each range is a combination of the sine and cosine functions. Applying the boundary conditions of continuity for the dynamic magnetization and its derivative, we get a linear eigenproblem, whose solution yields the generation frequency ω and the threshold current J_{th} . Both generation frequency and threshold current are determined from the following implicit equation:

$$\begin{aligned} k_1 (k_2 - ik_3 \tan[k_2\delta]) \tan[k_1 L_a/2] = \\ = -ik_2 (k_3 - ik_2 \tan[k_2\delta]). \end{aligned} \quad (2)$$

Here,

$$\begin{aligned} k_1 &= \sqrt{(\omega - \omega_0 + i(\Gamma - \sigma J_{\text{th}}))/D}, \\ k_2 &= \sqrt{(\omega - \omega_0 + i\Gamma)/D}, \\ k_3 &= \sqrt{(\omega - \omega_0 - \Delta\omega + i\Gamma)/D} \end{aligned} \quad (3)$$

are complex spin-wave wavenumbers in the active area, nonactive part of the field well, and the outer region, respectively, $\Gamma = \alpha_G \omega$ is the spin-wave damping rate, $\Delta\omega$ is the depth of the field well, ω_0 is the local FMR frequency within the well, and $\delta = (L_w - L_a)/2$ is the distance between boundaries of the active region and the field well (see Fig. 2). In the case of equal sizes of the active area and the field well, $L_a = L_w$, Eq. (2) simplifies to the well-known expression [10, 19]

$$k_1 \tan[k_1 L_w/2] = -ik_3. \quad (4)$$

If simultaneously, the well is of infinite depth, which corresponds to a finite-size magnetic dot, then $\text{Im}[k_3] \rightarrow \infty$, and the threshold is determined by Gilbert losses only, $J_{\text{th}} = \Gamma/\sigma$.

For the calculation of the bullet excitation threshold, we neglect the presence of a field well. As will be shown below, the nonlinear self-localization dominates over the linear one for relatively wide and/or shallow wells, which this assumption is reasonable for. The method of calculation of the threshold for

the bullet mode was described in [20]. The difference from the current work consists in a changed dimensionality of the problem, from two-dimensional to one-dimensional one. In the one-dimensional case, the bullet profile is given by the function $b(y) = b_0 \sqrt{2}/\text{ch}[y/l]$, with $l = \sqrt{D/|N|}/b_0$ being the characteristic bullet size, and b_0 being its amplitude. From the condition of energy balance, one can derive the expression for the excitation threshold of a bullet having the amplitude b_0 :

$$\frac{\sigma J_{\text{th}}}{\alpha_G \omega_0} = \text{cth} \left[\frac{L_a}{2l} \right] \left(1 - \frac{2}{3} b_0^2 \left(2 + \text{ch}^{-2} \left[\frac{L_a}{2l} \right] \right) \right)^{-1}. \quad (5)$$

The real excitation threshold is found as the minimum of expression (5) respective to the bullet amplitude b_0 (we recall that $l = l(b_0)$). The corresponding generation frequency is equal to $\omega = \omega_0 + N b_0^2$ (we recall that $N < 0$); the bullet size at the threshold is equal to $l = \sqrt{D/|N|}/b_0$ and, typically, is of the order of the active region length L_a .

3.2. Magnetization dynamics in a symmetric well

For the further consideration, we choose exemplary parameters of STO as follows: $\omega_M = 2\pi \times 30$ GHz, $D = 1.4 \times 10^{-5}$ m²/s, $\alpha_G = 0.01$, nonlinear frequency shift $N = -2\pi \times 3$ GHz, local FMR frequency is fixed within the well to $\omega_{0,w} = 2\pi \times 6.9$ GHz and is varying outside the well (this is done in order to fix Gilbert losses in the active region, which allows us to distinguish the pure effect of the well presence). These parameters correspond to a permalloy nanowire in the external field of 50 mT.

First, let us look at the simplest case where the sizes of the active region and the field well are equal. The excitation thresholds for the linear and bullet modes calculated by Eqs. (2), (5) are shown in Fig. 3, *a*. In our simplified calculations, the excitation threshold for the bullet mode does not depend on the field well depth and is equal to $J_{\text{th}} = 2.2\Gamma/\sigma$. Just as an additional example, we also show the bullet excitation threshold in the case of a twice larger nonlinear frequency shift of $N = -2\pi \times 6$ GHz in Fig. 3, *a*. It is clear that a higher nonlinear frequency shift leads to a decrease of the threshold, as the bullet mode becomes more localized within the active area.

The excitation threshold of the linear mode significantly depends on the field well depth. In the absence of a field well, it is much higher than the bullet

threshold. As the well becomes deeper, the threshold decreases and reaches the value $J_{\text{th}} = \Gamma/\sigma$ in the limit of infinitely deep well, i.e., in a confined free layer uniformly pumped by the spin current ($\Delta\omega \rightarrow \infty$ at a constant ω_0). The bullet mode cannot reach this minimal threshold value in a confined free layer, and one may expect the excitation of the linear mode in a confined layer of arbitrary sizes. It is, however, not always correct. One should be aware of the excitation of other linear and nonlinear modes. In a large sample (micron-sized in the 2D case; in 1D, it may be larger due to the dipolar interaction), the excitation thresholds for many modes are very close to each other, which results in a chaotic dynamics instead of the coherent generation [16].

From Fig. 3, *a*, one can expect the transition from the bullet mode excitation to the excitation of a linear mode, when the field well becomes deeper than $\Delta\omega = 2\pi \times 0.3$ GHz. We simulated the magnetization dynamics by solving numerically the initial equation (1) for two values of the field well depth, below and above this critical value (accounting the nonlinearity and the field well simultaneously). Corresponding stationary profiles of the excited spin-wave mode near the excitation thresholds are shown in Fig. 3, *b*. It is quite hard to distinguish normalized profiles even in simulations and will be completely impossible to do this in experiments. Of course, depending on the values of a nonlinear frequency shift and a field well depth, the characteristic sizes of the bullet and linear modes can become different. However, the localization law is the same. Indeed, the bullet mode $b(y) \sim 1/\text{ch}[y/l]$ is exponentially localized. The linear mode has a lower threshold than bullet ones, when its frequency is below the local FMR frequency outside the well, i.e., when it becomes the evanescent mode. The localization law of this mode outside the well is also exponential and is determined mainly by $b(y) \sim \exp[-\text{Im}[k_3]|y|]$. A small difference within the active region between inverse hyperbolic cosine $1/\text{ch}[y/l]$ and cosine $\cos[k_1 y]$ is too weak to be an evidence of the mode character.

The difference between the bullet and linear modes is pronounced in the dependence of the generation power on the driving current, which is shown in Fig. 3, *c*. For the linear mode, the power at the threshold is vanishingly small and monotonically increases above the threshold (until the nonlinear interaction with other modes becomes important). This

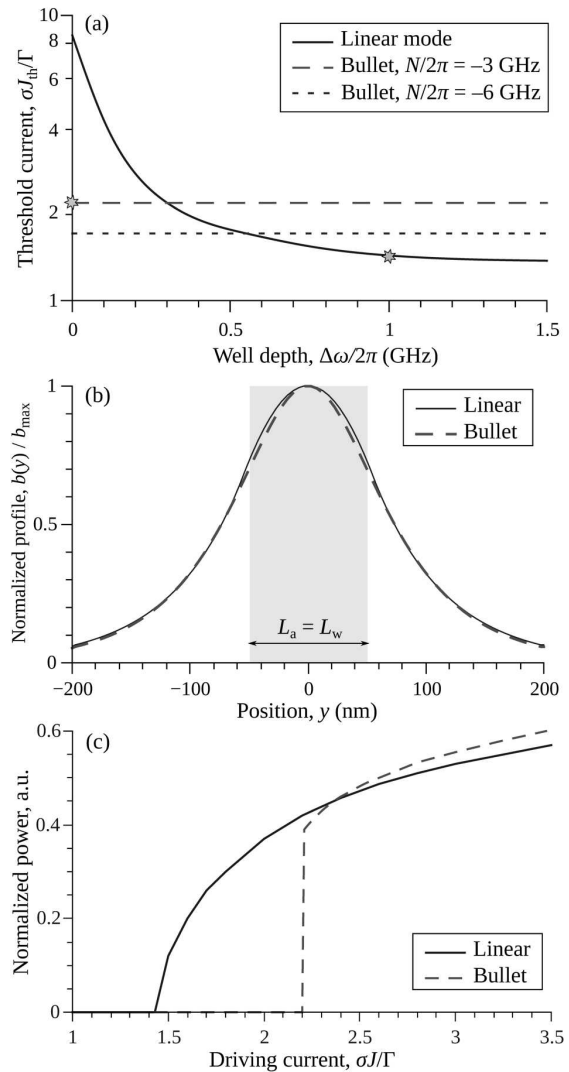


Fig. 3. *a* – calculated excitation threshold of a linearly localized mode as a function of the field well depth and the excitation threshold of the bullet mode at different nonlinear frequency shifts; $L_a = L_w = 100$ nm; stars show points of simulations in panels (*b*, *c*); *b* – normalized profiles of spin-wave modes close to the threshold for $\Delta\omega = 2\pi \times 1$ GHz (linear mode) and $\Delta\omega = 0$ (bullet); *c* – corresponding dependences of the generation power on the driving current for $\Delta\omega = 2\pi \times 1$ GHz (linear mode) and $\Delta\omega = 0$ (bullet). Panels (*b*, *c*) are obtained from the numerical solution of Eq. (1)

is the so-called “soft mode” of the excitation of an auto-oscillator. The bullet mode power at the threshold is finite and quite large (hard mode of excitation), because the bullet should have a large amplitude to support its self-localization. These features are the same as for the linear and bullet modes in

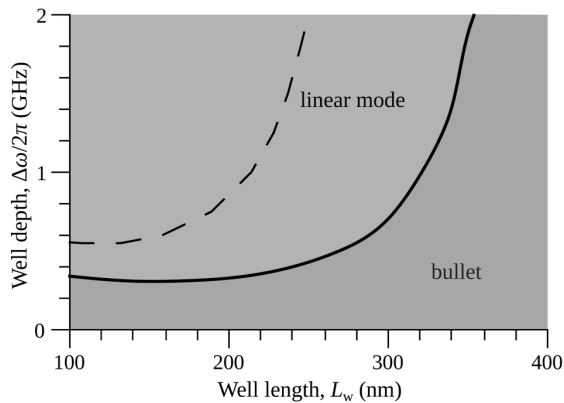


Fig. 4. Phase diagram of STO with the active region of the length $L_a = 100$ nm showing the excitation regions of the bullet and linear modes depending on the length and depth of the filed well; $N = -2\pi \times 3$ GHz. Dashed line show the boundary between the bullet and linear modes in the case of a higher nonlinear frequency shift of $N = -2\pi \times 6$ GHz

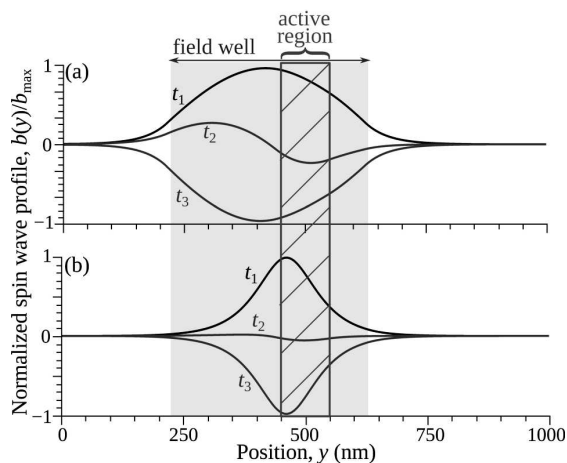


Fig. 5. Example profiles of the linear (a) and bullet (b) modes excited in STO with asymmetric position of the active region respective to the field well. Three instant profiles in each quarter of the oscillation period ($t_1 < t_2 < t_3$) are shown in both panels. Parameters: $L_a = 100$ nm, $L_w = 400$ nm, shift between the well active region centers is 75 nm, well depth $\Delta\omega = 2\pi \times 1$ GHz (a), and $\Delta\omega = 2\pi \times 0.25$ GHz (b)

a uniform ferromagnetic layer [14, 21] and are the main experimentally measured evidence of the nature of the excited spin-wave mode. However, such a simple picture is present only at vanishingly small thermal fluctuations. The sufficient thermal noise could spread the abrupt step in the power dependence, because of the nonstationary hopping between the bullet mode and the generation absence below the real excitation threshold of a bullet [23]. This spreading is

more pronounced, if the thresholds of the bullet and linear modes are close to each other, as will happen close to the well depth of 0.3 GHz in our case (see Fig. 3, a). In this complex case, only precise time-resolved measurements can distinguish a type of the magnetization dynamics [29].

Above, we considered the case of equal sizes of the active region and the field well, which is a good model for nanowire SHO (see Fig. 1, a, c). Figure 4 shows the phase diagram in a more general case of an arbitrary length of the field well, larger than the length of the active region. One can see that, in a sufficiently wide well, the bullet mode is excited in spite of a large well depth. In this case, the localization length of the bullet determined by a nonlinear frequency shift and the active region size becomes less than the field well length. Consequently, the magnetization dynamics does not feel the well and behaves as in a uniform ferromagnetic layer, in which the bullet mode should be excited, if $N < 0$. This characteristic critical well length is, naturally, inversely dependent on the nonlinear frequency shift, because the higher values of the nonlinear shift make the bullet mode more localized. Thus, we can conclude that the significantly narrow and deep field wells support the linearly localized mode formation. Otherwise, the bullet mode is excited.

3.3. Spin-wave profiles in a nonsymmetric well

In this section, we briefly discuss how the asymmetry of positions of the active region and the field well affects the STO dynamics. Such case of nonsymmetric well can appear in nanocontact STOs, as shown in Fig. 1, d. We model the asymmetry by a shift of the field well center respective to the active region center, while both still are of a rectangular profile. Simulations show that the asymmetry does not lead to a qualitative change of the STO phase diagram and the generation power dependence. The sufficiently narrow deep well supports the excitation of the linear mode in a soft excitation mode. Otherwise, the hard mode of the bullet excitation takes place. Simultaneously, the difference in spin-wave profiles could be substantial.

In Fig. 5, we show the profiles of the linearly localized and bullet modes in a nonsymmetric well. One can see that the presence of the well leads to a shift of

the bullet mode from the center of the active area toward to the center of the well (Fig. 5, *b*). This happens because “tails” of the bullet feel the boundaries of the well. This shift is more pronounced in a deeper well, if it stills support the bullet formation. The bullet has a standing-mode character, and the magnetization at different points oscillates with approximately the same phase, as it does in the case of a symmetric well or in the absence of a well. The effect of an asymmetry on a linearly localized mode is more pronounced. This mode becomes nonstanding, i.e., the magnetization oscillates not in the same phase in all the sample. The position of a maximum of the instant spin-wave profile changes during the oscillation period. Moreover, the profile varies from one having one maximum to that with two maxima, as shown in Fig. 5, *b* (number of maxima may differ depending on the well size). This complex dynamics is a result of the excitation of quasipropagating spin waves by the active region and its quantization in the well.

We believe that such a transition from a nonlinear to linear localization of the excited mode was observed in [33], but was incorrectly treated. In [33], it was stated that depending on external conditions, the one- or two-bullet mode, which are called *s*- or *p*-like bullets, is excited at the threshold. However, there is no other experimental or theoretical work, where the two-bullet solution (or the second bullet mode) was observed at the threshold. The second bullet mode always appears at a some higher threshold after the single-bullet mode is excited [23, 31]. We do not see any cause for why the two-bullet mode could be more energy-favorable than a single-bullet one. Indeed, the formation of the two-bullet mode always increases the exchange energy comparing to a single-bullet one. The nonuniformity of the energy landscape or bias current leads only to a shift of the single-bullet mode at the threshold, as is shown in this work and in [23], respectively. Simultaneously, the qualitative features of the mode observed in [33] are the same, as we found in a nonsymmetric well. Both the experiment and micromagnetic simulations in [33] showed that the mode, which was interpreted as a “*p*-like” soliton, has quasipropagating character with a variation in the number of instant maxima from one to two during the oscillation period. The nanocontact STO studied in [33] is similar to one shown in Fig. 1, *b*, which demonstrates a complex nonsymmetric magnetic field landscape. Therefore, we can state

that the observed excitation in that work was a linear mode localized in a field well.

4. Conclusions

In this work, the magnetization dynamics in a spin-torque oscillator with a nonuniform profile of the static magnetic field creating a field well has been studied. It is demonstrated that the presence of the field well can change the nature of the excited spin-wave mode. A shallow and/or wide well does not affect much the magnetization dynamics, and the bullet mode is excited in an STO having a negative nonlinear frequency shift, as it happens in the absence of a well. In contrast, if the well is sufficiently deep and narrow, the linear localization mechanism dominates over the nonlinear self-localization, despite a negative nonlinear frequency shift, and a linear localized spin-wave mode is excited. A change of the localization mechanism results in a qualitatively different dependence of the generation power on the driving current. For the dominant linear localization, the soft generation mode is realized, while we observe the hard mode of auto-generator excitation for the nonlinear self-localization. Simultaneously, in the case of a symmetric position of the well and the active region, the difference in the profiles of the linear and bullet spin-wave modes is weak. They have the exponential localization outside the well and the difference in the mode profiles within the active region is hardly distinguishable in experiment. But, in a nonsymmetric well, the profiles of the linear and bullet modes can differ drastically. While the bullet mode remains of a standing-mode character, the linear mode could acquire a quasipropagating character, which can be easily detected by a spatial mapping of the magnetization dynamics.

The work was sponsored by the Ministry of Education and Science of Ukraine (grant No. 0118U004007).

1. J.A. Katine, F.J. Albert, R.A. Buhrman, E.B. Myers, D.C. Ralph. Current-driven magnetization reversal and spin-wave excitations in Co/Cu/Co pillars, *Phys. Rev. Lett.* **84**, 3149 (2000).
2. R. Ramaswamy, J.M. Lee, K. Cai, H. Yang. Recent advances in spin-orbit torques: Moving towards device applications. *Appl. Phys. Rev.* **5**, 031107 (2018).
3. K. Ando, S. Takahashi, K. Harii, K. Sasage, J. Ieda, S. Maekawa, E. Saitoh. Electric manipulation of spin re-

- laxation using the spin Hall effect. *Phys. Rev. Lett.* **101**, 036601 (2008).
4. A. Hamadeh, O. d'Allivy Kelly, C. Hahn, H. Meley, R. Bernard, A.H. Molpeceres, V.V. Naletov, M. Viret, A. Anane, V. Cros, S.O. Demokritov, J.L. Prieto, M. Muñoz, G. de Loubens, O. Klein. Full control of the spin-wave damping in a magnetic insulator using spin-orbit torque. *Phys. Rev. Lett.* **113**, 197203 (2014).
 5. S.I. Kiselev, J.C. Sankey, I.N. Krivorotov, N.C. Emley, R.J. Schoelkopf, R.A. Buhrman, D.C. Ralph. Microwave oscillations of a nanomagnet driven by a spin-polarized current. *Nature* **425**, 380 (2003).
 6. W.H. Rippard, M.R. Pufall, S. Kaka, S.E. Russek, T.J. Silva. Direct-current induced dynamics in $\text{Co}_{90}\text{Fe}_{10}/\text{Ni}_{80}\text{Fe}_{20}$ point contacts. *Phys. Rev. Lett.* **92**, 027201 (2004).
 7. O. Prokopenko, E. Bankowski, T. Meitzler, V. Tiberkevich, A. Slavin. Spin-torque nano-oscillator as a microwave signal source. *IEEE Magn. Lett.* **2**, 3000104 (2011).
 8. S. Tsunegi, H. Kubota, K. Yakushiji, M. Konoto, S. Tamaru, A. Fukushima, H. Arai, H. Imamura, E. Grimaldi, R. Lebrun, J. Grollier, V. Cros, S. Yuasa. High emission power and Q factor in spin torque vortex oscillator consisting of FeB free layer. *Appl. Phys. Express* **7**, 063009 (2014).
 9. V.E. Demidov, S. Urazhdin, R. Liu, B. Divinskiy, A. Telegin, S.O. Demokritov. Excitation of coherent propagating spin waves by pure spin currents. *Nature Commun.* **7**, 10446 (2016).
 10. A. Giordano, R. Verba, R. Zivieri, A. Laudani, V. Puliafito, G. Gubbiotti, R. Tomasello, G. Siracusano, B. Azzzerboni, M. Carpentieri, A. Slavin, G. Finocchio. Spin-Hall nano-oscillator with oblique magnetization and Dzyaloshinskii-Moriya interaction as generator of skyrmions and nonreciprocal spin-waves. *Sci. Rep.* **6**, 36020 (2016).
 11. J. Torrejon, M. Riou, F.A. Araujo, S. Tsunegi, G. Khalsa, D. Querlioz, P. Bortolotti, V. Cros, K. Yakushiji, A. Fukushima, H. Kubota, S. Yuasa, M.D. Stiles, J. Grollier. Neuromorphic computing with nanoscale spintronic oscillators. *Nature* **547**, 428 (2017).
 12. V.E. Demidov, S. Urazhdin, H. Ulrichs, V. Tiberkevich, A. Slavin, D. Baither, G. Schmitz, S.O. Demokritov. Magnetic nano-oscillator driven by pure spin current. *Nat. Mater.* **11**, 1028 (2012).
 13. V.E. Demidov, S. Urazhdin, A. Zholud, A.V. Sadovnikov, A.N. Slavin, S.O. Demokritov. Spin-current nano-oscillator based on nonlocal spin injection. *Sci. Rep.* **5**, 8578 (2015).
 14. A. Slavin, V. Tiberkevich. Nonlinear auto-oscillator theory of microwave generation by spin-polarized current. *IEEE Trans. Magn.* **45**, 1875 (2009).
 15. V.S. Pribiag, I.N. Krivorotov, G.D. Fuchs, P.M. Braganca, O. Ozatay, J.C. Sankey, D.C. Ralph, R.A. Buhrman. Magnetic vortex oscillator driven by d.c. spin-polarized current. *Nature Phys.* **3**, 498 (2007).
 16. V.E. Demidov, S. Urazhdin, E.R.J. Edwards, M.D. Stiles, R.D. McMichael, S.O. Demokritov. Control of magnetic fluctuations by spin current. *Phys. Rev. Lett.* **107**, 107204 (2011).
 17. J. Slonczewski. Excitation of spin waves by an electric current. *J. Magn. Magn. Mater.* **195**, L261 (1999).
 18. M.A. Hofer, M.J. Ablowitz, B. Ilan, M.R. Pufall, T.J. Silva. Theory of magnetodynamics induced by spin torque in perpendicularly magnetized thin films. *Phys. Rev. Lett.* **95**, 267206 (2005).
 19. G. Consolo, L. Lopez-Diaz, B. Azzzerboni, I. Krivorotov, V. Tiberkevich, A. Slavin. Excitation of spin waves by a current-driven magnetic nanocontact in a perpendicularly magnetized waveguide. *Phys. Rev. B* **88**, 014417 (2013).
 20. A. Slavin, V. Tiberkevich. Spin wave mode excited by spin-polarized current in a magnetic nanocontact is a standing self-localized wave bullet. *Phys. Rev. Lett.* **95**, 237201 (2005).
 21. G. Consolo, B. Azzzerboni, G. Gerhart, G.A. Melkov, V. Tiberkevich, A.N. Slavin. Excitation of self-localized spin-wave bullets by spin-polarized current in in-plane magnetized magnetic nanocontacts: A micromagnetic study. *Phys. Rev. B* **76**, 144410 (2007).
 22. S. Bonetti, V. Tiberkevich, G. Consolo, G. Finocchio, P. Muduli, F. Mancoff, A. Slavin, J. Åkerman. Experimental evidence of self-localized and propagating spin wave modes in obliquely magnetized current-driven nanocontacts. *Phys. Rev. Lett.* **105**, 217204 (2010).
 23. L. Yang, R. Verba, V. Tiberkevich, T. Schneider, A. Smith, Z. Duan, B. Youngblood, K. Lenz, J. Lindner, A.N. Slavin, I.N. Krivorotov. Reduction of phase noise in nanowire spin orbit torque oscillators. *Sci. Rep.* **5**, 16942 (2015).
 24. K. Wagner, A. Smith, T. Hache, J.-R. Chen, L. Yang, E. Montoya, K. Schultheiss, J. Lindner, J. Fassbender, I. Krivorotov, H. Schultheiss. Injection locking of multiple auto-oscillation modes in a tapered nanowire spin Hall oscillator. *Sci. Rep.* **8**, 16040 (2018).
 25. Z. Duan, A. Smith, L. Yang, B. Youngblood, J. Lindner, V.E. Demidov, S.O. Demokritov, I.N. Krivorotov. Nanowire spin torque oscillator driven by spin-orbit torques. *Nature Commun.* **5**, 5616 (2014).
 26. M. Dvornik, A.A. Awad, J. Åkerman. Origin of magnetization auto-oscillations in constriction-based spin Hall nano-oscillators. *Phys. Rev. Applied* **9**, 014017 (2018).
 27. H. Mazraati, S.R. Etesami, S.A.H. Banuazizi, S. Chung, A. Houshang, A.A. Awad, M. Dvornik, J. Åkerman. Auto-oscillating spin-wave modes of constriction-based spin Hall nano-oscillators in weak in-plane fields. *Phys. Rev. Applied* **10**, 054017 (2018).
 28. M. Dvornik, J. Åkerman. Anomalous nonlinearity of the magnonic edge mode. arXiv:1804.01585 [cond-mat.mes-hall].
 29. B. Divinskiy, V.E. Demidov, S. Urazhdin, R. Freeman, A.B. Rinkevich, S.O. Demokritov. Controllable excitation of quasi-linear and bullet modes in a spin-Hall nano-oscillator. *Appl. Phys. Lett.* **114**, 042403 (2019).

30. A. Houshang, R. Khymyn, H. Fulara, A. Gangwar, M. Haidar, S.R. Etesami, R. Ferreira, P.P. Freitas, M. Dvornik, R.K. Dumas, J. Åkerman. Spin transfer torque driven higher-order propagating spin waves in nano-contact magnetic tunnel junctions. *Nature Commun.* **9**, 4374 (2018).
31. H. Ulrichs, V.E. Demidov, S.O. Demokritov. Micromagnetic study of auto-oscillation modes in spin-Hall nano-oscillators. *Appl. Phys. Lett.* **104**, 042407 (2014).
32. G. Consolo, G. Finocchio, G. Siracusano, S. Bonetti, A. Eklund, J. Åkerman, B. Azzerboni. Non-stationary excitation of two localized spin-wave modes in a nano-contact spin torque oscillator. *J. Appl. Phys.* **114**, 153906 (2013).
33. S. Bonetti, R. Kukreja, Z. Chen, F. Macià, J.M. Hernández, A. Eklund, D. Backes, J. Frisch, J. Katine, G. Malm, S. Urazhdin, A. D. Kent, J. Stöhr, H. Ohldag, H.A. Dürr. Direct observation and imaging of a spin-wave soliton with *p*-like symmetry. *Nature Commun.* **6**, 8889 (2015).

Received 18.04.19

P.B. Верб

КОНКУРЕНЦІЯ ЛІНІЙНОГО
ТА НЕЛІНІЙНОГО МЕХАНІЗМІВ
ЛОКАЛІЗАЦІЇ В СПІН-ТОРК ОСЦИЛЯТОРАХ
ЗА НАЯВНОСТІ ПОТЕНЦІАЛЬНОЇ ЯМИ

Резюме

Аналітично та числовими методами досліджується динаміка намагніченості у спін-торк осциляторах з неоднорідним профілем статичного магнітного поля, який утворює потенціальну яму. Продемонстровано, що у випадку достатньо глибокої та вузької потенціальної ями лінійний механізм локалізації домінує над нелінійною самолокалізацією, незважаючи на від'ємний нелінійний зсув частоти спінових хвиль. Зміна механізму локалізації відображається у якісно різних залежностях потужності генерації від струму накачки – у випадку лінійної локалізації реалізується м'який режим збудження автогенератора, тоді як у випадку нелінійної самолокалізації спостерігається жорсткий режим збудження. При цьому різниця профілів збуджених спін-хвильових мод стає помітною та такою, що може бути експериментально виміряною, лише у випадку несиметричного положення потенціальної ями.

4.4. Збудження невзаємних та спіральних спінових хвиль у спін-Холл осциляторах за наявності взаємодії Дзялошинського-Морія

www.nature.com/scientificreports

SCIENTIFIC REPORTS

OPEN

Received: 30 June 2016
Accepted: 06 October 2016
Published: 27 October 2016

Spin-Hall nano-oscillator with oblique magnetization and Dzyaloshinskii-Moriya interaction as generator of skyrmions and nonreciprocal spin-waves

A. Giordano¹, R. Verba², R. Zivieri³, A. Laudani⁴, V. Puliafito⁵, G. Gubbiotti⁶, R. Tomasello⁷, G. Siracusano¹, B. Azzerboni⁵, M. Carpentieri⁸, A. Slavin⁹ & G. Finocchio¹

Spin-Hall oscillators (SHO) are promising sources of spin-wave signals for magnonics applications, and can serve as building blocks for magnonic logic in ultralow power computation devices. Thin magnetic layers used as “free” layers in SHO are in contact with heavy metals having large spin-orbital interaction, and, therefore, could be subject to the spin-Hall effect (SHE) and the interfacial Dzyaloshinskii-Moriya interaction (*i*-DMI), which may lead to the nonreciprocity of the excited spin waves and other unusual effects. Here, we analytically and micromagnetically study magnetization dynamics excited in an SHO with oblique magnetization when the SHE and *i*-DMI act simultaneously. Our key results are: (i) excitation of nonreciprocal spin-waves propagating perpendicularly to the in-plane projection of the static magnetization; (ii) skyrmions generation by pure spin-current; (iii) excitation of a new spin-wave mode with a spiral spatial profile originating from a gyrotropic rotation of a dynamical skyrmion. These results demonstrate that SHOs can be used as generators of magnetic skyrmions and different types of propagating spin-waves for magnetic data storage and signal processing applications.

Spin-orbitronics combined with other sub-fields of spintronics, such as magnonics and spin-caloritronics, has created a novel paradigm in information processing which could become a viable alternative to Si-based electronics¹.

Recent experimental and theoretical developments in spin-orbitronics have clearly shown a great potential in generation of spin-currents able to compensate damping in magnetic materials^{2–6}. The spin-Hall effect (SHE) plays a dominant role in the above-mentioned experiments, as it converts the input *charge current*, flowing in a heavy metal, into a *spin-current*, diffusing perpendicularly into the adjacent ferromagnet, and creating a spin-transfer torque (STT) that acts on the ferromagnet magnetization⁷. Another interesting and highly non-trivial spin-orbital effect is the interfacial Dzyaloshinskii-Moriya interaction (*i*-DMI)⁸. Both SHE and *i*-DMI have been used to improve the performance of “racetrack” device prototypes in magnetic storage^{9,10}, to add a new degree of freedom in the design of magnetoresistive memories^{3,11}, to create nonreciprocity in the spin-wave (SW) propagation for signal processing applications^{12–14}, to excite coherent magnetization self-oscillations^{4,5}, and for the manipulation of skyrmions in ultrathin ferromagnetic materials^{15,16}. However, to the best of our knowledge, the influence of *i*-DMI on the performance of a spin-Hall oscillator (SHO) has not been studied so far^{4,5}.

¹Department of Mathematical and Computer Sciences, Physical Sciences and Earth Sciences, University of Messina, Messina, Italy. ²Institute of Magnetism, National Academy of Sciences of Ukraine, Kyiv, Ukraine. ³Department of Physics and Earth Sciences and CNISM Unit of Ferrara, University of Ferrara, Ferrara, Italy. ⁴Department of Engineering, University of Roma Tre, Roma, Italy. ⁵Department of Engineering, University of Messina, Messina, Italy. ⁶Istituto Officina dei Materiali del CNR (CNR-IOM), Sede Secondaria di Perugia, c/o Dipartimento di Fisica e Geologia, University of Perugia, Perugia, Italy. ⁷Department of Engineering, Polo Scientifico Didattico di Terni, University of Perugia, Terni, Italy. ⁸Department of Electrical and Information Engineering, Politecnico di Bari, I-70125 Bari, Italy. ⁹Department of Physics, Oakland University, Rochester, MI 48309, USA. Correspondence and requests for materials should be addressed to G.F. (email: gfinocchio@unime.it)

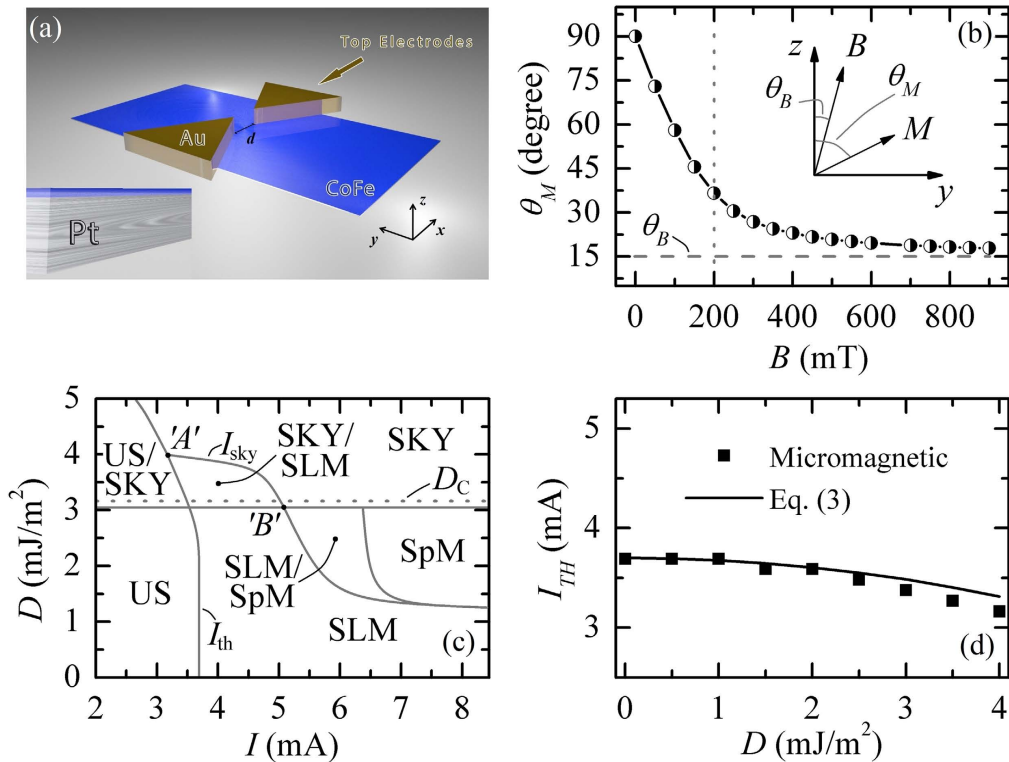


Figure 1. Sketch of the SHO device under investigation and dynamical phase diagram of this device. (a) Sketch of a bilayer composed of a CoFe ferromagnetic layer and a heavy metal layer (Pt) with a rectangular cross-section. The thick Au electrodes carry the charge current everywhere, except the inter-electrode gap of the width d , where the charge current flows inside the bilayer and excites perpendicular (vertical) spin current going into the CoFe ferromagnetic layer. A rectangular coordinate system for the above described SHO geometry is shown. (b) The angle θ_M characterizing the equilibrium direction of the static magnetization in the CoFe ferromagnetic layer as a function of the magnitude of the external bias magnetic field B . The vertical line at $B = 200$ mT separates the regions where it is possible to excite localized and propagating spin-wave modes, respectively. Inset: Cartesian coordinate reference system where the angles θ_M and θ_B are shown explicitly. (c) The phase diagram of the SHO excitations on the D vs. I plane. Seven different regions can be distinguished in this phase diagram: uniform states (US), Slonczewski linear modes (SLM), spiral modes (SpM), skyrmions (SKY), and the bistability regions uniform states/skyrmions (US/SKY), Slonczewski linear modes/spiral modes (SLM/SpM) and Slonczewski linear modes/skyrmions (SLM/SKY). The amplitude of the external field is $B = 400$ mT. The Oersted field is included in the model. D_C is the critical value of the i -DMI parameter (see explanations below), I_{th} is the threshold current, I_{sky} is the current needed to nucleate skyrmions (line between the points 'A' and 'B'); (d) Comparison between the threshold current of the SLM excitation obtained by means of micromagnetic simulations (symbols) and using the analytical formula (3) (solid line).

Here, we present the magnetization dynamics induced by the SHE in a realistic SHO structure, taking into account the influence of the i -DMI⁸. We have chosen a state-of-the-art SHO geometry (Fig. 1a) where the charge current I flows in the Pt layer along the x -axis between the golden electrodes and, due to the SHE in Pt, a spin-current is locally injected into the ultrathin extended CoFe ferromagnet (SHO “free” layer). The CoFe layer has an in-plane easy axis at zero bias field, so when a sufficiently large out-of-plane bias field is applied at an oblique angle in the “ yz ” plane (Fig. 1b), the static magnetization M of the “free” layer also goes out-of-plane, making the angle θ_M with the vertical axis “ z ”. In such a geometry, the Slonczewski *propagating* spin waves¹⁷ can be excited in any in-plane direction^{18–20} and, due to the influence of the i -DMI, they have the maximum nonreciprocity when propagating along the x -axis, perpendicular to the in-plane projection of the bias magnetic field. Our numerical simulations have shown that the wave numbers of SWs excited at a particular frequency ω and propagating along the positive and negative directions of the x -axis are different. The difference is proportional to the magnitude of the i -DMI parameter D . This result, well reproduced by a simple one-dimensional analytical model, can be used to establish a novel procedure for the experimental measurements of D . Micromagnetic simulations have also demonstrated that (i) a novel propagating spin-wave mode, characterized by a spiral spatial profile, can be excited at sufficiently large magnitudes of D and I , and (ii) skyrmions can be efficiently nucleated by the SHE in the SHO geometry. Similarly to optics^{21,22}, the excitation of spiral spin-waves in magnetism could be attractive for designing new information coding protocols. Recent experimental observations have demonstrated that skyrmions^{15,16,23–25} can be nucleated via conversion of domain walls in Ta/CoFeB/MgO²⁶, or by applying an

out-of-plane field in Ir/Co/Pt²⁷ and Pt/Co/MgO²⁸ multilayers. Although a single skyrmion can be nucleated by a spin-polarized scanning tunneling microscope²⁹, the control of its room temperature nucleation is still an experimental challenge. Earlier achievements have shown the possibility to solve this problem^{15,23,30}. Our results show an alternative method to control the nucleation of single skyrmions, based on the use of the SHE.

Results

Static characterization of the SHO structure and phase diagram of the SHO excitations. We have micromagnetically studied a Pt(5 nm)/CoFe(1 nm) SHO with a rectangular cross section of $1500 \times 3000 \text{ nm}^2$ (see Fig. 1a for the sketch of the device, including a Cartesian coordinate system where x and y are the in-plane axes, while z is the out-of-plane axis, Methods and Supplementary Note 1 for the detailed description of the micromagnetic framework and simulation parameters). Figure 1b shows the angle θ_M , characterizing the equilibrium orientation of the static magnetization in the SHO, as a function of the external bias magnetic field B . This field is applied at the tilting angle $\theta_B = 15^\circ$ with respect to the perpendicular of the SHO ferromagnetic layer in the y - z plane (see inset in Fig. 1b). As the bias field increases, the magnetization vector tends to align along the field direction.

Similarly to what is observed in STT oscillators based on the point-contact geometry, the type of the spin-wave mode excited by the SHE can be controlled by the direction of the bias magnetic field and the effective anisotropy. In particular, the materials with in-plane easy axis demonstrate excitation of self-localized spin-wave “bullets”, or co-existence of bullets and Slonczewski modes^{31,32}, for sufficiently large values of θ_M , and excitation of Slonczewski propagating spin-wave modes for sufficiently small values of θ_M ^{18,33}. In this study, numerical simulations showed that, for the bias field larger than 200 mT and $\theta_M < 37^\circ$, the Slonczewski propagating spin-wave modes were excited.

As it will be discussed below, the additional degree of freedom of the i -DMI can introduce qualitative differences in the spatial profile of the Slonczewski-type cylindrical mode, compared to the case when i -DMI is ignored. Hereafter, we focus on the results obtained at the bias field of 400 mT and active region (distance between the Au electrodes in Fig. 1a) of $d = 100 \text{ nm}$, however similar findings have been obtained at $d = 200 \text{ nm}$ and at larger bias fields (up to 800 mT).

Figure 1c shows a phase diagram of dynamical excitations in the SHO on the plane D -vs- I . Seven different regions can be identified: (i) uniform states (US), (ii) Slonczewski linear modes (SLM), (iii) spiral modes (SpM), (iv) skyrmions (SKY), as well as the bistability regions (v) uniform states/skyrmions (US/SKY), (vi) Slonczewski linear modes/skyrmions (SLM/SKY) and (vii) Slonczewski linear/spiral modes (SLM/SpM). At small values of the driving current, the SHO is in the US, i.e. in a region characterized by a uniform magnetic configuration. SLMs are excited at a critical current I_{th} that slightly decreases as a function of D (see Fig. 1d). The excited modes in the SLM region exhibit a two-dimensional radiation pattern that changes from the isotropic (see Supplementary Movies 1 and 2 for the SLM dynamics at $I = 4.22 \text{ mA}$ and $I = 5.28 \text{ mA}$ respectively, $B = 400 \text{ mT}$ and $D = 0.0 \text{ mJ/m}^2$) to the anisotropic cylindrical profile with the increase of the i -DMI parameter D (see Supplementary Movies 3 and 4 for the SLM at $I = 4.22 \text{ mA}$ and $I = 5.28 \text{ mA}$, respectively, $B = 400 \text{ mT}$ and $D = 1.5 \text{ mJ/m}^2$). The cylindrical profile of the spin-wave radiation evolves into a spiral-like profile for $1.5 \text{ mJ/m}^2 < D < 3.0 \text{ mJ/m}^2$, and a sufficiently large I (SpM region) (see as an example Supplementary Movie 5). The identification of the scenario leading to the radiation of these *spiral* spin-wave modes is one of the most important results of this study.

The SKY region is observed starting from D values near the critical value of $D_C = 3.16 \text{ mJ/m}^2$ ($D_C = 4\sqrt{A(K_u + (B_z - 0.5\mu_0 M_s)M_s)/\pi}$)³⁴. The skyrmion nucleation process, driven by the SHE, occurs together with the excitation of propagating spin-waves (see for an example Supplementary Movie 6), and at the current I_{sky} (solid line between the point ‘A’ and ‘B’). The I_{sky} curve coincides with I_{th} for D values larger than 4 mJ/m^2 (point ‘A’ in Fig. 1c). This fact constitutes the second key result of this study, i.e. the prediction that a pure spin-current with in-plane polarization can be used for the nucleation of skyrmions. The regions US/SKY, SKY/SLM and SLM/SpM are the bistability regions, obtained sweeping the current back and forth and using in each simulation the final state at the previous current. In the first of these regions, we have either a uniform ground state or skyrmions, depending on the excitation history. In particular, the US is achieved when the current is not sufficiently large to obtain the SKY region. On the other hand, when the current is large enough to reach the SKY region, skyrmions are nucleated and remain stable also at zero current, therefore the SKY state is achieved in the US/SKY region. Concerning the second region SKY/SLM, a SLM is excited if the current is increased from the US/SKY region. Skyrmions and a SLM coexist if the current is decreased from the SKY region. In the last region, an SLM (SpM) is observed, if the current is increased (decreased) from SLM (SpM) region. The origin of this hysteretic behavior will be discussed in detail below. We have also investigated the role of the Oersted field, finding that it does not influence qualitatively the results of Fig. 1c (see Supplementary Note 2 for more details).

Excitation of Slonczewski linear spin-wave mode. As it was pointed out earlier, the i -DMI leads to the excitation of nonreciprocal spin-waves. It can be observed qualitatively in the Supplementary Movies 3 and 4, and by comparing the mode profile in Fig. 2a,b. The largest nonreciprocal effect induced by the i -DMI occurs in the direction perpendicular to the in-plane projection of the static magnetization M_0 (x -axis), while the propagation along the in-plane projection of M_0 (y -axis) is reciprocal, and is characterized by the wave number that is the same as in the case of zero D (0.03 and 0.035 nm^{-1} at $I = 4.22 \text{ mA}$ and $I = 5.28 \text{ mA}$, respectively, see Supplementary Note 2). Those results are consistent with the previous experimental measurements³⁵ and the results of the analytical theory¹². The i -DMI-induced appearance of the nonreciprocal spin-waves leads to the decrease of the threshold current (Fig. 1d), and to a “red” shift of the generation frequency for increasing values of D , at a constant current (Fig. 2c). Figure 2d summarizes the dependence of the wave numbers ($|k_x|$ and $|k_{+x}|$) on D computed from the spatial distribution of the magnetization for $I = 4.22 \text{ mA}$ and $I = 5.28 \text{ mA}$. The difference between the $|k_x|$ and $|k_{+x}|$ is shown in Fig. 2e, and, as it can be noticed, is independent of I . All these numerically obtained features can

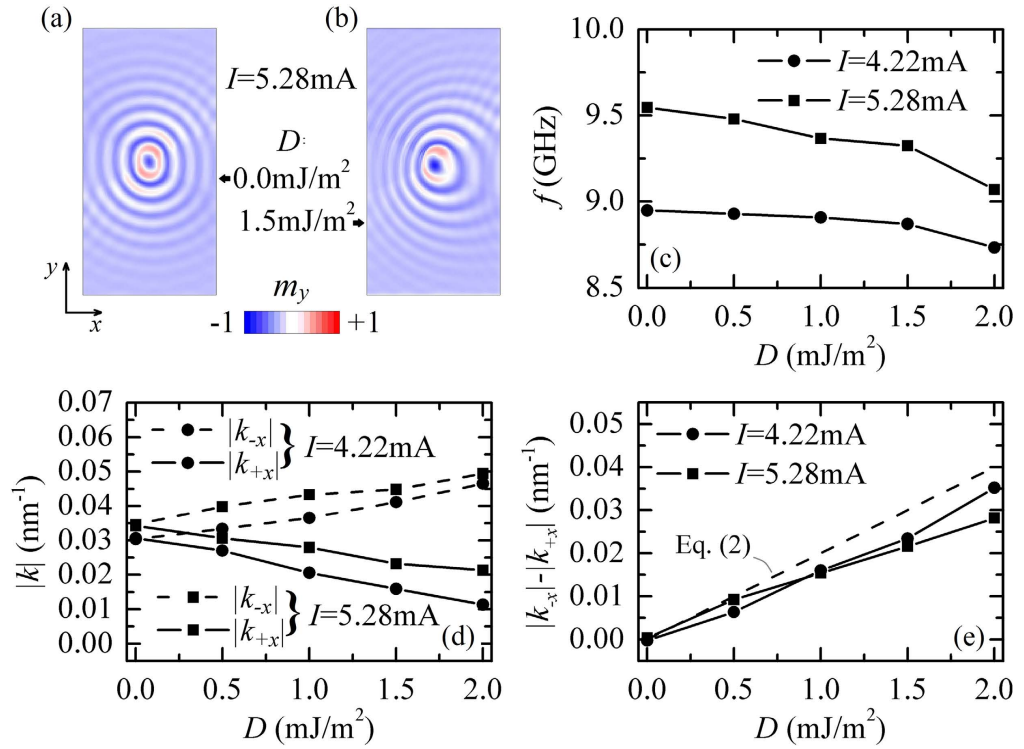


Figure 2. Non-reciprocal Slonczewski linear modes. (a,b) Example of the spatial profile of the reciprocal and nonreciprocal Slonczewski spin waves, respectively, calculated for $I=5.28$ A and $D=0.0$ and 1.5 mJ/m². (c) Oscillation frequency of the excited SLM as a function of D for two values of the driving current. (d) Wave numbers along the $-x$ and $+x$ directions as functions of D for two values of current; (e) Difference between the wave numbers along the positive and negative x -directions as a function D for the same two values of current (solid lines) and the same difference calculated analytically from Eq. (2) (dashed line).

be understood using a simple one-dimensional analytical model. In the framework of this model, we consider only the spin-waves propagating along the x -direction, where the spin-waves exhibit the largest nonreciprocity.

The frequency and wave vectors of the excited spin-waves are defined by the spatial quantization rule, which is determined by the spatial distribution of the spin-current J_s . In the case of a nonreciprocal spectrum, the general quantization rule can be written as $f(k_+ - k_-, J_s(x)) = 0^{36}$, or, equivalently $k_+ - k_- = \text{const} = f_1(J_s(x))$, where k_+ and k_- are the wave vectors of spin-waves propagating in opposite directions along the direction of maximum nonreciprocity and having the same frequency (for a reciprocal wave spectrum this rule is reduced to the condition $|k| = \text{const}$). The approximate spin-wave spectrum in the x -direction can be written as $\omega_k \approx \omega_0 + \omega_M \tilde{\lambda}^2 k_x^2 - \omega_M \tilde{D} k_x$ (see Methods), where ω_0 is the angular frequency of the ferromagnetic resonance in the SHO, $\tilde{D} = 2D/(\mu_0 M_S^2) \sin^2 \theta_M$, $\tilde{\lambda}^2 = \lambda^2 (2\omega_H + \omega_M (1 - H_{an}/M_S) \sin^2 \theta_M) / 2\omega_0$, λ is the exchange length in the material of the SHO ferromagnetic layer, and $H_{an} = 2K_u/(\mu_0 M_S)$ is the anisotropy field. From this equation, the wave vectors of counter-propagating nonreciprocal spin-waves, having the same frequency ω , can be computed as:

$$k_{\pm x} = \frac{1}{2\omega_M \tilde{\lambda}^2} (\omega_M \tilde{D} \mp \sqrt{\omega_M^2 \tilde{D}^2 + 4\omega_M \tilde{\lambda}^2 (\omega - \omega_0)}) \quad (1)$$

where k_{-x} (k_{+x}) is associated with the plus (minus) sign in the second term in the circular brackets in the equation (1). Substituting the wavenumber of equation (1) in the quantization rule, we get the condition $\sqrt{\omega_M^2 \tilde{D}^2 + 4\omega_M \tilde{\lambda}^2 (\omega - \omega_0)} = \text{const}_1$ that gives the following dependence of the generation frequency on D : $\Delta\omega = -\omega_M \tilde{D}^2 / (4\tilde{\lambda}^2)$. Thus, the generation frequency has a “red” shift with the increased D , as obtained from our micromagnetic simulations (see Fig. 2c). This effect could be easily understood by noting that the minimum spin-wave frequency in the spectrum becomes lower with the increase of D . From equation (1), it is easy to calculate the difference between the wave numbers of the excited waves:

$$k_{-x} - k_{+x} = \tilde{D} / \tilde{\lambda}^2 \quad (2)$$

and to verify that this difference is independent of the quantization constant and, therefore, of the spatial distribution of the spin-current. Hence, the condition (2) can be used for the experimental determination of the

magnitude and sign of the i -DMI parameter. Equation (2) gives a reasonable description of the simulation data, considering the same physical parameters of the SHO (Fig. 2e). Small deviation of Eq. (2) from micromagnetic results are related to the usage of approximate SW spectrum which allows us to give simple and clear qualitative explanation of the observed effect and derive explicit expression for Δk . The fact that the dependence $\Delta k(D)$ is almost the same for different I is linked to a weak nonlinear variation of the spin-wave spectrum with driving current, due to a small difference in amplitudes of the excited spin-waves. Therefore, the difference of the spin-wave numbers is mainly determined by the linear spin-wave spectrum. From an experimental point of view, a direct determination of D can be achieved by measuring the wavelength of the emitted spin-waves along the $+x$ and $-x$ direction, using the phase-resolved micro-focused Brillouin light scattering³⁷ or time-resolved Kerr microscopy³⁸. However, this method of determination of D may have practical limitations due to the fact that the wavelength of the excited spin-waves (see Fig. 2d) are in the range 0.13–0.63 μm , i.e. being comparable with the lateral resolution of the above mentioned optical techniques.

Within the above described one-dimensional model, we can also calculate the dependence of the threshold current for spin-wave excitation on D . Assuming a rectangular profile of the charge current density in the active region ($J(x) = J$ within $x = [0, d]$, and $J(x) = 0$ otherwise), one can get the following implicit expression (similar to equation (6c) in³⁹),

$$\left(\bar{k} + i \frac{\Gamma_G - \Gamma_J}{v} \right) \tan \left[\left(\bar{k} + i \frac{\Gamma_G - \Gamma_J}{v} \right) \frac{d}{2} \right] = -i \left(\bar{k} + i \frac{\Gamma_G}{v} \right) \quad (3)$$

where $\bar{k} = (k_{-x} - k_{+x})/2$ is the average wave number of excited nonreciprocal spin-waves (note, that in our notation $k_{-x} < 0$), d is the distance between the SHO golden electrodes characterizing the spatial localization of the spin-current, $v = [\omega_M^2 \tilde{D}^2 + 4\omega_M(\omega - \omega_0)\tilde{\chi}^2]^{(-1/2)}$ is the spin-wave group velocity, $\Gamma_G = \alpha_G \omega$ is the spin-wave damping, $\Gamma_J = \sigma J$ is the negative damping created by the spin-current, and $\sigma = g\mu_B \alpha_H \sin \theta_M / (2eM_s t_{\text{CoFe}})$ determines the spin-Hall efficiency (g is the Landé factor, μ_B the Bohr magneton, e the electronic charge and t_{CoFe} the CoFe layer thickness). The threshold current calculated from Eq. (3) is compared with numerical results in Fig. 1d. Here we use fitting coefficient C which relates threshold current density J_{th} found from Eq. (3) with the current $I_{\text{th}} = C J_{\text{th}}$, which value was determined from the coincidence of calculated and micromagnetic threshold currents $I_{\text{th}} = 3.7 \text{ mA}$ at $D = 0.0 \text{ mJ/m}^2$. One can see a good coincidence between the analytical and numerical results. Note that the decrease of the threshold current with D has the same nature, as a frequency “red” shift—lowering the bottom of the spin-wave spectrum with the increase of D and, consequently, the decrease of spin-wave damping $\Gamma_G = \alpha_G \omega$.

The SLM in SHOs have not been observed experimentally, since the threshold current for their excitation is expected to be very large ($> 10^9 \text{ A/cm}^2$)²⁰, around three times larger than the current necessary to excite a “bullet” spin-wave mode in an SHO with in-plane magnetization. In the SHO of this study, we were able to reduce the critical current density of one order of magnitude ($< 4 \times 10^8 \text{ A/cm}^2$) thanks to the additional perpendicular interface anisotropy in the CoFe ferromagnet. This additional anisotropy allows one to achieve the positive nonlinear frequency shift, required for the SLM excitation³³, at a higher magnetization angle θ_M , which results in the higher spin-Hall efficiency, since it is proportional to $\sin \theta_M$. A further reduction of the current density can be achieved by including an additional Ta layer above the CoFe ferromagnet²⁴.

Excitation of spin-wave modes with a spiral spatial profile. Figure 3a summarizes the spin-wave frequency as a function of I computed for $D = 0.0 \text{ mJ/m}^2$ and $D = 1.5 \text{ mJ/m}^2$ ($d = 100 \text{ nm}$). In the absence of the i -DMI, the oscillation frequency shows a monotonic increase with current, or a “blue” frequency shift, typical for the Slonczewski linear propagating spin-wave mode. A different frequency behavior is seen for $D = 1.5 \text{ mJ/m}^2$, where the frequency tunability with current becomes non-monotonic. This behavior is robust under the variation of d , as seen from Fig. 3b where $d = 200 \text{ nm}$. At sufficiently large I and D , the spin-wave is converted from the cylindrical to a spiral-like (SpM region in Fig. 1c). Figure 3c shows a spiral-type profile (the color is linked to the y -component of the magnetization).

In order to understand the origin of the spiral mode, we have performed a detailed analysis of the spatial distribution of the dynamic magnetization in the SHO ferromagnetic layer in this regime. Figure 3d–g illustrate four snapshots ($I = 6.33 \text{ mA}$) which clearly reveal the physics of the spiral mode formation. In the SpM region, the SHE is able to nucleate a dynamical soliton^{40–42}. It is characterized by a central core with the magnetization pointing along the negative out-of-plane direction (opposite to the equilibrium axis of the magnetization), and by the rotation of its boundary spins through 360° (see Fig. 3d–g). The dynamical skyrmion exhibits a rotational motion (gyration) along a circular trajectory within the region of the high current density, that is typical for solitons with nonzero topological charge under the influence of spin-current⁴³ (see Supplementary Movie 7). Dynamical skyrmion plays a role of a “source” for magnetization oscillations in the outer region, and, since the source is gyrating, the radiation acquires the form of a spiral wave, as it happens in many other fields with gyrating source^{44,45}. Note, also, that once it has been excited the SpM is still stable at lower current magnitudes in the SpM/SLM region, because the excitation of the dynamical skyrmion is linked to a sub-critical Hopf bifurcation⁴². Spiral mode is strongly nonlinear because it is originated by the interaction between a dynamical skyrmion and propagating spin-waves, this is the reason of the non-monotonic behavior of the frequency of the excited mode as a function of the current.

Generation of single skyrmions and “gas” of skyrmions. The last regions of the phase diagram of Fig. 1c are related to skyrmions. For the critical D_C , the skyrmions become energetically stable³⁴ and, after the nucleation driven by the SHE (SKY region) (see Supplementary Movie 6 for the nucleation of a single skyrmion),

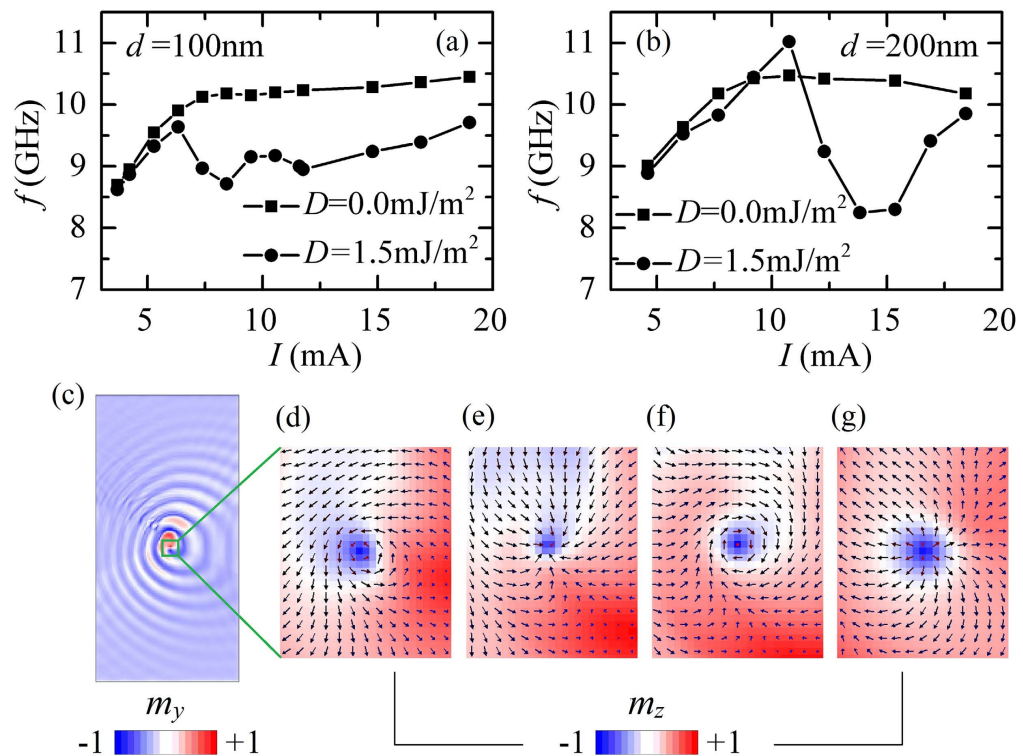


Figure 3. Excitation of a spin-wave with spiral profile. (a) Oscillation frequency of the excited mode as a function of I without and with i -DMI, for $d = 100$ nm. (b) Same as (a) but with $d = 200$ nm. (c) Example of a spatial profile of the spiral-type spin-wave for $I = 6.33$ mA and $D = 1.5$ mJ/m². (d–g) Spatial distributions of the magnetization characterizing a topological-type magnetic soliton, the current-induced gyration of which causes the radiation of a spiral-type spin wave mode.

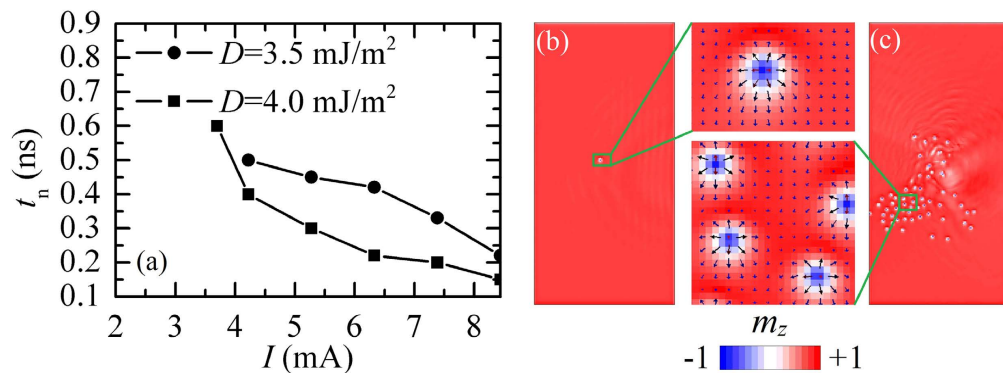


Figure 4. Skyrmion nucleation. (a) Nucleation time of a single skyrmion as a function of the current amplitude for $D = 3.5$ and 4.0 mJ/m². (b) Snapshot of a single skyrmion and zoom of the skyrmion nucleation region. (c) Snapshot of a skyrmion gas and zoom of the region indicated by a green square in the right frame.

they remain stable even when the driving current is switched off (US/SKY region). Once the skyrmion is nucleated, it is shifted along the spin-current direction, as expected for Néel skyrmions¹⁶. For D below 4.0 mJ/m² (point 'A' in Fig. 1c), I_{sky} and I_{th} split into different curves, and, hence, in the SKY/SLM region when the current increases from the uniform state, only the SLMs are excited. The presence of this region in the phase diagram is interesting from a fundamental point of view, as it identifies a scenario where the interaction between the spin-waves and skyrmions⁴⁶ can be studied. Figure 4a shows the nucleation time of a single skyrmion as a function of the current magnitude for two values of D (3.5 and 4.0 mJ/m²). It can be seen from Fig. 4a that a sub-nanosecond skyrmion nucleation time can be achieved (see Fig. 4b for a single skyrmion snapshot). Our results predict a new scenario for a single skyrmion nucleation driven by a pure spin-current. This method can be used as an alternative to the method based on the STT from a perpendicular spin-polarized current¹⁵, with the possible advantage of

the simpler fabrication process of the device. If current pulses are applied consecutively or if the current is not switched off, more skyrmions are nucleated up to a saturation value that marks a transition to a skyrmion gas phase⁴⁷. In detail, since the current is non-uniformly applied, the skyrmions tend to accumulate in one side of the ferromagnet until no more skyrmions can be hosted because of the skyrmion-skyrmion magnetostatic repulsion (see Fig. 4c for an example of the spatial distribution of the skyrmions). A skyrmion gas is, therefore, formed, and each skyrmion further nucleated is immediately annihilated (see Supplementary Movie 8). This result paves the way to study the magnetic properties of skyrmion gas described theoretically in⁴⁷.

Discussion

In our study, we propose an SHO device geometry that, combining SHE and *i*-DMI, offers a unique opportunity to study nonreciprocal effects of spin-wave propagation in two dimensional systems and to observe a new type of dynamical spin-wave modes having a spiral spatial profile. This novel spin-wave mode originates from the gyrotropic rotation of a dynamical skyrmion. From the technological point of view, the proposed SHO geometry could be useful for the development of novel generators of short propagating spin-waves in future magnonic signal processing devices. From the fundamental point of view, it is also very interesting, as it allows to study the interaction of spin-wave and skyrmions, as well as to control the number of the nucleated skyrmions by applying a properly designed current pulse.

Methods

Micromagnetic framework. Micromagnetic simulations were carried out by means of a *state-of-the-art* parallel micromagnetic solver, which numerically integrates the LLG equation including the Slonczewski-like torque due to SHE^{48,20}.

$$\frac{d\mathbf{m}}{d\tau} = -\mathbf{m} \times \mathbf{h}_{\text{EFF}} + \alpha_G \mathbf{m} \times \frac{d\mathbf{m}}{d\tau} - \frac{g\mu_B}{2\gamma_0 e M_S^2 t_{\text{CoFe}}} \alpha_H \mathbf{m} \times \mathbf{m} \times (\hat{z} \times \mathbf{J}) \quad (4)$$

where \mathbf{m} and \mathbf{h}_{EFF} are the normalized magnetization and the effective field of the ferromagnet. The effective field includes the standard magnetic field contributions, as well as the *i*-DMI and Oersted field (see also Supplementary Note 1). τ is the dimensionless time $\tau = \gamma_0 M_S t$, where γ_0 is the gyromagnetic ratio, and M_S is the saturation magnetization of the ferromagnet. α_G is the Gilbert damping, g is the Landè factor, μ_B is the Bohr Magneton, e is the electron charge, t_{CoFe} is the thickness of the ferromagnetic layer, α_H is the spin-Hall angle obtained from the ratio between the spin current and the electrical current. \hat{z} is the unit vector of the out-of-plane direction and \mathbf{J} is the in-plane current density injected via the heavy metal. The *i*-DMI energetic density expression, as derived considering the ultra-thin film hypothesis ($\frac{\partial \mathbf{m}}{\partial z} = 0$), is $\varepsilon_{i\text{-DMI}} = D[m_z \nabla \cdot \mathbf{m} - (\mathbf{m} \cdot \nabla)m_z]$, D being the parameter taking into account the intensity of the DMI, and m_z is the z -component of the normalized magnetization. By making the functional derivative of equation, the normalized *i*-DMI effective field is given by:

$$\mathbf{h}_{i\text{-DMI}} = -\frac{1}{\mu_0 M_S^2} \frac{\delta \varepsilon_{i\text{-DMI}}}{\delta \mathbf{m}} = -\frac{2D}{\mu_0 M_S^2} [(\nabla \cdot \mathbf{m})\hat{z} - \nabla m_z] \quad (5)$$

The boundary conditions related to the interfacial DMI are expressed by $\frac{d\mathbf{m}}{dn} = \frac{1}{\xi} (\hat{z} \times \mathbf{n}) \times \mathbf{m}$ where \mathbf{n} is the unit vector normal to the edge and $\xi = \frac{2A}{D}$ (being A the exchange constant) is a characteristic length in the presence of *i*-DMI.

We have studied a bilayer system Pt(5 nm)/CoFe(1 nm) with a rectangular cross section of $1500 \times 3000 \text{ nm}^2$. The electric current was locally injected into the ferromagnet via a thick Au electrode (thickness of 150 nm) with two tips located at a distance d from each other. The charge current flowing in the Pt layer gives rise to the SHE and then, to flow of perpendicular (along the “ z ” axis) pure spin current at the Pt/CoFe interface creating an anti-damping Slonczewski-like torque in the ferromagnetic layer. At sufficiently large magnitudes of the charge current his torque compensates the Gilbert losses in the ferromagnetic layer and excites in it persistent magnetization oscillations. For the results discussed in the main text, we have considered the following physical parameters of the SHO (Fig. 1a): saturation magnetization $M_S = 1 \times 10^6 \text{ A/m}$ ⁴⁹, exchange stiffness constant $A = 2.0 \times 10^{-11} \text{ J/m}$, interfacial perpendicular anisotropy induced at the boundary between CoFe and Pt characterized by the anisotropy constant $K_u = 5.5 \times 10^3 \text{ J/m}^3$ ⁵⁰, damping constant $\alpha_G = 0.03$ ⁵¹, and the spin-Hall angle $\alpha_H = 0.1$ ⁹. The ferromagnetic CoFe layer has an in-plane equilibrium magnetization at zero field which is directed along the y - in-plane direction due to the shape anisotropy of the ferromagnetic layer. The real spatial distributions of the density J_e of the charge current, density J_s of the spin current and the Oersted field were calculated numerically, as it is described in the Supplementary Note 1.

Derivation of analytical equations. The spin wave dispersion relation along the x -direction in the presence of *i*-DMI can be calculated analogously to ref. 12 and has the following form

$$\omega_k = \sqrt{(\omega_H + \omega_M \lambda^2 k_x^2)(\omega_H + \omega_M \lambda^2 k_x^2 + \omega_M(1 - H_{\text{an}}/M_S) \sin^2 \theta_M)} - \omega_M \tilde{D} k_x, \quad (6)$$

where $\omega_H = \gamma B_{\text{eff}}$, B_{eff} is the static effective field, $\omega_M = \gamma \mu_0 M_S$. In the range $\omega_M \lambda^2 k^2 \ll \omega_0$ it can be approximated as $\omega_k \approx \omega_0 + \omega_M \tilde{\lambda}^2 k_x^2 - \omega_M \tilde{D} k_x$, where $\omega_0 = \sqrt{\omega_H(\omega_H + \omega_M(1 - H_{\text{an}}/M_S) \sin^2 \theta_M)}$ is the angular frequency of the ferromagnetic resonance in the ferromagnetic layer, and $\tilde{\lambda}^2 = \lambda^2(2\omega_H + \omega_M(1 - H_{\text{an}}/M_S) \sin^2 \theta_M)/2\omega_0$.

Making a formal substitution $k_x \rightarrow -i(d/dx)$ in this dispersion equation, it is possible to obtain the following dynamical equation describing the spatial and temporal evolution of the spin wave complex amplitude a :

$$\frac{\partial a}{\partial t} = -i\omega a = -i \left(\omega_0 - \omega_M \tilde{\lambda}^2 \frac{\partial^2}{\partial x^2} + i\omega_M \tilde{D} \frac{\partial}{\partial x} \right) a - \alpha_G \omega a + \sigma J(x) a \quad (7)$$

The spin wave damping is accounted for by the term $\alpha_G \omega$ (spin wave ellipticity, which could modify the damping term⁵² in our case is small), while the influence of the spin current could be easily calculated from equation (4) within the framework of the perturbation theory⁵² and is given by the term $\sigma J(x)a$, with $\sigma = g\mu_B \alpha_H \sin \theta_M / (2eM_S t_{CoFe})$. Equation (3) for the threshold current can be obtained, analogously to ref. 13, by deriving general analytical solutions of equation (7) inside and outside the current-carrying region, and applying the boundary conditions of continuity for the spin wave complex amplitude a and its derivative. It is clear, that in the reciprocal case, when $k_x = -k_{+x}$, Eq. (3) is reduced to Eq. (6) from ref. 39.

References

- Hoffmann, A. & Bader, S. D. Opportunities at the frontiers of Spintronics. *Phys. Rev. Appl.* **4**, 047001 (2015).
- Miron, I. M. *et al.* Perpendicular switching of a single ferromagnetic layer induced by in-plane current injection. *Nature* **476**, 189–193 (2011).
- Liu, L. *et al.* Spin-Torque switching with the giant spin Hall effect of tantalum. *Science* **336**, 555–558 (2012).
- Demidov, V. E. *et al.* Magnetic nano-oscillator driven by pure spin current. *Nature Mater.* **11**, 1028–1031 (2012).
- Duan, Z. *et al.* Nanowire spin torque oscillator driven by spin orbit torques. *Nature Comm.* **5**, 5616 (2014).
- Bhowmik, D., You, L. & Salahuddin, S. Spin Hall effect clocking of nanomagnetic logic without a magnetic field. *Nature Nanotech.* **9**, 59–63 (2014).
- Sinova, J., Valenzuela, S. O., Wunderlich, J., Back, C. H. & Jungwirth, T. Spin Hall effects. *Rev. Mod. Phys.* **87**, 1213 (2015).
- Moriya, T. New mechanism of anisotropic superexchange interaction. *Phys. Rev. Lett.* **4**, 228 (1960).
- Emori, S., Bauer, U., Ahn, S.-M., Martinez, E. & Beach, G. S. D. Current-driven dynamics of chiral ferromagnetic domain walls. *Nature Mater.* **12**, 611–616 (2013).
- Ryu, K.-S., Thomas, L., Yang, S.-H. & Parkin, S. Chiral spin torque at magnetic domain walls. *Nature Nanotech.* **8**, 527–533 (2013).
- Garello, K. *et al.* Ultrafast magnetization switching by spin-orbit torques. *Appl. Phys. Lett.* **105**, 212402 (2014).
- Moon, J.-H. *et al.* Spin-wave propagation in the presence of interfacial Dzyaloshinskii-Moriya interaction. *Phys. Rev. B* **88**, 184404 (2013).
- Verba, R., Tiberkevich, V. & Slavin, A. Influence of interfacial Dzyaloshinskii-Moriya interaction on the parametric amplification of spin waves. *Appl. Phys. Lett.* **107**, 112402 (2015).
- Jamali, M., Kwon, J. H., Seo, S.-M., Lee, K.-J. & Yang, H. Spin wave nonreciprocity for logic device applications. *Sci. Rep.* **3**, 3160 (2013).
- Sampaio, J., Cros, V., Rohart, S., Thiaville, A. & Fert, A. Nucleation, stability and current-induced motion of isolated magnetic skyrmions in nanostructures. *Nature Nanotech.* **8**, 839–844 (2013).
- Tomasello, R. *et al.* A strategy for the design of skyrmion racetrack memories. *Sci. Rep.* **4**, 6784 (2014).
- Slonczewski, J. C. Excitation of spin waves by an electric current. *J. Magn. Magn. Mat.* **195**, L261–L268 (1999).
- Bonetti, S. *et al.* Experimental evidence of self-localized and propagating spin wave modes in obliquely magnetized current-driven nanocontacts. *Phys. Rev. Lett.* **105**, 217204 (2010).
- Madami, M. *et al.* Direct observation of a propagating spin wave induced by spin-transfer torque. *Nature Nanotech.* **6**, 635–638 (2011).
- Giordano, A. *et al.* Spin-Hall nano-oscillator: a micromagnetic study. *Appl. Phys. Lett.* **105**, 042412 (2014).
- Uchida, M. & Tonomura, A. Generation of electron beams carrying orbital angular momentum. *Nature* **464**, 737–739 (2010).
- Alieva, T., Rodrigo, J. A., Cámara, A. & Abramochkin, E. Partially coherent stable and spiral beams. *J. Opt. Soc. Am. A* **30**, 2237–2243 (2013).
- Iwasaki, J., Mochizuki, M. & Nagaosa, N. Current-induced skyrmion dynamics in constricted geometries. *Nature Nanotech.* **8**, 742–747 (2013).
- Woo, S. *et al.* Observation of room-temperature magnetic skyrmions and their current-driven dynamics in ultrathin metallic ferromagnets. *Nature Mater.* **15**, 501–506 (2016).
- Finocchio, G. *et al.* Skyrmion based microwave detectors and harvesting. *Appl. Phys. Lett.* **107**, 262401 (2015).
- Jiang, W. *et al.* Blowing magnetic skyrmion bubbles. *Science* **349**, 283–286 (2015).
- Moreau-Lucaire, C. *et al.* Additive interfacial chiral interaction in multilayers for stabilization of small individual skyrmions at room temperature. *Nature Nanotech.* **11**, 444–448 (2016).
- Boulle, O. *et al.* Room-temperature chiral magnetic skyrmions in ultrathin magnetic nanostructures. *Nature Nanotech.* **11**, 449–454 (2016).
- Romming, N. *et al.* Writing and deleting single magnetic skyrmions. *Science* **341**, 636–639 (2013).
- Ma, F., Ezawa, M. & Zhou, Y. Microwave field frequency and current density modulated skyrmion-chain in nanotrack. *Sci. Rep.* **5**, 15154 (2015).
- Dumas, R. K. *et al.* Spin-wave-mode coexistence on the nanoscale: a consequence of the Oersted-field-induced asymmetric energy landscape. *Phys. Rev. Lett.* **110**, 257202 (2013).
- Consolo, G. *et al.* Non-stationary excitation of two localized spin-wave modes in a nano-contact spin torque oscillator. *J. Appl. Phys.* **114**, 153906 (2013).
- Slavin, A. & Tiberkevich, V. Nonlinear auto-oscillator theory of microwave generation by spin-polarized current. *IEEE Trans. Magn.* **45**, 1875 (2009).
- Rohart, S. & Thiaville, A. Skyrmion confinement in ultrathin film nanostructures in the presence of Dzyaloshinskii-Moriya interaction. *Phys. Rev. B* **88**, 184422 (2013).
- Zhang, V. L. *et al.* In-plane angular dependence of the spin-wave nonreciprocity of an ultrathin film with Dzyaloshinskii-Moriya interaction. *Appl. Phys. Lett.* **107**, 022402 (2015).
- Glushchenko, A. G., Glushchenko, E. P., Ivanov, V. V. & Ustinova, E. S. Interference waves in nonreciprocal media. *World Scient. Discov.* **1**, 98–112 (2012).
- Madami M., Gubbiotti G., Tacchi S. & Carlotti G. Application of Microfocused Brillouin Light Scattering to the Study of Spin Waves in Low-Dimensional Magnetic Systems. *Sol. State Phys.* **63**, 79 (2012).
- Korner, H. S. *et al.* Interfacial Dzyaloshinskii-Moriya interaction studied by time-resolved scanning Kerr microscopy. *Phys. Rev. B* **92**, 220413(R) (2015).
- Consolo, G. *et al.* Excitation of spin waves by a current-driven magnetic nanocontact in a perpendicularly magnetized waveguide. *Phys Rev B* **88**, 014417 (2013).

40. Liu, R. H., Lim, W. L. & Urazhdin, S. Dynamical Skyrmion State in a Spin Current Nano-Oscillator with Perpendicular Magnetic Anisotropy. *Phys. Rev. Lett.* **114**, 137201 (2015).
41. Zhou, Y. *et al.* Dynamically stabilized magnetic skyrmions. *Nature Comm.* **6**, 8193 (2015).
42. Carpentieri, M., Tomasello, R., Zivieri, R. & Finocchio, G. Topological, non-topological and instanton droplets driven by spin-transfer torque in materials with perpendicular magnetic anisotropy and Dzyaloshinskii–Moriya Interaction. *Sci. Rep.* **5**, 16184 (2015).
43. Ivanov, B. A. & Zaspel, C. E. Excitation of Spin Dynamics by Spin-Polarized Current in Vortex State Magnetic Disks. *Phys. Rev. Lett.* **99**, 247208 (2007).
44. Kapral, R. & Showalter, K. *Chemical Waves and patterns* (Springer, 1994).
45. Loskutov, A. & Mikhailov, A. S. *Introduction to Synergetic* (Nauka, Moscow, 1990).
46. Zhang, X. *et al.* All-magnetic control of skyrmions in nanowires by a spin wave. *Nanotechnology* **26**, 225701 (2015).
47. Rodriguez, J. P. Magnetic properties of the Skyrmion gas in two dimensions. *Phys. Rev. B* **54**, 8345–8348 (1996).
48. Slonczewski, J. C. Current-driven excitation of magnetic multilayers. *J. Magn. Magn. Mat.* **159**, L1–L7 (1996).
49. Cubukcu, M. *et al.* Dzyaloshinskii–Moriya anisotropy in nanomagnets with in-plane magnetization. *Phys. Rev. B* **93**, 020401(R) (2016).
50. Emori, S. *et al.* Spin Hall torque magnetometry of Dzyaloshinskii domain walls. *Phys. Rev. B* **90**, 184427 (2014).
51. Ikeda, S. *et al.* A perpendicular-anisotropy CoFeB–MgO magnetic tunnel junction. *Nat. Mater.* **9**, 721–724 (2010).
52. Verba, R., Melkov, G., Tiberkevich, V. & Slavin, A. Collective spin-wave excitations in a two-dimensional array of coupled magnetic nanodots. *Phys. Rev. B* **85**, 014427 (2012).

Acknowledgements

This work was supported by the project PRIN2010ECA8P3 from Italian MIUR, the bilateral agreement Italy-Turkey (TUBITAK–CNR) project (CNR Grant #: B52I14002910005, TUBITAK Grant #113F378) “Nanoscale magnetic devices based on the coupling of Spintronics and Spinorbitronics”, and the executive programme of scientific and technological cooperation between Italy and China for the years 2016–2018 (code CN16GR09) title “Nanoscale broadband spin-transfer-torque microwave detector” funded by Ministero degli Affari Esteri e della Cooperazione Internazionale. The numerical simulations have been performed with the availability of SCL (Scientific Computing Laboratory) of the University of Messina, Italy. A.S. and R.V. acknowledge support from the Grant ECCS-1305586 from the National Science Foundation of the USA, from the contract with the US Army TARDEC, RDECOM, from DARPA MTO/MESO grant N66001-11-1-54114, and from the Center for NanoFerroic Devices (CNFD) and the Nanoelectronics Research Initiative (NRI). The authors thank Domenico Romolo for the graphical support. R. T. acknowledges Fondazione Carit - Projects – “Sistemi Phased-Array Ultrasonori”, and “Sensori Spintronici”.

Author Contributions

A.G., R.Z., M.C., G.G. and G.F. initiated the work and designed the numerical experiments. R.V. and A.S. developed the analytical theory and performed the analytical calculations. A.L. performed the computation of the spatial distribution of the current density and the Oersted field and wrote the supplementary note 1. A.G. performed micromagnetic simulations supported by V.P., G.S., B.A. and M.C. V.P. wrote the supplementary note 2 and prepared the last version of the figures. A.G. and G.F. analyzed the data. G.F. wrote the paper with input from R.V., A.S. and R.T. All authors contributed to the general discussion of the results and commented on the manuscript.

Additional Information

Supplementary information accompanies this paper at <http://www.nature.com/srep>

Competing financial interests: The authors declare no competing financial interests.

How to cite this article: Giordano, A. *et al.* Spin-Hall nano-oscillator with oblique magnetization and Dzyaloshinskii–Moriya interaction as generator of skyrmions and nonreciprocal spin-waves. *Sci. Rep.* **6**, 36020; doi: 10.1038/srep36020 (2016).

Publisher’s note: Springer Nature remains neutral with regard to jurisdictional claims in published maps and institutional affiliations.



This work is licensed under a Creative Commons Attribution 4.0 International License. The images or other third party material in this article are included in the article’s Creative Commons license, unless indicated otherwise in the credit line; if the material is not included under the Creative Commons license, users will need to obtain permission from the license holder to reproduce the material. To view a copy of this license, visit <http://creativecommons.org/licenses/by/4.0/>

© The Author(s) 2016

4.5. Теорія збудження невзаємних спінових хвиль у двовимірних спін-Холл осциляторах зі взаємодією Дзялошинського-Морія

PHYSICAL REVIEW B **97**, 134416 (2018)

Theory of nonreciprocal spin-wave excitations in spin Hall oscillators with Dzyaloshinskii-Moriya interaction

R. Zivieri,¹ A. Giordano,¹ R. Verba,² B. Azzarboni,³ M. Carpentieri,⁴ A. N. Slavin,⁵ and G. Finocchio^{1,*}

¹*Department of Mathematical and Computer Sciences, Physical Sciences and Earth Sciences, University of Messina, Messina, Italy*

²*Institute of Magnetism, Kyiv 03680, Ukraine*

³*Department of Engineering, University of Messina, Messina, Italy*

⁴*Department of Electrical and Information Engineering, Politecnico di Bari, I-70125 Bari, Italy*

⁵*Department of Physics, Oakland University, Rochester, Michigan 48309, USA*



(Received 27 February 2018; published 18 April 2018)

A two-dimensional analytical model for the description of the excitation of nonreciprocal spin waves by spin current in spin Hall oscillators in the presence of the interfacial Dzyaloshinskii-Moriya interaction (*i*-DMI) is developed. The theory allows one to calculate the threshold current for the excitation of spin waves, as well as the frequencies and spatial profiles of the excited spin-wave modes. It is found that the frequency of the excited spin waves exhibits a quadratic redshift with the *i*-DMI strength. At the same time, in the range of small and moderate values of the *i*-DMI constant, the averaged wave number of the excited spin waves is almost independent of the *i*-DMI, which results in a rather weak dependence on the *i*-DMI of the threshold current of the spin-wave excitation. The obtained analytical results are confirmed by the results of micromagnetic simulations.

DOI: [10.1103/PhysRevB.97.134416](https://doi.org/10.1103/PhysRevB.97.134416)

I. INTRODUCTION

In recent years, the excitation of microwave magnetization oscillations driven by a spin-polarized electric current or pure spin current has attracted much attention, both among theoreticians and experimentalists. Magnetization dynamics in spin torque oscillators (STOs) and spin Hall oscillators (SHOs) can exhibit various types of behavior, including highly nonlinear and nonstationary dynamics [1–3], making these oscillators an interesting test system for the investigation of nonlinear phenomena in ferromagnets. At the same time, STOs and SHOs demonstrate properties that make them suitable for a wide range of applications, such as generators of microwave signals [4–10], neuromorphic computing [11], microwave-assisted magnetic recording [12], etc.

The STOs and SHOs, in which spin-polarized electric current (or pure spin current) is injected locally in an unbounded ferromagnetic layer, are an important class of oscillators [13–15], because *propagating* spin waves can be excited in these oscillators in the case of out-of-plane magnetization [16–24]. The excitation of *propagating* spin waves makes these oscillators promising for signal processing applications in all spin-wave logic [25] and magnonics [26], and for the development of large arrays of phase-locked auto-oscillators efficiently coupled by the propagating spin waves [27–29].

In the case when the SHO free layer is influenced by the interfacial Dzyaloshinskii-Moriya interaction [30,31] (*i*-DMI), which is an antisymmetric exchange interaction, appearing at the interface between a ferromagnet and a heavy metal with large spin-orbit coupling [32], the SHO could acquire

an additional functionality. The *i*-DMI is known to introduce frequency nonreciprocity into the spectrum of propagating spin waves [32–36], leading to several potential physical and technological implications, such as the creation of unidirectional spin-wave emitters, the separation of signal and idler waves in frequency and wave-number domains in spin-wave devices, which use parametric and nonlinear spin-wave processes, etc. [37–40]. In recent theoretical works [41,42], it has been shown that the *i*-DMI in STO and SHO results in the excitation of two-dimensional nonreciprocal spin waves, and, at a sufficient strength of the *i*-DMI, in the generation of spiral spin-wave modes.

The main purpose of this paper is the development of an analytical model, which describes the excitation of *two-dimensional* nonreciprocal spin waves in a nanocontact SHO (the quasi-one-dimensional case of a nanowire-based SHO has been already considered theoretically in Ref. [41]). Our approach is based on an approximate solution of the linearized Landau-Lifshitz-Gilbert-Slonczewski (LLGS) equation and, in fact, is a generalization of the Slonczewski's theory [16] to the case of the presence of the *i*-DMI. The developed theory allows one to calculate profiles of the excited spin waves, which are approximately described by a combination of Laguerre's polynomials and Tricomi's hypergeometric functions, as well as to calculate the excitation threshold and frequency of excited spin waves, both of which become lower with increased *i*-DMI strength.

The paper is organized as follows. Section II describes the model system used in this study. In Sec. III, a step-by-step derivation of the analytical formalism is presented. Analytically calculated results are compared with micromagnetic modeling in Sec. IV. Finally, conclusions are given in Sec. V.

*gfinocchio@unime.it

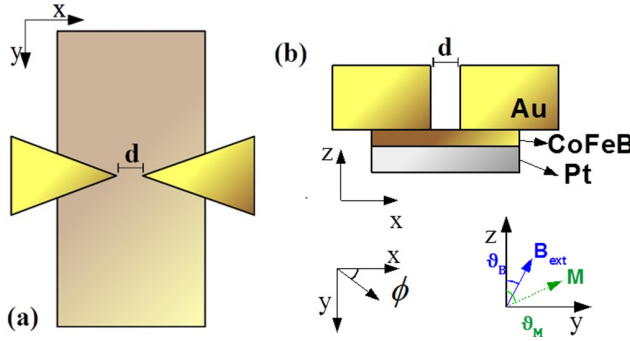


FIG. 1. Sketch of the device under investigation. (a) x - y in-plane view and (b) x - z cross section. The indication of azimuthal angle ϕ related to the wave vector, the direction of the applied field \mathbf{B}_{ext} , the angle θ_B , and the angle θ_M of the equilibrium magnetization \mathbf{M} vector are also shown.

II. DEVICE UNDER STUDY AND MICROMAGNETIC SIMULATIONS

The device under investigation is shown in Fig. 1. It is a typical SHO, consisting of a ferromagnetic/heavy-metal bilayer. The current is injected locally in the bilayer by using a gold concentrator of a double-triangular shape with a distance d between the tips. The system is biased by an external magnetic field \mathbf{B}_{ext} , applied in the y - z plane and making the angle θ_B with the film normal (axis z) [Fig. 1(b)]. A bias magnetic field is required in order to tilt the film static magnetization from the in-plane direction, and, if the angle θ_M between the static magnetization and film normal is sufficiently small, the SHO supports the excitation of propagating spin waves. Otherwise, either a nonlinear self-localized bullet mode is excited due to the negative nonlinear frequency shift, or a transient regime of mode coexistence is realized [19,43].

In our micromagnetic simulations we used the parameters of a Pt(5 nm)/CoFeB(1 nm) bilayer, having a rectangular in-plane cross section of $1500 \text{ nm} \times 3000 \text{ nm}$. The gold concentrator was assumed to be 150 nm thick, with the distance between the tips of $d = 100 \text{ nm}$. Details on the calculation of the electric current and the spin current profiles can be found in Ref. [41]. For the material parameters of the ferromagnetic layer we assumed a gyromagnetic ratio $\gamma = 2\pi \times 28 \text{ GHz/T}$, saturation magnetization $M_S = 1000 \times 10^3 \text{ A/m}$, exchange stiffness $A = 2.0 \times 10^{-11} \text{ J/m}$, constant of perpendicular surface anisotropy $K_s = 5.5 \times 10^{-4} \text{ J/m}^2$ (resulting in an effective volume anisotropy of $K_u = 5.5 \times 10^5 \text{ J/m}^3$), a Gilbert damping parameter $\alpha_G = 0.03$, and a spin Hall angle $\alpha_H = 0.1$. The i -DMI parameter D was varied in a range [44] in order to systematically study its effect on the nonreciprocal propagation of spin waves. Experimentally, an i -DMI parameter variation can be realized by the variation of the ferromagnetic film thickness or by use of a different material, covering the ferromagnetic film from another side. The external bias magnetic field was applied at an angle $\theta_B = 15^\circ$. For these parameters, the CoFeB layer had an easy-plane total (material plus shape) anisotropy. It is known that a partial compensation of the demagnetization field by perpendicular anisotropy allows one to reduce the critical

current density necessary to excite propagating spin-wave modes in a tilted external field [38]. All the micromagnetic simulations in this study have been performed using a state-of-the-art micromagnetic solver [45].

III. ANALYTICAL MODEL

In this section, we present a two-dimensional analytical model developed to study the nonreciprocal propagation of spin waves in the presence of an i -DMI interaction. In Sec. III A, we derive the linearized dynamical equation of motion for the magnetization, describing the spatial and temporal dependence of the spin-wave amplitude. Section III B is devoted to the general solution of the linearized equation of motion to obtain the analytical expression for the spatial profiles of the two-dimensional spin-wave mode, and to determine its angular-dependent wave number and group velocity. Section III C describes the calculation of the angular-dependent spin-wave wave vector, highlighting the influence of the i -DMI. In Sec. III D, the computation of the threshold current density is described, and the explicit quadratic dependence of the generation frequency on the i -DMI parameter is found. Finally, in Sec. III E, the main equations of our theoretical model are analyzed.

A. Initial equations

The dynamics of magnetization $\mathbf{M}(\mathbf{r}, t)$ of a ferromagnetic layer under the influence of spin current is described by the LLGS equation,

$$\frac{d\mathbf{M}}{dt} = \gamma \mathbf{B}_{\text{eff}} \times \mathbf{M} + \frac{\alpha_G}{M_S} \mathbf{M} \times \frac{d\mathbf{M}}{dt} - \frac{g\mu_B\alpha_H}{2eM_S^2 t_{\text{FM}}} \mathbf{M} \times \mathbf{M} \times (\mathbf{e}_z \times \mathbf{J}), \quad (1)$$

where g is the Landé factor, μ_B is the Bohr magneton, e is the electron charge, t_{FM} is the thickness of the ferromagnetic layer, α_H is the spin Hall angle, and \mathbf{J} is the electric current density flowing in the Pt layer. The effective field \mathbf{B}_{eff} includes the contributions of external field \mathbf{B}_{ext} , demagnetization, exchange, and i -DMI contributions ($\mathbf{B}_{i\text{-DMI}} = 2D/M_S^2[(\nabla \cdot \mathbf{M})\mathbf{e}_z - \nabla M_z]$, where D is the i -DMI constant).

Equation (1) is used in micromagnetic simulations, but it is too complex for the analytic analysis. From Eq. (1) one can derive a dispersion relation of linear spin waves propagating in the ferromagnetic film (for this purpose one needs to neglect the last two nonconservative terms and to represent the full magnetization of the film as a sum of its static magnetization and a small dynamic deviation) [46],

$$\omega_k = \sqrt{(\omega_H + \omega_M \lambda^2 k^2)(\omega_H + \omega_M \lambda^2 k^2 + \omega_M(1 - N_{\text{an}})\sin^2\theta_M)} + \omega_M \tilde{D} k_x, \quad (2)$$

where \mathbf{k} is the wave vector of a spin wave, $\omega_H = \gamma B_{\text{eff}}$, B_{eff} is the modulus of the effective static magnetic field, $\omega_M = \gamma\mu_0 M_S$, $N_{\text{an}} = 2K_u/(\mu_0 M_S^2)$ where K_u is the anisotropy constant, $\lambda = \sqrt{2A/(\mu_0 M_S^2)}$ is the material exchange length, and $\tilde{D} = 2D \sin\theta_M/(\mu_0 M_S^2)$ is the normalized i -DMI constant. One can see that the nonreciprocity, induced by the i -DMI, depends on the magnetization angle, and disappears in the case

of perpendicular static magnetization ($\theta_M = 0$). Therefore, it is desirable to choose a large magnetization angle, which, however, should be smaller than the critical value, corresponding to the change of sign of the nonlinear frequency shift from positive to negative, so that the propagating spin waves could be excited [19,23]. Since we consider an ultrathin ferromagnetic film, the in-plane dynamic dipolar contribution is neglected in Eq. (2). In the range $\omega_M \lambda^2 k^2 \ll \omega_0$, the dispersion relation can be approximated as

$$\omega_k \approx \omega_0 + \omega_M \tilde{\lambda}^2 k^2 + \omega_M \tilde{D} k_x, \quad (3)$$

where $\omega_0 = \sqrt{\omega_H[\omega_H + \omega_M(1 - N_{\text{an}})\sin^2\theta_M]}$ is the ferromagnetic resonance frequency and $\tilde{\lambda}^2 = \lambda^2[2\omega_H + \omega_M(1 - N_{\text{an}})\sin^2\theta_M]/2\omega_0$.

Making a formal substitution $k_x \rightarrow -i(d/dx)$, $k_y \rightarrow -i(d/dy)$ in the simplified dispersion equation, it is possible to obtain the following dynamical equation describing the spatial and temporal evolution of the spin-wave complex amplitude $a = a(x, y)$,

$$\frac{\partial a}{\partial t} = -i\omega a = -i\left(\omega_0 - \omega_M \tilde{\lambda}^2 \nabla^2 - i\omega_M \tilde{D} \frac{\partial}{\partial x}\right)a - \alpha_G \omega a + \sigma J(\mathbf{r})a, \quad (4)$$

which differs from the one used by Slonczewski [16] by the presence of the i -DMI term. The spin-wave damping is accounted for by the term $\alpha_G \omega$, while the influence of the spin current could be easily calculated from Eq. (1) within the framework of the perturbation theory [47], and is given by the term $\sigma J(\mathbf{r})a$ with the coefficient $\sigma = g\mu_B \alpha_H \sin\theta_M / (2eM_{\text{STFM}})$, describing the spin Hall efficiency and $\mathbf{r} = (x, y)$.

We have not included the Oersted field in the model (which results in a spatial dependence of ω_0), because it does not introduce any qualitative change [41]. Thus, the only spatially dependent parameter in Eq. (4) is the distribution of the current density. We approximate it in a cylindrical system (see Sec. III B) with the function $J(r) = J$ if $r < R_{\text{eff}}$ and $J(r) = 0$ otherwise with r the radial coordinate, i.e., we assume that current is flowing only within a circle of the radius R_{eff} . For spin Hall oscillators with concentrators such as the one shown in Fig. 1 it is an approximation, and the value of the effective radius R_{eff} , which is of the order of the half distance between the concentrator tips, should be determined by comparison with simulations (see Sec. IV). Simultaneously, such a case can be exactly realized in an STO [42].

B. General solution of the eigenvalue problem

Equation (4) can be considered as an eigenvalue problem, whose solution gives the values of the spin-wave excitation frequency ω and the critical current J . In the considered geometry it is convenient to express Eq. (4) in cylindrical coordinates (ρ, ϕ) ,

$$\left(\frac{\partial^2}{\partial \rho^2} + \frac{1}{\rho} \frac{\partial}{\partial \rho} + \frac{1}{\rho^2} \frac{\partial^2}{\partial \phi^2}\right)a + i\tilde{A} \left(\cos\phi \frac{\partial}{\partial \rho} - \frac{\sin\phi}{\rho} \frac{\partial}{\partial \phi}\right)a + (W + iG)a = 0. \quad (5)$$

Here, we introduce a dimensionless coordinate $\rho = r/R_{\text{eff}}$, and the following dimensionless parameters: $\tilde{A} =$

$\tilde{D}R_{\text{eff}}/\tilde{\lambda}^2$, describing the strength of the i -DMI, $W = (\omega - \omega_0)R_{\text{eff}}^2/(\omega_M \tilde{\lambda}^2)$, proportional to the generation frequency offset from the ferromagnetic resonance (FMR) frequency, and the normalized total damping G , which is equal to $G_1 = (\alpha_G \omega - \sigma J)R_{\text{eff}}^2/(\omega_M \tilde{\lambda}^2)$ within the active region ($\rho < 1$) and to $G_2 = (\alpha_G \omega)R_{\text{eff}}^2/(\omega_M \tilde{\lambda}^2)$ outside the active region.

Equation (5) does not allow an exact analytical solution, because the dependencies on the radial and azimuthal coordinates cannot be separated due to the presence of the i -DMI term. At the same time, in the absence of the i -DMI, this separation can be done rigorously, and the solution, corresponding to the lowest excitation threshold, has a simple form $a = a(\rho)$, i.e., it is radially symmetric, and does not depend on the azimuthal angle ϕ . Hence, we can assume that, at least in the range of a relatively weak i -DMI, the radially symmetric solution is only weakly modified, and the dependence on ϕ is also weak. This approximation allows us to consider the azimuthal coordinate not as an independent variable, but as a parameter which affects the radially symmetric solution $a = a_\phi(\rho)$, i.e., to neglect the derivative $\partial/\partial\phi$ in Eq. (4). As will be shown below, this approximation leads to correct dependencies of the generation frequency and threshold in the i -DMI range of interest.

Owing to the mentioned approximation, Eq. (5) is simplified to

$$\left(\frac{\partial^2}{\partial \rho^2} + \frac{1}{\rho} \frac{\partial}{\partial \rho} + i\tilde{A} \cos\phi \frac{\partial}{\partial \rho}\right)a + (W + iG)a = 0. \quad (6)$$

Equation (6) is a generalized confluent Riemann hypergeometric equation. Its general solution is a linear combination of a Laguerre's polynomial L (often known as a particular form of a Kummer's hypergeometric function) and a confluent hypergeometric function U (often known as a Tricomi's hypergeometric function) times an exponential function, namely,

$$a_\phi(\rho) = e^{-i(\alpha+\beta)\rho/2} \left[C_1 L\left(-\frac{1}{2} - \frac{\alpha}{2\beta}, i\beta\rho\right) + C_2 U\left(\frac{1}{2} + \frac{\alpha}{2\beta}, 1, i\beta\rho\right) \right], \quad (7)$$

where the parameters α and β are defined as $\alpha = \tilde{A} \cos\phi$ and $\beta_{1,2} = \sqrt{4(W + iG_{1,2}) + \tilde{A}^2 \cos^2\phi}$. The coefficients C_1, C_2 should be determined from the boundary conditions and proper asymptotes. Since the function U is divergent at $\rho \rightarrow 0$, the solution in the active region ($\rho < 1$) is given by the Laguerre's polynomial solely,

$$a_{\phi,1}(\rho) = e^{-i(\alpha+\beta_1)\rho/2} L\left(-\frac{1}{2} - \frac{\alpha}{2\beta_1}, i\beta_1\rho\right). \quad (8)$$

The solution outside the active region should have the asymptotic form of a decaying propagating wave, i.e., $a_{\phi,2}(\rho) \sim \rho^{-1/2} e^{i\kappa\rho} e^{-c_g G_2 \rho}$ with $c_g > 0$. This property is satisfied by the following combination,

$$a_{\phi,2}(\rho) = C e^{-i(\alpha+\beta_2)\rho/2} \left[L\left(-\frac{1}{2} - \frac{\alpha}{2\beta_2}, i\beta_2\rho\right) - \frac{i^{1+\alpha/\beta_2}}{\Gamma[1/2 - \alpha/(2\beta_2)]} U\left(\frac{1}{2} + \frac{\alpha}{2\beta_2}, 1, i\beta_2\rho\right) \right], \quad (9)$$

where $\Gamma[x]$ is the gamma function. The coefficient C is determined by the continuity of the solution at the boundary of the active region $a_{\phi,1}(1) = a_{\phi,2}(1)$. In the case of zero i -DMI, $\alpha = 0$, the above solutions are simplified to $a_1(\rho) = J_0(\beta_1\rho/2)$ and $a_2(\rho) = CH_0^{(1)}(\beta_2\rho/2)/2$, respectively, where J_0 and $H_0^{(1)}$ are the Bessel and Hankel functions of the zero order, which is in full accordance with Refs. [16,48].

C. Angular dependence of spin-wave wave number

Using asymptotic expansions of Laguerre polynomial and hypergeometric function, one can show that at $\rho \gg 1$ the solution expressed in Eq. (9) behaves as $a_{\phi,2}(\rho) \sim \rho^{-1/2-\alpha/2\beta_2} \exp[i(\beta_2 - \alpha)\rho/2]$, i.e., has a form of a wave, propagating from a point source, and having an angular-dependent wave number, which is determined by the term $\exp[ik_\phi r]$. The wave number is equal to $k_\phi = \text{Re}[\beta_2 - \alpha]/(2R_{\text{eff}})$, or, in the initial parameters, can be expressed as

$$k_\phi = \frac{1}{2\tilde{\lambda}^2} \left[-\tilde{D} \cos \phi + \sqrt{4 \frac{\omega - \omega_0}{\omega_M} \tilde{\lambda}^2 + \tilde{D}^2 \cos^2 \phi} \right]. \quad (10)$$

This expression can be also directly obtained from the spin-wave spectrum Eq. (3), which confirms the correct asymptotic behavior of the solution given by Eqs. (8) and (9). The exponential decay of the spin waves, caused by damping, is described by the term $\exp[-\alpha_G r/v_{\text{gr}}]$, with

$$v_{\text{gr}} = \omega_M(2\tilde{\lambda}^2 k + \tilde{D} \cos \phi) \quad (11)$$

being the spin-wave group velocity (to derive this expression we used the assumption of small damping, $\alpha_G \ll 1$).

The dependence of the spin-wave wave number on the azimuthal angle is nonreciprocal, in the sense that $k_\phi \neq k_{\pi-\phi}$, which is a consequence of the i -DMI. The averaged value of the wave number is equal to

$$\langle k \rangle = \frac{\sqrt{4(\omega - \omega_0)\tilde{\lambda}^2/\omega_M + \tilde{D}^2}}{\pi\tilde{\lambda}^2} E \left[\frac{\tilde{D}^2 \omega_M}{4(\omega - \omega_0)\tilde{\lambda}^2 + \tilde{D}^2 \omega_M} \right], \quad (12)$$

where $E[m]$ is the complete elliptic integral of the second kind. For small i -DMI it is simplified to $\langle k \rangle = \sqrt{4(\omega - \omega_0)\tilde{\lambda}^2/\omega_M + \tilde{D}^2}/(2\tilde{\lambda}^2)$. In the section below, we will find the excitation frequency ω , and will show that the averaged value of the spin-wave wave number is almost independent of \tilde{D} in the range of a relatively weak i -DMI.

D. Determination of the threshold current and generation frequency

The generation frequency and threshold current density can be determined by the application of the boundary conditions to the general solution Eqs. (8) and (9). The boundary conditions require continuity of the function $a_\phi(\rho)$ and its derivative at the boundary of the active region ($\rho = 1$). The first condition is satisfied automatically by the selection of the coefficient C in Eq. (9). However, since we use approximate solutions, the condition on the derivatives $da_{\phi,1}/d\rho|_{\rho=1} = da_{\phi,2}/d\rho|_{\rho=1}$ cannot be satisfied exactly for all the azimuthal angles ϕ simultaneously by any values of the generation frequency and the bias current density. Therefore, instead of the condition

of the exact matching of derivatives, we use the condition of the minimization of a total mismatch of the derivatives. This approach is analogous to the collocation and least squares method used to approximate numerical solutions of differential and integral equations [49–51].

For this purpose, we construct the functional of the quadratic deviation of the derivatives at the boundary of the active region,

$$\Phi[W, G_1] = \int_0^{2\pi} |\mathcal{F}(\phi)|^2 d\phi, \quad (13)$$

where

$$\mathcal{F}(\phi) = \left(\frac{da_{\phi,1}}{d\rho} - \frac{da_{\phi,2}}{d\rho} \right) \Big|_{\rho=1}. \quad (14)$$

The normalized generation frequency W and the threshold G_1 are then given by the minimum of $\Phi[W, G_1]$.

Let us find an analytical approximation for the generation frequency and threshold. Taking into account the structure of the functions $a_{\phi,i}(\rho)$, we can consider the function \mathcal{F} as the function of three variables, $\alpha = \tilde{A} \cos \phi$, β_1 , and β_2 . The value of α is proportional to the i -DMI strength, which is considered relatively small in the model. Thus, we can expand the function \mathcal{F} in a series leaving only a linear term in α , namely, $\mathcal{F} = \mathcal{F}_0 + C_f \tilde{A} \cos \phi$, where $\mathcal{F}_0 = \mathcal{F}(\tilde{A} = 0)$. After the integration, one gets $\Phi = \int_0^{2\pi} |\mathcal{F}_0| d\phi + |C_f|^2 \tilde{A}^2/2$. Consequently, the condition of the function minimum $\partial\Phi/\partial W = \partial\Phi/\partial G_1 = 0$ does not depend on C_f . This means that we can set $\alpha = 0$ in the definition of the function \mathcal{F} , at least for a small i -DMI. This property is, in fact, more general—the generation frequency and threshold should be the same for i -DMI of the same strength but opposite values, because the change $D \rightarrow -D$ corresponds to the simple inversion of the x axis. Thus, odd functions of D can be safely disregarded.

Setting $\alpha = 0$, the function in Eq. (13) is simplified to

$$\mathcal{F} = \frac{\beta_1}{2} J_0\left(\frac{\beta_1}{2}\right) H_1^{(1)}\left(\frac{\beta_2}{2}\right) - \frac{\beta_1}{2} J_1\left(\frac{\beta_1}{2}\right) H_0^{(1)}\left(\frac{\beta_2}{2}\right). \quad (15)$$

Following Ref. [16], we first consider the case of zero Gilbert damping. Then, the function of Eq. (15) has exact zero at the values $W + \tilde{A}^2 \cos^2 \phi/4 \approx 1.43$ and $G_1 = -\sigma J R_{\text{eff}}^2/(\omega_M \tilde{\lambda}^2) \approx -1.86$. One can see that the value of the normalized threshold current G_1 does not depend on the angle ϕ , thus it is the solution of the problem of minimization of the functional Φ . Since we disregard Gilbert damping at this moment, the found value of the current density J corresponds to the compensation of the radiation losses, and, as we see, this threshold value does not depend on the i -DMI. This feature will be explained below.

The last step is finding the generation frequency W . As it was pointed out, $\mathcal{F}(\phi) = 0$ if $W + \tilde{A}^2 \cos^2 \phi/4 = W_0 \approx 1.43$. The function $\mathcal{F}(\phi)$ close to this point can be expanded in a Taylor series as $\mathcal{F}(\phi) \approx C_\beta(\beta_1 - \beta_{1,0}) = C_\beta(\sqrt{W + \tilde{A}^2 \cos^2 \phi/4} - \sqrt{W_0})$ [one can directly verify that $\mathcal{F}(\phi)$ is approximately linear in $\beta_1 = \sqrt{W + \tilde{A}^2 \cos^2 \phi/4}$, but not in W]. Using this expression in Eq. (13), one finds that the minimum of the functional Φ is achieved at $W = W_0 - \tilde{A}^2/4$ with an accuracy of $O(\tilde{A}^4)$, that is, the solution we are

searching for. Returning to the initial variables, the generation frequency can be expressed as

$$\omega = \omega_0 + 1.43\omega_M \frac{\tilde{\lambda}^2}{R_{\text{eff}}^2} - \omega_M \frac{\tilde{D}^2}{4\tilde{\lambda}^2}. \quad (16)$$

The threshold current density is found after the addition of the Gilbert damping contribution. In the range of small values of the Gilbert damping (compared to the radiation losses) this contribution is simply equal to $\sigma J_G = \alpha_G \omega$ [16], because small damping does not change the spin-wave profiles, and, consequently, radiation losses. In this case its role is simply to increase the threshold current to the value $\sigma J = \sigma J_0 + \alpha_G \omega$, so that the “negative damping” in the active area $\Gamma_- = \sigma J - \alpha_G \omega$ reaches the threshold value $\Gamma_{-, \text{th}} = \sigma J_0$. Thus, summarizing all the contributions, the threshold current density turns out to be

$$\sigma J_{\text{th}} = 1.86\omega_M \frac{\tilde{\lambda}^2}{R_{\text{eff}}^2} + \alpha_G \omega. \quad (17)$$

Equations (16) and (17) are the central results of the presented analytical model. In the limit of a zero i -DMI, they are reduced to the ones derived in Ref. [16], as it should be.

E. Analysis of the obtained equations

According to Eq. (16), the presence of the i -DMI leads to a redshift of the generation frequency. This shift is *independent* of the geometry of the SHO active area, i.e., on R_{eff} , and is equal to $\Delta\omega = -\omega_M \tilde{D}^2 / 4\tilde{\lambda}^2$. The reason for the frequency shift is clear—the i -DMI results in a decrease of the minimum frequency in the spectrum of spin waves. Indeed, the expression for the spin-wave spectrum of Eq. (3) can be rewritten as

$$\omega_k = \omega_0 + \omega_M \tilde{\lambda}^2 [(k_x + \tilde{D}/2\tilde{\lambda}^2)^2 + k_y^2] - \omega_M \tilde{D}^2 / 4\tilde{\lambda}^2, \quad (18)$$

i.e., the spectrum is shifted in the k_x direction, and is lowered by a value of $\Delta\omega = -\omega_M \tilde{D}^2 / 4\tilde{\lambda}^2$. The last value is *exactly the same* as the redshift of the generation frequency. This is absolutely natural, because the exchange interaction results in a certain offset of the generation frequency from the minimum frequency in the spectrum. This offset is the same for any i -DMI, because the structure of the spectrum remains the same except for the k_x shift, to which the exchange interaction is not sensitive. Thus, one can expect that the redshift of the generation frequency $\Delta\omega = -\omega_M \tilde{D}^2 / 4\tilde{\lambda}^2$ remains the same in all the i -DMI range, not only in the range of relatively small values. Our simulations below confirm this expectation. Also, it becomes clear that in the one-dimensional case (nanowire along the x direction), the redshift is also given by the same expression, $\Delta\omega = -\omega_M \tilde{D}^2 / 4\tilde{\lambda}^2$, as shown by the exact one-dimensional analytical model in Ref. [41].

Above, we have also found that, in the absence of Gilbert damping, the generation threshold is independent of the i -DMI. In this case the threshold is determined by the compensation of the radiation losses Γ_{rad} . The radiation losses are proportional to the spin-wave group velocity given by Eq. (11), so the total radiation losses are obtained after integration over ϕ_k , and are proportional to $\Gamma_{\text{rad}} \sim \langle k \rangle$, where the averaged spin-wave wave number is given by Eq. (12). Substituting the expression

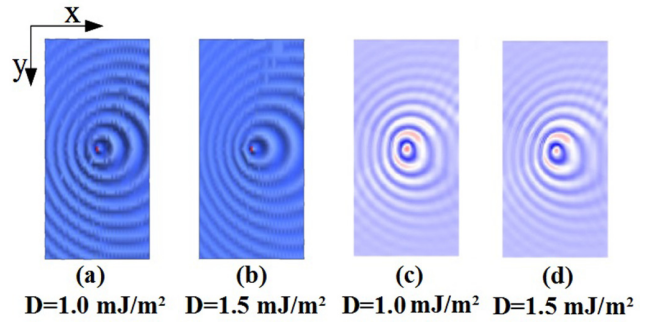


FIG. 2. Spatial profile of the excited spin-wave mode at different i -DMI strengths. (a) and (b) Theory [real part of the solution Eqs. (8) and (9)], and (c) and (d) micromagnetic simulations. The rectangular cross section is $1500 \text{ nm} \times 3000 \text{ nm}$.

for the generation frequency [Eq. (16) into Eq. (12)], one finds that, in the range of relatively small i -DMI, $\langle k \rangle \approx k_0(1 - [\tilde{D}/(2k_0\tilde{\lambda}^2)]^4/4)$, where $k_0 = \sqrt{1.43/R_{\text{eff}}}$. In the above presented model we have neglected the terms of the order of \tilde{D}^4 . Thus, the radiation losses are independent of the i -DMI within the model, and, naturally, the obtained threshold current is also independent of the i -DMI. The expression for $\langle k \rangle$ gives also the range of the i -DMI, where the model is valid, $[\tilde{D}/(2k_0\tilde{\lambda}^2)]^4/4 \ll 1$. Outside this range, one may expect a decrease of the threshold current since the averaged group velocity decreases. Moreover, if $|\tilde{D}| > 2k_0\tilde{\lambda}^2$, spin waves in certain directions become nonpropagating (evanescent), since their wave vector becomes imaginary [see Eq. (10)]. This feature was observed in simulations in Ref. [42]. However, to calculate the threshold dependence on this region analytically, one should find a way to describe a general solution without an approximation of the small values of i -DMI, which lies beyond the scope of this paper.

IV. COMPARISON WITH MICROMAGNETIC SIMULATIONS AND DISCUSSION

In this section, we compare predictions of the above presented analytical model with the results of our micromagnetic simulations. The geometry and parameters of our micromagnetic simulations are described in Sec. II, and the value of the bias magnetic field was 400 mT. In this case the parameters determined by means of the analytical model are equal to a FMR frequency $\omega_0 = 2\pi \times 7.81 \text{ GHz}$, effective exchange constant $\tilde{\lambda} = 5.64 \text{ nm}$, and an effective i -DMI parameter $\tilde{D} = D \times 0.62 \text{ nm}$, where D is expressed in mJ/m^2 . The effective radius of the active region is estimated from the difference of the generation frequency from the FMR frequency in the absence of the i -DMI. In the simulations we found $\omega_0 = 2\pi \times 7.8 \text{ GHz}$ and $\omega_{\text{gen}} = 2\pi \times 8.7 \text{ GHz}$, which, according to Eq. (16), results in the effective radius $R_{\text{eff}} = 42.2 \text{ nm}$. The effective radius is close to the half distance between the concentrator tips, as should be expected.

First, in Fig. 2 we compare the analytical approximations Eqs. (8) and (9) of the profile of an excited spin-wave mode with the micromagnetic ones. One can clearly see that spin-wave profiles deviate from a purely cylindrical symmetry, and this

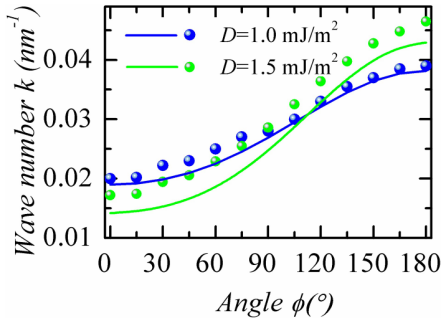


FIG. 3. Wave numbers of excited propagating spin-wave modes at different strengths of i -DMI. Symbols: micromagnetic simulation; lines: analytical expression [Eq. (10)].

deviation increases with the i -DMI, as expected. The analytical approximation describes micromagnetic spin-wave profiles reasonably well, and the weak deviation is related to the spatial distribution of the spin current, which is not of perfect radial symmetry (see, e.g., Supplemental Material in Ref. [41]), as was assumed in the model.

A quantitative comparison of the spin-wave profiles can be made via the calculation of the angular dependence of the spin-wave wave number (see Fig. 3). Analytically, this dependence is given by Eq. (10), in which one should calculate the generation frequency using Eq. (16). Micromagnetic dependence was found by a calculation of the distances between the zeros directly from the time evolution of the spatial distribution of the magnetization. The spin-wave wave number monotonically increases when the azimuthal angle is varied from $\phi = 0^\circ$ ($+x$ direction) to $\phi = 180^\circ$ ($-x$ direction); at negative angles the dependence is symmetric, $k(-\phi) = k(\phi)$. The maximum difference of the wave numbers $k(180^\circ) - k(0)$ is determined solely by the i -DMI strength, while the mean value mainly by the size of the active region. Again, we note quite a good description of the micromagnetic data by the analytical expression.

Next, we look at the dependence of the generation frequency on the i -DMI, which is shown in Fig. 4(a). Simulated frequencies follow the predicted trend, and decrease with the i -DMI as $\Delta\omega = -\omega_M \tilde{D}^2 / 4\lambda^2$. It should be noted that the equality of the characteristic contributions of the i -DMI and nonuniform exchange interaction, which corresponds to the condition $|\tilde{D}| = 2k_0\tilde{\lambda}^2$ [when the argument of the elliptic integral in Eq. (12) is equal to 1], in our case takes place at an i -DMI strength $D = 2.93 \text{ mJ/m}^2$. Thus, the redshift of the generation frequency follows the same trend not only in the range of relatively small i -DMI values, but remains the same for a large i -DMI, as was predicted in Sec. III E.

Additionally, to prove this feature, we analyzed the data of micromagnetic simulation in Ref. [42], where STO with an active area of exactly circular shape was studied. We use the data presented for the smallest bias current (3 mA), for which the nonlinear effects should be small. In that case, the characteristic value of the i -DMI, when its effect becomes the same as the effect of an exchange interaction, is 0.85 mJ/m^2 . As one can see from the inset in Fig. 4(a), the generation frequency follows the dependence of Eq. (16) in all the studied

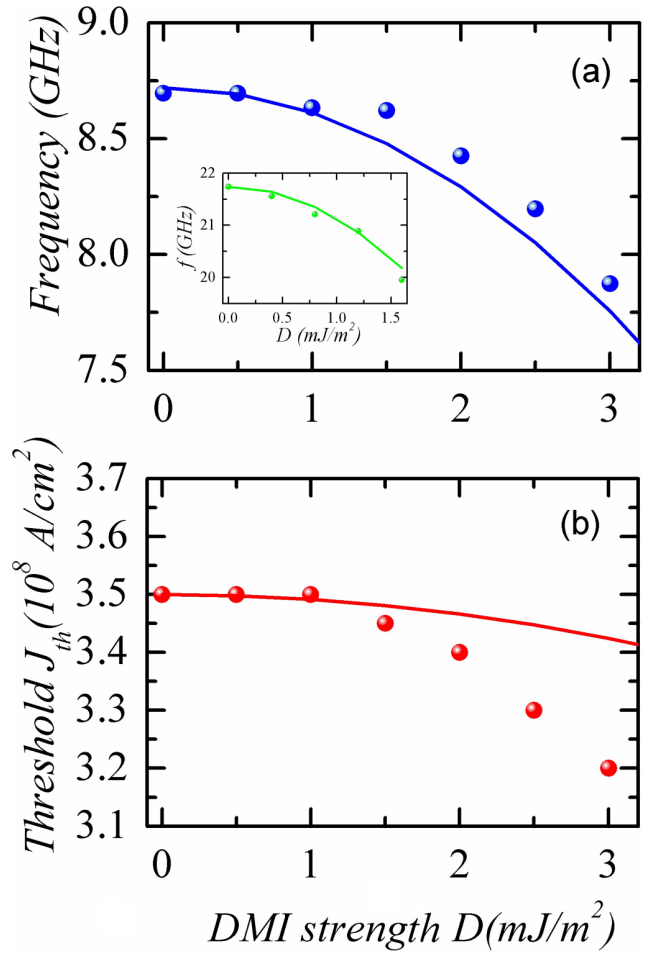


FIG. 4. Dependences of (a) the generation frequency and (b) threshold current density on the i -DMI strength. Symbols: micromagnetic data; lines: analytical model [Eqs. (16) and (17), respectively]. The inset in (a) shows the dependence of the generation frequency for the STO studied micromagnetically in Ref. [42]: Points are the micromagnetic data retrieved from Fig. 2(a) in Ref. [42] at a bias current of 3 mA, and the line shows the result of the analytical model [Eq. (16)].

i -DMI range, including the range where i -DMI becomes dominant ($D > 0.85 \text{ mJ/m}^2$).

For the calculation of the threshold current density [see Fig. 4(b)] one needs the value of the spin Hall efficiency $\sigma = \sigma_0 \sin \theta_M$. The theoretically calculated value is $\sigma_0 = 5.8 \times 10^{-3} \text{ m}^2/(\text{A s})$. By determining the value of σ_0 from the matching of the calculated threshold by means of Eq. (17) in the absence of i -DMI and the micromagnetic data, we get a slightly higher value of $\sigma_0 = 6.6 \times 10^{-3} \text{ m}^2/(\text{A s})$. This discrepancy is mainly attributed to a nonuniform spatial distribution of the current density, created by the concentrators. Below, we use the last value of the spin Hall efficiency for analytical calculations of the threshold current.

According to Eq. (17), which is valid in the range of relatively small i -DMI, the threshold current weakly depends on the i -DMI, because only the Gilbert losses are dependent on the i -DMI due to an i -DMI-induced redshift of the generation frequency, while the radiation losses do not depend

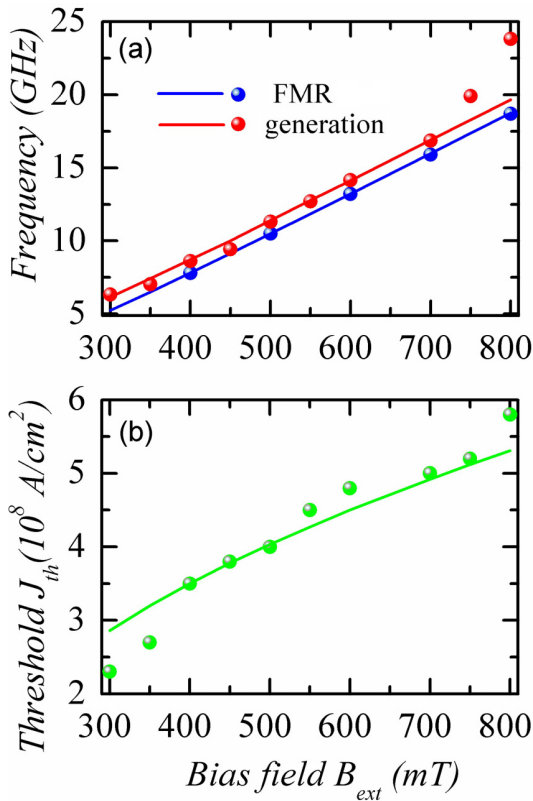


FIG. 5. (a) Frequency of FMR and frequency of the excited spin waves at the threshold as functions of the bias magnetic field. (b) Dependence of the threshold current on the bias magnetic field. Symbols: micromagnetic data; lines: analytical theory. The figures are plotted for the case of zero i -DMI.

on the i -DMI. In the range of relatively small i -DMI values ($D \leq 1.5$ mJ/m²) our micromagnetic simulations confirm this prediction. However, when the strength of the i -DMI becomes comparable to the strength of the exchange interaction, we observed a decrease of the generation threshold current. As was pointed out in Sec. III E, this decrease is related with a decrease of the averaged spin-wave group velocity, and, consequently, of the radiation losses.

Finally, we should note that the presented theory is rigorously valid for the STOs with a circular active region, while in the case of an SHO with concentrators one needs to use adjusting parameters, the effective radius R_{eff} and modified spin Hall efficiency σ . To check if these parameters are set solely by the geometry of the concentrators, we made simulations for different values of the bias magnetic field, which leads to a different magnetization angle, and compared these results with the corresponding curves calculated analytically. The i -DMI in this part of the study is not taken into account, since the effects of the i -DMI on the generation frequency and threshold do not depend on the R_{eff} [see Eqs. (16) and (17)]. As one can see from Fig. 5(a), the generation frequency has a constant offset from the FMR frequency, and it is almost perfectly described by the analytical expression Eq. (16) with a constant $R_{eff} = 42.2$ nm. The dependence of the threshold current density on the bias field [see Fig. 5(b)] also agrees very

well with the numerically calculated one in all the bias field range, especially noting that the accuracy of the determination of the critical parameters in simulations is often not very high, because of the properties of numerical noise. Summarizing this part, we found that the adjustable parameters of the analytical model are determined by the current density distribution, and could be found from one to two reference points of micromagnetic simulations.

V. CONCLUSIONS

In summary, in this paper, we have proposed an analytical model for the description of the excitation of two-dimensional nonreciprocal spin waves in spin torque and spin Hall oscillators in the presence of i -DMI. In the range of weak and moderate i -DMI the analytical problem of the spin-wave excitation is reduced to the eigenvalue problem for the generalized confluent Riemann equation. The profiles of the excited spin waves are described by a linear combination of a Laguerre's polynomial and a confluent hypergeometric function, and exhibit nonreciprocal behavior with the angular dependence of the spin-wave wave number.

It is shown that the frequency of the excited spin waves at the threshold exhibits a quadratic redshift with an increase of the i -DMI strength. This shift is a direct consequence of the lowering of the spin-wave spectrum bottom in the presence of the i -DMI. Therefore, this shift is proportional to the ratio between the characteristic i -DMI length and the exchange length, and could be expressed by the same functional dependence in all the studied i -DMI range, including the range where i -DMI makes a dominant contribution to the properties of the excited spin waves.

At the same time, the averaged spin-wave wave number and spin-wave group velocity are almost independent of the i -DMI in the range of small and moderate i -DMI. Consequently, the radiation losses remain the same, and the i -DMI affects the excitation threshold current only via its weak influence on the Gilbert losses, which are proportional to the generation frequency. However, when the effect of the i -DMI becomes comparable to or greater than that of the exchange interaction, we observed a decrease of the generation threshold, which is attributed to the decrease of the averaged group velocity.

ACKNOWLEDGMENTS

This work was supported by the executive programme of scientific and technological cooperation between Italy and China for the years 2016–2018 (code CN16GR09) title “Nanoscale broadband spin-transfer-torque microwave detector” funded by Ministero degli Affari Esteri e della Cooperazione Internazionale. This work was also supported in part by Grants No. EFMA-1641989 and No. ECCS-1708982 from the U.S. NSF, and by a DARPA M3IC grant under Contract No. W911-17-C-0031. R.Z. acknowledges support from the National Group of Mathematical Physics (GNFM-INdAM). R.V. acknowledges support from the Ministry of Education and Science of Ukraine (Project No. 0118U004007).

- [1] G. Bertotti, I. Mayergoyz, and C. Serpico, *Nonlinear Magnetization Dynamics in Nanosystems* (Elsevier, Amsterdam, 2009).
- [2] P. K. Muduli, O. G. Heinonen, and J. Åkerman, Decoherence and Mode Hopping in a Magnetic Tunnel Junction Based Spin Torque Oscillator, *Phys. Rev. Lett.* **108**, 207203 (2012).
- [3] G. Consolo, G. Finocchio, G. Siracusano, S. Bonetti, A. Eklund, J. Åkerman, and B. Azzèrboni, Non-stationary excitation of two localized spin-wave modes in a nano-contact spin torque oscillator, *J. Appl. Phys.* **114**, 153906 (2013).
- [4] A. Slavin and V. Tiberkevich, Nonlinear auto-oscillator theory of microwave generation by spin-polarized current, *IEEE Trans. Magn.* **45**, 1875 (2009).
- [5] Z. Zeng, G. Finocchio, and H. Jiang, Spin transfer nano-oscillators, *Nanoscale* **5**, 2219 (2013).
- [6] B. Wang, H. Kubota, K. Yakushiji, S. Tamaru, H. Arai, H. Imamura, A. Fukushima, and S. Yuasa, Diameter dependence of emission power in MgO-based nano-pillar spin-torque oscillators, *Appl. Phys. Lett.* **108**, 253502 (2016).
- [7] S. Tsunegi, K. Yakushiji, A. Fukushima, S. Yuasa, and H. Kubota, Microwave emission power exceeding 10 μ W in spin torque vortex oscillator, *Appl. Phys. Lett.* **109**, 252402 (2016).
- [8] L. Yang, R. Verba, V. Tiberkevich, T. Schneider, A. Smith, Z. Duan, B. Youngblood, K. Lenz, J. Lindner, A. N. Slavin, and I. N. Krivorotov, Reduction of phase noise in nanowire spin orbit torque oscillators, *Sci. Rep.* **5**, 16942 (2015).
- [9] A. Giordano, M. Carpentieri, A. Laudani, G. Gubbiotti, B. Azzèrboni, and G. Finocchio, Spin-Hall Nano-oscillator: A micromagnetic study, *Appl. Phys. Lett.* **105**, 042412 (2014).
- [10] V. Puliafito, A. Giordano, F. Garesci, M. Carpentieri, B. Azzèrboni, and G. Finocchio, Scalable synchronization of spin-Hall oscillators in out-of-plane field, *Appl. Phys. Lett.* **109**, 202402 (2016).
- [11] J. Torrejon, M. Riou, F. A. Araujo, S. Tsunegi, G. Khalsa, D. Querlioz, P. Bortolotti, V. Cros, K. Yakushiji, A. Fukushima, H. Kubota, S. Yuasa, M. D. Stiles, and J. Grollier, Neuromorphic computing with nanoscale spintronic oscillators, *Nature (London)* **547**, 428 (2017).
- [12] J. G. Zhu, X. Zhu, and Y. Tang, Microwave assisted magnetic recorder, *IEEE Trans. Magn.* **44**, 125 (2008).
- [13] M. V. Tsoi, A. G. M. Jansen, J. Bass, W. C. Chiang, M. Seck, V. Tsoi, and P. Wyder, Excitation of a Magnetic Multilayer by an Electric Current, *Phys. Rev. Lett.* **80**, 4281 (1998); Erratum: Excitation of a Magnetic Multilayer by an Electric Current, **81**, 493(E) (1998).
- [14] V. E. Demidov *et al.*, Magnetic nano-oscillator driven by pure spin current, *Nat. Mater.* **11**, 1028 (2012).
- [15] V. E. Demidov, S. Urazhdin, A. Zholud, A. V. Sadovnikov, A. N. Slavin, and S. O. Demokritov, Spin-current nano-oscillator based on nonlocal spin injection, *Sci. Rep.* **5**, 8578 (2015).
- [16] J. C. Slonczewski, Excitation of spin waves by an electric current, *J. Magn. Magn. Mater.* **195**, L261 (1999).
- [17] L. Berger, Emission of spin waves by a magnetic multilayer traversed by a current, *Phys. Rev. B* **54**, 9353 (1996).
- [18] M. A. Hofer, M. J. Ablowitz, B. Ilan, M. R. Pufall, and T. J. Silva, Theory of Magnetodynamics Induced by Spin Torque in Perpendicularly Magnetized Thin Films, *Phys. Rev. Lett.* **95**, 267206 (2005).
- [19] S. Bonetti, V. Tiberkevich, G. Consolo, G. Finocchio, P. Muduli, F. Mancoff, A. Slavin, and J. Åkerman, Experimental Evidence of Self-Localized and Propagating Spin Wave Modes in Obliquely Magnetized Current-Driven Nanocontacts, *Phys. Rev. Lett.* **105**, 217204 (2010).
- [20] V. E. Demidov, S. Urazhdin, and S. O. Demokritov, Direct observation and mapping of spin waves emitted by spin-torque nano-oscillators, *Nat. Mater.* **9**, 984 (2010).
- [21] T. J. Silva and W. H. Rippard, Developments in nano-oscillators based upon spin-transfer point-contact devices, *J. Magn. Magn. Mater.* **320**, 1260 (2008).
- [22] Z. Duan *et al.*, Nanowire spin torque oscillator driven by spin orbit torques, *Nat. Commun.* **5**, 5616 (2014).
- [23] G. Consolo, L. Lopez-Diaz, B. Azzèrboni, I. Krivorotov, V. Tiberkevich, and A. Slavin, Excitation of Spin Waves by a Current-Driven Magnetic Nanocontact in a Perpendicularly Magnetized Waveguide, *Phys. Rev. B* **88**, 014417 (2013).
- [24] V. E. Demidov, S. Urazhdin, R. Liu, B. Divinskiy, A. Telegin, and S. O. Demokritov, Excitation of coherent propagating spin waves by pure spin currents, *Nat. Commun.* **7**, 10446 (2016).
- [25] T. Schneider, A. A. Serga, B. Leven, B. Hillebrands, R. L. Stamps, and M. P. Kostylev, Realization of spin-wave logic gates, *Appl. Phys. Lett.* **92**, 022505 (2008).
- [26] B. Lenk, H. Ulrichs, F. Garbs, and M. Münzenberg, The building blocks of magnonics, *Phys. Rep.* **507**, 107 (2011).
- [27] A. N. Slavin and V. S. Tiberkevich, Theory of mutual phase locking of spin-torque nanosized oscillators, *Phys. Rev. B* **74**, 104401 (2006).
- [28] S. Kaka, M. R. Pufall, W. H. Rippard, T. J. Silva, S. E. Russek, and J. A. Katine, Mutual phase-locking of microwave spin torque nano-oscillators, *Nature (London)* **437**, 389 (2005).
- [29] A. Houshang, E. Iacocca, P. Dürrenfeld, S. R. Sani, J. Åkerman, and R. K. Dumas, Spin-wave-beam driven synchronization of nanocontact spin-torque oscillators, *Nat. Nanotechnol.* **11**, 280 (2016).
- [30] I. Dzyaloshinskii, A thermodynamic theory of “weak” ferromagnetism of antiferromagnetics, *J. Phys. Chem. Solids* **4**, 241 (1958).
- [31] T. Moriya, New Mechanism of Anisotropic Superexchange Interaction, *Phys. Rev. Lett.* **4**, 228 (1960).
- [32] L. Udvardi and L. Szunyogh, Chiral Asymmetry of the Spin-Wave Spectra in Ultrathin Magnetic Films, *Phys. Rev. Lett.* **102**, 207204 (2009).
- [33] J.-H. Moon, S.-M. Seo, K.-J. Lee, K.-W. Kim, J. Ryu, H.-W. Lee, R. D. McMichael, and M. D. Stiles, Spin-wave propagation in the presence of interfacial Dzyaloshinskii-Moriya interaction, *Phys. Rev. B* **88**, 184404 (2013).
- [34] A. A. Stashkevich, M. Belmeguenai, Y. Roussigné, S. M. Cherif, M. Kostylev, M. Gabor, D. Lacour, C. Tiusan, and M. Hehn, Experimental study of spin-wave dispersion in Py/Pt film structures in the presence of an interface Dzyaloshinskii-Moriya interaction, *Phys. Rev. B* **91**, 214409 (2015).
- [35] K. Di, V. Li Zhang, H. Siah Lim, S. Choon Ng, M. Hau Kuok, X. Qiu, and H. Yang, Asymmetric spin-wave dispersion due to Dzyaloshinskii-Moriya interaction in an ultrathin Pt/CoFeB film, *Appl. Phys. Lett.* **106**, 052403 (2015).
- [36] S. Tacchi, R. E. Troncoso, M. Ahlberg, G. Gubbiotti, M. Madami, J. Åkerman, and P. Landeros, Interfacial Dzyaloshinskii-Moriya Interaction in Pt/CoFeB films: Effect of the Heavy-Metal Thickness, *Phys. Rev. Lett.* **118**, 147201 (2017).

- [37] R. Verba, V. Tiberkevich, and A. Slavin, Influence of interfacial Dzyaloshinskii-Moriya interaction on the parametric amplification of spin waves, *Appl. Phys. Lett.* **107**, 112402 (2015).
- [38] F. Garcia-Sanchez, P. Borys, A. Vansteenkiste, J.-V. Kim, and R. L. Stamps, Nonreciprocal spin-wave channeling along textures driven by the Dzyaloshinskii-Moriya interaction, *Phys. Rev. B* **89**, 224408 (2014).
- [39] J. H. Kwon, J. Yoon, P. Deorani, J. M. Lee, J. Sinha, K.-J. Lee, M. Hayashi, and H. Yang, Giant nonreciprocal emission of spin waves in Ta/Py bilayers, *Sci. Adv.* **2**, e1501892 (2016).
- [40] T. Brächer, O. Boulle, G. Gaudin, and P. Pirro, Creation of unidirectional spin-wave emitters by utilizing interfacial Dzyaloshinskii-Moriya interaction, *Phys. Rev. B* **95**, 064429 (2017).
- [41] A. Giordano *et al.*, Spin-Hall nano-oscillator with oblique magnetization and Dzyaloshinskii-Moriya interaction as generator of skyrmions and nonreciprocal spin-waves, *Sci. Rep.* **6**, 36020 (2016).
- [42] L. Yang, P. Dürrenfeld, X. Ruan, W. Liu, L. He, Y. Xu, and Y. Zhou, Directional Spin Wave in Spin-Torque Oscillators Induced by Interfacial Dzyaloshinskii-Moriya Interaction, *IEEE Magn. Lett.* **8**, 3509504 (2017).
- [43] R. K. Dumas, E. Iacocca, S. Bonetti, S. R. Sani, S. M. Mohseni, A. Eklund, J. Persson, O. Heinonen, and J. Åkerman, Spin-Wave-Mode Coexistence on the Nanoscale: A Consequence of the Oersted-Field-Induced Asymmetric Energy Landscape, *Phys. Rev. Lett.* **110**, 257202 (2013).
- [44] M. Cubukcu, J. Sampaio, K. Bouzehouane, D. Apalkov, A. V. Khvalkovskiy, V. Cros, and N. Reyren, Dzyaloshinskii-Moriya anisotropy in nanomagnets with in-plane magnetization, *Phys. Rev. B* **93**, 020401(R) (2016).
- [45] L. Lopez-Diaz, D. Aurelio, L. Torres, E. Martinez, M. A. Hernandez-Lopez, J. Gomez, O. Alejos, M. Carpentieri, G. Finocchio, and G. Consolo, *J. Phys. D: Appl. Phys.* **45**, 323001 (2012).
- [46] D. Cortés-Ortuño and P. Landeros, Influence of the Dzyaloshinskii-Moriya interaction on the spin-wave spectra of thin films, *J. Phys.: Condens. Matter* **25**, 156001 (2013).
- [47] V. V. Naletov, G. de Loubens, G. Albuquerque, S. Borlenghi, V. Cros, G. Faini, J. Grollier, H. Hurdequint, N. Locatelli, B. Pigeau, A. N. Slavin, V. S. Tiberkevich, C. Ulysse, T. Valet, and O. Klein, Identification and selection rules of the spin-wave eigenmodes in a normally magnetized nanopillar, *Phys. Rev. B* **84**, 224423 (2011).
- [48] We use the definition of complex magnetization variable a , conjugated comparing to Ref. [16]. This results in the change of sign before the damping term in Eq. (4) and a consequent change of the Hankel function in our work to the one in Ref. [16].
- [49] E. A. Vlasova, V. S. Zarubin, and G. N. Kuvyrkin, *Approximate Methods of Mathematical Physics* (MSTU publishing, Moscow, 2001).
- [50] T. Zhu and S. N. Atluri, A modified collocation method and a penalty formulation for enforcing the essential boundary conditions in the element free Galerkin method, *Comput. Mech.* **21**, 211 (1998).
- [51] J. C. Newman, An improved method of collocation for the stress analysis of cracked plates with various shaped boundaries, NASA Technical Note D-6376, 1971.

РОЗДІЛ 5

**РОЗРАХУНОК ДИСПЕРСІЙНИХ ЗАЛЕЖНОСТЕЙ, СТАЛИХ ЗАТУХАННЯ,
ТА КОЕФІЦІЄНТІВ НЕЛІНІЙНОЇ ВЗАЄМОДІЇ СПІНОВИХ ХВИЛЬ У
НАНОРОЗМІРНИХ МАГНІТНИХ ХВИЛЕВОДАХ**

У цьому розділі розглядаються питання, які безпосередньо не пов'язані зі взаємодією електричних полів та струмів зі СХ, але є необхідними для розрахунку характеристик та проектування будь-яких нанорозмірних пристроїв та систем магنونіки, у тому числі електрично керованих.

У підрозділі 5.1 представлений метод розрахунку сталих затухання СХ мод, у тому числі за наявності нелокальних та/або неоднорідних механізмів дисипації. Такі механізми стають більш суттєвими саме при зменшенні характерних розмірів — неоднорідності динамічної чи/ти статичної намагніченості, розміру феромагнітного зразка, тощо — до наномасштабів. Крім того, такі нелокальні механізми як поздовжня та поперечна спінова дифузія характерна саме для провідних феромагнетиків, які розглядаються у попередніх розділах.

У підрозділі 5.2 розглядаються особливості структури СХ мод у нанорозмірних феромагнітних хвилеводах, які пов'язані, у першу чергу, зі змінами так званого “ефективного дипольного пінінгу” на краях хвилеводу. Зокрема, встановлено, коли класична теорія СХ мод у тонких хвилеводах стає незастосовною через сумірні масштаби неоднорідності динамічного дипольного поля з шириною хвилеводу і необхідно використовувати повні рівняння для розрахунку профілів та дисперсії СХ мод. У підрозділі розглядаються хвилеводи ЗІГ, для яких групою проф. А. Чумака (Технічний університет Кайзерслаутерна) були проведені експериментальні дослідження. Однак, ці явища не менш важливі і для надтонких хвилеводів з металевих феромагнетиків. Наприклад, оцінка характерної ширини w_{crit} хвилеводу, нижче якої профілі СХ мод перестають бути частково закріпленими на латеральних краях (рівняння (4) у підрозділі 5.2) для хвилеводу Fe товщиною 1 нм дає $w_{crit} \approx 25$ нм, що якраз знаходиться в області інтересу з точки зору магنونних застосувань.

У підрозділах 5.3-5.4 розглянуто роботу спрямованого СХ відгалужувача на основі дипольно взаємодіючих хвилеводів, який може стати важливим універсальним елементом магنونних кіл. Тут теоретичні розрахунки також проведені для хвилеводів ЗІГ, що дає можливість провести порівняння з експериментальними даними. Однак, такий СХ відгалужувач можна створити і на основі тонких металевих хвилеводів, адже суттєво більша намагніченість насичення та менша мінімально можлива відстань між хвилеводами (внаслідок простішої технології літографії порівняно з ЗІГ) дозволяє отримати суттєвий дипольний зв'язок незважаючи на малу товщину хвилеводів. Наприклад, для хвилеводів Fe товщиною 2 нм, шириною 20 нм, та відстанню між хвилеводами 5 нм довжина передачі енергії ("coupling length" нижче) на частотах 15-20 ГГц складає 60-300 нм, що є абсолютно прийнятним для застосувань. У підрозділі 5.3 представлена детальна теорія СХ відгалужувача та порівняння з результатами мікромагнітного моделювання (проведеного Ч. Вангом), а в підрозділі 5.4 проведене порівняння з експериментальними результатами та досліджено нелінійний режим роботи відгалужувача. Також, у підрозділі 5.4 проведені оцінки енергоспоживання пристроїв магنونної логіки на прикладі напівсуматора та параметричного підсилувача, в тому числі і з накачкою НВЧ електричним полем за рахунок ефекту ЕКМА.

Насамкінець, у підрозділі 5.5 узагальнено гамільтонів формалізм для нелінійної СХ динаміки на випадок присутності несиметричних взаємодій, найяскравішим представником яких у надтонких феромагнітних хвилеводах та плівках є ІВДМ, та, у якості прикладу застосування формалізму, проведені розрахунки невзаємності СХ спектру у структурах з ІВДМ залежно від потужності СХ.

Автором дисертації розроблено формалізм для розрахунку сталих затухання СХ та проведені розрахунки для випадку присутності спінової дифузії, запропоновано пояснення ефекту розкріплення профілів СХ мод у нанорозмірних хвилеводах, отримані аналітичні вирази для опису дипольної взаємодії СХ у сусідніх хвилеводах, проаналізовано механізми нелінійності спрямованого СХ

відгалужувача та отримані аналітичні рівняння для опису помірно нелінійного режиму роботи відгалужувача, зроблені оцінки енергоспоживання параметричного підсилювача на основі ЕКМА та магнетронного напівсуматора, а також проведений аналіз правил масштабування напівсуматора, та проведено узагальнення гамільтонового формалізму для розрахунку коефіцієнтів нелінійної СХ взаємодії на випадок присутності несиметричних взаємодій, за допомогою якого проведені розрахунки нелінійного зсуву частоти СХ у феромагнітній плівці та наносмушці за наявності ІВДМ.

5.1. Затухання спінових хвиль за наявності неоднорідних та нелокальних механізмів дисипації

PHYSICAL REVIEW B **98**, 104408 (2018)

Damping of linear spin-wave modes in magnetic nanostructures: Local, nonlocal, and coordinate-dependent damping

Roman Verba*

Institute of Magnetism, Kyiv 03680, Ukraine

Vasil Tiberkevich and Andrei Slavin

Department of Physics, Oakland University, Rochester, Michigan 48309, USA



(Received 29 May 2018; published 6 September 2018)

A general perturbation theory for the description of weak damping of linear spin-wave modes in magnetic nanostructures is developed. This perturbative approach allows one to account for the usual uniform Gilbert damping, as well as for the spatially nonuniform (coordinate-dependent) and nonlocal (magnetization-texture-dependent) Gilbert-like dissipation mechanisms. Using the derived general expression, it is possible to calculate the damping rate of a particular spin-wave mode if the frequency and the spatial profile of this mode, along with the relevant parameters of a magnetic material, are known. The examples demonstrating the applications of the developed general formalism include (i) generalization of the damping rate of a spin-wave mode propagating in a magnetic sample for the case of a nonuniform static magnetization or/and bias magnetic field, (ii) calculation of a damping rate of a gyrotropic mode in a vortex-state magnetic nanodot, (iii) evaluation of the spin diffusion influence on the damping rate of spin-wave modes in a conducting ferromagnet, and (iv) calculation of damping rates of spin-wave modes in a ferromagnetic film in the presence of a spin pumping into an adjacent nonmagnetic metal layer. The developed formalism is especially useful in micromagnetic simulations, as it allows one to calculate damping rates of spin-wave modes based on the numerical solution of a conservative eigenmode problem.

DOI: [10.1103/PhysRevB.98.104408](https://doi.org/10.1103/PhysRevB.98.104408)

I. INTRODUCTION

Understanding the mechanisms of magnetic damping and ability to calculate damping rates for magnetic eigenexcitations—spin-wave (SW) modes—is critically important for the applications of magnetic materials in data storage, information processing, and microwave technologies. In particular, the SW damping rate determines such important characteristics as the time of the magnetization reversal of a magnetic memory element (in precessional regime) [1], the linewidth of a ferromagnetic resonance [2], the threshold current in spin-torque devices [3], etc. A rigorous consideration of a magnetic damping, even in bulk ferromagnetics, is very complicated, since there are many different mechanisms of energy dissipation, such as magnon-electron and magnon-phonon scattering. Also multimagnon processes could contribute to the damping rate of some SW modes [2,4].

Instead of a rigorous consideration, magnetic damping is, usually, taken into account phenomenologically using the Gilbert model [5], within which the dissipative torque, acting on magnetization, is proportional to the time derivative of magnetization and the Gilbert damping parameter α_G . The damping rate of a SW mode is then given by $\Gamma_\nu = \alpha_G \epsilon_\nu \omega_\nu$, where ω_ν is the mode frequency and the coefficient ϵ_ν describes the effect of the magnetization precession ellipticity. Analytical expressions for ϵ_ν were derived in many important

particular cases, e.g., for spin waves propagating in a uniformly magnetized ferromagnetic film [6], for the gyrotropic mode of magnetic vortex [7], etc. The Gilbert model describes the magnetic damping in bulk ferromagnetic samples reasonably well within several limitations, in particular, when the damping rate is relatively small, and the magnitude of the dynamic magnetization is also not large. Recently, the Gilbert model of magnetic dissipation was also generalized to the case of a substantially nonlinear magnetization dynamics [8].

In thin ferromagnetic films and magnetic nanostructures, in addition to the bulk uniform damping, other damping mechanisms, such as spatially nonuniform (coordinate dependent) or nonlocal (dependent on the magnetization texture) damping could be present. These additional damping mechanisms include the spin pumping from a ferromagnetic layer into an adjacent normal metal layer [9,10], longitudinal and transverse spin diffusion [11–13], chiral damping [14], and spin-wave scattering on technological imperfections [15,16] (edge damage). In many cases, these coordinate-dependent and magnetization-texture-dependent damping mechanisms could be of the same order of magnitude or stronger than the traditional uniform Gilbert damping, and, also, could create different contribution to the SW modes having different spatial profiles [17–19]. Naturally, these mechanisms cannot be taken into account by a simple renormalization of a Gilbert damping constant α_G , same for all the SW modes.

In several particular cases, the influence of the interlayer spin pumping and transverse spin diffusion on the damping rate of SW modes with different spatial profiles has been

*corresponding author: verrv@ukr.net

already discussed [18–26]. In this paper, we present a general formalism, which allows one to calculate the SW mode damping rate in the presence of the uniform Gilbert damping, as well as the coordinate-dependent and magnetization-texture-dependent damping mechanisms. As shown below, when the damping rate is relatively small, it can be calculated, provided one knows the SW mode frequency and spatial profile, obtained in the *conservative* approach. It is especially important since for many practically important cases the problem of calculation of the SW mode profile has been already solved. In many cases, the SW mode profile can be obtained numerically using various powerful and general micromagnetic codes [27,28]. In contrast, accurate micromagnetic simulations of *dissipative* processes require much more simulation time. Also, common micromagnetic codes, typically, can take into account only the standard uniform Gilbert damping, while accounting for the additional dissipation mechanisms requires a substantial modification and a subsequent verification of the micromagnetic code.

The paper has the following structure. In Sec. II, following Refs. [29–31], we review the elements of the general theory of linear SW excitation in magnetic structures. Using this theory, a general expression for the SW mode damping rate under the influence of a linear magnetic damping is derived in Sec. III. Then, we present examples of application of the developed formalism, showing how its results are related to the previous results obtained in several known particular cases, as well as demonstrating some new results. In Sec. IV, we consider the SW damping caused by a uniform Gilbert damping in magnetic samples with nonuniform static magnetization, in particular, in vortex-state magnetic dots. The effects of additional dissipation mechanisms, such as spin diffusion and interlayer spin pumping, are considered in Secs. V and VI, respectively. Finally, conclusions are given in Sec. VII.

II. PRINCIPAL EQUATIONS

Let us consider the magnetization dynamics of a finite-size ferromagnetic sample, e.g., film, nanodot, etc. The conservative dynamics of a magnetization vector $\mathbf{M} = \mathbf{M}(\mathbf{r}, t)$ in such a case is described by the Landau-Lifshitz equation

$$\frac{\partial \mathbf{M}(\mathbf{r}, t)}{\partial t} = \gamma (\mathbf{B}_{\text{eff}} \times \mathbf{M}(\mathbf{r}, t)), \quad (2.1)$$

where γ is the modulus of the gyromagnetic ratio and $\mathbf{B}_{\text{eff}} = \mathbf{B}_e - \mu_0 \hat{\mathbf{G}} * \mathbf{M}$ is the effective magnetic field. Here, \mathbf{B}_e is an external magnetic field and the self-adjoint tensor operator $\hat{\mathbf{G}}$ describes the magnetic self-interaction: nonuniform exchange, magnetodipolar interaction, and magnetic anisotropy (explicit expression for $\hat{\mathbf{G}}$ could be found, e.g., in Refs. [29,31]).

Considering *linear* dynamical processes one can represent the magnetization vector as $\mathbf{M}(\mathbf{r}, t) = M_s [\boldsymbol{\mu}(\mathbf{r}) + \mathbf{m}(\mathbf{r}, t)]$, where M_s is the saturation magnetization, the unit vector $\boldsymbol{\mu}$ describes the static magnetic configuration of the ferromagnetic sample, and the dimensionless vector \mathbf{m} describes the small deviation from the static configuration. Using this representation in Eq. (2.1) one can, finally, obtain the following equation for frequencies ω_ν and profiles \mathbf{m}_ν of the SW eigenmodes of

a ferromagnetic body:

$$-i\omega_\nu \mathbf{m}_\nu = \boldsymbol{\mu} \times \hat{\boldsymbol{\Omega}} * \mathbf{m}_\nu, \quad (2.2)$$

where $\hat{\boldsymbol{\Omega}}$ is the Hamiltonian operator defined by the expression $\hat{\boldsymbol{\Omega}} = \gamma B \hat{\mathbf{I}} + \gamma \mu_0 M_s \hat{\mathbf{G}}$, B is the modulus of the static effective field, and $\hat{\mathbf{I}}$ is the identity matrix. In the same manner, one can, also, consider the propagating spin waves (e.g., in a ferromagnetic film), which are characterized by their wave vector \mathbf{k} . The only change in this case appears in the definition of the Hamiltonian operator, which should be defined as $\hat{\boldsymbol{\Omega}}_{\mathbf{k}} = \gamma B \hat{\mathbf{I}} + \gamma \mu_0 M_s e^{-i\mathbf{k}\cdot\mathbf{r}} (\hat{\mathbf{G}} * e^{i\mathbf{k}\cdot\mathbf{r}})$. Naturally, the Hamiltonian operators $\hat{\boldsymbol{\Omega}}$ and $\hat{\boldsymbol{\Omega}}_{\mathbf{k}}$ are also self-adjoint. Using this property, one can show that different SW modes of a ferromagnetic body satisfy the following orthogonality relation:

$$\langle \mathbf{m}_{\nu'}^* \cdot \boldsymbol{\mu} \times \mathbf{m}_\nu \rangle = -i A_\nu \delta_{\nu, \nu'}, \quad (2.3)$$

where index ν is used to enumerate the SW modes, symbols $\langle \dots \rangle$ denote averaging over all the volume of the ferromagnetic material, and A_ν is a real normalization constant of an SW eigenmode.

The influence of various small effects on the magnetization dynamics can be effectively considered in the framework of a perturbation theory. In a general case, accounting for a perturbation leads to the change of the effective field in Eq. (2.1) as $\mathbf{B}_{\text{eff}} \rightarrow \mathbf{B}_{\text{eff}} + \mathbf{b}$, where $\mathbf{b}(\mathbf{r})$ is an effective perturbation field, which could depend on time or/and on the magnetization \mathbf{M} . Considering only the processes that are linear in SW mode amplitudes, one can represent the dynamic magnetization as an infinite series in SW eigenmodes. Using this representation in the perturbed Landau-Lifshitz equation, one can obtain the following dynamical equation for the SW eigenmode amplitudes $c_\nu(t)$:

$$\frac{dc_\nu}{dt} = -i\omega_\nu c_\nu + i\gamma b_\nu - i\gamma \sum_{\nu'} (S_{\nu, \nu'} c_{\nu'} + \tilde{S}_{\nu, \nu'} c_{\nu'}^*). \quad (2.4)$$

Here, the summation goes only over modes with positive norms, $A_{\nu'} > 0$ (see details in Ref. [30]) and the coefficients are equal to

$$b_\nu = \frac{1}{A_\nu} \langle \mathbf{m}_\nu^* \cdot \mathbf{b} \rangle, \quad (2.5a)$$

$$S_{\nu, \nu'} = \frac{1}{A_\nu} \langle (\mathbf{m}_\nu^* \cdot \mathbf{m}_{\nu'}) (\boldsymbol{\mu} \cdot \mathbf{b}) \rangle, \quad (2.5b)$$

$$\tilde{S}_{\nu, \nu'} = \frac{1}{A_\nu} \langle (\mathbf{m}_\nu^* \cdot \mathbf{m}_{\nu'}^*) (\boldsymbol{\mu} \cdot \mathbf{b}) \rangle. \quad (2.5c)$$

The above derived equations allow one to effectively describe the excitation of SW modes by an external microwave field, parametric processes under the parallel pumping, thermal fluctuations, etc., and, as it will be shown below, also describe the damping of the SW eigenmodes.

III. GENERAL PERTURBATION FORMALISM FOR THE LINEAR SPIN-WAVE DAMPING

In the framework of a Gilbert model, magnetic damping is taken into account phenomenologically by an additional term in the right-hand side of the Landau-Lifshitz equation

Eq. (2.1):

$$\mathbf{T}_G = \frac{\alpha_G}{M_s} \left(\mathbf{M} \times \frac{\partial \mathbf{M}}{\partial t} \right). \quad (3.1)$$

Many other dissipation mechanisms could be introduced by a similar, Gilbert-like term,

$$\mathbf{T}_{ad} = \frac{1}{M_s} \left(\mathbf{M} \times \left(\hat{\mathbf{D}}_{ad} * \frac{\partial \mathbf{M}}{\partial t} \right) \right). \quad (3.2)$$

Here, $\hat{\mathbf{D}}_{ad}$ is, in general, a tensor operator which could depend both on the spatial coordinate \mathbf{r} and on the magnetization \mathbf{M} , but for the most common *linear* damping mechanisms it should not depend on the time derivative of the magnetization $\partial \mathbf{M} / \partial t$, since $\partial \mathbf{M} / \partial t$ is proportional to the SW amplitude. Note that for the dynamics of a constant-length magnetization vector \mathbf{M} , $|\mathbf{M}| = M_s$, only the component of the torque \mathbf{T}_{ad} that is parallel to the vector $(\mathbf{M} \times \partial \mathbf{M} / \partial t)$ corresponds to the change of a magnetic energy, and, therefore, is responsible for the magnetic dissipation [4,8]. The other torque component, which is parallel to $(\partial \mathbf{M} / \partial t)$, affects the conservative magnetization dynamics, i.e., makes a contribution to the SW mode eigenfrequencies. Thus the effects that are described by Eq. (3.2), in general, could lead both to a change of the SW mode damping rate and to the change of its eigenfrequency.

Using the additional torque term in the form (3.2) one can take into account various dissipation mechanisms. In general, Eq. (3.2) could describe any mechanism of the intrinsic magnetic energy dissipation of a “liquid friction” type, which are, typically, the most important linear intrinsic damping mechanisms in bulk ferromagnets and ferromagnetic nanostructures. Below we consider in detail the influence of the spin diffusion and interlayer spin pumping (see Secs. V and VI) on the resultant dissipation rate of an SW mode. Also, using the formalism, presented below, one can easily consider additional damping in ferromagnets and their structures having large Rashba spin-orbit coupling. In this case, the dissipative torque has exactly the structure (3.2) with the damping tensor dependent on the static magnetization configuration (see explicit expression in Ref. [32]). Another important dissipation mechanism is the dynamic feedback in the ferromagnet–spin-Hall-metal heterostructures [33]. The corresponding dissipative torque in this case has linear and nonlinear terms; the last one, naturally, is important only for large-amplitude dynamics. The linear term can be also derived in the form of Eq. (3.2) with the damping tensor $\hat{\mathbf{D}}_{fb} = \alpha_{fb} \mathbf{e}_{z'} \otimes \mathbf{e}_{z'}$, where \otimes denotes dyadic product of vectors, axis z' is directed perpendicularly to the ferromagnetic-normal metal interface and the coefficient α_{fb} determines the efficiency of the dynamic feedback (see explicit expression in Ref. [33]).

The extrinsic mechanisms of energy pumping or dissipation, like a spin-torque produced by an external spin-polarized current (or a pure spin current) are described by a different term in the equation of motion [3,34,35]. This term is not proportional to the derivative $\partial \mathbf{M} / \partial t$, but, it could also be taken into account by a formalism similar to the one presented below.

Thus, as it follows from Eqs. (3.1) and (3.2), the effects of the common Gilbert damping and additional Gilbert-like

damping mechanisms are described by the following effective field:

$$\mathbf{b} = \frac{1}{\gamma M_s} \hat{\mathbf{D}} * \frac{\partial \mathbf{M}}{\partial t}, \quad (3.3)$$

where $\hat{\mathbf{D}} = \alpha_G \hat{\mathbf{I}} + \hat{\mathbf{D}}_{ad}$. If the damping is relatively weak (i.e., if the damping rate of an SW mode is much smaller than the mode eigenfrequency), it can be considered using a perturbation theory.

In the above presented expression, we can use the zero-order approximation for the time derivative in the form

$$\partial \mathbf{M} / \partial t = M_s \sum_{\nu} [-i\omega_{\nu} c_{\nu} \mathbf{m}_{\nu} + \text{c.c.}], \quad (3.4)$$

which allows us to calculate explicitly the coefficients (2.5). The terms $S_{\nu\nu'} c_{\nu'}$ and $\tilde{S}_{\nu\nu'} c_{\nu'}^*$ in Eq. (2.4) correspond to three-magnon nonlinear interaction processes. These terms are of the second order of magnitude with respect to the SW amplitudes c_{ν} , and, thus, can be safely ignored in the consideration of the linear (small-amplitude) spin-wave dynamics. Finally, one gets the following equation describing the dynamics of the SW modes:

$$\frac{dc_{\nu}}{dt} = -i\omega_{\nu} c_{\nu} - \sum_{\nu'} (\Gamma_{\nu,\nu'} c_{\nu'} + \tilde{\Gamma}_{\nu,\nu'} c_{\nu'}^*), \quad (3.5)$$

where the coefficients are equal to

$$\Gamma_{\nu,\nu'} = \frac{\omega_{\nu'}}{A_{\nu}} \langle \mathbf{m}_{\nu}^* \cdot \hat{\mathbf{D}} * \mathbf{m}_{\nu'} \rangle, \quad \tilde{\Gamma}_{\nu,\nu'} = -\frac{\omega_{\nu'}}{A_{\nu}} \langle \mathbf{m}_{\nu}^* \cdot \hat{\mathbf{D}} * \mathbf{m}_{\nu'}^* \rangle. \quad (3.6)$$

It is clear, that the accounting for the magnetic dissipation leads to an additional dissipative coupling between the different SW modes, which results in a variation of the damping rates, mode profiles, and, to a smaller degree, the eigenfrequencies of the coupled modes in comparison with the case of zero intermode coupling. However, typically, the mode damping rates are small compared to the frequency difference between the neighboring SW eigenfrequencies, and one can safely ignore this damping-related coupling. In such a case, one obtains a standard equation for a damped oscillator, $dc_{\nu} / dt = -i\omega_{\nu} c_{\nu} - \Gamma_{\nu} c_{\nu}$, where the damping rate is defined as

$$\Gamma_{\nu} \equiv \Gamma_{\nu,\nu} = \frac{\omega_{\nu}}{A_{\nu}} \langle \mathbf{m}_{\nu}^* \cdot \hat{\mathbf{D}} * \mathbf{m}_{\nu} \rangle. \quad (3.7)$$

The damping-related coupling of the SW eigenmodes should be explicitly taken into account only near the points of SW mode degeneracy.

It follows from Eq. (3.7), that the common Gilbert damping in a ferromagnetic material could be described by the following expression for the SW mode damping rate:

$$\Gamma_{\nu} = \alpha_G \epsilon_{\nu} \omega_{\nu}, \quad (3.8)$$

where

$$\epsilon_{\nu} = \frac{\langle |\mathbf{m}_{\nu}|^2 \rangle}{A_{\nu}}. \quad (3.9)$$

The properties of the “ellipticity” coefficient ϵ_{ν} are discussed below. If one assumes that the Gilbert dissipation parameter is coordinate-dependent, $\alpha_G = \alpha_G(\mathbf{r})$, the SW mode damping

rate is defined as $\Gamma_v = \omega_v \langle \alpha_G |\mathbf{m}_v|^2 \rangle / A_v$. Such dependence takes place, for instance, near the boundaries of magnetic elements due to the technological imperfections [16,18]. Naturally, in such a case, the imperfections strongly affect the dissipation of the SW modes, which have greater oscillation power $|\mathbf{m}_v|^2$ in the spatial regions where the effective damping constant α_G is increased.

Representing the total damping rate of an SW mode, caused by different mechanisms, as

$$\Gamma_v = (\alpha_G + \Delta\alpha_{G,v})\epsilon_v\omega_v, \quad (3.10)$$

we arrive to the following expression for the effective enhancement of the Gilbert damping parameter, caused by additional dissipation mechanisms:

$$\Delta\alpha_{G,v} = \frac{\langle \mathbf{m}_v^* \cdot \hat{\mathbf{D}}_{ad} * \mathbf{m}_v \rangle}{\langle |\mathbf{m}_v|^2 \rangle}. \quad (3.11)$$

Obviously, the enhanced damping parameter affects differently the SW modes having a different spatial profiles, but this enhanced parameter does not depend directly on the SW mode eigenfrequency.

IV. EVALUATION OF A GILBERT DAMPING FOR SPIN-WAVE MODES

A. Relation of a Gilbert damping rate to the precession ellipticity and parameters of the spin-wave dispersion

As we have already pointed out, the damping rate of an SW mode, caused by common Gilbert damping, is determined by the mode structure via the coefficient ϵ_v [Eq. (3.8)]. In the case of a spatially uniform magnetization precession, this coefficient can be directly related to the precession ellipticity:

$$\epsilon = 1 + \frac{\mathcal{E}^2}{2(1 - \mathcal{E})}, \quad (4.1)$$

where $\mathcal{E} = 1 - m_{\min}/m_{\max}$ is the commonly used definition for the precession ellipticity [2]. It is clear that for circularly polarized magnetization precession, when $\mathcal{E} = 0$, the coefficient $\epsilon = 1$. When the magnetization precession becomes elliptically polarized, the value ϵ increases, and the damping rate becomes larger than $\alpha_G\omega_v$. This property of the SW mode damping is well-known in literature (see, e.g., Ref. [2]).

The value of the coefficient ϵ_v can be, also, related to the dispersion relation of a particular SW mode. As it was shown by D. Stancil [6], in the case of SWs, propagating in a ferromagnetic film having *uniform* static magnetization at an arbitrary angle to the film plane, the coefficient ϵ_v can be expressed as

$$\epsilon_v = \frac{\partial\omega_v}{\partial\omega_H}, \quad (4.2)$$

where ω_v is the SW mode dispersion relation, and $\omega_H = \gamma B$, where B is the static internal magnetic field. The relation of the damping rate to the derivative $\partial\omega_v/\partial\omega_H$ becomes clear if one notes that for a uniform static magnetization, accounting of the Gilbert damping leads to only one modification in the linearized equation of motion, $\omega_H \rightarrow \omega_H + i\alpha_G\omega$ (see Eq. (1.68) in Ref. [2]). For the cases of the in-plane or perpendicular static magnetization of a film, expression (4.2)

is simplified since $\partial\omega_v/\partial\omega_H = \gamma^{-1}\partial\omega_v/\partial B_e$, where B_e is the external magnetic field. This derivative can be easily calculated from the experimental data, and, therefore, can be used for the characterization of the SW modes and their damping rates.

Here we show that a relation similar to Eq. (4.2) can be derived in a general case when the static magnetization and the internal bias magnetic field of a magnetic sample can be coordinate-dependent. For this purpose, we take a variational derivative of both sides of Eq. (2.2) over some variable ξ . A straightforward calculation results in the following equation:

$$\begin{aligned} & -(i\omega_v + \boldsymbol{\mu} \times \hat{\boldsymbol{\Omega}}) * \frac{\delta\mathbf{m}_v}{\delta\xi} \\ & = \left(i \frac{\delta\omega_v}{\delta\xi} + \boldsymbol{\mu} \times \frac{\delta\hat{\boldsymbol{\Omega}}}{\delta\xi} + \frac{\delta\boldsymbol{\mu}}{\delta\xi} \times \hat{\boldsymbol{\Omega}} \right) * \mathbf{m}. \end{aligned} \quad (4.3)$$

Then, multiplying the above equation by $(\mathbf{m}_v^* \cdot \boldsymbol{\mu} \times)$, averaging the resulting equation over the volume of a magnetic sample, and taking into account the self-adjoint property of the operator $\hat{\boldsymbol{\Omega}}$, one can derive the following relation:

$$A_v \frac{\delta\omega_v}{\delta\xi} = - \left\langle \mathbf{m}_v^* \cdot \boldsymbol{\mu} \times \left(\boldsymbol{\mu} \times \frac{\delta\hat{\boldsymbol{\Omega}}}{\delta\xi} + \frac{\delta\boldsymbol{\mu}}{\delta\xi} \times \hat{\boldsymbol{\Omega}} \right) * \mathbf{m}_v \right\rangle. \quad (4.4)$$

Then, assuming that the static magnetization configuration of the sample is fixed, choosing the variable ξ as $\xi = \omega_H(\mathbf{r}) = \gamma B(\mathbf{r})$, and using the equality $\delta\hat{\boldsymbol{\Omega}}/\delta\omega_H = \hat{\mathbf{I}}$, we get the final expression for the ‘‘ellipticity’’ coefficient in the form

$$\epsilon_v = \frac{\langle |\mathbf{m}_v|^2 \rangle}{A_v} = \frac{\delta\omega_v}{\delta\omega_H}. \quad (4.5)$$

This expression is a generalization of Eq. (4.2) to the case of a nonuniform static magnetization and/or nonuniform static internal field in a magnetic sample. In the case when the static internal field is uniform, $\omega_H \notin f(\mathbf{r})$, Eq. (4.5) is reduced to Eq. (4.2), since the variational derivative is reduced to a simple partial derivative. The derived expression (4.4) is analogous to a well-known expression for a derivative of eigenvalues of a matrix [36], in which the vector $(\mathbf{m}_v^* \times \boldsymbol{\mu})$ has the meaning of a left-hand-side eigenvector.

B. Example: damping rate of gyrotropic mode of magnetic vortex

As an example of application of the above presented formalism, below we consider the damping of a gyrotropic mode in a vortex-state magnetic dot. The magnetization ground state in the form of a vortex is one of the simplest spatially nonuniform and topologically nontrivial magnetization configurations of a magnetic nanodot. It is characterized by a curling in-plane magnetization with a small out-of-plane core in the dot center (see inset in Fig. 1). The static magnetization distribution of a circular magnetic nanodot in a vortex state is given by

$$\boldsymbol{\mu}(\mathbf{r}) = p \cos\theta(r)\mathbf{e}_z + \chi \sin\theta(r)\mathbf{e}_\phi, \quad (4.6)$$

where p and χ are the vortex polarity and chirality, respectively. Here, we use the polar coordinate system (r, ϕ, z) both

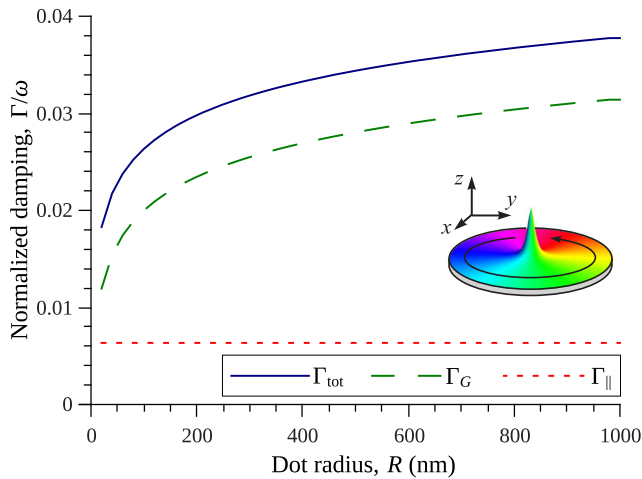


FIG. 1. Normalized damping rate of the gyrotropic mode in a vortex-state circular magnetic dot as a function of the dot radius: Γ_G is the Gilbert damping contribution, Γ_{\parallel} is the contribution from the longitudinal spin diffusion, and Γ_{tot} is the total damping rate. The dot material parameters (permalloy) are the exchange length $\lambda_{\text{ex}} = 5.5$ nm, $\alpha_G = 0.01$, and the constant of longitudinal spin diffusion [42] $\eta_{\parallel} = 0.5$ nm². The dot thickness is $L = 10$ nm, and the dependence of the vortex core radius on the dot radius and thickness is calculated according to Ref. [44]. (Inset) Circular magnetic nanodot in the vortex state. The spike in the dot center is the vortex core with the polarity $p = 1$, and the in-plane curling magnetization distribution is marked by different colors (vortex chirality $\chi = 1$).

for the description of vectors and coordinate positions inside the dot (the z axis is directed out of the dot's plane, see Fig. 1). In the case of a dot made from a soft ferromagnetic material (like permalloy) the function $\theta(r)$ can be approximated by the Usov-Peschany ansatz [37]: $\theta(r) = 2 \arctan[r/b]$ for $r \leq b$ and $\theta(r) = \pi/2$ for $r > b$. Here, b is the radius of the vortex core, which is determined by the competition between the exchange and magnetostatic interactions in the dot [38,39], and is of the order of several exchange lengths of the dot's material.

The spectrum of excitations of a vortex-state dot consists of one gyrotropic mode and a set of magnetostatic modes. The gyrotropic, or translational, mode describes the rotation of the vortex core around its equilibrium position (the dot center in the case of a zero bias magnetic field). This mode is the most interesting for our calculation, since in the out-of-core area the magnetization does not precess, but, instead, is oscillating along the linear trajectory in the \mathbf{e}_r direction. Therefore, locally, the precession ellipticity is maximal $\mathcal{E} = 1$, leading to a high averaged precession ellipticity of the SW mode, which should lead to a substantial increase of the damping rate of the gyrotropic mode. In the simplest “rigid vortex” model [39], the profile of the gyrotropic mode can be expressed as [40]

$$\mathbf{m}_G = R \left(\frac{\partial \boldsymbol{\mu}(\mathbf{r}, \mathbf{X})}{\partial X} + i \frac{\partial \boldsymbol{\mu}(\mathbf{r}, \mathbf{X})}{\partial Y} \right) \Big|_{\mathbf{x}=0}, \quad (4.7)$$

where $\mathbf{X} = (X, Y)$ is the two-dimensional vector characterizing the position of the vortex core inside the dot, and R is the dot radius. In terms of the magnetization components in a polar coordinate system, the spatial profile of the gyrotropic

mode is given by the expression

$$\mathbf{m}_G = R e^{-i\phi} \left(-\frac{i}{r} \sin \theta, \frac{d\theta}{dr} \cos \theta, -\frac{d\theta}{dr} \sin \theta \right). \quad (4.8)$$

Using the explicit expression for the gyrotropic mode profile and Eq. (2.3), one can easily calculate the mode's normalization constant to get $A = 4\pi R^2$. The averaged mode power can also be easily calculated to give $\langle |\mathbf{m}_G|^2 \rangle = 2\pi R^2 (2 + \ln[R/b])$. Thus, according to Eq. (3.9), the effective “ellipticity” coefficient for the gyrotropic mode can be evaluated as

$$\epsilon_G = 1 + \frac{1}{2} \ln \frac{R}{b}. \quad (4.9)$$

This expression has been previously derived in Ref. [7]. One can see, that the above presented general formalism allows one to easily reproduce this result, although the magnetization state of the considered magnetic sample is substantially nonuniform. The dependence of the gyrotropic mode damping rate on the dot radius is shown in Fig. 1 for a permalloy dot. It is clear that for a dot with a radius above 100–200 nm, this damping rate is substantially (2–3 times) larger than the value $\alpha_G \omega$ (result ignoring the mode ellipticity), which is a consequence of the increase of the averaged precession ellipticity of a gyrotropic mode taking place with the increase of a dot radius.

V. SPIN-WAVE DAMPING IN THE PRESENCE OF SPIN DIFFUSION

An important additional mechanism which affects the magnetization dynamics in conducting ferromagnets is the spin diffusion. The time variation of the magnetization in a conducting ferromagnet generates a flow of conduction electrons. The scattering of these electrons on the crystal lattice of a magnetic material contributes to the common Gilbert damping, which is described by the constant α_G . However, if the magnetization dynamics is spatially nonuniform, the flows of conduction electrons generated in different locations inside the ferromagnet become different, leading to the formation of a spin current. This spin current transfers the angular momentum from one point of a ferromagnet to another, thus, influencing the magnetization dynamics. It has been shown recently that this action of the spin current results in an additional damping torque acting on the dynamics of the magnetization [13,41,42].

A. Longitudinal spin diffusion

The spin diffusion is commonly considered to be composed of the longitudinal spin diffusion and the transverse spin diffusion, depending on which component of the spin angular momentum (parallel or perpendicular to the static magnetization, respectively) is transferred by the spin current.

The longitudinal spin diffusion is important for linear magnetization dynamics only in ferromagnets with a nonuniform spatial distribution of the static magnetization. Indeed, in the case of a uniformly magnetized ferromagnet, the excitation of an SW mode produces only a small (of the second order of smallness relative to the mode amplitude) variation of the longitudinal component of magnetization, and, therefore, the

effects of the longitudinal spin diffusion in this case are rather small. The influence of the longitudinal spin diffusion can be described by the term (3.2), where the tensor \hat{D}_{ad} is given by the expression [42]

$$\hat{D}_{ad} = \eta_{\parallel} \sum_{i=x,y,z} \left(\boldsymbol{\mu} \times \frac{\partial \boldsymbol{\mu}}{\partial x_i} \right) \otimes \left(\boldsymbol{\mu} \times \frac{\partial \boldsymbol{\mu}}{\partial x_i} \right). \quad (5.1)$$

Here, $\boldsymbol{\mu} = \mathbf{M}(\mathbf{r})/M_s$, as defined above, is the distribution of the dimensionless static magnetization, the symbol \otimes denotes the dyadic product of vectors, and the efficiency of the longitudinal spin diffusion is given by the coefficient

$$\eta_{\parallel} = \frac{\gamma \sigma_{\parallel}}{M_s}, \quad \sigma_{\parallel} = \frac{\hbar^2 G_0}{4e^2}, \quad (5.2)$$

where σ_{\parallel} is the longitudinal spin conductivity and G_0 is the common electric conductivity of a ferromagnetic metal.

Using Eq. (5.1) in Eq. (3.11), one can easily calculate the enhancement of the damping constant of a SW mode produced by the longitudinal spin diffusion. A typical value of the coefficient η_{\parallel} , for instance, for permalloy, is $\eta_{\parallel} \sim 0.5 \text{ nm}^2$. Noting that the common uniform Gilbert damping constant in permalloy is about $\alpha_G \approx 0.01$, it becomes clear that the longitudinal spin diffusion can become an important damping mechanism only if the characteristic length of the considered magnetization texture is less than 10–20 nm. However, the exact value of the enhanced Gilbert constant $\Delta\alpha_G$ could substantially vary for different SW modes, even for the same magnetization texture, and the difference in the magnitude of $\Delta\alpha_G$ in the case of different magnetization textures with similar characteristic lengths could also be significant. That becomes clear if one looks at the complex structure of the tensor \hat{D}_{ad} , Eq. (5.1) (see also the example presented below).

B. Transverse spin diffusion

In a uniformly magnetized ferromagnet, instead of the longitudinal spin diffusion, the transverse spin diffusion could play an important role in the damping of the linear magnetization dynamics. Naturally, a transverse spin transfer appears only in the case of a spatially nonuniform *dynamic* magnetization texture, i.e., when the spatially nonuniform SW modes are excited. The influence of the transverse spin diffusion on the magnetization dynamics is described by the term (3.2), where the tensor is defined by the expression [11]

$$\hat{D}_{\perp} = -\eta_{\perp} \nabla^2 \hat{\mathbf{I}}, \quad \eta_{\perp} = \frac{\gamma \sigma_{\perp}}{M_s}. \quad (5.3)$$

Here, σ_{\perp} is the transverse spin conductivity, which, in a general case, could differ significantly from σ_{\parallel} , and is not directly related to the electric conductivity of a ferromagnetic metal (see Ref. [11] for details).

Using Eq. (5.3), we arrive to the following expression for the enhanced Gilbert damping constant:

$$\Delta\alpha_G = -\eta_{\perp} \frac{\langle \mathbf{m}^* \cdot \nabla^2 \mathbf{m} \rangle}{\langle \mathbf{m}^* \cdot \mathbf{m} \rangle}. \quad (5.4)$$

For SW modes in a bulk ferromagnet, the transverse spin diffusion leads to the additional k^2 -dependent damping term, $\alpha_{G,\text{tot}} = \alpha_G + \eta_{\parallel} k^2$. Similarly, for volume SW modes of a magnetic nanoelement, the transverse spin diffusion leads to

the damping increase $\alpha_{G,\text{tot}} = \alpha_G + \eta_{\parallel} \kappa^2$, where $\kappa \sim n/w$ is the effective wave number of an SW mode, n is the quantization number of a mode, and w is the characteristic size of a nanoelement (i.e., radius, width, height, etc., depending on the mode structure). As a result, the damping rate of the spatially nonuniform higher-order SW modes is larger than for a quasiuniform one. This, in particular, leads to a suppression of the higher-order SW modes in the ferromagnetic resonance studies [21,24].

It is also clear that the damping increase for bulk SW modes is more pronounced in the case of smaller magnetic nanoelements. For an edge mode, however, as it has been shown in Ref. [18], the dependence $\Delta\alpha_G(w)$ could be opposite, due to the increase in the edge mode localization length with the decrease of the nanoelement size. Since the localization length of the edge mode can be, also, controlled by an external magnetic field, the measurement of the edge mode damping as a function of the external magnetic field could be used to probe the transverse spin conductance and to determine the additional mode damping caused by the transverse spin diffusion.

In bulk ferromagnetic metals, the transverse spin conductance is, typically, smaller than the longitudinal one [11,42]. In thin ferromagnetic films (10 nm thickness) the indirectly measured value of σ_{\perp} was found to be similar to the value of the longitudinal spin conductance [18]. Therefore the effect of the transverse spin diffusion on the SW damping will be pronounced only for the sufficiently short-wavelength SW modes, having wavelengths of the order of several tens of nanometers (for permalloy). Note that the transverse spin diffusion takes place, also, in the case of a nonuniform static magnetization distribution inside a ferromagnet. However, to the best of our knowledge, now it is unclear how the corresponding torque term in the Landau-Lifshitz equation should be derived in such a general case. Typically, when the characteristic lengths of the static and dynamic magnetization textures are similar, only the longitudinal spin diffusion is taken into account [42,43].

C. Example: additional damping of spin-wave excitations of a vortex state magnetic nanodot

As another example, we consider the additional damping caused by the longitudinal spin diffusion for an SW mode of a magnetic dot existing in a vortex state. As it was pointed out earlier, the vortex state is highly spatially nonuniform, and the characteristic length of its nonuniformity (the radius of the vortex core) is of the order of several exchange lengths of the dot magnetic material. Therefore one may expect a significant influence of the longitudinal spin diffusion on the damping of the SW modes in this case.

Using the expression for the magnetization distribution (4.6) and the definition of a damping tensor, Eq. (5.1), one can directly calculate the components of the damping tensor in the case of a vortex-state magnetic dot:

$$\hat{D}_{\parallel} = \frac{1}{r^2} \begin{pmatrix} (rd\theta/dr)^2 & 0 & 0 \\ 0 & \sin^2 \theta \cos^2 \theta & -\cos \theta \sin^3 \theta \\ 0 & -\cos \theta \sin^3 \theta & \sin^4 \theta \end{pmatrix}. \quad (5.5)$$

Here, $\hat{\mathbf{D}}_{\parallel}$ is derived in the polar components (i.e., its components are D_{rr} , $D_{r\phi}$, D_{rz} , etc.), and the values of the vortex polarity $p = 1$ and chirality $\chi = 1$ are used below for definiteness. Using this expression and the analytical expression for the profile of gyrotropic SW mode, Eq. (4.8), one finds that $(\mathbf{m}_G^* \cdot \hat{\mathbf{D}}_{\parallel} \cdot \mathbf{m}_G) = 2R^2(d\theta/dr)^2 \sin^2 \theta/r^2$. After averaging, the additional damping rate of a gyrotropic mode caused by the spin diffusion is expressed as

$$\Gamma_{\parallel} = \frac{7}{3} \frac{\eta_{\parallel}}{b^2} \omega. \quad (5.6)$$

The effective increase of the Gilbert damping constant in this case is, then, equal to

$$\Delta\alpha_G = \frac{14}{3} \frac{\eta_{\parallel}}{b^2(2 + \ln[R/b])}. \quad (5.7)$$

This expression has been previously derived in a more complex way, starting from the Landau-Lifshitz equation, in Ref. [22].

The radius of the vortex core is almost independent of the dot radius, and increases with the increase of the dot thickness L as $b \approx \lambda_{\text{ex}}(2.08 + 0.25(L/\lambda_{\text{ex}})^{0.85})$, where λ_{ex} is the material exchange length (≈ 5.5 nm for permalloy) [44]. Noting this dependence, it becomes clear that the damping enhancement for a gyrotropic mode is more pronounced in thinner magnetic dots. Also, due to the increase of the Gilbert damping rate, the relative effect of the spin-diffusion contribution to the total damping becomes smaller with an increase of the dot radius. As shown in Fig. 1, for a 10-nm-thick permalloy dots of radius $R = 100$ – 200 nm, the contribution of the spin diffusion to the gyrotropic mode damping rate reaches 20%–25%, which, of course, should be taken into account for the proper description of the vortex core dynamics. Spin diffusion is also important for a nonlinear vortex motion, as it has been pointed out in Ref. [43].

In contrast to the gyrotropic mode, all the other excitations of the vortex ground state—magnetostatic modes—are located outside the core region (see modes profiles, e.g., in Refs. [39,45]). Although outside the vortex core, the damping tensor is nonzero due to a curling in-plane magnetization [$D_{\parallel}^{(zz)} \neq 0$, see Eq. (5.5)], our calculations have shown that the longitudinal spin diffusion leads to a negligible damping enhancement, $\Delta\alpha_G < 10^{-3}$ even for a 50-nm dot radius. A rough estimation of the impact of the transverse spin diffusion using Eq. (5.4) (which, as pointed out above, is not rigorously applicable to the case of a nonuniform static magnetization distribution) has shown that this impact for the lowest magnetostatic modes is also negligible. Only if the characteristic wavelength of a magnetostatic mode becomes smaller than 10–20 nm (for permalloy) the transverse spin diffusion starts to be an important channel of the SW mode energy dissipation. Such a case may take place in thicker nanodots (above 40–50 nm in thickness), where the higher-order gyrotropic modes [46], and specific “curled” magnetostatic modes [47] appear, both having spatially nonuniform profiles along the dot thickness. The consideration of this case, however, lies beyond the scope of our current work.

VI. INFLUENCE OF THE INTERLAYER SPIN-PUMPING ON THE DAMPING RATE OF SPIN-WAVE MODES

In the previous section, we considered the case when the spin current, generated by magnetization dynamics, transfers the angular momentum within the ferromagnetic material. However, if a ferromagnet is in contact with another conducting material, the spin current can flow outside of the ferromagnet, or it can be generated in a ferromagnetic-nonmagnetic metal interface, if the ferromagnet is nonconducting. This transfer of angular momentum from a ferromagnet into an adjacent material is called the interlayer spin pumping [48,49].

The spin pumping plays an important role in the magnetization dynamics of ferromagnetic multilayers and heterostructures. In particular, in the case of several conducting ferromagnetic layers separated by ultrathin nonmagnetic spacers, the spin pumping leads to an additional coupling between the ferromagnetic layers [48,50]. If a ferromagnet is in contact with a nonmagnetic metal layer of a sufficient thickness (larger than the spin diffusion length), the spin current generated by time-varying magnetization in a ferromagnetic layer is simply absorbed in the nonmagnetic metal. Naturally, this leakage of the angular momentum plays a role of an additional damping channel for the magnetization dynamics in the ferromagnet [9,10].

The influence of the interlayer spin pumping on the magnetization dynamics is described by the term (3.2) with the damping tensor given by [19]

$$\hat{\mathbf{D}} = \eta_s \hat{\mathbf{I}} \delta(s(\mathbf{r})), \quad \eta_s = \frac{\gamma \hbar^2}{2e^2 M_s} g_{\perp}. \quad (6.1)$$

Here, g_{\perp} is the transverse “spin-mixing” conductance per unit area of ferromagnetic-nonmagnetic metal (FM-NM) interface, $\delta(s)$ is the Dirac delta function and the function $s(\mathbf{r})$ determines the position of the FM-NM interface. Thus, the expression $\delta(s(\mathbf{r}))$ in the equation above means that the interlayer spin pumping affects the magnetization dynamics only at the FM-NM interface. Note that the interlayer spin pumping takes place both in the case of conducting ferromagnets [9,10] and in the case of ferromagnetic insulators [17,19,20]. Equation (6.1) is applicable in both cases if the thickness of the NM layer is larger than the spin diffusion length (which varies from several nanometers up to hundreds of nanometers, depending on the material), and if the conductance of the NM layer is larger than the conductance of the ferromagnetic material.

In the opposite case, which is rather uncommon, one should take into account the effect of the spin accumulation and the back flow of the spin current into the ferromagnetic layer [48]. This, however, cannot be done by a simple modification of Eq. (6.1).

Using the general expression (3.11), we obtain that the enhancement of the damping constant produced by the interlayer spin pumping is equal to

$$\Delta\alpha_G = \eta_s \frac{S}{V} \frac{\langle |\mathbf{m}(\mathbf{r})|^2 \rangle_S}{\langle |\mathbf{m}(\mathbf{r})|^2 \rangle_V}, \quad (6.2)$$

where symbols $\langle \dots \rangle_V$ and $\langle \dots \rangle_S$ denote the averaging over the volume V of the ferromagnet and over the FM-NM interface, respectively, while S is the area of FM-NM interface. As

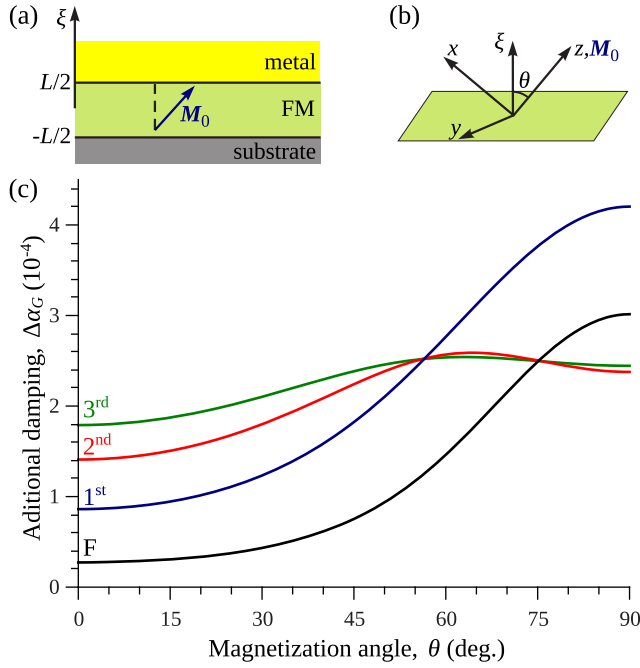


FIG. 2. Spin-pumping-related enhancement of the damping of spin wave modes in an obliquely magnetized magnetic film: (a) sketch of a ferromagnetic film (FM) having the static magnetization M_0 and thickness L contacting with a layer of a normal metal; (b) used coordinate system; (c) dependence of the additional damping caused by the interlayer spin pumping on the magnetization angle θ . Calculation parameters: YIG film of thickness 200 nm in contact with gold (Au) and external bias field $B_e = 0.2$ T. Calculations of the thickness profiles of the SW modes were made according to Ref. [51] in the long-wave limit.

one could expect, the enhancement of the damping constant is proportional to the ratio of the oscillation power $|\mathbf{m}|^2$ of an SW mode at the interface to the total mode power.

As an example, let us now consider the damping of SW modes in a ferromagnetic film of thickness L , covered on one side by a nonmagnetic metal layer [see Fig. 2(a)]. SW modes propagating in a ferromagnetic film are plane waves with the in-plane wave vector \mathbf{k} , and a transverse profile along the film thickness described by $\mathbf{m}_v(\xi)$. In this case, Eq. (6.2) for the damping rate enhancement is reduced to

$$\Delta\alpha_G = \frac{\eta_s}{L} \frac{|\mathbf{m}(\xi = L/2)|^2}{\langle |\mathbf{m}(\xi)|^2 \rangle_\xi}, \quad (6.3)$$

where in the denominator the averaging goes only over the film thickness. The above presented equation is general, and using this equation one can calculate numerically $\Delta\alpha_G$, provided the spatial profiles of the SW modes are known. In several particular cases, the mode profiles $\mathbf{m}(\xi)$ could be derived explicitly, which allows one to obtain analytical expressions for the enhanced damping parameters.

In particular, in the case of a negligible surface magnetic anisotropy $K_s \rightarrow 0$, which results in the “free” boundary conditions for the dynamic magnetization at the film boundaries, in the long-wave limit ($kL \ll 1$) the profiles of SW modes are given by simple harmonic functions [51]:

$\mathbf{m}(\xi) = \mathbf{m}_n \cos[\pi n(\xi + L/2)]$, $n \in \mathbb{Z}$. Noting that the averaged value $\langle |\mathbf{m}(\xi)|^2 \rangle = |\mathbf{m}_0|^2$ for the uniform mode ($n = 0$) and $\langle |\mathbf{m}(\xi)|^2 \rangle = |\mathbf{m}_n|^2/2$ for all the other modes, one obtains the following expressions for the mode damping enhancements:

$$\Delta\alpha_G = \frac{\eta_s}{L} \text{ for } n = 0, \quad \Delta\alpha_G = 2 \frac{\eta_s}{L} \text{ for } n \neq 0. \quad (6.4)$$

In a more complex way this result has been obtained previously in Ref. [19].

In the case of a nonzero surface anisotropy, the amplitude of the volume SW modes at the film boundary becomes smaller and, naturally, in that case the spin-pumping into the adjacent metallic layer leads to a smaller enhancement of the damping rate. The only exception from this rule is the surface mode, which exists if the pinning parameters are negative (for a perpendicularly magnetized film such a case is realized if $K_s < 0$, which means an easy-plane surface anisotropy). Since the surface mode is strongly localized at the surfaces, the interlayer spin-pumping has a much stronger effect on this surface mode. In the case of a relatively strong surface pinning, the profile of the surface mode can be approximated as $\mathbf{m} \sim \exp[Q(\xi - L/2)]$ (mode is localized at the $\xi = L/2$ surface), which leads to a thickness-independent enhanced of the mode damping rate:

$$\Delta\alpha_G = 2\eta_s \frac{|K_s|}{A}, \quad (6.5)$$

where $Q = |K_s|/A$ is the inverse localization length of the surface mode. Naturally, the other surface mode, localized at the opposite surface of the film [$\xi = -L/2$ in Fig. 2(a)], where the nonmagnetic metal layer is absent, experiences a negligible damping enhancement.

The above developed method allows one, also, to analyze a more general case of a nonuniform pinning of dynamical magnetization at the film surfaces, which is realized when the film is magnetized at an arbitrary angle θ to its normal. For instance, we calculated the damping enhancement for SW modes having different thickness profiles and propagating in an yttrium-iron-garnet (YIG) film contacting at one side with a layer of gold (Au). The calculation parameters were the saturation magnetization $\mu_0 M_s = 0.175$ T, the exchange stiffness $A = 3.5 \times 10^{-12}$ J/m, the easy-axis surface anisotropy constant $K_s = 5 \times 10^{-5}$ J/m, and the transverse spin-“mixing” conductance $hg_{\perp}/e^2 = 1.2 \times 10^{18} \text{ m}^{-2}$ [52].

The thickness profiles of the SW modes propagating in a magnetic film depend significantly on the magnetization angle. In particular, in the considered case of an easy-axis surface anisotropy, which was assumed to be the same at both interfaces of a ferromagnetic film, in the case of perpendicular magnetization ($\theta = 0$) all the SW modes are volume modes having sinusoidal thickness profiles. However, when the static magnetization tilts toward the in-plane direction ($\theta > 0$), the two lowest thickness SW modes are transformed into surface modes (in general, the number of the surface modes depends on the strength of the surface anisotropy at the film interfaces, and could be zero, one, or two [51]). This transformation is clearly seen in the dependencies of the damping parameter enhancement $\Delta\alpha_G$ on the magnetization angle, which are shown in Fig. 2(c).

For the second, third, and all the higher thickness SW modes, which remain volume modes at all values of the magnetization angle, the dependencies are nonmonotonic, having the maximum at $\theta \approx 50^\circ\text{--}60^\circ$. The appearance of this maximum is related to the angular dependence of the pinning parameters for both dynamic magnetization components, $d_x \sim \cos 2\theta$, $d_y \sim \cos^2 \theta$, [51] which, finally, results in the almost unpinned mode profiles at the considered magnetization angles. The maximum value of the damping enhancement is close to $\Delta\alpha_G \sim 2\eta_s/L$, which was obtained above for the case of “free” (unpinned) boundary conditions.

In contrast, the angular dependence of the damping enhancement $\Delta\alpha_G(\theta)$ for the lowest (fundamental, F) mode and the first thickness modes shows a monotonous increase with the magnetization angle θ , which is a direct consequence of the angular-dependent transformation of the mode “volume” to “surface,” and the consequent increase of the influence of the interlayer spin pumping on the SW mode damping.

Taking into account the fact that the natural Gilbert damping in a YIG film is $\alpha_G \approx (2\text{--}3) \times 10^{-4}$, it becomes clear that for the films of thickness $L \sim 200$ nm and less, the interlayer spin pumping could become an important, or even a dominant, source of the energy dissipation of the SW modes in YIG films.

In comparison, for the other widely used magnetic material, permalloy, the spin-mixing conductance is of the order of $hg_\perp/e^2 = 10^{19}$ m⁻² (for Py-Cu [10] and Py-Ta [18] interfaces), but due to the higher saturation magnetization of the permalloy [$\eta_s \sim 1/M_s$, see Eq. (6.1)] and the higher intrinsic Gilbert damping ($\alpha_G \sim 0.005\text{--}0.01$), the influence of the interlayer spin pumping becomes significant only for very thin films, having thicknesses less than 10 nm, or for a surface SW mode having a similar localization depth.

Finally, we would like to note that the dependencies $\Delta\alpha_G(\theta)$ shown in Fig. 2(c) with the maxima at $\theta \approx 50^\circ\text{--}60^\circ$ for all the SW modes except the one or two surface modes [51] provide a clear signature of the fact that the additional SW damping is caused by the interlayer spin pumping. Therefore such dependencies could be used to experimentally identify the cases when spin pumping provides an important additional damping channel for SW modes.

VII. CONCLUSIONS

In this work, we developed a general theoretical approach to describe the damping of spin-wave modes of ferromagnetic samples and nanostructures in the presence of different *linear* damping mechanisms, which could be spatially nonuniform or dependent on the magnetization texture (nonlocal). In the case of a relatively small magnetic damping, i.e., if the damping rate of an SW mode is significantly smaller than

the mode eigenfrequency, the SW damping rates could be successfully calculated in the framework of a perturbation theory. Using this perturbative approach, we derive a simple expression for the damping rate of an SW mode having an arbitrary spatial profile.

Using the developed formalism, we have shown that the SW damping rate due to the common Gilbert damping is directly related to the SW dispersion relation, namely, is determined by the variational derivative of the dispersion relation by the internal static magnetic field. In other words, it could be stated that the SW mode damping rate is related to the averaged precession ellipticity, and it increases when the ellipticity becomes larger. For this reason, for example, the gyrotropic mode of a vortex-state magnetic dot has a significantly larger damping rate than a fundamental SW mode in a uniformly magnetized magnetic film $\alpha_G\omega$, because the gyrotropic mode has an almost linear polarization (maximum ellipticity) away from the area of the vortex core.

To illustrate the power of the developed theoretical approach, we considered the influence of spin diffusion and interlayer spin-pumping on the damping rate of SW modes. In particular, it was shown that the longitudinal spin diffusion can substantially increase the damping rate of the gyrotropic mode of the vortex-state magnetic nanodot. In contrast, the magnetostatic modes of a vortex-state nanodot are practically unaffected by these dissipation mechanisms, as long as their characteristic wavelength is larger than 10–20 nm (for permalloy).

In the case of the interlayer spin pumping, the enhancement of the SW mode damping rate is proportional to the ratio of the SW mode oscillation power $|m|^2$ at the interface to the total power of the SW mode, and, naturally, the surface modes are the modes that are strongly affected by the spin pumping.

In a ferromagnetic film placed in contact with a layer of a normal metal, the dependence of the effective pinning parameters and, consequently, the SW mode thickness profiles, on the magnetization angle θ leads to a complex dependence of the damping constant enhancement on the magnetization angle θ . The characteristic features of the dependence $\Delta\alpha_G(\theta)$ —the existence of a local maximum at $\theta \approx 50^\circ\text{--}60^\circ$ for all the SW modes except one or two surface modes—could be used to experimentally detect the situations when the interlayer spin pumping has a significant influence on the magnetization dynamics.

ACKNOWLEDGMENTS

This work was supported by the Grants No. EFMA-1641989 and No. ECCS-1708982 from the NSF of the USA, and by the DARPA M3IC Grant under the Contract No. W911-17-C-0031. R.V. acknowledges support from the Ministry of Education and Science of Ukraine (Projects No. 0115U002716 and No. 0118U004007).

- [1] *Advanced Magnetic Nanostructures*, edited by D. J. Sellmyer and R. Skomski (Springer, New York, 2006).
 [2] A. G. Gurevich and G. A. Melkov, *Magnetization Oscillations and Waves* (CRC Press, New York, 1996).

- [3] A. Slavin and V. Tiberkevich, *IEEE Trans. Magn.* **45**, 1875 (2009).
 [4] M. Sparks, *Ferromagnetic Relaxation Theory* (McGraw-Hill, New York, 1964).

- [5] T. Gilbert, *IEEE Trans. Magn.* **40**, 3443 (2004).
- [6] D. D. Stancil, *J. Appl. Phys.* **59**, 218 (1986).
- [7] K. Y. Guslienko, *Appl. Phys. Lett.* **89**, 022510 (2006).
- [8] V. Tiberkevich and A. Slavin, *Phys. Rev. B* **75**, 014440 (2007).
- [9] Y. Tserkovnyak, A. Brataas, and G. E. W. Bauer, *Phys. Rev. Lett.* **88**, 117601 (2002).
- [10] T. Gerrits, M. L. Schneider, and T. J. Silva, *J. Appl. Phys.* **99**, 023901 (2006).
- [11] Y. Tserkovnyak, E. M. Hankiewicz, and G. Vignale, *Phys. Rev. B* **79**, 094415 (2009).
- [12] K. Gilmore and M. D. Stiles, *Phys. Rev. B* **79**, 132407 (2009).
- [13] C. H. Wong and Y. Tserkovnyak, *Phys. Rev. B* **80**, 184411 (2009).
- [14] C. A. Akosa, I. M. Miron, G. Gaudin, and A. Manchon, *Phys. Rev. B* **93**, 214429 (2016).
- [15] M. L. Schneider, J. M. Shaw, A. B. Kos, T. Gerrits, T. J. Silva, and R. D. McMichael, *J. Appl. Phys.* **102**, 103909 (2007).
- [16] H. T. Nembach, J. M. Shaw, T. J. Silva, W. L. Johnson, S. A. Kim, R. D. McMichael, and P. Kabos, *Phys. Rev. B* **83**, 094427 (2011).
- [17] C. W. Sandweg, Y. Kajiwara, K. Ando, E. Saitoh, and B. Hillebrands, *Appl. Phys. Lett.* **97**, 252504 (2010).
- [18] H. T. Nembach, J. M. Shaw, C. T. Boone, and T. J. Silva, *Phys. Rev. Lett.* **110**, 117201 (2013).
- [19] A. Kapelrud and A. Brataas, *Phys. Rev. Lett.* **111**, 097602 (2013).
- [20] H. Skarsvåg, A. Kapelrud, and A. Brataas, *Phys. Rev. B* **90**, 094418 (2014).
- [21] W. Wang, M. Dvornik, M.-A. Bisotti, D. Chernyshenko, M. Beg, M. Albert, A. Vansteenkiste, B. V. Waeyenberge, A. N. Kuchko, V. V. Kruglyak, and H. Fangohr, *Phys. Rev. B* **92**, 054430 (2015).
- [22] O. V. Sukhostavets, J. M. Gonzalez, and K. Y. Guslienko, *Low Temp. Phys.* **41**, 772 (2015).
- [23] A. Bisig, C. A. Akosa, J.-H. Moon, J. Rhensius, C. Moutafis, A. von Bieren, J. Heidler, G. Kiliani, M. Kammerer, M. Curcic, M. Weigand, T. Tyliszczak, B. Van Waeyenberge, H. Stoll, G. Schütz, K.-J. Lee, A. Manchon, and M. Kläui, *Phys. Rev. Lett.* **117**, 277203 (2016).
- [24] Y. Li and W. E. Bailey, *Phys. Rev. Lett.* **116**, 117602 (2016).
- [25] C. A. Akosa, P. B. Ndiaye, and A. Manchon, *Phys. Rev. B* **95**, 054434 (2017).
- [26] L. Rozsa, J. Hagemester, E. Y. Vedmedenko, and R. Wiesendanger, [arXiv:1805.01815](https://arxiv.org/abs/1805.01815) [*Phys. Rev. B* (to be published)].
- [27] A. Vansteenkiste, J. Leliaert, M. Dvornik, M. Helsen, F. Garcia-Sanchez, and B. Van Waeyenberge, *AIP Adv.* **4**, 107133 (2014).
- [28] L. Lopez-Diaz, D. Aurelio, L. Torres, E. Martinez, M. A. Hernandez-Lopez, J. Gomez, O. Alejos, M. Carpentieri, G. Finocchio, and G. Consolo, *J. Phys. D: Appl. Phys.* **45**, 323001 (2012).
- [29] V. V. Naletov, G. de Loubens, G. Albuquerque, S. Borlenghi, V. Cros, G. Faini, J. Grollier, H. Hurdequint, N. Locatelli, B. Pigeau, A. N. Slavin, V. S. Tiberkevich, C. Ulysse, T. Valet, and O. Klein, *Phys. Rev. B* **84**, 224423 (2011).
- [30] R. Verba, G. Melkov, V. Tiberkevich, and A. Slavin, *Phys. Rev. B* **85**, 014427 (2012).
- [31] R. V. Verba, *Ukrainian J. Phys.* **58**, 758 (2013).
- [32] K.-W. Kim, J.-H. Moon, K.-J. Lee, and H.-W. Lee, *Phys. Rev. Lett.* **108**, 217202 (2012).
- [33] R. Cheng, J.-G. Zhu, and D. Xiao, *Phys. Rev. Lett.* **117**, 097202 (2016).
- [34] K. Ando, S. Takahashi, K. Harii, K. Sasage, J. Ieda, S. Maekawa, and E. Saitoh, *Phys. Rev. Lett.* **101**, 036601 (2008).
- [35] L. Liu, T. Moriyama, D. C. Ralph, and R. A. Buhrman, *Phys. Rev. Lett.* **106**, 036601 (2011).
- [36] A. A. Mailybaev and A. P. Seiranian, *Multiparameter Stability Problems. Theory and Applications in Mechanics* (Fizmatlit, Moscow, 2009) (in Russian).
- [37] N. Usov and S. Peschany, *J. Magn. Magn. Mater.* **118**, L290 (1993).
- [38] K. L. Metlov and K. Y. Guslienko, *J. Magn. Magn. Matter.* **242-245**, 1015 (2002).
- [39] K. Y. Guslienko, *J. Nanosci. Nanotechnol.* **8**, 2745 (2008).
- [40] K. Y. Guslienko, A. N. Slavin, V. Tiberkevich, and S.-K. Kim, *Phys. Rev. Lett.* **101**, 247203 (2008).
- [41] J. Foros, A. Brataas, Y. Tserkovnyak, and G. E. W. Bauer, *Phys. Rev. B* **78**, 140402 (2008).
- [42] S. Zhang and S. S.-L. Zhang, *Phys. Rev. Lett.* **102**, 086601 (2009).
- [43] J.-H. Moon and K.-J. Lee, *J. Appl. Phys.* **111**, 07D120 (2012).
- [44] O. V. Sukhostavets, G. R. Aranda, and K. Y. Guslienko, *J. Appl. Phys.* **111**, 093901 (2012).
- [45] B. A. Ivanov and C. E. Zaspel, *Phys. Rev. Lett.* **94**, 027205 (2005).
- [46] J. Ding, G. N. Kakazei, X. Liu, K. Y. Guslienko, and A. O. Adeyeye, *Sci. Rep.* **4**, 4796 (2014).
- [47] R. V. Verba, A. Hierro-Rodriguez, D. Navas, J. Ding, X. M. Liu, A. O. Adeyeye, K. Y. Guslienko, and G. N. Kakazei, *Phys. Rev. B* **93**, 214437 (2016).
- [48] Y. Tserkovnyak, A. Brataas, G. E. W. Bauer, and B. I. Halperin, *Rev. Mod. Phys.* **77**, 1375 (2005).
- [49] A. Brataas, A. D. Kent, and H. Ohno, *Nat. Mater.* **11**, 372 (2012).
- [50] Y. Tserkovnyak, A. Brataas, and G. E. W. Bauer, *Phys. Rev. B* **67**, 140404 (2003).
- [51] B. A. Kalinikos and A. N. Slavin, *J. Phys. C: Solid State Phys.* **19**, 7013 (1986).
- [52] B. Heinrich, C. Burrowes, E. Montoya, B. Kardasz, E. Girt, Y.-Y. Song, Y. Sun, and M. Wu, *Phys. Rev. Lett.* **107**, 066604 (2011).

5.2. Дипольний пінінг та дисперсія спінових хвиль у нанорозмірних ферромагнітних хвилеводах

PHYSICAL REVIEW LETTERS **122**, 247202 (2019)

Spin Pinning and Spin-Wave Dispersion in Nanoscopic Ferromagnetic Waveguides

Q. Wang,^{1,*} B. Heinz,^{1,2,*} R. Verba,³ M. Kewenig,¹ P. Pirro,¹ M. Schneider,¹ T. Meyer,^{1,4} B. Lägél,⁵
C. Dubs,⁶ T. Brächer,¹ and A. V. Chumak^{1,†}

¹*Fachbereich Physik and Landesforschungszentrum OPTIMAS, Technische Universität Kaiserslautern, D-67663 Kaiserslautern, Germany*

²*Graduate School Materials Science in Mainz, Staudingerweg 9, 55128 Mainz, Germany*

³*Institute of Magnetism, Kyiv 03680, Ukraine*

⁴*THATec Innovation GmbH, Augustaanlage 23, 68165 Mannheim, Germany*

⁵*Nano Structuring Center, Technische Universität Kaiserslautern, D-67663 Kaiserslautern, Germany*

⁶*INNOVENT e.V., Technologieentwicklung, Prüssingstraße 27B, 07745 Jena, Germany*



(Received 9 July 2018; revised manuscript received 5 March 2019; published 19 June 2019)

Spin waves are investigated in yttrium iron garnet waveguides with a thickness of 39 nm and widths ranging down to 50 nm, i.e., with an aspect ratio thickness over width approaching unity, using Brillouin light scattering spectroscopy. The experimental results are verified by a semianalytical theory and micromagnetic simulations. A critical width is found, below which the exchange interaction suppresses the dipolar pinning phenomenon. This changes the quantization criterion for the spin-wave eigenmodes and results in a pronounced modification of the spin-wave characteristics. The presented semianalytical theory allows for the calculation of spin-wave mode profiles and dispersion relations in nanostructures.

DOI: [10.1103/PhysRevLett.122.247202](https://doi.org/10.1103/PhysRevLett.122.247202)

Spin waves and their quanta, magnons, typically feature frequencies in the gigahertz to terahertz range and wavelengths in the micrometer to nanometer range. They are envisioned for the design of faster and smaller next generational information processing devices where information is carried by magnons instead of electrons [1–9]. In the past, spin-wave modes in thin films or rather planar waveguides with thickness-to-width aspect ratios $a_r = h/w \ll 1$ have been studied. Such thin waveguides demonstrate the effect of “dipolar pinning” at the lateral edges, and for its theoretical description the thin strip approximation was developed, in which only pinning of the much-larger-in-amplitude dynamic in-plane magnetization component is taken into account [10–15]. The recent progress in fabrication technology leads to the development of nanoscopic magnetic devices in which the width w and the thickness h become comparable [16–23]. The description of such waveguides is beyond the thin strip model of effective pinning, because the scale of nonuniformity of the dynamic dipolar fields, which is described as “effective dipolar boundary conditions,” becomes comparable to the waveguide width. Additionally, both in-plane and out-of-plane dynamic magnetization components become involved in the effective dipolar pinning as they become of comparable amplitude. Thus, a more general model should be developed and verified experimentally. In addition, such nanoscopic feature sizes imply that the spin-wave modes bear a strong exchange character, since the widths of the structures are now comparable to the exchange length [24]. A proper description of the spin-wave eigenmodes in nanoscopic

strips which considers the influence of the exchange interaction, as well as the shape of the structure, is fundamental for the field of magnonics.

In this Letter, we discuss the evolution of the frequencies and profiles of the spin-wave modes in nanoscopic waveguides where the aspect ratio a_r evolves from the thin film case $a_r \rightarrow 0$ to a rectangular bar with $a_r \rightarrow 1$. Yttrium iron garnet (YIG) waveguides with a thickness of 39 nm and widths ranging down to 50 nm are fabricated and the quasiferromagnetic resonance (quasi-FMR) frequencies within them are measured using microfocused Brillouin light scattering (BLS) spectroscopy. The experimental results are verified by a semianalytical theory and micromagnetic simulations. It is shown that a critical waveguide width exists, below which the profiles of the spin-wave modes are essentially uniform across the width of the waveguide. This is fundamentally different from the profiles in state-of-the-art waveguides of micrometer [16–19] or millimeter sizes [25,26], where the profiles are nonuniform and pinned at the waveguide edges due to the dipolar interaction. In nanoscopic waveguides, the exchange interaction suppresses this pinning due to its dominance over the dipolar interaction and, consequently, the exchange interaction defines the profiles of the spin-wave modes as well as the corresponding spin-wave dispersion characteristics.

In the experiment and the theoretical studies, we consider rectangular magnetic waveguides as shown schematically in Fig. 1(a). In the experiment, a spin-wave mode is excited by a stripline that provides a homogeneous excitation field over the sample containing various waveguides

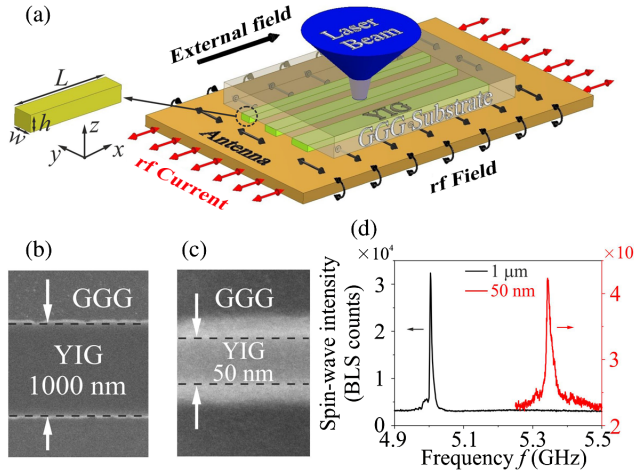


FIG. 1. (a) Sketch of the sample and the experimental configuration: a set of YIG waveguides is placed on a microstrip line to excite the quasi-FMR in the waveguides. BLS spectroscopy is used to measure the local spin-wave dynamics. (b) and (c) SEM micrograph of a 1 μm and a 50 nm wide YIG waveguide of 39 nm thickness. (d) Frequency spectra for 1 μm and 50 nm wide waveguides measured for a respective microwave power of 6 and 15 dBm.

etched from a $h = 39$ nm thick YIG film grown by liquid phase epitaxy [27] on gadolinium gallium garnet. The widths of the waveguides range from $w = 50$ nm to $w = 1$ μm with a length of 60 μm . The waveguides are patterned by Ar^+ ion beam etching using an electron-beam lithographically defined Cr/Ti hard mask and are well separated on the sample in order to avoid dipolar coupling between them [9]. The waveguides are uniformly magnetized along their long axis by an external field B (x direction). Figures 1(b) and 1(c) show scanning electron microscopy (SEM) micrographs of the largest and the narrowest waveguide studied in the experiment. The intensity of the magnetization precession is measured by microfocused BLS spectroscopy [28] (see Supplemental Material S3 [29]) as shown in Fig. 1(a). Black and red lines in Fig. 1(d) show the frequency spectra for a 1 μm and a 50 nm wide waveguide, respectively. No standing modes across the thickness were observed in our experiment, as their frequencies lie higher than 20 GHz due to the small thickness. The quasi-FMR frequency is 5.007 GHz for the 1 μm wide waveguide. This frequency is comparable to 5.029 GHz, the value predicted by the classical theoretical model using the thin strip approximation [12–14,34]. In contrast, the quasi-FMR frequency is 5.35 GHz for a 50 nm wide waveguide which is much smaller than the value of 7.687 GHz predicted by the same model. The reason is that the thin strip approximation overestimates the effect of dipolar pinning in waveguides with aspect ratio a_r close to one, for which the nonuniformity of the dynamic dipolar fields is not well localized at the waveguide edges. Additionally, in such nanoscale waveguides, the dynamic

magnetization components become of the same order of magnitude and both affect the effective mode pinning, in contrast to thin waveguides, in which the in-plane magnetization component is dominant.

In order to accurately describe the spin-wave characteristic in nanoscopic longitudinally magnetized waveguides, we provide a more general semianalytical theory which goes beyond the thin strip approximation. Please note that the theory is not applicable in transversely magnetized waveguides due to their more involved internal field landscape [16]. The lateral spin-wave mode profile $\mathbf{m}_{k_x}(y)$ and frequency can be found from [35,36]

$$-i\omega_{k_x} \mathbf{m}_{k_x}(y) = \boldsymbol{\mu} \times [\hat{\Omega}_{k_x} \cdot \mathbf{m}_{k_x}(y)], \quad (1)$$

with appropriate exchange boundary conditions, which take into account the surface anisotropy at the edges (see Supplemental Material S1 [29]). Here, $\boldsymbol{\mu}$ is the unit vector in the static magnetization direction and $\hat{\Omega}_{k_x}$ is a tensorial Hamilton operator, which is given by

$$\hat{\Omega}_{k_x} \cdot \mathbf{m}_{k_x}(y) = \left[\omega_H + \omega_M \lambda^2 \left(k_x^2 - \frac{d^2}{dy^2} \right) \right] \mathbf{m}_{k_x}(y) + \omega_M \int \hat{\mathbf{G}}_{k_x}(y-y') \cdot \mathbf{m}_{k_x}(y') dy'. \quad (2)$$

Here, $\omega_H = \gamma B$, B is the static internal magnetic field that is considered to be equal to the external field due to the negligible demagnetization along the x direction, $\omega_M = \gamma \mu_0 M_s$, γ is the gyromagnetic ratio. $\hat{\mathbf{G}}_{k_x}(y)$ is the Green's function (see Supplemental Material S1 [29]).

A numerical solution of Eq. (1) gives both the spin-wave profiles \mathbf{m}_{k_x} and frequency ω_{k_x} . In the following, we will regard the out-of-plane component $m_z(y)$ to show the mode profiles, representatively. The profiles of the spin-wave modes can be well approximated by sine and cosine functions. In the past, it was demonstrated that in microscopic waveguides, that the fundamental mode is well fitted by the function $m_z(y) = A_0 \cos(\pi y/w_{\text{eff}})$ with the amplitude A_0 and the effective width w_{eff} [12,13]. This mode, as well as the higher modes, are referred to as “partially pinned.” Pinning hereby refers to the fact that the amplitude of the modes at the edges of the waveguides is reduced. In that case, the effective width w_{eff} determines where the amplitude of the modes would vanish outside the waveguide [9,12,23]. With this effective width, the spin-wave dispersion relation can also be calculated by the analytical formula [9]

$$\omega_0(k_x) = \sqrt{[\omega_H + \omega_M(\lambda^2 K^2 + F_{k_x}^{yy})][\omega_H + \omega_M(\lambda^2 K^2 + F_{k_x}^{zz})]}, \quad (3)$$

where $K = \sqrt{k_x^2 + \kappa^2}$ and $\kappa = \pi/w_{\text{eff}}$. The tensor $\hat{F}_{k_x} = (1/2\pi) \int_{-\infty}^{\infty} (|\sigma_k|^2/\tilde{w}) \hat{\mathbf{N}}_k dk_y$ accounts for the dynamic

demagnetization, $\sigma_k = \int_{-w/2}^{w/2} m(y) e^{-ik_y y} dy$ is the Fourier transform of the spin-wave profile across the width of the waveguide, $\tilde{w} = \int_{-w/2}^{w/2} m(y)^2 dy$ is the normalization of the mode profile $m_z(y)$.

In the following, the experiment is compared to the theory and to micromagnetic simulations. The simulations are performed using MUMAX³ [37]. The structure is schematically shown in Fig. 1(a). The following parameters were used: the saturation magnetization $M_s = 1.37 \times 10^5$ A/m and the Gilbert damping $\alpha = 6.41 \times 10^{-4}$ were extracted from the plain film via ferromagnetic resonance spectroscopy before patterning [38]. Moreover, a gyromagnetic ratio $\gamma = 175.86$ rad/(ns T) and an exchange constant $A = 3.5$ pJ/m for a standard YIG film were assumed. An external field $B = 108.9$ mT is applied along the waveguide long axis (see Supplemental Material S2 [29]).

The central panel of Fig. 2 shows the spin-wave mode profile of the fundamental mode for $k_x = 0$, which corresponds to the quasi-FMR, in a $1 \mu\text{m}$ (a2) and 50 nm (b2) wide waveguide which has been obtained by micromagnetic simulations (red dots) and by solving Eq. (1) numerically (black lines) (higher width modes are discussed in Supplemental Material S6 [29]). The top panels (a1) and (b1) illustrate the mode profile and the local precession amplitude in the waveguide. As it can be seen, the two waveguides feature quite different profiles of their fundamental modes: in the $1 \mu\text{m}$ wide waveguide, the spins are

partially pinned and the amplitude of m_z at the edges of the waveguide is reduced. This still resembles the cosinlike profile of the lowest width mode $n = 0$ that has been well established in investigations of spin-wave dynamics in waveguides on the micron scale [19,23,39] and that can be well described by the simple introduction of a finite effective width $w_{\text{eff}} > w$ ($w_{\text{eff}} = w$ for the case of full pinning). In contrast, the spins at the edges of the narrow waveguide are completely unpinned and the amplitude of the dynamic magnetization m_z of the lowest mode $n = 0$ is almost constant across the width of the waveguide, resulting in $w_{\text{eff}} \rightarrow \infty$.

To understand the nature of this depinning, it is instructive to consider the spin-wave energy as a function of the geometric width of the waveguide normalized by the effective width w/w_{eff} . This ratio corresponds to some kind of pinning parameter taking values in between 1 for the fully pinned case and 0 for the fully unpinned case. The system will choose the mode profile which minimizes the total energy. This is equivalent to a variational minimization of the spin-wave eigenfrequencies as a function of w/w_{eff} . To illustrate this, the lower panels of Figs. 2(a3) and 2(b3) show the normalized square of the spin-wave eigenfrequencies ω^2/ω_M^2 for the two different widths as a function of w/w_{eff} . Here, ω^2 refers to a frequency square, not taking into account the Zeeman contribution ($\omega_H^2 + \omega_H \omega_M$), which only leads to an offset in frequency. The minimum of ω^2 is equivalent to the solution with the lowest energy corresponding to the effective width w_{eff} . In addition to the total ω^2 (black), also the individual contributions from the dipolar term (red) and the exchange term (blue) are shown, which can only be separated conveniently from each other if the square of Eq. (3) is considered for $k_x = 0$. The dipolar contribution is non-monotonic and features a minimum at a finite effective width w_{eff} , which can clearly be observed for $w = 1 \mu\text{m}$. The appearance of this minimum, which leads to the effect known as “effective dipolar pinning” [13,14], is a result of the interplay of two tendencies: (i) an increase of the volume contribution with increasing w/w_{eff} , as for common Damon-Eshbach spin waves, and (ii) a decrease of the edge contribution when the spin-wave amplitude at the edges vanishes ($w/w_{\text{eff}} \rightarrow 1$). This minimum is also present in the case of a 50 nm wide waveguide (red line), even though this is hardly perceivable in Fig. 2(b3) due to the scale. In contrast, the exchange leads to a monotonic increase of frequency as a function of w/w_{eff} , which is minimal for the unpinned case, i.e., $w/w_{\text{eff}} = 0$ implying $w_{\text{eff}} \rightarrow \infty$, when all spins are parallel. In the case of the 50 nm wide waveguide, the smaller width and the corresponding much larger quantized wave number in the case of pinned spins would lead to a much larger exchange contribution than this is the case for the $1 \mu\text{m}$ wide waveguide (please note the vertical scales). Consequently, the system avoids pinning and the solution with lowest energy is situated at

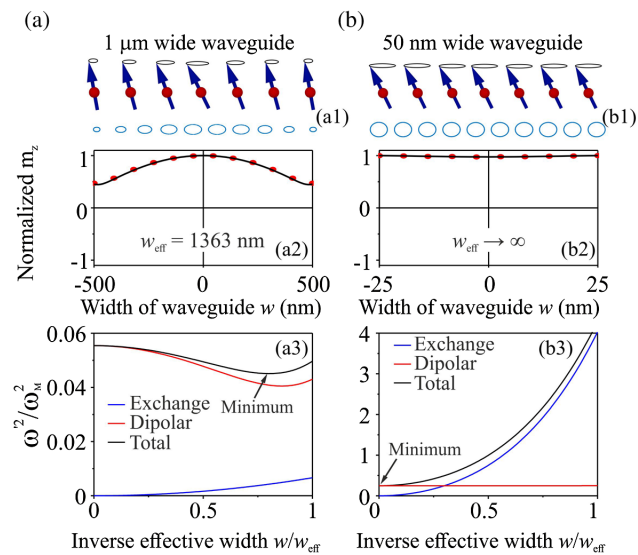


FIG. 2. Schematic of the precessing spins and simulated precession trajectories (ellipses in the second panel) and spin-wave profile $m_z(y)$ of the quasi-FMR. The profiles have been obtained by micromagnetic simulations (red dots) and by the quasianalytical approach (black lines) for an (a) $1 \mu\text{m}$ and a (b) 50 nm wide waveguide. Bottom panel: Normalized square of the spin-wave eigenfrequency ω^2/ω_M^2 as a function of w/w_{eff} and the relative dipolar and exchange contributions.

$w/w_{\text{eff}} = 0$. In contrast, in the $1\ \mu\text{m}$ wide waveguide, the interplay of dipolar and exchange energy implies that energy is minimized at a finite w/w_{eff} . The top panel of Fig. 2(b1) shows an additional feature of the narrow waveguide: as the aspect ratio of the waveguides approaches unity, the ellipticity of precession, a well-known feature of micron-sized waveguides which still resemble a thin film [23,40], vanishes and the precession becomes nearly circular. Also, in nanoscale waveguides, the ellipticity is constant across the width, while in the $1\ \mu\text{m}$ wide waveguide it can be different at the waveguide center and near its edges. Please note that the pinning phenomena and ellipticity of precession also influence the spin-wave lifetime which is described in the Supplemental Material S5 [29].

As it is evident from the lower panel of Fig. 2, the pinning and the corresponding effective width have a large influence on the spin-wave frequency. This allows for an experimental verification of the presented theory, since the frequency of partially pinned spin-wave modes would be significantly higher than in the unpinned case. Black squares in Fig. 3(a) summarize the dependence of the frequency of the quasi-FMR measured for different widths of the YIG waveguides. The magenta line shows the expected frequencies assuming pinned spins, the blue (dashed) line gives the resonance frequencies extrapolating the formula conventionally used for micron-sized waveguides [34] to the nanoscopic scenario, and the red line gives the result of the theory presented here, together with

simulation results (green dashed line). As it can be seen, the experimentally observed frequencies can be well reproduced if the real pinning conditions are taken into account.

As has been discussed along with Fig. 2, the unpinning occurs when the exchange interaction contribution becomes so large that it compensates the minimum in the dipolar contribution to the spin-wave energy. Since the energy contributions and the demagnetization tensor change with the thickness of the investigated waveguide, the critical width below which the spins become unpinned is different for different waveguide thicknesses. This is shown in Fig. 3(b), where the inverse effective width w/w_{eff} is shown for different waveguide thicknesses. Symbols are the results of micromagnetic simulations, lines are calculated semianalytically. As can be seen from the figure, the critical width linearly increases with increasing thickness. This is summarized in the inset, which shows the critical width (i.e., the maximum width for which $w/w_{\text{eff}} = 0$) as a function of thickness. The critical widths for YIG, Permalloy, CoFeB, and Heusler compound ($\text{Co}_2\text{Mn}_{0.6}\text{Fe}_{0.4}\text{Si}$) with different thicknesses are given in the Supplemental Material S9 [29]. A simple empirical linear formula is found by fitting the critical widths for different materials in a wide range of thicknesses:

$$w_{\text{crit}} = 2.2h + 6.7\lambda, \quad (4)$$

where h is the thickness of the waveguide and λ is the exchange length. Please note that additional simulations with rough edges and a more realistic trapezoidal cross section of the waveguides are also provided in the Supplemental Material S7, S8 [29]. The results show that these effects have a small impact on the critical width.

Up to now, the discussion was limited to the special case of $k_x = 0$. In the following, the influence of a finite wave vector will be addressed. The spin-wave dispersion relation of the fundamental ($n = 0$) mode obtained from micromagnetic simulations (color code) together with the semianalytical solution (white dashed line) are shown in Fig. 3(c) for the YIG waveguide of $w = 50\ \text{nm}$ width. The figure also shows the low-wave-number part of the dispersion of the first width mode ($n = 1$), which is pushed up significantly in frequency due to its large exchange contribution. Both modes are described accurately by the quasianalytical theory. As it is described above, the spins are fully unpinned in this particular case. In order to demonstrate the influence of the pinning conditions on the spin-wave dispersion, a hypothetical dispersion relation for the case of partial pinning is shown in the figure with a dash-dotted white line (the case of $w/w_{\text{eff}} = 0.63$ is considered that would result from the usage of the thin strip approximation [12]). One can clearly see that the spin-wave frequencies in this case are considerably higher. Figure 3(d) shows the inverse effective width w/w_{eff} as a function of the wave number k_x for three exemplary

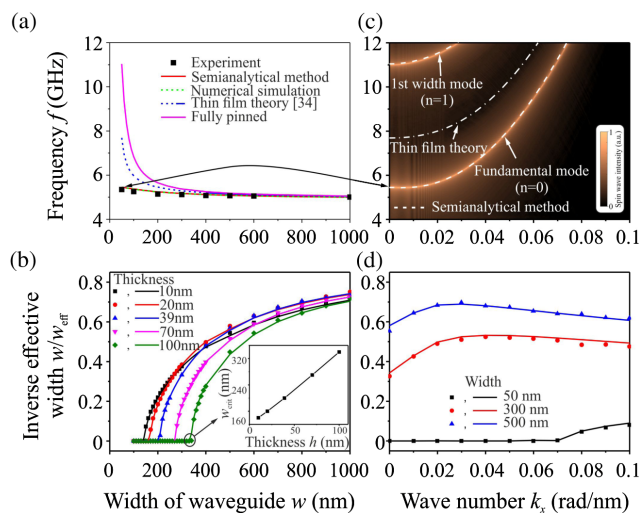


FIG. 3. (a) Experimentally determined resonance frequencies (black squares) together with theoretical predictions and micromagnetic simulations. (b) Inverse effective width w/w_{eff} as a function of the waveguide width. The inset shows the critical width (w_{crit}) as a function of thickness h . (c) Spin-wave dispersion relation of the first two width modes from micromagnetic simulations (color code) and theory (dashed lines). (d) Inverse effective width w/w_{eff} as a function of the spin-wave wave number k_x for different thicknesses and waveguide widths, respectively.

waveguide widths of $w = 50, 300,$ and 500 nm. As it can be seen, the effective width and, consequently, the ratio w/w_{eff} shows only a weak nonmonotonic dependence on the spin-wave wave number in the propagation direction. This dependence is a result of an increase of the inhomogeneity of the dipolar fields near the edges for larger k_x , which increases pinning [14], and of the simultaneous decrease of the overall strength of dynamic dipolar fields for shorter spin waves. Please note that the mode profiles are not only important for the spin-wave dispersion. The unpinned mode profiles will also greatly improve the coupling efficiency between two adjacent waveguides [9,41–43].

In conclusion, the quasi-FMR of individual wires with widths ranging from $1 \mu\text{m}$ down to 50 nm are studied by means of BLS spectroscopy. A difference in the quasi-FMR frequency between experiment and the prediction by the classical thin strip theory is found for 50 nm wide waveguides. A semianalytical theory accounting for the non-uniformity of both in-plane and out-of-plane dynamic demagnetization fields is presented and is employed together with micromagnetic simulations to investigate the spin-wave eigenmodes in nanoscopic waveguides with aspect ratio a_r approaching unity. It is found that the exchange interaction is getting dominant with respect to the dipolar interaction, which is responsible for the phenomenon of dipolar pinning. This mediates an unpinning of the spin-wave modes if the width of the waveguide becomes smaller than a certain critical value. This exchange unpinning results in a quasiuniform spin-wave mode profile in nanoscopic waveguides in contrast to the cosinelike profiles in waveguides of micrometer widths and in a decrease of the total energy and, thus, frequency, in comparison to the fully or the partially pinned case. Our theory allows us to calculate the mode profiles as well as the spin-wave dispersion, and to identify a critical width below which fully unpinned spins need to be considered. The presented results provide valuable guidelines for applications in nanomagnonics where spin waves propagate in nanoscopic waveguides with aspect ratios close to one and lateral sizes comparable to the sizes of modern CMOS technology.

The authors thank Burkard Hillebrands and Andrei Slavin for valuable discussions. This research has been supported by ERC Starting Grant No. 678309 MagnonCircuits and by the DFG through the Collaborative Research Center SFB/TRR-173 “Spin + X” (Projects B01) and through the Project No. DU 1427/2-1. R. V. acknowledges support from the Ministry of Education and Science of Ukraine, Project No. 0118U004007.

*These authors have contributed equally to this work.

†Corresponding author.

chumak@physik.uni-kl.de

[1] A. V. Chumak, V. I. Vasyuchka, A. A. Serga, and B. Hillebrands, *Nat. Phys.* **11**, 453 (2015).

- [2] V. V. Kruglyak, S. O. Demokritov, and D. Grundler, *J. Phys. D* **43**, 264001 (2010).
- [3] C. S. Davies, A. Francis, A. V. Sadovnikov, S. V. Chertopalov, M. T. Bryan, S. V. Grishin, D. A. Allwood, Y. P. Sharaevskii, S. A. Nikitov, and V. V. Kruglyak, *Phys. Rev. B* **92**, 020408(R) (2015).
- [4] A. Khitun, M. Bao, and K. L. Wang, *J. Phys. D* **43**, 264005 (2010).
- [5] M. Schneider, T. Brächer, V. Lauer, P. Pirro, D. A. Bozhko, A. A. Serga, H. Yu. Musiienko-Shmarova, B. Heinz, Q. Wang, T. Meyer, F. Heussner, S. Keller, E. Th. Papaioannou, B. Lägél, T. Löber, V. S. Tiberkevich, A. N. Slavin, C. Dubs, B. Hillebrands, and A. V. Chumak, [arXiv:1612.07305](https://arxiv.org/abs/1612.07305).
- [6] M. Krawczyk and D. Grundler, *J. Phys. Condens. Matter* **26**, 123202 (2014).
- [7] S. Wintz, V. Tiberkevich, M. Weigand, J. Raabe, J. Lindner, A. Erbe, A. Slavin, and J. Fassbender, *Nat. Nanotechnol.* **11**, 948 (2016).
- [8] T. Brächer and P. Pirro, *J. Appl. Phys.* **124**, 152119 (2018).
- [9] Q. Wang, P. Pirro, R. Verba, A. Slavin, B. Hillebrands, and A. V. Chumak, *Sci. Adv.* **4**, e1701517 (2018).
- [10] G. T. Rado and J. R. Weertam, *J. Phys. Chem. Solids* **11**, 315 (1959).
- [11] R. W. Doman and J. R. Eshbach, *J. Phys. Chem. Solids* **19**, 308 (1961).
- [12] K. Yu. Guslienko, S. O. Demokritov, B. Hillebrands, and A. N. Slavin, *Phys. Rev. B* **66**, 132402 (2002).
- [13] K. Yu. Guslienko and A. N. Slavin, *Phys. Rev. B* **72**, 014463 (2005).
- [14] K. Yu. Guslienko and A. N. Slavin, *J. Magn. Magn. Mater.* **323**, 2418 (2011).
- [15] R. E. Arias, *Phys. Rev. B* **94**, 134408 (2016).
- [16] T. Brächer, O. Boule, G. Gaudin, and P. Pirro, *Phys. Rev. B* **95**, 064429 (2017).
- [17] V. E. Demidov and S. O. Demokritov, *IEEE Trans. Magn.* **51**, 0800215 (2015).
- [18] F. Ciubotaru, T. Devolder, M. Manfrini, C. Adelman, and I. P. Radu, *Appl. Phys. Lett.* **109**, 012403 (2016).
- [19] P. Pirro, T. Brächer, A. V. Chumak, B. Lägél, C. Dubs, O. Surzhenko, P. Görnert, B. Leven, and B. Hillebrands, *Appl. Phys. Lett.* **104**, 012402 (2014).
- [20] M. Mruczkiewicz, P. Graczyk, P. Lupo, A. Adeyeye, G. Gubbiotti, and M. Krawczyk, *Phys. Rev. B* **96**, 104411 (2017).
- [21] A. Haldar and A. O. Adeyeye, *ACS Nano* **10**, 1690 (2016).
- [22] R. Verba, V. Tiberkevich, E. Bankowski, T. Meitzler, G. Melkov, and A. Slavin, *Appl. Phys. Lett.* **103**, 082407 (2013).
- [23] T. Brächer, P. Pirro, and B. Hillebrands, *Phys. Rep.* **699**, 1 (2017).
- [24] G. Abo, Y. Hong, J. Park, J. Lee, W. Lee, and B. Choi, *IEEE Trans. Magn.* **49**, 4937 (2013).
- [25] M. Vogel, A. V. Chumak, E. H. Waller, T. Langer, V. I. Vasyuchka, B. Hillebrands, and G. Von Greymann, *Nat. Phys.* **11**, 487 (2015).
- [26] A. A. Serga, A. V. Chumak, and B. Hillebrands, *J. Phys. D* **43**, 264002 (2010).
- [27] C. Dubs, O. Surzhenko, R. Linke, A. Danilewsky, U. Brückner, and J. Dellith, *J. Phys. D* **50**, 204005 (2017).

- [28] T. Sebastian, K. Schultheiss, B. Obry, B. Hillebrands, and H. Schultheiss, *Front. Phys.* **3**, 35 (2015).
- [29] See Supplemental Material at <http://link.aps.org/supplemental/10.1103/PhysRevLett.122.247202> for details of numerical solution and micromagnetic simulations, which includes Refs. [30–33].
- [30] V. V. Kruglyak, O. Yu. Gorobets, Yu. I. Gorobets, and A. N. Kuchko, *J. Phys. Condens. Matter* **26**, 406001 (2014).
- [31] D. D. Stancil, *J. Appl. Phys.* **59**, 218 (1986).
- [32] D. D. Stancil and A. Prabhakar, *Spin Waves: Theory and Applications* (Springer, New York, 2009).
- [33] R. Verba, V. Tiberkevich, and A. Slavin, *Phys. Rev. B* **98**, 104408 (2018).
- [34] B. A. Kalinikos and A. N. Slavin, *J. Phys. C* **19**, 7013 (1986).
- [35] R. Verba, G. Melkov, V. Tiberkevich, and A. Slavin, *Phys. Rev. B* **85**, 014427 (2012).
- [36] R. Verba, *Ukr. J. Phys.* **58**, 758 (2013).
- [37] A. Vansteenkiste, J. Leliaert, M. Dvornik, M. Helsen, F. García-Sánchez, and B. Van Waeyenberge, *AIP Adv.* **4**, 107133 (2014).
- [38] I. S. Maksymov and M. Kostylev, *Physica (Amsterdam)* **69E**, 253 (2015).
- [39] M. B. Jungfleisch, W. Zhang, W. Jiang, H. Chang, J. Sklenar, S. M. Wu, J. E. Pearson, A. Bhattacharya, J. B. Ketterson, M. Wu, and A. Hoffman, *J. Appl. Phys.* **117**, 17D128 (2015).
- [40] A. G. Gurevich and G. A. Melkov, *Magnetization Oscillations and Waves* (CRC Press, New York, 1996).
- [41] A. V. Sadovnikov, E. N. Beginin, S. E. Sheshukova, D. V. Romanenko, Yu. P. Sharaevskii, and S. A. Nikitov, *Appl. Phys. Lett.* **107**, 202405 (2015).
- [42] A. V. Sadovnikov, A. A. Grachev, S. E. Sheshukova, Yu. P. Sharaevskii, A. A. Serdobintsev, D. M. Mitin, and S. A. Nikitov, *Phys. Rev. Lett.* **120**, 257203 (2018).
- [43] A. V. Sadovnikov, S. A. Odintsov, E. N. Beginin, S. E. Sheshukova, Yu. P. Sharaevskii, and S. A. Nikitov, *Phys. Rev. B* **96**, 144428 (2017).

5.3. Передача енергії спінових хвиль у дипольно взаємодіючих хвилеводах, спрямований відгалужувач

SCIENCE ADVANCES | RESEARCH ARTICLE

PHYSICS

Reconfigurable nanoscale spin-wave directional coupler

Qi Wang,¹ Philipp Pirro,¹ Roman Verba,² Andrei Slavin,³ Burkard Hillebrands,¹ Andrii V. Chumak^{1*}

Spin waves, and their quanta magnons, are prospective data carriers in future signal processing systems because Gilbert damping associated with the spin-wave propagation can be made substantially lower than the Joule heat losses in electronic devices. Although individual spin-wave signal processing devices have been successfully developed, the challenging contemporary problem is the formation of two-dimensional planar integrated spin-wave circuits. Using both micromagnetic modeling and analytical theory, we present an effective solution of this problem based on the dipolar interaction between two laterally adjacent nanoscale spin-wave waveguides. The developed device based on this principle can work as a multifunctional and dynamically reconfigurable signal directional coupler performing the functions of a waveguide crossing element, tunable power splitter, frequency separator, or multiplexer. The proposed design of a spin-wave directional coupler can be used both in digital logic circuits intended for spin-wave computing and in analog microwave signal processing devices.

INTRODUCTION

Spin waves (SWs) are orders of magnitude shorter compared to electromagnetic waves of the same frequency, and therefore, the use of SWs allows one to design much smaller nanosized devices for both analog and digital data processing (1–15). Recently, several novel concepts of magnonic logic and signal processing have been proposed (2, 3, 6, 16–25), but one of the unsolved problems of the magnonic technology is an effective and controllable connection of separate magnonic signal processing devices into a functioning magnonic circuit (6). Unfortunately, a simple X-type crossing (21, 26) has a significant drawback because it acts as an SW re-emitter into all four connected SW channels. Thus, an alternative solution for an SW device connector is necessary.

We propose to use dipolar interaction between magnetized or self-biased, laterally parallel SW waveguides to realize a controlled connection between magnonic conduits. Originally, such an SW coupling has been studied theoretically in a “sandwich-like” vertical structure consisting of two infinite films separated by a gap (27, 28). However, experimental studies of this structure are rather complicated due to the lack of access to the separate layers, which is required for the excitation and detection of propagating SWs. The configuration of a connector based on two laterally adjacent waveguides is well studied in integrated optics because it can be conveniently implemented in applications (29). Recently, the dipolar coupling between two externally magnetized millimeter-sized laterally adjacent magnetic stripes has been studied experimentally using Brillouin light scattering spectroscopy by Sadovnikov and colleagues (30–32). It has been shown that SW coupling efficiency depends on both the geometry of a magnonic waveguides and the characteristics of the interacting SW modes (30). Also, a nonlinear regime of the SW waveguide coupling has been experimentally investigated in millimeter-sized waveguides (31).

However, to make a directional coupler based on the dipolar interaction between laterally adjacent SW waveguides usable in contemporary magnonic circuits, this device should be substantially more compact (nanometer instead of millimeter in size), should be able to function without permanent bias magnetic field, should have sufficiently low propagation losses (related to both Gilbert damping and

waveguide reflections), and should be easily integrable into large magnonic circuits without additional input and output transducers. Also, it is necessary to develop an analytic theory of operation of such a device, which would allow one to easily adjust and optimize the device characteristics for a particular application.

Here, we study dipolar coupling of nanoscale self-biased SW waveguides and propose a practical design of a nanoscale magnonic directional coupler. We do this using the combination of micromagnetic simulations and analytical theory, which we developed for easy optimization of the device characteristics. The proposed directional coupler consists of two bent nanosized and self-biased SW waveguides, where the bent regions are placed laterally close to each other, thus defining a region of the waveguides where the dipolar coupling is taking place. The chosen particular shape of the bent regions ensures a highly efficient (more than 95%) SW transmission that is difficult to achieve on the waveguides of a millimeter-size (33) or even micrometer-size (19, 21) scales. Using micromagnetic simulations, we demonstrate that the proposed SW directional coupler can have different functionalities (connector, power divider, frequency separator, multiplexer, etc.) controlled by the external parameters, such as the frequency (wave number) of the propagating SW, length of the “coupling” region of the waveguides, relative orientation of the static magnetizations in the coupled parallel waveguide segments, and the magnitude of the permanent bias magnetic field (which might be used but is not essential). It is also demonstrated that the working parameters and the functionality of the proposed device can be dynamically reconfigured by application of a short (tens of nanoseconds) pulse of an external bias magnetic field.

Operational principle of the directional coupler

In the case when two identical magnetic strip-line SW waveguides are placed sufficiently close to one another (see Fig. 1A), the dipolar coupling between the waveguides leads to a splitting of the lowest width SW mode of a single waveguide into the symmetric (“acoustic”) and antisymmetric (“optic”) collective modes of the coupled waveguides (see Fig. 1, B and C). Thus, in a system of two dipolarly coupled waveguides, at each frequency, two SW modes (symmetric and antisymmetric, whose profiles are shown in Fig. 1C) with different wave numbers k_s and k_{as} ($\Delta k_x = |k_s - k_{as}|$) will be excited simultaneously. The interference between these two propagating waveguide modes will lead to a periodic transfer of energy from one waveguide to the other (see Fig. 1A), so the energy of an SW excited in one of the waveguides

Copyright © 2018
The Authors, some
rights reserved;
exclusive licensee
American Association
for the Advancement
of Science. No claim to
original U.S. Government
Works. Distributed
under a Creative
Commons Attribution
NonCommercial
License 4.0 (CC BY-NC).

¹Fachbereich Physik und Landesforschungszentrum OPTIMAS, Technische Universität Kaiserslautern, Kaiserslautern 67663, Germany. ²Institute of Magnetism, Kyiv 03680, Ukraine. ³Department of Physics, Oakland University, Rochester, MI 48309, USA.
*Corresponding author. Email: chumak@physik.uni-kl.de

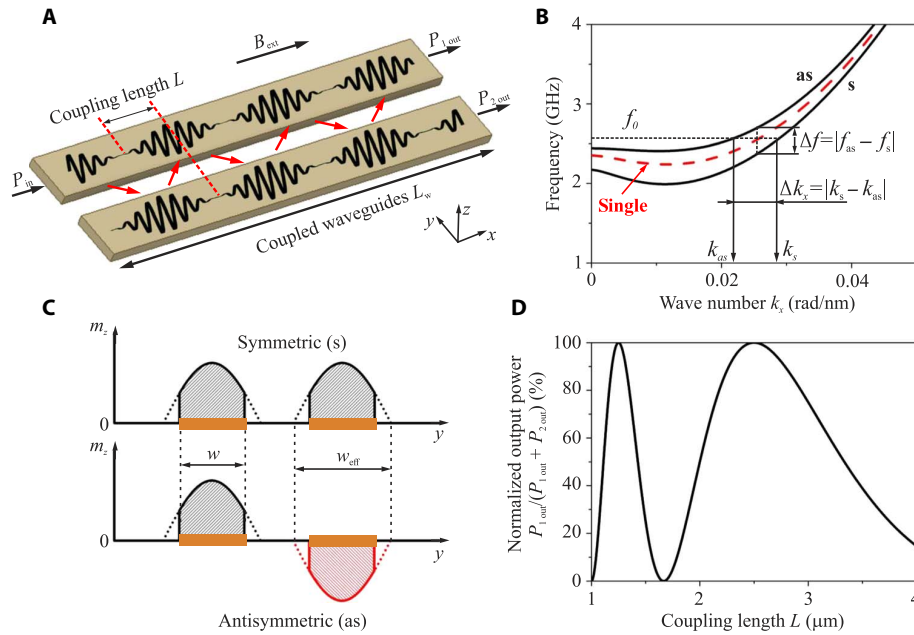


Fig. 1. The operational principle of a directional coupler based on two dipolarly coupled SW waveguides. (A) Sketch of two dipolarly coupled SW waveguides. Solid red lines illustrate the periodic energy exchange between the two interacting SW waveguides with a spatial periodicity of $2L$. (B) The red dashed line shows the dispersion characteristic of the lowest SW width mode in an isolated single SW waveguide. Solid black lines show the dispersion curves of the “symmetric” (s) and “antisymmetric” (as) lowest collective SW modes of a pair of dipolarly coupled SW waveguides. (C) Spatial profiles of the “symmetric” (s) and “antisymmetric” (as) collective SW modes partially pinned at the waveguide lateral boundaries ($w_{\text{eff}} > w$; see the main text). (D) Normalized output power of the first waveguide of the directional coupler as a function of the coupling length L (varied by varying the spin-wave wave number as will be shown later) for a fixed length of the coupled waveguides $L_w = 5 \mu\text{m}$, external field $B_{\text{ext}} = 10 \text{ mT}$, and vanishing damping in the system.

will be transferred to the other waveguide after propagation over a certain distance that will be defined as the coupling length L (28)

$$L = \pi / \Delta k_x = \pi / |k_s - k_{\text{as}}| \quad (1)$$

Note that, in our case, spins at the lateral boundaries are pinned only partially (34, 35), and therefore, we introduce the “effective width” of the waveguides w_{eff} that can be larger than the nominal waveguide width w (see Fig. 1C). This issue is discussed in more detail below.

The difference in the wave numbers Δk_x of the modes of the same frequency is equal to $\Delta k_x = \Delta\omega / (\partial\omega_0 / \partial k_x) = \Delta\omega / v_{\text{gr}}$, where $\Delta\omega = 2\pi\Delta f$, $\Delta f = |f_{\text{as}} - f_s|$ is the frequency separation between the symmetric (f_s) and antisymmetric modes (f_{as}) (see Fig. 1B), and $\omega_0 = 2\pi f_0$, f_0 is the SW frequency. With this last expression, the coupling length can be rewritten as

$$L = v_{\text{gr}} / (2\Delta f) \quad (2)$$

where v_{gr} is the SW group velocity in a single isolated waveguide.

The case interesting for applications is the one when an SW is originally excited in only one SW waveguide. The output powers for both waveguides can be expressed as follows (28): $P_{1 \text{ out}} = P_{\text{in}} \cos^2(\pi L_w / (2L))$ for the first waveguide and $P_{2 \text{ out}} = P_{\text{in}} \sin^2(\pi L_w / (2L))$ for the second one, where L_w is the length of the coupled waveguides as shown in Fig. 1A and P_{in} is the input SW power in the first waveguide. The

dependence of the normalized output power of the first waveguide $P_{1 \text{ out}} / (P_{1 \text{ out}} + P_{2 \text{ out}})$ can be expressed as

$$P_{1 \text{ out}} / (P_{1 \text{ out}} + P_{2 \text{ out}}) = \cos^2(\pi L_w / (2L)) \quad (3)$$

This dependence is shown in Fig. 1D as a function of the coupling length L for the case when damping is ignored.

Thus, the interplay between the length of the coupled waveguides L_w and the coupling length L , which is strongly dependent on several external and internal parameters of the system, allows one to define the ratio between the SW powers at the outputs of two coupled waveguides and, thus, define the functionality of the investigated directional coupler. In particular, we demonstrate below that the functionality of the directional coupler can be changed by varying the geometrical sizes of the waveguides and spacing in between them by changing the SW frequency (wave number) and/or the applied bias magnetic field and changing the relative orientations of static magnetizations of the interacting SW waveguides.

An analytical theory of coupled waveguides

To analytically describe the energy transfer in the system of two coupled waveguides, we first need to find the dispersion relation and the spatial profiles of the SW eigenmodes in them. When two waveguides are coupled, the SW branch existing in an isolated waveguide is split into two collective SW modes. In the simplest case of identical waveguides, these collective modes are symmetric and antisymmetric (see Fig. 1C).

To obtain the dispersion relation and the spatial structure of the collective modes in a general case, one needs to solve the Landau-Lifshitz (LL) equation of magnetization motion

$$\frac{d\mathbf{M}}{dt} = -|\gamma|\mathbf{M} \times \mathbf{B}_{\text{eff}} \quad (4)$$

in the linear approximation and neglecting the damping term. Here, \mathbf{M} is the magnetization vector, \mathbf{B}_{eff} is the effective field (which includes exchange, external, and demagnetization fields), and γ is the gyromagnetic ratio. In the following, we assume that the dynamic component of the magnetization is constant across the waveguide thickness (uniform thickness profile) that is a good approximation for waveguide thicknesses of the order of hundred nanometers and smaller. Within this approximation, the SW spectra can be calculated using the formalism developed by Verba and colleagues (36, 37) for the case of coupled magnetic nanodots but with the difference that SW propagation along the nanowire waveguides should be taken into account.

We consider two identical SW waveguides and identical SW modes propagating along these waveguides in the x direction. Then, the magnetization in a waveguide can be written as $\mathbf{M}(\mathbf{r}, t) = M_s(\boldsymbol{\mu} + \mathbf{m}(y)\exp(i(kx + \omega_k t)))$, where M_s is the saturation magnetization, $\boldsymbol{\mu}$ is the unit vector in the direction of the static magnetization, and $\mathbf{m} \ll 1$ is the small dynamic deviation of the magnetization from its equilibrium position. Using this representation in Eq. 4, we derive the following expression for the SW vector and amplitudes

$$-i\omega_{k_x} \mathbf{m}_{k_x,p} = \boldsymbol{\mu} \times \sum_q \hat{\mathbf{Q}}_{k_x,pq} \cdot \mathbf{m}_{k_x,q} \quad (5)$$

which is the Fourier representation (in time and x coordinate) of the linearized LL equation. Here, $\boldsymbol{\mu}$ is the unit vector along the direction of the static magnetization; indices $p, q = 1, 2$ enumerate waveguides; and the tensor $\hat{\mathbf{Q}}_{k_x,pq}$ has the form

$$\hat{\mathbf{Q}}_{k_x,pq} = \gamma(B + \mu_0 M_s \lambda^2 (k_x^2 + \kappa^2)) \delta_{pq} \hat{\mathbf{I}} + \omega_M \hat{\mathbf{F}}_{k_x}(d_{pq}) \quad (6)$$

where B is the static internal magnetic field, which in our case is considered to be equal to the external magnetic field due to the negligible demagnetization along the x direction, d_{pq} is the distance between the centers of the two waveguides (that is, $d_{pp} = 0$, $d_{12} = -d_{21} = w + \delta$), δ is the gap between the waveguides of width w , $\lambda = \sqrt{2A/(\mu_0 M_s^2)}$ is the exchange length, δ_{pq} is the Kronecker delta function, $\omega_M = \gamma \mu_0 M_s$, μ_0 is the vacuum permeability, γ is the gyromagnetic ratio, and $\hat{\mathbf{I}}$ is the identity matrix. Note that, due to the effective dipolar boundary conditions (34, 35) at the lateral boundaries of the waveguides, the width profiles of the collective SW modes will be, in general, partially pinned, resulting in a nonuniform width profile of the fundamental SW mode of the waveguide $m(y) \sim \cos(\kappa y) = \cos(\pi y/w_{\text{eff}})$. This nonuniformity is taken into account by the effective wave number $\kappa = \pi/w_{\text{eff}}$, where w_{eff} is the effective width of the waveguide (see illustration in Fig. 1C). In general, the effective width of the waveguides w_{eff} can be substantially larger than the nominal waveguide width w when the effective pinning decreases (see Fig. 1C). The influence of the dynamical magneto-dipolar interaction (both intra- and inter-waveguides) in Eq. 6 is described by the tensor $\hat{\mathbf{F}}_{k_x}$, which is con-

venient to calculate using a Fourier-space approach, developed by Beleggia *et al.* (38), namely

$$\hat{\mathbf{F}}_{k_x}(d) = \frac{1}{2\pi} \int \hat{\mathbf{N}}_k e^{ik_y d} dk_y \quad (7)$$

$$\hat{\mathbf{N}}_k = \frac{|\sigma_k|^2}{\tilde{w}} \begin{pmatrix} \frac{k_x^2}{k^2} f(kt) & \frac{k_x k_y}{k^2} f(kt) & 0 \\ \frac{k_x k_y}{k^2} f(kt) & \frac{k_y^2}{k^2} f(kt) & 0 \\ 0 & 0 & 1 - f(kt) \end{pmatrix} \quad (8)$$

where $f(kt) = 1 - (1 - \exp(-kt))/kt$, $k = \sqrt{k_x^2 + k_y^2}$, t is the waveguide thickness, $\sigma_k = \int_{-w/2}^{w/2} m(y) e^{-ik_y y} dy$ is the Fourier transform of the SW profile across the width of the waveguide, and $\tilde{w} = \int_{-w/2}^{w/2} m(y)^2 dy$ is the normalized constant of the mode profile $m(y)$. For $k = 0$, one should calculate the corresponding limit of $\hat{\mathbf{N}}_k$. In the case $d = 0$, the tensor $\hat{\mathbf{F}}_{k_x}(0)$ coincides with the dipolar self-interaction inside the waveguide. $\hat{\mathbf{F}}_{k_x}(d)$ is the dipolar interaction between the waveguides. In the case of an almost uniform SW profile $m(y) = 1$, which is realized if the waveguide size is close to or smaller than the material exchange length λ or if the effective boundary conditions are free (that is, $w_{\text{eff}} \rightarrow \infty$), the Fourier transform is described by the function $\sigma_k = w \text{sinc}(k_y w/2)$ and $\tilde{w} = w$. For any other spatially symmetric mode with the profile $m(y) \sim \cos(\kappa y)$, the Fourier transform σ_k can be evaluated as

$$\sigma_k = 2 \left[\frac{k_y \cos(\kappa w/2) \sin(k_y w/2) - \kappa \cos(k_y w/2) \sin(\kappa w/2)}{k_y^2 - \kappa^2} \right],$$

$$\tilde{w} = \frac{w}{2} (1 + \text{sinc}(\kappa w)) \quad (9)$$

Noting that the tensor $\hat{\mathbf{F}}_{k_x}(d)$ is diagonal and real (as long as the static magnetization is directed along one of the symmetry axes of the waveguide), we can obtain simple explicit expressions for the SW dispersion relations of the waveguide SW modes. The dispersion relation for the SW mode in an isolated waveguide is

$$f_0(k_x) = \frac{1}{2\pi} \sqrt{\Omega^{yy} \Omega^{zz}} \\ = \frac{1}{2\pi} \sqrt{(\omega_H + \omega_M(\lambda^2 K^2 + F_{k_x}^{yy}(0)))(\omega_H + \omega_M(\lambda^2 K^2 + F_{k_x}^{zz}(0)))} \quad (10)$$

The dispersion relation for two coupled waveguides (two modes) is

$$f_{1,2}(k_x) = \frac{1}{2\pi} \sqrt{(\Omega^{yy} \pm \omega_M F_{k_x}^{yy}(d))(\Omega^{zz} \pm \omega_M F_{k_x}^{zz}(d))} \quad (11)$$

where $\Omega^i = \omega_H + \omega_M(\lambda^2 K^2 + F_{k_x}^{ii}(0))$, $i = y, z$, $\omega_H = \gamma B$, $\omega_M = \gamma \mu_0 M_s$, and $K = \sqrt{k_x^2 + \kappa^2}$. Noting that the magneto-dipolar interaction between the waveguides is small compared to the dipolar self-interaction inside the waveguide, the dispersion relations of the two collective

modes (symmetric and antisymmetric) in a pair of coupled waveguides can be approximated as

$$f_{1,2}(k_x) \approx f_0(k_x) \pm \Delta f / 2 \quad (12)$$

where the frequency separation between the symmetric and antisymmetric collective modes is given by

$$\Delta f = \omega_M \frac{\Omega^z F_{k_x}^{yy}(d) + \Omega^y F_{k_x}^{zz}(d)}{4\pi^2 f_0(k_x)} \quad (13)$$

Equation 13 describes the dependence of the frequency separation between the symmetric and antisymmetric modes on all the geometrical and material parameters of the system consisting of two coupled waveguides. In general, Δf increases with an increase in dynamic magneto-dipolar interaction between the waveguides. This increase can be realized by decreasing the separation between the waveguides or by an increase of the thickness-to-width aspect ratio of the waveguides. In addition, Δf significantly depends on the saturation magnetization of the used materials. If the wave number of the excited SW, as well as the spin-pinning conditions (effective width w_{eff}), is fixed, then Δf can be approximated as $\Delta f \propto \omega_M \propto M_s$ in both the dipolar and exchange regions and is independent of the applied external field. As shown by Eq. 2, the coupling length $L = v_{\text{gr}} / (2\Delta f)$ is proportional to the ratio between the SW velocity and the frequency separation. Because in dipolar approximation the velocity $v_{\text{gr}} \propto M_s$ is practically proportional to the saturation magnetization, the coupling length L is independent of the choice of the material. Thus, the use of yttrium iron garnet (YIG), which has a smaller value of M_s compared to metallic materials, is preferable for dipolar waves due to the longer SW lifetimes in this material. In contrast, in the exchange-dominated region, the SW dispersion relation can be approximated as $f = \frac{1}{2\pi} \omega_M \lambda^2 k^2$, and the group velocity $v_{\text{gr}} = 2\pi \frac{\partial f}{\partial k} = 4\gamma \frac{A}{M_s} k$ is inversely proportional to the saturation magnetization. Thus, the exchange waves in metallic magnetic materials with large M_s are slower and, consequently, have smaller propagation decay lengths in comparison to YIG (even if to neglect much larger SW lifetimes in YIG). However, the coupling length $L \propto \frac{A}{M_s^2} \propto \lambda^2$ in the exchange region is smaller in the materials with high M_s , and another mechanism can be used to enhance the coupling between the SW waveguides as discussed later.

The developed analytical theory represents a method to calculate the characteristics of the magnonic SW couplers that are relatively simple and intuitive, compared to the traditional micromagnetic simulations. In the following, the analytic results are directly compared to the results of micromagnetic simulations.

RESULTS

Model and simulations

The structure of a directional coupler is schematically shown in Fig. 2A. Two parallel waveguides (length of 100 μm , width w ranging between 100 and 300 nm, and thickness t in the range of 10 to 50 nm) are placed laterally parallel with a gap δ (ranging between 10 and 100 nm). The numerical modeling of this structure is performed using the MuMax3 (39) micromagnetic package with the following parameters of a YIG nanometer-thick film (10, 40): saturation magnetization $M_s = 1.4 \times 10^5$ A/m, exchange constant $A = 3.5$ pJ/m, and Gilbert damping $\alpha =$

2×10^{-4} . In our numerical simulations, the Gilbert damping at the ends of the waveguides is set to exponentially increase to 0.5 to eliminate SW reflections at the waveguide ends [experimentally, this can be realized using tapered edges (30) or by placing a normal metal on top of the waveguide edges to use the phenomena of spin pumping (6, 10)]. Because of the ultralow Gilbert damping of YIG, the SW propagation distances in YIG waveguides reach up to dozens of micrometers (10, 14, 41, 42), which opens up the possibility for the realization of complex integrated SW circuits. A small external magnetic field $B_{\text{ext}} = 10$ mT is applied along the long axis of the waveguides (x direction in Fig. 2). To excite a propagating SW in one of the waveguides, we applied a sinusoidal magnetic field $b_y = b_0 \sin(2\pi f t)$ at the center of the second waveguide over an area of 20 nm in length (see yellow area shown in Fig. 2A), with the oscillation amplitude $b_0 = 1$ mT and a varying microwave frequency f .

Splitting of SW dispersion curves due to the dipolar coupling between waveguides

Figure 2B shows a snapshot of the dynamic magnetization profiles in the coupled waveguides with the following parameters: width $w = 100$ nm, thickness $t = 50$ nm, and gap $\delta = 100$ nm. The frequency of the excited SW in this case was 2.96 GHz, corresponding to a wave number $k_x = 0.02872$ rad/nm. It can be seen that the energy of the SW, excited in waveguide #2, is transferred completely to waveguide #1 after propagation over the coupling length L (see Fig. 2B). Figure 2 (C and D) shows the variations of the SW power in the two coupled waveguides as a function of the propagation distance x for the case of zero damping (Fig. 2C) and for the case of a typical damping of YIG film ($\alpha = 2 \times 10^{-4}$) (Fig. 2D). The coupling length of $L = 12 \mu\text{m}$ can be extracted from Fig. 2 (C and D). Note that the SW wavelength in our studies is of the order of 100 nm. The simulation performed for the damping-free waveguides shows the lossless oscillations of the SW energy between the waveguides. The blue line is a fit to the data using the dependence $P_1 = P_{\text{in}} \sin^2(x\pi/(2L))$, where P_{in} is the power launched into waveguide #2 and P_1 is the power in waveguide #1. In the case where realistic SW damping is taken into account, the SW power gradually decreases, as expected. The results can be fitted by a similar model that includes the damping term $P_1 = P_{\text{in}} \sin^2(x\pi/(2L)) \exp(-|2x|/\chi_{\text{freepath}})$, where $\chi_{\text{freepath}} = 88 \mu\text{m}$ is the exponential decay length, which is in good agreement with the analytical theory.

Figure 2E shows the dispersion characteristics of the two lowest width modes of a single isolated waveguide, and Fig. 2F shows the similar dispersion curves for a pair of the waveguides coupled across a gap of $\delta = 10$ nm. The color maps were calculated by micromagnetic simulations, whereas the black dashed lines for the lowest width SW mode were obtained using the analytic equations (Eqs. 10 and 11) for the single waveguide and the coupled waveguides, respectively.

It is seen that the dispersion curve corresponding to the lowest width mode of a single waveguide splits into two modes: antisymmetric (as) (top) and symmetric (s) (bottom) (see Figs. 1C and 2F). This splitting is caused by the dipolar interaction between the waveguides. The oscillations of the SW energy in the coupled waveguides can be interpreted as an interference of the symmetric and antisymmetric SW modes (28–30). These two SW modes have the same frequency but different wave numbers and, therefore, different phase velocities. Thus, these modes accumulate a phase difference during their propagation in the waveguides. When the accumulated phase difference is equal to π , the superposition of the two modes results in a destructive interference in one of the waveguides and in a constructive interference in the other one. The

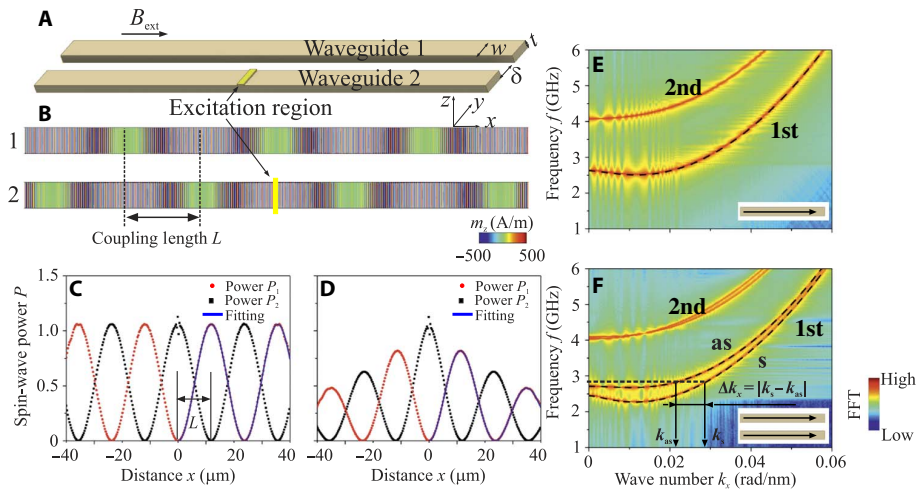


Fig. 2. Energy transfer in dipolarly coupled waveguides. A schematic view of the dipolarly coupled SW waveguides (A) and a snapshot of the SW profile excited in them (B). The excitation antenna (shown in yellow) is located in the center of one of the waveguides. Variation of the SW power in both waveguides as a function of propagation distance x for the case of zero SW damping (C) and for the typical damping in YIG film (D). (E) Dispersion characteristics of the two lowest width SW modes in a single isolated waveguide. (F) Similar dispersion curves for a pair of coupled waveguides. A color map represents the results of our numerical simulations, whereas the dashed lines represent the analytical theory. Splitting of the SW dispersion curves into antisymmetric (as) (top) and symmetric (s) (bottom) branches due to the dipolar coupling between the waveguides is shown.

SW energy is completely transferred from one waveguide to the other after propagation for a coupling length L . Analogously, the energy is transferred back to the first waveguide after the further propagation for the same distance L , and the process is periodic (see movie S1). Note that the complete SW energy periodic exchange between the coupled waveguides is possible only if the waveguides are identical, have parallel or antiparallel static magnetization, and experience the same internal magnetic field. In other cases, the SW energy is also transferred on a distance L , but the transfer is incomplete (43).

Coupling length

Figure 3 shows the dependence of the coupling length L on the geometrical parameters of the waveguides: the gap size δ (Fig. 3A), the thickness t (Fig. 3C), the width w (Fig. 3D) of the waveguides, and, on the SW, wave number k_x (Fig. 3B). In general, it can be seen that the increase of the dipolar coupling between the waveguides results in a decrease of L . The coupling between the waveguides is increased by a decrease of the gap δ between the waveguides, by a decrease in their width w , or by an increase in their thickness t . Note, also, that the coupling strength is decreased with increasing SW wave number k_x , due to the decreased dipolar interaction for short-wavelength exchange SWs. The latter is a challenge that should be addressed in the design of future nanomagnonics devices operating with SWs on the nanometer wavelength scale. One way to overcome this difficulty is to further decrease the gap between the waveguides. Another possible way to increase the coupling between the waveguides and, thus, to decrease the lateral sizes of the directional coupler is to fill the gap between the waveguides with another magnetic material [see, for example, the study of Wang *et al.* (44)]. For this purpose, it is preferable to use magnetic materials with higher values of M_s to ensure that the SW excitation in this material has higher frequencies and does not disturb the operational characteristics of the directional coupler (these studies are beyond the scope of the present work). The results obtained from the micromagnetic simulations (circle points) and from the analytical theory (lines) are consistent with those

in Fig. 3. In the waveguides with a width $w > 150$ nm, the SW profile across the width becomes essentially nonuniform due to dipolar pinning (34, 35), and the micromagnetically calculated SW profiles (in an isolated waveguide) are used for the calculation of the geometric form factor σ_k .

In the course of our simulations, a single-frequency SW was excited in one of the waveguides, and the width profile of this SW mode was extracted from the results of numerical simulation. The function $m_x(y) = A_0 \cdot \cos(\pi y/w_{\text{eff}})$, where A_0 is the amplitude, was used to fit the numerically calculated width profile of the SW mode to obtain the effective waveguide width w_{eff} . Then, this effective width was inserted into Eq. 9 for analytic calculations. The inset in Fig. 3D shows the dependence of the effective width on the geometrical width w of the waveguides. The effective width strongly increases with the decrease in w , which corresponds to the gradual decrease of the effective dipolar pinning at the lateral edges of the waveguides (34, 35).

Antiparallel magnetization configuration

In the previous sections, it was assumed that a small external bias magnetic field was applied along the x direction to orient the static magnetization along the waveguides' long axes. However, in nanoscale waveguides, the static magnetization orients itself parallel to the waveguides spontaneously without any external field due to the strong shape anisotropy of the elongated nature of a waveguide. Moreover, in the absence of an external field, waveguides can exist in two stable magnetic configurations—with parallel and antiparallel static magnetizations. The analytical calculations show that the SW dispersion and, therefore, the coupling length depend significantly on the static magnetization configuration. This is a result of the gyrotropic motion of the magnetization vector—in the parallel configuration, the magnetization vectors of both waveguides rotate in the same direction, whereas in the antiparallel configuration, they rotate in the opposite directions, which leads to a different dynamic magneto-dipolar interaction between the waveguides. In particular, for the antiparallel configuration of the

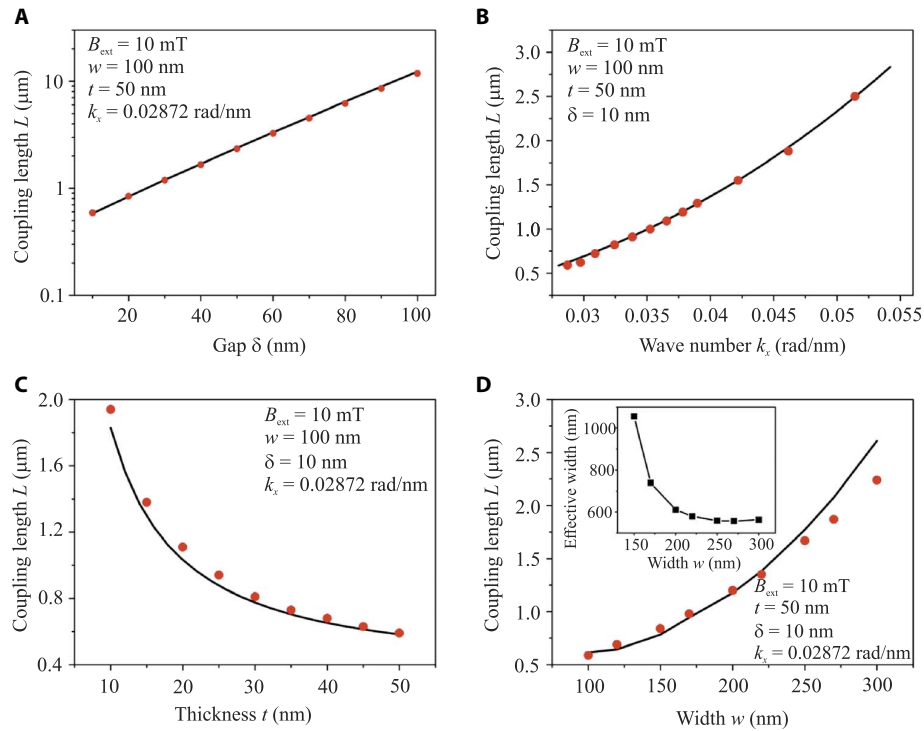


Fig. 3. Coupling length. The coupling length L , that is, the SW propagation length over which the SW energy is transferred from one waveguide to the other, is shown as a function of (A) the separation δ between the waveguides, (B) the longitudinal wave number k_x , (C) the thickness t of the waveguides, and (D) the width w of the waveguides. These results were obtained by means of numerical simulations (symbols) and analytical calculations (lines). The parameters for each particular case are shown directly inside the panels. The inset in (D) shows the dependence of the effective width w_{eff} of the waveguide on the nominal width w (the line is a guide for the eye). The decrease in the waveguide width results in the reduction of the effective dipolar pinning at the lateral edges of the waveguides and in the corresponding increase of the effective waveguide width.

waveguide static magnetizations, the splitting of the dispersion relation of the symmetric and antisymmetric collective modes is given by

$$\Delta f = \omega_M \frac{\Omega^{zz} F_{k_x}^{yy}(d) - \Omega^{yy} F_{k_x}^{zz}(d)}{4\pi^2 f_0(k_x)} \quad (14)$$

This equation is substantially different from the splitting Eq. 13 that takes place in the case of parallel static magnetization of the coupled waveguides. As one can see from Fig. 4 (A and B), the frequency splitting is stronger for the antiparallel magnetization configuration, which results from the stronger interaction of the oppositely precessing dynamic magnetizations in the two coupled waveguides. Consequently, the coupling length for the antiparallel configuration is always smaller than that for the parallel magnetization configuration, as one can see from the dependence of the coupling length L on the gap δ and on the SW wave number k_x shown in Fig. 4, C and D, respectively.

Design of a directional coupler

The dipolarly coupled SW modes in parallel waveguides have a large potential for applications. The functionality of a microwave signal processing device based on two laterally parallel coupled waveguides depends on the ratio between the coupling length L and the length of the coupled waveguides L_W . Thus, according to Eq. 3, if $L_W = (2n + 1)L$, where n is an integer value, then the entire energy will be transferred

from one waveguide to the other, and the directional coupler can be used as a connector of magnonic conduits. If $L_W = (n + 1/2)L$, then the coupler can be used as an equal divider (3 dB in each beam pass) for microwave power. Taking into account that the coupling length L strongly depends on the SW wave number k and, consequently, on the signal frequency, the directional coupler can be used as a frequency separator. Finally, the variation of the external bias magnetic field and/or of the direction of static magnetization in one of the coupled waveguides allows the switching of the functionality of the directional coupler having a fixed length L_W and fixed signal frequency.

One of the challenging tasks in the practical realization of a directional coupler is the design of the inputs (outputs) to (from) the coupled SW waveguides that are needed to precisely define the L_W/L ratio [note, for example, the absence of such inputs and outputs in the studies of Sadovnikov and colleagues (30–32)]. The design of directional couplers proposed here is somewhat analogous to the design of optical directional couplers (29) but needs a substantial modification because of the anisotropy of the SW dispersion laws and their qualitative dependence of the orientation of the static magnetization in an SW waveguide (21, 45). Moreover, the SW spectra typically have a multimode character, which can significantly complicate the SW microwave signal processing (19). Most of these problems are automatically solved, when the sizes of the magnonic signal processing devices are scaled down to below a micrometer. In this case, the frequencies of the SW modes are well separated due to the strong exchange interaction that shifts the frequency of the higher-order thickness and width modes by several gigahertz (see, for

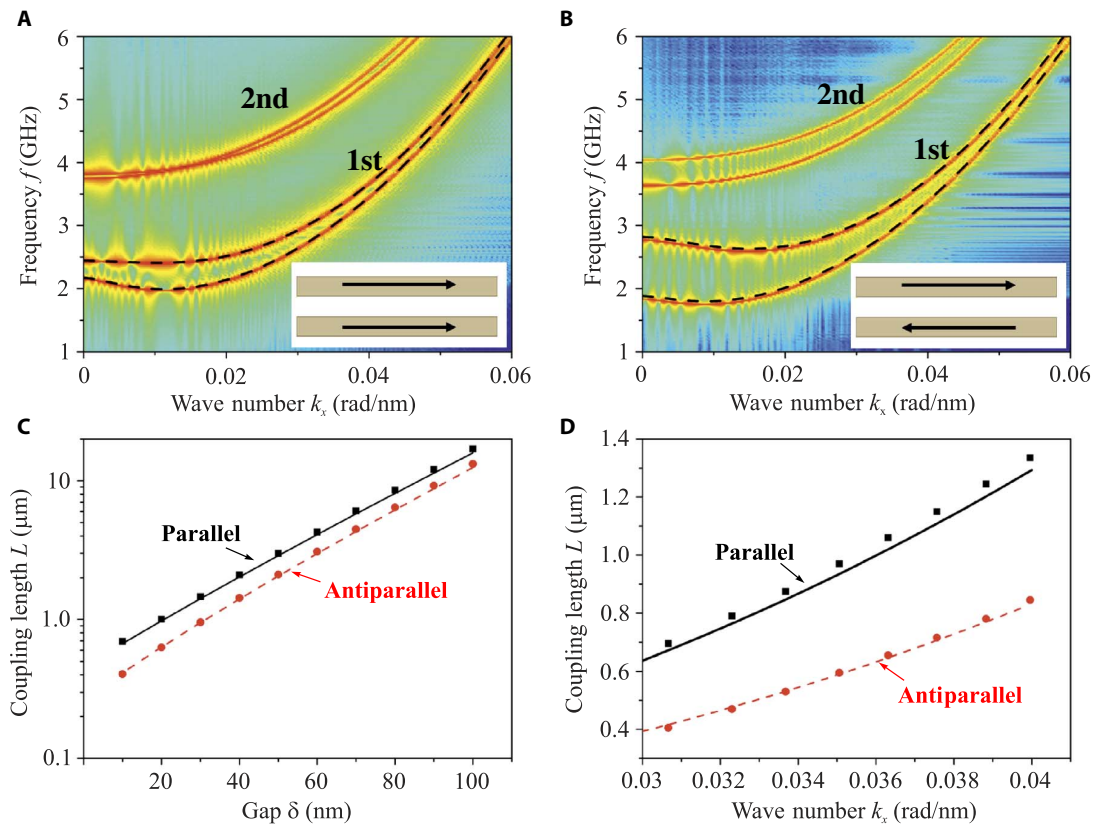


Fig. 4. Dependence on the static magnetization configuration. Dispersion characteristics of the lowest SW width modes in coupled waveguides for the cases of parallel (A) and antiparallel (B) orientation of the static magnetizations of the waveguides (see insets). Dashed lines show the results of the analytic theory. The waveguide parameters are as follows: width $w = 100$ nm, thickness $t = 50$ nm, and gap width $\delta = 10$ nm. Coupling length as a function of the gap width δ ($k_x = 0.03066$ rad/nm) (C) and as a function of the longitudinal wave number k_x ($\delta = 10$ nm) (D) for parallel (black squares and solid black lines) and antiparallel (red circles and dashed red lines) static magnetization configurations. The symbols show the numerical results, whereas lines correspond to the results calculated analytically.

example, Fig. 2E). Moreover, as described above, the strong shape anisotropy of the elongated SW waveguides makes the waveguides static magnetization parallel to the long axis of the waveguide and, therefore, along the direction of the SW propagation even in the presence of a small external bias magnetic field (see black arrows in Fig. 5A showing the direction of static magnetization). This quasi-isotropic condition for the SW propagation is one of the big advantages of the nanosized magnonic conduits when compared to the similar systems of the micro- and macroscale. The angle between the sections of the directional coupler is chosen to be 20° , as shown in the figure. This angle is small enough to show a good SW transmission through the bent point of the SW waveguide. Additional simulations are performed using the upper left region of the directional coupler (the region that contains two bents of the waveguide and is marked by dashed lines in Fig. 5A, bottom panel) and compared to the reference straight waveguide. The results show that the reflection weakly increases with the increase in the SW wave number but stays below 5% for the design shown in Fig. 5A.

Therefore, the structure shown in Fig. 5A, which is analogous to the directional coupler used in integrated optics (29), is also suitable for the realization of an SW directional coupler but on the nanometer scale. The main drawback of such a design is that the corners of the structure (marked with red circles in Fig. 5A) could act as secondary SW sources,

thus disrupting the operational characteristics of the device. To minimize these distortions, we introduced a translational shift $d_s = 100$ nm between the beams in the practical model of the proposed directional coupler, as shown in Fig. 5A. In the absence of this shift ($d_s = 0$ nm), the transmission of the SW power to the other waveguide drops down from 99.6 to 97.9% (for the case illustrated in Fig. 6A). The increase of the shift $d_s > 100$ nm, practically, does not influence the transmission anymore if the length L_W is fixed. The improvement of the transmission characteristics is independent of the direction of the translational shift. In the following studies, we fixed the width of the waveguides to $w = 100$ nm, the thickness to $t = 50$ nm, and the gap between the waveguides to $\delta = 30$ nm. The length of the coupled waveguides L_W was fixed to be equal to $L_W = D - d_s = 4900$ nm.

Figure 5B shows the normalized output power in the first beam pass $P_{1 \text{ out}}/(P_{1 \text{ out}} + P_{2 \text{ out}})$ as a function of the SW wave number k_x . The symbols represent the results of the micromagnetic simulations, and the lines are obtained from the analytical theory for the parallel (black) and antiparallel (red) configuration of the waveguides' static magnetizations, respectively.

Note that, despite the fact that the directional coupler as a whole was studied by micromagnetic simulations, although only the parallel parts (of the length L_W) of the coupled waveguides were considered in the

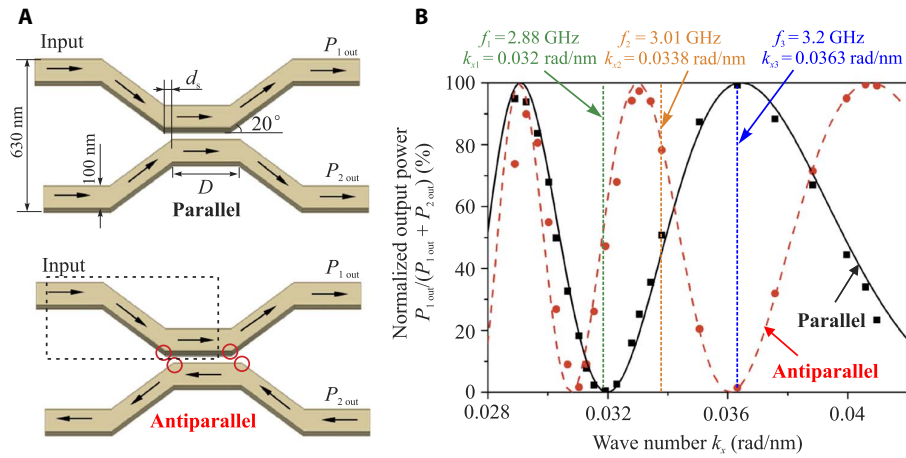


Fig. 5. Reconfigurable SW directional coupler. (A) Schematic view of the parallel and antiparallel magnetization configuration of the directional coupler. The widths of the waveguides are $w = 100$ nm, thickness is $t = 50$ nm, and gap is $\delta = 30$ nm; the angle between the coupler waveguides is 20° ; and the working length of the coupled waveguides is $L_W = D - d_s = 4900$ nm. The arrows show the direction of the static magnetization. The SWs are excited in the first beam pass of the directional coupler marked as "Input." (B) Wave number dependence of the normalized power at the output of the first beam pass $P_{1\text{ out}}/(P_{1\text{ out}} + P_{2\text{ out}})$ (%) of the directional coupler. The symbols and lines were obtained by micromagnetic simulations and the analytical theory for parallel (black squares and solid black line) and antiparallel (red circles and dashed red line) configurations, respectively. The vertical dashed lines indicate the wave numbers (and corresponding frequencies), which are chosen for the demonstration of different functionalities of the directional coupler in Fig. 6.

framework of the analytical theory, the difference in the results is very small. This is an indication of the high efficiency (small SW reflections) of the proposed directional coupler design. It can be seen in Fig. 5 that the operational characteristics of the directional coupler can be easily tuned by the variation of the SW wave number (that is, by the frequency of the input microwave signal). Moreover, this tuning is different for parallel and antiparallel configurations of the static magnetization that provides an additional degree of freedom to the utilization of the coupler. In the following, we choose three different values of the SW wave number, which are shown by vertical dashed lines in Fig. 5B, and perform separate simulations for the case of a single-frequency input signal. The design and all the sizes of the directional coupler are kept the same for all the simulations shown in Fig. 6. There is no biasing magnetic field applied in all cases shown in Fig. 6 excluding Fig. 6 (H and J).

Functionalities of a directional coupler

Figure 6 shows the color maps of the SW amplitude (represented by the variable component of the dynamic magnetization m_x) in a directional coupler for different input frequencies and, consequently, wave numbers. Because it is expected from the results shown in Fig. 5B, the SW of the frequency $f_1 = 2.88$ GHz is almost fully transferred to the second waveguide. After a few oscillations between the waveguides, 99.6% of the output SW energy (here, we show the fraction of the output SW power between two outputs) is detected at the second pass of the device in our simulations. The coupling length ($L = 1630$ nm in this case) satisfies the ratio $L_W = 3 \times L$. Thus, this directional coupler can be used to effectively connect two magnonic conduits. If the SW of the same frequency is excited in the other pass of the coupler, then the SW energy will be transferred into the opposite pass in a similar way.

The situation is different for the SW of the frequency $f_3 = 3.2$ GHz (see Fig. 6C) that corresponds to a longer coupling length of $L = 2450$ nm. The length of the waveguides is $L_W = 2 \times L$ in this case (see also Fig. 5B), and the SW energy is transferred back to the input pass of the directional coupler. This means that the directional coupler can be used as a frequen-

cy separator (multiplexer): If SWs of different frequencies f_1 and f_3 are simultaneously excited in the same beam pass of the waveguide, then the SW of frequency f_1 will exit from one pass of the coupler, whereas the signal of frequency f_3 will exit from the other pass, as shown in Fig. 6 (D to F) (see also movie S2). Figure 6B shows that the directional coupler can be used as a 3-dB power divider in which half of the energy is transferred to the second pass of the coupler and half of the energy stays in the first pass. A propagating SW of the frequency $f_2 = 3.01$ GHz corresponding to $L = 1960$ nm has been excited in this case to ensure the condition $L_W = 2.5 \times L$. The ratio between the output energies in both beam passes of the waveguide can be easily tuned by the frequency of the input signal.

Furthermore, the ratio between the output powers can be adjusted by shifting the dispersion curves up or down using an applied external magnetic field. An SW of the frequency $f_3 = 3.2$ GHz has a coupling length $L = 2450$ nm (unbiased case). In this case, the SW energy is transferred back to the same input pass of the directional coupler (see Fig. 6G). When the external bias magnetic field is increased to 7.1 mT, the coupling length decreases to 1960 nm, and the directional coupler acts as a 3-dB power divider (see Fig. 6H). The continuing increase of the bias field to 12 mT results in the coupling length further decreasing to 1630 nm, and in such a situation, most of the SW energy is transferred to the second pass of the directional coupler, as shown in Fig. 6I. The energy of the propagating SW can be switched from one pass to the other during a few nanoseconds using the application of an abrupt step in the external bias field. Movie S3 shows the situation in which the biasing magnetic field B_{ext} is changed from 0 to 12 mT within 10 ns. Because the magnetization ground state is not changed in this case (as opposed to the process of the switching of the magnetization direction discussed further), the switching time is limited only by the time that the SW needs to pass the directional coupler (around 20 ns in our simulations).

Finally, we study the case when an SW of frequency f_3 is excited (see Fig. 6J), but the relative orientation of the static magnetizations in the

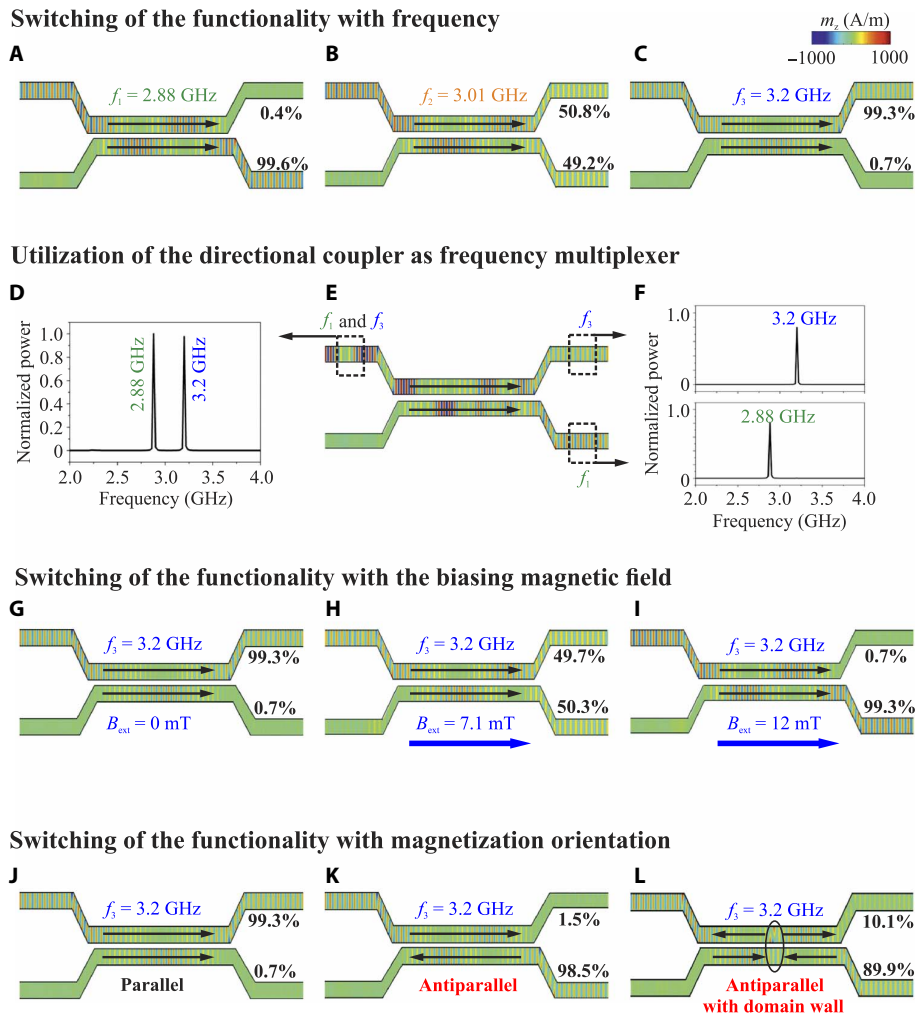


Fig. 6. Dynamically reconfigurable SW directional coupler. (A to C) Switching of the device functionality by changing the signal frequency. Directional coupler acts as a connector of magnonic conduits, as a 3-dB power divider, or as a simple transmission line (delay line). (D to F) Utilization of the directional coupler as a frequency separator (multiplexer). The directional coupler can be used as a frequency multiplexer. SWs of two frequencies simultaneously excited in the first beam pass of the coupler will reach different output beams. (G to I) Switching of the device functionality by changing the bias magnetic field. The ratio of the output powers in two beam passes can be changed by the variation of the bias magnetic field. The demagnetization fields were taken into account in the simulations. (J and K) Switching of the device functionality by changing the static magnetization orientation. Switching the relative orientation of the static magnetization in two beam passes leads to the switching of the output signal between the beam passes. (L) Even in the case when the remagnetization process leads to the formation of a domain wall in the device beam passes, the main part (90%) of the output signal power is still transferred from the upper to the lower beam pass. The SW amplitude is shown by a color map. Note that the width of the waveguides is constant in all parts of the directional coupler, as shown in Fig. 5A. The structures are compressed in the direction along the waveguide for a better illustration of the coupling effects.

beam passes has been switched from parallel to antiparallel (see Fig. 6K). As expected, on the basis of the results presented in Fig. 5B, most of the SW energy is transferred in that case from one pass of the directional coupler to the other one due to the shorter coupling length L for the antiparallel magnetization configuration ($L = 1640$ nm in this case satisfies the condition $L_W = 3 \times L$). Thus, the proposed directional coupler turns out to be fully dynamically reconfigurable and can be used as an effective and fast switch and/or multiplexer (9).

Obviously, the operational frequency of the device can be easily varied with the length of the directional coupler L_W by the geometry of the waveguides that defines the coupling length L or by the external bias magnetic field. However, it is important to note that the maximum

operating power of such a frequency multiplexer is limited by different nonlinear SW phenomena (18, 30, 45).

Switching of the orientation of static magnetization in a directional coupler

Here, we would like to discuss the practical realization of the switching of the relative orientation of the static magnetizations in the passes of the directional coupler (see Fig. 4). Taking into account a very short separation distance between the parallel passes of the coupler, it is difficult to remagnetize the passes of the coupler independently using external magnetic fields. Instead, here, we propose to use a method similar to the one used in previous studies (12, 46–48) for the switching of

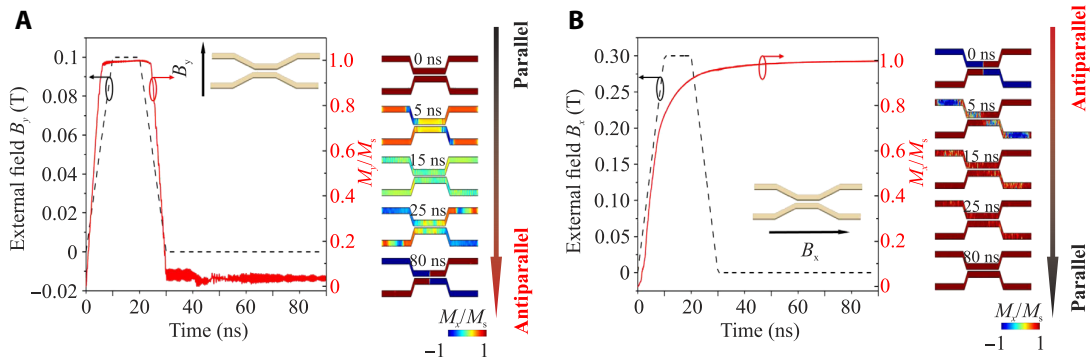


Fig. 7. Switching of the directional coupler. (A) Application of a magnetic field pulse in the direction transverse to the coupled waveguide direction results in the switching of the magnetization from the parallel to the antiparallel state (see color map in the right panels for M_x component). Two domain walls are formed in the centers of the coupler beam passes in such antiparallel magnetization configuration. (B) Profile of the longitudinal magnetic field pulse for the switching of the directional coupler magnetization back into the parallel state. The magnetization configuration is shown in the same way as in (A).

the magnetic state in arrays of dipolarly coupled magnetic nanodots. Namely, we apply a short (~ 20 ns) magnetic field (0.1 T) pulse in the perpendicular direction (y direction), which temporarily magnetizes both waveguides in the y direction (Fig. 7A).

Then, the applied field is decreased to zero within 10 ns. This evolution not only allows the static magnetization in the coupler to be spontaneously directed along the long axes of the waveguides (see movie S4) but also results in the excitation of parasitic SWs in the structure (see the long tail in the M_y characteristics). In general, the device is ready for operation after a time period exceeding at least one SW life cycle, which, in our case, is equal to 252 ns (for the 3-GHz frequency).

However, even 50 ns after the bias field has been turned off, one can see that the magnetization distribution in the directional coupler assumes the form shown in the right panels of Fig. 7A. Each pass of the waveguide contains a domain wall in the center of the structure (due to the energy minimum condition) and is therefore separated into two regions with opposite directions of the static magnetization. The magnetization orientations in both regions are antiparallel to each other as desired.

To prove that the domain walls do not substantially disturb the operational characteristics of the device, we performed additional simulations for a single SW waveguide with the same domain wall structure and showed that the SW reflection coefficient due to the domain wall is only 3%. Figure 6L demonstrates that the magnetization configuration with the presence of the domain walls does not have much influence on the operational characteristics of the directional coupler when compared to the ideal antiparallel aligned magnetization configuration shown in Fig. 6K.

To switch the magnetization configuration of the directional coupler back to the parallel state, we applied a field of 0.3 T in the x direction (parallel to the waveguides), as shown in Fig. 7B. The magnetic field is switched on again for 30 ns with a rise and fall time of 10 ns. Note that these time intervals are important because the switching of the magnetic field for a shorter period will not necessarily result in the switching of the magnetization configuration. The magnetization orientation is shown in the same way as in Fig. 7A. One can see that approximately 50 ns after the external field was switched off, the directional coupler stays in its original parallel magnetization configuration (see movie S5). Figure 6J shows the SW amplitude in this case, and one can see that the SW energy reaches the same beam pass in which it was originally excited. Thus, the proposed methodology allows the realization of the SW switch.

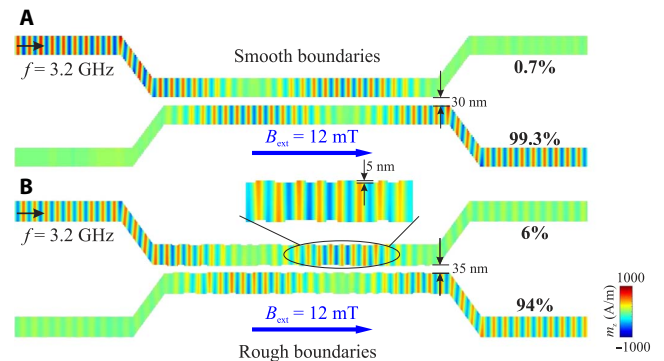


Fig. 8. Influence of rough boundaries on the characteristics of a directional coupler. A snapshot of the SW profile in (A) smooth boundaries and (B) rough boundaries.

Robustness of the directional coupler characteristics

We would like to mention that the simulations presented here were performed without taking into account temperature, that is, for zero effective temperature. Additional numerical simulations, identical to those shown in Fig. 6A (at an SW frequency of 2.88 GHz), were performed at an effective temperature of 300 K (using the embedded MuMax3 package) to explore the influence of temperature on the characteristics of the directional coupler (see movies S6 and S7). Only a small difference between the operational characteristics of the device was obtained for different temperatures: The output power of the device is 99.6% at zero temperature and 86.3% at room temperature. The difference is mainly caused by a slight shift of the dispersion characteristics of SWs due to the decrease in the saturation magnetization (49) that results, consequently, in a change of the coupling length. This behavior is analogous to the temperature-induced change of the coupling length in optical directional couplers due to the change of the refractive index (29, 50). The role of temperature can be decreased by an adjustment of the coupling length via a slight variation of the signal frequency. The output power of the device can be increased to 94.5% at room temperature by slightly decreasing the frequency to 2.84 GHz (see movie S8).

Finally, we would like to discuss the influence of rough boundaries at the edges of the SW waveguides (that might result from the fabrication

process) on the characteristics of a magnonic directional coupler. Additional numerical simulations, similar to those shown in Fig. 6I (in the presence of a weak external magnetic field of 12 mT), were performed with rough boundaries (see Fig. 8B). Five-nanometer-wide and randomly defined long (from 50 to 400 nm to be comparable to the SW wavelength) rectangular magnetic elements are additionally introduced on both sides of each SW waveguide to act as roughness. The introduction of the roughness results in the increase of the average width of the waveguides. To compensate it, we increased the gap δ from 30 to 35 nm. Only a small difference in the operational characteristics of the directional coupler was found for different boundary conditions: The output power of the device is 99.3% for the smooth boundaries and 94% for the rough boundaries. These robust operational characteristics are due to the “diluted” SW dispersion spectra in the nanoscale waveguide shown in Fig. 2F, in which the frequencies of higher thickness and width modes are separated by several gigahertz. As a result, the elastic two-magnon scattering damping mechanism is absent (19, 21). This is an additional advantage given to the directional coupler by its nanometer sizes.

CONCLUSION

In conclusion, a practical design of a nanoscale SW directional coupler is proposed and studied by means of micromagnetic simulations and analytical theory. The interference between the two collective SW modes of two laterally parallel and dipolarly coupled magnetic waveguides separated by a gap provides a mechanism responsible for the operation of the device. The coupling length L , over which the energy of an SW is transferred from one waveguide to the other, is studied as a function of the SW wave number, geometry of the coupler, relative orientation of the static magnetization in the coupled waveguides, and the magnitude of the applied magnetic field (if it is used). The proposed design of the device allows one to use it as a directional coupler, as a controlled multiplexer, as a frequency separator, or as a power divider for microwave signals. Our micromagnetic simulations have also shown that the proposed device has an additional benefit: Its functionality can be dynamically reconfigured within tens of nanoseconds by application of a short pulse of an external bias magnetic field. Finally, the robustness of the coupler has been tested in additional numerical simulations, where geometric sizes were varied. These simulations ensured us that the experimental realization of the device is possible. The nanometer sizes of the proposed directional coupler and its ability to operate without external bias field make the proposed device interesting and useful for the processing of both digital and analog microwave signals at the nanoscale.

MATERIALS AND METHODS

Extraction of the dispersion relations from the results of micromagnetic simulation

The micromagnetic simulations were performed using the MuMax3 (39) code. It uses the Dormand-Prince method (51) for the integration of the LL-Gilbert equation

$$\frac{d\mathbf{M}}{dt} = -\gamma|\mathbf{M} \times \mathbf{B}_{\text{eff}} + \frac{\alpha}{M_s}(\mathbf{M} \times \frac{d\mathbf{M}}{dt}) \quad (15)$$

where \mathbf{M} is the magnetization vector; \mathbf{B}_{eff} is the effective field that includes exchange, external, and demagnetization fields; γ is the gyromagnetic ratio; and α is the damping constant. The material parameters

were given in the main text. There were three steps involved in the calculation of the SW dispersion curve in our simulation: (i) The external field was applied along the waveguide, and the magnetization was relaxed to a stationary state (ground state). This state was consequently used as the ground state in the following simulations. (ii) To excite odd and even SW width modes, a sinc field pulse was applied to a 20-nm-wide area located on one side of the waveguide. The sinc field is $b_y = b_0 \text{sinc}(2\pi f_c t)$, with an oscillation field $b_0 = 1$ mT and a cutoff frequency $f_c = 20$ GHz. The $M_z(x, y, t)$ of each cell was collected over a period of $T = 100$ ns and recorded in $T_s = 25$ -ps intervals, which allows a frequency resolution of $\Delta f = 1/T = 0.01$ GHz, whereas the highest resolvable frequency was $f_{\text{max}} = 1/(2T_s) = 20$ GHz. The fluctuations in $m_z(x, y, t)$ were calculated for all the cells, $m_z(x, y, t) = M_z(x, y, t) - M_z(x, y, 0)$, where $M_z(x, y, 0)$ corresponds to the ground state obtained from the first step. (iii) To obtain the SW dispersion curves, we performed two-dimensional (2D) fast Fourier transformation (FFT) (52, 53)

$$m_z(k_x, f) = \frac{1}{N} \sum_{i=1}^N |\mathcal{F}_2[m_z(x, y_i, t) - m_z(x, y_i, 0)]|^2 \quad (16)$$

where \mathcal{F}_2 is the 2D FFT, y_i is the i th cell along the width of the waveguide, and N is the total number of the cells along the width of the waveguide. To visualize the dispersion curve, we recorded a 3D color map of $P(k_x, f) \propto m_z(k_x, f)$ in logarithmic scale versus f and k_x , which is shown in Figs. 2 (E and F) and 4 (A and B). We performed 2D FFT on the time evolution and along the waveguide. Next, the average FFT amplitude was taken along the width of the waveguide. This method allows us to obtain information about all the SW modes (even and odd) existing in the waveguide.

SUPPLEMENTARY MATERIALS

Supplementary material for this article is available at <http://advances.sciencemag.org/cgi/content/full/4/1/e1701517/DC1>

- movie S1. SW propagation in coupled waveguides.
- movie S2. SW directional coupler acts as a multiplexer.
- movie S3. Switching of the device functionality by changing the bias magnetic field.
- movie S4. Ground-state switching: parallel to antiparallel.
- movie S5. Ground-state switching: antiparallel to parallel.
- movies S6 to S8. The effects of temperature on the directional coupler properties.

REFERENCES AND NOTES

1. V. V. Kruglyak, S. O. Demokritov, D. Grundler, *Magnonics*. *J. Phys. D Appl. Phys.* **43**, 264001 (2010).
2. A. Khitun, M. Bao, K. L. Wang, *Magnonic logic circuits*. *J. Phys. D Appl. Phys.* **43**, 264005 (2010).
3. D. E. Nikonov, I. A. Young, Overview of beyond-CMOS devices and a uniform methodology for their benchmarking. *Proc. IEEE* **101**, 2498–2533 (2013).
4. A. V. Chumak, A. A. Serga, B. Hillebrands, *Magnonic crystals for data processing*. *J. Phys. D Appl. Phys.* **50**, 244001 (2017).
5. M. Krawczyk, D. Grundler, Review and prospects of magnonic crystals and devices with reprogrammable band structure. *J. Phys. Condens. Matter* **26**, 123202 (2014).
6. A. V. Chumak, V. I. Vasyuchka, A. A. Serga, B. Hillebrands, *Magnon spintronics*. *Nat. Phys.* **11**, 453–461 (2015).
7. Y. Kajiwara, K. Harii, S. Takahashi, J. Ohe, K. Uchida, M. Mizuguchi, H. Umezawa, H. Kawai, K. Ando, K. Takanashi, S. Maekawa, E. Saitoh, Transmission of electrical signals by spin-wave interconversion in a magnetic insulator. *Nature* **464**, 262–266 (2010).
8. S. Urazhdin, V. E. Demidov, H. Ulrichs, T. Kendziorczyk, T. Kuhn, J. Leuthold, G. Wilde, S. O. Demokritov, *Nanomagnonic devices based on the spin-transfer torque*. *Nat. Nanotechnol.* **9**, 509–513 (2014).
9. K. Vogt, F. Y. Fradin, J. E. Pearson, T. Sebastian, S. D. Bader, B. Hillebrands, A. Hoffmann, H. Schultheiss, Realization of a spin-wave multiplexer. *Nat. Commun.* **5**, 3727 (2014).

10. P. Pirro, T. Brächer, A. V. Chumak, B. Lägler, C. Dubs, O. Surzhenko, P. Gönert, B. Leven, B. Hillebrands, Spin-wave excitation and propagation in microstructured waveguides of yttrium iron garnet/Pt bilayers. *Appl. Phys. Lett.* **104**, 012402 (2014).
11. V. E. Demidov, S. Urzhidin, R. Liu, B. Divinskiy, A. Telegin, S. O. Demokritov, Excitation of coherent propagating spin waves by pure spin currents. *Nat. Commun.* **7**, 10446 (2016).
12. A. Haldar, D. Kumar, A. O. Adeyeye, A reconfigurable waveguide for energy-efficient transmission and local manipulation of information in a nanomagnetic device. *Nat. Nanotechnol.* **11**, 437–443 (2016).
13. H. Yu, O. d'Allivy Kelly, V. Cros, R. Bernard, P. Bortolotti, A. Anane, F. Brandl, F. Heimbach, D. Grundler, Approaching soft x-ray wavelengths in nanomagnet-based microwave technology. *Nat. Commun.* **7**, 11255 (2016).
14. M. Collet, O. Gladii, M. Evelt, V. Bessonov, L. Soumah, P. Bortolotti, S. O. Demokritov, Y. Henry, V. Cros, M. Bailleul, V. E. Demidov, A. Anane, Spin-wave propagation in ultra-thin YIG based waveguides. *Appl. Phys. Lett.* **110**, 092408 (2017).
15. D. Bossini, S. Dal Conte, Y. Hashimoto, A. Secchi, R. V. Pisarev, Th. Rasing, G. Cerullo, A. V. Kimel, Macrospin dynamics in antiferromagnets triggered by sub-20 femtosecond injection of nanomagnons. *Nat. Commun.* **7**, 10645 (2016).
16. T. Schneider, A. A. Serga, B. Hillebrands, R. L. Stamps, M. P. Kostylev, Realization of spin-wave logic gates. *Appl. Phys. Lett.* **92**, 022505 (2008).
17. K.-S. Lee, S.-K. Kim, Conceptual design of spin wave logic gates based on a Mach-Zehnder-type spin wave interferometer for universal logic functions. *J. Appl. Phys.* **104**, 053909 (2008).
18. A. V. Chumak, A. A. Serga, B. Hillebrands, Magnon transistor for all-magnon data processing. *Nat. Commun.* **5**, 4700 (2014).
19. S. Klingler, P. Pirro, T. Brächer, B. Leven, B. Hillebrands, A. V. Chumak, Design of a spin-wave majority gate employing mode selection. *Appl. Phys. Lett.* **105**, 152410 (2014).
20. O. Zografos, B. Sorée, A. Vaysset, S. Cosemans, L. Amarù, P.-E. Gaillardon, G. D. Micheli, R. Lauwereins, S. Sayan, P. Raghavan, I. P. Radu, A. Thean, Design and benchmarking of hybrid CMOS-spin wave device circuits compared to 10nm CMOS, *IEEE Proceedings of the 15th International Conference on Nanotechnology*, Rome, Italy, 27 to 30 July 2015 (IEEE, 2016).
21. S. Klingler, P. Pirro, T. Brächer, B. Leven, B. Hillebrands, A. V. Chumak, Spin-wave logic devices based on isotropic forward volume magnetostatic waves. *Appl. Phys. Lett.* **106**, 212406 (2015).
22. S. Dutta, S.-C. Chang, N. Kani, D. E. Nikonov, S. Manipatruni, I. A. Young, A. Naeemi, Non-volatile clocked spin wave interconnect for beyond-CMOS nanomagnet pipelines. *Sci. Rep.* **5**, 9861 (2015).
23. A. A. Nikitin, A. B. Ustinov, A. A. Semenov, A. V. Chumak, A. A. Serga, V. I. Vasyuchka, E. Lähderanta, B. A. Kalinikos, B. Hillebrands, A spin-wave logic gate based on a width-modulated dynamic magnonic crystal. *Appl. Phys. Lett.* **106**, 102405 (2015).
24. K. Ganzhorn, S. Klingler, T. Wimmer, S. Geprägs, R. Gross, H. Huebl, S. T. B. Goennenwein, Magnon based logic in a multi-terminal YIG/Pt nanostructure. *Appl. Phys. Lett.* **109**, 022405 (2016).
25. N. Sato, K. Sekiguchi, Y. Nozaki, Electrical demonstration of spin-wave logic operation. *Appl. Phys. Express* **6**, 063001 (2013).
26. M. Balynsky, D. Gutierrez, H. Chiang, A. Kozhevnikov, G. Dudko, Y. Filimonov, A. A. Balandin, A. Khitun, A magnetometer based on a spin wave interferometer. *Sci. Rep.* **7**, 11539 (2017).
27. A. K. Ganguly, C. Vittoria, Magnetostatic wave propagation in double layers of magnetically anisotropic slabs. *J. Appl. Phys.* **45**, 4665–4667 (1974).
28. H. Sasaki, N. Mikoshiba, Directional coupling of magnetostatic surface waves in a layered structure of YIG films. *J. Appl. Phys.* **52**, 3546–3552 (1981).
29. A. V. Krasavin, A. V. Zayats, Active nanophotonic circuitry based on dielectric-loaded plasmonic waveguides. *Adv. Opt. Mater.* **3**, 1662–1690 (2015).
30. A. V. Sadovnikov, E. N. Beginin, S. E. Sheshukova, D. V. Romanenko, Y. P. Sharaevskii, S. A. Nikitov, Directional multimode coupler for planar magnonics: Side-coupled magnetic stripes. *Appl. Phys. Lett.* **107**, 202405 (2015).
31. A. V. Sadovnikov, E. N. Beginin, M. A. Morozova, Y. P. Sharaevskii, S. V. Grishin, S. E. Sheshukova, S. A. Nikitov, Nonlinear spin wave coupling in adjacent magnonic crystals. *Appl. Phys. Lett.* **109**, 042407 (2016).
32. A. V. Sadovnikov, A. A. Grachev, E. N. Beginin, S. E. Sheshukova, Y. P. Sharaevskii, S. A. Nikitov, Voltage-controlled spin-wave coupling in adjacent ferromagnetic-ferroelectric heterostructures. *Phys. Rev. Appl.* **7**, 014013 (2017).
33. T. Fischer, M. Kewenig, D. A. Bozhko, A. A. Serga, I. I. Syvorotka, F. Ciubotaru, C. Adelman, B. Hillebrands, A. V. Chumak, Experimental prototype of a spin-wave majority gate. *Appl. Phys. Lett.* **110**, 152401 (2017).
34. K. Y. Guslienko, S. O. Demokritov, B. Hillebrands, A. N. Slavin, Effective dipolar boundary conditions for dynamic magnetization in thin magnetic stripes. *Phys. Rev. B* **66**, 132402 (2002).
35. K. Y. Guslienko, A. N. Slavin, Boundary conditions for magnetization in magnetic nanoelements. *Phys. Rev. B* **72**, 014463 (2005).
36. R. Verba, G. Melkov, V. Tiberkevich, A. Slavin, Collective spin-wave excitations in a two-dimensional array of coupled magnetic nanodots. *Phys. Rev. B* **85**, 014427 (2012).
37. R. V. Verba, Spin waves in arrays of magnetic nanodots with magnetodipolar coupling. *Ukr. J. Phys.* **58**, 758–768 (2013).
38. M. Beleggia, S. Tandon, Y. Zhu, M. De Graef, On the magnetostatic interactions between nanoparticles of arbitrary shape. *J. Magn. Magn. Mater.* **278**, 270–284 (2004).
39. A. Vansteenkiste, J. Leliaert, M. Dvornik, M. Helsen, F. Garcia-Sanchez, B. Van Waeyenberge, The design and verification of MuMax3. *AIP Adv.* **4**, 107133 (2014).
40. C. Dubs, O. Surzhenko, R. Linke, A. Danilewsky, U. Brückner, J. Dellith, Sub-micrometer yttrium iron garnet LPE films with low ferromagnetic resonance losses. *J. Phys. D Appl. Phys.* **50**, 204005 (2017).
41. H. Yu, O. d'Allivy Kelly, V. Cros, R. Bernard, P. Bortolotti, A. Anane, F. Brandl, R. Huber, I. Stasinopoulos, D. Grundler, Magnetic thin-film insulator with ultra-low spin wave damping for coherent nanomagnonics. *Sci. Rep.* **4**, 6848 (2014).
42. A. A. Serga, A. V. Chumak, B. Hillebrands, YIG magnonics. *J. Phys. D Appl. Phys.* **43**, 264002 (2010).
43. B. E. A. Saleh, M. C. Teich, *Fundamentals of Photonics* (John Wiley & Sons Inc., 1991).
44. Z. K. Wang, V. L. Zhang, H. S. Lim, S. C. Ng, M. H. Kuok, S. Jain, A. O. Adeyeye, Observation of frequency band gaps in a one-dimensional nanostructured magnonic crystal. *Appl. Phys. Lett.* **94**, 083112 (2009).
45. A. G. Gurevich, G. A. Melkov, *Magnetization Oscillations and Waves* (CRC Press, 1996).
46. R. Verba, G. Melkov, V. Tiberkevich, A. Slavin, Fast switching of ground state of a reconfigurable array of magnetic nano-dots. *Appl. Phys. Lett.* **100**, 192412 (2012).
47. R. Verba, V. Tiberkevich, K. Guslienko, G. Melkov, A. Slavin, Theory of ground-state switching in an array of magnetic nanodots by application of a short external magnetic field pulse. *Phys. Rev. B* **87**, 134419 (2013).
48. A. Haldar, A. O. Adeyeye, Deterministic control of magnetization dynamics in reconfigurable nanomagnetic networks for logic applications. *ACS Nano* **10**, 1690–1698 (2016).
49. M. Vogel, A. V. Chumak, E. H. Waller, T. Langer, V. I. Vasyuchka, B. Hillebrands, G. von Freymann, Optically reconfigurable magnetic materials. *Nat. Phys.* **11**, 487–491 (2015).
50. J. Goscinia, S. I. Bozhevolnyi, T. B. Andersen, V. S. Volkov, J. Kjelstrup-Hansen, L. Markey, A. Dereux, Thermo-optic control of dielectric-loaded plasmonic waveguide components. *Opt. Express* **18**, 1207–1216 (2010).
51. J. R. Dormand, P. J. Prince, A family of embedded Runge-Kutta formulae. *J. Comput. Appl. Math.* **6**, 19–26 (1980).
52. D. Kumar, O. Dmytriiev, S. Ponraj, A. Barman, Numerical calculation of spin wave dispersions in magnetic nanostructures. *J. Phys. D Appl. Phys.* **45**, 015001 (2012).
53. G. Venkat, D. Kumar, M. Franchin, O. Dmytriiev, M. Mruczkiewicz, H. Fangohr, A. Barman, M. Krawczyk, A. Prabhakar, Proposal of a standard micromagnetic problem: Spin wave dispersion in a magnonic waveguide. *IEEE Trans. Magn.* **49**, 524–529 (2013).

Acknowledgments

Funding: This research was supported by the European Research Council Starting Grant 678309 MagnonCircuits. R.V. acknowledges support from the Ministry of Education and Sciences of Ukraine (project 0115U002716). A.S. was supported by grants ECCS-1305586 and EFMA-1641989 from the U.S. NSF, by a contract from the U.S. Army TARDEC (Tank Automotive Research, Development and Engineering Center) and RDECOM (Research, Development and Engineering Command), and by the Center for NanoFerroic Devices (CNFD) and the Nanoelectronics Research Initiative (NRI). **Author contributions:** Q.W. proposed the spin-wave directional coupler design, performed micromagnetic simulation, and wrote the first version of the manuscript. P.P. and A.V.C. devised and planned the project. R.V. and A.S. developed the general analytical theoretical model. A.V.C. led the project. All authors discussed the results and contributed to writing the manuscript. **Competing interests:** The authors declare that they have no competing interests. **Data and materials availability:** All data needed to evaluate the conclusions in the paper are present in the paper and/or the Supplementary Materials. Additional data related to this paper may be requested from the authors.

Submitted 9 May 2017

Accepted 14 December 2017

Published 19 January 2018

10.1126/sciadv.1701517

Citation: Q. Wang, P. Pirro, R. Verba, A. Slavin, B. Hillebrands, A. V. Chumak, Reconfigurable nanoscale spin-wave directional coupler. *Sci. Adv.* **4**, e1701517 (2018).



A magnonic directional coupler for integrated magnonic half-adders

Q. Wang^{1,2}✉, M. Kewenig², M. Schneider^{1,2}, R. Verba³, F. Kohl², B. Heinz^{1,2,4}, M. Geilen², M. Mohseni², B. Lägél⁵, F. Ciubotaru⁶, C. Adelmann^{1,6}, C. Dubs^{1,7}, S. D. Cotofana^{1,8}, O. V. Dobrovolskiy¹, T. Brächer², P. Pirro^{1,2} and A. V. Chumak^{1,2}✉

Magnons, the quanta of spin waves, could be used to encode information in beyond-Moore computing applications, and magnonic device components, including logic gates, transistors and units for non-Boolean computing, have already been developed. Magnonic directional couplers, which can function as circuit building blocks, have also been explored, but have been impractical because of their millimetre dimensions and multimode spectra. Here, we report a magnonic directional coupler based on yttrium iron garnet that has submicrometre dimensions. The coupler consists of single-mode waveguides with a width of 350 nm. We use the amplitude of a spin wave to encode information and to guide it to one of the two outputs of the coupler depending on the signal magnitude, frequency and the applied magnetic field. Using micromagnetic simulations, we also propose an integrated magnonic half-adder that consists of two directional couplers and we investigate its functionality for information processing within the magnon domain. The proposed half-adder is estimated to consume energy in the order of attojoules.

Spin waves (and their quanta magnons) in magnetic structures could potentially be used as data carriers in future low-energy computing devices^{1–5}. Spin waves can transfer information with low losses^{1–4,6,7} and can be used to implement logic functionality based on a wide range of nonlinear spin-wave phenomena^{8–10}. The phase of a coherent spin wave provides an additional degree of freedom (beyond amplitude) in data processing, thus decreasing the footprint of logic units^{11–13}, and magnonic structures can be scaled down to the nanometre regime^{14,15} and use spin waves with nanometre wavelengths^{16–18}. Nanoscale single-mode magnonic waveguides can also overcome the issue of parasitic magnon scatterings into higher modes¹⁹. Furthermore, reducing the dimensions of magnonic structures to the atomic scale could potentially shift the frequency of the spin waves from the GHz to the THz range^{20,21}.

Several magnon-based data-processing devices have already been demonstrated, including spin-wave logic gates^{11,22–25}, majority gates^{26,27}, magnon transistors and valves^{8,28}, spin-wave multiplexers^{29,30} and unconventional and neuromorphic computing elements^{31–33}. However, an integrated all-magnonic circuit, which is suitable for the cascading of multiple magnonic units, has not yet been developed. Nanoscale spin-wave directional couplers with reconfigurable functionality can constitute the core of integrated all-magnonic circuits³⁴. However, while spin-wave directional couplers have been explored experimentally³⁵, their millimetre dimensions and multimode spectrum limit their practical implementation.

In this Article, we report a magnonic directional coupler with single-mode waveguides of submicrometre width and based on yttrium iron garnet (YIG). Using space-resolved micro-focused Brillouin light scattering (μ BLS) spectroscopy³⁶, we investigate its functionality as a building block for integrated magnonic circuits.

In the linear regime, the directional coupler exhibits the functionality of a microwave filter for the processing of analogue and digital information, a power splitter for fan-out logic gates and a frequency divider or signal multiplexer. In the nonlinear regime, the outputs of the directional coupler can be controlled by varying the spin-wave amplitude, which can be useful for logic gates. We also combine linear and nonlinear directional couplers numerically to construct a half-adder—a prototype of a magnonic integrated circuit. Numerical benchmarking of the proposed half-adder (based on 30-nm technology) against a 7-nm complementary metal-oxide-semiconductor (CMOS) half-adder shows that the proposed device has a 10-fold lower energy consumption and a comparable device footprint.

Magnonic directional coupler structure

Our submicrometre directional coupler (Fig. 1a) was fabricated from an 85-nm-thick YIG film^{6,7} (Methods) and consists of two spin-wave waveguides with a width of 350 nm. Near the point of spin-wave excitation, the waveguides are physically separated by a narrow gap of 320 nm. To transfer spin waves out of the coupled waveguides into an ‘isolated’ conduit, the waveguides bend at an angle of 12° until achieving a gap of 1.32 μ m. A U-shaped antenna is placed on top of the first YIG waveguide to excite spin waves and at a distance of 2 μ m to the second waveguide to avoid spin-wave excitation in both waveguides (Extended Data Fig. 1 and Supplementary Note 1). When a field of 56 mT is applied along the waveguides, spin-wave frequencies ranging from 3.4 GHz to 3.63 GHz are excited well by the U-shaped antenna in the first waveguide (Extended Data Fig. 2 and Supplementary Note 2). Only the first width mode can be excited in this frequency range (single-mode nano-waveguide), as shown in the dispersion curve in Fig. 1b. To detect the spin-wave

¹Faculty of Physics, University of Vienna, Vienna, Austria. ²Fachbereich Physik and Landesforschungszentrum OPTIMAS, Technische Universität Kaiserslautern, Kaiserslautern, Germany. ³Institute of Magnetism, Kyiv, Ukraine. ⁴Graduate School Materials Science in Mainz, Mainz, Germany. ⁵Nano Structuring Center, Technische Universität Kaiserslautern, Kaiserslautern, Germany. ⁶imec, Leuven, Belgium. ⁷INNOVENT e.V., Technologieentwicklung, Jena, Germany. ⁸Department of Quantum and Computer Engineering, Delft University of Technology, Delft, The Netherlands.

✉e-mail: qi.wang@univie.ac.at; andrii.chumak@univie.ac.at

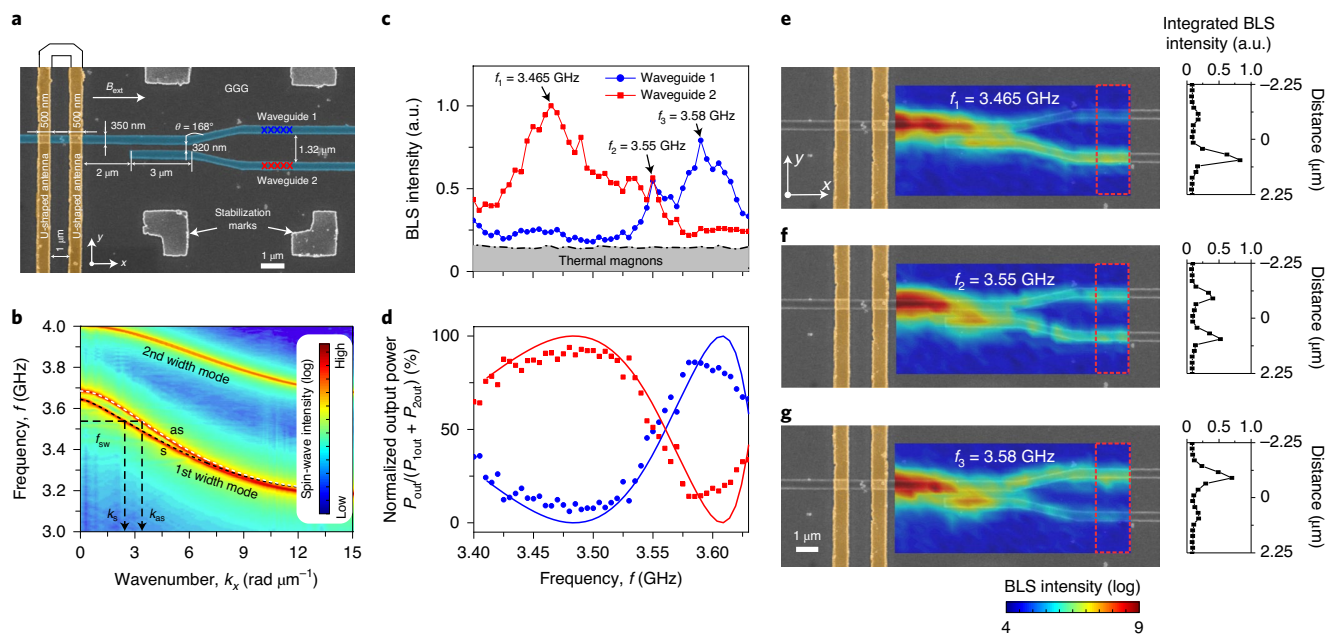


Fig. 1 | Sample geometry and working principle of the directional coupler in the linear regime. **a**, Scanning electron microscopy (SEM) image of the directional coupler (shaded in blue) with the U-shaped antenna. An external magnetic field, $B_{\text{ext}} = 56$ mT, is applied along the YIG conduits (x axis) to saturate the directional coupler in a backward volume geometry³⁴ and a radiofrequency (RF) current with power $P_{\text{mw}} = 0$ dBm is applied to the antenna to excite spin waves. GGG, gadolinium gallium garnet. **b**, Spin-wave dispersion relation of the first two width modes obtained using micromagnetic simulation (colour-coded) and analytic theory (dashed lines). YIG waveguides of 350-nm width and with a 320-nm gap between are considered. **c**, Averaged spin-wave spectra measured by μ BLS spectroscopy on the first (blue circles) and second (red squares) output waveguides. The arrows indicate the frequencies chosen for the demonstration of different functionalities of the directional coupler in **e–g**. **d**, The frequency dependence of the normalized output powers $P_{\text{out}}/(P_{\text{out}} + P_{\text{2out}})$ with subtracted thermal background for both waveguides. Circles and squares represent experimental results and solid lines are theoretical calculations of the normalized output spin-wave intensity at the first (blue) and second (red) output waveguides. **e–g**, Two-dimensional (2D) BLS maps (the laser spot was scanned over an area of $9.4 \times 4.5 \mu\text{m}^2$ with 30×20 points) of the BLS intensity for $f_1 = 3.465$ GHz (**e**), $f_2 = 3.55$ GHz (**f**) and $f_3 = 3.58$ GHz (**g**). The right panels show the spin-wave intensity integrated over the red dashed rectangular regions at the end of the directional coupler.

intensity in the directional coupler, space-resolved μ BLS spectroscopy was used (Methods)³⁶.

Linear functionality

As a first step, we measured the spin-wave intensity at five points along each output waveguide, as marked by blue and red crosses in Fig. 1a. Figure 1c shows the spin-wave intensities for the two output waveguides averaged over these points as a function of the excitation frequency. It can be seen that the two spectra show quite different features. In the first waveguide, the maximum spin-wave intensity is observed at 3.58 GHz. By contrast, the maximum spin-wave intensity in the second waveguide is found around 3.465 GHz, and only very weak spin-wave intensities are detected above 3.575 GHz. To understand the nature of this frequency separation, the dispersion relations of the first two spin-wave width modes for coupled waveguides are shown in Fig. 1b (Methods). The colour coding represents the results of micromagnetic simulations, whereas the dashed lines were calculated using analytical theory (Methods)^{15,19}. The dispersion curve of the first width mode splits into antisymmetric (as) and symmetric (s) modes due to the dipolar interaction between the waveguides. This results in an oscillation of the spin-wave energy between the coupled waveguides^{19,35}. Thus, once the spin-wave energy is injected into only one of the waveguides, it will be transferred entirely to the other one after propagation through a certain distance, known as the coupling length L . This is defined by the wavenumbers of the spin-wave modes k_{as} and k_{s} , $L = \pi/\Delta k = \pi/|k_{\text{as}} - k_{\text{s}}|$, and depends strongly on the spin-wave frequency and other parameters¹⁹.

Because the length of the coupled waveguides is fixed, the ratio of this length to the coupling length L defines in which of the two output waveguides of the directional coupler the spin wave is guided. Figure 1d shows the frequency dependence of the normalized output spin-wave intensities for both output waveguides. The experimental data are well fitted by the developed analytical model (Methods), indicating the high robustness of the proposed directional coupler design. The measured maximal transfer of the spin-wave energy takes place at a spin-wave frequency of around 3.48 GHz and is equal to 93.8%, which is only slightly below the theoretical value of 100%. This difference is likely due to imperfections in the fabricated structure and might be decreased by further improvement of the nanostructuring process³⁷.

It should be emphasized that complex magnonic circuits are only possible using single-mode waveguides. In these waveguides, width modes are well separated in energy to prevent elastic intermode scatterings³⁸. Parasitic scatterings would introduce an energy loss in the signal-carrying mode and create complex interference patterns due to the simultaneous presence of waves with different wavevectors. This is especially critical for concepts based on directional couplers, because different wavevectors also possess different coupling lengths. The waveguides used in our studies are single-mode due to their nanoscopic size, which ensures separation of the modes (Fig. 1b). An additional advantage of the nanoscopic waveguides is spin-wave propagation in longitudinally self-magnetized waveguides, which allows for the efficient two-dimensional (2D) guiding of information¹⁹.

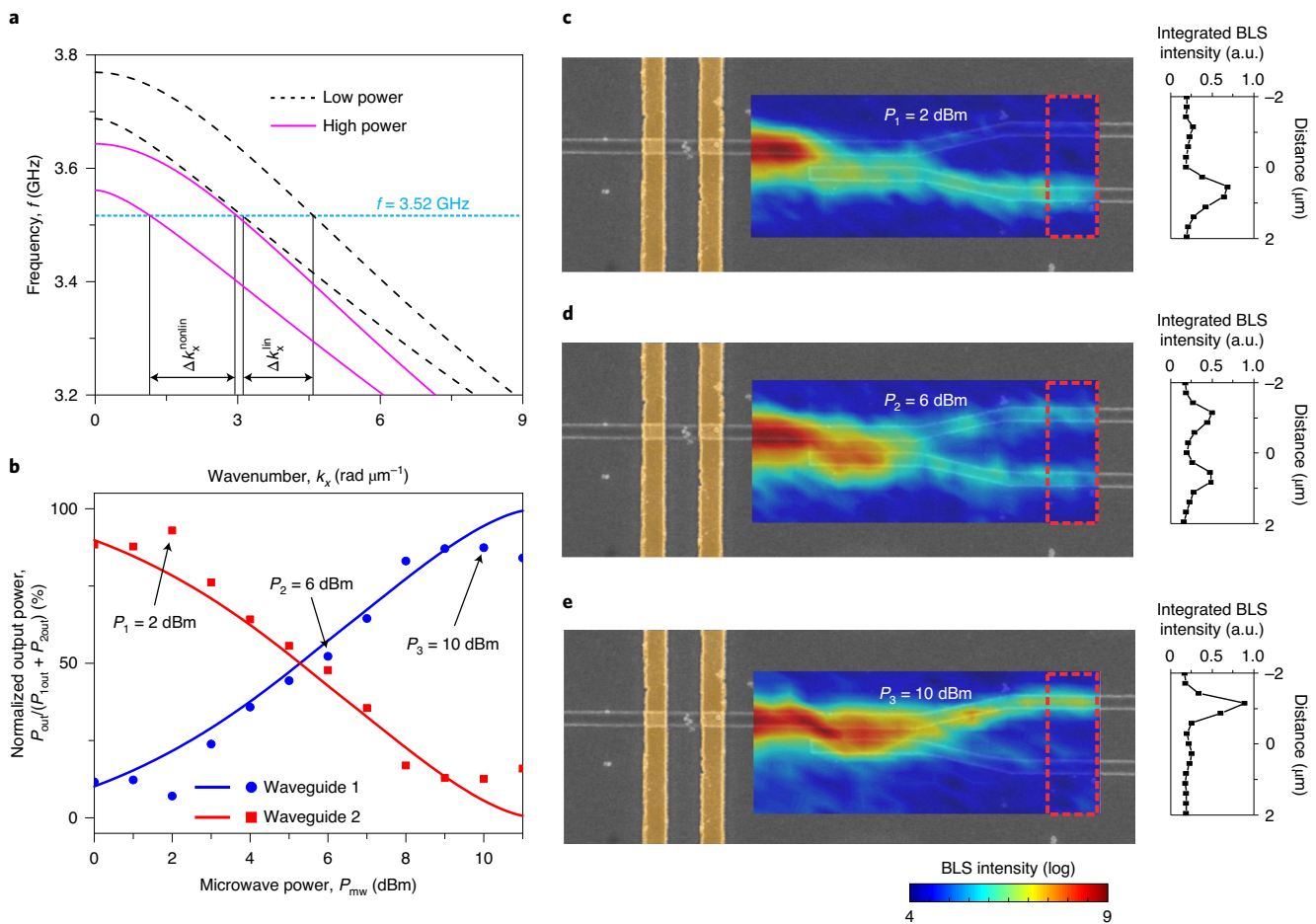


Fig. 2 | Nonlinear functionality of the directional coupler. **a**, The dispersion relations of symmetric and antisymmetric spin-wave modes in the coupled waveguides for small (black dashed lines) and large (magenta solid lines) powers. The increase in spin-wave amplitude results in a downshift of the dispersion curves. **b**, Averaged output spin-wave intensity as a function of microwave power P_{mw} (dots, experimental results; lines, theoretical fits). **c–e**, 2D BLS maps of the spin-wave intensity for a frequency of $f = 3.52$ GHz and different input powers $P_1 = 2$ dBm (**c**), $P_2 = 6$ dBm (**d**) and $P_3 = 10$ dBm (**e**). The right panels show the spin-wave intensity integrated over the regions indicated by red dashed rectangles.

Two-dimensional BLS spectroscopy scans of the spin-wave intensity are presented in Fig. 1e–g to demonstrate directly the frequency-dependent functionality of the directional coupler. Figure 1e shows the case where most of the spin-wave energy is transferred to the second waveguide at a spin-wave frequency of 3.465 GHz. This planar 2D directional coupler can thus be used to efficiently connect two magnonic conduits without the need for complex and costly 3D bridges, as used in modern electronic circuits. Figure 1g shows an entirely different spin-wave path in the directional coupler. The increase in the spin-wave frequency to $f_3 = 3.58$ GHz results in a decrease of the coupling length L by a factor of approximately two. As a result, the spin wave transfers all its energy from the first waveguide to the second one and back. Thus, 86% of the total output spin-wave energy is guided back into the first output waveguide of the directional coupler. This demonstrates the potential use of the directional coupler as a frequency division demultiplexer: if different frequencies are applied to the same input of the directional coupler, they will be transferred to the different outputs of the device. Finally, Fig. 1f demonstrates that the directional coupler can also be used as a 50/50 power splitter, in which half of the spin-wave energy is transferred to the second waveguide and half of it remains in the first one. Such a splitter can also be used as a fan-out logic gate if an amplifier^{39–41} is installed at the outputs of the device to

compensate the split in energy. Furthermore, for a fixed frequency, the output signal of the directional coupler can be switched from one output to the other by changing the external field in a small range of $\Delta B_{ext} = 4.7$ mT (Extended Data Fig. 3 and Supplementary Note 3). Thus, magnetic fields from switchable nanosized magnets⁴² could be used to realize a non-volatile nanosecond-fast reconfigurability of the directional coupler.

Nonlinear switching functionality

The processing of data, in general, requires the utilization of elements with nonlinear characteristics, as provided, for example, by a semiconductor transistor in CMOS. As mentioned above, the key benefits of spin waves for data processing are their pronounced natural nonlinearity, which allows for all-magnon control of one magnonic unit by another. In our studies, the phenomenon of a nonlinear shift of the dispersion relation^{9,10} is used, in contrast to the multi-magnon scattering exploited in the realization of a magnon transistor⁸. In the relatively weak nonlinear regime, where the dipolar coupling between the waveguides is larger than the nonlinear frequency shift of the spin waves, nonlinear operation of the directional coupler can be described simply by taking into account the nonlinear frequency shift of the symmetric and antisymmetric collective modes. The shift is the same for both modes and can be well approximated

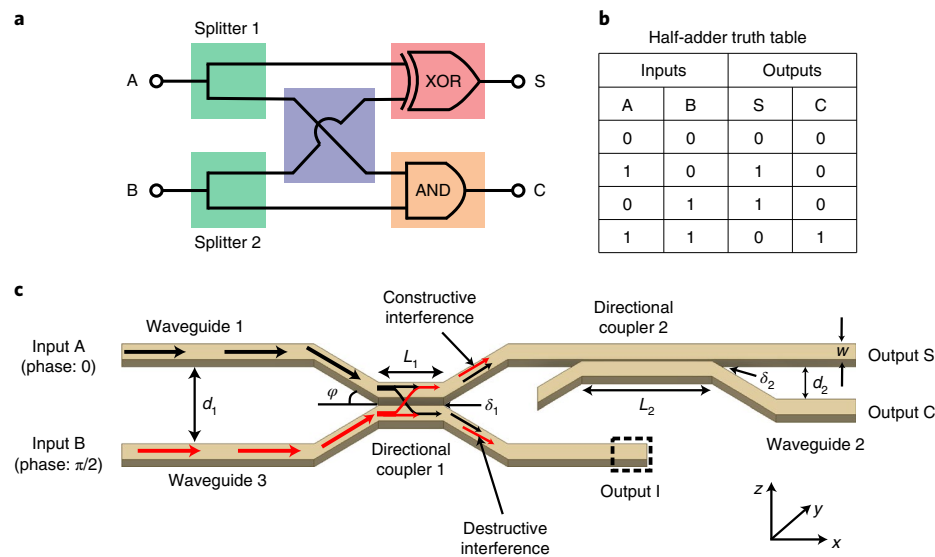


Fig. 3 | The operational principle of the magnonic half-adder. a, Sketch of the half-adder in electronics format. Building blocks are highlighted by different colours. **b**, Half-adder truth table. **c**, Schematic view of the magnonic half-adder. In this work we consider the following parameters: YIG waveguide width, $w = 100$ nm; thickness, $h = 30$ nm; edge-to-edge distances between waveguides, $d_1 = 450$ nm, $d_2 = 210$ nm; angle between waveguides, $\varphi = 20^\circ$; gaps between coupled waveguides, $\delta_1 = 50$ nm, $\delta_2 = 10$ nm; lengths of coupled waveguides, $L_1 = 370$ nm and $L_2 = 3$ μ m. Red and black arrows show the flow path of magnons from the inputs to the logic gates.

by the nonlinear frequency shift of waves in isolated waveguides⁴³: $f_{s,as}^{(nl)}(k_x, a_k) = f_{s,as}^{(0)}(k_x) + T_k |a_k|^2$, where $f_{s,as}^{(0)}(k_x)$ are the dispersion relations of the symmetric and antisymmetric modes of the coupled waveguides in the linear region¹⁹, a_k is the canonical spin-wave amplitude and T_k is the nonlinear shift coefficient (Methods). For the backward volume geometry ($M_s \parallel k_x$, where M_s is the saturation magnetization and k_x is the wavenumber) used here, the nonlinear shift coefficient is negative^{9,43}, so the spin-wave dispersion curves shift down with an increase in the spin-wave amplitude, defined by the applied RF power. The calculated spin-wave dispersions are shown in Fig. 2a for small and large applied microwave powers. As can be seen, for a fixed spin-wave frequency of 3.52 GHz, the coupling length L decreases from $\pi/\Delta k_x^{\text{lin}}$ to $\pi/\Delta k_x^{\text{nonlin}}$ with an increase in input power, resulting in changed device characteristics.

To study the nonlinear switching functionality of the presented directional coupler, the microwave power P_{mw} was varied in the range from 0 dBm to 11 dBm. Figure 2b clearly shows that the respective output spin-wave intensity strongly depends on the input microwave power due to the discussed nonlinear effects. Figure 2c shows that, for a relatively low input power 2 dBm, the output spin-wave energy is transferred to the second waveguide. This regime can be considered a linear one. For an increased power of 6 dBm, the spin-wave dispersion shift implies that half of the output spin-wave energy is transferred back to the first waveguide and thus the directional coupler; accordingly, it works as a 50/50 splitter. A further increase of the input power to 10 dBm results in a further dispersion shift, a decrease of the coupling length L and a transfer of the spin-wave energy back to the first waveguide, as can be seen in Fig. 2e.

Design of the all-magnon half-adder

According to the obtained experimental results, we propose an integrated magnonic circuit on the example of a half-adder consisting of two directional couplers and investigate its functionality by means of micromagnetic simulations. The simulations allow us to check the working principle of this design at a size comparable to a CMOS device and also to perform benchmarking. For the simulations, we chose a minimal waveguide width of 100 nm (see Fig. 3 for the sizes

of the structure), which can be reliably fabricated using modern patterning techniques^{14,15,37,44} (Methods).

A general schematic layout of a half-adder, in electronics form, is presented in Fig. 3a. This combines an XOR logic gate and an AND logic gate using 3D bridge constructions. It adds two single binary digital inputs 'A' and 'B' and has two outputs, sum ('S') and carry ('C'). The truth table of a half-adder is shown in Fig. 3b and a sketch of the proposed magnonic half-adder is presented in Fig. 3c. Directional coupler 1 in the magnonic half-adder acts as a power splitter for each of the two inputs and, at the same time, replaces the 3D bridge required for sending the signals from input A to the AND gate and from input B to the XOR gate (compare Fig. 3a). The spin-wave flow paths in the magnonic half-adder are shown by the black and red arrows in Fig. 3c: spin waves from both inputs are split into two identical spin waves of half intensity by directional coupler 1. One pair of waves is directed to directional coupler 2 via waveguide 1 and the other pair is guided into the idle output 'I' via waveguide 3. In the present simulation, output 'I' just features a high damping region at the end (shown in the figure by a dashed rectangle) and it does not contribute to the half-adding function. However, it acts as an XOR logic gate and, with the use of another directional coupler, can perform the same half-adder operation (Extended Data Fig. 4 and Supplementary Note 4). Thus, the modified half-adder can be considered as a combination of a half-adder with a fan-out logic gate, which doubles each output of the device. Directional coupler 2 performs the actual half-adder logic operation and its operational principle is described in the next section.

Modelling of the nonlinear functionality

The nonlinear functionality of the directional coupler shown above qualitatively takes place for any spin-wave directional coupler. Nevertheless, as shown below, realization of the logic operation requires a full switch of the spin-wave path by the change in the spin-wave intensity exactly four times. To achieve this value, modifications of the directional coupler, discussed below, are required.

Directional coupler 2 consists of a coupled straight parallel waveguide with 3- μ m coupled length as shown in Fig. 4a. The split

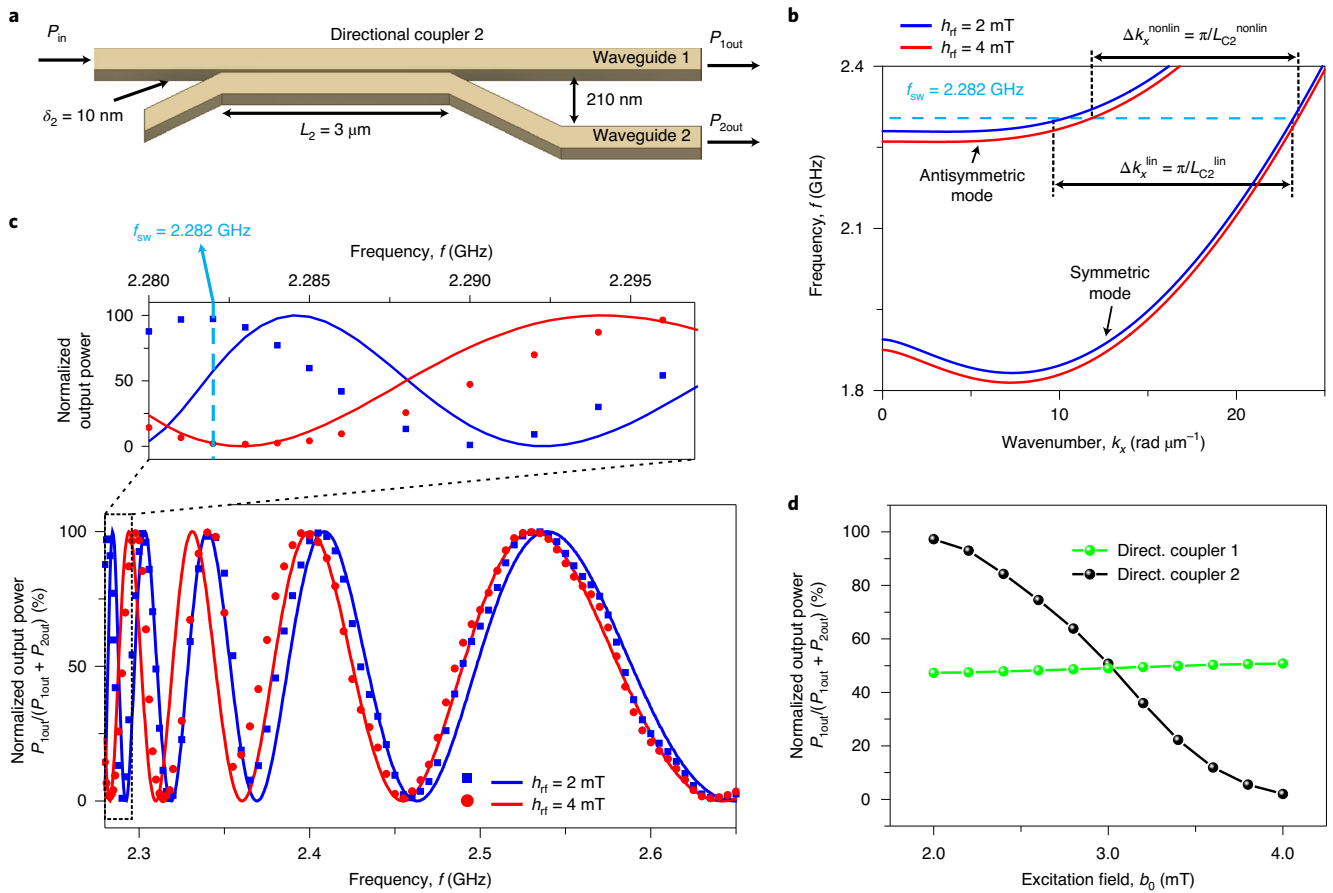


Fig. 4 | Modelling and characteristics of directional coupler 2. **a**, Schematic of directional coupler 2. **b**, Analytically calculated dispersion curves for the coupled waveguides for small (blue lines) and large (red lines) excitation fields h_{rf} . The change in coupling length L_{C2} is clearly visible, and is associated with the increase in spin-wave amplitude. **c**, Normalized output power in the first waveguide $P_{1out}/(P_{1out} + P_{2out})$ as a function of frequency for different excitation field h_{rf} (symbols, simulations; lines, analytic theory). An enlarged view of the region marked with the dashed rectangle is shown in the top panel. **d**, Simulated normalized output power P_{1out} as a function of excitation field b_0 for a fixed frequency of $f = 2.282$ GHz for directional couplers 1 and 2.

dispersion relations in the linear regime in the coupled waveguides are shown in Fig. 4b as blue lines. To obtain the linear dispersion, small spin-wave amplitudes are excited by a microwave field of $h_{rf} = 2$ mT. The output power in the first waveguide normalized by the total power $P_{1out}/(P_{1out} + P_{2out})$ can be expressed using the characteristic coupling length L_{C2} : $\frac{P_{1out}}{P_{1out} + P_{2out}} = \cos^2(\pi L_2 / (2L_{C2}))$, where $L_2 = 3 \mu\text{m}$ is the length of the coupled waveguide in directional coupler 2. Figure 4c shows the normalized output power in the first waveguide as a function of spin-wave frequency f , in the frequency range from 2.28 GHz to 2.65 GHz. The result of numerical simulations in the linear regime is shown with blue symbols and the analytic calculation with solid blue lines. One can clearly see that the output power P_{1out} strongly depends on the spin-wave frequency, as shown experimentally in Fig. 2. This is due to the strong dependence of the coupling length L_{C2} on the spin-wave wavenumber^{19,35,45}. The coupling length consequently defines the energy distribution between the output waveguides for a given length of the coupled waveguides. The small mismatch between simulations and theory in the region below 2.3 GHz is mainly caused by the damping, which is not taken into account in the theory, and by the large sensitivity of the coupling coefficient to the dispersion of the antisymmetric mode, which is practically flat in this region.

When the input spin-wave power increases, spin-wave dispersion shifts down (red lines in Fig. 4b). Thus, for a fixed spin-wave frequency of 2.282 GHz, the wavenumber difference $\Delta k_x = \pi/L_{C2}$

changes from Δk_x^{lin} to $\Delta k_x^{\text{nonlin}}$ with an increase in the excitation field from $b_0 = 2$ mT to 4 mT. Consequently, the coupling length L_{C2} of the directional coupler also changes. Using the Taylor expansion of the frequency dependence of the coupling length, the power dependence of the output of directional coupler 2 can be found:

$$\frac{P_{1out}}{P_{1out} + P_{2out}} = \cos^2\left(\frac{\pi L_2}{2L_{C2}^{\text{lin}}} - \frac{L_2}{L_{C2}^{\text{lin}}} \frac{\pi}{2L_{C2}^{\text{lin}}} \frac{\partial L_{C2}}{\partial f} T_k |a_k|^2\right) \quad (1)$$

The power-independent term is proportional to the ratio of the directional coupler length to the coupling length in the linear regime L_2/L_{C2}^{lin} . The output power P_{1out} periodically changes with a change in the coupling length and is maximal for the cases $L_2/L_{C2}^{\text{lin}} = 0, 2, 4, \dots$ (Fig. 4c). Simultaneously, as seen from equation (1), the sensitivity to the nonlinear effect increases with an increase in the ratio L_2/L_{C2}^{lin} . Therefore, the longer the directional coupler is and the more coupling lengths it spans, the higher the nonlinear phase accumulation. This is the reason why directional coupler 2 in our half-adder design is long and features a strong coupling provided by the small gap between the waveguides of only 10 nm. It has a length of $L_2 = 14L_{C2}^{\text{lin}}$ and is very sensitive to the increase in the spin-wave amplitude passing through it. As a result, a complete energy transfer from output 1 to output 2 is observed in the micromagnetic simulations if the spin-wave intensity is increased by a factor of four ($L_2 = 13L_{C2}^{\text{nonlin}}$, black line in Fig. 4d). The normalized

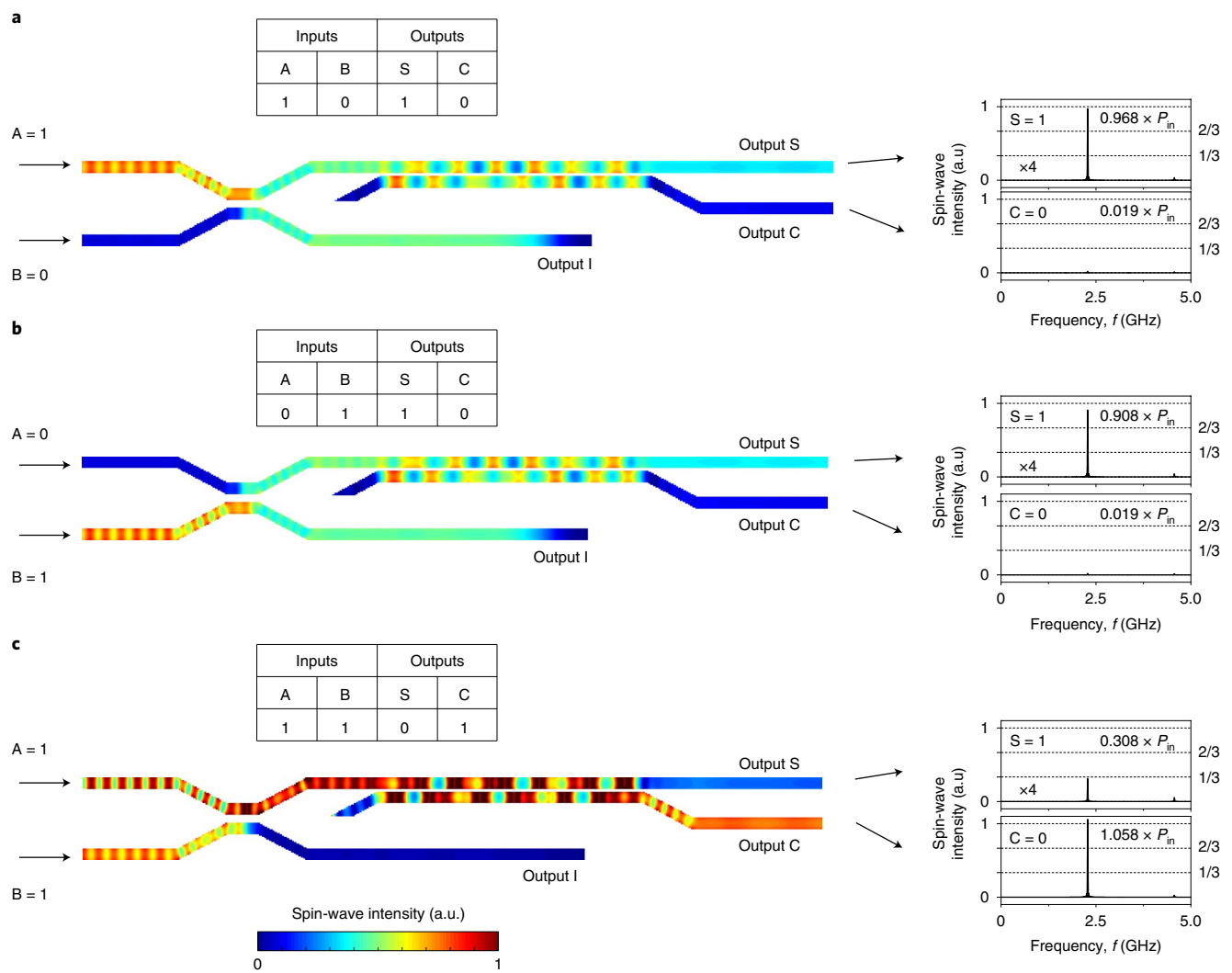


Fig. 5 | Operational principle of the magnonic half-adder. **a–c**, Spin-wave intensity distributions for different inputs combinations: $A = 1, B = 0$ (**a**), $A = 0, B = 1$ (**b**) and $A = 1, B = 1$ (**c**). The truth tables for each input combination are shown above the structures. The normalized output spin-wave intensities in the outputs are shown on the right. All outputs S are multiplied by a factor of four.

output spin-wave power in the first waveguide decreases from 97.3% at $b_0 = 2 \text{ mT}$ to 2.0% at $b_0 = 4 \text{ mT}$. Owing to this nonlinear switching effect, directional coupler 2 performs a combined AND and XOR logic function, as will be described in the following. At the same time, the first directional coupler 1 in the half-adder design should remain in the linear regime and its coupling length should be independent of the spin-wave power. This is achieved by its smaller length of 370 nm as well as via an increased spacing between the waveguides of 50 nm. As a result, directional coupler 1 spans only half of the coupling length $L_1 = 0.5L_{C1}^{\text{lin}}$, independent of the excitation field (green symbols in Fig. 4d). The directional coupler studied experimentally above was designed for linear functionality. Nevertheless, the increase of the spin-wave power from 0 dBm to 10 dBm, which is a more than four times increase of the spin-wave intensity required by the half-adder design, also results in the nonlinear switch (Fig. 2).

Operational principle of the magnonic half-adder

The operational principle of the half-adder is shown in Fig. 5. Binary data are coded into the spin-wave amplitude; namely, in the ideal case, a spin wave of a given amplitude (for example, $M_z/M_s = 0.057$, where

M_z is the out-of-plane (z) component of dynamic magnetization) corresponds to logic state ‘1’, while zero spin-wave amplitude corresponds to ‘0’. In the following, we normalize output spin-wave intensity to the input spin-wave intensity. In the more realistic cases considered below, we utilize an approach from CMOS: a normalized spin-wave intensity below 1/3 is considered to be logic ‘0’ and above 2/3, logic ‘1’.

The operational principle of the half-adder is as follows. Let us first consider the case of logic inputs $A = 1$ and $B = 0$ (Fig. 5a). In this case, the spin wave injected into input A is split into two equal parts by directional coupler 1. One part is directly guided to directional coupler 2 by the upper conduit. The spin-wave intensity is chosen in such a way that directional coupler 2 remains in the linear regime ($L_{C2}^{\text{lin}} \approx 214 \text{ nm} \approx 14/L_2$) and, after initial oscillations, the spin wave is guided into output S, as shown in Fig. 5a. Only about 1.9% of the spin-wave energy goes into output C. This corresponds to logic outputs $S = 1$ and $C = 0$. If a spin wave is injected in input B only, this corresponds to logic inputs $A = 0$ and $B = 1$ (Fig. 5b). The situation in this case is quite similar to the previous one. The situation is different for input logics states $A = 1$ and $B = 1$ (Fig. 5c). It is assumed that the phase of the spin wave injected into input

B is permanently shifted by $\pi/2$ with respect to the one in input A (to compensate the $-\pi/2$ phase shift caused by directional coupler 1), which can be easily realized by many means⁴⁶. In this case, constructive interference of the two spin waves will take place in waveguide 1 and destructive interference in waveguide 3. As a result of this coherent superposition, the entire spin-wave energy from both inputs goes to directional coupler 2, resulting in four times larger spin-wave intensity with respect to the single-input cases when only 50% of the spin-wave energy is guided to this coupler. As discussed above, this increase in spin-wave intensity by a factor of four switches the coupler to the nonlinear regime ($L_{c2}^{\text{nonlin}} \approx 230 \text{ nm} \approx 13/L_2$) and the spin wave is guided to output C. This corresponds to logic outputs $S=0$ and $C=1$ (Fig. 5c) and, thus, the whole truth table of the half-adder is realized.

Note that the all-magnon circuit concept^{8,34} requires that the signal from the output of a magnonics gate be directly guided into the input of the next one. To satisfy this condition, the spin-wave intensity at outputs S still has to be amplified by a factor of approximately four due to the energy splitting in directional coupler 1 and also parasitic reflections and spin-wave damping in the waveguides. The output signals S shown in Fig. 5 are artificially multiplied by four. The most promising realization of such an amplifier is based on the utilization of voltage-controlled magnetic anisotropy (VCMA) parametric pumping^{43,47,48} (Extended Data Fig. 5 and Supplementary Note 5). By contrast, no amplifier is required for the ‘carry’ output of the half-adder. In general, the idea presented here and the concept of the half-adder are applicable to any magnetic material. Nevertheless, the requirement that the device length L_{de} be smaller than the spin-wave decay length should be satisfied. This is the case not only for YIG, but also for low-damping Heusler compounds⁴⁹.

Benchmarking of the proposed technology

A summary of the key parameters of two versions of the proposed half-adder is provided in Table 1 (Methods): the first one is the device that was simulated and discussed above. The second device is an estimation performed for a device with $w=30 \text{ nm}$, $h=10 \text{ nm}$ and minimal gap $\delta=10 \text{ nm}$. It has to be mentioned that the second device does not constitute a fundamental limit but is merely an estimation based on the current state of the art of fabrication technology^{15,37}. A further improvement in all characteristics is potentially achievable.

According to Table 1, the area of the simulated 100-nm-feature-size half-adder is $5.58 \mu\text{m}^2$ (the spaces between neighbouring logic gates are included) and is thus only a few times larger than a corresponding 7-nm-feature-size CMOS device. In contrast to a CMOS realization, the magnonic half-adder core part (without amplifier) consists of only three nanowires made of the material and of only one planar layer. This drastically simplifies its fabrication and decreases its potential costs. The area can be readily decreased to $1.016 \mu\text{m}^2$ for the second 30-nm-based device, which is comparable to the 7-nm-based CMOS device. In addition, it should be noted that the largest part of the half-adder is provided by directional coupler 2; this could be further decreased by utilizing exchange-coupling mechanisms between the waveguides instead of dipolar coupling. To achieve this, the air gap between the coupled waveguides should be filled with another magnetic material.

Operational frequency is an important requirement. In the presented half-adder, the delay time is defined by the whole length of the device with respect to the spin-wave group velocity. In our design, the spin-wave propagation time from input to output is $\sim 150 \text{ ns}$. According to Table 1, the calculation time can be reduced to 18 ns in the second device. This value is larger than the 60-ps delay time obtained for 7-nm CMOS and suggests that magnon logic would be more suitable for slow but low-energy applications. At the same time, one has to note that CMOS does not operate at its maximal speed because of the drastically increasing Joule heating (a typical clock rate is 3 GHz, which corresponds to $\sim 0.3\text{-ns}$ delay).

Table 1 | Magnonic half-adder benchmarking

Parameters	YIG ^a (100 nm)	YIG ^b (30 nm)	CMOS ^c (7 nm)
Area (μm^2)	5.58	1.016	1.024
Delay time (ns)	150	18	6×10^{-2}
Total energy consumption without amplification (aJ)	24.6	1.96	35.3
Spin-wave frequency (GHz)	2.282	2.39	-
Spin-wave wavelength (nm)	340	510	-
Spin-wave group velocity (m s^{-1})	25	137	-
Type of amplifier	Energy consumption		
Electric current-based parametric pumping ^{39,41}	10^5 (aJ per operation)		
Voltage-controlled magnetic anisotropy parametric pumping ^{43,47}	3 (aJ per operation)		

^aThe values in this column are extracted from the micromagnetic simulation of the half-adder investigated in this Article. ^bThe values are estimated characteristics of a device miniaturized down to 30 nm using equations (8) to (10) (Methods). ^cThe values are calculated using Cadence Genus by Sorin D. Cotofana for 7-nm CMOS technology.

In computing systems, small energy consumption is probably the most crucial requirement, given the constantly increasing amount of information that has to be processed. In our simulations, we recorded the total energy of the device as a function of simulation time. The energy injected into the device per nanosecond is equal to $4.1 \times 10^{-20} \text{ J ns}^{-1}$ for the input combinations $A=1$ and $B=1$. Note that only the energy propagating along the positive direction is taken into account. For the 300-ns pulse duration the energy consumption is thus 12.3 aJ. For all operations, the total energy consumption is 24.6 aJ. This is similar to current CMOS values (35.3 aJ), calculated using Cadence Genus (Methods). It should be highlighted that the energy consumption of the miniaturized 30-nm-based device is more than one order of magnitude smaller ($\sim 1.96 \text{ aJ}$). At the same time, we have to underline that this energy consumption is related to the energy within the magnonic domain only and the energy consumption of the amplifier should be added (Table 1 and Supplementary Note 5). The most promising approach is VCMA parametric pumping, which has been reported recently^{43,47,48} and allows for an energy consumption of an amplifier of $\sim 3 \text{ aJ}$ per device.

Conclusions

We have fabricated a submicrometre spin-wave directional coupler operating in a single-mode regime and studied its functionality in the linear and nonlinear regime using μBLS spectroscopy. Our experimental results are supported by numerical simulations and analytical theory. By varying the applied microwave frequency or an applied magnetic field, spin waves can be guided to different coupler outputs, demonstrating the reconfigurability of the device. Our spin-wave directional coupler could therefore be used as a microwave filter for processing analogue and digital information, a power splitter for fan-out logic gates, a frequency divider or signal multiplexer, and a planar interconnecting element for magnonic conduits. Furthermore, the output of the directional coupler can be switched by changing the spin-wave amplitude, demonstrating nonlinear functionality.

We have also proposed and tested numerically an integrated magnonic circuit—a half-adder—based on the fabricated directional

coupler. This half-adder consists of two directional couplers: one that functions as a linear power splitter and one that functions as a nonlinear switch (as demonstrated experimentally). The proposed device is all-magnonic—the magnons are controlled by magnons without any conversion to the electric domain—ensuring low energy consumption. The proposed magnonic half-adder consists only of three planar magnetic nanowires with one amplifier and can potentially substitute 14 transistors in electronics circuits. A magnonic half-adder developed with 30-nm technology is predicted to have a footprint comparable to a 7-nm CMOS half-adder, with around 10 times smaller energy consumption.

Methods

Liquid-phase epitaxial film growth and sample fabrication. An 85-nm-thick YIG film was grown on a 1-inch (111) 500- μm -thick gadolinium gallium garnet (GGG) substrate by liquid-phase epitaxy from $\text{PbO-B}_2\text{O}_3$ -based high-temperature solutions at 860 °C using the isothermal dipping method (for example, ref. 50). Nominally pure $\text{Y}_3\text{Fe}_5\text{O}_{12}$ films with smooth surfaces were obtained on horizontally rotated substrates applying rotation rates of 100 r.p.m. (refs. 6,7). The saturation magnetization of the YIG film is $1.42 \times 10^5 \text{ A m}^{-1}$ and its Gilbert damping $\alpha = 2.1 \times 10^{-4}$, as extracted by ferromagnetic resonance spectroscopy⁵¹.

The directional coupler was fabricated using electron-beam lithography, Ar^+ ion-beam etching and electron-beam evaporation. First a double layer of polymethyl methacrylate was spin-coated on the YIG film and the directional coupler structures were created afterwards by electron-beam lithography. To obtain well-shaped waveguides, titanium and chromium were deposited by electron-beam evaporation as a bilayer hard mask, defining the shape of the directional coupler structures. These were then etched out of the film by Ar^+ ion-beam etching. Finally, the U-shaped antenna was defined by electron-beam lithography and a liftoff process. This consisted of $\sim 230\text{-nm}$ -thick gold and 20-nm-thick titanium (for adhesion).

BLS spectroscopy and spin-wave excitation. μBLS spectroscopy is a technique for the measurements of spin-wave intensities with frequency, space, phase and time resolution⁵⁶. It is based on inelastic light scattering of the incident laser beam by magnons. In our measurements, a laser beam of 491-nm wavelength and power of 1.8 mW was focused on the directional coupler with an effective spot diameter of 400 nm using a $\times 100$ microscope objective with a large numerical aperture ($\text{NA} = 0.75$). The scattered light was collected and guided into a tandem Fabry–Pérot interferometer (TFP-1, JRS Scientific Instruments) for further analysis. To perform 2D scans, the sample was moved with respect to the laser spot in steps of a few hundred nanometres in each direction using a piezoelectric stage. Stabilization marks were grown on the sample to maintain the same relative position of the laser spot during the long measuring cycles.

An external magnetic field, $B_{\text{ext}} = 56 \text{ mT}$, was applied along the YIG conduits (x axis) to saturate the directional coupler in a backward volume geometry⁵⁴, and a RF current with power $P_{\text{mw}} = 0 \text{ dBm}$ (in the linear regime) was applied to the antenna to excite spin waves. Spin-wave frequencies ranging from 3.4 GHz to 3.63 GHz were excited well by the U-shaped antenna in the isolated waveguide (Extended Data Fig. 2 and Supplementary Note 2). Only the first width mode was excited in this frequency range, as shown in the dispersion curve in Fig. 1b.

Calculation of the nonlinear frequency shift coefficient. The nonlinear shift coefficient T_k in the isolated waveguide can be calculated using the framework of ref. 9 and by assuming a uniform mode profile across the waveguide thickness and width. Accounting for the negligible static demagnetization of a waveguide along its length, $F_0^{\text{xx}} = 0$, the nonlinear shift coefficient becomes equal to⁴⁰

$$T_k = \left((\omega_{\text{H}} - A_k) + \frac{B_k^2}{2\omega_0^2} (\omega_{\text{M}} (4\lambda^2 k_x^2 + F_{2k}^{\text{xx}}(0)) + 3\omega_{\text{H}}) \right) / 2\pi \quad (2)$$

where

$$A_k = \omega_{\text{H}} + \frac{\omega_{\text{M}}}{2} (2\lambda^2 k_x^2 + F_k^{\text{yy}}(0) + F_k^{\text{zz}}(0)) \quad (3)$$

$$B_k = \frac{\omega_{\text{M}}}{2} (F_k^{\text{yy}}(0) - F_k^{\text{zz}}(0)) \quad (4)$$

The relation between the dynamic magnetization component and the canonical spin-wave amplitude a_k is given by

$$M_z = M_s a_k \sqrt{2 - |a_k|^2} (u_k - v_k) \quad (5)$$

with

$$u_k = \sqrt{\frac{A_k + \omega_0}{2\omega_0}} \text{ and } v_k = -\text{sign}[B_k] \sqrt{\frac{A_k - \omega_0}{2\omega_0}} \quad (6)$$

Calculation of the directional coupler characteristics. The theory of the directional coupler is described in our previous paper¹⁹. However, in ref. 19 we accounted only for the straight part of the coupler where the distance between waveguides is minimal and constant. For the device reported in this Article, this approach is not sufficient, because the gap between the coupled waveguides is quite large (320 nm). In such a case, the region of the bent waveguides could also notably contribute to the coupling characteristics, because the gap in this region is not much larger than the minimal gap over a considerable distance. To take this bent region into account, we calculated the splitting of the symmetric and antisymmetric spin-wave modes as a function of the gap, $\Delta k = \Delta k(d)$. The coordinate dependence of the spin-wave power in the waveguides is then given by

$$\begin{aligned} P_1(x) &= \cos^2 \left[\frac{1}{2} \int_0^x \Delta k(d(x')) dx' \right] \\ P_2(x) &= \sin^2 \left[\frac{1}{2} \int_0^x \Delta k(d(x')) dx' \right] \end{aligned} \quad (7)$$

Furthermore, an additional coupling, which is especially pronounced for large spin-wave wavelengths, must be taken into account due to the large wavelength studied in this work: the part of the first waveguide located before the second one starts also contributes to the coupling 'diagonally'. Indeed, the dynamic magnetization of a large spin-wave wavelength varies slowly and, thus, the mentioned part of the first waveguide creates a non-negligible dipolar field at the beginning of the second one. By contrast, for short-wavelength spin waves, these additional contributions vanish, because contributions from neighbouring half-wavelength parts almost cancel each other. In this work, we account for it through the introduction of an 'additional effective length' of the coupler, which, by itself, depends on the spin-wave wavelength. Because the strength of the dipolar fields decays with the distance approximately proportional to x^{-3} , the effective length is expected to depend on spin-wave wavenumber as $L_{\text{eff}} = C_1 / (k + C_2)^2$. Here, the second power in the spin-wave wavenumber comes from the integration $\int_0^{1/k} (x + d_0)^{-3} dx$, and the constant C_2 reflects the fact that the effective length cannot increase infinitely for an infinitely large spin-wave wavelength. By fitting the experimental data, we found $C_1 = 25 \mu\text{m}^{-1}$ and $C_2 = 2 \mu\text{m}^{-1}$. Using this expression for the effective additional length, both frequency and field dependencies of the power transmission rates are described well (Figs. 1d and 2b).

The variation of the power transmission rate in the coupler with increasing spin-wave power is mainly attributed to the nonlinear frequency shift of the symmetric and antisymmetric spin-wave modes in coupled waveguides, as shown in Fig. 3b. The shift of the dispersion results in a change of spin-wave wavenumbers at a given frequency and, consequently, in a change of the coupling between the waveguides. Knowing the frequency dependence of the power transmission rates $P_{1,2}^{(\text{lin})}(\omega)$ in the linear regime, the nonlinear characteristics can be calculated simply as $P_{1,2}^{(\text{nl})}(\omega, a) = P_{1,2}^{(\text{lin})}(\omega - T_k |a|^2)$, where a is the canonical spin-wave amplitude and T_k is the nonlinear frequency shift ($T_k / 2\pi = -1.8 \text{ GHz}$ in our case). Given that the experimental data measured for 0-dBm excitation power also correspond to a weakly nonlinear regime, for the description of power dependence we use the relation $P_{1,2}^{(\text{nl})}(\omega, a) = P_{1,2}^{(0)}(\omega - T_k (|a|^2 - |a_0|^2))$, where $P_{1,2}^{(0)}$ is the dependence for 0 dBm (measured and fitted by the calculations shown above) and a_0 is the spin-wave amplitude at 0-dBm excitation power. The relation of the spin-wave amplitude with the excitation power was obtained by measuring the BLS intensity in the first waveguide before the coupler and fitting one adjusting parameter (the ratio of BLS counts to the square of the spin-wave amplitude). We get the following relation $a = 0.035 \sqrt{1 + p/17.4}$, where p is the excitation power in dBm. The appearance of an almost linear dependence of the spin wave power on p , instead of an exponential one, which could be expected, is mediated by the strong variation of the spin-wave group velocity with spin-wave wavenumber and, consequently, with the excitation power at a given frequency. The described simple model fits the experimental data well for the applied powers below 10 dBm (Fig. 3a). For higher powers, higher-order nonlinear effects should be taken into account as well⁵².

Micromagnetic simulations. Dispersion curve presented in Fig. 1b. The micromagnetic simulations were performed by the GPU-accelerated simulation program Mumax3 to calculate the space- and time-dependent magnetization dynamics in the investigated structures using a finite-difference discretization⁵³. The following material parameters were used: saturation magnetization $M_s = 1.33 \times 10^5 \text{ A m}^{-1}$ (94% comparing to the value of the plain film^{6,7} due to the Ar^+ ion-beam etching) and Gilbert damping $\alpha = 2 \times 10^{-4}$. A standard exchange constant for YIG of $A = 3.5 \text{ pJ m}^{-1}$ was assumed. There were three steps involved in calculation of the spin-wave dispersion curve⁵⁴: (1) the external field was applied along the waveguide and the magnetization was relaxed to a stationary state (ground state); (2) a sinc field pulse $b_y = b_0 \text{sinc}(2\pi f_c t)$, with an oscillation field of $b_0 = 1 \text{ mT}$ and a cutoff frequency of $f_c = 10 \text{ GHz}$, was used to excite a wide range of spin waves; (3) the spin-wave dispersion relations were obtained by performing 2D fast Fourier transformation (FFT) of the time- and space-dependent data.

Magnonic half-adder. The simulated structure of the magnonic half-adder is shown in Fig. 1c. The parameters of the nanometre-thick YIG were obtained from experiments and are as follows^{6,7}: saturation magnetization $M_s = 1.4 \times 10^5 \text{ A m}^{-1}$, exchange constant $A = 3.5 \text{ pJ m}^{-1}$ and Gilbert damping $\alpha = 2 \times 10^{-4}$. The damping at the ends of the simulated structure and the high damping absorber was set to exponentially increase to 0.5 to prevent spin-wave reflection⁵⁵. The high damping

region could be realized in the experiment by putting another magnetic material or metal on top of the YIG to enhance the damping or it can just correspond to waves guided into further parts of the magnonic network. No external bias field was applied. The static magnetization oriented itself parallel to the waveguides spontaneously due to the strong shape anisotropy in the nanoscale waveguides. The mesh was set to $10 \times 10 \times 30 \text{ nm}^3$. To excite propagating spin waves, a sinusoidal magnetic field $b = b_0 \sin(2\pi ft)$ was applied over an area of 100 nm in length, with a varying oscillation amplitude b_0 and microwave frequency f . $M_z(x, y, t)$ of each cell was collected over a period of 300 ns, which is long enough to reach the steady state. The fluctuations $m_z(x, y, t)$ were calculated for all cells via $m_z(x, y, t) = M_z(x, y, t) - M_z(x, y, 0)$, where $M_z(x, y, 0)$ corresponds to the ground state. The spin-wave spectra of the output signals were calculated by performing a fast Fourier transformation from 250 ns to 300 ns, which corresponds to the steady state. We mention that all these simulations were performed for defect-free waveguides and without taking temperature into account. The influences of edge roughness, trapezoidal cross-sections of the waveguides and temperature can be ignored due to their smallness, as has been shown in our previous studies^{5,19}.

Energy consumption. For the estimation of energy consumption in the magnonic system (neglecting transducers), the minimal energy consumption can be expressed as (Supplementary Note 6)

$$E = \frac{20\pi M_s v_{gr} \sqrt{S}}{3 \gamma T_k} \quad (8)$$

where $v_{gr} = 2\pi \frac{\partial f}{\partial k}$ is the spin-wave group velocity and S is the cross-section of the waveguide. As one can see, the energy consumption is independent of the characteristics of spin-wave couplers and spin-wave amplitude. Note that the nonlinear frequency shift T_k is of the order of the spin-wave frequency f ($T_k \propto f$), especially in the exchange-dominated region. The conclusion is reached that the feasible way to reduce energy consumption is to decrease the waveguide cross-section S . Another alternative is to search for specific points or mechanisms with anomalously high nonlinearity. It should be noted that the relation of equation (8) is universal and occurs in other realizations of magnonic half-adders that are based on the nonlinear shift. For the other designs, the only change is the pre-factor $20\pi/3$.

Scalability and delay time. The width of the device can be estimated by

$$w_{de} = 2w + 4 \quad 5h \quad (9)$$

where w is the width of the waveguide and h is the thickness of the waveguide. This equation accounts for the minimal distance between all waveguides and neighbouring devices of $5h$ to make the dipolar interaction relatively weak. The gaps between different logic gates are taken into account in this width.

The length of the device is given by

$$L_{de} = (N + 0.5)L_C + 4 \frac{5h}{\sin \varphi} \quad (10)$$

where φ is the angle of the bent waveguide, L_C is the coupling length and $N = L_d/L_C$ is the ratio between the coupled length of directional coupler 2 and the coupling length. The minimal N can be estimated from the condition that directional coupler 1, working at half the coupling length, does not substantially change its characteristics at power that is sufficient to switch directional coupler 2. Simple calculations yield that the change of directional coupler 1 transmission is given by $\cos^2(\pi(N-1)/(4N))$, while in the linear regime the transmission rate is equal to $1/2$. This gives the restriction $N_{min} = 6$. The area of the magnonic half-adder is equal to $w_{de}L_{de}$. The processing delay is $\tau_{de} = L_{de}/v_{gr}$.

Calculation of the energy consumption of the 7-nm CMOS half-adder. We considered a 7-nm half-adder standard cell afferent to the typical processor corner (room temperature, 0.7-V power supply) and evaluated its power consumption using Cadence Genus. To this end, we set an inverter standard cell as driver and a capacitance of 2.5 fF as the output load, and assumed for the nets a 50% probability of logic '1' and a toggle rate of 0.02 per ns. The simulation results indicate a total power consumption of 587.994 nW, of which the dynamic component (divided into nets' power and internal power, which account for 87.7% and 13.3% of the dynamic power, respectively) dominates the less than 1-nW leakage component.

Data availability

The data that support the plots within this paper and other findings of this study are available from the corresponding author upon reasonable request.

Received: 7 February 2019; Accepted: 11 September 2020;

Published online: 19 October 2020

References

1. Kruglyak, V. V., Demokritov, S. O. & Grundler, D. Magnonics. *J. Phys. D* **43**, 264001 (2010).

- Lenk, B. et al. The building blocks of magnonics. *Phys. Rep.* **507**, 107–136 (2011).
- Krawczyk, M. & Grundler, D. Review and prospects of magnonic crystals and devices with reprogrammable band structure. *J. Phys. Cond. Matter* **26**, 123202 (2014).
- Chumak, A. V. et al. Magnon spintronics. *Nat. Phys.* **11**, 453–461 (2015).
- Dieny, B. et al. Opportunities and challenges for spintronics in the microelectronics industry. *Nat. Electron.* **3**, 446–459 (2020).
- Dubs, C. et al. Sub-micrometer yttrium iron garnet LPE films with low ferromagnetic resonance losses. *J. Phys. D* **50**, 204005 (2017).
- Dubs, C. et al. Low damping and microstructural perfection of sub-40-nm-thin yttrium iron garnet films grown by liquid phase epitaxy. *Phys. Rev. Mater.* **4**, 024426 (2020).
- Chumak, A. V., Serga, A. A. & Hillebrands, B. Magnon transistor for all-magnon data processing. *Nat. Commun.* **5**, 4700 (2014).
- Krivovik, P. & Patton, C. E. Hamiltonian formulation of nonlinear spin-wave dynamics: theory and applications. *Phys. Rev. B* **82**, 184428 (2010).
- Sadovnikov, A. V. et al. Nonlinear spin wave coupling in adjacent magnonic crystals. *Appl. Phys. Lett.* **109**, 042407 (2016).
- Khitun, A., Bao, M. & Wang, K. L. Magnonic logic circuits. *J. Phys. D* **43**, 264005 (2010).
- Manipatruni, S., Nikonov, D. E. & Young, I. A. Beyond CMOS computing with spin and polarization. *Nat. Phys.* **14**, 338–343 (2018).
- Zografos, O. et al. Design and benchmarking of hybrid CMOS-spin wave device circuits compared to 10-nm CMOS. In *Proceedings of the 15th IEEE International Conference on Nanotechnology* 686–689 (IEEE, 2015).
- Duan, Z. et al. Nanowire spin torque oscillator driven by spin-orbit torques. *Nat. Commun.* **5**, 5616 (2014).
- Wang, Q. et al. Spin pinning and spin-wave dispersion in nanoscopic ferromagnetic waveguides. *Phys. Rev. Lett.* **122**, 247202 (2019).
- Wintz, S. et al. Magnetic vortex cores as tuneable spin-wave emitters. *Nat. Nanotechnol.* **11**, 948–953 (2016).
- Liu, C. et al. Current-controlled propagation of spin waves in antiparallel, coupled domains. *Nat. Nanotechnol.* **14**, 691–697 (2019).
- Che, P. et al. Efficient wavelength conversion of exchange magnons below 100 nm by magnetic coplanar waveguides. *Nat. Commun.* **11**, 1445 (2020).
- Wang, Q. et al. Reconfigurable nanoscale spin-wave directional coupler. *Sci. Adv.* **4**, e1701517 (2018).
- Kirilyuk, A., Kimel, A. V. & Rasing, T. Ultrafast optical manipulation of magnetic order. *Rev. Mod. Phys.* **82**, 2731 (2010).
- Kampfthaler, T. et al. Coherent terahertz control of antiferromagnetic spin waves. *Nat. Photon.* **5**, 31–34 (2011).
- Lee, K.-S. & Kim, S.-K. Conceptual design of spin wave logic gates based on a Mach-Zehnder-type spin wave interferometer for universal logic functions. *J. Appl. Phys.* **104**, 053903 (2008).
- Schneider, T., Serga, A. A. & Hillebrands, B. Realization of spin-wave logic gate. *Appl. Phys. Lett.* **92**, 022505 (2008).
- Goto, T. et al. Three port logic gate using forward volume spin wave interference in a thin yttrium iron garnet film. *Sci. Rep.* **9**, 16472 (2019).
- Khivintsev, Y. V. et al. Spin waves in YIG-based networks: logic and signal processing. *Phys. Metals Metallogr.* **120**, 1318–1324 (2019).
- Fischer, T. et al. Experimental prototype of a spin-wave majority gate. *Appl. Phys. Lett.* **110**, 152401 (2017).
- Talmelli, G. et al. Reconfigurable nanoscale spin wave majority gate with frequency-division multiplexing. Preprint at <https://arxiv.org/pdf/1908.02546.pdf> (2019).
- Wu, H. et al. Magnon valve effect between two magnetic insulators. *Phys. Rev. Lett.* **120**, 097205 (2018).
- Vogt, K. et al. Realization of a spin-wave multiplexer. *Nat. Commun.* **5**, 3727 (2014).
- Heussner, F. et al. Experimental realization of a passive gigahertz frequency-division demultiplexer for magnonic logic networks. *Phys. Status Solidi* **14**, 1900695 (2020).
- Papp, A. et al. Nanoscale spectrum analyzer based on spin-wave interference. *Sci. Rep.* **7**, 9245 (2017).
- Torrejon, J. et al. Neuromorphic computing with nanoscale spintronic oscillators. *Nature* **547**, 428–431 (2017).
- Brächer, T. & Pirro, P. An analog magnon adder for all-magnonic neurons. *J. Appl. Phys.* **124**, 152119 (2018).
- Chumak, A. V. in *Spintronics Handbook: Spin Transport and Magnetism* (eds Tsymbal, E. Y. & Žutić, I.) 247–303 (Taylor & Francis, 2019).
- Sadovnikov, A. V. et al. Directional multimode coupler for planar magnonics: side-coupled magnetic stripes. *Appl. Phys. Lett.* **107**, 202405 (2015).
- Sebastian, T. et al. Micro-focused Brillouin light scattering: imaging spin waves at the nanoscale. *Front. Phys.* **3**, 35 (2015).
- Heinz, B. et al. Propagation of spin-wave packets in individual nanosized yttrium iron garnet magnonic conduits. *Nano Lett.* **20**, 4220–4227 (2020).
- Clausen, P. et al. Mode conversion by symmetry breaking of propagating spin waves. *Appl. Phys. Lett.* **99**, 162505 (2011).

39. Brächer, T., Pirro, P. & Hillebrands, B. Parallel pumping for magnon spintronics: amplification and manipulation of magnon spin currents on the micron-scale. *Phys. Rep.* **699**, 1–34 (2017).
40. Verba, R. et al. Amplification and stabilization of large-amplitude propagating spin waves by parametric pumping. *Appl. Phys. Lett.* **112**, 042402 (2018).
41. Mohseni, M. et al. Parametric generation of propagating spin waves in ultrathin yttrium iron garnet waveguides. *Phys. Status Solidi RRL* **14**, 2000011 (2020).
42. Imre, A. et al. Majority logic gate for magnetic quantum-dot cellular automata. *Science* **311**, 205–208 (2006).
43. Verba, R. et al. Excitation of propagating spin waves in ferromagnetic nanowires by microwave voltage-controlled magnetic anisotropy. *Sci. Rep.* **6**, 25018 (2016).
44. Schneider, M. et al. Bose–Einstein condensation of quasi-particles by rapid cooling. *Nat. Nanotechnol.* **15**, 457–461 (2020).
45. Bauer, H. G. et al. Nonlinear spin-wave excitations at low magnetic bias fields. *Nat. Commun.* **6**, 8274 (2015).
46. Dobrovolskiy, O. V. et al. Spin-wave phase inverter upon a single nanodot. *ACS Appl. Mater. Interfaces* **11**, 17654–17662 (2019).
47. Chen, Y. et al. Parametric resonance of magnetization excited by electric field. *Nano. Lett.* **17**, 572–577 (2017).
48. Sadovnikov, A. V. et al. Magnon straintronics: reconfigurable spin-wave routing in strain-controlled bilateral magnetic stripes. *Phys. Rev. Lett.* **120**, 257203 (2018).
49. Guillemard, C. et al. Ultralow magnetic damping in Co₂Mn-based Heusler compounds: promising materials for spintronics. *Phys. Rev. Appl.* **11**, 064009 (2019).
50. Robertson, J. Liquid phase epitaxy of garnets. *J. Cryst. Growth* **45**, 233–242 (1978).
51. Maksymov, I. S. & Kostylev, M. Broadband stripline ferromagnetic resonance spectroscopy of ferromagnetic films, multilayers and nanostructures. *Physica E* **69**, 253–293 (2015).
52. Morozova, M. A. et al. Suppression of periodic spatial power transfer in a layered structure based on ferromagnetic films. *J. Magn. Magn. Mater.* **466**, 119–124 (2018).
53. Vansteenkiste, A. et al. The design and verification of MuMax3. *AIP Adv.* **4**, 107133 (2014).
54. Kumar, D. et al. Numerical calculation of spin wave dispersions in magnetic nanostructures. *J. Phys. D* **45**, 015001 (2012).
55. Venkat, G., Fangohr, H. & Prabhakar, A. Absorbing boundary layers for spin wave micromagnetics. *J. Magn. Magn. Mater.* **450**, 34–39 (2018).

Acknowledgements

We thank B. Hillebrands for support and valuable discussions. This research has been supported by ERC Starting Grant 678309 MagnonCircuits, FET-OPEN project CHIRON (contract no. 801055), the Deutsche Forschungsgemeinschaft (DFG, German Research Foundation) TRR-173 – 268565370 (Collaborative Research Center SFB/TRR-173 ‘Spin+X’, project B01) and DFG project no. 271741898, the Austrian Science Fund (FWF) through project I 4696-N and the Ministry of Education and Science of Ukraine, project 0118U004007. B.H. acknowledges support from the Graduate School Material Science in Mainz (MAINZ).

Author contributions

Q.W. proposed the directional coupler and half-adder design, preformed the BLS measurements, carried out the evaluation and wrote the first version of the manuscript. C.D. provided the YIG film. M.K., B.H. and B.L. fabricated the nanoscale directional coupler. M.S., B.H. and M.G. developed the BLS set-up. T.B. acquired the SEM micrograph. M.K. performed the VNA-FMR measurements. R.V. developed the analytical theory and performed the theoretical calculations. Q.W. and M.M. performed the micromagnetic simulations. F.C., C.A. and S.D.C. performed the benchmarking and calculated the parameters of the 7-nm CMOS half-adder. O.V.D. and T.B. discussed the interpretation and the relevance of the results. P.P. and A.V.C. led this project. All authors contributed to the scientific discussion and commented on the manuscript.

Competing interests

The authors declare no competing interests.

Additional information

Extended data is available for this paper at <https://doi.org/10.1038/s41928-020-00485-6>.

Supplementary information is available for this paper at <https://doi.org/10.1038/s41928-020-00485-6>.

Correspondence and requests for materials should be addressed to Q.W. or A.V.C.

Reprints and permissions information is available at www.nature.com/reprints.

Publisher’s note Springer Nature remains neutral with regard to jurisdictional claims in published maps and institutional affiliations.

© The Author(s), under exclusive licence to Springer Nature Limited 2020

Supplementary Materials

Realization of a nanoscale magnonic directional coupler for integrated magnonic half-adders

**Q. Wang, M. Kewenig, M. Schneider, R. Verba, F. Kohl, B. Heinz, M. Geilen, M. Mohseni, B. Lagel,
F. Ciubotaru, C. Adelman, C. Dubs, S. D. Cotozana, T. Bracher, P. Pirro, and A. V. Chumak**

S1. Effect of far-field excitation by the U-shaped antenna	2
S2. Spin-wave spectra in the isolated waveguide	2
S3. Field-dependent guiding of the spin-wave signal	4
S4. Modified half-adder with fan-out gate	5
S5. Energy consumption of parametric amplification	6
S6. Energy consumption for magnonic half-adder	9

Supplementary Section 1 | Effect of far-field excitation by the U-shaped antenna

In order to investigate the effect of the far-field spin-wave excitation in the second waveguide of the directional coupler, a set of additional measurements was performed on the special sample in which a single spin-wave waveguide is located $2\ \mu\text{m}$ away from the antenna as shown in Fig. S1b. The spin-wave spectra were measured using μBLS spectroscopy in the normal and displaced waveguides at the points which are marked by red and blue dots in Fig. S1a-b. The thermal background is obtained in the absence of microwave excitation. As one can see in the Fig. S1c, the spin-wave intensity in the displaced waveguide (blue points) is comparable to the thermal background (black points) in the working region and is much smaller than the intensity of the excited spin waves (red points). Therefore, the effect of the parasitic far-field excitation can be neglected in our experiments.

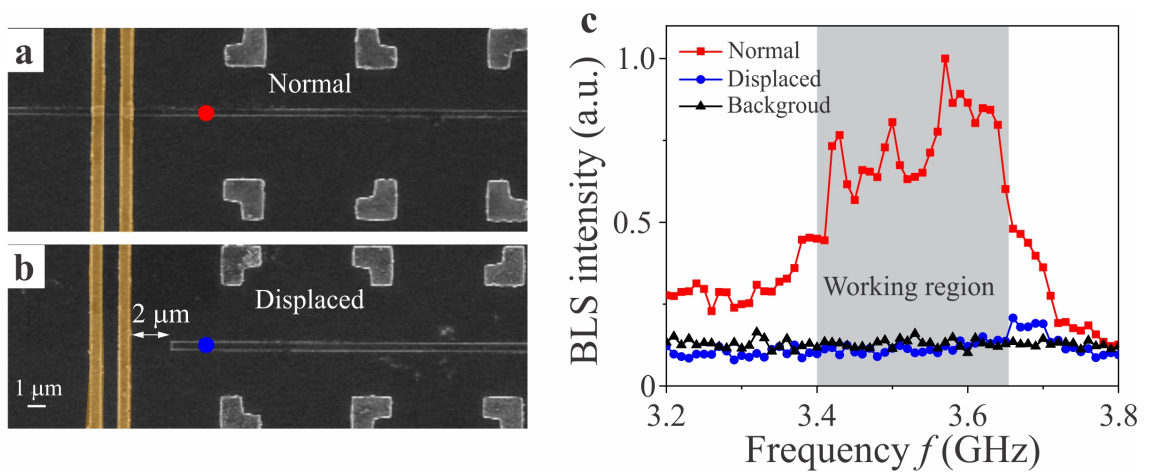


Figure S1 | Effect of far-field excitation by the U-shaped antenna. SEM images of the (a) normal and (b) displaced waveguides. c. The spin-wave intensities for normal (red dot line), displaced waveguides (blue dot line) and thermal background (black dot line). The grey area shows the working frequency range in the paper.

Supplementary Section 2 | Spin-wave spectra in the isolated waveguide

In this section, a comparison between the theoretical spin-wave spectra in the single waveguide and experimental results is given. For this calculation, all the parameters have already been provided in the methods section of the manuscript. In order to obtain the spectra of the excited spin waves in the isolated waveguides theoretically, we calculated the in-plane and the out-of-plane field distribution (see Fig. S2a) using the method reported in Ref. [S1]. Figure S2b shows the normalized excitation efficiency, which is obtained by performing the fast Fourier transformation of the out-of-plane field distribution. Please note the in-plane field did not directly excite spin waves in the used backward volume geometry. Figure S2c shows the spin-wave dispersion curve in the single waveguide of the width of $350\ \text{nm}$, which is calculated using the analytical theory [S2] with an effective width of $1400\ \text{nm}$ [S3] taking into account partial unpinning. Finally, the excited spin-wave intensity as a function of the

frequency is obtained as shown in Fig. S2d (black line) and compared to the spectra measured with μ BLS spectroscopy. The first two peaks of the spin-wave intensity are found at frequencies of about 3.6 GHz and 3.4 GHz, respectively, which correspond to the first two maxima of the excitation efficiency of the U-shaped antenna (see the black dashed line in Fig. S2b-d). A minimum spin-wave intensity is found at the frequency of 3.48 GHz, which corresponds to the minimum excitation efficiency of the antenna (see the blue dashed line). A set of additional measurements is performed on an isolated waveguide to confirm the analytical description. The spin-wave intensities are measured for different microwave powers (P_{mw}) at 4 μm distance from the antenna as shown on the top of Fig. S2d. When the input power $P_{\text{mw}} < -10$ dBm, the spin-wave intensity shows two peaks separated by a minimum point at $f = 3.48$ GHz which fits well with the analytical theory. However, the minimum point of the spin-wave spectrum disappears due to the nonlinearity when the excitation power is above 0 dBm. So, the spin-wave frequencies ranging from 3.4 GHz to 3.63 GHz are well excited by the U-shaped antenna.

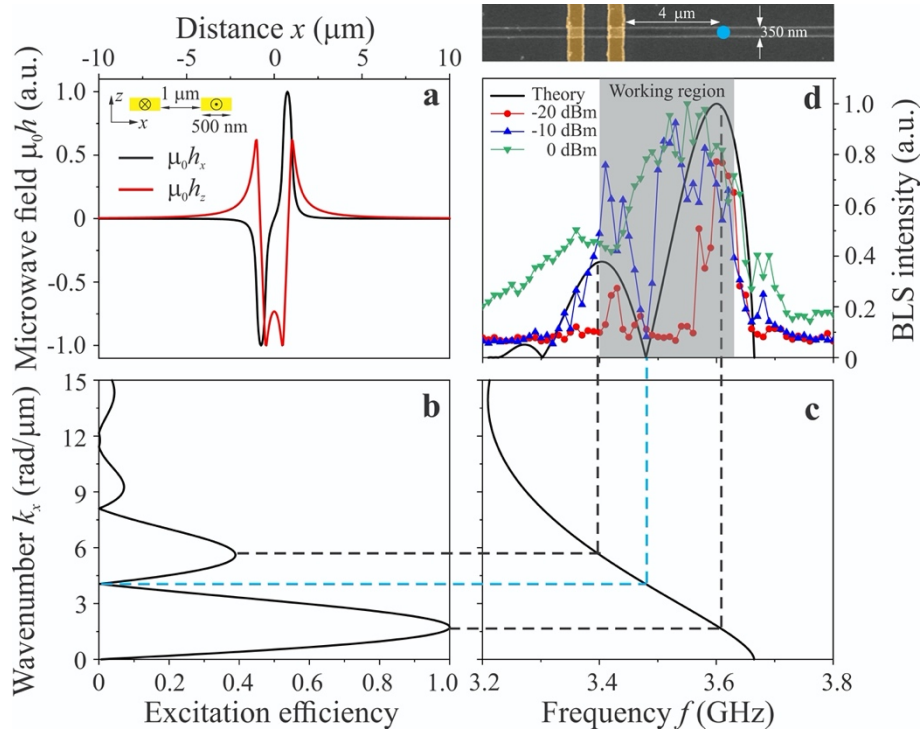


Fig. S2 | Spin-wave spectra in the isolated waveguide. *a.* The in-plane (black line) and out-of-plane (red line) field distribution created by the U-shape antenna. The schematic cross section of a U-shaped antenna is shown inset. *b.* The excitation efficiency as a function of spin-wave wavenumber. *c.* Spin-wave frequency as a function of spin-wave wavenumber. *d.* Spin-wave intensities are measured 4 μm far from the antenna for different excitation powers. The black line shows the analytical calculation of the spin-wave intensity. A SEM image of the isolated waveguide is shown on the top of Fig. S2d.

Supplementary Section 3 | Field-dependent guiding of the spin-wave signal

One of the most significant advantages of spin-wave directional couplers is their (re-)configurability via the magnetic field or magnetization orientation that allows to change the functionality while conserving the frequency of the signal. To demonstrate this feature, Fig. S3a shows the output spin-wave intensity for a frequency of $f_1 = 3.465$ GHz as a function of the applied external magnetic field at the output waveguides 1 and 2. Figure S3b presents the experimental and theoretical field dependencies of the normalized spin-wave intensity at the outputs. It can be seen from both figures that the variation of the applied field can tune the distribution of the spin-wave energy between the output waveguides. This is due to the fact that the coupling length L is strongly dependent on the spin-wave wavelength which is defined by the applied field at constant spin-wave frequency. For the field $B_{\text{ext}} = 56$ mT, the spin-wave energy is transferred to the second output waveguide, as shown in Fig. S3c. When the external field is decreased to 53.2 mT, the coupling length decreases due to a downward shift of the spin-wave dispersion curve and the directional coupler works as a 50/50 power splitter (see Fig. S3d). A further decrease of the external field to 51.3 mT results in a further decrease of the

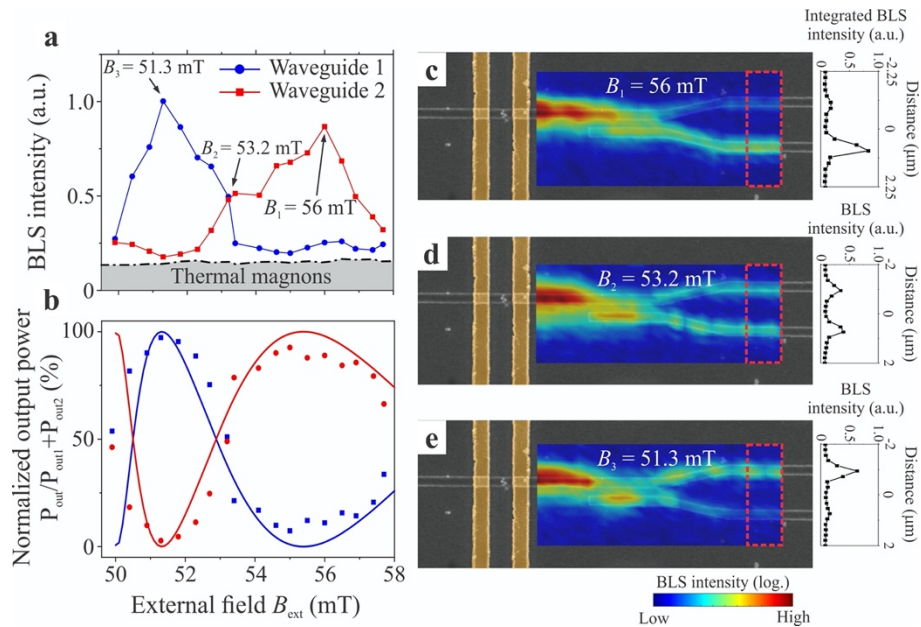


Fig. S3. Reconfigurability of the directional coupler by an applied magnetic field. *a.* The averaged spin-wave intensity for a frequency of 3.465 GHz as function of the external field for the first (blue circles) and the second (red squares) output waveguide of the directional coupler. *b.* Measured (circles and squares) and theoretically calculated (solid lines) normalized output spin-wave intensities at the first (blue) and second (red) output waveguide for different external fields. *c-e:* Two-dimensional BLS maps of the spin-wave intensity for the different external magnetic fields: *c.* $B_1 = 56$ mT, *d.* $B_2 = 53.2$ mT, and *e.* $B_3 = 51.3$ mT. The right panels show the BLS intensity integrated over the red dashed rectangular regions.

coupling length and most of the spin-wave energy is transferred back to the first waveguide as it is shown in Fig. S3e. Thus, the directional coupler can act as a signal multiplexer since its output configuration can be switched from one output to another within a small field range of only $\Delta B_{\text{ext}} = 4.7$ mT. In future circuits, an electric current applied to a metallic strip could be used to create a local Oersted field and to realize a switching of the directional coupler output via electric current control [S4]. As an energy-efficient alternative, a magnetic field from switchable nanosized magnets [S5] could be used to realize a non-volatile reconfigurability of the directional coupler.

Supplementary Section 4 | Modified half-adder with fan-out gate

In this manuscript, the Output “I” features high damping to avoid the reflection at the end of the waveguide. However, the SW amplitude in this waveguide satisfies the XOR logic gate – see truth table Table S1. In the further, it could also be used for logical operation.

Inputs		Output
A	B	I
0	0	0
1	0	1
0	1	1
1	1	0

Table S1. Truth of Output “I”

Furthermore, the Output “I” could also be used to perform the half-adder operation. In order to do that, an additional coupler was introduced to the Output “I” as shown in Fig. S4(a)-(c). For this, another waveguide is closely placed to the Output “I” and the phase difference between the inputs “A” and “B” has been changed from $\pi/2$ to 0 [S6]. The operation principle is identical to the original half-adder for the inputs combinations “A” = “1”, “B” = “0” and “A” = “0”, “B” = “1” as shown in Fig. S4 (a)-(b). If the inputs are “A” = “1”, “B” = “1”, the excitation of spin waves in both inputs results in the transfer of spin waves of the same intensities to both directional couplers. In this case, the SW intensity reaching the nonlinear directional coupler is twice compared to the single input (but not four times larger like in the original half-adder design). Nevertheless, even the increase in the SW intensity twice between the logic states allowed for the triggering of the nonlinear switching phenomenon (after adapting working frequency and the coupled length of the device) - see Fig. S4(c). This device operates as a combination of half-adder with fan-out gate and each logic output is doubled.

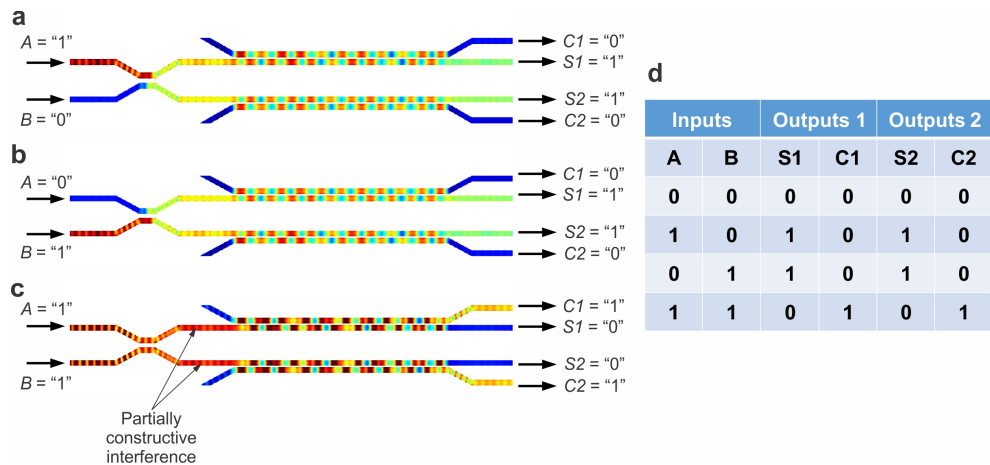


Fig. S4 | Modified half-adder with fan-out gate. (a-c) The operational principle and (d) truth table of two half-adders with shared inputs (corresponds to the half-adder with added fan-out logic gate).

Supplementary Section 5 | Energy consumption of parametric amplification

The amplifier is a very important point for the whole all-magnon data processing concept since the amplitude of the output signal should always be equal to the input one. The energy consumption of the amplifier might be crucial. To find the answer which amplifier is the most suitable, we analyzed three different approaches: the Spin-Orbit Torque-based approach, the electric current-based parametric pumping, and the Voltage Control Magnetic Anisotropy (VCMA) electric field-based parametric pumping.

1) The first one is based on the usage of the, so-called Spin-Orbit Torque (the combination of spin Hall effect (SHE) with spin transfer torque (STT)) [e.g., described in the review [S7]]. Unfortunately, this approach does not seem to be suitable since the amplification of the propagating spin waves was not demonstrated so far. Even the result reported in Ref. [S8] hardly can be used to amplify the propagation spin waves since the final smallest damping parameter in bilayer YIG/Pt with the current was comparable to the original damping of pure single layer YIG. The spin-orbit torque can only compensate for the damping caused by spin pumping due to the introduction of the Pt layer. To sum up, the output spin-wave intensity is always lower than the input in this system. Moreover, this approach requires the applications of electric currents of high densities and, therefore, hardly can ensure small energy consumption.

2) The second way is a classical parallel parametric pumping process in which the pumping rf magnetic Oersted field is created by sending of rf signal through a metallic strip

[S9]. This is the most well-studied approach in magnonics. In order to find the energy consumption of parametric amplification, we perform simulations in a single waveguide with a pumping antenna. Figure S5(a) shows the schematic picture of the parametric pumping region where an antenna (width: $w_a = 500$ nm, thickness: $t_a = 300$ nm) is placed on top of the YIG waveguide.

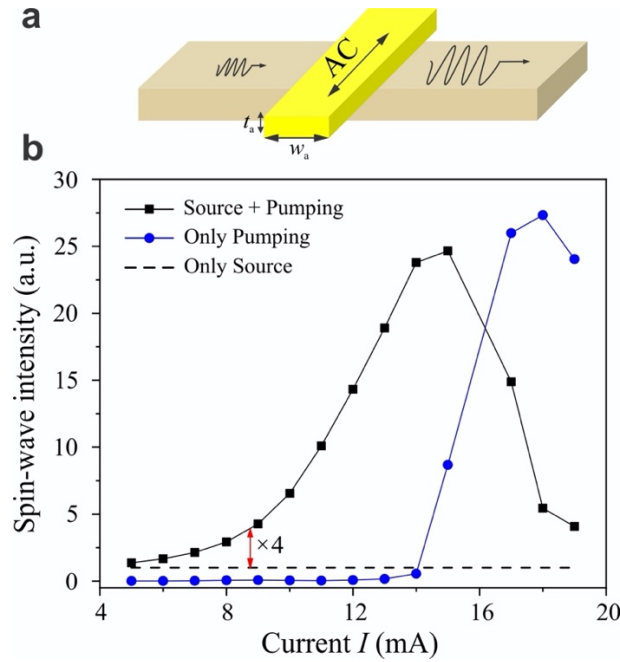


Fig. S5 | Parametric amplification. (a) A schematic picture of the parametric amplifier. (b) Output spin-wave intensity as a function of pumping current for different conditions.

In the simulations, the pumping frequency ($2f$) is twice the frequency of the initial spin wave. The spin-wave intensity at the frequency of f is extracted after the pumping region and is plotted as a function of pumping current. The blue dotted line shows the spin-wave intensity when only the pumping current is applied, where a clear threshold is observed. The intensity of the initial spin wave is marked by the dashed line. The black dotted line presents the total energy of the output spin-wave after the amplification when the pumping current and initial spin wave are applied simultaneously. The gap between the dashed line and the black dotted line indicates the amplification due to the parallel pumping. It is worth to mention that the parametric pumping starts to amplify the initial spin wave before it reaches the threshold of the parametric generation. This means that the parametric pumping will not directly excite parasitic spin waves in the magnonic circuits. The spin-wave intensity drops down in the high pumping current region due to the four magnon scattering.

In order to obtain a 4 times amplification of SW intensity, which is needed for the magnonic half-adder, the pumping current should be around 8.8 mA as shown in Fig. S5(b). For each output “S”, the length of the pumping antenna is at least $L_a=100$ nm (the width of waveguide). Then, the resistance of the pumping antenna can be calculated using $R=\rho L_a/(w_a t_a)=0.016$ Ohm ($\rho = 2.44 \times 10^{-8}$ Ohm/m is the resistivity of gold at room temperature). The pumping time is 300 ns. Thus, the energy consumption of amplification is around 10^5 aJ, which can be further decreased one or two orders of magnitude by optimizing the size of the pumping antenna and the half-adder. In general, this energy consumption is much higher than the energy used to process data within the magnonic domain.

3) The most suitable approach appeared to be the VCMA parametric pumping that has been reported in Ref. [S10]. In this case, the parametric process is similar to the previous one but instead of the magnetic rf field (which requires large currents), an electric rf field is used. This allows for the drastic decrease in the energy consumption of the amplification down to 3 aJ as was estimated for the example of a nm-thick CoFeB waveguide. The functionality of such kind of parametric pumping was recently reported experimentally in [S11].

The detail of estimation is given below. For VCMA parametric pumping, the electric field required is equal to:

$$E = \frac{hM_s b_{th}}{2\beta} \quad (7)$$

with β – magnetoelectric coefficient and h – waveguide thickness. Losses consists of dielectric losses and Ohmic ones,

$$W = \left(E^2 d \omega \varepsilon \varepsilon_0 w L \tan \delta + \frac{E^2 d^2}{R} \right) \tau \quad (8)$$

where d – dielectric thickness, ε – dielectric permittivity, $\tan \delta$ – tangents of dielectric losses, R – tunnel resistance. Both terms depend on the thickness d and the total losses are minimal at certain optimal d .

In the estimation, we use $L = 100$ nm (the length of pumping area), CoFeB thickness $h = 1$ nm (for perpendicular anisotropy), $\beta = 100$ fJ/Vm, for MgO $\varepsilon = 9.6$ and $\tan \delta = 10^{-5}$, tunnel resistance per area product $10^6 \Omega \mu\text{m}^2$ for $d = 2.2$ nm and increases in order per each 0.4 nm [S12]. Then pumping electric field is $E \sim 1-1.5$ V/nm, optimal MgO thickness $d \sim 2.6$ nm, energy consumption ~ 3 aJ.

Supplementary Section 6 | Energy consumption for magnonic half-adder

For the estimation of energy consumption in the magnonic system (neglecting transducers), we can simply calculate the energy of the SW pulse. The energy of SW pulse is given by

$$E = \frac{M_s V}{\gamma} \omega_k |a_k|^2 \quad (1)$$

where SW amplitude a_k is defined so that SW norm $A_k = 1$ (which is the same as common u - v transformation), and V is the volume of SW pulse. Naturally, $V = S v_{gr} \tau$, with S being the cross-section of the waveguide, v_{gr} – SW group velocity and τ – pulse duration.

The SW amplitude is determined from the condition that it should be enough to switch the nonlinear directional coupler. From Eq. (3) of the paper, we obtain the following condition

$$\frac{L}{L_c} \frac{\pi}{2L_c} \frac{\partial L_c}{\partial f} T_k |a_k|^2 = \frac{\pi}{2} \quad (2)$$

For simplicity, we neglect the sign of T_k and $\partial L_c / \partial f$ – they are not important. Then, using the definition of the coupling length via the coupling frequency Ω , and setting $L/L_c = N$, $N = 0, 2, 4, \dots$ (i.e., in the linear regime we work on the $N/2$ - the transmission maximum), we get

$$\frac{N}{\Omega} \frac{\partial \Omega}{\partial f} T_k |a_k|^2 = 1 \quad (3)$$

The duration of the SW pulse is determined by the maximal frequency width of the pulse $\Delta\omega$, $\tau = 2\pi/\Delta\omega$, which should be small enough for stable operation of both linear and nonlinear couplers. In the case of the nonlinear coupler, which works near the maximum or minimum of transmission,

$$\cos \frac{\Omega L}{v_{gr}} \approx 1 - \frac{1}{2} \left(\frac{L}{v_{gr}} \right)^2 \Delta\Omega^2 \quad (4)$$

where $\Delta\Omega = (\partial\Omega/\partial\omega)\Delta\omega$ and the last term should be $\ll 1$. Using the convention that $x \ll 1$ meaning $x \leq 0.1$, we get

$$\frac{\Delta\Omega}{\Omega} < \frac{0.3}{N} \quad (5)$$

Performing the same calculations for a linear coupler (assuming its length $L=L_c/2$), we get $\Delta\Omega/\Omega < 0.2$. In fact, the condition for the nonlinear case is more severe, as $N \geq 2$. More rigorously, the minimal size of the nonlinear coupler N can be estimated from the condition that the linear coupler, working at half the coupling length, does not significantly change its characteristics at the power which is enough to the switch nonlinear coupler. Simple

calculations yield that the change of linear coupler transmission is given by $\cos^2(\pi(N-1)/(4N))$, while the linear regime transmission rate is equal to $1/2$. This gives the restriction $N_{\min} = 6$. In this estimations, we disclose the worse possible case assuming that the linear and nonlinear coupler have the same gap. In the optimized case when the gaps are different, the energy consumption will be reduce further.

Combining Eqs. (5, 3, 1), we get the final expression for the minimal energy consumption (Eq. 8 in the paper)

$$E = \frac{20\pi}{3} \frac{M_s}{\gamma} \frac{v_{gr} f S}{T_k} \quad (6)$$

References

- S1. Chumakov, D. High Frequency Behaviour of Magnetic Thin Film Elements for Microelectronics. Dissertation, Technische Universität Dresden, Dresden, Germany (2007).
- S2. Wang, Q. *et al.* Reconfigurable nanoscale spin-wave directional coupler. *Sci. Adv.* **4**, e1701517 (2018).
- S3. Wang, Q. *et al.* Spin pinning and spin-wave dispersion in nanoscopic ferromagnetic waveguides, *Phys. Rev. Lett.* **122**, 247202 (2019).
- S4. Heussner, F. *et al.* A switchable spin-wave signal splitter for magnonic networks. *Appl. Phys. Lett.* **111**, 122401 (2017).
- S5. Imre, A. *et al.* Majority logic gate for magnetic quantum-dot cellular automata. *Science* **311**, 205 (2006).
- S6. Please note that the phase shift in the manuscript is $\pi/2$. It is easy to get any phase shift in magnonic system. Since the spin-wave wavelength is fixed as well as the required phase shift, in practice, the phase shifter can be realized by varying, e.g., the length of the magnonic conduits the waveguide width or by creating inhomogeneities in the biasing magnetic field.
- S7. Demidov, V. E. *et al.* Magnetization oscillations and waves driven by pure spin currents. *Phys. Rep.* **673**, 1-32 (2017).
- S8. Evelt, M. *et al.* High-efficiency control of spin-wave propagation in ultra-thin yttrium iron garnet by the spin-orbit torque. *Appl. Phys. Lett.* **108**, 172406 (2016).
- S9. Brächer, T. Pirro, P, & Hillebrands, B. Parallel pumping for magnon spintronics: Amplification and manipulation of magnon spin currents on the micron-scale. *Phys. Rep.* **699**, 1-34 (2017).

- S10. Verba, R. *et al.* Amplification and stabilization of large-amplitude propagating spin waves by parametric pumping. *App. Phys. Lett.* **112**, 042402 (2018).
- S11. Chen, Y. *et al.* Parametric resonance of magnetization excited by electric field. *Nano. Lett.* **17**, 572-577 (2017).
- S12. D. Mazumdar, Coherent magnetotunneling based on (001) magnesium oxide barrier, PhD thesis, Brown University, (2007).

5.5. Узагальнення гамільтонового формалізму нелінійної взаємодії спінових хвиль на випадок несиметричних магнітних взаємодій

PHYSICAL REVIEW B **99**, 174431 (2019)

Hamiltonian formalism for nonlinear spin wave dynamics under antisymmetric interactions: Application to Dzyaloshinskii-Moriya interaction

Roman Verba,¹ Vasil Tiberkevich,² and Andrei Slavin²

¹*Institute of Magnetism, Kyiv 03142, Ukraine*

²*Department of Physics, Oakland University, Rochester, Michigan 48309, USA*



(Received 21 March 2019; published 28 May 2019)

A Hamiltonian formalism is applied for the investigation of nonlinear spin wave dynamics under the influence of antisymmetric magnetic interactions. In the framework of this formalism we account not only for symmetric magnetic interactions (exchange, dipole-dipole, magnetocrystalline anisotropy), but also for antisymmetric interactions, such as Dzyaloshinskii-Moriya exchange interaction. The account of antisymmetric exchange, in general, could lead to the appearance of an additive nonreciprocal term in the spin wave dispersion law. We present the generalization of the linear transformation for the diagonalization of quadratic part of the Hamiltonian (so-called “third Holstein-Primakoff transformation”) for the antisymmetric case, which allowed us to obtain generalized expressions for the coefficients of the nonlinear three- and four-magnon interactions. As an example, nonlinear spin wave interactions in ultrathin ferromagnetic nanowires and films subjected to interfacial Dzyaloshinskii-Moriya interaction (IDMI) are considered. It was found that three-magnon interaction coefficients in the “Damon-Eshbach” geometry are nonzero only in the case of the noncollinear interacting spin waves, and vanish in the case of the collinear spin waves. It was also found that the nonlinear spin wave frequency shift caused by the four-magnon interaction is nonreciprocal, and has the sign opposite to that of the nonreciprocal term in linear spin wave dispersion, so that the IDMI-induced nonreciprocity of the spin wave spectrum decreases with the increase of the spin wave amplitude.

DOI: [10.1103/PhysRevB.99.174431](https://doi.org/10.1103/PhysRevB.99.174431)

I. INTRODUCTION

One of significant advantages of spin waves (SWs) as signal carriers for microwave signal processing is the relatively low amplitude levels at which SWs (or magnons) start to demonstrate nonlinearity, and can be involved in nonlinear processes, including parametric interaction with electromagnetic pumping, three-wave, four-wave, and higher-order magnon-magnon interaction processes [1–3]. Nonlinear SW properties manifest themselves in various phenomena, such as parametric SW instability [4–7], saturation of the ferromagnetic resonance and foldover effect [8–12], nonlinear decay of SWs [13,14], and SW turbulence and chaos [2,15,16]. Exploration of these nonlinear phenomena made possible the development of nonlinear microwave signal processing devices, such as frequency-selective power limiters and signal-to-noise enhancers based on three-wave interaction [1,17,18], nonlinear delay lines based on formation, propagation and manipulation of SW solitons caused by the four-wave interactions [19–25], as well as the nonlinear spin wave switches and logic devices [26–29].

To understand and explore nonlinear SW processes, one needs to know which processes are allowed for a particular group of SWs, and needs to be able to evaluate the efficiency of these processes. Obviously, the understanding of nonlinear SW properties is also necessary for the successful development of *linear* SW devices since the nonlinear processes often limit the power dynamic range of these linear devices. Theoretically, the most general and powerful approach for the quantitative analysis of nonlinear SW interactions and calculation of the efficiencies of multimagnon interaction

(that is, nonlinear SW coefficients) is the classical Hamiltonian formalism for SW that was originally proposed by Schlömann [30], and, then, developed in Ref. [2]. In the framework of this formalism the components of the dynamical magnetization vector are represented in terms of two scalar canonical Hamiltonian variables $a(\mathbf{r}, t)$ and $a^*(\mathbf{r}, t)$ [2]. The coefficients of the nonlinear multimagnon interactions are derived using the expansion of the Hamiltonian function for the magnetization dynamics into a series of spatial Fourier harmonics of the above-mentioned canonical variables, while the dynamics is governed by standard Hamiltonian equations [31]. This Hamiltonian formalism for the magnetization dynamics was extensively used for the investigation of nonlinear SW dynamics under parametric pumping (see Refs. [2,32] and references therein) and SW parametric instabilities in different geometries [6,7,14]. More recently, the large-angle magnetization dynamics induced by spin-transfer torque, was explored in Refs. [33,34].

Calculation of nonlinear coefficients in the framework of the above-described Hamiltonian approach is straightforward, but rather cumbersome algebraically when applied to particular geometries (e.g., thin films) [35,36], and cannot be easily generalized. Krivosik and Patton, using effective SW tensor formulation [6], derived explicit general expressions for nonlinear coefficients (up to four-wave coefficients) in a uniformly magnetized sample, assuming that normal modes of the system are plane waves [37]. Their theory is suitable for bulk samples, fundamental modes of ferromagnetic films and nanowires, ferromagnetic resonance of nanostructures, and allows one to take into account *symmetric* magnetic

self-interactions, quadratic in magnetization. Nonuniform exchange, magnetodipolar interaction, and uniaxial anisotropy, which often are the most important interactions, belong to the family of symmetric quadratic interactions, and are described by symmetric tensor operators.

However, not all the quadratic magnetic self-interactions are symmetric. In magnetic multilayers and materials with a specific crystal structure the *antisymmetric* exchange interaction, which is usually called “Dzyaloshinskii-Moriya” interaction (DMI), can appear and play an important role [38,39]. The DMI became of a significant research interest recently when it became possible to fabricate ultrathin ferromagnetic (Fe, permalloy, CoFe, etc.) films on a substrate made of a heavy metal characterized by a large spin-orbit coupling (W, Pt, etc.). In such systems at the interface between the ferromagnet and the heavy metal, the interfacial Dzyaloshinskii-Moriya interaction (IDMI) manifests itself and significantly influences the magnetization dynamics [40–42]. In particular, IDMI can stabilize topologically nontrivial magnetization states [43,44], or lead to the nonreciprocity of the SW spectrum in magnetic films or nanowires magnetized to saturation [41,45–48].

SW nonreciprocity could be very important for microwave signal processing [49–55], and the use of IDMI in thin ferromagnetic films is the most promising way to achieve substantial nonreciprocity of SWs with the wavelength of 100 nm and below. Therefore, it is important to investigate linear and nonlinear SW properties in magnetic materials with IDMI. In particular, it is critical to investigate the variation of SW spectrum at high SW amplitudes and calculate the three-wave nonlinear SW coefficients that determine the threshold of the SW parametric instability. This knowledge is especially important for the successful development of parametric [54] and spin-torque [56–58] IDMI-based devices, in which high amplitudes of SWs are easily realized.

The IDMI is not the only example of antisymmetric magnetic interactions. Different kinds of bulk Dzyaloshinskii-Moriya interactions, which exist in magnetic crystals with specific broken symmetries, are nonsymmetric too [38,39,59,60]. Also, the spin-flexoelectric interaction, which was predicted to manifest itself in ferromagnetic insulators under applied electric field [61,62], also belongs to the family of antisymmetric interactions.

The main aim of our current work is to generalize the existing theory of nonlinear spin wave dynamics based on the Hamiltonian approach [2,35,37] to the case of *any* magnetic self-interactions, quadratic in magnetization. Similarly to Ref. [37] we assume that ferromagnetic sample is in the saturated state, and elementary excitations in this sample are plane SWs. Throughout our current work we keep the notations of Ref. [37], and point out explicitly the main differences which appear due to the presence of nonsymmetric magnetic interactions.

The paper is organized as follows. In Sec. II an overview of the Hamiltonian formalism is given, and magnetic Hamiltonian function is derived in terms of the magnetization components and complex amplitudes of the plane spin waves. The expansion of the Hamiltonian function in a series of Fourier amplitudes of canonic variables $a_k(t)$ and $a_k^*(t)$ up to the fourth-order terms is presented in Sec. II E. The

diagonalization of the quadratic part of the SW Hamiltonian using the generalized third Holstein-Primakoff transformations and expansion of the Hamiltonian function into linear modes are given in Sec. III. In Sec. IV, as an example of application of the developed formalism, we derive general expressions to calculate three-wave splitting efficiency and four-wave nonlinear frequency shift of the SWs in ferromagnetic films subjected to IDMI. Finally, conclusions are given in Sec. V.

II. MAGNETIC HAMILTONIAN FUNCTION

A. Overview of the Hamiltonian formalism

The most important step in the classical Hamiltonian approach is the transformation of the natural dynamic variables of the problem (in our case, components of the dynamical magnetization) into canonical variables a , a^* in which the energy of the studied system becomes a Hamiltonian function. The Hamiltonian function is, commonly, a functional of the full energy of the system E . In the study of ferromagnetic materials, however, it is more convenient to use a reduced Hamiltonian function [30,37]

$$\mathcal{H} = \mathcal{H}[\mathbf{M}(\mathbf{r}, t)] = \frac{\gamma E}{M_s V}, \quad (2.1)$$

where γ is the modulus of the gyromagnetic ratio, M_s is the saturation magnetization, and V is the volume of the ferromagnetic material. The Hamiltonian function (2.1) is measured in the units of frequency. The canonical variables $a(\mathbf{r}, t)$ and $a^*(\mathbf{r}, t)$ are introduced as

$$\alpha_{\perp}(\mathbf{r}, t) = a(\mathbf{r}, t)\sqrt{2 - a(\mathbf{r}, t)a^*(\mathbf{r}, t)}, \quad (2.2a)$$

$$\alpha_z(\mathbf{r}, t) = 1 - a(\mathbf{r}, t)a^*(\mathbf{r}, t). \quad (2.2b)$$

Here, $\alpha_{x,y,z} = M_{x,y,z}/M_s$ are the normalized magnetization components and $\alpha_{\perp} = i\alpha_x + \alpha_y$ is the complex dynamic magnetization variable. Equations (2.2) use the convention that static magnetization is directed along the z axis. It is clear that $|\alpha_{\perp}|^2 + \alpha_z^2 = 1$, i.e., the transformation (2.2) satisfies the condition of conservation of the magnetization vector length.

When Hamiltonian function of the system is expressed in terms of the canonical variables, the dynamical equations for the variables $a(\mathbf{r}, t)$ and $a^*(\mathbf{r}, t)$ can be written in a standard Hamiltonian form:

$$i\frac{da(\mathbf{r}, t)}{dt} = \frac{\delta\mathcal{H}}{\delta a^*(\mathbf{r}, t)}, \quad -i\frac{da^*(\mathbf{r}, t)}{dt} = \frac{\delta\mathcal{H}}{\delta a(\mathbf{r}, t)}. \quad (2.3)$$

The next step in the Hamiltonian formalism for SW is the expansion of $a(\mathbf{r}, t)$ into a series of plane waves (in the case when the plane waves are the normal modes of the system):

$$a(\mathbf{r}, t) = \sum_k a_k(t)e^{i\mathbf{k}\cdot\mathbf{r}}, \quad (2.4)$$

where new canonical variables $a_k(t)$ describe amplitudes of SWs with the wave vector \mathbf{k} . Since the Fourier transform is canonical, the dynamical equations for $a_k(t)$ have the same form as Eq. (2.3), namely,

$$i\frac{da_k(t)}{dt} = \frac{\partial\mathcal{H}}{\partial a_k^*(t)}, \quad -i\frac{da_k^*(t)}{dt} = \frac{\partial\mathcal{H}}{\partial a_k(t)}. \quad (2.5)$$

The change of the variational derivative in Eq. (2.3) to the partial derivative in Eq. (2.5) is related with the fact that \mathcal{H} is a functional in terms of $a(\mathbf{r}, t)$, but becomes a polynomial function in terms of the Fourier amplitudes $a_k(t)$.

After the transformation (2.2), the Hamiltonian function can be developed as a series in the SW Fourier amplitudes a_k and a_k^* and, thus, can be represented as $\mathcal{H} \approx \mathcal{H}^{(0)} + \mathcal{H}^{(1)} + \mathcal{H}^{(2)} + \dots$, where the superscripts indicate the number of amplitudes a_k and a_k^* in the corresponding term. The term $\mathcal{H}^{(0)}$ which does not contain any SW amplitudes determines the energy of the ground state, $\mathcal{H}^{(1)}$ describes the linear excitation of SWs by external forces (e.g., by a microwave magnetic field), the term $\mathcal{H}^{(2)}$ determines the “kinetic” energy of the system in the linear regime defined by the linear spectrum of the system SW eigenmodes, and all the higher-order terms describe the nonlinear interactions between the SWs. It has been shown in Ref. [2] that in most cases it is sufficient to consider the expansion of the Hamiltonian function up to the fourth order $\mathcal{H}^{(4)}$ in terms of the variables a_k and a_k^* .

Finally, it is, usually, convenient to diagonalize the quadratic part $\mathcal{H}^{(2)}$ of the SW Hamiltonian using the third Holstein-Primakoff (or u - v Bogoljubov) transformation, and introduce the new (elliptically polarized) variables c_k and c_k^* , which describe the amplitudes of the normal linear SW modes. The derivation of the nonlinear terms $\mathcal{H}^{(3)}$ and $\mathcal{H}^{(4)}$ of the Hamiltonian function in terms of the variables c_k and c_k^* is the final step, which gives the coefficients of the nonlinear (three- and four-wave) SW interactions.

B. Terms of the magnetic Hamiltonian function

The first step in the Hamiltonian formalism is the derivation of the Hamiltonian function \mathcal{H} in terms of the magnetization vector $\mathbf{M}(\mathbf{r}, t)$. A generic expression for \mathcal{H} can be written as

$$\mathcal{H} = -\frac{\gamma}{M_s V} \int \mathbf{M}(\mathbf{r}, t) \cdot \mathbf{B}_e(\mathbf{r}, t) d\mathbf{r} - \frac{1}{2} \frac{\gamma}{M_s V} \int \mathbf{M}(\mathbf{r}, t) \cdot \mathbf{B}_M(\mathbf{r}, t) d\mathbf{r} - \dots \quad (2.6)$$

Here, the first term corresponds to the Zeeman energy of magnetization in the *external* magnetic field \mathbf{B}_e , which can be both space and time dependent. The second term represents the interaction of the magnetization with the *internal* field \mathbf{B}_M , which is produced by the magnetization itself. For most common magnetic self-interactions, which are quadratic functionals in terms of magnetization, the field \mathbf{B}_M can be conveniently expressed as

$$\mathbf{B}_M(\mathbf{r}, t) = -\mu_0 \int \hat{\mathbf{N}}(\mathbf{r}, \mathbf{r}') \cdot \mathbf{M}(\mathbf{r}', t) d\mathbf{r}', \quad (2.7)$$

where $\hat{\mathbf{N}}(\mathbf{r}, \mathbf{r}')$ is the tensor operator describing magnetic self-interactions. It consists of the sum of different contributions, the most important of which are exchange, magnetodipolar, and anisotropy contributions. The isotropic exchange interaction is described by the operator

$$\hat{\mathbf{N}}_{\text{ex}}(\mathbf{r}, \mathbf{r}') = -\lambda_{\text{ex}}^2 \delta(\mathbf{r} - \mathbf{r}') \hat{\mathbf{I}} \nabla_{\mathbf{r}} \cdot \nabla_{\mathbf{r}'}, \quad (2.8)$$

where $\lambda_{\text{ex}} = \sqrt{2A/\mu_0 M_s^2}$ is the exchange length of the magnetic material, A is the exchange stiffness, $\hat{\mathbf{I}}$ is the unit matrix,

and subscripts of the nabla operators denote the coordinates (\mathbf{r} or \mathbf{r}') to which the operator is applied. Magnetodipolar interaction in the magnetostatic approximation, i.e., neglecting retardation effects, is expressed via the magnetostatic Green's function [63]

$$\hat{\mathbf{N}}_{\text{dip}} = \frac{1}{4\pi} \nabla_{\mathbf{r}} \left(\nabla_{\mathbf{r}'} \frac{1}{|\mathbf{r} - \mathbf{r}'|} \right). \quad (2.9)$$

The uniaxial magnetic anisotropy is given by

$$\hat{\mathbf{N}}_{\text{an}}(\mathbf{r}, \mathbf{r}') = -\frac{B_{\text{an}}}{\mu_0 M_s} \delta(\mathbf{r} - \mathbf{r}') \mathbf{e}_{\zeta} \otimes \mathbf{e}_{\zeta}, \quad (2.10)$$

where $B_{\text{an}} = 2K_u/M_s$ is the anisotropy field, K_u is the constant of uniaxial anisotropy, \mathbf{e}_{ζ} is the unit vector in the direction of the anisotropy axis (ζ direction), and the symbols \otimes are denoting the dyadic product of vectors. Dirac delta function $\delta(\mathbf{r} - \mathbf{r}')$ in Eqs. (2.8) and (2.10) indicates the local character of the exchange interaction and the crystalline anisotropy, in contrast with the nonlocal long-range character of the magnetodipolar interaction.

In a general case, the Hamiltonian function (2.1) may contain higher-order terms (in respect to the magnetization), in particular, if the other than uniaxial crystalline anisotropy is taken into account. For example, cubic magnetic anisotropy is described by the third order in respect to \mathbf{M} term [1]. Below, for simplicity, we skip these possible higher-order contributions, although, if necessary they can be accounted for in a similar way.

The energy of the IDMI in a thin ferromagnetic film or nanowire can be expressed as

$$E_{\text{IDMI}} = \int \frac{\tilde{D}}{M_s^2} [M_z \nabla \cdot \mathbf{M} - \mathbf{M} \cdot (\nabla M_z)] d\mathbf{r}, \quad (2.11)$$

where z axis is a normal to the ferromagnetic-heavy-metal interface, $\tilde{D} = Db/h$ is the effective IDMI parameter, D is the IDMI constant, h is the thickness of the film or nanowire, and b is the thickness of the ferromagnetic monolayer [47]. It is clear that the term representing IDMI in the Hamiltonian function can be also expressed in the form of Eqs. (2.6) and (2.7) with the tensor operator given by

$$\hat{\mathbf{N}}_{\text{IDMI}}(\mathbf{r}, \mathbf{r}') = \frac{2\tilde{D}}{\mu_0 M_s^2} \delta(\mathbf{r} - \mathbf{r}') [\mathbf{e}_{z'} \otimes \nabla_{\mathbf{r}'} - \nabla_{\mathbf{r}'} \otimes \mathbf{e}_{z'}] \quad (2.12)$$

or in the explicit matrix form

$$\hat{\mathbf{N}}_{\text{IDMI}}(\mathbf{r}, \mathbf{r}') = \frac{2\tilde{D}}{\mu_0 M_s^2} \delta(\mathbf{r} - \mathbf{r}') \begin{pmatrix} 0 & 0 & -\partial_{x'} \\ 0 & 0 & -\partial_{y'} \\ \partial_{x'} & \partial_{y'} & 0 \end{pmatrix}. \quad (2.13)$$

From Eq. (2.13) one can clearly see the main difference of the IDMI term compared to the other magnetic self-interactions, mentioned above. The tensor operator $\hat{\mathbf{N}}_{\text{IDMI}}$ is *antisymmetric*, while the operators of the uniaxial anisotropy, dipolar and exchange interactions are all *symmetric*. The antisymmetric nature of the IDMI is also reflected by the fact that $\hat{\mathbf{N}}_{\text{IDMI}}$ changes its sign to the opposite under the space inversion operation $\mathbf{r} \rightarrow -\mathbf{r}$, in contrast to the other self-interaction operators, which remain unchanged in respect to the space inversion.

The bulk Dzyaloshinskii-Moriya interaction, which is present in ferromagnetic crystals with lack of the inversion symmetry, could be also accounted in the same manner as the IDMI, and is represented by an antisymmetric tensor operator [60]. Below, we will not use any specific features of the operator \hat{N} , related to the IDMI or other interactions. We assume that tensor operator $\hat{N}(\mathbf{r}, \mathbf{r}')$ is *nonsymmetric* in a general case, i.e., consists of symmetric and antisymmetric contributions. Thus, the formalism presented below is applicable to *any* magnetic self-interaction, quadratic in magnetization.

C. Conversion to the complex variables

The next step in the Hamiltonian approach is the conversion to the canonic variables $\alpha(\mathbf{r}, t)$, $\alpha^*(\mathbf{r}, t)$. This step is just a simple algebraic operation. For convenience and brevity, we, following Ref. [37], introduce the dimensionless complex vector $\alpha(\mathbf{r}, t) = [\alpha_\perp, \alpha_\perp^*, \alpha_z]$, where $\alpha_\perp(\mathbf{r}, t)$ and $\alpha_z(\mathbf{r}, t)$ are related to the canonical variables according to Eq. (2.2). The real magnetization vector $\mathbf{M}(\mathbf{r}, t)$ is connected with α through the relation $\mathbf{M} = M_s \hat{T} \cdot \alpha$, where

$$\hat{T} = \frac{1}{2} \begin{pmatrix} -i & i & 0 \\ 1 & 1 & 0 \\ 0 & 0 & 2 \end{pmatrix}. \quad (2.14)$$

It is also useful to establish the relation $\alpha^* = \hat{S} \cdot \alpha$, where

$$\hat{S} = \begin{pmatrix} 0 & 1 & 0 \\ 1 & 0 & 0 \\ 0 & 0 & 1 \end{pmatrix}. \quad (2.15)$$

Here, we should recall that the introduction of the canonical variables in the form of Eq. (2.2) assumes that the static magnetization of a ferromagnetic sample is uniform, and is pointed in the $+z$ direction. Therefore, all the self-interaction operators $\hat{N}(\mathbf{r}, \mathbf{r}')$ should be derived in this coordinate system. A more complex case of nonuniform static magnetization configurations is considered in a similar way, with the difference that the relation between \mathbf{M} and α becomes coordinate dependent, i.e., $\hat{T} = \hat{T}(\mathbf{r})$. The examples of application of the Hamiltonian formalism to nonuniform magnetic states can be found in Refs. [64,65].

The direct calculation allows one to obtain the Hamiltonian function in the form

$$\mathcal{H} = -\frac{\gamma}{V} \int \alpha^*(\mathbf{r}, t) \cdot \tilde{\mathbf{B}}(\mathbf{r}, t) d\mathbf{r} + \frac{1}{2V} \iint \alpha^*(\mathbf{r}, t) \cdot \hat{\Gamma}(\mathbf{r}, \mathbf{r}') \cdot \alpha(\mathbf{r}', t) d\mathbf{r} d\mathbf{r}', \quad (2.16)$$

where

$$\tilde{\mathbf{B}}(\mathbf{r}, t) = \hat{S} \cdot \hat{T}^T \cdot \mathbf{B}_e(\mathbf{r}, t) \quad (2.17a)$$

and

$$\hat{\Gamma}(\mathbf{r}, \mathbf{r}') = \omega_M \hat{S} \cdot \hat{T}^T \cdot \hat{N}(\mathbf{r}, \mathbf{r}') \cdot \hat{T}, \quad (2.17b)$$

with $\omega_M = \gamma \mu_0 M_s$. Here, analogously to the complex magnetization vector α , we introduce the complex vector field $\tilde{\mathbf{B}}(\mathbf{r}, t) = [\tilde{B}_\perp/\sqrt{2}, \tilde{B}_\perp^*/\sqrt{2}, B_{e,z}]$, where $\tilde{B}_\perp(\mathbf{r}, t) = (iB_{e,x} + B_{e,y})/\sqrt{2}$ is the circular component of the external field \mathbf{B}_e (the “tilde” sign over the complex vector field is added

in order not to mix this vector with the real external field \mathbf{B}_e). The explicit derivation of the components of the tensor operator $\hat{\Gamma}(\mathbf{r}, \mathbf{r}')$ is not necessary at this step. It is convenient to preserve the vector structure of this expression during the operation of the Fourier transform (next step).

D. Conversion to the plane waves

The goal of the current and following sections in the paper is to represent the Hamiltonian function in terms of the Fourier amplitudes of the SW canonical variables a_k and a_k^* . It should be noted that the introduction of the SW amplitudes a_k and a_k^* in the form of Eq. (2.4) implies that the linear eigenmodes of the considered ferromagnetic sample are plane waves. This statement is correct for the bulk samples and for fundamental SW modes in ferromagnetic films and nanowires, which have almost uniform profiles along the thickness and width coordinate of the sample. In other cases, e.g., when considering quantized modes of a magnetic nanodot, Eq. (2.4) should be modified taking into account the spatial profiles of the quantized modes (see, e.g., Refs. [7,64,65]).

When performing Fourier transform, it is convenient to preserve the vector structure of the Hamiltonian (2.16). Then, all the terms of the Hamiltonian function change to their Fourier images. Namely, the dimensionless complex magnetization vector is represented via its Fourier image as

$$\alpha(\mathbf{r}, t) = \sum_k \alpha_k(t) e^{ik \cdot \mathbf{r}}, \quad (2.18)$$

where $\alpha_k = [\mathcal{F}_k[\alpha_\perp(\mathbf{r}, t)], \mathcal{F}_k[\alpha_\perp^*(\mathbf{r}, t)], \mathcal{F}_k[\alpha_z(\mathbf{r}, t)]]$, and \mathcal{F}_k denotes the operator of the Fourier transform. The derivation of the explicit relation between the components of α_k and canonical variables a_k requires application of the Taylor expansion, and is given in the next subsection. The transformation of the complex vector of the external field is also trivial, and is given by

$$\tilde{\mathbf{B}}(\mathbf{r}, t) = \sum_k \tilde{\mathbf{B}}_k(t) e^{ik \cdot \mathbf{r}}, \quad (2.19)$$

with $\tilde{\mathbf{B}}_k(t) = [\tilde{B}_{\perp,k}(t), \tilde{B}_{\perp,k}^*(t), \tilde{B}_{z,k}(t)]$.

It should be noted that the Fourier transformation of the operator of magnetic self-interactions is not so trivial in a general case. Here, we restrict ourselves to the case when the operator $\hat{N}(\mathbf{r}, \mathbf{r}')$ depends only on the difference of arguments $\hat{N}(\mathbf{r}, \mathbf{r}') = \hat{N}(\mathbf{r} - \mathbf{r}')$. This implies that the considered magnetic sample is spatially *homogeneous*, having no spatial variations of the material parameters. In this case, the Fourier transform of the operator $\hat{N}(\mathbf{r}, \mathbf{r}')$ is introduced as

$$\hat{N}_k e^{ikr} = \int \hat{N}(\mathbf{r} - \mathbf{r}') e^{ikr'} d\mathbf{r}'. \quad (2.20)$$

The tensor N_k is often called the “effective spin wave tensor” [6]. It is the most important universal characteristic of a ferromagnetic sample for the description of the propagating SWs in it. Together with the direction of the static magnetization, and the value of the external field, it contains all the information about the linear SW spectrum and nonlinear interactions. With certain modifications, the effective spin wave tensor can be also introduced in the problems of spatially nonuniform

propagating SW modes, e.g., for higher thickness or width modes of ferromagnetic films or nanowires [66–68].

The properties of the tensor \hat{N}_k follow from the symmetry of the magnetic self-interactions. Obviously, \hat{N}_k is self-adjoint, i.e., $(\hat{N}_k^T)^* = \hat{N}_k$, which ensures that the Hamiltonian function is real valued. Another general property is $\hat{N}_{-k} = \hat{N}_k^*$. For symmetric self-interactions, e.g., exchange, dipolar interaction, or anisotropy, the tensor \hat{N}_k is *symmetric*, $\hat{N}_k^T = \hat{N}_k$, and is *real*. In a general case, however, magnetic self-interactions are not required to bear these properties. For example, in the case of the IDMI the tensor \hat{N}_k is *antisymmetric* and *imaginary*. Namely, in the coordinate system with z axis being perpendicular to the ferromagnetic interface we get

$$\hat{N}_{k,\text{IDMI}} = \frac{2\tilde{D}}{\mu_0 M_s^2} \begin{pmatrix} 0 & 0 & -ik_x \\ 0 & 0 & -ik_y \\ ik_x & ik_y & 0 \end{pmatrix}. \quad (2.21)$$

Therefore, in a general case we should consider a complex-valued nonsymmetric self-interaction tensor \hat{N}_k , having a symmetric real part and antisymmetric imaginary part. Mathematically, the appearance of an antisymmetric imaginary contribution of \hat{N}_k is the only difference from the previous analysis of symmetric interactions, performed in Ref. [37]. However, it leads to significant modifications of all the expressions in the following analysis.

Using the above-defined Fourier images of the complex magnetization vector, the complex vector of external field and the operator of magnetic self-interactions, the Hamiltonian function can be represented in the following form:

$$\mathcal{H} = -\gamma \sum_k \alpha_k^* \cdot \hat{B}_k(t) + \frac{1}{2} \sum_k \alpha_k^*(t) \cdot \hat{\Gamma}_k \cdot \alpha_k, \quad (2.22)$$

where $\hat{\Gamma}_k = \omega_M \hat{S} \cdot \hat{T}^T \cdot \hat{N}_k \cdot \hat{T}$. Straightforward calculations give the explicit form of the tensor $\hat{\Gamma}_k$:

$$\hat{\Gamma}_k = \begin{pmatrix} \frac{1}{2} \mathcal{Q}_k & \frac{1}{2} \mathcal{B}_k & \frac{1}{\sqrt{2}} \mathcal{D}_k \\ \frac{1}{2} \mathcal{B}_k^* & \frac{1}{2} \mathcal{Q}_{-k} & \frac{1}{\sqrt{2}} \mathcal{D}_{-k}^* \\ \frac{1}{\sqrt{2}} \mathcal{D}_k^* & \frac{1}{\sqrt{2}} \mathcal{D}_{-k} & \Gamma_{zz,k} \end{pmatrix}, \quad (2.23)$$

where

$$\mathcal{Q}_k = \frac{\omega_M}{2} (N_{xx,k} + N_{yy,k} - 2 \text{Im} N_{xy,k}), \quad (2.24)$$

$$\mathcal{B}_k = \frac{\omega_M}{2} (-N_{xx,k} + N_{yy,k} + 2i \text{Re} N_{xy,k}), \quad (2.25)$$

$$\mathcal{D}_k = \frac{\omega_M}{\sqrt{2}} (iN_{xz,k} + N_{yz,k}), \quad (2.26)$$

and

$$\Gamma_{zz,k} = \omega_M N_{zz,k}. \quad (2.27)$$

Using the above-described general properties of the tensor \hat{N}_k , one can prove that $\mathcal{B}_k = \mathcal{B}_{-k}$, $\Gamma_{zz,k} = \Gamma_{zz,-k}$, and that the values \mathcal{Q}_k and $\Gamma_{zz,k}$ are real. Simultaneously, in a general case $\mathcal{Q}_k \neq \mathcal{Q}_{-k}$ and $\mathcal{D}_k \neq \mathcal{D}_{-k}$, while corresponding equalities take place in the case of symmetric self-interactions. These inequalities lead to the appearance of terms with both k and $-k$ in the definition of the tensor $\hat{\Gamma}_k$. Another evident difference from the symmetric case is the appearance of real and

imaginary parts of $N_{xy,k}$ in the definitions of the coefficients \mathcal{Q}_k and \mathcal{B}_k .

E. Expansion coefficients of the Hamiltonian function

Finally, in order to derive the Hamiltonian function in terms of the canonical variables, one needs to express the Fourier components of the complex magnetization vector α_k in terms of the variables a_k and a_k^* . For the component α_z this operation is trivial, and, taking into account Eq. (2.2), we get

$$\mathcal{F}_k[\alpha_z(\mathbf{r}, t)] = \Delta(\mathbf{k}) - \sum_{12} a_1(t) a_2^*(t) \Delta(\mathbf{1} - \mathbf{2} - \mathbf{k}). \quad (2.28)$$

Here, Δ is the Kronecker delta function, and the abbreviated notations $\mathbf{1} \equiv k_1$, $\mathbf{2} \equiv k_2$, etc., are used. The transformation of the components α_\perp , α_\perp^* is not so trivial, as Eq. (2.2a) contains a square root. Therefore, to proceed, one needs to expand it into a Taylor series. Limiting the expansion to the first two terms, we get

$$\alpha_\perp(\mathbf{r}, t) \approx \sqrt{2} a(\mathbf{r}, t) \left[1 - \frac{1}{4} a(\mathbf{r}, t) a^*(\mathbf{r}, t) \right]. \quad (2.29)$$

The error coming from this approximation is rather small. Indeed, it gives $|\alpha_\perp|^2 + \alpha_z^2 = 1 + |a|^6/8$, while the exact value is 1. Even for the precession angles close to 90° , for which $|a| \approx 1$, the expansion (2.29) gives the error not exceeding 12%. The straightforward Fourier transform of Eq. (2.29) and its complex conjugate yields the following relations:

$$\begin{aligned} \mathcal{F}_k[\alpha_\perp(\mathbf{r}, t)] \\ \approx \sqrt{2} \left(a_k(t) - \frac{1}{4} \sum_{123} a_1(t) a_2(t) a_3^*(t) \Delta(\mathbf{1} + \mathbf{2} - \mathbf{3} - \mathbf{k}) \right), \end{aligned} \quad (2.30a)$$

$$\begin{aligned} \mathcal{F}_k[\alpha_\perp^*(\mathbf{r}, t)] \\ \approx \sqrt{2} \left(a_{-k}^*(t) - \frac{1}{4} \sum_{123} a_1^*(t) a_2^*(t) a_3(t) \Delta(\mathbf{1} + \mathbf{2} - \mathbf{3} + \mathbf{k}) \right). \end{aligned} \quad (2.30b)$$

Using the above expansions in Eq. (2.22), it is possible to represent the Hamiltonian function \mathcal{H} in terms of canonical SW amplitudes a_k, a_k^* . Then, it is easy to collect the terms of the same power in the SW amplitudes, representing, thus, the Hamiltonian function as $\mathcal{H} \approx \mathcal{H}^{(0)} + \mathcal{H}^{(1)} + \mathcal{H}^{(2)} + \dots$, where the superscript denotes the power of the terms respective to the SW amplitudes. Here, we limit the expansion to the fourth-order term $\mathcal{H}^{(4)}$, which corresponds to the four-magnon processes. Usually, this expansion is sufficient as the four-magnon processes are almost never prohibited by the conservation laws, and the higher-order terms in the expansion are rather small [2].

1. Zeroth-order terms

The zeroth-order term of the Hamiltonian function is expressed as

$$\mathcal{H}^{(0)} = -\gamma \tilde{B}_{z,0}(t) + \frac{1}{2} \Gamma_{zz,0}. \quad (2.31)$$

This term does not contain any SW amplitudes, and, consequently, does not affect the magnetization dynamics. It

determines the energy of the static magnetization state, which consists of the Zeeman energy of the magnetization in a uniform magnetic field [recall that $\tilde{B}_{z,0}$ is the spatially uniform component of the external field $B_{e,z}(\mathbf{r}, t)$] and the static demagnetization energy of a uniformly magnetized body.

2. First-order terms

The first-order terms of the Hamiltonian function have the following form:

$$\mathcal{H}^{(1)} = - \sum_k \gamma \tilde{B}_{\perp,k}^*(t) a_k + \mathcal{D}_0^* a_0 + \text{c.c.}, \quad (2.32)$$

where for brevity we omit the explicit notation of the time dependence of the SW amplitudes $a_k \equiv a_k(t)$. To analyze these terms it is convenient to split the external field into a static and dynamic components: $\tilde{B}_{\perp,k}(t) = \tilde{B}_{\perp,k} + \tilde{b}_{\perp,k}(t)$. Hereafter, we denote the static part of the external field by a capital symbol, and the time-dependent one (e.g., microwave field) by a lowercase symbol $\tilde{b}(t)$. First, let us look at the static part. Using the relations (2.5), one can derive the dynamic equations for the SW amplitudes, associated with the first-order terms of the Hamiltonian function:

$$\frac{da_k}{dt} = -i \frac{\partial \mathcal{H}^{(1)}}{\partial a_k^*} = i(\gamma \tilde{B}_{\perp,k} - \mathcal{D}_0 \Delta(\mathbf{k})). \quad (2.33)$$

If the considered static magnetization state is stable, then, in the absence of a time-dependent field, the time derivative vanishes, $da_k/dt = 0$ (note that this is a necessary, but not a sufficient condition). Then, we get the following condition: $\tilde{B}_{\perp,k} = 0$ for $\mathbf{k} \neq 0$, i.e., the static field perpendicular to the direction of static magnetization should be spatially uniform. It is an absolutely natural condition for the stability of a uniform magnetization state which is considered here. Simultaneously, the parallel component of the external field $B_{e,z}(\mathbf{r})$ can remain spatially nonuniform. From the dynamic equations for a_0 one gets the following condition:

$$\gamma \tilde{B}_{\perp,0} = \mathcal{D}_0. \quad (2.34)$$

Recalling the definitions (2.26) and $\tilde{B}_{\perp}(\mathbf{r}) = (iB_{e,x} + B_{e,y})/\sqrt{2}$, this condition can be transformed to the standard conditions of the static equilibrium in a uniformly magnetized sample $B_{e,x} = \mu_0 M_s N_{xz,0}$, $B_{e,y} = \mu_0 M_s N_{yz,0}$.

If the static equilibrium conditions are satisfied, the first-order terms of the Hamiltonian function are simplified to

$$\mathcal{H}^{(1)} = - \sum_k \gamma \tilde{b}_{\perp,k}^*(t) a_k + \text{c.c.} \quad (2.35)$$

These terms describe the interaction of the SWs with the time-dependent magnetic field which is perpendicular to the direction of static magnetization. Such an interaction is responsible for the linear excitation of SWs. In the opposite case, when the equilibrium conditions are not satisfied, one can not follow the formalism below and should find a real equilibrium magnetization state (possibly, nonuniform), and introduce canonical variables on the background of this real equilibrium state.

3. Second-order terms

After collecting all the terms, the quadratic part $\mathcal{H}^{(2)}$ of the Hamiltonian function can be expressed as

$$\begin{aligned} \mathcal{H}^{(2)} = & \sum_k \left[\mathcal{A}_k a_k^* a_k + \left(\frac{\mathcal{B}_k}{2} a_k^* a_{-k}^* + \text{c.c.} \right) \right] \\ & + \sum_{\mathbf{1} \neq \mathbf{2}} \gamma \tilde{B}_{z,2-1} a_1 a_2^* + \sum_{\mathbf{1}, \mathbf{2}} \gamma \tilde{b}_{z,2-1}(t) a_1 a_2^*. \end{aligned} \quad (2.36)$$

The first sum is familiar from the linear SW theory. It involves pairs of SWs with the same wave vectors, and coupling of the SWs with opposite wave vectors, which can be present in a general case. In fact, this coupling reflects the fact that the magnetization precession is not circular, but is elliptical, as it is shown in the next section. The coefficient \mathcal{A}_k is equal to

$$\begin{aligned} \mathcal{A}_k &= \gamma B_{z,0} - \Gamma_{zz,0} + \mathcal{Q}_k \\ &= \omega_H + \frac{\omega_M}{2} (N_{xx,k} + N_{yy,k} - 2 \text{Im} N_{xy,k}), \end{aligned} \quad (2.37)$$

where $\omega_H = \gamma(B_{z,0} - \mu_0 M_s N_{zz,0})$. A general assumption of the existence of nonsymmetric magnetic self-interactions used in this work results in the appearance of the last term $\text{Im} N_{xy,k}$ in the definition of \mathcal{A}_k . As a consequence, \mathcal{A}_k loses the symmetry in respect to the wave-vector inversion $\mathcal{A}_k \neq \mathcal{A}_{-k}$, while such a symmetry is valid for the symmetric magnetic self-interactions. As it will be shown below, this inequality qualitatively affects the procedure of diagonalization of the quadratic part of the Hamiltonian function.

The second term in Eq. (2.36) describes the coupling of plane waves with arbitrary unequal wave vectors. This coupling is present only in the case of a spatially inhomogeneous external field $B_{e,z}(\mathbf{r})$, and the coupling strength is proportional to the Fourier component of the external field at nonzero \mathbf{k} . In fact, it means that in the case of an inhomogeneous field the plane waves having a definite \mathbf{k} cease to be the normal modes of a ferromagnetic body. Instead, normal modes are formed by the sums of plane waves, which are finite in the case of harmonic (e.g., sinelike or cosinelike) field, and are infinite otherwise. In the following, we will not address this case and will assume that the static external field is spatially uniform.

Finally, the last term represents the coupling of the SW pairs having, in general, different wave vectors with the time-dependent external field. It is a well-known ‘‘parametric’’ coupling in the so-called ‘‘parallel pumping geometry’’ [1,2], which can be understood as a ‘‘three-quasiparticle’’ interaction when one microwave photon splits into two magnons. The spatially uniform parametric pumping couples with the SWs having opposite wave vectors, while a spatially nonuniform pumping can lead to a coupling of SWs with arbitrary wave vectors [69]. The different condition of the summation in the second and last terms ($\mathbf{1} \neq \mathbf{2}$ in the second term) appears because the term $\tilde{B}_{z,0} a_1 a_1^*$ is already accounted in the first sum $\sum_k \mathcal{A}_k a_k a_k^*$.

4. Third-order terms

The part of the Hamiltonian, which includes three SW amplitudes a_k , can be written as

$$\begin{aligned} \mathcal{H}^{(3)} = & -\frac{1}{2} \sum_{123} [(\mathcal{D}_1^* + \mathcal{D}_2^*) a_1 a_2 a_3^* + \text{c.c.}] \Delta(\mathbf{1} + \mathbf{2} - \mathbf{3}) \\ & + \frac{1}{4} \sum_{123k} [\gamma \tilde{b}_{\perp,k}^*(t) a_1 a_2 a_3^* + \text{c.c.}] \Delta(\mathbf{1} + \mathbf{2} - \mathbf{3} - \mathbf{k}). \end{aligned} \quad (2.38)$$

In the derivation of this third-order contribution we took into account the stability conditions (2.34). The expression for $\mathcal{H}^{(3)}$ is absolutely the same as in the case of symmetric magnetic self-interactions [37]. However, one should remember that the presence of antisymmetric interactions changes the properties of the coefficients \mathcal{D}_k (see above).

The first term in Eq. (2.38) represents a pure three-magnon scattering process, namely, splitting of a magnon $\mathbf{3}$ into a pair of magnons $\mathbf{1}$ and $\mathbf{2}$, and the opposite process. These scattering processes are allowed only when the momentum and energy conservation conditions are satisfied, which depends on the sample geometry and material, and on the external field. It should be noted that if the resonant three-magnon processes are not allowed (i.e., if the conservation laws for the three-magnon process are not satisfied), but the three-magnon interaction efficiency ($\mathcal{D}_1^* + \mathcal{D}_2^*$) is nonzero, these “prohibited” processes may affect the strength of the nonlinear processes of higher orders (see Sec. III C).

The second term in Eq. (2.38) describes the scattering of a microwave photon and a magnon into two other magnons. Such a process is, typically, weak, compared to the common parametric interaction of SW pairs by a microwave photon and the three-magnon splitting processes. Nevertheless, in certain cases such a process can be involved in the limitation of the FMR amplitude at high excitation fields [6].

5. Fourth-order terms

The highest-order nonlinear SW processes, which we consider in this work, are the fourth-order processes. The importance of these processes is related with the fact that some of them are always allowed, as the energy and momentum conservation laws for such processes can be satisfied for any SW spectrum. For example, a scattering of a pair of magnons with wave vectors $\mathbf{1}$ and $\mathbf{2}$ into a pair of magnons with the same wave vectors $(\mathbf{1}, \mathbf{2}) \rightarrow (\mathbf{1}, \mathbf{2})$, but, possibly, different phases, is always allowed. Obviously, the process $(\mathbf{1}, \mathbf{1}) \rightarrow (\mathbf{1}, \mathbf{1})$ is also allowed in any case. While this kind of the four-magnon processes does not change the number of magnons, these processes affect the magnon phase, being, in particular, responsible for the nonlinear frequency shift (process $(\mathbf{1}, \mathbf{1}) \rightarrow (\mathbf{1}, \mathbf{1})$), or the “phase mechanism” of the limitation of the parametric instability growth [process $(\mathbf{1}, \mathbf{2}) \rightarrow (\mathbf{1}, \mathbf{2})$] [2].

In a general case, the fourth-order terms of the Hamiltonian function can be written as

$$\begin{aligned} \mathcal{H}^{(4)} = & \frac{1}{2} \sum_{1234} \Psi_{12,(-3)(-4)} a_1 a_2 a_3^* a_4^* \Delta(\mathbf{1} + \mathbf{2} - \mathbf{3} - \mathbf{4}) \\ & + \frac{1}{3} \sum_{1234} [\Phi_{123,4} a_1 a_2 a_3 a_4^* + \text{c.c.}] \Delta(\mathbf{1} + \mathbf{2} + \mathbf{3} - \mathbf{4}), \end{aligned} \quad (2.39)$$

where the coefficients are equal to

$$\begin{aligned} \Psi_{12,34} = & -\frac{1}{4} (\mathcal{Q}_1 + \mathcal{Q}_2 + \mathcal{Q}_{-3} + \mathcal{Q}_{-4}) \\ & + \frac{1}{4} (\Gamma_{zz,1+3} + \Gamma_{zz,1+4} + \Gamma_{zz,2+3} + \Gamma_{zz,2+4}) \end{aligned} \quad (2.40)$$

and

$$\Phi_{123,4} = -\frac{1}{4} (\mathcal{B}_1 + \mathcal{B}_2 + \mathcal{B}_3). \quad (2.41)$$

In the notations of the above-presented coefficients we used a common convention, when the indices, which can be interchanged without any effect on the coefficient, are not separated by a comma, while the indices (or groups of indices) separated by a comma can not be interchanged. For example, $\Psi_{12,34} = \Psi_{21,34}$, but $\Psi_{12,34} \neq \Psi_{13,24}$, as one can check from the definition (2.40).

The properties of the four-magnon coefficients follow from Eqs. (2.24), (2.25), and (2.27). Namely, the coefficient $\Psi_{12,34}$ is real valued: $\Psi_{12,34} = \Psi_{(-3)(-4),(-1)(-2)}$. At the same time, $\Psi_{12,34} \neq \Psi_{(-1)(-2),(-3)(-4)}$ in the general case, while the equality in this equation is fulfilled in the case of symmetric magnetic self-interactions.

III. CONVERSION TO THE LINEAR NORMAL MODES

A. Diagonalization of the quadratic part of the SW Hamiltonian function

The Hamiltonian expansion presented in the previous section gives, in principle, the full description of the linear and nonlinear SW processes up to the fourth order. However, this description is rather cumbersome since SWs with different wave numbers remain coupled even in the second-order terms of the Hamiltonian, which describe the *linear* SW dynamics. This demonstrates that *circularly polarized* plane waves are not the normal modes (or eigenmodes) of a considered ferromagnetic sample. It turns out that the normal SW modes have the elliptical polarization because of the presence of the anisotropy in a magnetic material and because of the anisotropic nature of the dipolar interaction. Only in some specific cases, and in the limit of purely exchange SWs, the polarization of SWs becomes circular.

The transformation from the circularly polarized plane waves to elliptically polarized linear SW normal modes is called the diagonalization of the quadratic part of the SW Hamiltonian, and is performed using a canonical linear transformation. In the SW theory, this transformation was introduced by Hostein and Primakoff [70], and is often called “third Holstein-Primakoff transformation.” The similar transformation was later introduced by Bogoliubov and Valatin in the theory of superconductivity [71,72]. By this transformation, new SW variables c_k [73] are introduced, and in terms

of these variables the quadratic part of the SW Hamiltonian function assumes a diagonal form

$$\mathcal{H}^{(2)} = \sum_k \omega_k c_k c_k^*. \quad (3.1)$$

Then, it becomes clear that in terms of the variables c_k [73], the Hamiltonian equations of motion, in which only a quadratic part of the Hamiltonian function is retained, become uncoupled from each other and assume the simple form $dc_k/dt = -i\omega_k c_k$, which demonstrates that c_k are the linear eigenmodes of the system. Naturally, the quantity ω_k has the meaning of an eigenfrequency of a linear SW mode c_k .

In the case of a uniform external field, when the second sum in Eq. (2.36) is identically zero, the relation between the new variables c_k and the old variables a_k is given by

$$\begin{aligned} a_k(t) &= u_k c_k(t) + v_k c_{-k}^*, \\ a_{-k}^*(t) &= v_k^* c_k(t) + u_k c_{-k}^*, \end{aligned} \quad (3.2)$$

where the coefficients are equal to

$$u_k = \sqrt{\frac{\mathcal{A}_k + \omega_k}{2\omega_k}}, \quad v_k = -\frac{\mathcal{B}_k}{|\mathcal{B}_k|} \sqrt{\frac{\mathcal{A}_k - \omega_k}{2\omega_k}}, \quad (3.3)$$

and the SW frequency is defined as

$$\omega_k = \sqrt{\mathcal{A}_k^2 - |\mathcal{B}_k|^2}. \quad (3.4)$$

It is important to note that the third Holstein-Primakoff transformation (3.2) was derived in the case of *symmetric* magnetic self-interactions, and is not applicable in our more general case of nonsymmetric interactions. Using the mathematical procedure of a matrix diagonalization, we found that the quadratic part of the Hamiltonian function in the presence of antisymmetric interactions can be diagonalized by the transformation (3.2), but with the coefficients defined by the following relations:

$$\begin{aligned} u_k &= \sqrt{\frac{\mathcal{A}_{-k} + \omega_k}{2\omega_k + \mathcal{A}_{-k} - \mathcal{A}_k}}, \\ v_k &= -\frac{\mathcal{B}_k}{|\mathcal{B}_k|} \sqrt{\frac{\mathcal{A}_k - \omega_k}{2\omega_k + \mathcal{A}_{-k} - \mathcal{A}_k}}. \end{aligned} \quad (3.5)$$

The SW frequency in this case is given by

$$\omega_k = \frac{\mathcal{A}_k - \mathcal{A}_{-k}}{2} + \sqrt{\left(\frac{\mathcal{A}_k + \mathcal{A}_{-k}}{2}\right)^2 - |\mathcal{B}_k|^2}. \quad (3.6)$$

The above-derived transformation (3.5) represents an important result of this work, which allows us to derive explicit expressions for the coefficients of nonlinear interactions of *normal SW modes*.

One can easily verify that these transformations are canonical, as $(u_k^2 - |v_k|^2) = 1$, that allows to fulfill the conditions of the canonical transformations: $\{c_k, c_{k'}\} = 0$, $\{c_{-k}^*, c_{-k'}^*\} = 0$, and $\{c_k, c_{-k'}^*\} = \Delta(\mathbf{k} - \mathbf{k}')$, where $\{f, g\}$ denotes the Poisson's brackets respective to a_k, a_{-k}^* . It is also clear that in the case of symmetric magnetic self-interactions, when $\mathcal{A}_k = \mathcal{A}_{-k}$, the expressions (3.5) are reduced to the standard Holstein-Primakoff transformations (3.3).

It is important to note that in a general case $\omega_k \neq \omega_{-k}$, which means that the SW spectrum can be nonreciprocal. We also have $u_k = u_{-k}$ and $v_k = v_{-k}$, meaning that the SW structure (ellipticity) does not change with the reversal of the propagation direction. Moreover, using the definition (2.37) of \mathcal{A}_k , one can find that the coefficients u_k and v_k are completely independent of the term $\text{Im}N_{xy,k}$, which is the only term in \mathcal{A}_k and \mathcal{B}_k reflecting the presence of the antisymmetric interactions. Thus, we can conclude that the presence of antisymmetric magnetic self-interactions affects the SW dispersion relation ω_k , but does not affect SW polarization properties. For the case of IDMI, this fact has been previously pointed in Refs. [55,58].

B. Transformation of the nonlinear coefficients

Now, using the transformations (3.2) and (3.5) in the SW Hamiltonian function, we can represent it in terms of the amplitudes of the SW normal modes $c_k(t)$. Although this action is straightforward, it is a rather tedious and cumbersome algebraic operation. Below, we present the general expressions for all the third- and fourth-order nonlinear coefficients in the Taylor expansion of the SW Hamiltonian function. These general expressions for the nonlinear interaction coefficients of SWs having arbitrary wave vectors are rather cumbersome, but in many important particular cases they could be significantly simplified due to a symmetry of the considered nonlinear processes. For example, among the fourth-order nonlinear processes, the most important are the processes $(\mathbf{1}, \mathbf{1}) \rightarrow (\mathbf{1}, \mathbf{1})$ and $(\mathbf{1}, \mathbf{2}) \rightarrow (\mathbf{1}, \mathbf{2})$.

The zeroth-order term of the SW Hamiltonian function, naturally, remains unchanged. The first-order term (2.35) is transformed to the following form:

$$\mathcal{H}^{(1)} = -\sum_k \gamma [u_k \tilde{b}_{\perp,k}^*(t) + v_k^* \tilde{b}_{\perp,-k}] c_k + \text{c.c.} \quad (3.7)$$

The term in the brackets here describes the effect of the precession ellipticity on the interaction of a SW with an external magnetic field.

The second-order term, including the interaction of magnons with dynamic magnetic fields, can be written as

$$\begin{aligned} \mathcal{H}^{(2)} &= \sum_k \omega_k c_k c_k^* + \sum_{12} \tilde{b}_{z,2-1} (u_1 u_2 + v_1^* v_2) c_1 c_2^* \\ &+ \sum_{12} \left[\frac{1}{2} \tilde{b}_{-1-2} (u_1 v_2^* + v_1^* u_2) c_1 c_2 + \text{c.c.} \right]. \end{aligned} \quad (3.8)$$

The first term here, as discussed above, defines the eigenfrequencies of the SW normal modes. The second term describes interaction of a microwave photon with two different magnons. This interaction, usually, is not very strong since the resonance condition for such a process is rather difficult to satisfy because it requires a highly spatially nonuniform distribution of the microwave magnetic field. The last term corresponds to the familiar (and much more efficient) parametric excitation of SWs under parallel microwave pumping [1,2].

In the consideration of the third-order terms in the SW Hamiltonian function, we limit ourselves to the pure nonlinear magnon-magnon interactions, and neglect the processes of the

photon-stimulated three-magnon interactions caused by the second term in Eq. (2.38). Then, the third-order term in the Hamiltonian function describing only the magnon-magnon interactions in terms of the amplitudes of the normal SW modes is expressed as

$$\mathcal{H}^{(3)} = \frac{1}{3} \sum_{123} [U_{123}^* c_1 c_2 c_3 + \text{c.c.}] \Delta(\mathbf{1} + \mathbf{2} + \mathbf{3}) + \sum_{123} [V_{12,3}^* c_1 c_2 c_3^* + \text{c.c.}] \Delta(\mathbf{1} + \mathbf{2} - \mathbf{3}). \quad (3.9)$$

The coefficients of the three-magnon interaction are

$$U_{123} = -\frac{1}{2} [(\mathcal{D}_1 u_1 + \mathcal{D}_{-1}^* v_1)(u_2 v_3 + v_2 u_3) + (\mathcal{D}_2 u_2 + \mathcal{D}_{-2}^* v_2)(u_1 v_3 + v_1 u_3) + (\mathcal{D}_3 u_3 + \mathcal{D}_{-3}^* v_3)(u_1 v_2 + v_1 u_2)] \quad (3.10)$$

and

$$V_{12,3} = -\frac{1}{2} [(\mathcal{D}_1 u_1 + \mathcal{D}_{-1}^* v_1)(u_2 u_3 + v_2 v_3^*) + (\mathcal{D}_2 u_2 + \mathcal{D}_{-2}^* v_2)(u_1 u_3 + v_1 v_3^*) + (\mathcal{D}_3^* u_3 + \mathcal{D}_{-3} v_3^*)(u_1 v_2 + v_1 u_2)]. \quad (3.11)$$

Although these expressions appear to be cumbersome, they have a clear structure, if one recalls the above introduced rules of indices interchange in the SW nonlinear interaction coefficients.

It should be noted that the ellipticity of the magnetization precession results in the appearance of qualitatively new term in the expansion of the SW Hamiltonian function: the first term in Eq. (3.9). From a formal point of view, this term and its complex conjugate correspond to the appearance of three magnons from “vacuum” or to the annihilation of three magnons. Such a term, however, can not become resonant since, although the momentum conservation $\mathbf{1} + \mathbf{2} + \mathbf{3} = \mathbf{0}$ can be satisfied, the energy conservation condition $\omega_1 + \omega_2 + \omega_3 = 0$ can not be satisfied for any stable magnetization configuration $\omega_k \geq 0$. Nevertheless, these nonresonant three-magnon processes can play a role in the resonant nonlinear processes of a higher (fourth) order (see explanation presented in the next subsection).

The fourth-order terms in the expansion of the Hamiltonian function after the transformation to normal SW modes acquire the following form:

$$\mathcal{H}^{(4)} = \frac{1}{2} \sum_{1234} W_{12,34} c_1 c_2 c_3^* c_4^* \Delta(\mathbf{1} + \mathbf{2} - \mathbf{3} - \mathbf{4}) + \sum_{1234} [G_{123,4}^* c_1 c_2 c_3 c_4^* + \text{c.c.}] \Delta(\mathbf{1} + \mathbf{2} + \mathbf{3} - \mathbf{4}) + \frac{1}{4} \sum_{1234} [R_{1234}^* c_1 c_2 c_3 c_4 + \text{c.c.}] \Delta(\mathbf{1} + \mathbf{2} + \mathbf{3} + \mathbf{4}). \quad (3.12)$$

As in the case of the third-order terms, the SW ellipticity results in the appearance of new terms in the Hamiltonian expansion, in particular, the last sum in the above-presented expression. These terms are always nonresonant and, therefore, can effectively contribute only to the five-wave and higher-order magnon-magnon interaction processes. For this

reason, we do not present here the explicit expression for the corresponding nonlinear coefficient R_{1234} .

The remaining coefficients of four-magnon nonlinear interaction are given by the following expressions:

$$W_{12,34} = \Psi_{12,(-3)(-4)} u_1 u_2 u_3 u_4 + \Psi_{(-1)(-2),34} v_1^* v_2^* v_3 v_4 + \Psi_{2(-3),1(-4)} v_1^* u_2 v_3 u_4 + \Psi_{(-2)3,(-1)4} u_1 v_2^* u_3 v_4 + \Psi_{1(-3),2(-4)} u_1 v_2^* v_3 u_4 + \Psi_{(-1)3,(-2)4} v_1^* u_2 u_3 v_4 + \Phi_{123,4} v_1^* v_2^* u_3 v_4 + \Phi_{123,4}^* u_1 u_2 v_3 u_4 + \Phi_{412,3} v_1^* v_2^* v_3 u_4 + \Phi_{412,3}^* u_1 u_2 u_3 v_4 + \Phi_{341,2} v_1^* u_2 u_3 u_4 + \Phi_{341,2}^* u_1 v_2^* v_3 v_4 + \Phi_{234,1} u_1 v_2^* u_3 u_4 + \Phi_{234,1}^* v_1^* u_2 v_3 v_4 \quad (3.13)$$

and

$$G_{123,4} = \frac{1}{3} [\Psi_{12,3(-4)} u_1 u_2 v_3 u_4 + \Psi_{(-1)(-2),(-3)4} v_1 v_2 u_3 v_4^* + \Psi_{23,1(-4)} v_1 u_2 u_3 u_4 + \Psi_{(-2)(-3),1(-4)} u_1 v_2 v_3 v_4^* + \Psi_{13,2(-4)} u_1 v_2 u_3 u_4 + \Psi_{(-1)(-3),(-2)4} v_1 u_2 v_3 v_4^* + \Phi_{123,4} u_1 u_2 u_3 u_4 + \Phi_{123,4}^* v_1 v_2 v_3 v_4^* + \Phi_{412,3} u_1 u_2 v_3 v_4^* + \Phi_{412,3}^* v_1 v_2 u_3 u_4 + \Phi_{341,2} u_1 v_2 u_3 v_4^* + \Phi_{341,2}^* v_1 u_2 v_3 u_4 + \Phi_{234,1} v_1 u_2 v_3 v_4^* + \Phi_{234,1}^* u_1 v_2 v_3 u_4]. \quad (3.14)$$

One can easily derive these expressions by direct substitution of the transformations (3.2) to (2.39), accounting for the symmetry properties of the coefficients $\Psi_{12,34}$ and $\Phi_{123,4}$.

Using the above-presented expressions, one can calculate the efficiency of any relevant nonlinear SW interaction up to the fourth order. In the limit of symmetric magnetic self-interactions, when $\mathcal{D}_k = \mathcal{D}_{-k}$ and $\Psi_{12,34} = \Psi_{(-1)(-2),(-3)(-4)}$, these expressions are reduced to Eqs. (60)–(65) from Ref. [37]. Also, in the case of a circular polarization of SWs (e.g., in the limit of purely exchange SWs), when $u_k = 1$ and $v_k = 0$, one can find $U_{123} = 0$, $V_{12,3} = -(\mathcal{D}_1 + \mathcal{D}_2)/2$, $W_{12,34} = \Psi_{12,(-3)(-4)}$, $G_{123,4} = \Phi_{123,4}/3$, and $R_{1234} = 0$, in full agreement with Eqs. (2.38) and (2.39).

C. Elimination of the nonresonant three-wave terms

Using the above-derived expansion of the SW Hamiltonian function in terms of the normal mode amplitudes c_k , one can investigate the nonlinear SW dynamics. Naturally, in practical particular cases it is not necessary to take into account all the existing nonlinear magnon-magnon interactions as, typically, only the resonant ones, which satisfy both the momentum and energy conservation laws, play a significant role in the interaction outcome. In real magnetic systems, due to the effect of dissipation, the frequency (energy) conservation laws can be satisfied only approximately to the accuracy of the SW damping rate. Therefore, in most practical cases it is sufficient to take into account only the “resonant” nonlinear processes since the influence of other processes, which are far from the resonance conditions, is typically negligible.

However, in certain cases the nonresonant processes cannot be simply neglected. It is known that the nonresonant nonlinear processes of a lower order can significantly influence the resonant processes of a higher order. In particular, the

nonresonant three-wave processes can contribute to the intensity of the resonant four-wave processes, as it was pointed out by Zakharov [74]. This contribution can be understood as a four-wave process, mediated by the creation and annihilation of a “virtual” magnon. For example, a four-magnon process $(1, 2) \rightarrow (3, 4)$ can be a combination of two subsequent three-magnon processes $(1, 2) \rightarrow 5$ and $5 \rightarrow (3, 4)$, mediated by a “virtual” magnon 5. To account for the effect of such nonresonant interaction processes, one needs to perform an additional transformation of variables, which is nonlinear and, strictly speaking, only approximately canonical. The presence of the antisymmetric interactions does not lead to any changes in this additional transformation, and we will not reproduce it here. The complete description of this transformation can be found, e.g., in Refs. [7,75,76].

IV. APPLICATION: THREE-MAGNON SPLITTING AND NONLINEAR FREQUENCY SHIFT OF SPIN WAVES SUBJECTED TO IDMI

A. Ferromagnetic nanowire

In this section we apply the above-developed formalism to the investigation of nonlinear SW interaction in a magnetic sample subjected to IDMI. Specifically, we study a nanowire made of a ferromagnetic–heavy-metal bilayer (e.g., CoFeB-Pt), having the width w_x and the ferromagnetic layer thickness h , as shown in Fig. 1. The nanowire is magnetized in its plane by an external field \mathbf{B}_e , so that the static magnetization \mathbf{M}_0 makes the angle ϕ_M with the direction of the SW propagation (axis of the nanowire). The spectrum of a nanowire, in general, contains a set of SW modes with different width profiles. Here, we restrict our analysis to the case of a quasiuniform width mode. If the nanowire is sufficiently narrow (the width is less than 100–200 nm, typically [67]), the quasiuniform mode is the fundamental mode of the nanowire, being the lowest in frequency. Also, in a certain frequency range this mode is not frequency degenerate with any other width mode of the nanowire, meaning that it can be the only one excited, and that the magnetization dynamics in this frequency range is determined by the fundamental mode only.

To apply the above-developed formalism, one needs to derive expressions for effective SW tensor \hat{N}_k for the nanowire sample. It is convenient, first, to derive the tensor \hat{N} in a standard coordinate system, having axes aligned with the axes of the nanowire [coordinate system (xyz) in Fig. 1]. The

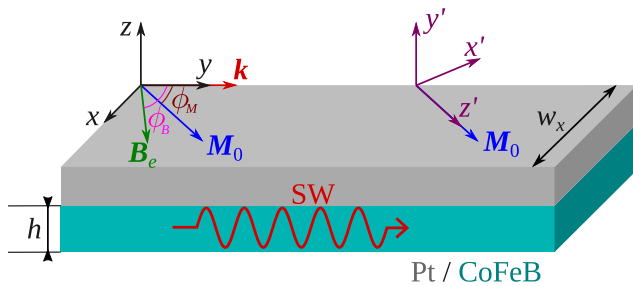


FIG. 1. A sketch of the considered bilayer nanowire, showing the directions of the bias magnetic field \mathbf{B}_e , static magnetization \mathbf{M}_0 , and the principal and auxiliary coordinate systems (see text).

contribution of the IDMI in this “principal” coordinate system is described by the expression (2.21). Since in our case the SW wave vector is always parallel to the y axis, $\mathbf{k} = k_y \mathbf{e}_y$, in Eq. (2.21) we set $k_x = 0$. The exchange interaction is described by the diagonal tensor $\hat{N}_{\text{ex},k} = \lambda_{\text{ex}}^2 k_y^2 \hat{\mathbf{I}}$ [see Eqs. (2.8) and (2.20)]. The dipolar interaction in the considered case of quasiuniform mode is described by the tensor [66,67]

$$\hat{N}_{\text{dip},k} \equiv \hat{F}_k = \frac{1}{2\pi w_x} \int_{-\infty}^{\infty} \text{sinc}^2\left(\frac{k_x w_x}{2}\right) \hat{N}_{\text{dip},K} dk_x, \quad (4.1)$$

where

$$\hat{N}_{\text{dip},K} = \begin{pmatrix} \frac{k_x^2}{K^2} f(Kh) & \frac{k_x k_y}{K^2} f(Kh) & 0 \\ \frac{k_x k_y}{K^2} f(Kh) & \frac{k_y^2}{K^2} f(Kh) & 0 \\ 0 & 0 & 1 - f(Kh) \end{pmatrix}, \quad (4.2)$$

with $K = \sqrt{k_x^2 + k_y^2}$ and $f(x) = 1 - (1 - e^{-|x|})/|x|$. In fact, the integration in Eq. (4.1) yields identical zeros for all the off-diagonal components, so the tensor \hat{F}_k has only three nonzero components $F_{xx,k}$, $F_{yy,k}$, and $F_{zz,k}$. Finally, we also need to take into account the perpendicular surface magnetic anisotropy, which is especially important for ultrathin magnetic films. According to Eqs. (2.10) and (2.20), the corresponding contribution to the SW tensor has only one nonzero component $(\hat{N}_{\text{an},k})_{zz} = n_{\text{an}} = -2K_s/(\mu_0 M_s^2 h)$, where K_s is the constant of the surface magnetic anisotropy.

In the Hamiltonian formalism the effective SW tensor should be expressed in the coordinate system having axis z' parallel to the static magnetization ($x'y'z'$ system in Fig. 1). The rotation of the coordinate system is expressed via the rotation tensor

$$\hat{T} = \begin{pmatrix} -\cos \phi_M & \sin \phi_M & 0 \\ 0 & 0 & 1 \\ \sin \phi_M & \cos \phi_M & 0 \end{pmatrix}. \quad (4.3)$$

Then, the effective SW tensor in the new (auxiliary) coordinate system is expressed as $\hat{N}_k^{(x'y'z')} = \hat{T} \cdot \hat{N}_k^{(xyz)} \cdot \hat{T}^{-1}$. By direct calculations, one finds the following expressions for the components of the effective SW tensor:

$$\begin{aligned} N_{x'x',k} &= \lambda_{\text{ex}}^2 k_y^2 + F_{xx,k} \cos^2 \phi_M + F_{yy,k} \sin^2 \phi_M, \\ N_{x'y',k} &= -N_{y'x',k} = -ik_y \tilde{d} \sin \phi_M, \\ N_{x'z',k} &= N_{z'x',k} = (F_{yy,k} - F_{xx,k}) \sin \phi_M \cos \phi_M, \\ N_{y'y',k} &= \lambda_{\text{ex}}^2 k_y^2 + F_{zz,k} - n_{\text{an}}, \\ N_{y'z',k} &= -N_{z'y',k} = ik_y \tilde{d} \cos \phi_M, \\ N_{z'z',k} &= \lambda_{\text{ex}}^2 k_y^2 + F_{xx,k} \sin^2 \phi_M + F_{yy,k} \cos^2 \phi_M, \end{aligned} \quad (4.4)$$

where we used the short notation $\tilde{d} = 2\tilde{D}/(\mu_0 M_s^2)$. Using these expressions for the components of the effective SW tensor, we derived the following expressions for the coefficients (2.24)–(2.27):

$$\begin{aligned} Q_k &= \frac{\omega M}{2} (2\lambda_{\text{ex}}^2 k_y^2 + F_{xx,k} \cos^2 \phi_M + F_{yy,k} \sin^2 \phi_M \\ &\quad + F_{zz,k} - n_{\text{an}} + 2k_y \tilde{d} \sin \phi_M), \\ B_k &= \frac{\omega M}{2} (F_{zz,k} - n_{\text{an}} - F_{xx,k} \cos^2 \phi_M - F_{yy,k} \sin^2 \phi_M), \end{aligned}$$

$$\mathcal{D}_k = \frac{i\omega_M}{\sqrt{2}} [(F_{yy,k} - F_{xx,k}) \sin \phi_M + k_y \tilde{d}] \cos \phi_M,$$

$$\Gamma_{z'z',k} = \omega_M (\lambda_{\text{ex}}^2 k_y^2 + F_{xx,k} \sin^2 \phi_M + F_{yy,k} \cos^2 \phi_M). \quad (4.5)$$

The equilibrium condition (2.34) in our case is reduced to $\mu_0 M_s F_{xx,0} \sin \phi_M \cos \phi_M = B_e \sin(\phi_B - \phi_M)$, which is a pretty standard condition for a ferromagnetic nanowire. Naturally, this condition is not affected by the IDMI. For the derivation of this condition we used the identities $F_{yy,0} = 0$ and $\tilde{B}_{\perp,0} = iB_{e,x'}/\sqrt{2} = -iB_e \sin(\phi_B - \phi_M)/\sqrt{2}$.

According to Eq. (2.37), the coefficient $\mathcal{A}_k = \omega_H + \mathcal{Q}_k$, where $\omega_H = \gamma B_e \cos(\phi_B - \phi_M) - \omega_M F_{xx,0} \sin^2 \phi_M$. Using these expressions in the general equation (3.6), we can directly calculate the dispersion relation of the linear SWs propagating in the nanowire:

$$\omega_k = \sqrt{\omega_H + \omega_M (\lambda_{\text{ex}}^2 k_y^2 + F_{xx,k} \cos^2 \phi_M + F_{yy,k} \sin^2 \phi_M)}$$

$$\times \sqrt{\omega_H + \omega_M (\lambda_{\text{ex}}^2 k_y^2 + F_{zz,k} - n_{\text{an}})} + \omega_M k_y \tilde{d} \sin \phi_M. \quad (4.6)$$

A similar SW dispersion equation in different particular cases was previously derived in Refs. [46,47,55,60]. The influence of the IDMI results in the appearance of the last term, which is linear in the SW wave number, and is *nonreciprocal*. Note that this peculiarity is general. The nonreciprocity coming from an antisymmetric magnetic self-interaction always appears as an additive term in the dispersion relation for SWs, as can be seen from Eq. (3.6).

Next, let us look at the three-wave terms of the Hamiltonian. The coefficients of the three-magnon interaction $V_{12,3}$ and U_{123} are proportional to the values $\mathcal{D}_1, \mathcal{D}_2, \mathcal{D}_3$. The \mathcal{D}_i values are proportional to $\mathcal{D}_k \sim \cos \phi_M$, independently of the length of the SW wave vector. Thus, in the case $\phi_M = 90^\circ$ (often called the ‘‘Damon-Eshbach geometry’’), i.e., when the nanowire is magnetized in its plane perpendicularly to the nanowire axis, the three-magnon interaction efficiency is identically zero for all the SWs independently of the magnitude of their wave vector. Thus, the fundamental SW mode of a transversely magnetized nanowire cannot split into two other SWs of the fundamental SW branch (notes on the splitting of a propagating fundamental SW into *different* SW branches are given below).

This feature could be very useful, as the three-magnon splitting is often an undesirable process, which limits the maximum power at which the SW propagation is stable. It is also important that the three-magnon splitting is prohibited for the propagation angle $\phi_M = 90^\circ$, at which the nonreciprocity of a linear SW dispersion is maximum. Thus, the nanowires made of the ferromagnetic–heavy-metal bilayers with a proper magnetization direction can support the propagation of stable nonreciprocal SWs of a relatively large amplitude.

Now, we consider the influence of the IDMI on the nonlinear frequency shift of SWs propagating in a ferromagnetic nanowire. This nonlinear frequency shift is a result of the four-magnon interaction of the type $(\mathbf{k}, \mathbf{k}) \rightarrow (\mathbf{k}, \mathbf{k})$, and leads to the following power-dependent modification of the SW dispersion:

$$\omega_k(c_k) = \omega_k(0) + T_k |c_k|^2, \quad (4.7)$$

where $\omega_k(0)$ describes the linear SW dispersion, given by Eq. (4.6), and the coefficient $T_k \equiv W_{kk,kk}$. For this particular four-wave process, the general expression (3.13) is greatly simplified, and yields

$$W_{kk,kk} = \Psi_{kk,(-k)(-k)} u_k^4 + 4\Psi_{k(-k),k(-k)} u_k^2 |v_k|^2$$

$$+ \Psi_{(-k)(-k),kk} |v_k|^4$$

$$+ 2[\Phi_{kkk,k} u_k v_k^* (u_k^2 + |v_k|^2) + \text{c.c.}]. \quad (4.8)$$

For simplicity, we consider here only the case of the Damon-Eshbach geometry, i.e., $\phi_M = \phi_B = 90^\circ$. As it was pointed out above, in this geometry all the three-magnon splitting processes have zero efficiency, and, therefore, one does not need to calculate the contribution from the nonresonant three-magnon processes to the four-magnon scattering efficiency.

Calculating the values of the coefficients $\Psi_{12,34}$ according to Eq. (2.24), and using the definitions (3.5), we finally arrive to the following compact expression for the coefficient of the nonlinear frequency shift:

$$T_k = (\gamma B_e - \bar{\mathcal{A}}_k) + \frac{\mathcal{B}_k^2}{2\tilde{\omega}_k^2} (\omega_M [4\lambda_{\text{ex}}^2 k_y^2 + F_{xx,2k} - F_{xx,0}]$$

$$+ 3\gamma B_e) - k_y \tilde{d} \frac{\omega_M \bar{\mathcal{A}}_k}{\tilde{\omega}_k}. \quad (4.9)$$

Here, for brevity, we introduce $\bar{\mathcal{A}}_k \equiv (\mathcal{A}_k + \mathcal{A}_{-k})/2$ and $\tilde{\omega}_k = (\omega_k + \omega_{-k})/2$, which are, in fact, the values of \mathcal{A}_k and ω_k in the absence of the IDMI. The first two terms in the expression (4.9) are standard ones for a ferromagnetic nanowire without the IDMI [77]. The influence of the IDMI is reflected in the appearance of the last term, which is *nonreciprocal*. It is important that this nonreciprocal contribution to the nonlinear frequency shift has the sign that is opposite to the sign of the IDMI contribution to the linear SW dispersion [see Eqs. (4.6) and (4.9)]. This means that with the increase of the SW amplitude, the nonlinear nonreciprocal term in the dispersion law will partly compensate the linear one. Thus, the nonreciprocal splitting of the SW dispersion will decrease with the increased SW power, and the dispersion relation of a nonlinear SW becomes less nonreciprocal with the increase of the wave amplitude.

To illustrate this effect, we calculated the dispersion relation of SWs having different amplitudes for the example of a CoFeB/Pt bilayer nanowire of the width $w_x = 50$ nm, and CoFeB thickness $h = 1.5$ nm. The material parameters used in calculations are [56] saturation magnetization $\mu_0 M_s = 1.28$ T, exchange stiffness $A = 2 \times 10^{-11}$ J/m (corresponding exchange length $\lambda_{\text{ex}} = 5.5$ nm), constant of the surface magnetic anisotropy $K_s = 5.5 \times 10^{-4}$ J/m², and the effective IDMI strength per 1.5 nm film is $Db/h = 6.6 \times 10^{-4}$ J/m (corresponding value $\tilde{d} = 1$). The value of the external bias magnetic field is assumed to be $B_e = 0.2$ T.

The calculated SW spectra are shown in Fig. 2. For all the SW wave vectors the nonlinear frequency shift is negative (which is typical for the in-plane magnetized ferromagnetic films and nanowires), and increases with the SW wave number. It is also clearly seen that the nonreciprocity of the SW spectrum decreases with the increase of the SW amplitude. While for small-amplitude linear SWs the spectrum is clearly nonreciprocal, having the nonreciprocal linear frequency shift

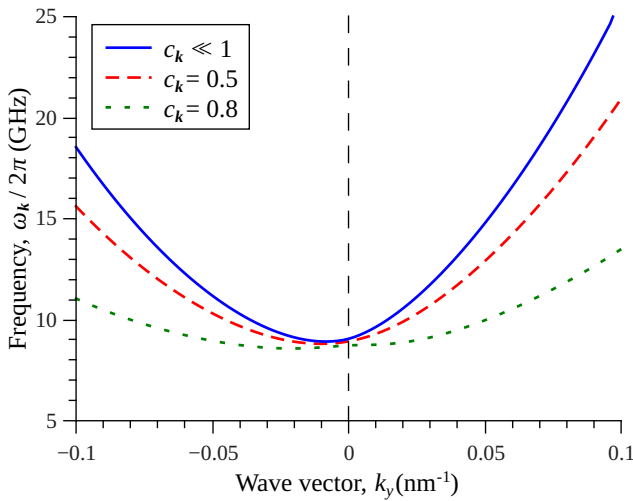


FIG. 2. SW spectrum of a CoFeB/Pt bilayer nanowire for different dimensionless amplitudes c_k of the propagating SWs. The calculation parameters are given in the text.

of $(\omega_k - \omega_{-k})/2\pi = 7.2$ GHz at $|k_y| = 0.1$ nm⁻¹, the spectrum of nonlinear SWs with the amplitude $c_k = 0.8$ looks much more reciprocal, and the corresponding nonreciprocal spectral shift at the same value of the SW wave number is only 2.4 GHz. This effect can be useful for the development of power-dependent nonreciprocal devices.

B. Ferromagnetic film

The case of a ferromagnetic film, magnetized in its plane, is considered in a similar way. All the expressions (4.4) for the effective SW tensor remain the same with only the change of the dynamic dipolar contribution, namely, $F_{xx,k} = 0$, $F_{yy,k} = f(kh)$, and $F_{zz,k} = 1 - f(kh)$ [note that $f(x) = 1 - (1 - e^{-|x|})/|x|$]. Making this substitution in Eq. (4.6), one gets a well-known dispersion relation for the linear SWs in a thin ferromagnetic film [46,56].

Considering three-magnon splitting, we arrive at the same conclusion, that an SW, which propagates perpendicular to the static magnetization, cannot split into two SWs, propagating *in the same direction*. Indeed, in this case we get $\mathcal{D}_1 = \mathcal{D}_2 = \mathcal{D}_3 = 0$ and, consequently, $V_{12,3} = 0$.

However, in the case of a film that is unrestricted in its plane, the SWs can propagate at an arbitrary angle to the static magnetization, and the three-magnon splitting into *non-collinear* SWs is allowed. To analyze this case, it is convenient to use the components of the SW wave vectors instead of the angles ϕ in respect to the static magnetization direction. The reference coordinate system is shown in Fig. 3(a). Then, the coefficient \mathcal{D}_k for an arbitrary SW can be obtained from Eqs. (4.5) in the form

$$\mathcal{D}_k = \frac{i\omega_M}{\sqrt{2}} \left(\frac{k_x k_y}{k^2} f(kh) + k_x \tilde{d} \right). \quad (4.10)$$

Denoting the initial SW as the third one, and the secondary SWs as the first and second [i.e., considering the three-wave splitting process $\mathbf{k}_3 \rightarrow (\mathbf{k}_1, \mathbf{k}_2)$], we get $\mathcal{D}_{k_3} = 0$. Additionally, the momentum conservation rule requires that $\mathbf{k}_3 = \mathbf{k}_1 +$

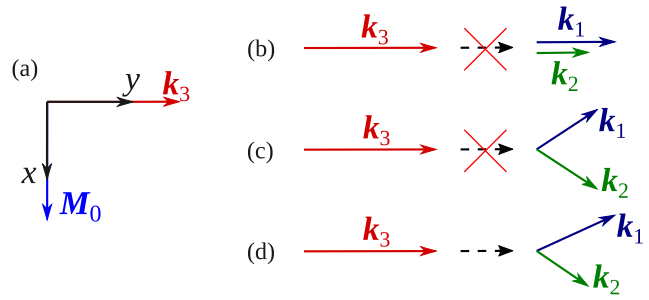


FIG. 3. Three-magnon splitting in a ferromagnetic–heavy-metal bilayer film: (a) considered geometry of the static magnetization and initial SW propagation direction, (b), (c) prohibited splitting processes, (d) allowed splitting process.

\mathbf{k}_2 or, in terms of the wave-vector components, $k_{y,3} = k_{y,1} + k_{y,2}$ and $k_{x,1} = -k_{x,2}$.

Substituting these expressions into the definition of the three-magnon scattering coefficient (3.11), we found, that in a general case, the splitting coefficient $V_{12,3}$ is not required to be zero, and the three-magnon splitting processes are allowed. There are only two exceptions: (i) splitting of an SW into two collinear SWs, and (ii) a symmetric splitting, when the wave vectors of the resulting waves possess a mirror symmetry relative to the initial SW, i.e., when $k_{y,1} = k_{y,2}$. Thus, in a ferromagnetic–heavy-metal bilayer film, three-magnon splitting can occur even in the Damon-Eshbach geometry if, of course, the resonance conditions are satisfied. A schematic illustration of the prohibited and allowed splitting processes is shown in Fig. 3.

These results can be generalized qualitatively to the case of a relatively wide ferromagnetic nanowire, in which many different width modes are degenerate, and the three-magnon splitting resonance condition $\omega_3 = \omega_1 + \omega_2$ can be satisfied for the SWs belonging to different branches of the SW spectrum (i.e., to the modes having different width profiles).

If we consider a higher-order SW width mode as a superposition of a plane wave with a transverse component of the wave vector k_x and $-k_x$, it becomes clear that in the Damon-Eshbach geometry a fundamental (uniform) SW mode cannot scatter into higher-order SWs of the same SW branch. At the same time, the scattering into SW modes having different width profiles could be allowed. The SW property that in a symmetric system a symmetric three-magnon SW splitting is prohibited, while a nonsymmetric one is allowed, is not unique, and was described for the SWs in bulk ferromagnets [2] and for SW modes of a magnetic vortex [65].

Finally, we note that the nonlinear frequency shift in the case of a bilayer film and magnetization angle $\phi_M = 90^\circ$ is also expressed by Eq. (4.9) with corresponding substitution of the dipolar tensor components. Indeed, as it is shown in Refs. [2,75], only the nonresonant three-magnon processes involving the SWs with wave vectors $\pm\mathbf{k}$, $\pm 2\mathbf{k}$, and $\mathbf{k} = 0$ contribute to the renormalization of the four-magnon nonlinear coefficients. In the considered case, all the three-magnon processes that involve the SWs, which are collinear, and propagate perpendicular to the static magnetization, have zero efficiency and, therefore, it is not necessary to calculate

corrections caused by these three-wave processes to the expression (4.9).

V. SUMMARY

In this work we presented a generalization of the theory of nonlinear spin wave dynamics based on the Hamiltonian approach to the case when the antisymmetric magnetic interactions are present. The developed formalism allows one to calculate the linear SW dispersion and the coefficients of nonlinear SW interactions for propagating SWs in a uniformly magnetized sample with arbitrary symmetric and antisymmetric magnetic self-interactions, quadratic in magnetization. In particular, it allows to account for the various types of a bulk and interfacial Dzyaloshinskii-Moriya interactions, spin flexoelectric interaction, etc.

It was shown that the presence of antisymmetric magnetic self-interactions reduces the symmetry of the effective SW tensor and, consequently, the symmetry of the coefficients of the Hamiltonian function expansion, both for quadratic terms, three-magnon, four-magnon, and higher-order terms. We derived the generalized third Holstein-Primakoff transformation, which diagonalizes the quadratic part of the SW Hamiltonian function in a general case, as well as the explicit expressions for the three- and four-magnon interaction coefficients. At the same time, it was shown that the antisymmetric interactions can lead to the frequency nonreciprocity of the SW spectrum, and could affect the nonlinear SW processes. Also, it turned out that the structure (ellipticity) of the linear SWs is not affected by the antisymmetric interactions, and the SWs propagating in opposite directions have the same ellipticity (in the case of a uniform SW spatial profile).

As an example of application of the developed generalized formalism, we considered nonlinear SW interactions

in ferromagnetic-heavy-metal bilayer nanowires and films, subjected to the IDMI. It was shown that three-magnon splitting, that is often undesirable in practical signal-processing applications, can be completely avoided in a nanowire, which is in-plane magnetized perpendicularly to the nanowire axis.

In the case of a magnetic film which is unrestricted in plane, however, the three-magnon splitting for noncollinear SWs could be allowed. Thus, the three-magnon splitting into noncollinear SWs can occur for any magnetization direction if, of course, the resonance conditions for this splitting are satisfied.

It was also shown that the nonlinear frequency shift, which is caused by the four-magnon interaction processes, is nonreciprocal, and the sign of the nonreciprocal term in the nonlinear frequency shift is opposite to the sign of the term describing the frequency nonreciprocity of linear (small-amplitude) SWs. Consequently, the nonreciprocal shift of the SW dispersion decreases with the increase of the SW amplitude. This fact can be used for the development of power-dependent nonreciprocal devices.

ACKNOWLEDGMENTS

This work at the Oakland University was supported by the National Science Foundation of the USA (Grants No. EFMA-1641989 and No. ECCS-1708982), and by the Oakland University Foundation. R.V. acknowledges support from the State Fund for Fundamental Research of Ukraine (President's of Ukraine grant for young scientists Grant No. F75/151-2018), and from the Ministry of Education and Sciences of Ukraine (Project No. 0118U004007).

-
- [1] A. G. Gurevich and G. A. Melkov, *Magnetization Oscillations and Waves* (CRC Press, New York, 1996), p. 464.
 - [2] V. S. L'vov, *Wave Turbulence under Parametric Excitation* (Springer, New York, 1994).
 - [3] G. Bertotti, I. Mayergoyz, and C. Serpico, *Nonlinear Magnetization Dynamics in Nanosystems* (Elsevier, Oxford, 2009).
 - [4] H. Suhl, *J. Phys. Chem. Solids* **1**, 209 (1957).
 - [5] C. E. Patton, *Phys. Status Solidi B* **92**, 211 (1979).
 - [6] A. Nazarov, C. Patton, R. Cox, L. Chen, and P. Kabos, *J. Magn. Magn. Mater.* **248**, 164 (2002).
 - [7] K. L. Livesey, M. P. Kostylev, and R. L. Stamps, *Phys. Rev. B* **75**, 174427 (2007).
 - [8] H. Suhl, *J. Appl. Phys.* **31**, 935 (1960).
 - [9] P. Gottlieb and H. Suhl, *J. Appl. Phys.* **33**, 1508 (1962).
 - [10] W. Chen, G. de Loubens, J. M. L. Beaujour, J. Z. Sun, and A. D. Kent, *Appl. Phys. Lett.* **95**, 172513 (2009).
 - [11] Y. S. Gui, A. Wirthmann, N. Mecking, and C.-M. Hu, *Phys. Rev. B* **80**, 060402(R) (2009).
 - [12] G. A. Melkov, D. V. Slobodianiuk, V. S. Tiberkevich, G. de Loubens, O. Klein, and A. N. Slavin, *IEEE Magn. Lett.* **4**, 4000504 (2013).
 - [13] A. D. Boardman and S. A. Nikitov, *Phys. Rev. B* **38**, 11444 (1988).
 - [14] A. Y. Dobin and R. H. Victora, *Phys. Rev. Lett.* **90**, 167203 (2003).
 - [15] G. Gibson and C. Jeffries, *Phys. Rev. A* **29**, 811 (1984).
 - [16] F. M. de Aguiar and S. M. Rezende, *Phys. Rev. Lett.* **56**, 1070 (1986).
 - [17] S. N. Stitzer and P. R. Emtage, *Circuits Syst. Signal Process.* **4**, 227 (1985).
 - [18] W. S. Ishak, *Proc. IEEE* **76**, 171 (1988).
 - [19] B. A. Kalinikos, N. G. Kovshikov, and A. N. Slavin, *Zh. Eksp. Teor. Fiz.* **94**, 159 (1988) [*Sov. Phys.-JETP* **67**, 303 (1988)].
 - [20] M. Chen, M. A. Tsankov, J. M. Nash, and C. E. Patton, *Phys. Rev. Lett.* **70**, 1707 (1993).
 - [21] B. A. Kalinikos and M. P. Kostylev, *IEEE Trans. Magn.* **33**, 3445 (1997).
 - [22] G. A. Melkov, Y. V. Kobljanskyj, A. A. Serga, V. S. Tiberkevich, and A. N. Slavin, *J. Appl. Phys.* **89**, 6689 (2001).
 - [23] A. Slavin and V. Tiberkevich, *Phys. Rev. Lett.* **95**, 237201 (2005).
 - [24] S. Bonetti, V. Tiberkevich, G. Consolo, G. Finocchio, P. Muduli, F. Mancoff, A. Slavin, and J. Åkerman, *Phys. Rev. Lett.* **105**, 217204 (2010).
 - [25] O. R. Sulymenko, O. V. Prokopenko, V. S. Tyberkevych, A. N. Slavin, and A. A. Serga, *Low Temp. Phys.* **44**, 602 (2018).

- [26] A. V. Sadovnikov, S. A. Odintsov, E. N. Beginin, S. E. Sheshukova, Y. P. Sharaevskii, and S. A. Nikitov, *Phys. Rev. B* **96**, 144428 (2017).
- [27] M. Morozova, D. Romanenko, O. Matveev, S. Grishin, Y. Sharaevskii, and S. Nikitov, *J. Magn. Magn. Mater.* **466**, 119 (2018).
- [28] T. Meyer, T. Brächer, F. Heussner, A. A. Serga, H. Naganuma, K. Mukaiyama, M. Oogane, Y. Ando, B. Hillebrands, and P. Pirro, *IEEE Magn. Lett.* **9**, 1 (2018).
- [29] Q. Wang, R. Verba, T. Brächer, P. Pirro, and A. V. Chumak, Integrated magnonic half-adder, [arXiv:1902.02855](https://arxiv.org/abs/1902.02855).
- [30] E. Schlömann, *Phys. Rev.* **116**, 828 (1959).
- [31] L. D. Landau and E. M. Lifshitz, *Mechanics (Vol. 1 of Course of Theoretical Physics)* (Pergamon, Oxford, 1960).
- [32] V. E. Zakharov, V. S. L'vov, and S. S. Starobinets, *Uspekhi Fiz. Nauk.* **114**, 609 (1974) [*Sov. Phys.-Usp.* **17**, 896 (1975)].
- [33] A. N. Slavini and P. Kabos, *IEEE Trans. Magn.* **41**, 1264 (2005).
- [34] A. Slavin and V. Tiberkevich, *IEEE Trans. Magn.* **45**, 1875 (2009).
- [35] A. N. Slavin and I. V. Rojdestvenski, *IEEE Trans. Magn.* **30**, 37 (1994).
- [36] O. Dzyapko, I. Lisenkov, P. Nowik-Boltyk, V. E. Demidov, S. O. Demokritov, B. Koene, A. Kirilyuk, T. Rasing, V. Tiberkevich, and A. Slavin, *Phys. Rev. B* **96**, 064438 (2017).
- [37] P. Krivosik and C. E. Patton, *Phys. Rev. B* **82**, 184428 (2010).
- [38] I. E. Dzialoshinskii, *Zh. Eksp. Teor. Fiz.* **32**, 1547 (1957) [*Sov. Phys.-JETP* **5**, 1259 (1957)].
- [39] T. Moriya, *Phys. Rev.* **120**, 91 (1960).
- [40] M. Bode, M. Heide, K. von Bergmann, P. Ferriani, S. Heinze, G. Bihlmayer, A. Kubetzka, O. Pietzsch, S. Blügel, and R. Wiesendanger, *Nature (London)* **447**, 190 (2007).
- [41] L. Udvardi and L. Szunyogh, *Phys. Rev. Lett.* **102**, 207204 (2009).
- [42] K.-S. Ryu, L. Thomas, S.-H. Yang, and S. Parkin, *Nat. Nanotechnol.* **8**, 527 (2013).
- [43] M. Heide, G. Bihlmayer, and S. Blügel, *Phys. Rev. B* **78**, 140403(R) (2008).
- [44] K.-W. Kim, H.-W. Lee, K.-J. Lee, and M. D. Stiles, *Phys. Rev. Lett.* **111**, 216601 (2013).
- [45] K. Zakeri, Y. Zhang, J. Prokop, T.-H. Chuang, N. Sakr, W. X. Tang, and J. Kirschner, *Phys. Rev. Lett.* **104**, 137203 (2010).
- [46] J.-H. Moon, S.-M. Seo, K.-J. Lee, K.-W. Kim, J. Ryu, H.-W. Lee, R. D. McMichael, and M. D. Stiles, *Phys. Rev. B* **88**, 184404 (2013).
- [47] M. Kostylev, *J. Appl. Phys.* **115**, 233902 (2014).
- [48] V. L. Zhang, K. Di, H. S. Lim, S. C. Ng, M. H. Kuok, J. Yu, J. Yoon, X. Qiu, and H. Yang, *Appl. Phys. Lett.* **107**, 022402 (2015).
- [49] G. A. Melkov, V. I. Vasyuchka, V. V. Lazovskiy, V. S. Tiberkevich, and A. N. Slavin, *Appl. Phys. Lett.* **89**, 252510 (2006).
- [50] B. K. Kuanr, V. Veerakumar, R. Marson, S. R. Mishra, R. E. Camley, and Z. Celinski, *Appl. Phys. Lett.* **94**, 202505 (2009).
- [51] T. J. Fal and R. E. Camley, *J. Appl. Phys.* **110**, 053912 (2011).
- [52] J. Wu, X. Yang, S. Beguhn, J. Lou, and N. X. Sun, *IEEE Trans. Microwave Theory Tech.* **60**, 3959 (2012).
- [53] M. Mruczkiewicz, M. Krawczyk, G. Gubbiotti, S. Tacchi, Y. A. Filimonov, D. V. Kalyabin, I. V. Lisenkov, and S. A. Nikitov, *New J. Phys.* **15**, 113023 (2013).
- [54] R. Verba, V. Tiberkevich, and A. Slavin, *Appl. Phys. Lett.* **107**, 112402 (2015).
- [55] T. Brächer, O. Boulle, G. Gaudin, and P. Pirro, *Phys. Rev. B* **95**, 064429 (2017).
- [56] A. Giordano, R. Verba, R. Zivieri, A. Laudani, V. Puliafito, G. Gubbiotti, R. Tomasello, G. Siracusano, B. Azzerboni, M. Carpentieri, A. Slavin, and G. Finocchio, *Sci. Rep.* **6**, 36020 (2016).
- [57] L. Yang, P. Dürrenfeld, X. Ruan, W. Liu, L. He, Y. Xu, and Y. Zhou, *IEEE Magn. Lett.* **8**, 1 (2017).
- [58] R. Zivieri, A. Giordano, R. Verba, B. Azzerboni, M. Carpentieri, A. N. Slavin, and G. Finocchio, *Phys. Rev. B* **97**, 134416 (2018).
- [59] R. L. Melcher, *Phys. Rev. Lett.* **30**, 125 (1973).
- [60] D. Cortés-Ortuño and P. Landeros, *J. Phys.: Condens. Matter* **25**, 156001 (2013).
- [61] D. L. Mills and I. E. Dzialoshinskii, *Phys. Rev. B* **78**, 184422 (2008).
- [62] T. Liu and G. Vignale, *Phys. Rev. Lett.* **106**, 247203 (2011).
- [63] K. Y. Guslienko and A. N. Slavin, *J. Magn. Magn. Mater.* **323**, 2418 (2011).
- [64] A. Y. Galkin, B. A. Ivanov, and C. E. Zaspel, *Phys. Rev. B* **74**, 144419 (2006).
- [65] K. Schultheiss, R. Verba, F. Wehrmann, K. Wagner, L. Körber, T. Hula, T. Hache, A. Kákay, A. A. Awad, V. Tiberkevich, A. N. Slavin, J. Fassbender, and H. Schultheiss, *Phys. Rev. Lett.* **122**, 097202 (2019).
- [66] R. Verba, M. Carpentieri, G. Finocchio, V. Tiberkevich, and A. Slavin, in *Spin Wave Confinement: Propagating Waves*, 2nd ed., edited by S. O. Demokritov (Pan Stanford Publishing Pte. Ltd., Singapore, 2017), pp. 385–426.
- [67] Q. Wang, B. Heinz, R. Verba, M. Kewenig, P. Pirro, M. Schneider, T. Meyer, B. Lägél, C. Dubs, T. Brächer, and A. V. Chumak, Spin pinning and spin-wave dispersion in nanoscopic ferromagnetic waveguides [Phys. Rev. Lett. (to be published)], [arXiv:1807.01358](https://arxiv.org/abs/1807.01358).
- [68] In Refs. [66,67] the effective spin wave tensor is denoted by the symbol \hat{F}_k .
- [69] G. A. Melkov, A. A. Serga, V. S. Tiberkevich, Y. V. Kobljanskij, and A. N. Slavin, *Phys. Rev. E* **63**, 066607 (2001).
- [70] T. Holstein and H. Primakoff, *Phys. Rev.* **58**, 1098 (1940).
- [71] N. N. Bogoljubov, *Nuovo Cimento* **7**, 794 (1958).
- [72] J. G. Valatin, *Nuovo Cimento* **7**, 843 (1958).
- [73] In the most of papers these new variables are denoted as b_k . Here, we use notations c_k , in order to not confuse with the notations of microwave external field.
- [74] V. E. Zakharov, *Zh. Eksp. Teor. Fiz.* **51**, 1107 (1967) [*Sov. Phys.-JETP* **24**, 740 (1967)].
- [75] V. L. Safonov, *Nonequilibrium Magnons: Theory, Experiment and Applications* (Wiley, Weinheim, 2013).
- [76] Q. Shi, V. L. Safonov, M. Mino, and H. Yamazaki, *Phys. Lett. A* **238**, 258 (1998).
- [77] R. Verba, M. Carpentieri, G. Finocchio, V. Tiberkevich, and A. Slavin, *Sci. Rep.* **6**, 25018 (2016).

ВИСНОВКИ

У дисертаційній роботі запропоновано та обґрунтовано шлях вирішення проблеми створення енергоефективних та придатних до застосування на наномасштабах способів збудження та контролю СХ у пристроях магنونіки, а також покращення характеристик та надання додаткової функціональності магнітним наногенераторам на основі ефекту СТ. Проведені аналітичні та числові дослідження лінійної та нелінійної динаміки СХ у надтонких феромагнітних плівках і наноструктурах під дією електричного поля (за рахунок ефекту ЕКМА) або спінового струму та одержані наступні наукові результати:

1. Вперше продемонстровано можливість збудження СХ НВЧ електричним полем за допомогою ефекту ЕКМА у феромагнітному хвилеводі чи нанoelementі за відсутності зовнішнього магнітного поля. Встановлено, що у цьому випадку збудження можливе лише за механізмом параметричного збудження, тобто, на половині частоти НВЧ електричного поля. При цьому, у випадку перпендикулярної статичної намагніченості взаємодія НВЧ модульованої анізотропії, викликаної НВЧ електричним полем, зі СХ аналогічна до параметричної взаємодії з паралельною накачкою і визначається еліптичністю прецесії СХ. Натомість, у випадку площинної намагніченості параметричний зв'язок відбувається через перпендикулярну компоненту динамічної намагніченості. Останній механізм є більш ефективним і, найголовніше, не має обмежень щодо довжини СХ, зокрема, він ефективно працює і в обмінній області спектру СХ, де еліптичність, а, отже, і ефективність взаємодії з паралельною накачкою, прямує до нуля. Теоретичні розрахунки успішно підтверджені спільним експериментом по параметричному збудженню основної моди магнітної наноточки за допомогою НВЧ напруги.
2. Розроблено нелінійну теорію параметричного збудження СХ у нанорозмірних хвилеводах локалізованою накачкою. Вперше встановлено, що окрім фазового механізму обмеження росту параметричної нестійкості, який є єдиним суттєвим механізмом в об'ємних зразках, у нанорозмірних хвилеводах стає важливим

додатковий механізм, а саме нелінійна зміна групової швидкості СХ внаслідок нелінійного зсуву спектру. Поява цього механізму призводить не лише до зменшення амплітуд збуджених СХ, а й до якісно інших залежностей потужності збуджених СХ від потужності накачки при невеликих перевищеннях порогу збудження — замість кореневої залежності $|a|^2 \sim \sqrt{V^2 - V_{th}^2}$, яка реалізується при великих (макроскопічних) довжинах області накачки, у нанорозмірних зразках має місце лінійна залежність $|a|^2 \sim (V^2 - V_{th}^2)$.

3. Продемонстровано вплив різниці поляризації СХ, яка, зокрема, виникає при локальному прикладанні квазістатичного електричного поля внаслідок суттєвої зміни магнітної анізотропії, на проходження СХ через внутрішню границю розділу. По-перше, поблизу границі розділу з'являються експоненційно локалізовані СХ, з довжиною локалізації рівною або меншою за довжину біжучої СХ відповідної частоти та поляризацією, ортогональною до поляризації біжучої СХ. По-друге, з'являється додатковий зсув фаз відбитої та переданої хвиль, який, залежно від різниці поляризацій, може приймати будь-яке значення в діапазоні $[-\pi, \pi]$, на відміну від скалярного випадку, у якому фаза переданої хвилі завжди рівна фазі падаючої хвилі, а відбита хвиля може бути у фазі або в протифазі з нею. По-третє, різниця поляризації призводить до зменшення коефіцієнту проходження та збільшення коефіцієнту відбивання СХ. При цьому, зміна фази лінійна щодо різниці поляризації, а зміна коефіцієнтів проходження та відбивання — квадратична, тому при помірних прикладених електричних полях помітно проявляється тільки перший ефект. Незважаючи на різницю поляризації, СХ може проходити скінченну область з відмінною анізотропією резонансно, однак резонансні умови відрізняються від класичних внаслідок вищеприписаного додаткового зсуву фаз. Встановлені залежності є характерними для СХ з домінантною обмінною взаємодією. У дипольній області спектру вплив поляризації може зникати повністю. Вищевказані властивості, однак, не стосуються розповсюдження СХ в геометрії Деймона-Ешбаха. Внаслідок іншої симетрії динамічних дипольних полів, розсіяння та відбивання цих хвиль має

суттєві особливості. Зокрема, такі СХ демонструють стійкість до розсіювання на поверхневих дефектах і зменшене відбивання, навіть в короткохвильовій (переважно обмінній) частині спектру та плівках і хвилеводах нанорозмірної товщини, в яких локалізація СХ на поверхні практично відсутня.

4. Досліджено динаміку біжучих СХ при проходженні області локалізованої параметричної накачки. Вперше продемонстровано ефект зменшення ефективності параметричного підсилення при збільшенні амплітуди вхідної хвилі, що пояснюється нелінійною чотиримагнетною взаємодією сигнальної та холостої хвиль (“S-взаємодія”). Характерна амплітуда вхідної СХ, за якої проявляється ефект, обернено залежить від довжини області накачки, тому для підсилення СХ відносно великої амплітуди необхідно використовувати накачку з довжиною локалізації, суттєво меншою за довжину вільного пробігу СХ. За певного значення вхідної амплітуди СХ, яке визначається довжиною та величиною накачки, можлива реалізація стабілізації амплітуди СХ — амплітуда вхідної та вихідної хвиль стають однаковими, а розкид амплітуд (шуми) зменшуються після проходження області накачки. Ефект стабілізації амплітуди краще проявляється за великих довжин накачки.
5. Вперше запропоновано використання неадіабатичної параметричної накачки для корекції фази СХ. Продемонстровано, що фазова прохідна характеристика СХ у цьому випадку стає нелінійною і проявляє “плато стабілізації”, розділені між собою різницею фаз у π радіан, що ідеально підходить для корекції фазових помилок у системах магнетної логіки. Внаслідок залежності амплітуди вихідної СХ від її фази досяжна на практиці величина помилок, які можуть бути успішно виправленими, обмежена величиною приблизно $|\Delta\phi| < \pi/4$. Встановлено, що ефект фазової стабілізації є стійким по відношенню до амплітуди вхідної хвилі.
6. Пояснено ряд експериментів по збудженню СХ у спін-торк та спін-Холл осциляторах. Вперше встановлено вирішальну роль дипольної взаємодії у стабілізації магнетних солітонів — СХ булетів — в квазіодновимірних СТО, що дозволяє реалізувати стійку монохроматичну генерацію в осциляторах з активною областю довжиною в одиниці мікрометрів і, таким чином, підвищити

потужність осцилятора. При цьому, на відміну від обмінних СХ булетів, дипольні СХ булети є чисто дисипативними солітонами і можуть утворюватись тільки в активному середовищі. Продемонстровано, що неоднорідний профіль густини спінового струму (наприклад, внаслідок змінного перерізу активної зони осцилятора) призводить до появи додаткової зворотної сили, що діє на СХ булет, а також до просторового рознесення булетів у режимі двомодової генерації. У підсумку, така неоднорідність густини струму накачки призводить до збільшення когерентності та стабільності режиму одномодової генерації СТО. Також продемонстровано, що наявність потенціальної ями може змінювати тип збудженої моди у СТО з нелінійного булету на лінійно локалізовану моду за умови достатньої глибини потенціальної ями та її розмірів, сумірних із розмірами активної зони. На експерименті така зміна типу моди буде проявлятися зміною типу збудження автогенератора — з жорсткого на м'який режим збудження, а у випадку несиметричного розташування ями та активної зони також можлива суттєва якісна зміна профілів СХ моди, яку можна детектувати на експерименті.

7. Досліджено вплив ІВДМ на параметричні процеси та динаміку СХО. Вперше запропоновано спосіб збільшення ефективності та завадостійкості параметричного підсилювача за рахунок невзаємності СХ, викликаній ІВДМ — при цьому стає можливим вибір робочої точки так, що холоста хвиля стає еванесцентною. Розроблено теорію збудження невзаємних СХ у СТО з квазіодновимірною та двовимірною активною зоною за наявності ІВДМ. Пояснено появу червоного зсуву частоти генерації зі збільшенням ІВДМ, який, як виявилось, рівний пониженню дна спектра СХ, та слабку залежність порогу генерації від ІВДМ при помірних величинах ІВДМ. Пояснено природу появи спіральних СХ мод при відносно великій ІВДМ — ці СХ є наслідком гіротропного руху динамічного скіріміону в активній області осцилятора.
8. Розроблені методики для розрахунку дисперсійних характеристик, сталих затухання СХ у нанорозмірних ферромагнітних хвилеводах за наявності неоднорідних та/або нелокальних механізмів дисипації, а також коефіцієнтів

зв'язку між СХ у дипольно взаємодіючих хвилеводах. Виявлено явище “розкріплення” профілю моди при зменшенні ширини хвилеводу менше за певне критичне значення, яке пов'язане не тільки зі зростанням впливу обмінної взаємодії, а й зі зменшенням неоднорідності динамічних дипольних полів на краях хвилеводу. Проаналізовано нелінійні механізми, які впливають на СХ у дипольно взаємодіючих хвилеводах. Встановлено, що при помірних амплітудах СХ єдиним суттєвим механізмом є нелінійний зсув спектру СХ, як цілого, у той час як нелінійність безпосередньо дипольного зв'язку та просторова залежність потужності СХ є несуттєвими; розроблено метод розрахунку характеристик спрямованого СХ відгалужувача у помірно нелінійному режимі.

9. Узагальнено метод розрахунку коефіцієнтів нелінійної СХ взаємодії на випадок наявності несиметричних магнітних взаємодій, наприклад, ІВДМ, отримані готові для використання рівняння для розрахунку нелінійних коефіцієнтів у намагнічених до насичення феромагнітних плівках та наносмужках. Вперше продемонстровано нелінійність невзаємного зсуву спектру СХ, викликаного ІВДМ — при збільшенні амплітуди СХ невзаємне розщеплення спектру СХ зменшується, що може бути використаним для створення невзаємних пристроїв, керованих потужністю.

Насамкінець, варто відзначити, що частина з описаних явищ є загальною і не обмежуються СХ динамікою під дією ефекту ЕКМА. Зокрема, виявлені явища стабілізації амплітуди та фази СХ можуть бути реалізовані і з будь-яким іншим типом НВЧ параметричної накачки. Те ж саме стосується і способу підвищення завадостійкості параметричного підсилювача, у якому, до того ж, можливо використання не лише невзаємності, наведеної ІВДМ, а й невзаємності СХ у ґратках магнітних нанoeлементів, синтетичних антиферомагнетиках, тощо. Загальні ж методики розрахунку дисперсії, сталих затухання та коефіцієнтів нелінійної взаємодії СХ знайдуть своє застосування при розрахунку і проектуванні будь-яких магнітних систем на основі нанорозмірних феромагнітних хвилеводів.

ДОДАТОК А

СПИСОК ОПУБЛІКОВАНИХ ПРАЦЬ ЗА ТЕМАТИКОЮ ДИСЕРТАЦІЇ

Наукові праці, в яких опубліковані основні наукові результати дисертації:*Розділи в колективних монографіях:*

1. **R. Verba**, M. Carpentieri, G. Finocchio, V. Tiberkevich, and A. Slavin, Chapter 13 - Parametric excitation and amplification of spin waves in ultrathin ferromagnetic nanowires by microwave electric field. In: *Spin wave confinement: Propagating waves (2nd edition)*, ed. by S. O. Demokritov (Pan Stanford Publishing, Singapore, 2017), - P. 385-426. [Автор дисертації брав участь у написанні розділу, підготовці ілюстрацій, автором проведені аналітичні та числові розрахунки.]

Статті у фахових наукових журналах:

2. **R. Verba**, V. Tiberkevich, I. Krivorotov, and A. Slavin, Parametric excitation of spin waves by voltage-controlled magnetic anisotropy, *Phys. Rev. Appl.* **1**, 044006 (2014). [Автором проведені аналітичні та числові розрахунки]
3. **R. Verba**, V. Tiberkevich, and A. Slavin, Influence of interfacial Dzyaloshinskii-Moriya interaction on the parametric amplification of spin waves, *Appl. Phys. Lett.* **107**, 112402 (2015). [Автором проведені аналітичні та числові розрахунки]
4. L. Yang, **R. Verba**, V. Tiberkevich, T. Schneider, A. Smith, Z. Duan, B. Youngblood, K. Lenz, J. Lindner, A. N. Slavin, and I. N. Krivorotov, Reduction of phase noise in nanowire spin orbit torque oscillators, *Sci. Rep.* **5**, 16942 (2015). [Автором проведено числове моделювання рівняння Гінзбурга-Ландау (рис. 5, 6), на основі якого дане якісне пояснення експериментальних результатів]
5. **R. Verba**, M. Carpentieri, G. Finocchio, V. Tiberkevich, and A. Slavin, Excitation of propagating spin waves in ferromagnetic nanowires by microwave voltage-controlled magnetic anisotropy, *Sci. Rep.* **6**, 25018 (2016). [Автором розроблена нелінійна теорія збудження СХ, проведений аналіз мікромагнітних даних та їх порівняння з теоретичними розрахунками]

6. A. Giordano, **R. Verba**, R. Zivieri, A. Laudani, V. Puliafito, G. Gubbiotti, R. Tomasello, G. Siracusano, B. Azzerboni, M. Carpentieri, A. Slavin, and G. Finocchio, Spin-Hall nano-oscillator with oblique magnetization and Dzyaloshinskii-Moriya interaction as generator of skyrmions and nonreciprocal spin-waves, *Sci. Rep.* **6**, 36020 (2016). [Автором розроблена теоретична модель 1D СТО з ІВДМ, проведені відповідні теоретичні розрахунки, а також пояснено природу спіральних СХ мод]
7. Y.-J. Chen, H. K. Lee, **R. Verba**, J. A. Katine, I. Barsukov, V. Tiberkevich, J. Q. Xiao, A. N. Slavin, and I. N. Krivorotov, Parametric resonance of magnetization excited by electric field, *Nano Lett.* **17**, 572 (2017). [Автором проведені розрахунки порогів збудження, допорогової та запорогової поведінки амплітуди СХ моди (п. S4, S5 додаткових матеріалів). Автор також брав участь в аналізі експериментальних даних та надавав рекомендації щодо вимірювань]
8. **R. Verba**, M. Carpentieri, G. Finocchio, V. Tiberkevich, and A. Slavin, Excitation of spin waves in an in-plane-magnetized ferromagnetic nanowire using voltage-controlled magnetic anisotropy, *Phys. Rev. Appl.* **7**, 064023 (2017). [Автором проведені аналітичні розрахунки, також автор брав участь у розробці методики мікромагнітного моделювання та обробці мікромагнітних даних]
9. Q. Wang, P. Pirro, **R. Verba**, A. Slavin, B. Hillebrands, and A. V. Chumak, Reconfigurable nanoscale spin-wave directional coupler, *Sci. Adv.* **4**, e1701517 (2018). [Автором розроблена теорія спрямованого СХ відгалужувача]
10. **R. Verba**, M. Carpentieri, G. Finocchio, V. Tiberkevich, and A. Slavin, Amplification and stabilization of large-amplitude propagating spin waves by parametric pumping, *Appl. Phys. Lett.* **112**, 042402 (2018). [Автором проведені числові розрахунки на базі вкорочених рівнянь та аналітичні розрахунки, представлені у додаткових матеріалах. Також автор брав участь у розробці методики мікромагнітного моделювання та обробці мікромагнітних даних]
11. R. Zivieri, A. Giordano, **R. Verba**, B. Azzerboni, M. Carpentieri, A. N. Slavin, and G. Finocchio, Theory of nonreciprocal spin-wave excitations in spin Hall oscillators

- with Dzyaloshinskii-Moriya interaction, *Phys. Rev. B* **97**, 134416 (2018). [Автором запропоновано методику розрахунку частоти генерації та критичного струму, та проведені відповідні розрахунки]
12. **R. Verba**, V. Tiberkevich, and A. Slavin, Damping of linear spin-wave modes in magnetic nanostructures: Local, nonlocal, and coordinate-dependent damping, *Phys. Rev. B* **98**, 104408 (2018). [Автором проведені аналітичні та числові розрахунки]
13. M. Mohseni, **R. Verba**, T. Brächer, Q. Wang, D. A. Bozhko, B. Hillebrands, and P. Pirro, Backscattering Immunity of Dipole-Exchange Magnetostatic Surface Spin Waves, *Phys. Rev. Lett.* **122**(19), 197201 (2019). [Автором запропоноване пояснення стійкості ПМСХ до розсіювання, розраховані профілі дипольних полів ПМСХ та проаналізовано їх симетрію]
14. **R. Verba**, M. Carpentieri, Y.-J. Chen, I. N. Krivorotov, G. Finocchio, V. Tiberkevich, and A. Slavin, Correction of Phase Errors in a Spin-Wave Transmission Line by Nonadiabatic Parametric Pumping, *Phys. Rev. Appl.* **11**, 054040 (2019). [Автором проведені аналітичні розрахунки, також автор брав участь у розробці методики мікромагнітного моделювання та обробці мікромагнітних даних]
15. **R. Verba**, V. Tiberkevich, and A. Slavin, Hamiltonian formalism for nonlinear spin wave dynamics under antisymmetric interactions: Application to Dzyaloshinskii-Moriya interaction, *Phys. Rev. B* **99**, 174431 (2019). [Автором виведені загальні рівняння формалізму та проаналізовано нелінійний зсув спектру СХ за наявності ІВДМ]
16. Q. Wang, B. Heinz, **R. Verba**, M. Kewenig, P. Pirro, M. Schneider, T. Meyer, B. Lägel, C. Dubs, T. Brächer, and A. V. Chumak, Spin Pinning and Spin-Wave Dispersion in Nanoscopic Ferromagnetic Waveguides, *Phys. Rev. Lett.* **122**(24), 247202 (2019). [Автором проведені аналітичні розрахунки та запропоновано якісне пояснення ефекту розкріплення профілю СХ мод]
17. **R. V. Verba**, Interplay of linear and nonlinear localization mechanisms in spin-torque oscillators with a field well, *Ukr. J. Phys.* **64** (10), 947 (2019).

18. **R. Verba**, V. Tiberkevich, and A. Slavin, Spin-wave transmission through an internal boundary: Beyond the scalar approximation, *Phys. Rev. B* **101**, 144430 (2020). [Автором проведені всі аналітичні розрахунки, а також серію мікромагнітних моделювань, результати якої представлені на Рис. 5]
19. **R. V. Verba**, V. S. Tiberkevich and A. N. Slavin, Dipole-dominated dissipative magnetic solitons in quasi-one-dimensional spin-torque oscillators, *Фізика низьких температур* **46**, 920 (2020) [*Low Temp. Phys.* **46**, 773 (2020)]. [Автором проведені числові моделювання СХ динаміки та аналіз отриманих залежностей]
20. Q. Wang, M. Kewenig, M. Schneider, **R. Verba**, F. Kohl, B. Heinz, M. Geilen, M. Mohseni, B. Lägel, F. Ciubotaru, C. Adelman, C. Dubs, S. D. Cotofana, O. V. Dobrovolskiy, T. Brächer, P. Pirro and A. V. Chumak, A magnonic directional coupler for integrated magnonic half-adders, *Nature Electronics* **3**, 765 (2020). [Автором проведені аналітичні розрахунки характеристик СХ відгалужувача у лінійному та нелінійному режимі, зроблені оцінки енергоспоживання параметричного підсилювача на основі ефекту ЕКМА та магنونного напівсуматора]

Публікації, які засвідчують апробацію матеріалів дисертації:

21. **R. V. Verba**, V. S. Tiberkevich, I. N. Krivorotov, and A. N. Slavin, Parametric excitation of spin waves in thin films by electric field. In: *58th Annual Conference on Magnetism and Magnetic Materials. Abstracts. (Denver, CO, USA, November 4 - 8, 2013)*, GB-04, p. 621.
22. **R. V. Verba**, V. S. Tiberkevich, and A. N. Slavin, Voltage control of spin waves in ultra-thin ferromagnetic waveguide. In: *INTERMAG 2014. Digest book (Dresden, Germany, 4 - 8 May 2014)*, AH-11, p. 237.
23. **R. V. Verba**, V. S. Tiberkevich, and A. N. Slavin, Damping of spin wave modes in the presence of spin pumping and spin diffusion. In: *INTERMAG 2014. Digest book (Dresden, Germany, 4 - 8 May 2014)*, HH-2, p. 3210.

24. **R. Verba**, V. Tiberkevich, O. Gorobets, and A. Slavin, Resonant and nonresonant transmission of spin waves through a barrier induced by voltage-controlled magnetic anisotropy. In: *59th Annual Conference on Magnetism and Magnetic Materials. Abstracts (Honolulu, HI, USA, November 3 - 7, 2014)*, CE-05, p. 250.
25. **R. V. Verba**, V. S. Tyberkevych, and A. N. Slavin, Excitation of propagating spin waves in an in-plane magnetized ferromagnetic strip by voltage-controlled magnetic anisotropy. In: *2015 IEEE International Magnetism Conference (INTERMAG) (Beijing, China, 11 - 15 May 2015)*, DB-02.
26. **R. V. Verba**, V. S. Tyberkevych, and A. N. Slavin, Influence of interfacial Dzyaloshinskii-Moriya interaction on parametric amplification of spin waves in ultrathin magnetic films. In: *2015 IEEE International Magnetism Conference (INTERMAG) (Beijing, China, 11 - 15 May 2015)*, GT-12.
27. **Verba R. V.**, Dipolar stabilization of a large size bullet mode in one-dimensional spin-torque oscillators. In: *Proceedings of the XI international conference "Electronics and applied physics" (Kyiv, October 21-24, 2015)*, p. 28.
28. **R. V. Verba**, L. Yang, V. Tyberkevych, T. Schneider, A. Smith, Z. Duan, J. Lindner, A. N. Slavin, and I. Krivorotov, Enhancement of single bullet mode stability in nanowire spin-Hall oscillator with spatially nonuniform current bias. In: *MMM | INTERMAG 2016 Joint Conference. Abstracts (San Diego, CA, USA, 11 – 15 January 2016)*, GU-07, p. 899.
29. Y. Chen, H. Lee, **R. V. Verba**, J. Katine, I. Barsukov, V. Tyberkevych, A. N. Slavin, and I. Krivorotov, Parametric excitation of magnetization by electric field. In: *MMM | INTERMAG 2016 Joint Conference. Abstracts (San Diego, CA, USA, 11 – 15 January 2016)*, GW-13, p. 915.
30. **R. V. Verba**, M. Carpentieri, G. Finocchio, V. Tyberkevych, and A. N. Slavin, Excitation of propagating spin waves in ferromagnetic nanowires by microwave voltage-controlled magnetic anisotropy. In: *MMM | INTERMAG 2016 Joint Conference. Abstracts (San Diego, CA, USA, 11 – 15 January 2016)*, HF-04, p. 956.

31. **R. Verba**, L. Yang, V. Tiberkevich, T. Schneider, A. Smith, Z. Duan, B. Youngblood, K. Lenz, J. Lindner, A. Slavin, and I. Krivorotov, Effect of dipolar interaction and bias nonuniformity on nanowire spin-Hall oscillator dynamics. In: *Baltic Spin 2016. Abstract book (Jurmala, Latvia, 9-13 August 2016)*, p. 22.
32. A. Giordano, **R. V. Verba**, R. Zivieri, A. Laudani, V. Puliafito, G. Gubbiotti, R. Tomasello, G. Siracusano, B. Azzerboni, M. Carpentieri, A. N. Slavin, and G. Finocchio, Spin-Hall nano-oscillator with oblique magnetization and Dzyaloshinskii-Moriya interaction as generator of skyrmions and nonreciprocal spin-waves. In: *61th Annual Conference on Magnetism and Magnetic Materials. Abstracts (New Orleans, LA, USA, 31 October – 4 November 2016)*, BB-08, p. 122.
33. A. Chumak, Q. Wang, P. Pirro, B. Hillebrands, **R. V. Verba**, and A. N. Slavin, Reconfigurable nano-scale spin-wave directional coupler. In: *61th Annual Conference on Magnetism and Magnetic Materials. Abstracts (New Orleans, LA, USA, 31 October – 4 November 2016)*, DB-02, p. 344.
34. **R. V. Verba**, V. Tyberkevych, and A. N. Slavin, Stabilization of spin wave amplitude by parametric pumping in ferromagnetic nanowires. In: *61th Annual Conference on Magnetism and Magnetic Materials. Abstracts (New Orleans, LA, USA, 31 October – 4 November 2016)*, DB-06, p. 346.
35. Y. Chen, **R. V. Verba**, V. Tyberkevych, A. N. Slavin, and I. Krivorotov, Parametric amplifier of spin waves using electric field. In: *61th Annual Conference on Magnetism and Magnetic Materials. Abstracts (New Orleans, LA, USA, 31 October – 4 November 2016)*, FE-09, p. 603.
36. **R. V. Verba**, V. S. Tiberkevich, and A.N. Slavin, Linear and nonlinear spin-wave mode localization in a spin-torque oscillator with a field well. In: *2017 IEEE International Magnetism Conference (INTERMAG) (Dublin, Ireland, 24-28 April 2017)*, BC-08.
37. **R. V. Verba**, M. Carpentieri, Y. Chen, V. Tyberkevych, G. Finocchio, I. Krivorotov, and A. N. Slavin. Correction of phase errors in spin wave signals by nonadiabatic parametric pumping. In: *62nd Annual Conference on Magnetism and Magnetic Materials. Abstracts (Pittsburgh, PA, USA, 6-10 November 2017)*, AE-04, p. 24.

38. A. Chumak, Q. Wang, B. Heinz, M. Kewenig, M. Schneider, T. Fischer, T. Meyer, B. Laegel, T. Löber, P. Pirro, C. Dubs, **R. V. Verba**, and T. Brächer. Spin-wave dynamics in yttrium iron garnet nano-structures. In: *62nd Annual Conference on Magnetism and Magnetic Materials. Abstracts (Pittsburgh, PA, USA, 6-10 November 2017)*, AE-10, p. 27.
39. **R. V. Verba**, V. Tyberkevych, and A. N. Slavin. Nonlinear spin-wave interaction in ultrathin ferromagnetic films with interfacial Dzyaloshinskii-Moriya interaction. In: *62nd Annual Conference on Magnetism and Magnetic Materials. Abstracts (Pittsburgh, PA, USA, 6-10 November 2017)*, FD-10, p. 556.
40. **R. Verba**, Voltage-controlled magnonics. In: *3rd International Advanced School on Magnonics 2018 (17–21 September, 2018, Kyiv, Ukraine)*, p. 36.
41. **R. V. Verba**, R. Zivieri, A. Giordano, B. Azzerboni, M. Carpentieri, A. N. Slavin, and G. Finocchio, Nonreciprocal spin waves in spin-Hall oscillators with Dzyaloshinskii-Moriya interaction. In: *2019 Joint MMM-INTERMAG conference. Book of Abstracts (January 14-18, 2019, Washington, DC, USA)*, AJ-10, p. 66.
42. A. Chumak, Q. Wang, B. Heinz, **R. V. Verba**, M. Kewenig, P. Pirro, M. Schneider, B. Lägél, C. Dubs, and T. Brächer, Spin-Wave Modes in sub-100 nm YIG Waveguides. In: *2019 Joint MMM-INTERMAG conference. Book of Abstracts (January 14-18, 2019, Washington, DC, USA)*, HE-07, p. 791.
43. **R. Verba**, Q. Wang, A. Chumak, Nonlinear Operation of Nanoscale Spin-Wave Directional Coupler. In: *Proceedings of the 2019 IEEE 9th International Conference on Nanomaterials: Applications & Properties (NAP-2019) (September 15-20, 2019, Odesa, Ukraine)*, p. 02M03-1.
44. Q. Wang, M. Kewenig, M. Schneider, **R. V. Verba**, B. Heinz, M. Geilen, M. Mohseni, B. Lägél, F. Ciubotaru, C. Adelman, S. Cotofana, C. Dubs, T. Brächer, P. Pirro and A. Chumak, Realization of a Nanoscale Magnonic Directional Coupler for All-Magnon Circuits. In: *64th Annual conference on Magnetism and Magnetic Materials. Abstracts (November 4-8, 2019, Las Vegas, NV, USA)*, CE-08, p. 258.

Наукові праці, які додатково відображають наукові результати дисертації:

45. M. Mohseni, M. Kewenig, **R. Verba**, Q. Wang, M. Schneider, B. Heinz, F. Kohl, C. Dubs, B. Lägel, A. A. Serga, B. Hillebrands, A. V. Chumak, and P. Pirro, Parametric Generation of Propagating Spin Waves in Ultrathin Yttrium Iron Garnet Waveguides, *Phys. Status Solidi RRL* **14**, 2000011 (2020). [Автором проведені розрахунки порогів параметричного збудження та залежностей на Рис.3]
46. O. V. Prokopenko, D. A. Bozhko, V. S. Tyberkevych, A. V. Chumak, V. I. Vasyuchka, A. A. Serga, O. Dzyapko, **R. V. Verba**, A. V. Talalaevskij, D. V. Slobodianiuk, Yu. V. Kobljanskyj, V. A. Moiseienko, S. V. Sholom, and V. Yu. Malyshev, Recent trends in microwave magnetism and superconductivity, *Ukr. J. Phys.* **64** (10), 888 (2019). [Автором написаний розділ 7]
47. B. Heinz, Q. Wang, **R. Verba**, V. Vasyuchka, M. Kewenig, P. Pirro, M. Schneider, T. Meyer, B. Lägel, C. Dubs, T. Brächer, O. Dobrovolskiy, and A. Chumak, Temperature Dependence of Spin Pinning and Spin-Wave Dispersion in Nanoscopic Ferromagnetic Waveguides, *Ukr. J. Phys.* **65** (12), 1094 (2020). [Автором проведені розрахунки температурних залежностей та написані пункти 2.4, 2.5, 3.5]